

Oct 98

JOURNAL OF THE MECHANICS AND PHYSICS OF SOLIDS

EDITORS

Vol. 46, No. 10

L. B. FREUND

Brown University
Division of Engineering

J. R. WILLIS

Cambridge University
Department of Applied Mathematics
and Theoretical Physics

SPECIAL ISSUE

Proceedings of a Symposium on the Dynamic
Deformation and Failure Mechanics of Materials,
honoring Professor R. J. Clifton

GUEST EDITORS

G. Ravichandran

A. J. Rosakis

M. Ortiz

Y. D. S. Rajapakse

K. Iyer

DISTRIBUTION STATEMENT A

Approved for Public Release
Distribution Unlimited



PERGAMON

DTIC QUALITY INSPECTED 4

20000612 043

AIMS AND SCOPE

Journal of the Mechanics and Physics of Solids. The Journal publishes papers reporting original research on the mechanics of solids. Emphasis is placed on the development of fundamental concepts of mechanics and novel applications of these concepts based on theoretical, experimental or computational approaches, drawing upon the various branches of engineering science and the allied areas within applied mathematics, materials science, structural engineering, applied physics and geophysics. The main purpose of the Journal is to foster scientific understanding of the processes of deformation and mechanical failure of all solid materials, both technological and natural, and the connections between these processes and their underlying physical mechanisms. In this sense, the content of the Journal should reflect the current state of the discipline in analysis, experimental observation and numerical simulation. In the interest of achieving this goal, authors are encouraged to consider the significance of their contributions for the field of mechanics and the implications of their results, in addition to describing the details of their work.

© 1998 Elsevier Science Ltd. All rights reserved.

This journal and the individual contributions contained in it are protected under copyright by Elsevier Science Ltd, and the following terms and conditions apply to their use:

Photocopying

Single photocopies of single articles may be made for personal use as allowed by national copyright laws. Permission of the publisher and payment of a fee is required for all other photocopying, including multiple or systematic copying, copying for advertising or promotional purposes, resale, and all forms of document delivery. Special rates are available for educational institutions that wish to make photocopies for non-profit educational classroom use.

Permissions may be sought directly from Elsevier Science Rights & Permissions Department, P.O. Box 800, Oxford OX5 1DX, U.K.; phone: (+44) 1865 843830, fax: (+44) 1865 853333, e-mail: permissions@elsevier.co.uk. You may also contact Rights & Permissions directly through Elsevier's home page (<http://www.elsevier.nl>), selecting first 'Customer Support', then 'General Information', then 'Permissions Query Form'.

In the U.S.A., users may clear permissions and make payments through the Copyright Clearance Center, Inc., 222 Rosewood Drive, Danvers, MA 01923, U.S.A.; phone: (978) 7508400, fax: (978) 7504744, and in the U.K. through the Copyright Licensing Agency Rapid Clearance Service (CLARCS), 90 Tottenham Court Road, London W1P 0LP, U.K.; phone: (+44) 171 436 5931; fax: (+44) 171 436 3986. Other countries may have a local reprographic rights agency for payments.

Derivative works

Subscribers may reproduce tables of contents or prepare lists of articles including abstracts for internal circulation within their institutions. Permission of the publisher is required for resale or distribution outside the institution.

Permission of the publisher is required for all other derivative works, including compilations and translations.

Electronic storage or Usage

Permission of the publisher is required to store or use electronically any material contained in this journal, including any article or part of an article. Contact the publisher at the address indicated.

Except as outlined above, no part of this publication may be reproduced, stored in a retrieval system or transmitted in any form or by any means, electronic, mechanical, photocopying, recording or otherwise, without prior written permission of the publisher.

Address permissions requests to: Elsevier Rights & Permissions Department, at the mail, fax and e-mail addresses noted above.

Notice

No responsibility is assumed by the publisher for any injury and/or damage to persons or property as a matter of products liability, negligence or otherwise, or from any use or operation of any methods, products, instructions or ideas contained in the material herein. Because of rapid advances in the medical sciences, in particular, independent verification of diagnoses and drug dosages should be made.

Although all advertising material is expected to conform to ethical (medical) standards, inclusion in this publication does not constitute a guarantee or endorsement of the quality or value of such product or of the claims made of it by its manufacturer.

∞™ The paper used in this publication meets the requirements of ANSI/NISO Z39.48-1992 (Permanence of Paper)



ContentsDirect delivers the table of contents of this journal, by e-mail, approximately two to four weeks prior to each issue's publication. To subscribe to this free service, complete and return the form at the back of this issue or send an e-mail to cdsubs@elsevier.co.uk, or register online at <http://www.elsevier.nl/locate/ContentsDirect>.

36707.1-55-47
VOLUME 46, NUMBER 10, OCTOBER 1978

ISSN 0022-5096

JOURNAL OF THE MECHANICS AND PHYSICS OF SOLIDS

EDITORS

L. B. FREUND

Brown University
Division of Engineering

J. R. WILLIS

Cambridge University
Department of Applied Mathematics
and Theoretical Physics

EDITORIAL ADVISERS

R. HILL (Editor-in-Chief 1952-68)—Cambridge, UK

R. J. CLIFTON—Providence, U.S.A.

H. HORII—Tokyo, Japan

J. W. HUTCHINSON—Cambridge, U.S.A.

R. D. JAMES—Minneapolis, U.S.A.

K. L. JOHNSON—Cambridge, U.K.

M. ORTIZ—Pasadena, U.S.A.

J. R. RICE—Cambridge, U.S.A.

P. SUQUET—Marseille, France

SPECIAL ISSUE

Proceedings of a Symposium on the Dynamic Deformation and Failure
Mechanics of Materials, honoring Professor R. J. Clifton

GUEST EDITORS

G. Ravichandran

A. J. Rosakis

M. Ortiz

Y. D. S. Rajapakse

K. Iyer



PERGAMON

REPORT DOCUMENTATION PAGE

Form Approved
OMB NO. 0704-0188

Public Reporting burden for this collection of information is estimated to average 1 hour per response, including the time for reviewing instructions, searching existing data sources, gathering and maintaining the data needed, and completing and reviewing the collection of information. Send comment regarding this burden estimates or any other aspect of this collection of information, including suggestions for reducing this burden, to Washington Headquarters Services, Directorate for information Operations and Reports, 1215 Jefferson Davis Highway, Suite 1204, Arlington, VA 22202-4302, and to the Office of Management and Budget, Paperwork Reduction Project (0704-0188,) Washington, DC 20503.

1. AGENCY USE ONLY (Leave Blank)		2. REPORT DATE 17 May 2000	3. REPORT TYPE AND DATES COVERED Final Report 24 February 1997-23 February 1998	
4. TITLE AND SUBTITLE Dynamic Deformation and Failure of Materials			5. FUNDING NUMBERS DAAG55-97-1-0107	
6. AUTHOR(S) Guruswami Ravichandran				
7. PERFORMING ORGANIZATION NAME(S) AND ADDRESS(ES) California Institute of Technology Graduate Aeronautical Laboratories Pasadena, CA 91125			8. PERFORMING ORGANIZATION REPORT NUMBER GR-ARO-00-33	
9. SPONSORING / MONITORING AGENCY NAME(S) AND ADDRESS(ES) U. S. Army Research Office P.O. Box 12211 Research Triangle Park, NC 27709-2211			10. SPONSORING / MONITORING AGENCY REPORT NUMBER <i>36707.1-EG-CP</i>	
11. SUPPLEMENTARY NOTES The views, opinions and/or findings contained in this report are those of the author(s) and should not be construed as an official Department of the Army position, policy or decision, unless so designated by other documentation.				
12 a. DISTRIBUTION / AVAILABILITY STATEMENT Approved for public release; distribution unlimited.			12 b. DISTRIBUTION CODE	
13. ABSTRACT (Maximum 200 words) The grant provided support for the organization of a conference on "Dynamic Deformation and Failure of Materials." The conference was held at the California Institute of Technology campus in Pasadena during May 22-24, 1997. The conference attracted researchers from all over the world and provided a forum to assess the state-of-the-art in this field. More than 30 presentations were made on a wide range of subjects including, high strain rate behavior of materials, dynamic fracture and shear banding, topics that are of interest to the Army. The talks were focussed on various physical phenomena including failure waves and factors influencing strength at high temperatures and high loading rates. There were a number of participants from the Army and included two presentations by scientists from the Army Research Laboratories. The proceedings of the conference was published in a bound volume by Elsevier and as a special issue of the Journal of the Mechanics and Physics of Solids.				
14. SUBJECT TERMS Solid mechanics; conference; dynamic deformation; dynamic failure			15. NUMBER OF PAGES	
			16. PRICE CODE	
17. SECURITY CLASSIFICATION OR REPORT UNCLASSIFIED	18. SECURITY CLASSIFICATION ON THIS PAGE UNCLASSIFIED	19. SECURITY CLASSIFICATION OF ABSTRACT UNCLASSIFIED	20. LIMITATION OF ABSTRACT UL	

NSN 7540-01-280-5500

Standard Form 298 (Rev.2-89)
Prescribed by ANSI Std. Z39-18
298-102

DEDICATION

RODNEY J. CLIFTON, Rush C. Hawkins University Professor and Professor of Engineering at Brown University, reached sixty years of age in July 1997. In recognition of his more than thirty years of distinguished contributions to teaching, research and leadership in the field of solid mechanics, a special symposium on *Dynamic Deformation and Failure Mechanics of Materials* was held in May of 1997 at the California Institute of Technology. His students, colleagues and friends from around the world joined his family in a tribute to the distinguished record of excellence he has established. The speakers were invited to submit papers based on their lectures to the *Journal of the Mechanics and Physics of Solids*, which kindly agreed to publish this special issue marking the occasion. A copy of the complete program appears in this issue.

This issue is dedicated to Rod Clifton, with the gratitude, admiration and affection of his many friends and colleagues, with their hope that he will enjoy a long and healthy life, and continue to lead his field for many years to come.

G. Ravichandran
A. J. Rosakis
M. Ortiz
Y. D. S. Rajapakse
K. Iyer

JOURNAL OF THE MECHANICS AND PHYSICS OF SOLIDS

VOLUME 46, NUMBER 10

1998

CONTENTS

SPECIAL ISSUE: Proceedings of a Symposium on the Dynamic
Deformation and Failure Mechanics of Materials, honoring
Professor R. J. Clifton

iii Dedication

vii Preface

- | | | |
|--|------|---|
| Y. ZHANG and K. T. RAMESH | 1699 | On the compressibility of a glass-forming lubricant: experiments and molecular modeling |
| K. J. FRUTSCHY and
R. J. CLIFTON | 1723 | High-temperature pressure-shear plate impact experiments on OFHC copper |
| P. ARCHER and V. GUPTA | 1745 | Measurement and control of ice adhesion to aluminum 6061 alloy |
| P. KUMAR and
N. N. KISHORE | 1773 | Initiation and propagation toughness of delamination crack under an impact load |
| A. J. ROSAKIS,
O. SAMUDRALA, R. P. SINGH
and A. SHUKLA | 1789 | Intersonic crack propagation in bimaterial systems |
| G. XU, A. F. BOWER and
M. ORTIZ | 1815 | The influence of crack trapping on the toughness of fiber reinforced composites |
| L. B. FREUND | 1835 | A surface chemical potential for elastic solids |
| R. MILLER, R. PHILLIPS,
G. BELTZ and M. ORTIZ | 1845 | A non-local formulation of the Peierls dislocation model |
| G. I. KANEL | 1869 | Some new data on deformation and fracture of solids under shock-wave loading |
| N. BOURNE, J. MILLETT,
Z. ROSENBERG and
N. MURRAY | 1887 | On the shock induced failure of brittle solids |

Contents continued

K. BHATTACHARYA, M. ORTIZ and G. RAVICHANDRAN	2171	Energy-based model of compressive splitting in heterogeneous brittle solids
---	------	--



RODNEY JAMES CLIFTON

Rodney James Clifton was born on 10 July 1937 in Orchard, Nebraska, a small town in the northeastern corner of the state. His parents were descended from Europeans who had immigrated to the region in the latter part of the 19th century. His early education was received in small rural schools where he excelled in science, mathematics and athletics. Following secondary school, he enrolled in the program in civil engineering at the University of Nebraska in Lincoln, where he received his B.Sc. degree in 1959.

Upon his graduation from Nebraska, Rod was employed as a structural engineer by the Paxton and Vierling Steel Co. of Omaha. However, his interests were in the fundamental precepts of structural mechanics, and he decided to pursue graduate study in the field. In the fall of 1960, taking advantage of opportunities for graduate study in the U.S.A. created as a consequence of the launch of the Soviet satellite sputnik in 1957, he enrolled in the department of civil engineering at Carnegie Institute of Technology, now part of Carnegie Mellon University. He received his Ph.D. in 1964.

Rod's thesis was concerned with the numerical solution of the partial differential equations which describe the propagation of stress waves in solids. The general approach for two space dimensions and time was based on integration of the system of hyperbolic equations along bi-characteristic strips, tangent to characteristic cones. The second-order-accurate method was applied for both elastic and elastic-plastic waves in solids. This work marked the beginning of his long and productive interest in wave propagation in solids.

While at the University of Nebraska, he met Mercadee Bonde and they were married in December of 1958. Their first son Brad was born in 1960, followed by Jeff in 1962, Greg in 1966 and, finally, daughter Ann, born in 1970. Rod and Merc presently have two grandchildren.

Upon completion of his dissertation, Rod inquired at Brown University about the prospects for continuing his research in the Division of Engineering, having become

aware of the research tradition there in both plasticity and stress waves. At the time, Brown was the site of one of the national interdisciplinary Materials Research Laboratories, which provided excellent opportunities for short term research visits. (As will be noted below, Rod currently serves as the director of Brown's Materials Research Science and Engineering Center, the direct descendant of the original MRL program.) The senior faculty at Brown concerned with filling research positions were at first curious, and then totally delighted, upon discovering this young person who had written a thesis of consequence in an area of great current interest at Brown, and that he had done so working largely on his own. This work has become broadly known in the area and is still cited frequently today.

Rod and his young family arrived in providence in January of 1964, and he began a very productive period of research which established the framework for much of the work done subsequently in the area which has become known as dynamic plasticity. He developed solution procedures for analyzing plastic wave propagation, especially combined-stress plastic waves. A beautiful discussion entitled 'An analysis of combined longitudinal and torsional plastic waves in a thin-walled tube' appeared in the proceedings of the 5th U.S. National Congress of Applied Mechanics held in Minnesota in 1966. Then, with his first Ph.D. student, Joel Lipkin, he carried out the corresponding experiment. This work was reported in 'An experimental study of combined longitudinal and torsional plastic waves in a thin-walled tube' which appeared in the proceedings of the 12th International Congress of Theoretical and Applied Mechanics in 1968. This blend of creative experimental investigation with sound analysis was to become the hallmark of his work in the field. Among the many innovations in experimental dynamic plasticity which were developed in his laboratory are the pressure-shear plate impact configurations, which opened the way for the broad study of combined-stress plastic waves of one-dimensional strain on the basis of interpretable experiments, and the transverse displacement interferometer for detecting lateral motion of a specimen surface in the plate impact apparatus. Both the standard and the pressure-shear configurations of the plate impact apparatus were also modified to measure plane strain fracture toughness of steels under high rates of loading, the nucleation and propagation of shear bands in metals, the pressure-shear characteristics of lubricants at high rates of deformation, the high-rate response of fragmented brittle materials, and nucleation of failure in brittle polycrystalline ceramics. In each of these situations, novel experimental procedures supported by sound analysis or numerical modeling led to significant advances.

Largely through his association with Terra Tek Inc. of Salt Lake City, first as a consultant and subsequently as a member of the Board of Directors, he also made important contributions to the area of hydraulic fracture of geological materials and secondary oil recovery technology. His contributions included both fundamental studies on applications of fracture mechanics and the development of commercial software for prediction of hydraulic fracturing patterns around bore holes.

Over the years at Brown, more than twenty-five graduate students have completed their Ph.D. thesis research under his direction. He is well-known for the close personal attention given to the work of each student and for fostering an independent and discriminating point of view within each student over the course of his or her work. These former students, who now contribute at leading universities, research lab-

oratories and industrial laboratories throughout the U.S.A. and abroad, are having a major impact on the area of experimental mechanics.

In addition to his research contributions, Rod has been very generous with his time in service to his university and profession. Through his leadership and sound judgement, he has had a profound influence on the programs in the Division of Engineering at Brown over the years. He served as Chair of the Engineering Executive committee (1974–79), as Director of the Central Facility for Mechanical Testing (1980–86), on the University Research Council (1987–91), as Principal Investigator and Director of the NSF Materials Research Group (1989–96), as Principal Investigator and Director of the NSF Materials Research Science and Engineering Center (1996–date), and on many other committees and panels. He has also served as Associate Editor of the *Journal of Applied Mechanics* (1981–88), on the Board of Directors of the Society of Engineering Science (1977–83), president of the Society of Engineering Science (1982–83), on the editorial advisory board of the *Journal of the Mechanics and Physics of Solids* (1982–date), on the Board of Directors of the NSF Institute for Mechanics and Materials (1992–date), on the mechanical engineering peer committee of the national Academy of Engineering (Vice Chair 1995, Chair 1996), and on advisory boards of several federal agencies.

For his many contributions in both research and service, Rod has been recognized by election as a Fellow of the American Academy of Mechanics, through receipt of the ASME Melville Medal (joint with K. S. Kim), the SES Prager medal, the best paper award of the ASME Tribology Division, (joint with K. T. Ramesh), by the Distinguished Alumni Award of Carnegie Mellon University, and by election to membership in the National Academy of Engineering.

Most of the foregoing information has been drawn from the public record, where Rod's impressive professional accomplishments are evident for all to see. However, the full dimension of Rod Clifton is most appreciated by those who have had the privilege of a direct association. He is devoted to his family and has been tireless in quest of their happiness and interests. He has been active in his church and generous on behalf of its causes, including Habitat for Humanity and others. Within the Division of Engineering at Brown, he has had a long-standing interest in the undergraduate programs of instruction, often volunteering for the most difficult teaching assignments in an effort to improve the educational experiences of the students. The door of his office has always been open to students who require extra help to surmount some barrier, and it is not unusual to find students waiting their turn outside his office door long after closing hours in the department. Those who have had the good fortune of having been a faculty colleague have benefited immeasurably from Rod's leadership, sound judgement and enormous efforts for the common good, and have appreciated his good humor and collegiality. He is a model of integrity and dedication.

RODNEY J. CLIFTON'S PUBLICATIONS

- V. Vitols, R.J. Clifton and T. Au, Analysis of Composite Beam Bridges by Orthotropic Plate Theory. *Journal of Struct. Div.*, ASCE, August (1963).
- R.J. Clifton, J.C.L. Chang and T. Au, Analysis of Orthotropic Plate Bridges. *Journal of Struct. Div.*, ASCE, (1963).
- R.J. Clifton, An Analysis of Combined Longitudinal and Torsional Plastic Waves in a Thin-Walled Tube, *Proceedings, 5th U.S. National Congress of Applied Mechanics*, University of Minnesota, (1966), 465-480.
- R.J. Clifton, A Difference Method for the Dynamic Elastic-Plastic Equations under Conditions of Plane Strain, (abstract only). *Proceedings, 5th US National Congress of Applied Mechanics*, University of Minnesota, (1966), 546.
- S.R. Bodner and R.J. Clifton, An Experimental Investigation of Elastic-Plastic Pulse Propagation in Aluminum Rods, *Journal of Applied Mechanics*, **34**, (1967), 91-99.
- R.J. Clifton, A Difference Method for Plane Problems in Dynamic Elasticity, *Quarterly of Applied Mathematics*, **25**, (1967), 96-116.
- D.L. Vitiello, and R.J. Clifton, The Numerical Solution of a Problem in the Propagation of Plastic Waves of Combined Stress, *Technical Report No. 4 under contract DA-31-124-ARO-D 358*, Division of Applied Mathematics, Brown University, (1967).
- L.R. Oliver, R.W. Armstrong, R.J. Clifton, and H. Kolsky, Stress Wave Produced Cleavage of Zinc Monocrystals and Investigation of the Associated Deformation by Optical Microscopy and X-ray Diffraction, *Technical Report No. 6 under contract NSF-GP-2010*, Division of Applied Mathematics, Brown University, (1967).
- L.R. Oliver, R.W. Armstrong, R.J. Clifton, and H. Kolsky, Cleavage of Zinc Single Crystals Induced by Stress Waves, *Nature*, **216**, No. 5118, (1967), 910.
- R.J. Clifton, Snap-Buckling of a Pre-Stressed Shallow Arch, *Proceedings of the ASCE Joint Specialty Conference on Optimization and Non-linear Problems*, held in Chicago, Illinois, (1968), 53-56.
- J. Lipkin and R.J. Clifton, An Experimental Study of combined Longitudinal and Torsional Plastic Waves in a Thin-Walled Tube, *Proceedings, 12th International Congress of Applied Mechanics*, Stanford University, (1968).
- R.J. Clifton, High-Speed Testing of Armor Materials, in *National Academy of Sciences, National Research Council report on The Development of Lightweight Armor*, (1968), 77-89.
- R.J. Clifton, Elastic-Plastic Boundaries in Combined Longitudinal and Torsional Plastic Wave Propagation, *Journal of Applied Mechanics*, **35**, (1968), 782-786.
- R.J. Clifton, and T.C.T. Ting, The Elastic-Plastic Boundary in One-Dimensional Wave Propagation, *Journal of Applied Mechanics*, **35**, (1968), 812-814.
- R.J. Clifton, Initial Thrust Effects in Snap-Buckling of Shallow Arches, *Journal of Engineering Mechanics Division*, ASCE, (1970), 1157-1170.
- J. Lipkin and R.J. Clifton, Plastic Waves of Combined Stresses due to Longitudinal Impact of a Pre-Torqued Tube, Part I: Experimental Results, *Journal of Applied Mechanics*, **37**, (1970), 1107-1112.
- J. Lipkin and R.J. Clifton, Plastic Waves of Combined Stresses due to Longitudinal Impact of a Pre-Torqued Tube, Part II: Comparison of Theory with Experiment, *Journal of Applied Mechanics*, **37**, (1970), 1113-1120.
- R.J. Clifton, On the Analysis of the Laser Velocity-Interferometer, *Journal of Applied Physics*, **41**, (1970), 5335-5337.
- R.J. Clifton, Thermal Buckling of Shallow Bimetallic Two Hinged Arches, (discussion of a paper by B. Vahidi and N.C. Huang), *Journal of Applied Mechanics*, **37**, (1970), 1199-1202.
- R.J. Clifton, Dislocation Velocity for Combined Viscous Glide and Thermally Activated Jumps Past Dispersed Local Obstacles, *Technical Report No. 3 on contract DASD05-69-C-0290* with Brown University, (1970).
- R.J. Clifton, On the Analysis of Elastic/Visco-Plastic Waves of Finite Uniaxial Strain, *Shock Waves and the Mechanical Properties of Solids*, edited by J. Burke and V. Weiss, Syracuse University Press, (1971), 73-119.

- J.C. Hsu, and R.J. Clifton, Waves in a Thin-Walled Tube Due to the Sudden Release of a Radial Ring Pressure, *Journal of the Acoustical Society of America*, **50**, (1971), 230–240.
- R.J. Clifton, On the Equivalence of the Fe Fp and Fp Fe, *Journal of Applied Mechanics*, **39**, (1972), 287–289.
- S. Ranganath, and R.J. Clifton, Normal Impact of an Infinite Elastic-Plastic Beam by a Semi-Infinite Elastic Rod, *International Journal of Solids & Structures*, **8**, (1972), 41–67.
- S. Ranganath, and R.J. Clifton, A Second Order Accurate Difference Method for Systems of Hyperbolic Partial Differential Equations, *Computer Methods in Applied Mechanics and Engineering*, **1**, (1972), 173–188.
- R.J. Clifton, solutions of Wave Problems in Inelastic Materials, *Dynamics of Inelastic Materials* (P. Perzyna, ed.), *Polish Academy of Sciences*, Summer Course held in Jablonna, Poland, 8–13 May, (1972), 175–254.
- R.J. Clifton, Guided Interfacial Waves with Applications to Cochlear Mechanics, *Institute of Sound and Vibration Research Memorandum*, **466**, Southampton University, England, (1972).
- R.J. Clifton, Plastic Waves: Theory and Experiment, *Mechanics Today*, **1**, edited by S. Nemat-Nasser, Pergamon Press, Inc., (1973), 102–168.
- J.C.C. Hsu, and R.J. Clifton, Plastic Waves in a Rate Sensitive Material Part I: Waves of Uniaxial Stress, *J. Mech. Phys. Solids*, **22**, (1974), 253–255.
- J.C.C. Hsu, and R.J. Clifton, Plastic Waves in a Rate Sensitive Material Part II: Waves of Combined Stress, *J. Mech. Phys. Solids*, **22**, (1974), 255–266.
- S. Ranganath, and R.J. Clifton, Finite Deflection Dynamics of Elastic Beams, *Int'l. J. Solids and Structures*, **10**, (1974), 557–568.
- L.B. Freund, and R.J. Clifton, On the Uniqueness of Plane Elastodynamics Solutions for Running Cracks, *J. of Elasticity*, **4**, (1974), 293–299.
- C.C. Chen, and R.J. Clifton, Asymptotic Solutions for Wave Propagation in Elastic and Viscoelastic Bilaminates. (with C.C. Chen), *Proceedings of the 14th Midwestern Mechanics Conference*, **8**, (1975), 399–417.
- A.S. Abou-Sayed, R.J. Clifton, and L. Hermann, The Oblique Plate Impact Experiment, *Experimental Mechanics*, **16**, (1976), 127–132.
- R.J. Clifton, Some Recent Developments in Plate Impact Experiments, *Proceedings of Symposium on Shock Waves in Solids*, ASME Applied Mechanics Conference, (1976), 27–40.
- E.R. Simonson, R.J. Clifton, A.H. Jones, and S.J. Green, Determination of the Critical-Stress-Intensity K_{Ic} from Internally Pressurized Thick-Walled Vessels, *Experimental Mechanics*, **16**, (1976), 233–238.
- A.S. Abou-Sayed, and R.J. Clifton, Pressure-Shear Waves in Fused Silica, *J. Appl. Phys.*, **47**, (1976), 1762–1770.
- J. Guldenphennig, and R.J. Clifton, An Application of Self-Consistent Slip Models to Plastic Waves of Combined Stress, *Proceedings of International Congress of Applied Mechanics*, Delft, (1976).
- P. Kumar, and R.J. Clifton, Optical Alignment of Impact Faces for Plate Impact Experiments, *J. Appl. Phys.*, **48**, (1977), 1366–1367.
- K.S. Kim, R.J. Clifton, and P. Kumar, A Combined Normal and Transverse Displacement Interferometer with an Application to Impact of Y-Cut Quartz, *J. Appl. Phys.*, **48**, (1977), 4132–4139.
- P. Kumar, and R.J. Clifton, A Star-Shaped Flyer for Plate Impact Recovery Experiments, *J. Appl. Phys.*, **48**, (1977), 4850–4852.
- A.S. Abou-Sayed, and R.J. Clifton, Analysis of Combined Pressure-Shear Waves in an Elastic/Visco-plastic Material, *J. Appl. Mech.*, **99**, Series E, No. 1, (1977), 79–84.
- A.S. Abou-Sayed, and R.J. Clifton, Pressure-Shear Waves in 6061-T6 Aluminum Due to Oblique-Plate-Impact, *J. Appl. Mech.*, **99**, Series E, No. 1, (1977), 85–88.
- C.E. Washington, R.J. Clifton, and B.W. Costerus, Tests of Torispherical Pressure Vessel Heads Convex to Pressure, *Welding Research Council Bulletin*, **227**, (1977), 1–9.
- J. Guldenpfennig, and R.J. Clifton, On the Computation of Plastic Stress-Strain Relations for Polycrystalline Metals, *Comp. Meth. in Appl. Mech. and Engin.*, **10**, (1977), 141–149.
- R.J. Clifton, and P. Kumar, Dislocation Configurations Due to Plate Impact, *Proc. IUTAM Symposium on High Velocity Deformation of Solids* held in Tokyo, Japan, 24–27 Aug., (1977).

- Belytschko, T., Ting, T.C.T., and Clifton, R.J., co-editors, Nonlinear Waves in Solids, *Proceedings of NSF-ARO sponsored Workshop held at University of Illinois at Chicago Circle*, March (1977).
- E.R. Simonson, A.S. Abou-Sayed, and R.J. Clifton, Containment of Massive Hydraulic Fractures, *Society of Petroleum Engineers Journal*, **18**, (1978), 27–32.
- A.S. Abou-Sayed, C.E. Brechtel, and R.J. Clifton, In Situ Stress Determination by Hydrofracturing—A Fracture mechanics Approach, *Journal of Geophysical Research*, **83**, (1978), 2851–1862.
- P. Kumar, and R.J. Clifton, Dislocation Motion and Generation in LiF Single Crystals Subjected to Plate-Impact, *J. Appl. Phys.*, **50**, (1979), 4747–4762.
- R.J. Clifton, Adiabatic Shear Banding, *National Academy of Sciences*, National Research Council National Materials Advisory Board Report No. **356**, Materials Response to Ultra-High Loading rates, (1979), Chapter 8, 129–142.
- R.J. Clifton, Plastic Wave Theory—Supported by Experiments?, *Conference on Mechanical Properties of Materials at High Rates of Strain*, Oxford University, 28–30 March, (1979); Inst. Phys. Conf. Ser. **47**: Chapter 2, 174–186.
- R.J. Clifton, and A.S. Abou-Sayed, On the Computational of the Three-Dimensional Geometry of Hydraulic Fractures, *Proceedings of SPE-AIME Symposium on Low-Permeability Gas Reservoirs*, Denver, Colorado, 20–22 May, (1979).
- P.S. Steif, and R.J. Clifton, On the Kinetics of a Frank-Read Source, *Materials Science and Engineering*, **41**, (1979), 251–258.
- R.J. Clifton, Dynamic Plastic Deformation for Non-Proportional Loading Paths, *Proceedings of Euromech Colloquium* **115**, Villard-de-Lans, France, 19–22 June, (1979).
- J. Guldenpfennig, and R.J. Clifton, Plastic Waves of Combined Stress Based on Self-Consistent Slip Models, *J. Mech. Phys. Solids*, **28**, (1980), 201–219.
- K.-S. Kim, and R.J. Clifton, Pressure-Shear Impact of 6061-T6 Aluminum, *J. Appl. Mech.*, **47**, (1980), 11–16.
- R.J. Clifton, and X. Markenscoff, Elastic Precursor Decay and Radiation from Nonuniformly Moving Dislocations, *J. Mech. Phys. Solids*, **29**, (1981), 227–251.
- X. Markenscoff, and R.J. Clifton, The Nonuniformly Moving Edge Dislocation, *J. Mech. Phys. Solids*, **29**, (1981), 253–262.
- R.J. Clifton, and A.S. Abou-Sayed, A Variational Approach to the Prediction of the Three-Dimensional Geometry of Hydraulic Fractures, *Proceedings of the 1981 SPE/DOE Low Permeability Symposium held in Denver, Colorado*, 27–29 May, (1981), 457–465.
- C.H. Li, and R.J. Clifton, Dynamic Stress-Strain Curves at Plastic Shear Strain Rates of 105s⁻¹, *Proceedings of the American Physical Society's 1981 Topical Conference on Shock Waves in Condensed Matter held at Stanford Research Institute*, 23–25 June (1981).
- X. Markenscoff, and R.J. Clifton, Re-examination of the Precursor Decay Anomaly, *Ibid.* **64.**, Radiation from expanding Circular Dislocation Loops and Elastic Precursor Decay, *J. Appl. Mech.*, **49**, (1982), 792–796.
- X. Markenscoff, and R.J. Clifton, Radiation From Expanding Circular Dislocation Loops and Elastic Precursor Decay, *J. Appl. Mech.*, **49**, (1982), 792–796.
- R.J. Clifton, A. Gilat, and C.H. Li, Dynamic Plastic Response of Metals under Pressure-Shear Impact, *Proceedings of the 29th Sagamore Army Materials Research Conference*, held at Lake Placid, New York, (1982), 1–19.
- R.J. Clifton, and A.S. Abou-Sayed, On the Mechanics of Hydraulic Fracturing, *Proceedings of the 9th US Nat'l Congress of Applied Mechanics*, Cornell University, (1982), 443–451.
- A. Molinari, and R.J. Clifton, Localisation de la Deformation Viscoplastique en Cisaillement Simple: Resultats Exacts en Theorie Non Lineaire, *C.R. Acad. Sc. Paris*, t. **296**, (1983), 1–4.
- R.J. Clifton, and G. Ravichandran, A Plate Impact Experiment for Studying Crack Initiation at Loading Rates MPa m/2s⁻¹, *Proceedings of the NSF-ARO Workshop on Dynamic Fracture*, held at Caltech, February (1983).
- R.J. Clifton, Dynamic Plasticity, 50th Anniversary Issue of the *Journal of Applied Mechanics*, **50**, December (1983), 941–952.

- R.J. Clifton, Pressure-Shear Impact and the Dynamic Plastic Response of Metals, *Proceedings of the American Physical Society 1983 Topical Conference on Shock Waves in Condensed Matter*, edited by J.R. Asay, G.K. Straub and R.A. Graham, July (1983), 105–111.
- R.J. Clifton, Experiments and the Micromechanics of Viscoplasticity, *Proceedings of the Symposium Plasticity Today* held at Udine, Italy, edited by G. Bianchi and A. Sawczuk, June (1983), 105–111.
- T.G. Shawki, R.J. Clifton, and G. Majda, An Analysis of Shear Strain Localization in Thermal, Viscoplastic Materials, *Brown University Report No.*, ARO DAAG 29-81-K-0121/3, October (1983).
- P. Blinot, C.Y. Chiem, P. Kumar, and R.J. Clifton, Dislocation Mobility in Fe-3% Si Single Crystals under Plate Impact, in *Proceedings of Third Oxford Conference on the Mechanical Properties of Materials at High Rates of Strain*, Oxford, (1984).
- R.J. Clifton, J. Duffy, K.A. Hartley, and T.G. Shawki, On Critical Conditions for Shear Band Formation at High Strain Rates, *Scripta Met*, **18**, (1984), 443–448.
- K.-S. Kim, and R.J. Clifton, Dislocation Motion in MgO Crystals Under Plate Impact, *J. Matls. Sci.*, **19**, (1984), 1428–1438.
- A. Gilat, and R.J. Clifton, Pressure-Shear Waves in 6061-T6 Aluminum and Alpha-Titanium, *J. Mech. Phys. Solids*, **33**, (1985), 263–284.
- R.J. Clifton, Stress Wave Experiments in Plasticity, *International Journal of Plasticity*, **1**, (1985), 289–302.
- R.J. Clifton, and R.W. Klopp, Pressure-Shear Plate Impact Testing, *Metals Handbook: Mechanical Testing*, **8**, 9th Edition, (1985), 230–239.
- S. Huang, and R.J. Clifton, Dynamic Plastic Response of OFHC Copper at High Shear Strain Rates, *Proceedings of the IUTAM Symposium on Macro- and Micro-Mechanics of High Velocity Deformation and Fracture*, Tokyo, Japan, August, (1985).
- R.J. Clifton, Metal Plasticity, *Appl. Mech. Rev.*, **38**, (1985), 1261–1263.
- R.J. Clifton, Stress Wave Propagation, Dynamic Material Response, and Quantitative Non-destructive Evaluation, *Appl. Mech. Rev.*, **38**, (1985), 1276–1278.
- F.P. Chiang, and R.J. Clifton, Experimental Mechanics, *Appl. Mech. Rev.*, **38**, (1985), 1279–1281.
- R.J. Clifton, Recent Advances in the Three Dimensional Simulation of Hydraulic Fracturing, *Developments in Mechanics 13, Proceedings of the 19th Midwestern Mechanics Conference*, Ohio State University, September (1985), 311–319.
- T.G. Shawki, J.P. Yang, and R.J. Clifton, Calculation of the Visco-plastic Response of Polycrystals from Slip Theory for F.C.C. Single Crystals, (preprint) *22nd Annual Meeting, Society of Engineering Science*, Penn State University, October (1985).
- R.W. Klopp, R.J. Clifton, and T.G. Shawki, Pressure-Shear Impact and the Dynamic Viscoplastic Response of Metals, *Mechanics of Materials*, **4**, (1985), 375–385.
- G. Meir, and R.J. Clifton, Dislocation Mobility in High Purity LiF from 100oK to 300oK, *Shock Compression of Condensed Matter*, APS, (1985).
- G. Meir, and R.J. Clifton, The Effects of Dislocation Generation at Surfaces and Subgrain Boundaries on Precursor Decay in High Purity LiF, *J. Appl. Phys.*, **59**, (1986), 124–148.
- K.T. Ramesh, and R.J. Clifton, A Pressure-Shear Plate Impact Experiment for Studying the Rheology of Lubricants at High Pressures and High Shearing Rates, *Journal of Tribology*, **109**, (1987), 215–222.
- A. Molinari, and R.J. Clifton, Analytical Characterization of Shear Localization in Thermoviscoplastic Materials, *Journal of Applied Mechanics*, **109**, (1987), 806–812.
- R.J. Clifton, Constitutive Models for Plastic Flow at Ultra High Strain Rates, *Proceedings of the Symposium on Dynamic Constitutive/Failure Models*, University of Dayton, May (1988), 28–55.
- R.J. Clifton, and J.J. Wang, Multiple Fluids, Proppant Transport, and Thermal Effects in Three-Dimensional Simulation of Hydraulic Fracturing, SPE 18198, *Proceedings of the 63rd Annual Technical Conference and Exhibition*, Houston, October (1988), 175–188.
- G. Ravichandran, and R.J. Clifton, Dynamic Fracture Under Plane Wave Loading, *International Journal of Fracture*, **40**, (1989), 157–201.

- R.J. Clifton, Three-Dimensional Fracture-Propagation Models, *Chapter 5 in Recent Advances in Hydraulics Fracturing*, SPE Monograph, J.L. Gidley, ed., (1989).
- R. Godse, G. Ravichandran, and R.J. Clifton, Micromechanisms of Dynamic Crack Propagation in an AISI 4340 Steel, *Materials Science and Engineering*, **A112**, (1989), 79–88.
- T.G. Shawki, and R.J. Clifton, Shear Band Formation in Thermal Viscoplastic Materials, *Mechanical Behavior of Materials*, **8**, (1989), 13–43.
- G. Raiser, R.J. Clifton, and M. Ortiz, A Soft Recovery Plate Impact Experiment for Studying Microcracking in Ceramics, *Mechanical Behavior of Materials*, **10**, (1990), 43–58.
- R.W. Klopp, and R.J. Clifton, Analysis of Tilt in the High-Strain-Rate Pressure-Shear Plate Impact Experiment, *J. of Appl. Phys.*, **67**, (1990), 7171–7173.
- R.J. Clifton, G. Raiser, M. Ortiz, and H. Espinosa, A Soft Recovery Experiment for ceramics, *Shock Compression of Condensed Matter—1989*, eds. S.C. Schmidt, J.N. Johnson, L.W. Davissou, Elsevier Science Publishers, 437–440, (1990).
- R.J. Clifton, High Strain Rate Behavior of Metals, *Applied Mechanics Reviews*, **43**, (1990), S9–S22.
- V. Prakash, and R.J. Clifton, Experimental and Analytical Investigation of Dynamic Fracture under Conditions of Plane Strain. To appear in the *Proceedings of the 22nd National Symposium on Fracture Mechanics*, (1990).
- R.J. Clifton, and J.J. Wang, Numerical Modeling of Hydraulic Fracturing in Layered Formation with Multiple Elastic Moduli, *Rock Mechanics Contributions and Challenges, Proceedings of the 31st US Symposium*, edited by Hustrulid, W.A. and Johnson, G.A., (1990).
- M. Zhou, and R.J. Clifton, Dynamic Ductile Rupture in a Spheroidized 1045 Steel, *Proceedings of Army Symposium on Solid Mechanics*, S.C. Chou, editor, (1991), 451–472.
- R.J. Clifton, and J.J. Wang, Modeling of Poroelastic Effects in Hydraulic Fracturing, *SPE22107 SPE Joint Rocky Mountain Regional Meeting and Low Permeability Reservoirs Symposium*, Denver, Colorado, (1991).
- R.J. Clifton, and J.J. Wang, Modeling of In-Situ Stress Change Due to Cold Fluid Injection, *SPE International Arctic Technology Conference*, Anchorage, Alaska, (1991).
- R.J. Clifton, and J.J. Wang, Adaptive Optimal Mesh Generator for Hydraulic Fracturing Modeling, *Rock Mechanics as Multidisciplinary Science, Proceedings of the 32nd US Symposium*, edited by J.C. Roegiers, (1991).
- H.D. Espinosa, and R.J. Clifton, An Experimental Investigation of Inelasticity in Shock Loaded ALN/AL Composites, *Symposium on Experiments in Micromechanics of Failure-Resistant Materials*, edited K.-S. Kim, ASME, 37–56, (1991).
- W. Tong, R.J. Clifton, and S. Huang, Pressure-Shear Impact Investigation of Strain-Rate History Effects in OFHC Copper, *Journal of the Mechanics and Physics of Solids*, **40**, (1992), 1251–1294.
- V. Prakash, L.B. Freund, and R.J. Clifton, Stress Wave Radiation from a Crack Tip during Dynamic Fracture Initiation, *Journal of Applied Mechanics*, **59**, (1992), 356–365.
- K.T. Ramesh, and R.J. Clifton, Finite Deformation Analysis of Pressure-Shear Plate Impact Experiments on Elastohydrodynamic Lubricants, *Journal of Applied Mechanics*, **59**, (1992), 754–761.
- M.C. Mello, V. Prakash, and R.J. Clifton, Multi-Point Interferometer for Monitoring Two Dimensional Wave Motions, *Shock Compression of Condensed Matter*, 1991, R.D. Dick, J.W. Forbes, D.G. Tasker eds, (1992), 763–766, Elsevier Science Publishers, B.V.
- M. Kurashige, and R.J. Clifton, Integral Equations for the Problem of a 3D Crack in an Infinite Fluid-Filled Porous Elastic Solid. *SPE Production Engineering*, February (1992), 34–38.
- V. Prakash, L.B. Freund, and R.J. Clifton, Plane Strain Fracture in Plate Impact, *Shock Compression of Condensed Matter 1991*, R.D. Dick, J.W. Forbes, D.G. Tasker, editors, (1992), 515–518, Elsevier Science Publishers, B.V.
- H.D. Espinosa, G. Raiser, R.J. Clifton, and M. Ortiz, Experimental Observations and Numerical Modeling of Inelasticity in Dynamically Loaded Ceramics, *Journal of Hard Materials*, **3**, (1992), 285–313.
- V. Prakash, and R.J. Clifton, Pressure-Shear Plate Impact Measurement of Dynamic Friction

- for High Speed Machining Applications, to appear in *Proceedings VII International Congress on Experimental Mechanics*, Society of Experimental Mechanics, Las Vegas, Nevada, June (1992).
- H.D. Espinosa, G. Raiser, R.J. Clifton, and M. Ortiz, Performance of the Star-Shaped Flyer in the Study of Brittle Materials: Three-Dimensional Computer Simulations and Experimental Observations, *J. of Appl. Phys.*, **71**, (1992), 3451–3457.
- M. Zhou, R.J. Clifton, and A. Needleman, Shear Band Formation in a W-Ni-Fe Alloy under Plate Impact, *Proceedings, 1992 International Conference on Tungsten and Tungsten Alloys*, Metal Powder Industries Federation, Princeton, New Jersey, 343–356.
- J. Escobar, and R.J. Clifton, On Pressure-Shear Plate Impact for Studying the Kinetics of Stress-Induced Phase Transformations, *J. Materials Science and Engineering*, **A170**, (1993), 125–142.
- G. Raiser, and R.J. Clifton, High Strain Rate Deformation and Damage in Ceramic Materials, *Journal of Engineering Materials and Technology*, **115**, (1993), 292–299.
- V. Prakash, and R.J. Clifton, Time-Resolved Dynamic Friction Measurements in Pressure-Shear, *AMD-Vol. 165, Experimental Techniques in the Dynamics of Deformable Solids*, ASME, (1993), 33–48.
- M. Zhou, R.J. Clifton, and A. Needleman, Shear Bands in Pressure-Shear Plate Impact, *Proceedings of the Army Symposium on Solid Mechanics*, Plymouth, Massachusetts, August, (1993).
- R.J. Clifton, Analysis of Failure Waves in Glasses, *Applied Mechanics Reviews*, **48**, (1993), 540–546.
- R.J. Clifton, Shear Waves and Phase Transformations, in *Shock Induced Transitions and Phase Structures in General Media*, eds., J.E. Dunn, R. Fosdick, M. Slemrod, Springer-Verlag, New York, (1993), 45–60.
- G.F. Raiser, and R.J. Clifton, Failure Waves in Uniaxial Compression of an Aluminosilicate Glass, *High-Pressure Science and Technology*, 1993, edited by S.C. Schmidt, J.W. Shaner, G.A. Samara and M. Ross, AIP Press, 1039–1042.
- M. Zhou, A. Needleman, and R.J. Clifton, Finite Element Simulations of Shear Localization in Plate Impact, *J. Mech. Phys. Solids*, **42**, (1994), 423–458.
- G.F. Raiser, J.L. Wise, R.J. Clifton, D.E. Grady, and D.E. Cox, Plate Impact Response of Ceramics and Glasses, *J. Appl. Phys.*, **75**, (1994), 3862–3869 G.F.
- J.J. Wang, and R.J. Clifton, Application of a Quasi-Newton Method in 3D Hydraulic Fracturing Simulations, in *Proceedings 8th International Conference of the Association for Computer Methods and Advances in Geomechanics*, (1994).
- S. Sundaram, and R.J. Clifton, Pressure-Shear Impact Investigation of Dynamic Fragmentation and Flow of Ceramics, *Symposium on the Mechanical Testing of Ceramics and Ceramic Composites*, ASME, (1994), 23–40.
- Q. Guo, J.J. Wang, and R.J. Clifton, Three-Dimensional Analysis of Planar Cracks in Composites, *Durability of Composite Materials*, MD-51, edited by R.C. Wetherhold, ASME, (1994), 159–175.
- R.-R. Chien, R.J. Clifton, and S.R. Nutt, Stress-Induced Phase Transformation in Single Crystal Titanium Carbide, *J. Amer. Cer. Soc.*, **78**, (1995), 1537–1545.
- Q. Guo, J.J. Wang, R.J. Clifton, and L. Mertaugh, Elastic Analysis of Planar Cracks of Arbitrary Shape, *J. Appl. Mech.*, **62**, (1995), 1–8.
- J.C. Escobar, and R.J. Clifton, Pressure-shear Impact Induced Phase Transformations in Cu-14.44Al-4.19 Ni Single Crystals, *SPIE*, **2427**, (1995), 186–197.
- J.C. Escobar, and R.J. Clifton, Stress-Wave Induced Martensitic Phase Transformations, Metallurgical and Materials Applications of Shock-Wave and High-Strain-Rate Phenomena edited by L.E. Murr, K.P. Staudhammer and M.A. Meyers, *Elsevier Science*, (1995), 451–462.
- M. Kurashige, and R.J. Clifton, Integral Equations for a 3-D Crack in an Infinite Fluid-Filled Poroelastic Medium with Zero Permeability in One Direction, *J. Appl. Mech.*, **63**, (1996), 62–68.
- Q. Guo, J.J. Wang, and R.J. Clifton, Three Dimensional Analysis of Surface Cracks in an Elastic Half Space, *J. Appl. Mech.*, **63**, (1996), 287–294.

- R.J. Clifton and S.R. Bodner, An Analysis of Longitudinal Elastic-Plastic Pulse Propagation, *Journal of Applied Mechanics*, **33**, Trans. ASME, (1996), 248–255.
- R.J. Clifton, Pressure-Shear Impact Investigation of the Dynamic Response of Ceramics, Advances in Failure Mechanisms in Brittle Materials, R.J. Clifton and H.D. Espinosa, eds., *ASME AMD.*, **219**, (1996), 59–80.
- K.J. Frutschy, and R.J. Clifton, High Temperature Pressure-Shear Plate Impact Experiments on OFHC Copper, *Proceedings, US Army Symposium on Solid Mechanics, Myrtle Beach, South Carolina*, October, (1996).
- Z. Zhang, and R.J. Clifton, Dynamic Failure of 4340 VAR Steel in Shear, *Proceedings US Army Symposium on Solid Mechanics held in Myrtle Beach, South Carolina*, October, (1996).
- T. Nonaka, T. Okazaki, and R.J. Clifton, Longitudinal Elastic Waves in Columns Due to Earthquake Motion, *Int'l. J. of Impact Engineering*, **18**, (1996), 889–898.
- M. Zhou, and R.J. Clifton, Dynamics Ductile Rupture Under Conditions of Plane Strain, to appear in *Int. J. Impact Engineering*, **19**, (1997), 189–206.
- K.J. Frutschy, and R.J. Clifton, Plate-Impact Technique for Measuring Dynamic Friction at High Temperatures, *J. of Tribology*, **119**, *ASME*, (1997), 590–593.
- K.E. Duprey, and R.J. Clifton, Dynamic Constitutive Response of Tantalum at High Strain Rates, *Proceedings of 1994 APS Meeting on Shock Compression of Condensed Matter held at Univ. of Massachusetts@Amherst*, 27 July–1 August, 1997.
- K.J. Frutschy, and R.J. Clifton, High-Temperature Pressure-Shear Plate Impact Studies on OFHC Copper and Pure WC, *Proceedings of 1997 APS Meeting on Shock Compression of Condensed Matter held at Univ. of Massachusetts@Amherst*, 27 July–1 August 1997.
- M. Zhou, and R.J. Clifton, Dynamic Constitutive and Failure Behavior of a Two-Phase Tungsten Composite, *J. Appl. Mechs.*, **64**, (1997), 487–494.
- K.E. Duprey, and R.J. Clifton, Plastic Flow of Tantalum at High Strain Rates, *Proceedings, International Conference on Tungsten and Refractory Metals—1194, Metal Powder Industries Federation*, Princeton, New Jersey.
- K.J. Frutschy and R.J. Clifton, High-Temperature Pressure-Shear Plate Impact Experiments on OFHC Copper, (to appear in *J. Mechs. Phys. Solids*).
- K.J. Frutschy and R.J. Clifton, High-Temperature Pressure-Shear Plate Impact Experiments Using Pure Tungsten Carbide Impactors, (to appear in *Experimental Mechanics*).

DYNAMIC DEFORMATION AND FAILURE MECHANICS OF MATERIALS

Conference in honor of Professor Rodney J. Clifton, Brown University, on the occasion of his 60th Birthday, Beckman Institute Auditorium, California Institute of Technology, Pasadena, CA, U.S.A. May 22–24, 1997.

Coordinating Committee

G. Ravichandran, A.J. Rosakis, M. Ortiz (Caltech); Y. Rajapakse (Office of Naval Research); K. Iyer (Army Research Office).

Sponsors

The sponsorship of the Office of Naval Research, the Army Research Office and the Provost's Office of the California Institute of Technology is gratefully acknowledged.

PROGRAM

Thursday, 22 May

Session I

Chair: Y. D. S. Rajapakse, Office of Naval Research
(a) Dynamic Constitutive Laws

- K. T. Ramesh (Johns Hopkins University): Grace under Pressure: The Strength of Liquids.
K. J. Fruttschy (Brown University): High-Temperature Pressure-Shear Plate Impact Experiments.
A. Gilat (Ohio State University): Experiments with the torsional Split Hopkinson Bar at Strain Rates Above $10,000 \text{ s}^{-1}$.

(b) : Dynamic Fracture-I

- J. W. Morrissey and J. R. Rice (Harvard University): 3D Elastodynamics of Cracking through Heterogeneous Solids: A New Type of Wave on Moving Crack Fronts and Implications for Growth of Disorder.
V. Gupta (University of California-Los Angeles): Measurement of in-situ Interface Strength at Elevated and Cryogenic Temperatures.
P. Kumar (Indian Institute of Technology-Kanpur): Initiation and Propagation Toughness of Delamination Cracks under an Impact Load.
A. J. Rosakis, S. Omprakash, R. P. Singh and D. Coker (Caltech): Intersonic Crack Propagation in Layered Systems.

Session II

Chair : K. Iyer, Army Research Office
 (a) : Mechanics in Multiple Length Scales

A. Xu, J. Wang, Q. Guo (Terra Tek, Inc) and R. J. Clifton (Brown University) : Application of Fluid Fracturing of Poro-Inelastic Media.

L. B. Freund (Brown University) : A Surface Chemical Potential for Elastic Solids.

R. Phillips (Brown University) : Failure of Materials : A View from the Atomic Scale.

(b) : Failure under Shock Wave Loading

G. I. Kanel (Russian Academy of Sciences) : Some New Data on Deformation and Fracture of Solids Under Shock-Wave Loading.

N. K. Bourne (University of Cambridge) : Failure Waves in Glasses.

D. P. Dandekar (Army Research Laboratory) : Behavior of Glass under Shock-Induced Tension

Friday, 23 May

Session III

Chair : J. Blume, Brown University
 (a) : Dynamic Failure of Brittle Solids

K. S. Kim (Brown University) : Micromechanics of Dynamic Comminution and Fragmentation of Ceramics

H. D. Espinosa (Purdue University) : A Finite Deformation Multiple-Plane Model for Brittle Materials.

V. Prakash (Western Reserve University) : Numerical Simulations of Dynamic Brittle Failure under Fully Plane Strain Conditions.

(b) : Materials Modeling

R. Abeyaratne (MIT) and J. K. Knowles (Caltech) : On the Kinetics of the Austenite-Martensite Transformation Observed in the Escobar-Clifton Experiments.

R. D. James (University of Minnesota) : New Materials with Exceptionally Large Magnetostriction.

X. Markenscoff (University of California-San Diego) : Applications of Cosserat Spectrum Theory to Viscoelasticity.

P. Rosakis (Cornell University) and J. K. Knowles (Caltech) : Unstable Kinetic Relations and the Dynamics of Solid-Solid Phase Transitions.

Session IV

Chair: G. Yoder, Office of Naval Research
(a): Plasticity and Nonlinear Mechanics

- L. Anand (Massachusetts Institute of Technology): Plastic Deformation of F.C.C. Materials by Slip and Twinning.
M. Ortiz (Caltech): Nonconvex Energy Minimization and Dislocation Structures in Ductile Single Crystals.
J. G. Gonzalez and W. G. Knauss (Caltech): Strain Inhomogeneity and Discontinuous Crack Growth in a Particulate Composite.

(b): Dynamic Fracture-II

- A. Needleman (Brown University): Modeling of Dynamic Ductile Fracture.
G. Ravichandran, P. R. Guduru, R. P. Singh and A. J. Rosakis (Caltech): Dynamic Crack Initiation in Ductile Steels.
K. W. Klopp (SRI International): Validation of Railroad Tank Car Accident Damage Assessment Guidelines.

Saturday, 24 May

Session V

Chair: D. Barnett, Stanford University
(a): Wave Propagation

- T. J. Ahrens (Caltech): Impact of Shoemaker-Levy-9 and Chains of Craters on Other Planets.
D. E. Grady (Applied Research Associates, Inc.): Shock-Wave Dispersion in Heterogeneous Solids.
T. W. Wright (Army Research Laboratories): Wave Propagation through a Material with Dispersed Particles.

(b): Plasticity and Damage

- M. R. Begley and J. W. Hutchinson (Harvard University): Size Dependent Indentation Hardness.
P. S. Steif (Carnegie Mellon University): Damage in Gamma Titanium Aluminides Due to Small Particle Impacts.
W. Tong (Yale University): Strain Characterization of Propagative Deformation Bands.

Session VI: Shear Localization
Chair: K. S. Kim, Brown University

- A. Molinari (University of Metz): Steady Propagation of a Shear Band under Dynamic Conditions.
J. R. Klepaczko (University of Metz): Remarks on Impact Shearing.
M. Zhou (Georgia Institute of Technology): Dynamic Shear Failure Resistance of Structural Metals.



Pergamon

J. Mech. Phys. Solids, Vol. 46, No. 10, pp. 1699–1722, 1998

© 1998 Elsevier Science Ltd. All rights reserved

Printed in Great Britain

0022–5096/98 \$—see front matter

PII: S0022-5096(98)00068-4

ON THE COMPRESSIBILITY OF A GLASS-FORMING LUBRICANT: EXPERIMENTS AND MOLECULAR MODELING

Y. ZHANG and K. T. RAMESH*

Laboratory for Impact Dynamics and Rheology, Department of Mechanical Engineering,
The Johns Hopkins University, Baltimore, MD 21218, U.S.A.

(Received 20 December 1997; in revised form 6 April 1998)

ABSTRACT

A very large number of technologically important liquids, including lubricants, undergo a glass transition under increasing pressure, decreasing temperature, or increasing rate of deformation (one may consider the glassy solid to be a supercooled liquid). The compressibility of glass-forming lubricants has a strong influence on the modeling of elastohydrodynamic (EHD) contacts, where pressures (as high as several GPa) are sufficient to induce the glass transition. This paper presents both experimental and analytical studies of the compressibility of a low-molecular-weight synthetic organic lubricant known as 5P4E, which has a simple molecular structure amenable to molecular modeling. The experimental results are obtained using the compression Kolsky bar and pressure–shear plate impact techniques, and show that this lubricant has substantial compressibility under high pressures.

An analytical and computational investigation of the nonlinear compressibility of this simple material based on estimates of the molecular structure and intermolecular interactions is then presented. The molecular structure and the various molecular conformations of the material are examined using relatively simple “molecular mechanics” calculations. An intermolecular interaction energy potential is obtained by examining the interactions of a molecule pair, and the molecular structure and interaction potential estimates are used together to provide a prediction of the material’s nonlinear compressibility (although thermal effects are not completely accounted for in the model). All but one of the parameters in the model are obtained directly from the molecular mechanics computations; the one parameter that must be independently specified is the volume at room temperature and atmospheric pressure, obtained from a simple density measurement. The predicted compressibility is found to be in remarkably good agreement with the experimental data. © 1998 Elsevier Science Ltd. All rights reserved.

Keywords: A. thermomechanical processes, B. constitutive behavior, glass material, C. Kolsky bar, molecular structure.

1. INTRODUCTION

A very large number of technologically important liquids, including lubricants, undergo a glass transition under increasing pressure, decreasing temperature, or increasing rate of deformation. This transition to a glass state can occur under the typical operating conditions of devices and machinery, and so the mechanical properties of the glassy solid are of great interest. For example, lubricants are commonly in the glassy state within typical elastohydrodynamic contacts such as meshing gear

* Author to whom correspondence should be addressed. E-mail: ramesh@jhu.edu

teeth, ball and roller bearings, and precision mechanical devices. Biological liquids such as synovial fluid may be forced into the glassy state within animal joints. And recent work (Prosperetti, 1997) suggests that the phenomenon of sonoluminescence in single water bubbles may be the result of the impact of a water jet (developed during bubble collapse) on the bubble wall, where the water has been rendered glassy by the very short times and high rates of the interaction.

The organic substances that form glassy solids may be separated into two classes with substantially different behaviors: low-molecular weight organics such as oils and hydrocarbons, and high-molecular weight organics such as polymers. Low-molecular weight organics ($M_w < 10^3$) undergo a direct liquid-to-glass transition; high molecular weight organics ($M_w > 10^4$) develop an intermediate rubbery phase (liquid-to-rubbery-to-glass). This difference in behavior reflects an important distinction in mechanism for large molecular weight organics, the statistics of chain entanglements are extremely important, whereas such entanglements are rare at low molecular weights. This paper focuses on a low-molecular-weight organic glass-forming material, so that chain entanglements are not an issue. Inorganic glasses such as metallic glasses evince peculiarities in their behavior that require special treatment, and will not be considered here.

Low-molecular-weight organic glassy solids are interesting from a continuum viewpoint, since such solids are real examples of isotropic homogeneous media with the added benefit that the internal molecular mechanisms are directly manifested in the continuum properties. For most traditional engineering materials, it is extremely difficult to properly make the connection between atomic or molecular structure and the macroscopic properties, because intermediate microstructural variables (such as grain size and dislocation substructure in metals or degree of polymerization in polymers) control the behavior. However, in the case of low-molecular-weight organic glasses, there are no intermediate microstructural features to obscure the molecular mechanisms. At the same time, these materials (generally hydrocarbons) are sufficiently simple that their molecular structures can be studied, and understanding the molecular mechanisms that determine macroscopic mechanical behavior will provide a theoretical basis for the molecular design of new materials.

This paper focuses on the characterization of the compressibility of a glass-forming synthetic lubricant that is a low-molecular-weight hydrocarbon. The choice of material is dictated by the technological importance of lubrication within today's mechanized civilization. Proper lubrication is required for the satisfactory operation of all contacting machine elements with relative motion. Within these machine elements, especially in elastohydrodynamic (EHD) contacts, lubricants are subjected to pressures as high as several GPa (at these pressures, most lubricants are glassy solids). The compressibility of the lubricant influences the oil film shape and thickness and thus has a strong influence on the functioning of the contact. Thus, knowledge of the compressibility is of great importance for the accurate modeling of lubrication. At the same time, the compressibility is the macroscopic property most amenable to simple mechanistic modeling in terms of molecular structure.

The next section reviews some of the literature on the compressibility of glassy solids and simple liquids. A section describing the specific lubricant investigated follows. The basic experimental techniques used to measure compressibility and their

results are then reviewed. Next, the molecular structure of the lubricant is estimated using simple molecular mechanics computations, and the computed intermolecular interactions are used to estimate the compressibility of this synthetic lubricant. Finally, the predicted compressibility is compared to the experimental data on this material.

2. BACKGROUND

The compressibility of materials has been extensively studied in the context of the pressure–volume–temperature (*PVT*) relation known as the Equation of State (EOS). The characterization of the EOS is of interest to a number of fields, including geophysics, condensed matter physics, and mechanics. A large fraction of the literature, driven by geophysics, focuses on the EOS of minerals and ceramics. A substantial amount of work has been performed on metallic materials from a shock physics viewpoint, and some work has also been done on the compression of liquids such as benzene under extremely high pressures through shock waves (e.g. Dick, 1970; Nellis, 1994). Progress in describing the equation of state has proceeded along two fronts. A very large effort has been expended on the experimental characterization of material behavior, and a number of empirical models have been constructed to describe the observed behavior. A substantial literature has recently evolved on the theoretical (and even first principles) development of equations of state.

The experimental effort has been driven by the availability of techniques for high-pressure measurements, beginning with the early work of Bridgman (1940) using full-scale quasistatic compression. The advent of shock loading techniques, especially with the two-stage gas gun, significantly accelerated the characterization of the EOS of materials. More recently, the development of the diamond anvil cell and associated instrumentation has allowed the independent measurement of material parameters for comparison with the shock physics data. Measurement of the variation of moduli with pressure using ultrasonics has also been a potent experimental tool. Put together, these techniques have provided a fairly clear picture of the volumetric behavior of solids under large compressions, but comparatively few results are available for liquids.

Theoretical developments in the understanding of the compressibility on the equation of state can be broadly classified within two categories: those approaches that are based on an atomistic or molecular understanding of the microphysics, and those approaches that examine the behavior from a macroscopic viewpoint. A very large activity currently exists in the development of models of material behavior from a first-principles or a quantum mechanical viewpoint. These models generally involve vast computations, and while fascinating from a purely scientific viewpoint, are not yet sufficiently advanced to provide general utility. At one level up in scale, models have been developed based on interatomic pair potentials, with parameters based on other experimental measurements or obtained from first principles calculations. A large variety of potentials has been used, with the most common being the Lennard–Jones and Born–Mayer forms; a number of these are semi-empirical functions. Since such potential-based models typically are only valid at zero K, thermal corrections are typically incorporated in the Mie–Grüneisen form through the Grüneisen

parameter. At the macroscopic scale, models for the EOS have been developed in terms of finite elastic deformations, such as the Birch–Murnaghan equation, and on an essentially empirical basis, such as the Murnaghan equation. Vinet (1986) provides a succinct review of such equations of state. A more recent review of several of these topics (and an outstanding exposition of the physics) is provided by Anderson (1995).

In a series of papers (Rose *et al.*, 1984, Vinet *et al.*, 1987, 1989), a number of researchers have proposed a universal scaled energy relation for all classes of solids (metallic, covalent, ionic, van der Waals). The form of this universal relation was inferred from analysis of energetics and determined by fittings to experimental isothermal compression data. Vinet *et al.* (1989) have shown that compressibility relations derived from this universal form can be fitted fairly well to a great variety of materials (e.g., Ne, Kr, H₂, NaCl, KI and silicone). These “universal” relations are discussed more completely later in the modeling section of the paper.

2.1. *The compressibility of simple organic liquids*

The EOS for the liquid state of matter is not as well characterized as that for the solid state, and this is even more so when one considers organic liquids rather than atomic or simple inorganic liquids. Several hard sphere and soft sphere models have been proposed for the liquid state, and have found some success in dealing with liquid metals, but are generally unable to handle organic liquids (larger, more complex molecules generally lead to flaws in the sphere assumption). There is as yet no simple theoretical equation of state for liquids, although some of the empirical models previously mentioned for solids have been used to describe their behavior. Indeed, a common assumption is that models applied to solids can also be applied to liquids, ignoring the intrinsically disordered nature of the liquid state. Sanchez *et al.* (1993) found universal aspects of the compression of liquids and solids; their interaction potential was approximated by a series expansion with parameters determined from fittings to experimental data. Similar work can be found in Baonza *et al.* (1994). Of the empirical relationships, the Murnaghan equation appears to provide a reasonable description of the real behavior of liquids at low pressures. A theoretical basis for this fact has been presented by Song *et al.* (1993) in terms of a statistical mechanics-based equation of state.

Extensive experimental research has been performed on the compression of liquids under extremely high pressures through shock waves (e.g. Dick, 1970; Nellis, 1994). Experimental work at lower pressures is scattered widely in the literature, depending on the materials studied (e.g. Linton, 1920; Wahid, 1993). Computational studies of liquid compressibility are largely limited to very simple liquids such as water (e.g. Motakabbir and Berkowitz, 1990).

The focus of this paper is on the compressibility of lubricants, which are simple organic liquids at room temperature and atmospheric pressure. The compressibility of lubricants is critical to the understanding of elastohydrodynamic (EHD) lubrication, which is one of the most significant problems in tribology. Unfortunately, none of the studies mentioned above provide information on the compressibility of such materials. The materials studied to date in the literature generally have molecular weights that are either too high (as in polymer solids) or too small (as in simple

liquids, although benzene and the alkanes come close). Moreover, the pressures in the majority of the studies are not in the range 1–5 GPa developed within elastohydrodynamic contacts. Most liquid and polymer data to date has been obtained under pressures below 300 MPa, while most data for solids are for pressures above 10 GPa. Thus, despite the rich literature on the compressibility and the equation of state of solids and liquids, it is necessary to obtain both experimental data on the compressibility of lubricants and to develop a model to describe their volumetric behaviors.

2.2. The compressibility of lubricants

Almost all of the literature on lubricant compressibility is experimental (e.g. Barlow *et al.*, 1972). Dowson and Higginson (1977) measured the compressibility of a mineral oil at pressures up to 400 MPa and suggested an empirical compressibility equation based on their data:

$$\frac{\rho}{\rho_0} = 1 + \frac{0.6P}{1 + 1.7P} \quad (1)$$

where the unit of pressure P is GPa, ρ is the density of the oil in kg/m³, and ρ_0 is the density at atmospheric pressure. This relation has been widely used in simulations of EHD lubrication (e.g., Jacobson and Hamrock, 1984). However, its validity under high pressure is questionable, since eqn (1) was obtained by fitting data from measurements that were only made at relatively low pressures, and pressures over 1 GPa are commonly encountered within elastohydrodynamic contacts. Hamrock *et al.* (1987) performed a series of quasistatic measurements of the compressibility of several hydrocarbons up to pressures of 2.2 GPa; they observed that the Dowson–Higginson relationship was not valid at higher pressures for synthetic lubricants, and suggested another empirical pressure–volume relation that was parabolic in the liquid state and linear in the glassy state. Measurements of the high frequency longitudinal and bulk moduli of the polyphenyl ether 5P4E were made by Bezot *et al.* (1986) over a small range of pressures (up to 400 MPa) and over a range of temperatures using a light scattering technique. A very strong dependence of the moduli on pressure and temperature was observed. Jacobson and Vinet (1987) were able to fit an equation of state developed by Vinet *et al.* (1987) to the data published by Hamrock *et al.* (1987) for pressures as high as 2.2 GPa.

Ramesh (1991) and Feng and Ramesh (1993) measured the dynamic compressibility of two lubricants for pressures as high as 5 GPa and (at lower pressures) over a range of temperatures using the compression Kolsky bar (Feng and Ramesh, 1993) and pressure–shear plate impact techniques (Ramesh and Clifton, 1987; Ramesh, 1991; Zhang and Ramesh, 1996). Based on these results, Feng and Ramesh (1993) presented a model for the pressure–volume relationship derived from a linear shock–velocity/particle–velocity Hugoniot:

$$P = \frac{K[1 - V/V_0]}{[1 + a\{(V/V_0) - 1\}]^2} \quad (2)$$

Here K and a are material constants related to the low-pressure bulk modulus and

the slope of the Hugoniot respectively. The current paper will make extensive use of the experimental compressibility measurements from the Ramesh (1991) and Feng and Ramesh (1993) papers; the experimental techniques themselves are briefly described in the interests of completeness.

This paper develops an analytical prediction of lubricant compressibility based on a characterization of molecular interactions. A P - V relation (similar to that developed by Vinet *et al.*, 1989) is established for a simple synthetic lubricant based largely on molecular mechanics calculations, and the predictions of this model are compared with experimental data on the material. A brief description of the material itself follows.

3. A MODEL MATERIAL: THE SYNTHETIC LUBRICANT 5P4E

The material examined in this paper is a synthetic lubricant, a five-ring polyphenyl ether known as 5P4E. 5P4E is a polyphenyl ether of molecular weight 446. Because of this simple structure, the range of isomers is limited and the possible forms are very similar. One form is known as bis- (m- (m-phenoxy phenoxy) phenyl) ether or bis- (phenoxy phenoxy) benzene. Figure 1 is a schematic drawing of this molecular structure. Note the five phenyl rings and the four ether linkages—hence the name 5P4E.

There are three reasons for the choice of 5P4E as a model material for this work :

- it has been widely studied, and so there is extensive experimental data on its properties available in the literature;
- as a synthetic, it has relatively uniform properties from batch to batch, so that a comparison of several experimental results is appropriate (a particular issue with lubricants);
- it has a relatively simple molecular structure, amenable to molecular mechanics computations.

At room temperature and ambient pressure 5P4E is a viscous, clear, light yellow liquid with the consistency of a thin shampoo. This material undergoes a transition to the glassy state on cooling at a temperature of about -40°C at ambient pressure. As is the case with most simple organic liquids, the glass transition can also be developed by increasing the pressure at constant temperature: in the case of 5P4E, the glassy state is achieved on increasing the pressure to above 160 MPa at room temperature. The glass transition itself is not discussed in this paper, and most of

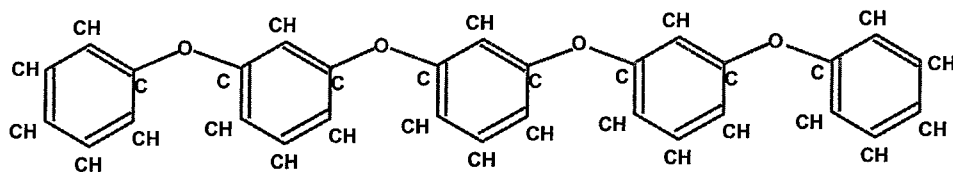


Fig. 1. Schematic diagram of the chemical structure of an isomer of 5P4E.

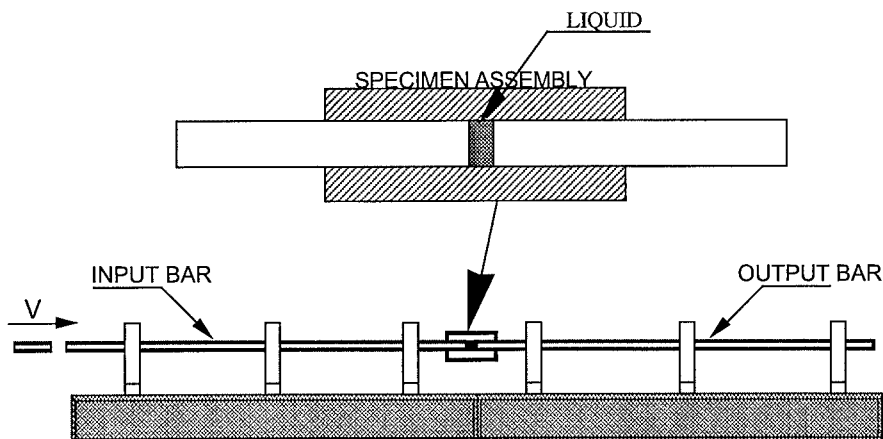


Fig. 2. The modified compression Kolsky bar experiment for compressibility measurement. The inset shows the specimen assembly used for the experiments.

the pressures that are considered are above the glass transition pressure at room temperature (thus the properties of the glassy solid are being discussed, rather than those of the liquid). The fact that the glass transition can be achieved either by cooling at constant pressure or by pressurizing at constant temperature indicates that a volume-driven molecular mechanism is involved. A molecular basis for the evaluation of the glass transition itself is presented in a separate paper (Zhang and Ramesh, 1998).

4. EXPERIMENTAL TECHNIQUES AND RESULTS

Two experimental techniques are briefly described for measurement of the dynamic compressibility: the compression Kolsky bar technique and pressure-shear plate impact experiments. Both of these techniques employ stress waves to induce compression in the specimen; they can achieve high pressure levels in very short times and therefore measure the adiabatic compressibility.

4.1. *The compression Kolsky bar technique for measurement of the compressibility*

The traditional Kolsky bar (Kolsky, 1949) or split-Hopkinson pressure bar was modified to be able to measure the compressibility of lubricants (details may be found in Ramesh, 1991; Feng and Ramesh, 1993). The Kolsky bar itself consists of an input bar, an output bar and a specimen assembly (Fig. 2). A projectile fired from a gas gun impacts one end of the input bar and generates a compressive stress pulse propagating down the bar into the specimen. The specimen assembly is a thick-walled cylinder containing a thin layer of the material to be studied confined between two pistons. The incident pulse reverberates within the lubricant layer until the layer reaches an equilibrium stress state. The pulse transmitted into the output bar carries

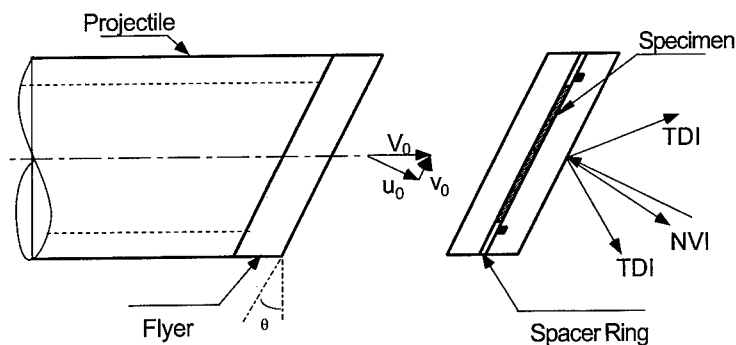


Fig. 3. Schematic diagram of the experimental configuration used for pressure-shear plate impact experiments on simple organic liquids and glasses.

information about the magnitude of this stress, and the pulse reflected into the input bar carries information about the displacement of the bar-specimen interfaces. The bars are designed to remain elastic throughout the test.

Since the cylinder is nearly rigid, essentially uniaxial strain conditions are generated so that the volume ratio is related to the relative displacement of the two bar-specimen interfaces. Detailed analysis (Ramesh, 1991) shows that the axial stress in the specimen approaches a uniform hydrostatic pressure (essentially the difference between the axial and transverse stress is proportional to a shear stress, and this shear stress relaxes if the material has a viscous response). Thus the pressure-volume response of the lubricant can be determined from the strain gauge measurements of the incident, reflected and transmitted pulses. By changing the initial temperature of the specimen, the pressure-volume-temperature behavior can be determined. The technique is limited to pressures of about 1.2 GPa because of yielding in the bars and cylinder.

4.2. Plate impact experiments

Pressure-shear plate impact experiments have been used in the study of both the compressibility and the shear rheology of liquids under high pressures and high shear rates (e.g. Ramesh and Clifton, 1987; Ramesh, 1991; Zhang and Ramesh, 1996). The experimental configuration is shown in Fig. 3. A projectile carrying a two-inch diameter plate (the "flyer") is accelerated down the barrel of a light gas gun and impacts a parallel stationary target. Impact occurs at a known projectile velocity v_0 and at a skew angle θ in an evacuated chamber. The target consists of two flat plates which confine a thin ($\sim 25 \mu\text{m}$) layer of the lubricant sealed into the assembly by means of an O-ring. The thickness of the lubricant layer is determined by a ring of aluminium shim stock. All of the plates remain elastic during the test, so that stresses at the interface between the lubricant and the rear plate can be computed from measured particle velocities at the rear surface of the target. Laser interferometers are set up to measure the transverse particle displacement and normal particle velocity at the rear surface of the target. The experiments are designed such that no unloading waves from the periphery of the specimen arrive at the point of observation during the time

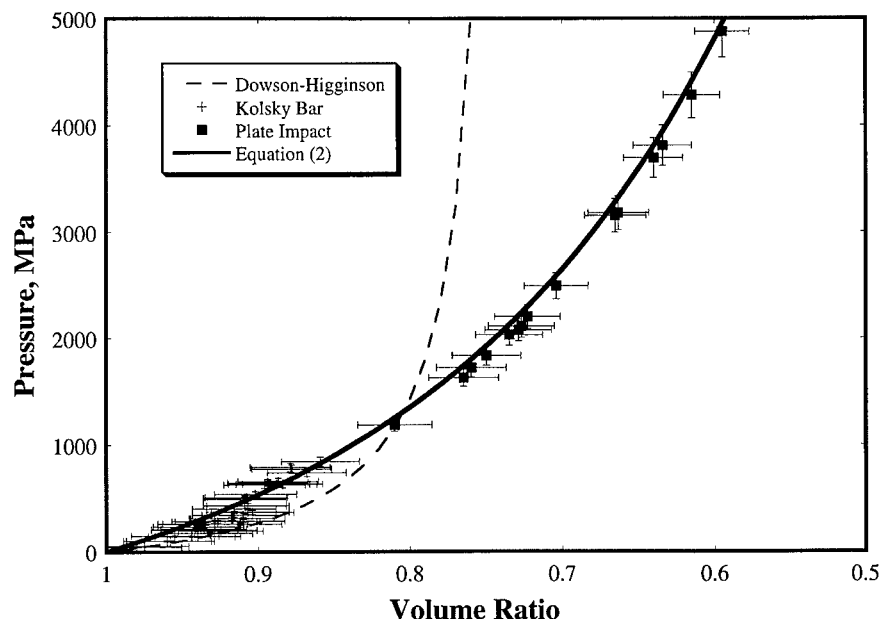


Fig. 4. Experimental compressibility data obtained from Kolsky bar and plate impact experiments. The dotted line is the Dowson-Higginson relation, eqn (1) extrapolated to these pressures (the original Dowson-Higginson parameters were obtained up to 400 MPa), and the solid line is the Hugoniot relation, eqn (2).

of data acquisition, thus ensuring that the experimental results can be interpreted entirely in terms of the propagation of plane waves. This is thus a truly one-dimensional problem, and the specimen is subjected to very well-characterized loading conditions.

Upon impact, both longitudinal and transverse waves are sent into the flyer and front plates. Since the longitudinal wave travels faster than the transverse wave, it arrives at the lubricant first and reverberates within the lubricant layer. Because of the finite compressibility of the layer, and because the lubricant is surrounded by higher impedance materials, the longitudinal stress in the lubricants rings up to a constant value. Eventually a nearly hydrostatic state of compression is developed in the lubricant (Ramesh and Clifton, 1992). A series of tests at different pressures gives the compressibility of the lubricant over a range of pressures. Shearing information is obtained from the transverse waves, but is not of interest to this paper.

4.3. Experimental results

The experimental data presented by Feng and Ramesh (1993) on the compressibility of 5P4E are shown in Fig. 4 (all of the tests were performed at room temperature, $\sim 30^\circ\text{C}$). Although not shown in Fig. 4, the compressibility results at low pressures are very consistent (Feng and Ramesh, 1993) with the results obtained (using completely different techniques) by Barlow *et al.* (1972), Alsaad *et al.* (1978) and Bezot *et al.* (1986). It is obvious that this material exhibits substantial compressibility,

especially in the high-pressure regime; this is of importance to the modeling of elastohydrodynamic contacts, where pressures of 2–3 GPa may be developed. Note that the traditional Dowson–Higginson relation, eqn (1), underestimates the compressibility of this lubricant at high pressures. Note also that most of this data is well above the glass transition pressure, and represents the compressibility of the glassy solid. The error bands on this data at low pressures are such that the change in compressibility through the glass transition cannot be captured through these techniques. A fit obtained using eqn (2) is also presented in Fig. 4. Clearly such a two-parameter model can describe the observed behavior, but the parameters, while physically motivated, must be determined from the data.

In the remainder of this paper, a model is developed that is able to capture the experimental behavior shown in Fig. 4. The model is based on a fundamental analysis of the molecular structure of the material and the corresponding intermolecular interactions. Note that the experimental techniques presented here are essentially adiabatic, since the timescales of the experiments ($\sim 10^2 \mu\text{s}$ for the Kolsky bar and $\sim 1 \mu\text{s}$ for plate impact) are so short that there is no time for a significant heat flux. Thus, the measurements are of the adiabatic pressure–volume behavior rather than of the isothermal behavior.

5. A MOLECULAR BASIS FOR THE COMPRESSIBILITY

For adiabatic deformations that involve only the volume changes considered here, the pressure can be obtained directly from the internal energy E :

$$P = -\left(\frac{\partial E}{\partial V}\right)_S \quad (3)$$

For isothermal deformations the corresponding relation would be

$$P = -\left(\frac{\partial F}{\partial V}\right)_T \quad (4)$$

where F is the Helmholtz free energy of the glass solid and:

$$F = E - TS. \quad (5)$$

Here E is the internal energy, T is the temperature and S is the entropy. The traditional approach to the equation of state (Anderson, 1995) for glasses would consist of separating the Helmholtz free energy into two parts: $F = E_0 + E_{\text{TH}}$, where E_0 is the internal energy at absolute zero and E_{TH} is the thermal contribution to the Helmholtz free energy of the molecules (for these organic materials, the contribution due to the free electrons is negligible). The use of eqn (4) would then provide the isothermal pressure–volume response. However, the experimental data of Fig. 4 in fact represents the adiabatic response, and so eqn (3) is the appropriate approach to developing the compressive response of the material. Once the form of the internal energy E has been determined, the compressibility can be obtained directly from eqn (3).

Previous researchers have used several different ways to establish E . For example,

Sanchez *et al.* (1993) used a series expansion to approximate E with all of the parameters determined by curve-fitting to experimental data. Porter (1995) used group interaction modeling theory to relate E to the "cohesive energy," which is also obtained from experiments. However, most of these methods rely on experimental measurements of the compressibility to determine the free parameters, and thus are not truly predictive.

The intent here is to provide a molecular basis for the prediction of compressibility. E is viewed as the internal energy of a system consisting of a collection of 5P4E molecules. The internal energy at absolute zero (E_0) of a system of molecules of the type shown in Fig. 1 is first computed, and then a correction for the thermal effects is employed to obtain E . Equation (3) is then used to estimate the adiabatic compressibility of the material. Note that at absolute zero the Helmholtz free energy reduces to just the internal energy, and the adiabatic and isothermal compressibilities are identical.

A well-developed branch of computational chemistry known (in that literature) as "molecular mechanics" provides the information needed for the computation of E_0 . Thus, the potential E_0 is obtained directly from molecular level information rather than from macroscopic mechanical measurements. A brief description of this branch of computational chemistry is provided below, and a much more detailed description can be found in Zhang (1997).

5.1. The molecular mechanics approach and associated assumptions

The basic ideas of "molecular mechanics" are the following (Allinger, 1992). A molecule is described in terms of a collection of nuclei distributed on a potential energy field provided by the electrons. The potential surface can be described by a series expansion about the point of minimum energy; in the typical approximation, only the first and second-order terms in the expansion are used. The typical bond energies used may be expressed as follows (e.g. Gelin, 1994):

$$\text{stretching: } E_{\text{bond}} = K_b(R - R_0)^2 \quad (6)$$

$$\text{bending: } E_{\text{angle}} = K_\theta(\theta - \theta_0)^2 \quad (7)$$

$$\text{torsion: } E_{\text{torsion}} = K_\varphi\{1 + \cos(n\varphi - \delta)\} \quad (8)$$

$$\text{van der Waals: } E_{ij}^{\text{vdw}} = \frac{A_{ij}}{R_{ij}^n} - \frac{B_{ij}}{R_{ij}^m} \quad (9)$$

$$\text{electrostatic: } E_{ij}^{\text{es}} = \frac{Cq_i q_j}{\epsilon R_{ij}} \quad (10)$$

In these equations R is the bond length, R_0 is the bond length at the equilibrium position, θ is the bending angle, θ_0 is the bond angle at the equilibrium position, φ is the torsion angle, R_{ij} is the bond length between atoms i and j , and q_i is the electric charge corresponding to atom i . The force constants K_b , K_θ , K_φ , A_{ij} and so forth in eqns (6–10) are usually obtained by either curve-fitting to non-mechanical experimental data, such as spectroscopic and X-ray diffraction measurements, or from *ab*

initio calculations. Note that the energy approximations represented by eqns (6–10) are by no means unique; other (generally similar) approximations exist and are used. The collection of parameters required for each set of approximations is called a “force field” within the computational chemistry literature, and specific force fields have been established for particular types of compounds. Spectroscopists have shown (Allinger, 1992) that the force parameters obtained from one kind of molecule can be transferred to another with a high degree of precision if both kinds of molecules form part of a series of closely related compounds. The particular parameter set used here, corresponding to eqns (6–10), is a variant of the Amber force field (Weiner *et al.*, 1984) which was developed specifically for modeling complex organic compounds. The parameters in Amber were chosen so that computations on simple organic compounds (e.g. ethane, propane, and dimethyl ether) will yield results consistent with experimental observations (the molecular structure of 5P4E is similar to that of the calibration compounds).

The total energy of one conformation of a single molecule can be calculated by summing all of the energy terms in eqns (6–10):

$$E_{\text{total}} = \Sigma E_{\text{bond}} + \Sigma E_{\text{angle}} + \Sigma E_{\text{torsion}} + \Sigma [E_{ij}^{\text{dw}} + E_{ij}^{\text{cs}}] \quad (11)$$

Note that the thermal vibration energy term is not included in the above equation. Physically, this means that the total energy calculated in eqn (11) is essentially the energy at absolute zero (the small quantum mechanical vibration term at zero temperature is also ignored). One may therefore view these calculations as molecular statics rather than molecular dynamics; the thermal effects are incorporated in due course. Different molecular conformations will have different energies through eqn (11), and the most stable conformations will be those with the lowest total energies. In order to obtain a qualitative idea of the size and shape of individual molecules, the next step is to find the low-energy conformations of the molecule (at zero K). This is achieved by a process of energy minimization.

The molecular mechanics computations in this work were performed using Macro-Model (V5.0) developed by Mohamadi *et al.* (1990). The total energy of the collection of atoms and bonds constituting a single 5P4E molecule is minimized by exploring configuration changes that lower the energy. The numerical approach consists of applying the method of steepest descent, followed by Polak–Ribiere conjugate gradient minimization, followed by a full-matrix Newton–Raphson algorithm (in that sequence, with increasing algorithmic efficiency as one approaches the minimum). Using these techniques for the energy minimization, one obtains the minimum-energy conformation (at zero K) of a single 5P4E molecule presented in Fig. 5. While there is no way of proving that this is an absolute minimum, an extensive Monte-Carlo conformational search about this minimum was unable to find other minima. The molecular conformation of Fig. 5 will henceforth be referred to as the minimal conformation. Note that this minimal conformation is quite different from the linear chain conformation evoked by the schematic of Fig. 1. Instead, the minimal conformation closely resembles a rounded tetrahedron with a 10 Å base to vertex height, and with insufficient space within the conformation to accommodate even another hydrogen atom. Of course, other higher energy conformations of the molecule will

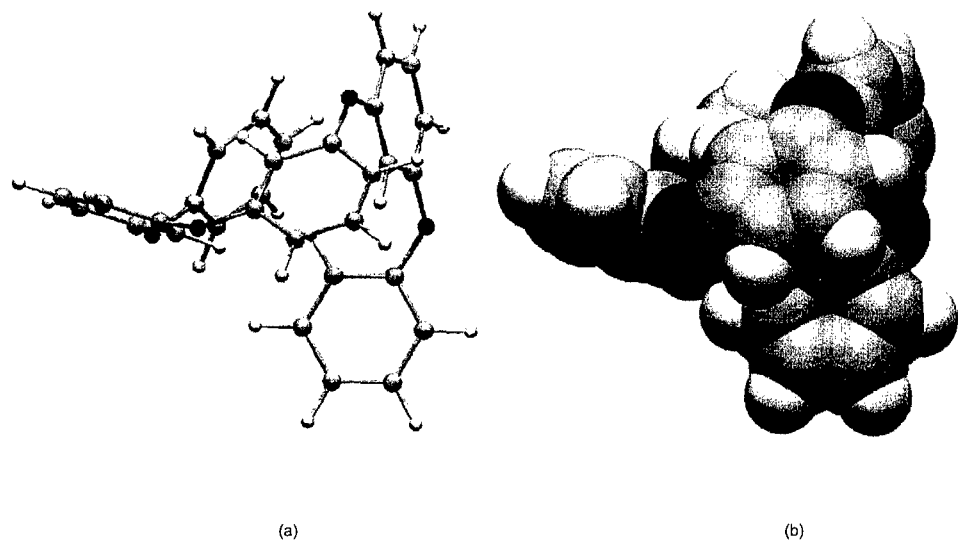


Fig. 5. Computed minimal conformation of the 5P4E molecule: (a) in ball-and stick mode, showing the relationship to Fig. 1; (b) with atomic radii shown at 70% of the known van der Waals radii. The darkest atoms are oxygen atoms, the gray atoms are carbon, and the light gray atoms are hydrogen. There is insufficient space between the atoms to incorporate even another hydrogen atom, so that all of the space within an envelope surrounding the molecule is effectively excluded.

also exist in the real material at room temperature, with a probability distribution largely determined by Boltzmann statistics.

The material compressibility, however, is a function of the interactions between molecules rather than solely of the molecular conformations themselves. Consider the simple case of the interactions of a pair of molecules, and for the moment, assume that those interactions are indicative of the response of the entire material (for hydrostatic compressions). When the two molecules are sufficiently far apart, neither feels the influence of the other, and the single molecule solutions hold. However, as the two molecules are brought closer together the total energy of the system becomes dependent on more than just the internal energies of each individual molecule, since the interaction energies begin to contribute strongly to the energy of the system. Of particular importance is the fact that each molecule will change its conformation because of the interactions with the other molecule, in order to minimize the total energy (the system is most stable when the energy is a minimum). Therefore, computations of the total energy E of the two-molecule system should include the effects of conformational changes.

The total energy $E(d)$ as a function of the intermolecular distance d is obtained through the following procedure. Initially two 5P4E molecules (each in the minimal conformation) are placed far apart so that the interactions between them are negligible, and the total energy of this system is calculated. The total system energy is now minimized by allowing the two molecules to approach each other and simultaneously change their conformations. Computational estimates of E and d are obtained by evaluating these quantities repeatedly during the minimization process. The inter-

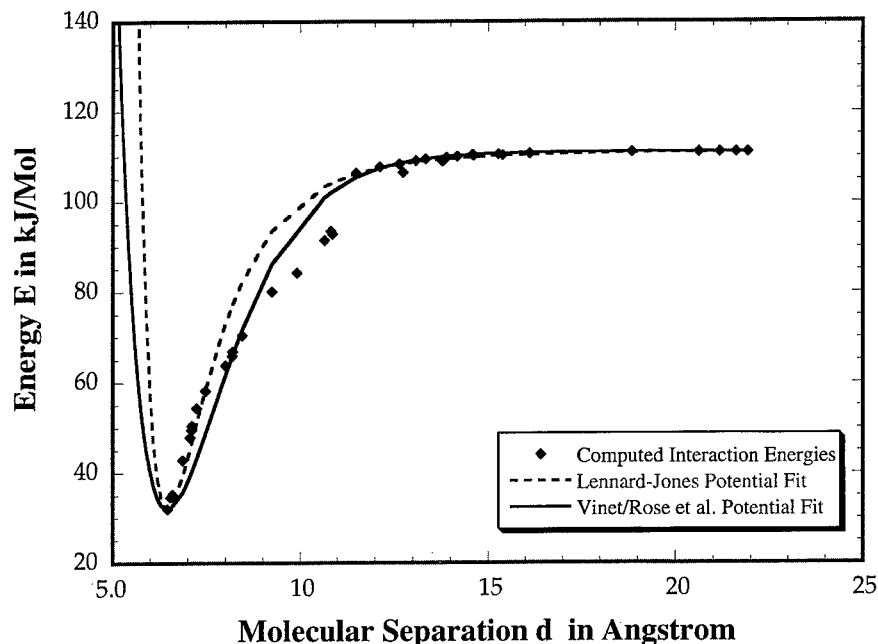


Fig. 6. The internal energy of a two-molecule 5P4E system as a function of intermolecular separation, as computed through the energy minimization process discussed in the text. The dashed line is a fit to a Lennard-Jones potential, eqn (14), and the solid line is the fit to the Vinet/Rose *et al.* potential, eqn (16).

molecular distance d is strictly the distance between the centers of the molecules as computed from the instantaneous positions of all atoms in the molecule. However, an approximate molecular center is defined in terms of the positions of the oxygen atoms in the molecule; this approximation is found to be very good (error $\leq 1\%$) for the extremal (i.e. initial and final) molecular conformations developed. The energy minimization is continued until the two-molecule system reaches a minimum; the gradient at the minimum is as close to zero as can be achieved with the available computing capacity (an SGI Power Challenge with six processors). The resulting $E(d)$ is the function used to derive the P - V relation using eqn (3).

However, energy minimization processes starting with different initial positions or orientations of the two molecules may develop different $E(d)$ relations, since the 5P4E molecule does not possess spherical symmetry. An extensive computational evaluation of such intermolecular interactions was performed over a representative range of possible initial orientations (discretized in terms of Euler angles). While the form of the $E(d)$ relation did not change significantly, the depth of the energy well at the minimum does change with varying initial relative orientations of the molecules in each molecular pair. The question arises: what is the appropriate $E(d)$ that represents the average interactions among molecule pairs, each of which may have a range of initial orientations? In this work, it is assumed that the $E(d)$ relation that provides the lowest energy in the equilibrium position is the appropriate representation of the average interactions among molecule pairs, and the resulting computed data are presented in Fig. 6 (this data includes the output of two separate minimizations to

show the consistency of the results of the search algorithm). Note that this $E(d)$ relation still represents behavior at zero K: the configurational space that has been explored at this point is entirely an orientational space, not a conformational space (which could reflect thermal effects). Conformational changes are necessarily developed as the two molecules approach each other and individual atoms in the molecules begin to interact: one (2D) view of the final conformations of the two molecules in the equilibrium (lowest energy) state of the two-molecule system is presented in Fig. 7.

The important idealizations and assumptions used so far are summarized below:

- (i) Thermal vibrations are ignored within the computations.
- (ii) No statistical distribution of molecular conformations is considered.
- (iii) Entropic changes are neglected.
- (iv) It is assumed that the macroscopic compressibility can be determined by examining the pair-wise interactions between molecules.

Furthermore, all the computations reported here were performed on the isomer shown in Fig. 1. However, less extensive computations on some of the other isomers show that very similar results are obtained. While the above restrictions correspond to a very strong idealization, this approach will be shown to capture the most significant physics for the hydrostatic compressive state considered.

5.2. Computation of the compressibility from $E(d)$

Since $E(d)$ has been obtained for this material (Fig. 6), a direct application of eqn (3) should give us the pressure-volume relation for 5P4E. However, the application

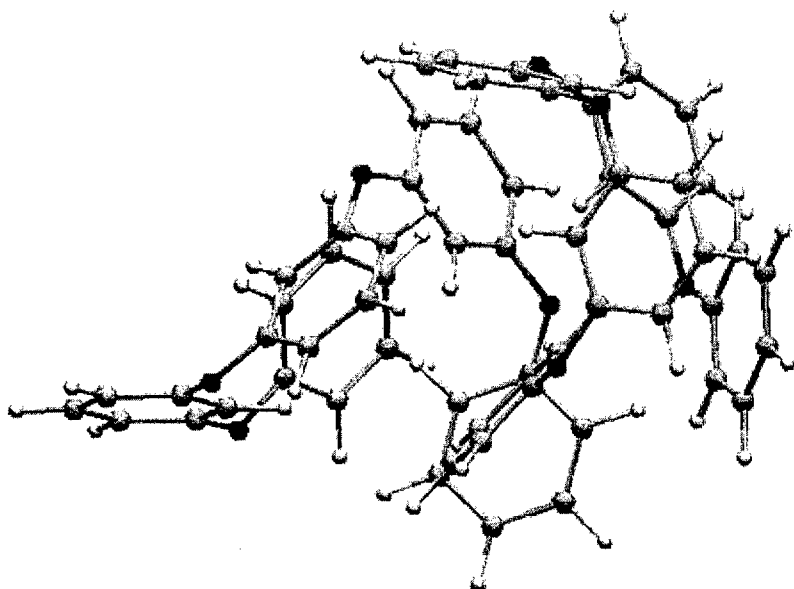


Fig. 7. One view (in ball-and-stick mode) of the final conformations of the two molecules in the two-molecule system at equilibrium. Note the substantial change in conformation from Fig. 5(a).

of eqn (3) requires the use of a derivative, so it is convenient first to develop an analytical form for $E(d)$ that provides a good fit to the computed data. Two analytic forms for $E(d)$ are examined *et seq*: the Lennard-Jones form and the Vinet form. In each case, the corresponding functions are fit to the computed data of Fig. 6, so that in effect the parameters within these energy forms are determined on the basis of molecular-level computations.

It is important to recognize that there are both attractive and repulsive parts to the interactions between molecules. When the molecules are very far apart and are then brought together, the interactions are primarily attractive, and the internal energy of a two-molecule system decreases as the molecules approach (this is the part that has been computed in Fig. 6). Once the minimum in the internal energy is reached (defining the equilibrium separation of the two molecules), further attempts to bring the molecules together results in a repulsive interaction, with the internal energy increasing as the molecules approach. These repulsive interactions may be due, for instance, to an effective interpenetration of electronic orbits and thus a manifestation of the Pauli exclusion principle. Note that similar repulsive interactions would exist for all classes of materials, whether one considers inert gases, ionic crystals, metals, or simple organic molecules (conformational stiffnesses would also contribute in the case of large-molecule systems). Compression away from the equilibrium state would correspond to climbing up the repulsive side of the interaction energy curve; the increase in pressure required to attain this compression is a macroscopic consequence of the repulsive mechanisms at the molecular level. The molecular mechanics approach used here is unable to directly compute the repulsive side of the interaction energy curve, since only energy minimization is feasible and the initial conformations of the highly compressed molecules are unknown. However, the molecular mechanics computations of the attractive side of the interaction energy curve are sufficient to determine the parameters in the analytic forms (Lennard-Jones and Vinet) that are used, and the forms then determine the repulsive interactions.

One should expect that the decohesion of materials (which is strongly determined by the attractive side of the interaction) will be very different depending on the material type (e.g. inert gas, metal or ionic crystal). However, Vinet (1986) espouses the idea of a "universal" equation of state for solids (based on the Rose *et al.*, 1984 model but applying only to the compressive behavior) by assuming that the compressibility of materials is determined primarily by short-range electronic forces.

Since eqn (3) involves a derivative with respect to the volume V , while $E(d)$ is a function only of the intermolecular separation d , one must first determine the connection between the separation d of two molecules and the volume occupied by a collection of molecules. This connection is developed as follows: the intermolecular separation d is identified as being twice the average radius r of the coordination cell occupied by each molecule within a collection of such molecules, so that $r = d/2$. The coordination cell referred to here is that polyhedron formed by the planes which are the perpendicular bisectors of the line joining the centers of any two nearest-neighbor molecules (Fig. 8); a collection of such coordination cells is space-filling and generates the total volume occupied by the material. The specific volume per molecule is then assumed proportional to the cube of the average radius of the coordination cell:

Coordination Cell

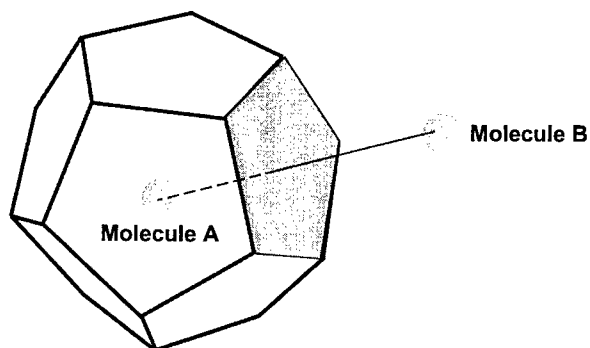


Fig. 8. Schematic diagram of a coordination cell, defined as that polyhedron developed by the perpendicular bisectors of every line drawn between the centers of two nearest neighbor molecules (an example is shown). A collection of such coordination cells (of various sizes and shapes in an amorphous medium) fills the volume occupied by the material.

$$V = \alpha r^3 = \alpha \left(\frac{d}{2} \right)^3 \quad (12)$$

where α is a proportionality constant related to cell/molecule shape (e.g., if the cell is spherical, then $\alpha = 4\pi/3$). The zero-pressure volume (i.e., the equilibrium volume) is then

$$V_0 = \alpha r_0^3 = \alpha \left(\frac{d_0}{2} \right)^3. \quad (13)$$

Using eqns (12–13) in $E(d)$ provides a function of the volume that is suitable for use in eqn (3).

5.2.1. *The Lennard-Jones approximation.* If $E(d)$ is assumed to be in the Lennard-Jones form, then:

$$E(d) = \epsilon \left[\left(\frac{d_0}{d} \right)^{12} - 2 \left(\frac{d_0}{d} \right)^6 \right] \quad (14)$$

where d_0 is the equilibrium molecular separation; the parameters ϵ and d_0 are determined by fitting the molecular mechanics results shown in Fig. 6.

Using eqns (12–14) in eqn (3):

$$P = - \frac{dE}{dV} = \frac{4\epsilon}{V_0} \left[\left(\frac{V_0}{V} \right)^5 - \left(\frac{V_0}{V} \right)^3 \right]. \quad (15)$$

This is the pressure-volume equation with parameters obtained solely from the molecular mechanics computations. The parameter ϵ has already been determined directly by fitting eqn (14) to the data of Fig. 6; however, the zero-pressure volume V_0 must still be determined (since it incorporates both d_0 and α). The obvious way to estimate

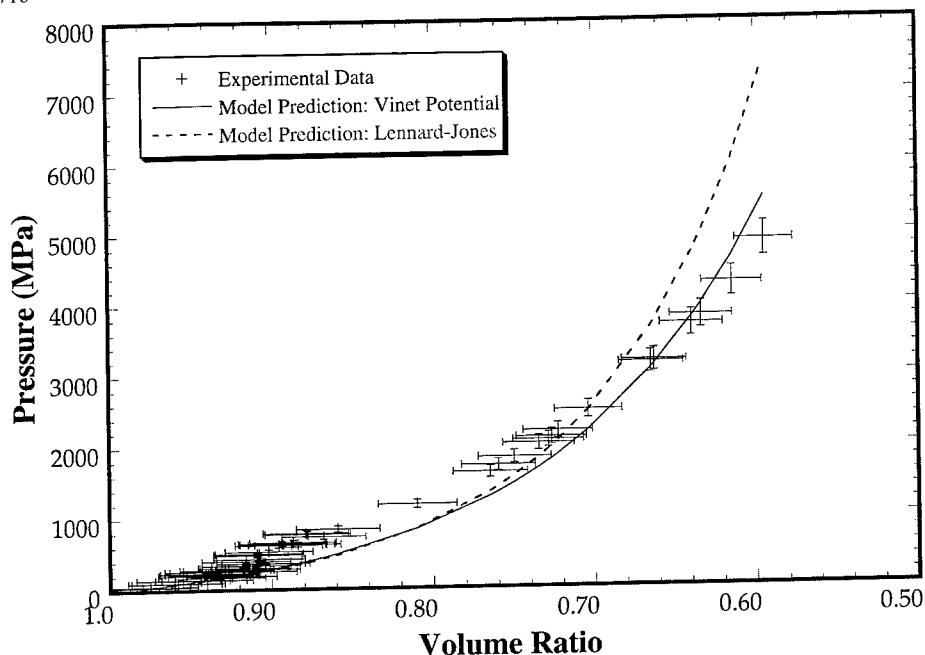


Fig. 9. Comparison of the pressure-volume relations predicted by the Lennard-Jones approximation and the Vinet potential (each fit to the molecular data of Fig. 6) with the macroscopic experimental results obtained on 5P4E. All of the parameters in the model predictions are obtained from the molecular-level computations, with the exception of the density of the material at room temperature and atmospheric pressure.

V_0 is to obtain it from eqn (13) using the molecular mechanics calculations for d_0 and an estimate of molecular shape to determine α . The corresponding V_0 would be the zero-pressure volume at zero K, and then eqn (15) would give us the P - V relation at zero K.

However, the desired comparison is of the predictions with the measured compressibility at room temperature. Therefore, the zero-pressure volume V_0 is instead estimated using the known room temperature density of the material (5P4E) at ambient pressure. A discussion of the implications of this choice of V_0 is presented in the discussion section; essentially this procedure lumps all of the thermal effects into a single parameter that then scales the compressibility relation. Using this room-temperature normalized value for V_0 , eqn (15) can now be used to predict the room temperature pressure-volume behavior of 5P4E. This prediction (the dashed line) is compared with the experimental results on 5P4E in Fig. 9. Note that eqn (15) provides a much better description of the actual behavior than the traditional Dowson-Higginson relation does (Fig. 4).

5.2.2. The Vinet approximation. Vinet *et al.* (1989) developed a "universal" equation of state in which all classes of solids (metallic, covalent, ionic, van der Waals) can be described by a universal scaled energy relation. The Vinet EOS is based on the

Rose *et al.* (1984) binding energy model but is applied only to the compressive behavior. Universality is claimed by assuming that the compressibility of materials is determined primarily by short-range electronic forces, which do not vary significantly across the classes of materials of interest. The corresponding binding energy relation (initially developed for metals) is:

$$E(a^*) = -\Delta E(1 + a^*)e^{-a^*} \quad (16)$$

where $E(a^*)$ is the binding energy per atom, ΔE scales the energy, and a^* is a scaled atomic separation given by:

$$a^* = \frac{a - a_0}{l} \quad (17)$$

where a itself is the separation between atoms (here molecules), a_0 is the equilibrium separation between two atoms (molecules), and l is a scaling length. Note that this form has been found to be good for the binding energies between atoms or small molecules (the materials on which this approach has been tested include hydrogen, Ar, Ne, Kr, Mo, K, Cu, Li, MgO and SiC). The 5P4E molecule has a molecular weight of 446, and so conformational stiffnesses may contribute to the compressibility, but the applicability of the Vinet approach is assumed for our analysis. Equation (16) is applied to the molecular-level data on the interaction energy by associating the separation a with the separation d and a_0 with the equilibrium molecular separation d_0 . The corresponding fit of eqn (16) to the computed energy-distance data is shown in Fig. 6 as the solid line (note that the Vinet relation provides a marginally better fit than the Lennard-Jones form). The corresponding value of the scaling length parameter is 1.17 Å.

Following the same procedures used previously, eqns (12–13), a pressure–volume equation based on the Vinet potential can be derived using eqn (3), with parameters determined solely from the molecular mechanics computations:

$$P = \frac{\Delta E}{3l^2\alpha} \left(\frac{1 - (V/V_0)^{1/3}}{(V/V_0)^{2/3}} \right) \exp \left(\frac{r_0}{l} (1 - (V/V_0)^{1/3}) \right) \quad (18)$$

ΔE and l are obtained directly from the curve fit of Fig. 6. One additional parameter (α) must be specified in order to use eqn (18): as a first approximation, the cell is assumed to be spherical, so that $\alpha = 4\pi/3$. Given α , then,

$$r_0 = \left(\frac{3}{4\pi} V_0 \right)^{1/3}. \quad (19)$$

If the r_0 (and hence V_0) computed from the molecular mechanics results of Fig. 6 are used, the resulting eqn (18) will provide the pressure–volume response of the material at zero K. However, the interest is in comparison with room-temperature pressure–volume data, and so for V_0 the volume corresponding to each molecule at room temperature is again used (computed using the room temperature density and Avogadro's number). Use of this V_0 (and the corresponding r_0) in eqn (18) then provides a relation for the room temperature pressure–volume behavior of the material, with

all of the parameters obtained either directly from the molecular-level computations or from a simple density point at room temperature. Using these parameters, the predictions of eqn (18) are compared with the experimental room-temperature pressure–volume results in Fig. 9 (the solid line). The agreement is remarkably good, and appears to be a significant improvement over the Lennard–Jones approximation (given the error bars on the data).

One must distinguish the model prediction developed here from the compressibility equation provided by Jacobson and Vinet (1987) for lubricants. Although the form of the compressibility relation (18) is exactly the same in their work, the process by which they determine the parameters is completely different, since Jacobson and Vinet obtain the parameters simply by fitting their experimental compressibility data. In contrast, in this work the parameters in the compressibility relation are obtained independently from molecular-level computations and from the room-temperature density. Thus molecular-level information, and one macroscopic density data point that accounts for the thermal effects, are sufficient to predict completely the macroscopic compressibility of this simple organic substance in the glassy state.

6. DISCUSSION

Our approach to the modeling of the compressibility of this simple organic substance is to compute the interactions between a pair of molecules, using bond parameters (a “force field”) obtained from computational chemistry. Each molecule is in fact a collection of atoms, and the total intermolecular interaction is a result of all of the interatomic interactions (both within one molecule and with atoms in the other molecule). However, the interactions between the molecule pair are then consolidated within a single potential of either the Lennard–Jones or Vinet types (such consolidation is a common idealization, e.g. Smith and Srolovitz, 1995). This two-body interaction is then idealized as representative of the interactions within the bulk of the material. The latter approximation, while acceptable for the study of compression under hydrostatic pressures, would be a very poor approximation if any deviatoric behaviors were considered. Consideration of shearing itself may require both a full incorporation of the kinetics and an evaluation of the statistical distributions of molecular shapes, energies and orientations.

Note that in reality the material is in a glassy state over most of the pressure range presented in Fig. 9. The modeling approach presented here is unable to capture a change in compressibility through the glass transition, since the intermolecular interaction is idealized in terms of a single overall potential. The glass transition itself can be predicted using these computations and Cohen–Turnbull theory (Zhang and Ramesh, 1998), but this amounts to a prediction of a point in pressure–temperature space rather than prediction of material response through the glass transition. An accurate characterization of material behavior through the glass transition would require a true molecular dynamics calculation, since it is the loss of mobility associated with a reduction in volume that leads to the glassy behavior. Further, an entire ensemble of molecules would have to be considered rather than the single pair of molecules within our molecular micromechanics approach. Molecular dynamics com-

putations of material response through a glass transition have been presented in the literature, although generally on much simpler molecules (or on polymers, where the statistical mechanics dominates the problem).

The "molecular mechanics" computations themselves were performed without consideration of the thermal energies of the molecules, and therefore correspond to an evaluation of intermolecular interactions at zero K. In contrast, the experimental data were obtained under near-adiabatic conditions with an initial temperature of 300 K (room temperature). The direct use of the parameters for each potential obtained by fitting the molecular-level calculation would give us the compressibility at zero K, and this is of course a much stiffer response than is observed at room temperature. The model uses the idealization that all of the thermal effects can be incorporated into a single scaling parameter represented by V_0 , the effective volume occupied by a molecule at the equilibrium state at any given temperature. In essence, it is assumed that the V_0 corresponding to room temperature contains all of the major thermal effects, including the statistical distribution of various molecular conformations, the thermal vibration and the expansion of the coordinate cells up to room temperature. All these are effects that were not taken into account in the molecular mechanics computations. Such effects can only be fully incorporated into the model by performing full-scale molecular dynamics computations. Instead, this single scalar parameter is used to scale the entire behavior, and the approach seems to work remarkably well. The parameter V_0 itself is obtained very simply from the known room-temperature density of the material under ambient pressure.

It should also be noted that the experimental data in Fig. 4 is obtained from compression Kolsky bar and pressure-shear plate impact experiments, in which compression is near-adiabatic, so that the temperature will rise during compression. This is thus not an isothermal compressibility curve. Further, the error of the measurement of volume ratio is not negligible (Ramesh, 1991). Given all of these approximations, the fact that the theory is very primitive, and the assumptions made in the development of eqn (18), the quality of the model's prediction of the measured compressibility is considered to be good.

7. CONCLUSION

Experimental data from two different experimental techniques (the compression Kolsky bar and pressure-shear plate impact) are presented, describing the compressibility of a simple organic glass-forming liquid (the lubricant 5P4E) under pressures ranging from 100 MPa to 5 GPa. 5P4E is observed to exhibit substantial compressibility over this range of pressures. In an effort to determine the molecular basis for this large compressibility, the branch of computational chemistry known as "molecular mechanics" is used to obtain the interaction energy potential between two molecules, with all of the interatomic interactions described through parameters that are obtained independent of the experimental compressibility data. The resulting estimate of the intermolecular potential at 0 K is used to estimate the compressibility of the material; correction to room temperature is performed by incorporating all of the thermal effects into a parameter representing the average size of the coordination

cell in a collection of such molecules. The resulting predicted room-temperature compressibility provides a very good comparison to the experimental compressibility data. The model prediction is independent of compression experiments, with all of the parameters obtained from the molecular mechanics computations except for the room-temperature zero-pressure coordination cell volume (which is a macroscopic quantity).

ACKNOWLEDGEMENTS

The research presented here was made possible in part by support from the National Science Foundation's Program in Surface Engineering and Tribology through Grant No. MSS-9114781. The experiments and computations described here would not have been possible without the support also of the U.S. Army Research Office to the Laboratory for Impact Dynamics and Rheology at Johns Hopkins through Grants DAAH04-94-G-0086 and DAAH05-95-1-0417. The authors would also like to thank Prof. Townsend and Dr Smith of the Johns Hopkins Department of Chemistry for introducing us to the wonders of computational chemistry, and Prof. M. O. Robbins of the Johns Hopkins Department of Physics and Astronomy for several enlightening discussions.

REFERENCES

- Allinger, N. L. (1992) Molecular mechanics. In *Accurate Molecular Structures: Their Determination and Importance*, ed. A. Domenicano and I. Hargittai. Oxford University Press, New York.
- Alsaad, M. A., Winer, W. O., Medina, F. D. and O'Shea, D. C. (1978) Light scattering study of the glass transition in lubricants. *ASME Journal of Lubrication Technology* **100**, 418–422.
- Anderson, O. L. (1995) *Equations of State of Solids for Geophysics and Ceramic Science*. Oxford University Press, Oxford.
- Baonza, V. G. *et al.* (1994) Universal behavior of compressed liquids. *Journal of Physical Chemistry* **98**, 4955.
- Barlow, A. H., Harrison, G., Irving, J. B., Kim, M. G., Lamb, J. and Pursley, W. C. (1972) The effect of pressure on the viscoelastic properties of liquids. *Proceedings of Royal Society London A* **327**, 403–412.
- Bezot, P., Hesse-Bezot, C., Berthe, D., Dalmaz, G. and Vergne, P. (1986) Viscoelastic properties of 5P4E as a function of pressure and temperature by light scattering technique. *ASME Journal of Tribology* **108**, 579–583.
- Bridgman, P. W. (1940) The compression of 46 substances to 50,000 kg/cm². *Proceedings of American Academy of Arts and Sciences* **74**, 21–51.
- Bridgman, P. W. (1948a) Recent work in the field of high pressure. *Review of Modern Physics*, **18**.
- Bridgman, P. W. (1948b) Rough compressions of 177 substances to 40,000 kg/cm². *Proceedings of American Academy of Arts and Science*, **76**, 71.
- Dick, R. (1970) Shock wave compression of benzene, carbon disulfide, carbon tetrachloride, and liquid nitrogen. *Journal of Chemical Physics* **32**, 6021–6032.
- Dowson, D. and Higginson, G. R. (1977) *Elastohydrodynamic Lubrication*. Pergamon, Oxford.
- Feng, R. and Ramesh, K. T. (1993) On the compressibility of elastohydrodynamic lubricants. *Journal of Tribology* **115**, 557–559.
- Gelin, B. R. (1994) *Molecular Modeling of Polymer Structures and Properties*. Hanser/Gardner Publications, Inc., Cincinnati, OH.
- Hamrock, B. J., Jacobson, B. O. and Bergstrom, S.-I. (1987) Measurement of the density of base fluids at pressures to 2.2 GPa. *Transactions of ASLE* **30** (2), 196.

- Haward, R. N. (1969) Compressibility of polymers. *Journal of Polymer Science, Polymer Physics Edition*, **7**, 219.
- Jacobson, B. O. and Hamrock, B. J. (1984) Non-Newtonian fluid model incorporated into elastohydrodynamic lubrication of rectangular contacts. *ASME Journal of Tribology* **106**, 275.
- Jacobson, B. O. and Vinet, P. (1987) A model for the influence of pressure on the bulk modulus and the influence of temperature on the solidification pressure for liquid lubricants. *Journal of Tribology* **109**, 709–714.
- Kolsky, H. (1949) An investigation of the mechanical properties of materials at very high rates of loading. *Proceedings of Physics Society of London* **62B**, 676.
- Linton, W. L. (1920) The compressibility of liquids and mixed organic liquids. Ph.D. dissertation. The Johns Hopkins University, Baltimore, MD.
- Matsuoka, S. and Maxwell, B. (1958) Response of linear high polymers to hydrostatic pressure. *Journal of Polymer Science* **32**, 131.
- Mohamadi, F. *et al.* (1990) MacroModel—An integrated software system for modeling organic and bioorganic molecules using molecular mechanics. *Journal of Computational Chemistry* **11**, 440.
- Motakabbir, K. A. and Berkowitz, M. (1990) Isothermal compressibility of SPC/E water. *Journal of Physical Chemistry* **94** 8359–8362.
- Nellis, W. J. (1994) Fluids at high shock pressures and temperatures and some thoughts about future possibilities. *AIP Conference Proceedings* **309**, 61–63.
- Porter, D. (1995) *Group Interaction Modeling of Polymer Properties*. Marcel Dekker, Inc., New York.
- Prosperetti, A. (1997) A new mechanism for sonoluminescence. *Journal of the Acoustic Society of America* **101** (4), 2003–2007.
- Ramesh, K. T. (1991) The short-time compressibility of EHD lubricants. *Journal of Tribology* **113**, 361–371.
- Ramesh, K. T. and Clifton, R. J. (1987) A pressure–shear plate impact experiment for studying the rheology of lubricants at high pressures and high shearing rates. *Journal of Tribology* **109**, 215–222.
- Ramesh, K. T. and Clifton, R. J. (1992) Finite deformation analysis of pressure–shear plate impact experiments on an elastohydrodynamic lubricant. *Journal of Applied Mechanics* **59**, 754–761.
- Rose, J. H., Smith, J. R., Guinea, F. and Ferrante, J. (1984) Universal features of the equation of state of metals. *Physical Review B* **29** (6), 2963.
- Sanchez, I. C. *et al.* (1993) Compression of liquids and solids: universal aspects. *Journal of Physical Chemistry* **97**, 6120–6123.
- Smith, R. W. and Srolovitz, D. J. (1995) Simulation of dynamic fracture of an impact-loaded brittle solid: microcracked and polycrystalline solids. *Modeling Simul. Mater. Sci. Eng.* **3**, 665.
- Song, Y., Caswell, B. and Mason, E. A. (1991) Compressibility of liquids: theoretical basis for a century of empiricism. *International Journal of Thermophysics* **12** (5), 855.
- Spencer, R. S. and Gilmore, G. D. (1950) Equation of state for high polymers. *Journal of Applied Physics* **21**, 523.
- Tait, R. G. (1888) Report of some of the physical properties of fresh water and sea water. *Physical Chemistry* **2**, 1.
- Vinet, P. (1986) Equation of state of condensed materials: Physical principles and applications. Ph.D. thesis, Ecole Centrale, Lyon, France.
- Vinet, P. *et al.* (1987) Temperature effects on the universal equation of state of solids. *Physical Review B* **35** (4), 1945–1953.
- Vinet, P. *et al.* (1989) Universal features of the equation of state of solids. *Journal of Physics: Condensed Matter* **1**, 1941–1963.
- Wahid, H. (1993) Light scattering techniques for measuring the compressibility of liquids. *Journal of Molecular Liquids* **55**, 1.
- Warfield, R. W. (1966) Compressibility of bulk polymers. *Polymer Engineering Science* **6**, 176.

- Warfield, R. W. (1967) Compressibility of linear polymers. *Journal of Applied Chemistry* **17**, 263.
- Weiner, S. J. *et al.* (1984) A new force field for molecular mechanical simulation of nucleic acids and proteins. *Journal of American Chemistry Society* **106**, 765.
- Zhang, Y. (1997) An experimental and analytical study of lubricant behavior under EHD conditions. Ph.D. dissertation. The Johns Hopkins University, Baltimore, MD.
- Zhang, Y. and Ramesh, K. T. (1996) The behavior of an elastohydrodynamic lubricant at moderate pressure and high shear rates. *Journal of Tribology* **118**, 162–168.
- Zhang, Y. and Ramesh, K. T. (1998) Prediction of the glass transition in a synthetic lubricant. *Submitted for publication.*



Pergamon

J. Mech. Phys. Solids, Vol. 46, No. 10, pp. 1723–1743, 1998

© 1998 Elsevier Science Ltd. All rights reserved

Printed in Great Britain

0022-5096/98 \$—see front matter

PII: S0022-5096(98)00055-6

HIGH-TEMPERATURE PRESSURE-SHEAR PLATE IMPACT EXPERIMENTS ON OFHC COPPER

K. J. FRUTSCHY* AND R. J. CLIFTON

Brown University, Division of Engineering, Providence, Rhode Island 02912, U.S.A.

(Received 20 December 1997; in revised form 10 March 1998)

ABSTRACT

Experimental results are presented on the dynamic plastic response of OFHC copper at strain rates of 10^5 – 10^6 s $^{-1}$ and temperatures up to 700°C. Measurements in this previously unexplored regime of high temperatures and very high strain rates are made possible by recent extensions of the pressure-shear plate impact methodology to allow testing at high temperatures. A thin foil of the specimen material is sandwiched between two pure tungsten carbide plates which have sufficient high temperature strength to remain elastic under the temperature and loading conditions of the experiment. This target assembly is heated by an induction heating coil. To overcome possible misalignment of the impact face of the target due to thermal expansion of the target supports, a laser beam reflected from the rear surface of the target is used as an optical lever to detect changes in the orientation of the target. Remote controls are used to make the necessary adjustments in the orientation of the target assembly to maintain its original alignment with the impact face of the flyer plate. To withstand the high temperatures, the photoresist gratings which normally provide the diffracted beams used in recording the transverse velocity of the target assembly are replaced by titanium phase gratings produced by SEM lithography. Over temperatures from 300 to 700°C and strain rates from 10^5 to 10^6 s $^{-1}$ the flow stress of OFHC copper increases with increasing strain rate, and decreases with increasing temperature. Numerical simulations of the experiments, based on popular constitutive models, exhibit lower flow stresses than those measured in the experiments. The models also fail to predict the softening that is observed at large strains in the tests at strain rates of 10^6 s $^{-1}$. © 1998 Elsevier Science Ltd. All rights reserved.

1. INTRODUCTION

Measurements of the plastic response of materials at high temperatures and high strain rates are important for the development of constitutive models for flow in this regime—especially for applications in which shear bands occur under high strain rates as in high-speed machining, automotive crash tests, dynamic fracture, and terminal ballistics. For such so-called *adiabatic* shear bands, the localization of deformation into a narrow band occurs as a thermoplastic instability in which thermal softening allows both strain rate and temperature to increase sharply within the band. For martensitic steels, temperatures within the bands have been measured to be over 600°C (e.g. Marchand and Duffy, 1988; and Zhou, Rosakis and Ravichandran, 1996); strain rates in the range of 10^5 – 10^6 s $^{-1}$ are often inferred (e.g. Marchand and Duffy, 1988; and Giovanola, 1987).

*To whom correspondence should be addressed at Intel Corporation, 5000 West Chandler Boulevard, Chandler, Arizona, 85226, U.S.A.

The pressure-shear plate impact experiment, because of the high strain rates obtained and the comparatively straightforward interpretation made possible by the plane wave loading, is well-suited for measuring the plastic response of materials at shear strain rates of 10^5 – 10^6 s $^{-1}$ and large shear strains ($\sim 100\%$). The new high-temperature capability of the experiment allows the constitutive response of materials to be measured at high strain rates *and* high temperatures. OFHC copper was chosen as the first material to be tested in the high-temperature pressure-shear configuration because of its well documented response under other loading conditions. Also, the low melting point of copper makes possible the measurement of the high-strain rate flow stress of a solid near its transition to liquid.

This paper presents experimental results for three temperatures, at each of two high strain rates, as a means of characterizing independently the effects of temperature and strain rate. Probably the most striking feature of the observed response is the high shearing resistance that copper maintains as its temperature approaches the melting point.

2. EXPERIMENTAL APPROACH

The basic pressure-shear plate impact experiment for high strain rate deformation of a thin foil has been described by Clifton and Klopp (1985). The time-distance diagram for such experiments, adapted for the experiments to be reported here, is shown in Fig. 1. The specimen foil is sandwiched between the center and right tungsten carbide plates which are heated prior to impact. The heating is provided by an

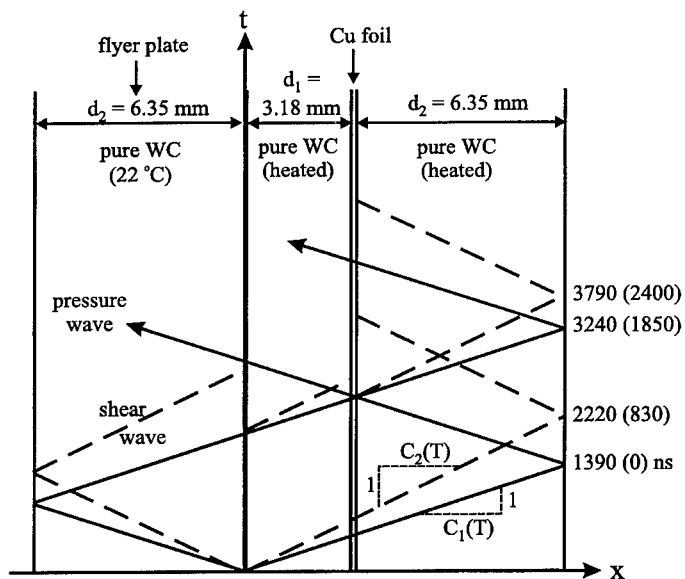


Fig. 1. Time/distance diagram for high-strain rate, high temperature experiment.

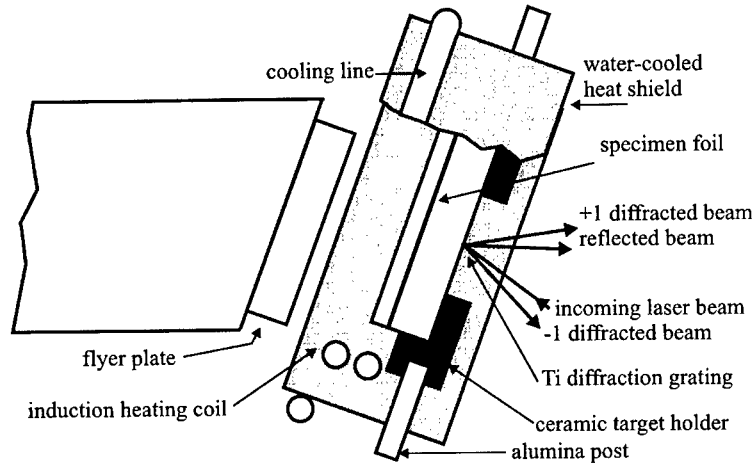


Fig. 2. Impact schematic for high-temperature, pressure-shear experiment.

induction heater (Frutschy and Clifton, 1997); the induction heating coil is wrapped around the circumference of the target sandwich as shown in Fig. 2. The target sandwich is supported by a machinable ceramic holder and attached to the frame of the target holder with alumina pins that eventually break away. The inner diameter of the induction heating coil is larger than the diameter of the projectile tube to ensure that the coil is untouched throughout the experiment. The target holder (not shown) is shielded from the heat of the target sandwich and the electromagnetic field of the induction heating coil by a water-cooled copper housing that surrounds the target sandwich. The flyer plate on the left is at room temperature.

Upon impact, a pressure wave and a shear wave are generated in both the flyer and the central tungsten carbide plates. The pressure wave arrives at the specimen first and induces a small amount of longitudinal plastic deformation ($\sim 2\%$ according to simulations). More importantly, the pressure wave subjects the specimen/tungsten carbide interfaces to a large normal pressure so that sufficient frictional resistance is generated to allow the shear wave to be transmitted across the specimen without slip. The principal plastic deformation comes from the shear wave which arrives after the specimen is under pressure. The experiment is regarded as completed once the pressure wave—after reflecting from the rear surface of the target sandwich—returns to the specimen. At this time, the normal pressure drops to zero, and shear stress can no longer be transmitted. Clifton and Klopp (1985) describe how the stress and strain in the specimen foil are calculated from the measured free surface velocities. Briefly, the shear stress and normal stress in the specimen are given by

$$\tau = \frac{1}{2} \rho c_2 v_{fs}, \quad \sigma = \frac{1}{2} \rho c_1 u_{fs} \quad (1)$$

where ρc_2 , ρc_1 are, respectively, the elastic shear wave impedance and the elastic longitudinal wave impedance of the rear target plate; the quantities v_{fs} , u_{fs} are the transverse and normal components of the velocity measured at the traction-free rear

Table 1. *Material properties from literature*

Property (at 22°C)	Copper (OFHC)	WC (pure)
c_1 (mm/ μ s)	4.978	6.858
c_2 (mm/ μ s)	2.322	4.300
ρ (g/cm ³)	8.96	15.4
ρc_1 (GPa/(mm/ μ s))	44.6	107.0
ρc_2 (GPa/(mm/ μ s))	20.8	67.1
E(GPa)	129.8	609.1
μ (GPa)	48.3	287
ν	0.343	0.20
σ_{yield} (MPa)	40	4460
T_{melt} (°K)	1356	3058
k (W/m°K)	399.0	102
C_p (J/kg°K)	386.0	204
α (°K ⁻¹ $\times 10^{-6}$)	18	5.9

surface of the target assembly. The room temperature properties of the OFHC copper and the pure tungsten carbide plates (manufactured by Cercom Inc.) are given in Table 1. Data for this table was given by Cercom Inc. and taken from Smithells and Brandes (1976), Exner (1979), and Storms (1967). The experiment is described more fully by Frutschy (1997) and Frutschy and Clifton (1997).

Because of the 1 GHz frequency response of the latest photodiodes, the normal displacement interferometer (NDI) can now be used to measure normal free surface velocities up to 0.2 mm/ μ s. A transverse displacement interferometer (TDI) (Kim, Clifton and Kumar, 1977) is used to measure the transverse free surface velocity. The diffraction gratings used for these experiments consist of titanium strips put on the rear surface of the target assembly by means of electron-beam lithography together with a standard "lift-off" procedure. Figure 3 is an SEM photo of the final grating.

3. EXPERIMENTAL RESULTS

Experiments were conducted at two nominal strain rates: $\dot{\gamma} = 2.5 \times 10^5 \text{ s}^{-1}$ and $\dot{\gamma} = 1.2 \times 10^6 \text{ s}^{-1}$, and at three initial temperatures: 298°C, 495°C and 691°C. The normal free surface velocities for the experiments at $\dot{\gamma} = 2.5 \times 10^5 \text{ s}^{-1}$ are shown in Fig. 4 and those for $\dot{\gamma} = 1.2 \times 10^6 \text{ s}^{-1}$ are shown in Fig. 5. The normal component of the free surface velocity for all of these tests jumps to 0.06 mm/ μ s and quickly ramps to roughly 0.14 mm/ μ s. For the cases involving the highest shear strain rates, shown in Fig. 5, the risetime increases significantly with increasing temperature. However, even the risetime of approximately 0.4 μ s at the highest temperature is much less than the 0.74 μ s required for the incident shear wave to reach the specimen. Thus, the specimen is under a nearly uniform state of stress before the shear wave arrives. The arrival of

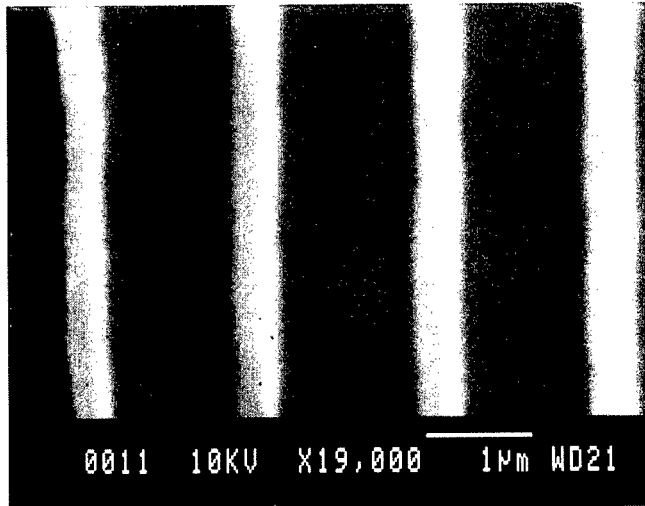


Fig. 3. 600 lines/mm grating on rear surface of tungsten carbide plate (narrow strips are 200 Å Ti/800 Å Au).

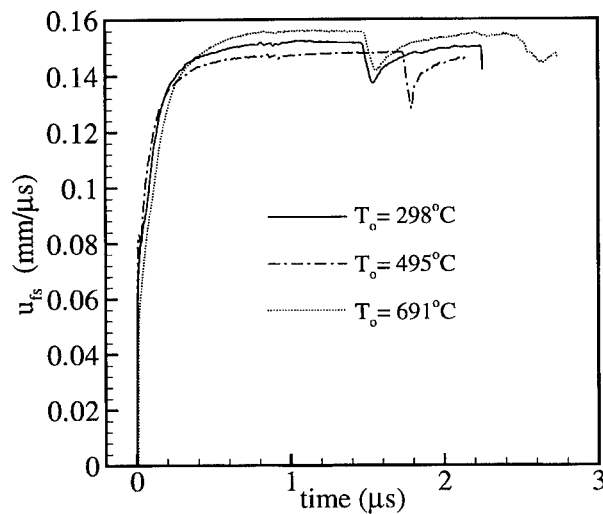


Fig. 4. Normal free surface velocity from 10^5 s^{-1} tests on OFHC Cu.

the shear wave can be identified on some of the normal velocity records by the appearance of a small wiggle in the record at approximately $0.83 \mu\text{s}$ after the arrival of the longitudinal wave, as expected from the $t-X$ diagram, Fig. 1. The sharp dip in the velocity around $1.8 \mu\text{s}$ is the arrival of the longitudinal wave that reflected off the rear surface of the flyer plate (see Fig. 1). The sharp dip arrives later for one shot at each of the nominal strain rates because thicker pure-WC loading plates were used.

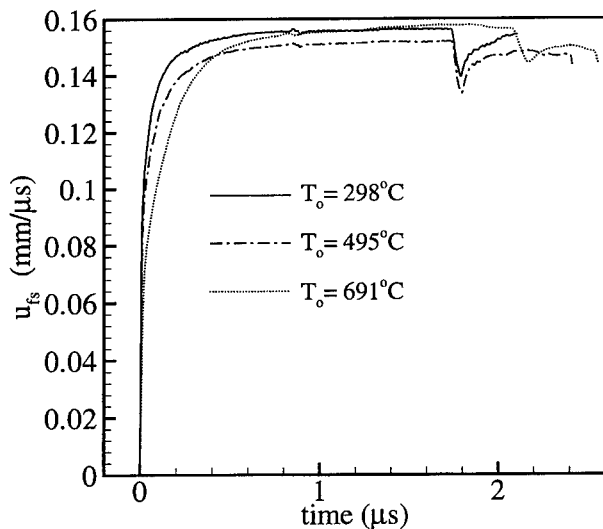


Fig. 5. Normal free surface velocity from 10^6 s^{-1} tests on OFHC Cu.

The normal velocity profiles are almost identical to those for the symmetric impact tests on pure-WC (see Frutschy, 1997; or Frutschy and Clifton, 1997). Because for uniaxial strain the longitudinal strain in the copper foil is small, say less than 3%, and the thickness of the foil is small, the effect of the deformation of the specimen on the curvature in the upper part of the normal velocity profile is small.

The transverse free surface velocities corresponding to the experiments for which the normal free surface velocities are shown in Figs 4 and 5 are shown in Figs 6 and

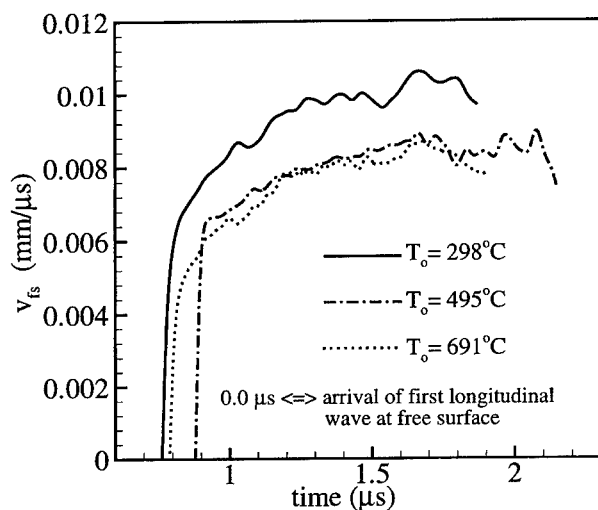


Fig. 6. Transverse free surface velocity from 10^5 s^{-1} tests on OFHC Cu.

7, respectively. The difference in arrival times of the shear wavefronts in these figures is due primarily to differences in thicknesses of the WC loading plates. Prior to the arrival times the transverse free surface velocity is shown to be zero, indicating that the small transverse velocity corresponding to the small tilt-induced inclination of the longitudinal wavefront is being neglected. Tilt effects are neglected throughout the data reduction leading to these velocity-time profiles because Klopp and Clifton (1990) have shown tilt effects to have negligible effect on the inferred shearing resistance of the material for tilts up to 4 mrad which is approximately an order of magnitude larger than the tilts (i.e. the values of α in Table 2) obtained in the reported experiments. These velocity-time profiles have been smoothed to remove noise associated with the data reduction—primarily noise introduced through differentiation of the corresponding displacement-time profiles.

The nominal shear strain rates for these tests, is obtained from the relation (e.g. Clifton and Klopp, 1985)

$$\dot{\gamma} = \frac{v_0 - v_{fs}}{h} \quad (2)$$

where v_0 is the transverse component of the projectile velocity and h is the specimen thickness. From eqn (2) and Figs 6 and 7 it is evident that the shear strain rate varies somewhat during the test, becoming larger when the transverse velocity becomes smaller. However, the variation is not more than about 10% over most of the time interval of interest so the experiments can be regarded as conducted at approximately constant strain rates at the nominal rates reported in Table 2.

For the experiments at shear strain rates of 10^5 s^{-1} shown in Fig. 6 the transverse velocity increases essentially monotonically until unloading occurs due to the reduction of the normal pressure on the faces of the specimen. From eqn (1), the shear stress τ is proportional to the transverse component of the free surface velocity

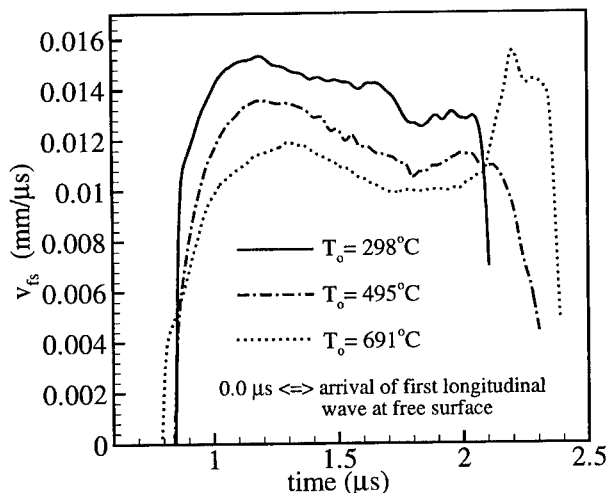


Fig. 7. Transverse free surface velocity from 10^6 s^{-1} tests on OFHC Cu.

Table 2. OFHC copper experiment summary

Parameter	KF9707	KF9611*	KF9709	KF9612*	KF9609*	KF9708
$\bar{T}_{T/C}$	300	500	700	300	500	700
$T_0(^{\circ}\text{C})$	298	495	691	298	495	691
$T_f(^{\circ}\text{C})$	319	518	709	466	634	846
$\dot{\gamma}_{\text{nom}}(\text{s}^{-1})$	2.2×10^5	2.6×10^5	2.5×10^5	1.1×10^6	1.1×10^6	1.4×10^6
$\tau_{\text{peak}}(\text{MPa})$	340	280	280	500	440	360
$p(\text{GPa})$	7.8	7.4	7.8	8.0	7.7	7.8
γ_{tot}	0.26	0.34	0.28	1.4	1.5	1.8
$h(\mu\text{m})$	102	95	102	28	28	25
$V_0(\text{mm}/\mu\text{s})$	0.155	0.152	0.159	0.163	0.158	0.163
$\theta(\text{deg.})$	12.0	12.5	12.0	16.0	16.0	16.0
$\alpha(\text{mrad})$	0.35	0.40	0.39	0.75	0.22	0.42
$\Omega(\text{deg.})$	20	37	11	86	90	27
$d_1(\text{mm})$	3.05	3.18	3.05	3.18	3.18	3.05
$d_2(\text{mm})$	5.46	6.35	5.44	6.35	6.35	7.62

* Denotes 1.9 inch dia. plate shots. All others were 2.0 inch dia.

† Foil annealed for 20 min at 495°C.

and is therefore also essentially monotonically increasing. On the other hand, for the experiments at the higher shear strain rates and larger shear strains shown in Fig. 7, the transverse velocity and the shear stress show a peak followed by a reduction to a plateau-like region before the unloading waves arrive.

Figure 8 shows the dynamic stress-strain curves inferred from the velocity-time

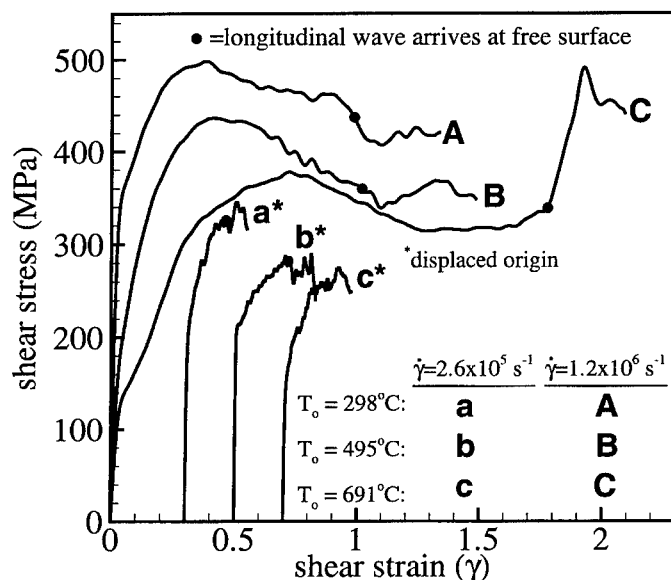


Fig. 8. Shots on OFHC copper.

profiles of Figs 6 and 7. The shear strains γ are obtained by integrating the shear strain rates obtained from eqn (2). The shear stresses are obtained from the transverse velocity-time profiles by means of eqn (1). For the three tests conducted at a nominal shear rate of $2.5 \times 10^5 \text{ s}^{-1}$ the copper hardens to a steady flow stress within a shear strain of 0.1 for all three tests. With the exception of the last portion of the 691°C test, the flow stress decreases with increasing temperature. It is important to note that the curves represent the intrinsic constitutive response of the material only after the stress becomes uniform across the thickness of the specimen. From numerical simulations, such a uniform state of stress is reached at strains of $\gamma \approx 0.04 - 0.1$.

For the three tests conducted at a nominal shear rate of $1.2 \times 10^6 \text{ s}^{-1}$ the flow stresses at a given temperature and shear strain are substantially higher. The copper hardens, as for the lower strain rates, but then softening occurs around a shear strain of $\gamma = 0.5$. This softening continues for a significant period, and then the copper stabilizes (or rehardens as in the 691°C test). The black circles in Fig. 8 correspond to the times at which a longitudinal wave arrives at the free surface of the target sandwich (see Fig. 1). If there is any tilt at impact, this wave will induce a small transverse velocity to the free surface. Hence, the late strain behavior in the plots—especially in the 691°C test—may be inaccurate due to this offset. From numerical simulations, the curves for the high strain rate experiments represent the inherent constitutive response of copper after a strain of approximately $\gamma = 0.3$ when the stress has become nominally uniform through the thickness of the sample.

4. FINITE DIFFERENCE SIMULATIONS OF OFHC COPPER EXPERIMENTS

Complete numerical simulations of the experiments were carried out using a finite difference method introduced by Ranganath and Clifton (1972), applied to the pressure-shear impact problems by Gilat and Clifton (1985), and extended to the case of finite deformation by Ramesh and Clifton (1992). The difference method is explicit, second order accurate, and conditionally stable. Stability of the method for the governing system of hyperbolic PDEs is ensured by taking the time step Δt to be less than the time required for an elastic longitudinal wave, with wavespeed c_1 , to cross a mesh spacing Δx . That is, the Courant-Friedrichs-Levy number, ($CFL \equiv c_1 \Delta t / \Delta x$) must be less than unity; the value $CFL = 0.95$ was used for the calculations. Stability of the parabolic equations governing heat flow places an additional restriction on the time step. The composite stability condition was taken to be (e.g. Shawki and Clifton, 1989),

$$\frac{\Delta t}{\Delta x} \leq \min\left(\frac{1}{c_1}, \frac{\Delta x}{2D}\right) \quad (3)$$

where D is the thermal diffusivity. With $CFL = 1$, the smallest mesh spacing for stable heat flow calculations for copper is 49 nm which is well below the spacing used in the calculations.

For the computations, the flyer plate and the heated pure-WC target plates on each

side of the copper foil were assumed to respond linear elastically. This assumption appears valid given the measured response of the pure-WC plates in high-temperature symmetric impact experiments (see Frutschy and Clifton, 1997).

The copper foils are modeled as elastic/viscoplastic with thermal softening. Due to the large strains measured during these experiments, finite deformation kinematics are used in the computations. Ramesh and Clifton (1992) describe in detail the modeling of the finite deformation of elastic visco-plastic materials. The only difference for this calculation is in the form of the plastic strain rate function:

$$\Phi(\bar{\tau}, \bar{\gamma}_p, T, \dots) = \dot{\gamma}_p = (2D_{ij}^p D_{ij}^p)^{1/2} \quad (4)$$

which—in the current modeling of copper—is a function of the effective shear stress ($\bar{\tau}$), the effective plastic shear strain ($\bar{\gamma}_p = \int_0^t \dot{\gamma}_p dt$), and the temperature (T). The plastic rate of deformation tensor (\mathbf{D}^p) is defined by

$$\mathbf{D}^p = \mathbf{D} - \mathbf{D}^e \quad (5)$$

where \mathbf{D}^e is the elastic rate of deformation. The total rate of deformation, \mathbf{D} , is equal to the symmetric part of the spatial velocity gradient ($\dot{\mathbf{F}}\mathbf{F}^{-1}$) where \mathbf{F} is the deformation gradient. \mathbf{D}^p is related to stress through the flow law

$$\mathbf{D}^p = \left(\frac{\Phi}{2\bar{\tau}} \right) \mathbf{S}, \quad (6)$$

where $\bar{\tau}^2 = \frac{1}{2} S_{ij} S_{ij}$ is the effective shear stress, $\mathbf{S} = \boldsymbol{\sigma} - \frac{1}{3} (\text{trace } \boldsymbol{\sigma}) \mathbf{I}$ is the deviatoric stress, and $\boldsymbol{\sigma}$ is the Cauchy stress tensor.

4.1. Follansbee/Kocks model

Complete numerical analyses were carried out using three popular constitutive models for the function Φ for OFHC copper. The first is the Mechanical Threshold Stress (MTS) model developed by Follansbee and Kocks (1988). This model describes the current hardened state of the copper in terms of an internal state variable called the mechanical threshold stress which is the extrapolated flow stress of the material as the temperature approaches 0°K. Dislocation/dislocation interactions (i.e. hardening), and dynamic recovery (i.e. softening) are included in the evolution of the MTS. For this model the hardening rate θ_0 —proposed initially as increasing linearly with increasing strain rate—increases too strongly with strain rate; therefore, a modified hardening rate suggested by Johnson and Tonks (1991) was used; the latter hardening rate increases with the square root of the strain rate. The resulting constitutive law (cf. eqn (5) from Follansbee and Kocks, 1988), written for shearing deformation becomes

$$\Phi = \dot{\gamma}_1 = \dot{\gamma}_0 \exp \left(\frac{-g_0 \mu b^3}{kT} \left[1 - \left(\frac{\bar{\tau} - \tau_a}{\tau_m - \tau_a} \right)^p \right]^q \right) \quad (7)$$

where $\dot{\gamma}_0 = \sqrt{3} \dot{\epsilon}_0$, $\bar{\tau} = \hat{\sigma}/\sqrt{3}$, $\tau_m = \hat{\sigma}/\sqrt{3}$ is the mechanical threshold stress, $\tau_a = \hat{\sigma}_a/\sqrt{3}$ is the long range internal back stress, μ is the shear modulus, b is the Burgers vector, g_0 is the normalized activation energy, k is the Boltzmann constant;

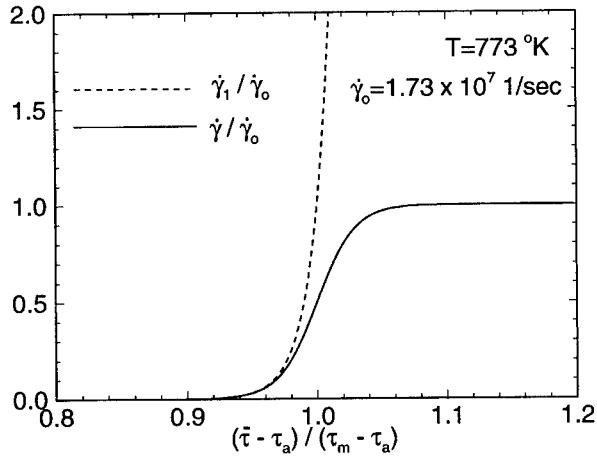


Fig. 9. Applied shear strain rate for Follansbee/Kocks model.

p and q are constants that characterize the shape of the dislocation obstacle profile. Because the strain rate for this model grows exponentially with the applied shear stress, a limiting strain rate had to be imposed to handle the high stresses due to the initial elastic response. The limiting strain rate is introduced while maintaining a continuous slope in the stress/strain-rate relation by combining the model's strain rate, $\dot{\gamma}_1$, with a limiting strain rate, $\dot{\gamma}_2 = \dot{\gamma}_0$, according to

$$\dot{\gamma} = \frac{\dot{\gamma}_1 \dot{\gamma}_2}{\dot{\gamma}_1 + \dot{\gamma}_2} \quad (8)$$

so that the *lowest* shear strain rate dominates. The resulting dependence of the shear strain rate on the shear stress is shown as the solid curve in Fig. 9. This strain-rate limited approximation of the MTS model agrees well with the MTS model up to approximately the highest nominal strain rates (i.e. 10^6 s^{-1}) of the experiments being simulated. The evolution of the mechanical threshold stress, τ_m , with strain follows from (cf. eqn (17) of Follansbee and Kocks, 1988),

$$\frac{\partial \tau_m}{\partial \gamma} = \frac{1}{3} \frac{\partial \sigma_m}{\partial \varepsilon} = \frac{\theta_0}{3} \left[1 - \tanh \left(\frac{2(\tau_m - \tau_a)}{\tau_s - \tau_a} \right) / \tanh(2) \right] \quad (9)$$

where τ_s is the saturation stress, and θ_0 evolves according to (cf. eqn (19) of Johnson and Tonks, 1991),

$$\theta_0 (\text{Pa}) = C_1 + C_2 \ln(\dot{\gamma}) + C_3 \sqrt{\dot{\gamma}}. \quad (10)$$

The saturation stress, τ_s , is a function of shear strain rate (cf. (11) of Follansbee and Kocks, 1988):

$$\tau_s = \tau_{s0} \left(\frac{\dot{\gamma}}{\dot{\gamma}_{s0}} \right)^\alpha; \quad \alpha = \frac{kT}{A\mu b^3}. \quad (11)$$

Table 3. *Definition of experimental parameters*

Parameter	Definition
$\bar{T}_{T/C}$	average thermocouple temperature measurement
T_0	calculated initial temperature of foil
T_f	estimated final temperature in foil (see eqn (16))
$\dot{\gamma}_{nom}$	average strain rate during test
τ_{peak}	peak shear flow stress measured during test
p	longitudinal normal stress in foil during test
γ_{tot}	total shear deformation in foil
h	foil thickness
V_0	impact velocity
θ	impact angle
α	calculated tilt angle
Ω	calculated closure angle
d_1	pure-WC front plate thickness
d_2	pure-WC back plate thickness (= pure-WC flyer plate thickness)

Table 4. *Parameters for Follansbee/Kocks model with Johnson/Tonks modification*

	Value		Value
p	2/3	τ_a	23.1 (MPa)
q	1	C_1	2.37 (GPa)
$\dot{\gamma}_0$	1.73×10^7 1/s	C_2	8.30 MPa · ln(sec)
g_0	1.6	C_3	2.67 MPa $\sqrt{\text{sec}}$
μ	44.0 GPa	τ_{so}	519.6 MPa
b	0.25 nm	$\dot{\gamma}_{so}$	10.74×10^{10} 1/s
k	1.38×10^{-23} J/°K	A	0.312

In the simulation of shot KF9609, constants used for this model are those, from (Follansbee and Kocks, 1988), listed in Table 4.

4.2. Zerilli/Armstrong model

Another constitutive model that was used in simulations of the experiments on OFHC copper is that of Zerilli and Armstrong (1987). For f.c.c. metals, their eqn (21) has the form

$$\sigma = \Delta\sigma'_G + kl^{-1/2} + C_2\epsilon^{1/2} \exp(-C_3T + C_4T \ln \epsilon) \quad (12)$$

where $\Delta\sigma'_G$ is the contribution to the flow stress from solute atoms and/or the original dislocation density. The dislocation pileups at grain boundaries add to the flow stress through $kl^{-1/2}$ where k is the microstructural stress intensity factor, and l is the average

Table 5. *Parameters for Zerilli/Armstrong model*

	Value
$\Delta\sigma_G$	46.5 MPa
k	5 MPa mm ^{1/2}
l	5 μ m
C_2	890 MPa
C_3	2.8×10^{-3} 1/K
C_4	1.15×10^{-4} 1/K
$\dot{\gamma}_0$	10^7 1/s

grain diameter. Rearranging eqn 12 and expressing it in terms of shear stress and shear strain one obtains

$$\dot{\gamma}_1 = \sqrt{3}\dot{\epsilon} = \sqrt{3} \exp\left(\frac{C_3}{C_4}\right) \left[\frac{\sqrt{3}\bar{\tau} - (\Delta\sigma'_G + kl^{-1/2})}{C_2[(\gamma + \gamma_0)/\sqrt{3}]^{1/2}} \right]^{1/(C_4 T)}. \quad (13)$$

Because the original model has a strain singularity at $\gamma = 0$ which causes computational difficulties, a small offset strain, γ_0 , was introduced. Only positive strains are present during the calculation, and the small exponential, $1/(C_4 T)$, allowed a minuscule offset ($\gamma_0 = 10^{-8}$) to be used. Parameter values for the Zerilli/Armstrong model are given in Table 5.

4.3. Johnson/Cook model

The third copper model considered was that of Johnson and Cook (1985). Their model—like the Zerilli/Armstrong model—is a constitutive relation for OFHC copper that predicts accurately the final shapes of rods deformed in Taylor impact tests. Their constitutive law (cf. eqn (1) of Johnson and Cook, 1985) is

$$\sigma = (\sigma_0 + B\epsilon^n) \left[1 + C \ln\left(\frac{\dot{\epsilon}}{\dot{\epsilon}_0}\right) \right] (1 - \Theta^m), \quad \Theta = \left(\frac{T - T_0}{T_m - T_0} \right) \quad (14)$$

where $\sigma = \sqrt{3}\bar{\tau}$, $\dot{\epsilon} = \dot{\gamma}/\sqrt{3}$, is the temperature, T_0 is the ambient temperature, T_m is the melting temperature, and the rest of the parameters are constants. Rearranging equation 14 one obtains

$$\dot{\gamma}_1 = \sqrt{3}\dot{\epsilon} = \sqrt{3}\dot{\epsilon}_0 \exp\left[\frac{\sqrt{3}\sigma}{C(\sigma_0 + B\epsilon^n)(1 - \Theta^m)} - \frac{1}{C} \right]. \quad (15)$$

The constants for this model are given in Table 6. A limiting strain rate, $\dot{\gamma}_2$, was imposed as discussed earlier (see eqn 8).

4.4. Numerical results

The computed stress-strain curves for all simulations of KF9609 and KF9611 are shown in Figs 10 and 11, respectively. The calculated stress on the front surface of the foil is large initially due to the instantaneous elastic response of the foil when the shear wave first arrives at the front surface. This overstress is quickly attenuated as shown by the lack of a stress spike at the back of the foil. The deformation becomes nominally uniform after $\gamma = 0.2$ in Fig. 10 and $\gamma = 0.05$ in Fig. 11. The flow stresses

Table 6. *Parameters for Johnson/Cook model*

	Value
σ_0	90.0 MPa
B	292.0 MPa
C	0.25
n	0.31
$\dot{\epsilon}_0$	10^{-3} 1/s
T_0	298°K
T_m	1356°K
$\dot{\gamma}_2$	10^7 1/s

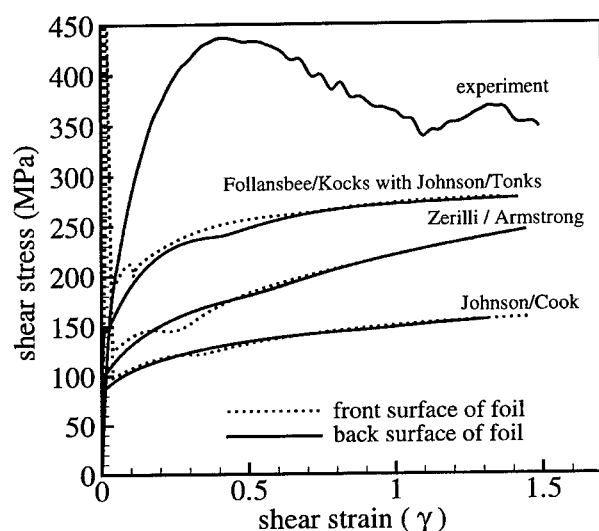


Fig. 10. Computed responses for experiment KF9609 (1.2×10^6 s⁻¹, 495°C) with 400 mesh points.

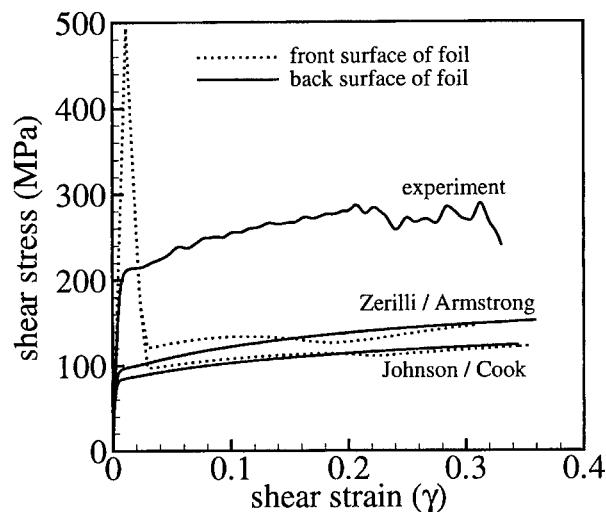


Fig. 11. Computed responses for experiment KF9611 ($2.8 \times 10^5 \text{ s}^{-1}$, 495°C) with 1000 mesh points.

predicted by the various models are lower than those measured in the experiments. It appears that all of the models overestimate the thermal softening at very high strain rates and elevated temperatures. Additionally, none of the current models predict the softening and rehardening observed at larger strains. The predictions of the Follansbee/Kocks model are not shown for the simulation of KF9611 because of excessive numerical oscillations—even with 1600 mesh points.

The plastic work done on a foil during a test increases the temperature of the foil because a large percentage of the plastic work is converted into heat, and there is insufficient time for this heat to be conducted into the neighbouring tungsten carbide plates. An estimate of the final temperature in the foil, T_f , can be found by assuming adiabatic heating, and that 90% of the plastic work is converted to heat:

$$T_f \approx T_0 + 0.9 \left(\frac{\bar{\tau} \bar{\gamma}_p}{\rho C_p} \right) \quad (16)$$

where T_0 is the initial temperature, $\bar{\tau}$ is the average effective flow stress, $\bar{\gamma}_p$ is the final effective plastic strain, ρ is the mass density, and C_p is the specific heat of the material. Values for the estimated final temperatures using eqn 16 are included in Table 2. The experimental record, not a computed simulation, is used to obtain the average flow stress for these estimates.

The evolution of the temperature field in a foil is computed concurrently with the mechanical fields, including heat transfer within the foil and into the neighboring WC plates. Figures 12 and 13 show temperature as a function of position in the foil during the simulation of shot KF9609 for two of the models. The field eventually becomes symmetric about the centerline once the predicted strain rate in the foil becomes homogeneous. The temperature gradients at 0 and $25 \mu\text{m}$ arise from heat conduction into the neighboring plates. The peak in the final temperature plot for the Zerilli/

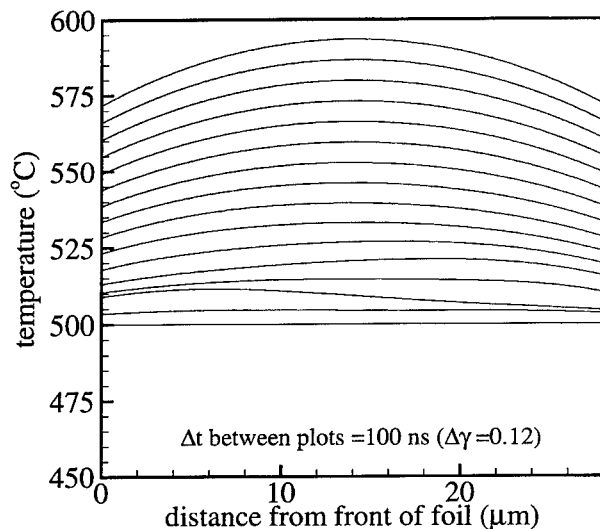


Fig. 12. Zerilli/Armstrong model temperature field prediction for KF9609 ($1.2 \times 10^6 \text{ s}^{-1}$, 495°C).

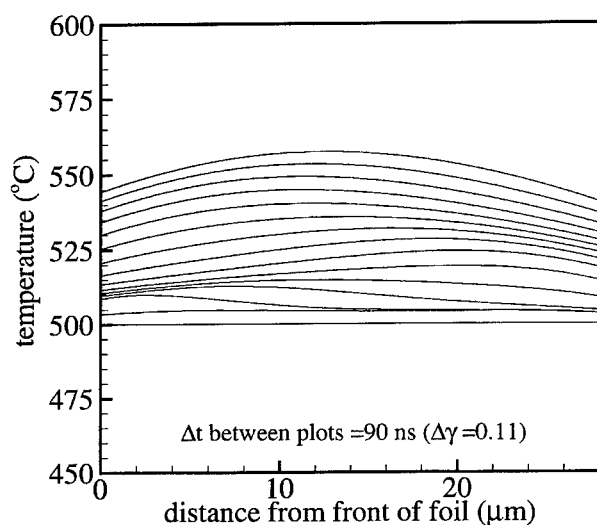


Fig. 13. Johnson/Cook model temperature field prediction for KF9609 ($1.2 \times 10^6 \text{ s}^{-1}$, 495°C).

Armstrong model in Fig. 12 is 580°C which is lower than the 634°C prediction of eqn 16 when using $\bar{\tau} = 363 \text{ MPa}$ and $\bar{\gamma}_p = 1.4$. A lower value is obtained from the simulation because the computed flow stress is less than that observed and because the simulation accounts for heat loss to the neighboring WC plates. The temperature rise predicted by the Johnson/Cook model is still smaller because the simulation for this model results in an even lower flow stress.

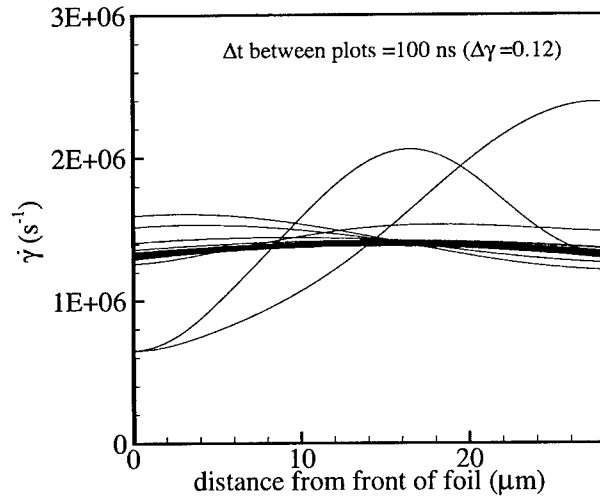


Fig. 14. Zerilli/Armstrong model strain rate profiles for KF9609 ($1.2 \times 10^6 \text{ s}^{-1}$, 495°C).

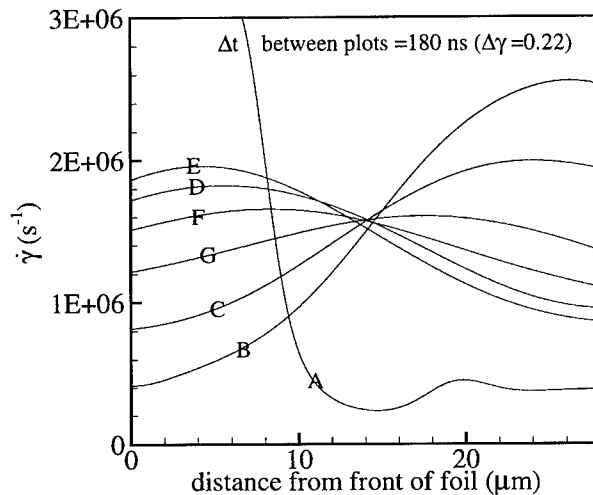


Fig. 15. Johnson/Cook model strain rate profiles for KF9609 ($1.2 \times 10^6 \text{ s}^{-1}$, 495°C).

The strain rate profiles through the foil are plotted in Figures 14 and 15 for the simulations of KF9609. For the Zerilli/Armstrong model a steady-state profile is obtained after approximately 600 ns as shown by the dark band of profiles at $1.3 \times 10^6 \text{ s}^{-1}$. On the other hand, it is evident that for the Johnson/Cook model a constant, uniform strain rate is never obtained. The continued fluctuation of the strain rate for the simulation using the Johnson/Cook model reflects the weaker strain rate sensitivity of this model relative to the Zerilli/Armstrong model (cf. Figs 10 and 11). The weaker the strain rate sensitivity the stronger the fluctuation in strain rate for a given

fluctuation in stress. Or, in computational terms, the weaker the strain rate sensitivity the smaller the time step required to obtain an accurate, stable solution. For the simulation using the Johnson/Cook model, reducing the time step did not change the solution significantly. Thus, the fluctuations appear to be those expected of an exact solution of the equations, not an artifact of the numerical methodology. The modest fluctuations in strain rate in Fig. 15 are not viewed as having a substantial effect on the reported principal features of the stress and temperature histories for the specimen.

Clifton (1971) developed a stability condition for the finite difference simulation of elastic/visco-plastic waves of uniaxial strain (cf. eqn (102) of Clifton, 1971):

$$\Delta t < \frac{2}{\kappa \left(\frac{\partial \phi}{\partial T_{11}} - \frac{1}{\rho_0 c_1^2} \frac{\partial \phi}{\partial \lambda_1} - \frac{2}{\kappa} \frac{\partial \phi}{\partial \lambda_1^p} \right)} \quad (17)$$

where Δt is the time step in the simulation, ϕ is the effective plastic strain rate, T_{11} is uniaxial compressive stress, λ_1 and λ_1^p are the total and plastic axial stretches (respectively), and κ is effectively a shear modulus for finite deformations. The first term in the denominator of eqn 17 illustrates the effect just described: If ϕ has a strong sensitivity to stress, the model is less stable and small time steps must be used to avoid instability. From the remaining terms in the denominator, one can see that if ϕ increases as the compression increases, even smaller time steps must be used. Strain hardening in the Follansbee/Kocks model acts to make these derivatives with respect to the stretches positive (thus helping to increase the time step), but thermal softening counteracts the effect. The model may be exceptionally sensitive to changes in stress under the particular conditions of KF9611, and an extremely small time step may have to be used for a stable finite-difference simulation. For 1600 mesh points, the Follansbee/Kocks simulation of KF9611 was also unstable with the original hardening rate (θ_0) that scaled linearly with strain rate. A full stability analysis of this model including thermal softening is warranted.

5. DISCUSSION

Two particularly interesting features of the reported response of OFHC copper at elevated temperatures and very high strain rates are the relatively strong rate sensitivity and the relatively weak thermal softening. The latter is especially striking in that at absolute temperatures approaching 83% of the melting point the flow stress (≈ 340 MPa) is not only as high or higher than measured values at room temperature at comparable strains and strain rates, but it appears to be either constant or increasing with further straining. One possible explanation for this behavior is that, at these elevated temperatures and very high strain rates, the thermally activated motion of dislocations past obstacles is no longer the only important rate controlling mechanism for plastic flow. In particular, the results suggest that phonon drag on the motion of dislocations may be playing an increasingly important role as this mechanism can be expected to lead to enhanced rate sensitivity and to increased resistance to dislocation mobility with increasing temperature. Also, the high shear stresses and high tem-

peratures should make it possible for dislocations to glide past a larger fraction of the obstacles with less need for thermal activation to overcome the potential barriers. A pilot TEM study of samples cut from the specimens used in the higher strain rate, higher temperature experiments appears to support this possibility in that dislocation cell structures commonly observed at lower temperatures (e.g. Staker and Holt, 1972; Jarrell, 1988; Tong, *et al.*, 1992; Andrade *et al.*, 1994) either are not observed or occur on a much larger length scale.

Tong *et al.* (1992) attributed the major part of the rate sensitivity to the rate sensitivity of the hardening rate, not the rate sensitivity of the flow stress at constant dislocation structure in their high strain rate experiments on OFHC copper. The explanation given for the relatively strong rate sensitivity of the strain hardening was that, without time for recovery, the dislocation density for a given strain increases quite significantly with applied strain rate. Whether or not such an explanation remains valid at elevated temperature requires further investigation as the elevated temperature can be expected to facilitate the dynamic recovery processes.

The peak flow stress in the higher strain rate experiments is higher than that measured in room temperature pressure-shear plate impact experiments done on similar copper specimens by Tong *et al.* (1992). For example, for a room temperature test (Shot 89-02) at $\dot{\gamma} \approx 1.5 \times 10^6 \text{ s}^{-1}$, Tong *et al.* (1992) reported a flow stress of 318 MPa which is comparable to the flow stress, at large strains, for the highest temperature, highest strain rate experiment reported here. The reason for the relatively large shearing resistance at elevated temperatures is not yet known. One difference between the current tests and the earlier tests is that for the higher impedance plates used in the elevated temperature experiments the initial loading pressure ($\approx 8 \text{ GPa}$) is roughly twice that in the room-temperature experiments of Tong *et al.* (1992). At room temperature, shock wave pre-compression can be expected to cause greater pre-hardening of the specimens (e.g. Rajendran *et al.*, 1990); whether or not such pre-hardening continues to have a significant effect on the flow stress at the large strains that are obtained in the experiments reported here is questionable. Another difference between the current tests and the former tests is that in the former tests the samples were diffusion bonded to the front face of a hard steel target plate. Annealing during the diffusion bonding as well as the introduction of residual stresses during cooling could have affected the initial state of the samples. Also, the loading path is different for the two types of tests since in the former tests the pressure and shear loading begin simultaneously whereas in the current tests the pressure loading has equilibrated at its final level before the shear loading begins. While the interpretation of the comparison with the earlier room temperature experiments remains unclear, the series of elevated temperature experiments appear to show consistent trends.

Andrade *et al.* (1994) deformed OFHC copper at room temperature and high strain rates using hat-shaped specimens in the split Hopkinson bar. The copper specimens were first shock-loaded at 50 GPa leaving a longitudinal residual strain of ~ 0.05 . The final shear strains in the geometrically induced shear bands were of the order 3–4. Their transmission electron microscopy study of the deformed material indicated that the microstructure evolves in three stages: An initial large dislocation cell structure breaks down into long, narrow dislocation cells which then break down into smaller equiaxed cells as the deformation continues. Dynamic recrystallization finally

occurs when the angular mismatch between the cells becomes sufficiently large. This qualitative argument appears to be consistent with the TEM observations made by Jarrell (1988) on the samples from the experiments from Tong *et al.* (1992). Pilot TEM analysis of samples cut from the central region of the specimen for KF9612 (298°C, $1.1 \times 10^6 \text{ s}^{-1}$) supports this sequence of events. However, such dislocation patterns are not nearly as well defined in the higher temperature shots (495°C, 691°C) at this same strain rate. Dynamic recovery processes may play a greater role in these high temperature tests. Static recovery is also possible since the foil takes a few seconds to cool after the pressure-shear test is done and the plates are being caught in the room-temperature catcher tank. Full static recovery is not evident since the dislocation cell walls are ragged and not sharp (as in the work of Staker and Holt (1972) on copper).

6. CONCLUSIONS

The high-temperature pressure-shear plate impact experiment has been established as a viable technique for measuring the shearing resistance of materials at high strain rates and high temperatures. The major obstacles overcome for this project include: producing metallic diffraction gratings, developing an *in situ* alignment technique, and establishing the elastic response of pure-WC loading plates at high temperature over a large stress range. Symmetric impact experiments on the pure tungsten carbide loading plates confirm that their response is characterized adequately by linear elasticity over the stress and temperature ranges of the tests on OFHC copper (Frutschy, 1997; Frutschy and Clifton, 1997). OFHC copper exhibits strain rate sensitivity and thermal softening over the temperature range of 300–700°C and strain rate range of $2.5\text{--}14 \times 10^5 \text{ s}^{-1}$. Current constitutive models predict lower flow stresses than those measured at high strain rates and high temperatures. More modeling work is needed not only to account for the higher flow stresses, but also to capture the evolution of flow stress with plastic strain.

ACKNOWLEDGEMENTS

This support was funded by the Army Research Office through Grant No. DAAH04-94-G-0233. Facilities used for computing and TEM were made possible by the Materials Research Science and Engineering Center at Brown University. The authors are very grateful to Jennifer Martin and Alan Schwartzman for their contributions to the metallography and TEM components of this investigation.

REFERENCES

- Andrade, U., Meyers, M., Vecchio, K. and Chokshi, A. (1994) Dynamic recrystallization in high-strain, high-strain-rate, plastic deformation of copper. *Acta. Metall. Mater.* **42**, 3183–3195.
- Clifton, R. J. (1971) On the analysis of elastic/visco plastic waves of finite uni-axial strain.

- Shock Waves and the Mechanical Properties of Solids*. Syracuse University Press, Syracuse, New York.
- Clifton, R. J. and Klopp, R. W. (1985) Pressure-shear plate impact testing. *Metals Handbook: Mechanical Testing*, American Society for Metals, Metals Park, Ohio, **8**(9), 230–239.
- Exner, N. E. (1979) Physical and chemical nature of cemented carbides. *International Metals Reviews* **4**, 149–173.
- Follansbee, P. S. and Kocks, U. F. (1988) A constitutive description of the deformation of copper based on the use of the mechanical threshold stress as an internal state variable. *Acta Metall.*, **36**(1), 81–93.
- Frutschy, K. J. (1997) *High-Temperature Pressure Shear Plate Impact Experiments on OFHC Copper and Pure Tungsten Carbide*, Ph.D. Thesis, Brown University.
- Frutschy, K. J. and Clifton, R. J. (1998) High-temperature pressure shear plate impact experiments and results for pure tungsten carbide. *Experimental Mechanics* **38**(2), 116–125.
- Gilat, A. and Clifton, R. J. (1985) Pressure-shear waves in 6061-T6 aluminum and alpha-titanium. *J. Phys. Mech. Solids* **33**, 263–284.
- Giovanola, J. (1987) *Proceedings on Impact Loading and Dynamic Behavior of Materials*, Bremen, Federal Republic of Germany.
- Jarrell, J. D. (1988) *The Dislocation Structure of OFHC Copper Deformed by High Rate Pressure Shear*, Sc.M. Thesis, Brown University.
- Johnson, G. R. and Cook, W. H. (1985) Fracture characteristics of three metals subjected to various strains, strain rates, temperatures, and pressures. *Engin. Fracture Mech.* **21**(1), 31–48.
- Johnson, J. N. and Tonks, D. L. (1991) Dynamic plasticity in transition from thermal activation to viscous drag. *Shock Compression of Condensed Matter*, pp. 371–378. Elsevier Science Publishers B. V., New York.
- Kim, K. S., Kumar, P. and Clifton, R. J. (1977) A combined normal and transverse displacement interferometer with an application to impact of Y-cut quartz. *J. Appl. Physics* **48**, 4132–4139.
- Klopp, R. W. and Clifton, R. J. (1990) Analysis of tilt in the high-strain-rate pressure-shear plate impact experiment. *J. Appl. Physics* **67**, 7171–7173.
- Marchand, A. and Duffy, J. (1988) An experimental study of the formation process of adiabatic shear bands in a structural steel. *J. Mech. Phys. Solids* **36**(3), 251–283.
- Rajendran, A., Brar, N. and Khobaib, M. (1990) Effects of dynamic pre-strain on the subsequent tensile flow strength. *Shock Compression of Condensed Matter*, pp. 401–404. Elsevier Science Publishers B.V.
- Ramesh, K. T. and Clifton, R. J. (1992) Finite deformation analysis of pressure-shear plate impact experiments on an elastohydrodynamic lubricant. *J. of Appl. Mech.* **59**, 754–761.
- Ranagath, S. and Clifton, R. J. (1972) A second order accurate difference method for systems of hyperbolic partial differential equations. *Computer Methods in Applied Mechanics and Engineering* **1**, 173–188.
- Shawki, T. G. and Clifton, R. J. (1989) Shear band formation in thermal viscoplastic materials. *Mechanics of Materials* **8**, 13–43.
- Smithells, C. J. and Brandes, E. A. (1976) *Metals Reference Book*, 5th edn, pp. 953–975. Butterworths, Boston.
- Staker, M. R. and Holt, D. L. (1972) The dislocation cell size and dislocation density in copper deformed at temperatures between 25 and 700°C. *Acta Metall.*, Vol. 20, pp. 569–579.
- Storms, E. K. (1967) *Refractory Metals*, p. 152. Academic Press, New York.
- Tong, W., Clifton, R. J. and Huang, S. (1992) Pressure-shear impact investigation of strain rate history effects in oxygen-free high-conductivity copper. *J. Mech. Phys. Solids* **40**(6), 1251–1294.
- Zerilli, F. J. and Armstrong, R. W. (1987) Dislocation-mechanics-based constitutive relations for material dynamics calculations. *J. Appl. Phys.* **61**(5), 1816–1825.
- Zhou, M., Rosakis, A. J. and Ravichandran, G. (1996) Dynamically propagating shear bands in impact-loaded prenotched plates—I. Experimental investigations of temperature signatures and propagation speed. *J. Mech. Phys. Solids* **44**(6), 981–1006.



Pergamon

J. Mech. Phys. Solids, Vol. 46, No. 10, pp. 1745–1771, 1998

© 1998 Elsevier Science Ltd. All rights reserved

Printed in Great Britain

0022-5096/98 \$—see front matter

PII: S0022-5096(98)00014-3

MEASUREMENT AND CONTROL OF ICE ADHESION TO ALUMINUM 6061 ALLOY

PAUL ARCHER¹ AND VIJAY GUPTA*

Department of Mechanical and Aerospace Engineering, University of California,
Los Angeles, CA 90095, U.S.A.

(Received 20 December 1997; in revised form 15 January 1998)

ABSTRACT

A new experimental strategy for measuring the tensile strength of ice coatings to structural surfaces is presented. In this experiment, a laser-induced compressive stress pulse travels through a 1 mm-thick substrate disc that has a layer of ice grown on its front surface. The compressive stress pulse reflects into a tensile wave from the free surface of the ice and pulls the ice/interface apart, given a sufficient amplitude. The interface strength was calculated by recording the free surface velocity of an Al substrate using a Doppler interferometer and calculating the stress at the interface using a finite-difference elastic wave mechanics simulation with the free surface velocity as an input. The test procedure was used to study ice adhesion on 6061 aluminum alloy sheets. It was found that the adhesion strength of ice to unpolished aluminum substrates was 274 MPa at -10°C . This value decreased with temperature, down to 179 MPa at -40°C . Interestingly, this decrement in the tensile strength could be directly related to the existence of a liquid-like layer that is known to exist on the surface of solid ice till -30°C . The interface strength was also shown to decrease by polishing the Al substrate surface or by adding thin polymer coatings on the unpolished Al substrate. The sensitivity of the technique to such microstructural changes in the interfacial region is indicative of the experiments ability to provide basic adhesion data, which in turn, can be used to solve the deicing problem from a fundamental standpoint. © 1998 Elsevier Science Ltd. All rights reserved.

Keywords: A. adhesion and adhesives, A. fracture, B. ice and snow, B. stress waves, C. optical interferometry.

1. INTRODUCTION

In cold climates all over the world, icing on structural surfaces is a common phenomenon. Examples include, ice build-up on power and high-tension lines, radio and television transmitting and receiving towers, offshore oil platforms in cold environments, roads and foot paths, automobile windshields and headlights, and airplane fuselages and wings, among many others. Removal of ice coatings from these structures is usually necessary for their safe and reliable operation.

Most research related to deicing has focused on mechanical ice removal strategies because of practical considerations, and very little has been directed towards gaining

* Author to whom all correspondences should be addressed.

¹ Current address: Raytheon Electronic Systems, 50 Apple Hill Drive, P.O. Box 1201, Tewksbury, MA 01876-0901, M/S ANMN23, U.S.A.

a fundamental understanding of the ice adhesion process. In this regard, this paper is different from the rest and provides a quantitative measurement of basic adhesion and its influence on such variables as the ice microstructure, temperature, and the type (metal, polymer, etc.) and quality (polishing, roughness) of the structural surface. Before presenting the results, some terms related to adhesion are introduced and the available literature is reviewed.

Basic adhesion is an intrinsic property of the interface and is solely determined by the atomic structure and chemistry of the interfacial region. It can be characterized by either the intrinsic tensile strength (σ_i) or the intrinsic toughness (G_i) of the interface, both of which are related to each other via the fundamental interface stress-separation curve (Gupta *et al.*, 1994; Mittal, 1978). In contrast, the total toughness of the interface or the energy consumed in propagating a unit area of a crack along an ice/structure interface (or in its vicinity) as may occur during any ice removal process, depends upon many extrinsic parameters such as the specimen geometry, loading rate, temperature, substrate roughness, adsorbed impurities, interface flaw density, and the ratio of the tensile to shear stress ratio separating the interface. Each of these extrinsic parameters influence the inelastic (creep) dissipative mechanisms in the vicinity of the crack tip; and consequently, the fracture resistance or the total toughness of the interface becomes larger than the basic adhesion by two orders of magnitude and higher.

Ice literature is replete with studies that have measured directly or indirectly the total interface toughness. Jellinek (1957a, b, 1962, 1960, 1967), examined the adhesive properties of snow-ice sandwiched between stainless steel, optically flat quartz plates, and various polymers and block copolymers applied to aluminum substrates under both tensile and shear loading. His tensile experiments were essentially a direct pull-type test and only cohesive breaks through the bulk ice were observed at a maximum stress of about 7 MPa, implying the interface strength of the ice-solid bond to be greater than the cohesive strength of the ice. Shear experiments were conducted in a setup resembling the classical charpy impact test apparatus, where the impacting pendulum head was made to strike the ice plug almost horizontally. Such tests resulted in adhesive breaks at the interface. The *overall* interface shear strength was found to depend upon the loading rate, degree of surface roughness, temperature and the type of the substrate material being tested. In shear experiments with ice on steel, adhesive breaks were predominantly found down to -13°C . Below -13°C , only cohesive breaks through the ice were found at a peak stress of only 2 MPa. The difference between the shear and tensile strengths was related to the existence of a liquid-like layer that is known to exist between ice and the structural solid till -30°C . The existence of this layer which was proposed by Faraday (1859) are given in more detail later while discussing the basic adhesion studies.

Landy and Freiberger (1967) investigated the adhesion strength of ice to various plastics using a shear apparatus similar to that used by Jellinek. They attempted to correlate the adhesion strengths to physical and chemical properties such as critical surface tension of wetting, contact angle, coefficient of thermal conductivity and thermal expansion, porosity, dielectric constant, and flexural modulus. They were unsuccessful in this attempt probably because such tests are unable to discriminate between the effects of various variables separately. Rather, they measure a combined effect which can best be considered an average failure stress, far away from the local interface stress of interest.

More recently, solid-ice adhesion was investigated using a Raman microprobe shear apparatus (Sonwalkar *et al.*, 1993). Ice samples of thickness 100–200 μm were vapor-deposited on polished substrates of titanium, copper, aluminum, stainless steel, and Teflon. The results indicated that the adhesive bonds between the ice and the solid substrates are formed primarily by the interaction of oxygen atoms in the ice lattice with the atoms of the solid surface. When the solid lattice closely matched the ice lattice, high values of adhesive strength were obtained. The adhesive strength was also found to be proportional to the extent of mechanical interlocking and inversely proportional to the contact angle of a water droplet on the substrate. Values for the adhesive strengths obtained in the shear apparatus were in relative agreement with the values obtained by Jellinek (1957), in his experiments on steel and polymeric substrates.

All tests discussed above, provide only a relative measure of the adhesion of ice to the substrate of interest. This is due to the influence in all cases of the large extrinsic components. For example, Jellinek's direct tension and pure shear tests (Jellinek, 1957a, b) contained the effect of residual stresses at the metal-ice interface trapped during sample preparation. These tests also contained the effects of dust particle-induced interfacial flaws as indicated by the low measured bond strength value of about 2 MPa, which is two–three orders of magnitude lower than the expected strength from quantum mechanical calculations. Also included, are the effects of local creep relaxations as indicated by the measured non-linear stress-strain response, effects of strain rate as indicated by different stress-strain curves at different loading rates, effects of substrate surface roughness, and finally, the effects of the different local tensile to shear stress ratios at the interface—even though the far-field loading was either pure tension or pure shear. In fact, shortly after Jellinek carried out many of his studies on ice adhesion, breakthroughs in interfacial fracture mechanics were made by Rice and Sih (1965); they found that when a crack resides at an interface between dissimilar materials, the local stress state is a combination of shear and tension, even when the interfacial crack is loaded under far-field uniaxial tension (Mode I) or shear (Mode II) loads. The exact ratio of the tensile to shear stresses depends upon the mismatch in the elastic properties of the two materials. For the steel-ice interface, a shear stress of about 15% of the far-field tensile stress will develop under pure Mode I loading. So, without knowing the exact local stress state which is responsible for either the cohesive, adhesive, or mixed failure, the conclusions drawn by Jellinek assuming the locus of failure caused by either pure applied tension or shear, remain questionable. It seems unlikely that the bond strength of the stainless steel-ice interface is as low as 2 MPa, so there must be concentration sites at the interface which lead to higher local stresses.

Attempts to understand basic adhesion dates back to the 1850s, when Faraday (1859) studied the adhesion between two spheres of ice brought into contact. He correctly explained this adhesion by postulating that there is a thin "liquid-like" layer at the surface of ice which seemed to persist until temperatures as low as -30°C . Weyl (1951) later proposed a plausible structure to this liquid layer, claiming that it is oriented in such a way that the negative oxygen atoms of the water molecules are uppermost in the layer. In this orientation, a liquid-like electrical double layer is formed and the surface free energy is minimized. The thickness of the layer (several

hundred molecular layers thick and decreasing with temperature) was required to gradually pass from the outer electrical double layer to the proper structure of solid ice. Since this initial attempt to describe the liquid-like layer on the surface of ice, many other models have been proposed to describe the ice surface. A good summary of these is given by Petrenko (1994).

Most fundamental experimental studies of the ice adhesion process to date have been accomplished using the contact angle measurement technique, where the contact angle θ , made by a drop of water on a solid surface is measured, and related to the work of adhesion W_{ad} and free energy of the liquid-vapor interface γ_{lv} using the relationship (Jellinek, 1957a)

$$W_{ad} = \gamma_{lv}(1 + \cos\theta) + \pi_e, \quad (1)$$

where π_e represents the increment in the solid-vapor free energy on account of adsorbed gases and liquids on the solid surface. The values of W_{ad} obtained from eqn (1) for the water/solid interface cannot be directly taken as a measure of the work of adhesion for the ice/solid interface, especially when a liquid-like layer of varying thickness is present at the ice/solid interface at different temperatures. Nevertheless, such contact angle studies can be used for qualitatively determining the degree of hydrophobicity of various engineering metallic and polymeric substrates as demonstrated by Jellinek (1957a).

Scanning force microscopy (SFM) has recently been used by Nicolayev and Petrenko (1995) to study the surface of ice and the adhesive forces between the ice surface and cantilever tip of the apparatus. This method allows the study of the ice surface and ice adhesion to solids (the tip of the cantilever) at the molecular level. In this experiment, a very sharp tip, mounted to a flexible cantilever of the SFM, is dragged over the surface of an ice sample. Deflections in the flexible cantilever are detected by a laser beam reflected from the cantilever, providing a vertical resolution of about 0.1 nm. Measurements of the force interaction between the tip and the surface, as a function of relative tip-sample position, yield a force curve. From this force curve, the adhesion force between the tip and the ice surface can be deduced. Then, the adhesion strength is defined as the adhesion force per unit area of the tip. For silicon nitride cantilever tips, Nicolayev and Petrenko (1995) found an adhesion strength of 2.7 MPa at -5°C , with the strength decreasing with decreasing temperature. Although this technique is promising, there are a number of questions that pertain to converting the measured force to the local stress. First, the mechanistic considerations should include the sharp tip geometry-related singularity effects while converting the force to the stress. This should increase the calculated interface stress significantly. When operated in the contact mode, the surface tension effects between the tip and the liquid layer will significantly depend upon the tip geometry, and hence, so would the calculated adhesion stress. Finally, the technique is rather impractical, since one will have to change the tip material to aluminum or other materials of interest. Unfortunately, putting a coating on nitride cantilever tips will not yield basic adhesion data between the coating material and ice, since it is well known that the influence of tip material could persist through 70–100 monolayers of the intervening layers of different materials (Yuan and Gupta, 1995). Additionally, the grain orien-

tation and geometry that is known to influence the adhesion strongly will become a significant factor in interpreting the data, given the rather small diameter of the cantilever tip. In light of the above discussion, the values obtained from this procedure can only be considered qualitative at the present time.

In summary, a quantitative measure of basic adhesion between ice and structural solids has not been obtained so far, and yet this appears to be a basic quantity that is needed to solve the deicing problem, from a fundamental standpoint. The aim of the research leading to this paper was to develop an experimental procedure for measuring the tensile strength of ice/structural aluminum interfaces by adapting the recently developed technology of laser-generated stress pulses. Previously, the tensile strengths of interfaces formed by a variety of metal, ceramic, and dielectric films and a number of engineering substrates were measured under ambient conditions by using laser-generated stress pulses (Gupta *et al.*, 1990 and 1992; Yuan *et al.*, 1993; Gupta and Yuan, 1993; Yuan and Gupta, 1993; Gupta *et al.*, 1994). As discussed below, this so-called laser spallation experiment is capable of measuring the intrinsic tensile strength of flaw-free interfaces. The present investigation was focused on developing this procedure further for carrying out ice adhesion measurements at cryogenic temperatures, and to study the effects of the type and quality of the substrate surface, including the effects of intervening hydrophobic coatings and the interface strength dependence on temperature. The basic laser spallation test methodology is discussed first, and this is followed by the sample preparation procedures and the new test apparatus for examining the ice/6061 Al bond strength.

2. THE LASER SPALLATION TECHNIQUE

In this experiment (Fig. 1), a 2.5 nanosecond (ns) long Nd:YAG laser pulse is made to impinge over a 3 mm-dia area on a 0.3 μm -thick aluminum film which is sandwiched between the back surface of a substrate disc and a 5–10 μm thick layer of solid water glass. This layer is provided as a liquid solution of sodium silicate, which dehydrates within a few minutes when exposed to air, and leaves behind a continuous layer of solid SiO_2 , covering the aluminum film. The melting-induced expansion of aluminum under confinement generates a compressive stress pulse with 1 ns ($= 10^{-9}$ s) rise time directed towards the test coating which is deposited on the substrate's front surface. The compressive stress wave reflects into a tensile pulse from the coating's free surface and leads to its spallation (complete removal) at a sufficiently high amplitude. The critical stress at the interface is calculated by measuring the transient displacement history of the coating's free surface (induced during pulse reflection) by using an optical interferometer (shown towards the right and top in Fig. 1) which is capable of recording fringes from even optically rough surfaces and with a resolution of only 0.2 ns in the single shot mode. For a coating of density ρ , thickness h , and longitudinal wave velocity, c , the interface stress σ is calculable from the measured transient velocity $v(t)$ using

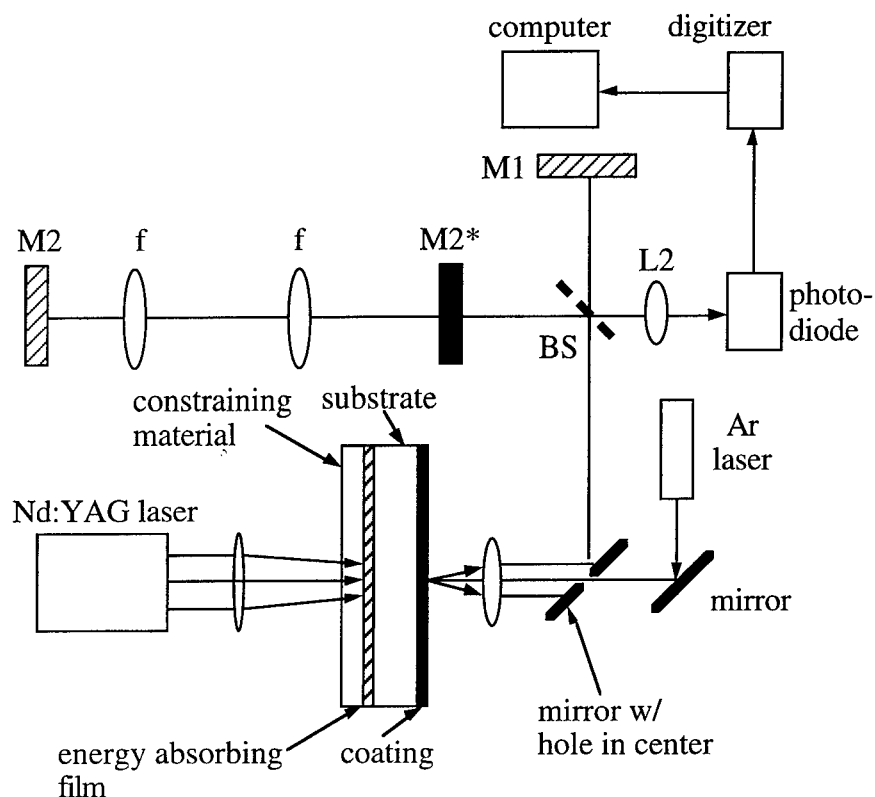


Fig. 1. A schematic diagram of the laser spallation setup along with the laser Doppler differential displacement-velocity interferometer.

$$\sigma(h, t) = \frac{1}{2} \rho c \left[v \left(t + \frac{h}{c} \right) - v \left(t - \frac{h}{c} \right) \right]. \quad (2)$$

The major advantage of this technique over its counterparts is in its ability to provide a fundamental measure of the bond strength, since interface decohesion is achieved at a relatively high strain rate (10^7 s^{-1}) during which all inelastic dislocation-related processes are essentially suppressed, and the measured values relate directly to the atomic structure and chemistry of the interfacial region. Additionally, the short rise time of the stress pulse is able to invoke a rather local response of the interface such that minute changes in the atomic structure and chemistry are reflected directly in the measured strength values. This was recently demonstrated (Yuan and Gupta, 1995) on interfaces between sputter-deposited polycrystalline Nb coatings and sapphire substrates where structural changes brought about by different heat treatment cycles and different thicknesses of the intervening Cr and Sb layers were shown to directly affect the interface's tensile strength.

3. MODIFICATIONS TO THE LASER SPALLATION TECHNIQUE FOR ICE ADHESION STUDIES

3.1. Sample preparation

The current investigation involved testing the adhesion strength of ice frozen to sheets of Al-6061 alloy with different surface treatments. The first set of samples were tested in the as-manufactured condition. The second set were polished on a metallographic wheel using α -alumina powder of sizes 1.0 μm , 0.3 μm and 0.05 μm . The third set were prepared with the aim of investigating the influence of hydrophobic coatings. For this purpose, unpolished Al substrates were coated with 1 μm -thick coatings of polymethylmethacrylate (PMMA) and a polyimide (PI) and tested at -10°C . The polymer coatings were spin-cast onto the Al substrates, and then baked for 1 h in an oven at 100°C . The coatings were transparent. Finally, the last set of samples were used for studying the effects of temperature on bond strength. For this, only the as-manufactured Al surfaces were used and bond strength determined at -20°C , -30°C , and -40°C .

All aluminum sheets, regardless of the surface treatment, were 0.8 mm thick and roughly 25–50 mm in length and width. The back side (i.e., other than the one treated above) of each sample was cleaned in an ultrasonic cleaner in a bath of acetone, rinsed in de-ionized water, then again cleaned in a bath of de-ionized water in the ultrasonic cleaner. The samples were then air dried and a thin layer (30–50 μm) of liquid water glass ($\text{H}_2\text{SiO}_3 \cdot (\text{H}_2\text{O})_x$) was applied to one surface of the aluminum. After exposure to the air for several minutes, the water evaporated and a layer of solid water glass (SiO_2) was left on the aluminum. This layer of water glass serves as the confining layer, which is critical for the generation of the high-amplitude and quickly decaying stress pulse discussed by Yuan *et al.* (1993). Previously, it was found that the generated stress pulse amplitudes and profiles are quite insensitive to the solid water glass in the above thickness range, which in turn, could be applied reproducibly.

Once the water glass hardened, samples were placed in a freezer held at -10°C . The samples were allowed to equilibrate to this temperature for about 1 h and then the ice was grown on the *treated* surface of the aluminum, opposite to the one covered with the water glass coating. To grow ice, an O-ring with a 25 mm inner diameter was placed on the surface. Then, room temperature de-ionized water was placed inside the O-ring, with the meniscus of the water rising above the thickness of the O-ring (≈ 2 –3 mm). Normally, ice formed several minutes after the water was filled inside the O-ring. If ice did not form within this time, a slight movement of the O-ring would cause the water to crystallize. Figure 2 shows a schematic of such a sample.

After ice formation, the sample was allowed to sit for an hour in the freezer at -10°C . The O-ring was then carefully removed from the sample and the ice puck was shaved flat, using a razor blade. This was done to remove bubbles from the upper part of the ice which would inhibit examination of the interface by optical microscopy. The ice samples were polycrystalline in nature with columns perpendicular to the interface. In all experiments the thickness of the ice was about 0.74 mm and the variation of the thickness over the entire surface area was normally less than ± 0.05 mm. Due to the internal reflection of the stress pulse that occurs at each boundary,

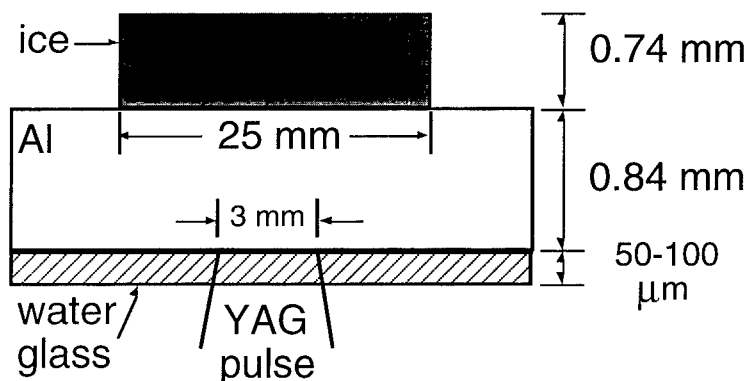


Fig. 2. A schematic showing the geometry of the ice plug/aluminum sample.

variation of the ice thickness could lead to a different stress state at the interface due to different arrival times of the compressive and tensile pulses. Therefore, only samples with ice thicknesses in the range of 0.74 ± 0.05 mm were used in actual experiments.

Figure 3(a) and (b) show high magnification view of the unpolished and polished Al substrates, respectively. These surfaces were typical of the surfaces which were used in the present study. It should be noted that no quantization of the surface roughness was performed (such as surface profilometry, etc.), so that any conclusions based on surface roughness are qualitative in nature.

As expected, the ice microstructure was strongly influenced by that of the substrate surface below. Figure 4(a) and (b) show ice grains on unpolished and polished Al substrates, respectively, using reflected light in an optical microscope. The grains are visible as shadows on the surface of the aluminum substrates. The grains on the unpolished Al (Fig. 4(a)) are generally hexagonal in nature, having grain sizes of about 1.5 mm and under, and oriented perpendicular to the interface (so the grains are visible in the plane of the aluminum). On the polished Al substrates (Fig. 4(b)), the grains are smaller in size (averaging less than 1 mm in width) and, in general, more irregular in shape than on the unpolished substrates.

Figure 5(a) and (b) show the grain structure of the ice grown on the substrates coated with $1 \mu\text{m}$ of PMMA and PI, respectively. The grains in these micrographs are viewed under double-polarized light. In order to view the samples in this way, the light illuminating the samples had to be polarized in one direction before hitting the sample. After reflection from the sample, the light was polarized along the other direction and gathered by the microscope objective. Figure 5(a) and (b) do not show the hexagonal structure for the ice grains that is seen on the uncoated aluminum samples.

Before performing experiments on new samples, all samples were examined using an optical microscope. Occasionally, some samples would show bubbles or other contaminants either in the bulk ice or close to the ice-aluminum interface. These samples were discarded and not used in any laser spallation experiments since these contaminants could have caused premature failure and skew the data.

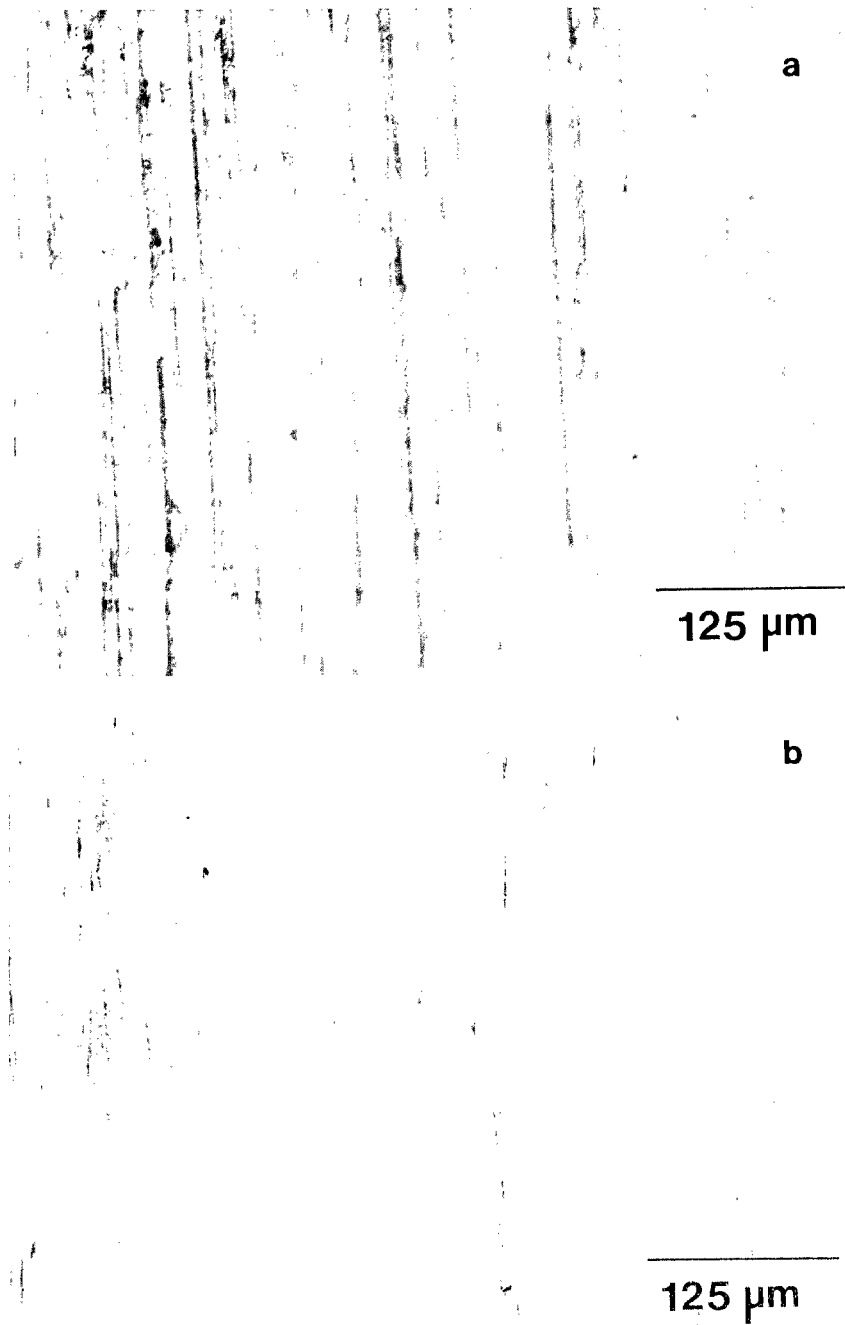


Fig. 3. Micrographs showing high magnification views of (a) unpolished Al and (b) polished Al.

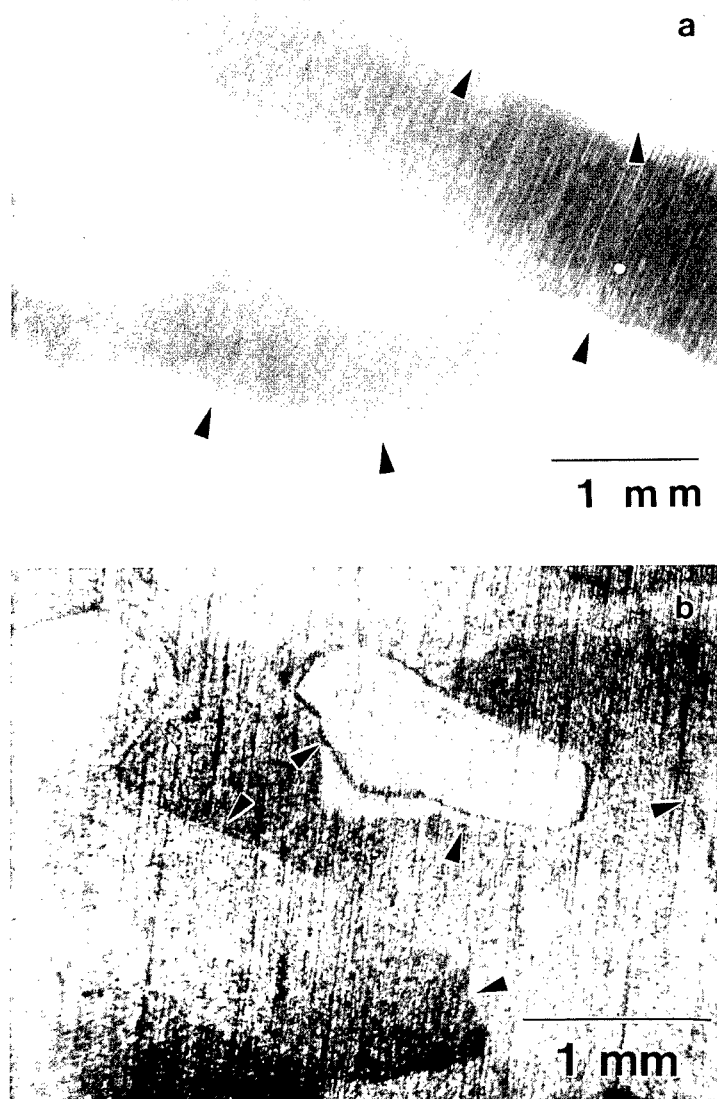


Fig. 4. Micrographs showing the grain structure of ice grown on (a) unpolished Al and (b) polished Al substrates under reflected light in an optical microscope. The grains show up as shadows on the Al substrate.

3.2. Test apparatus

A sample holder similar to the one used by Gupta and Tian (1994), was constructed to incorporate the new geometry of the current investigation (Fig. 6). In this holder, stainless steel clips held the aluminum-ice sample in the inner chamber (fig. 6(a)) which was held in the freezer at -10°C until the outer chamber (Fig. 6(b)), already in place in front of the YAG laser) was cooled to the desired test temperature. Once

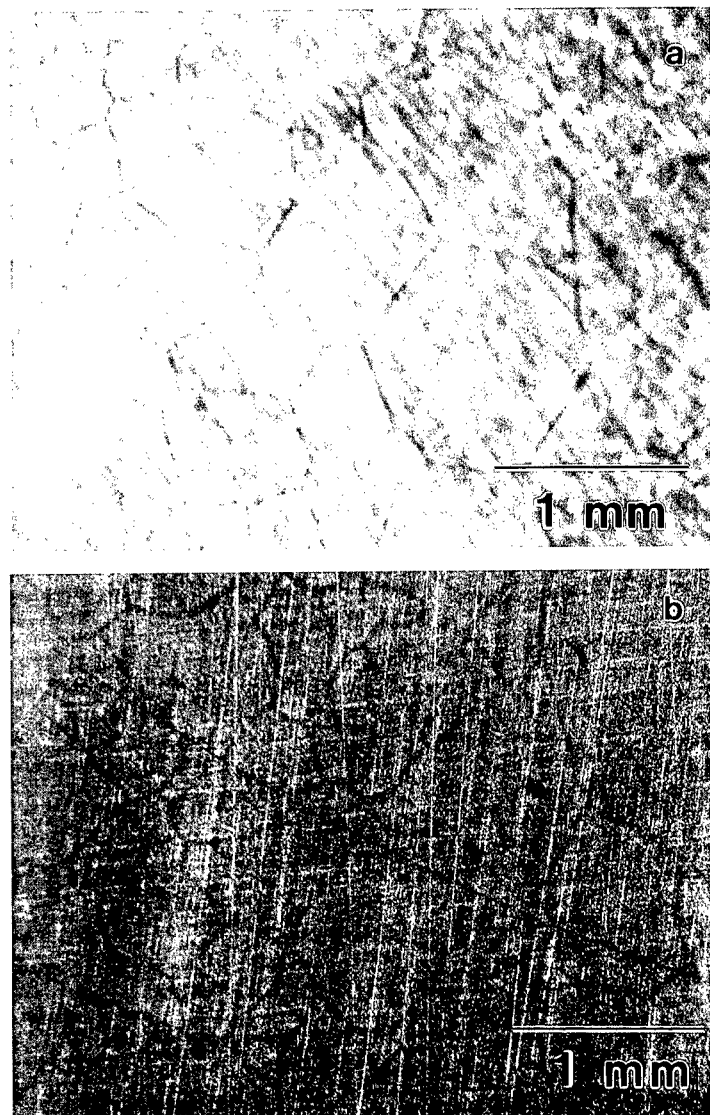


Fig. 5. Micrographs showing the grain structure of ice grown on Al substrates coated with 1 μm of (a) PI and (b) PMMA viewed under double-polarized reflected light in an optical microscope. Grain boundaries are indicated by arrows.

the outer chamber was at the desired temperature, the inner chamber was placed inside such that the water glass-covered surface of the sample was facing towards the YAG laser source. Both chambers were then allowed to equilibrate to the desired test temperature for several minutes. As before, a copper coil was immersed in a liquid nitrogen bath and gas flowed through the coil and into the chambers to control the temperature. Due to its availability in the laboratory, compressed air was used as the

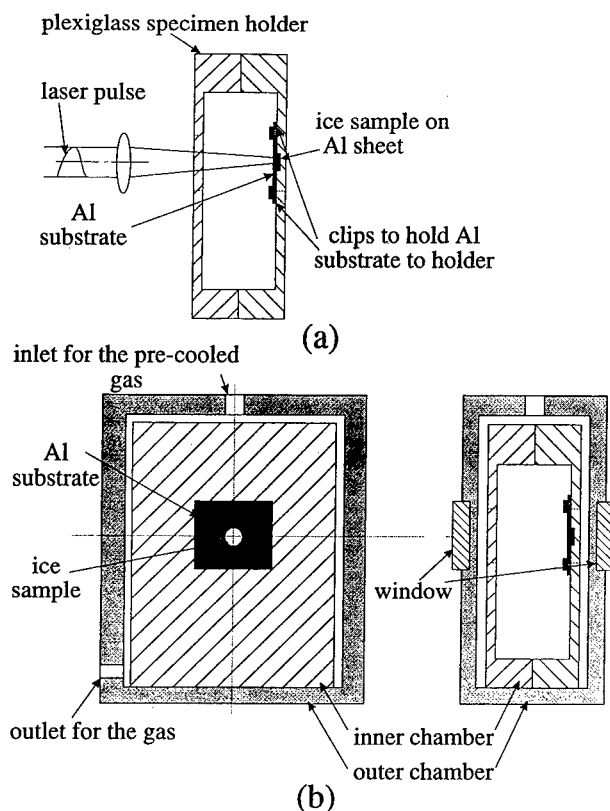


Fig. 6. A schematic diagram of the ice sample holder used in the aluminum-ice adhesion experiments: (a) inner chamber; (b) outer chamber.

cooling gas, as opposed to nitrogen used in the cleavage strength measurements of ice crystals of Gupta and Tian (1994). Occasionally, water vapor and oxygen would freeze inside the coils and the flow of air was restricted, but this never prevented the setup from cooling the chamber to the desired temperature. The temperature of the chamber was controllable to within $\pm 1^\circ\text{C}$ by adjusting the flow rate of the air. The lowest test temperature investigated, -40°C , was easily achieved using this experimental assembly,

The Nd:YAG laser pulse communicated with the constrained aluminum surface via one of the quartz windows that was provided on the outer chamber. Similarly, a rear quartz window provided the view of the ice surface as needed to inspect the spall phenomenon. The quartz used for constructing the window facing the YAG laser source was transparent to the $1.06\ \mu\text{m}$ wavelength of the YAG laser. A continuous flow of room temperature air was blown on the windows to prevent condensation of vapor.

3.3. Test procedure

3.3.1. *Procedure summary.* The basic structure of the laser spallation experiment described in Section II was used without change except that a different quantification strategy had to be adopted because of the difficulties encountered in measuring the free surface velocity of the ice surface. In the new procedure, the threshold laser fluence causing the onset of damage at the ice/aluminum interface was determined first. Next, a bare aluminum surface having identical geometry and stress pulse generation conditions, was subjected to the same laser fluence that led to the initiation of interface damage in the first step, and the transient free surface velocity resulting from the reflecting stress pulse was recorded by using an interferometer. This free surface velocity was used as an input to a finite-difference program which solved the one-dimensional elastic wave equation in an aluminum/ice plug assembly and resulted in the desired peak interface tensile stress. Although this procedure is not as direct as the one based on the measurement of the coating's free surface velocity (as discussed in Section II above), it is still less complicated than the original procedure of Gupta, *et al.* (1992) which used a simulation to convert the threshold laser energy into the desired interface stress, without the use of any interferometer. In this latter approach (Gupta *et al.*, 1992), the entire process of stress pulse generation resulting from the melting and associated volumetric expansion of the aluminum film, and its subsequent propagation to build the tensile stress at the interface, was modeled. The various aspects of the quantification procedure outlined above are preliminary and well established, and hence only a brief description of each is provided below.

3.3.2. *Determination of the threshold laser energy.* At the desired test temperature, a Nd:YAG laser pulse was fired through the quartz window onto a 3 mm dia area of the aluminum surface constrained by the water glass layer (Fig. 6). After each shot of the YAG laser, the ice samples were returned to the cold room and examined under an optical microscope. For the purpose of interface strength measurement, quantification of the initiation of interface damage and not propagation of such damage was desired. Three types of damage were typically seen in most samples, as is shown in Fig. 7. First, damage occurs at the outer reaches of the incident area or the stress pulse (labeled A in Fig. 7). This damage is caused by the momentum of the volume of ice under the influence of the stress pulse and the constraint of this volume of ice by the surrounding ice. So, the axial stress σ_x (normal to the ice surface, see Fig. 2) and the confinement by the surrounding ice create a shear stress which causes the cracking around the periphery of the stressed spot. A second type of failure (labeled B in Fig. 7) is damage within the ice, that is, the cracking of columns along the grain boundaries. This damage is caused by the transverse tensile stress, σ_t , that develops in the yz plane due to the plane strain constraints of the sample. The final type of failure (labeled C in Fig. 7) is the interface damage consisting of a void formation at the interface due to the axial stress σ_x . The first two types of damage will not be discussed any further here. It is the interface damage which is of interest in this investigation.

Interface damage and void formation are more easily seen in Fig. 8(a) where the large decohered regions appear dark compared with the bonded regions immediately to the outside and are labeled A. Normally, the formation of voids (or one large void

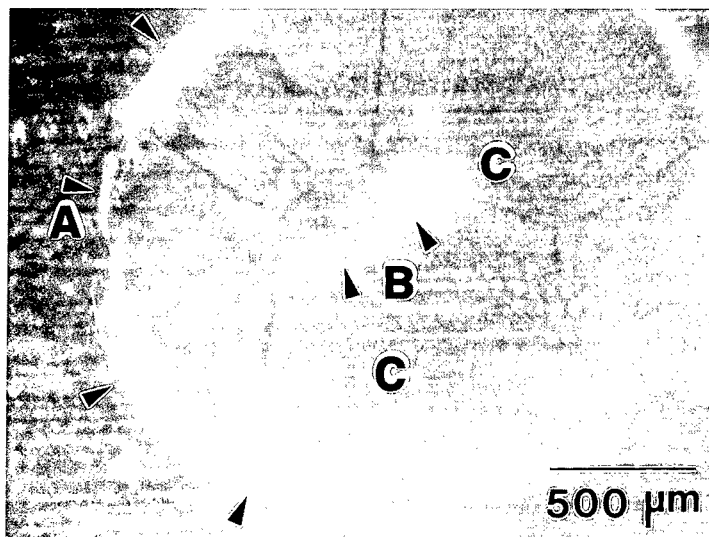


Fig. 7. A micrograph showing the three types of failure observed during ice adhesion experiments viewed under reflected light in an optical microscope. (A) pulling out of ice plug; (B) cracking of ice columns; (C) interface voids.

in some cases) occurred within the central region of the incident area of the stress pulse, sometimes extending to the edges of the stress pulse area. This damage occurred as a result of the axial tensile stress acting to pull the ice away from the aluminum at the interface. These voids were easily discernible under the optical microscope, even when they were small in size, Fig. 8(b).

It is noteworthy that the compressive pulse should not predamage ice since grain boundaries are normal to the interface and hence experience no shear. Furthermore, the deformation occurs at a strain rate of 10^{-7} s^{-1} , which is about five orders of magnitude higher than the rate at which Picu and Gupta (1995b) observed the grain boundary sliding phenomenon in freshwater columnar ice.

Once damage at the interface was discovered using the optical microscope, the experiments were repeated several times to verify that interface damage actually occurred and was repeatable. Then, the laser output energy was measured using an energy meter, and the laser fluence (or energy per incident area) was calculated. The laser fluence at which damage at the interface first occurred was then found by repeated experimentation, and this was termed the threshold laser fluence for the particular aluminum surface treatment at the particular test temperature. The stress causing this damage initiation at the interface is a direct measure of the bond strength between the ice and the aluminum. The method to calculate this stress from the recorded threshold laser fluence is discussed next.

3.3.3. Determination of the aluminum free surface velocity using interferometry. The wide angle interferometer shown in Fig. 1 was used for recording the free surface velocities from a highly reflective aluminum surface whose backside was subjected to

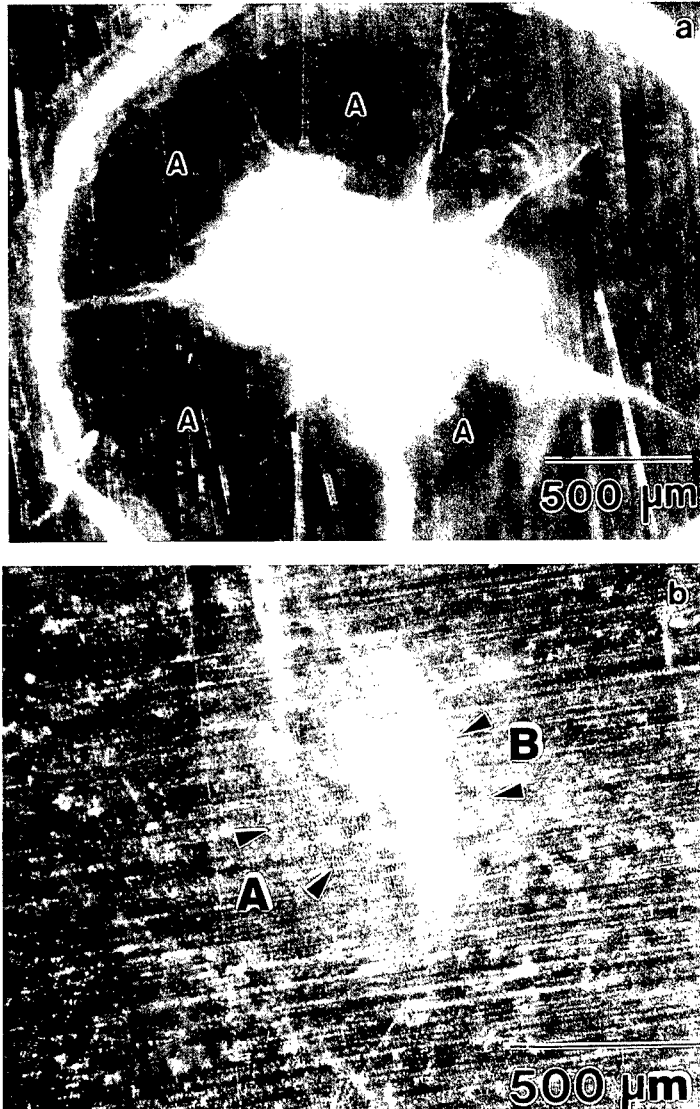


Fig. 8. (a) A micrograph showing interface voids (labeled A) on a polished Al substrate viewed under reflected light in an optical microscope; (b) Interfacial microbubbles viewed using an optical microscope at the ice interface with a polished aluminum surface.

the same laser fluence that led to crack nucleation at the ice/aluminum interface. Except for the ice layer, every other aspect of the previous sample geometry including the water glass layer was identically reproduced. The interferometer design is somewhat similar to that proposed by Amery (1976) and its details have been given earlier (Pronin and Gupta, 1993). A typical fringe record obtained from an Al surface is shown by the solid line in Fig. 9. Since the useful duration of the signal is well within

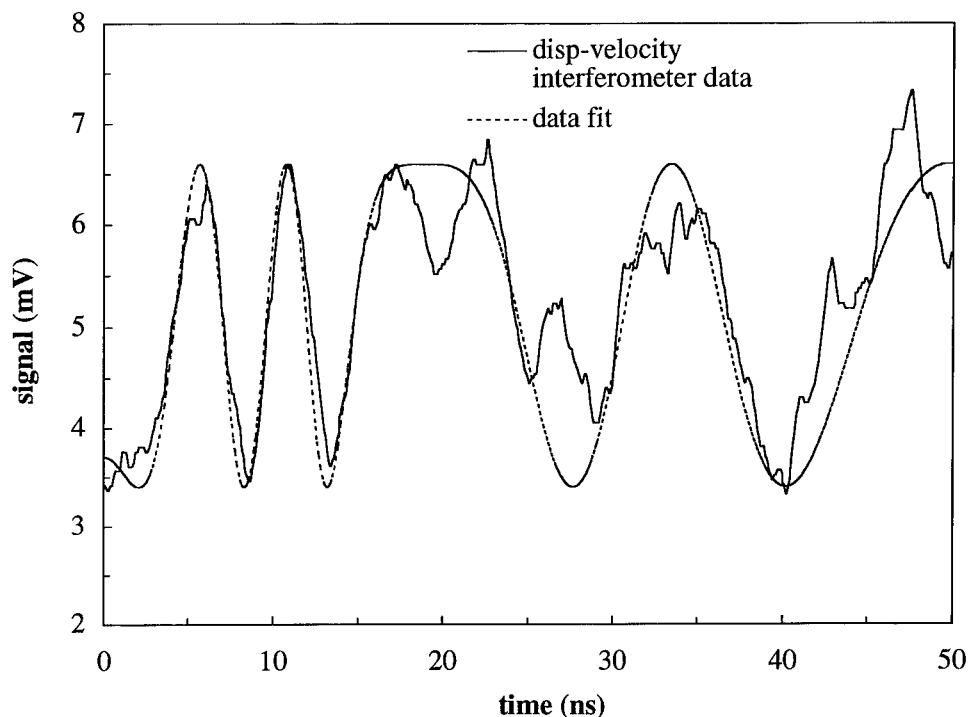


Fig. 9. The fringe pattern recorded by using the differential displacement-velocity interferometer of Fig. 1, is shown by the bold line.

the delay time τ_d of the interferometer ($= 13.3$ ns), the fringes obtained during this time are directly related to the surface displacements. Due to the rather sharp rise time and duration of the signal in the laser spallation setup, the signal to noise ratio of the recorded fringes is not ideal. This requires information on the expected velocity profile before the fringe data can be unambiguously reduced to the transient velocity profile. To get such information, a linear velocity interferometer was constructed. In this type of interferometer, the delay length between the two optical paths is made much smaller than the rise time of the velocity pulse so that the photodetector output is directly proportional to the free surface velocity (Barker, 1972).

In this modified interferometer (shown in Fig. 10), the delay leg of two lenses and one mirror of the interferometer shown in Fig. 1 is replaced by a de-ionized water-filled etalon with a mirror on one end. The etalon was constructed of a plexiglas tube of 2 in inner diameter and about 7 in length, capped at the ends by fused silica windows of 0.5 in thickness. The fused silica window on the left end had a $5\text{ }\mu\text{m}$ thick layer of aluminum deposited on the outside to act as mirror M2 as shown in Fig. 10. Once again, the apparent position of M2 (M2*) and M1 are equidistant from the BS. Due to the higher index of refraction of water compared to air (≈ 1.3 compared to 1), the actual optical position of M2 is at M2**, yet this is much less than the actual optical position of M2 in Fig. 3. This reduction in actual optical distance traveled

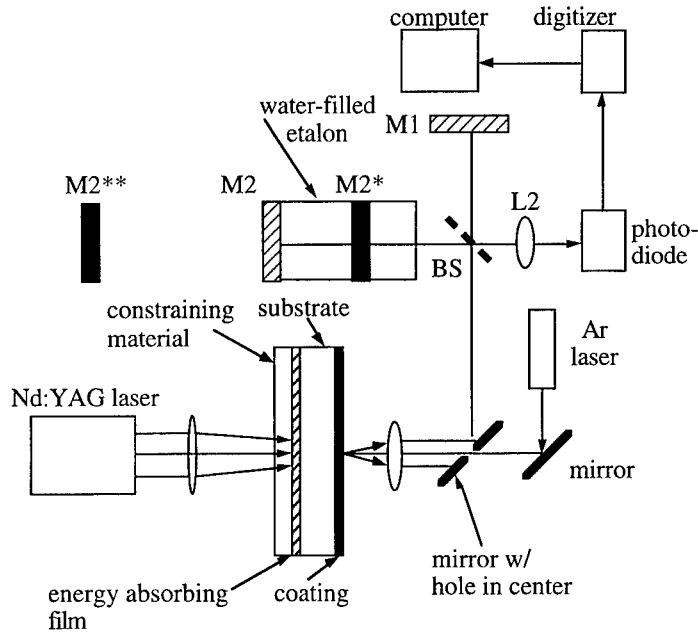


Fig. 10. A schematic diagram of the laser spallation technique along with the velocity interferometer with etalon to verify the assumed shape of the velocity pulse.

between the two interferometers reduces the time lag between the delayed beam and the signal beam to approximately 0.67 ns. Since the expected rise time of the velocity pulse recorded in this experiment is appreciably larger than 0.67 ns, the photodetector output is directly proportional to the transient surface velocity. Figure 11 shows the fringe record (or proportional to velocity profile) obtained from the linear interferometer at the same laser fluence as the one that resulted in the displacement fringe record of Fig. 9. It is noteworthy that the linear interferometer only provides information proportional to the actual velocity, with the amplitude of the actual velocity undefined. This was of no concern here as the aim was just to obtain the profile of the surface velocity so that it could be used to judiciously reduce the displacement fringe data of Fig. 9 obtained using the interferometer of Fig. 1. It was found that the velocity profile remained almost identical, except for the amplitude over the range of laser fluences that were needed to initiate damage at the ice/aluminum interface. The expected displacement fringe data corresponding to the recorded velocity profile with an assumed amplitude, was determined via integration and matched with the displacement fringe pattern recorded using the interferometer of Fig. 1. The amplitude of the recorded velocity pulse was varied till the match between the calculated and recorded displacement fringes was the closest. The dashed line in Fig. 9 corresponds to the calculated fringe record obtained via the above procedure. The complete velocity information was next used as an input to the wave propagation simulation to arrive at the desired interface stress history.

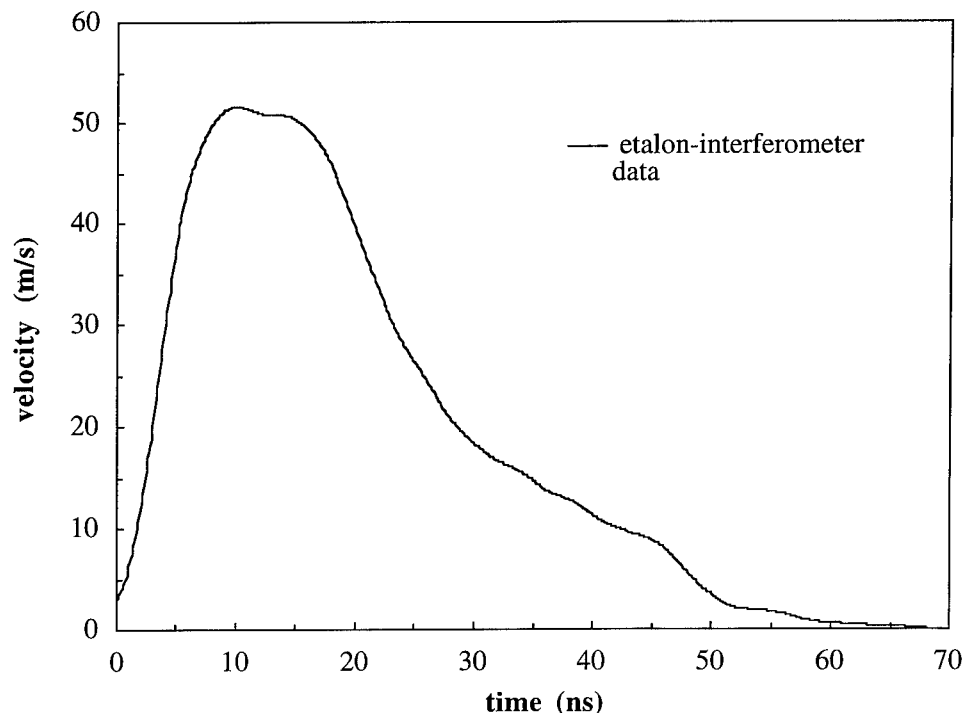


Fig. 11. The velocity fringe profile as obtained from the etalon interferometer. The ordinate of the fringe record was adjusted till a close fit to the recorded fringes in Fig. 9 was obtained. Thus, the as-recorded fringe record ordinate in units, of mV was converted into m/s .

3.3.4. *Interface stress calculation using a finite-difference simulation.* The geometry of the ice/aluminum assembly used for the computation is shown in Fig. 2. In the central region of the stressed area, the normal strains in the plane of the interface can be considered fully constrained and hence, the stress wave propagation through the assembly can be idealized as one-dimensional. Further, for ice, a strain rate of 10^{-1} s^{-1} is plenty to invoke an elastic dislocation motion-free response from a polycrystal (Picu and Gupta, 1995a and b). The stress-velocity data in aluminum at strain rates in the laser spallation experiment, near 10^7 sec^{-1} , is currently unavailable. Linear extrapolation of data from lower rates, however, suggests an elastic response. Therefore, the stress state within the aluminum and ice was taken to be elastic throughout with the displacements and the resulting stresses in the assembly calculated by solving the classical one-dimensional elastic wave equation, albeit modified by the condition of zero lateral strains. Due to this latter condition, the transverse stresses σ_t develop and their magnitude equals the product of the axial stress σ_x with the term $\nu/(1-\nu)$, where ν is the Poisson's ratio. The wave equation was solved subject to: (1) the traction free condition at the ice's free surface; (2) continuity of traction and velocity

at the ice/aluminum interface; and (3) the initial stress condition at the back aluminum surface given by

$$\sigma = 0.5 \rho_{\text{Al}} c_{\text{Al}} V(t) \quad (3)$$

where ρ_{Al} is the Al density, c_{Al} is the speed of a longitudinal wave traveling through aluminum, and $V(t)$ is the Al free surface velocity determined from the experiments discussed above.

The simulation modeled the propagation of the stress wave through the aluminum-ice sample (Fig. 2) for 1 μs by using the finite difference approach. The Al thickness used in the program was 0.84 mm while the ice thickness was 0.74 mm. Furthermore, because of the rather small thickness of the polymeric (1 μm) and liquid-like layer (few hundred \AA thick) compared with the stress wave, they were not identified in the simulation. The model incorporated 1000 space nodes and 12,000 time steps, giving $\Delta x = 1.58 \mu\text{m}$ and $\Delta t = 0.083 \text{ ns}$. The density, one dimensional Young's modulus ($\lambda + 2\mu$), Poisson's ratio, and longitudinal speed of sound for both Al and ice that were used in the simulation are summarized in Table 1. Specific ice adhesion results on differently treated aluminum surfaces are provided next.

4. RESULTS

For all experiments performed, regardless of the surface finish, applications of coatings on the Al, or test temperature, it was found that damage initiation at the interface with ice always occurred between YAG laser fluences of $1.3 \times 10^4 \text{ J/m}^2$ and $2.15 \times 10^4 \text{ J/m}^2$. The interface stress was calculated at three values of laser fluence within this range (as discussed in Section III), and fitted to a curve, as shown in Fig. 12. Each data point on the curve is the average of seven runs of the finite-difference program with each run using a different velocity record obtained from a fringe record output of the interferometer shown in Fig. 1. In all cases, the velocity pulses input

Table 1. *Material properties for aluminum and ice as used in the finite difference simulation*

Property	Aluminum	Ice
Density (kg/m^3)	2700	918
One-dimensional Modulus ($\lambda + 2\mu$) (GPa)	111	9.4
ν	0.345	0.33
c (m/s)	6409	3200
Reference	Brandes and Brook (1992)	Hobbs (1974)

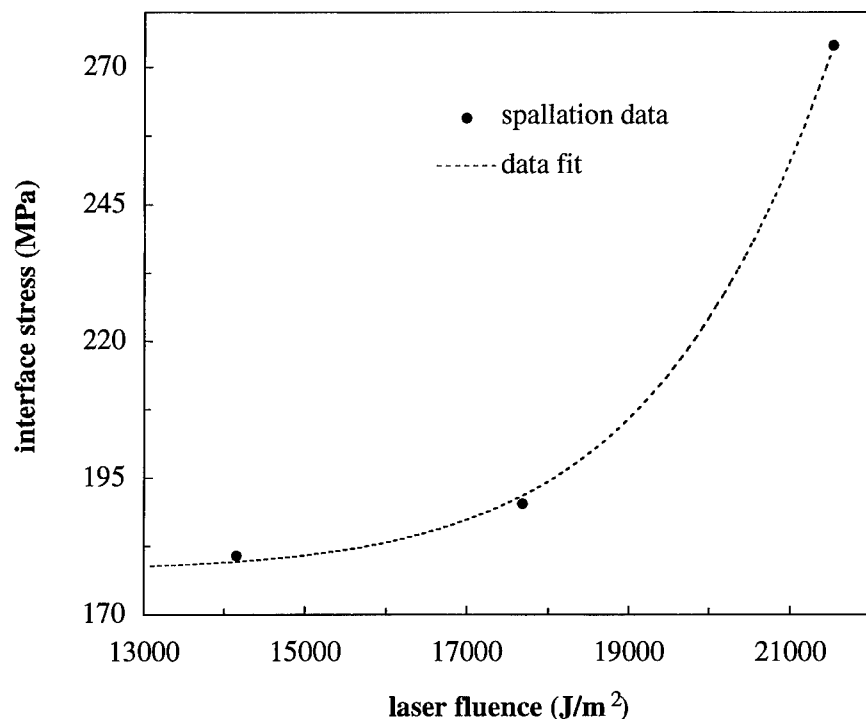


Fig. 12. A plot of the calculated interface stress as a function of laser fluence.

into the finite-difference program, were of similar shape (that is, similar rise and decay times) and varied only in amplitude for different threshold laser fluence levels. This was confirmed experimentally. This method of determining the interface stress expedited the data collection process.

The results for the ice adhesion experiments performed in this investigation are summarized in Table 2. Those results which show a \pm value were calculated from the methods described in Section III. The others were determined by reading the interface stress from Fig. 12 according to the experimentally determined threshold laser fluence. The number of experiments in which interface damage was observed at the indicated interface stress is shown after the stress level in Table 2. The number after \pm represents the error range resulting from the laser pulse-to-pulse variation, recording and reducing the interferometer data, and sample preparation procedures. Details of this estimation can be found in Archer (1996).

The maximum strain rate calculated in the finite-difference program was found to be about $2 \times 10^7 \text{ s}^{-1}$. This, of course, depends upon the exact shape of the stress pulse and the actual stress amplitudes, but since the velocity pulses found with the interferometer were of the same shape and varied only slightly in amplitude, the stress

Table 2. Results for the laser spallation experiments on the Al-ice interface system with various aluminum surface treatments

Substrate Surface	Temp (°C)	Interface strength (MPa)	No. of experiments
Unpolished Al	-10	274 ± 17.1	6
Unpolished Al	-20	192	4
Unpolished Al	-30	183	6
Unpolished Al	-40	179	5
Polished Al	-10	180.8 ± 6.4	8
Al + 1 µm PMMA	-10	190.3 ± 8.0	8
Al + 1 µm PI	-10	181	5

All temperatures shown for the experiments are $\pm 1^\circ\text{C}$. The number of experiments in which interface damage was observed at the indicated stress is shown after the stress.

pulses in all experiments were very similar in shape. Therefore, the strain rate in all experiments is in the order of 10^7 s^{-1} , high enough to justify the elastic wave propagation simulation.

5. DISCUSSION

As discussed in Section I, many studies have been performed attempting to measure the ice adhesion strength to various substrates. yet none, to date, have been able to characterize the intrinsic interface tensile strength. The current investigation provides data closer to the true value of intrinsic interface stress than any other report to date. Thus, data obtained here cannot be directly compared with the results of previous studies, but the results are very promising in that the trends of the data follow intuition and current theories on the existence of the liquid-like layer at the interface. Qualitative comparisons are made with other investigations wherever appropriate.

5.1. Temperature dependence

Table 2 shows the adhesion strength of ice to the unpolished Al substrates to be temperature-dependent. This temperature dependence is plotted in Fig. 13 along with a best fit of an exponential function of the form

$$\sigma_x = \sigma_0 + a \exp^{2.5T/b} \quad (4)$$

where σ_0 is 179 MPa and a and b are fitting parameters whose values are shown in the figure. with falling temperatures, the interface strength falls, leveling off to a value of about 179 MPa at -40°C . This temperature dependence is contrary to that found by Jellinek in tensile tests of ice on polystyrene substrates (Jellinek, 1957a), but in

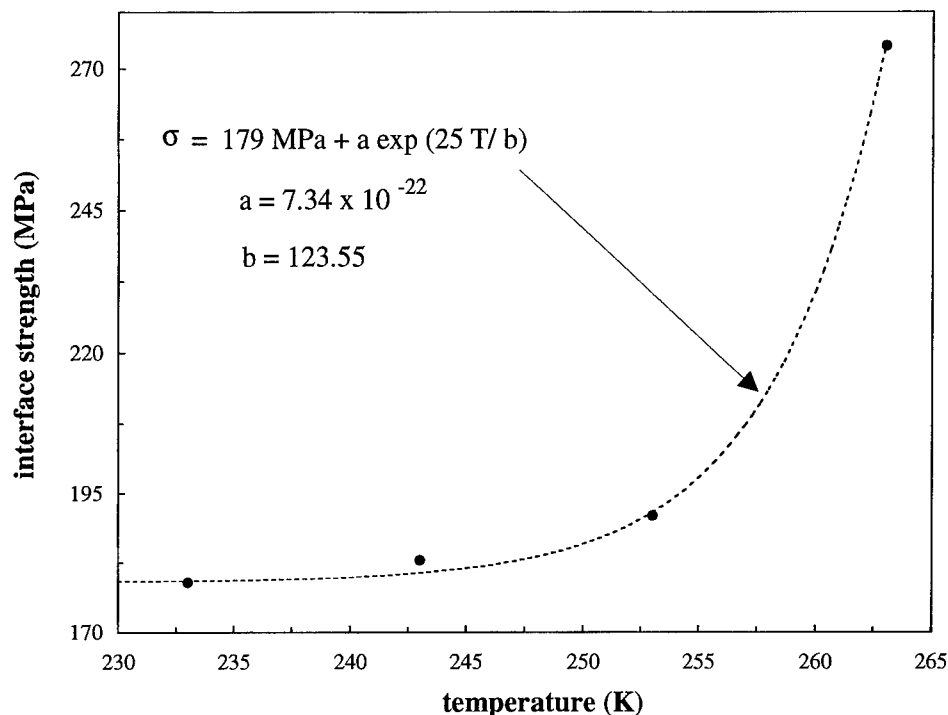


Fig. 13. A plot of the temperature dependence of the interface strength of ice on unpolished aluminum substrates and the best fit of an exponential function.

agreement with Nickolayev and Petrenko (1995) in SFM tests of ice adhesion to metals.

This temperature-dependence of adhesion data on unpolished Al substrates can be explained using the existence of a liquid-like layer at the Al-ice interface. At relatively high temperatures (-10°C), the value of adhesion is the largest. The liquid-like layer is largest at temperatures close to the freezing point of water and decays with decreasing temperature (Weyl, 19510). Since the layer is liquid-like, it should be treated as incompressible with Poisson's ratio equal to 0.5. In this case, the transverse stress (σ_t) developed within the liquid-like layer equals the axial stress (σ_x), and now more energy is dissipated in the transverse direction. Because of this, a much larger stress is needed to accomplish interface separation. At -20°C , the interface strength has dropped dramatically, which also correlates with a corresponding decrement in the liquid layer thickness. Below -20°C , the value of the interface strength levels off to about 180 MPa. It is a temperature between -25°C and -30°C where the liquid-like layer disappears (Weyl, 1951; Jellinek, 1967; Hosler *et al.*, 1957). In this case, the

damping effects of the liquid-like layer would be removed completely, and the interface stress would correspond directly to the bond strength between the aluminum and ice. The final two data points (for -30°C and -40°C) support this view, as they are the same. In order to verify this hypothesis, however, more experiments would have to be performed at intermediate temperatures (between -10°C and -30°C), as well as temperatures between 0°C and -10°C . Interestingly, the decrement of the liquid-like layer with temperature follows an exponential curve, too, (Weyl, 1951), and this provides further credence to the above explanation tying the strength decrement to the features of the liquid-like layer.

5.2. Surface roughness

As stated earlier, the discussion of the relationship of substrate surface roughness to adhesion strength is purely qualitative, meaning no data on surface roughness was collected and can be compared to actual values of adhesion strength. This should not preclude a discussion of such a relationship, however, as repeatable experiments reported herein attest to the fact that such a relationship does exist.

As shown in Table 2, the adhesion strength of ice on aluminum can be greatly reduced by decreasing the surface roughness of the aluminum. That is, by refining the surface quality from that shown in Fig. 3(a) to that shown in Fig. 3(b), the stress causing interface damage was reduced from 274 MPa to 181 MPa. This decrease in the adhesion strength can be explained as follows: the smooth Al surface shows many small, thin scratches, while the rougher surface appears to have only larger hills and valleys (as evident in Fig. 3). These scratches on the polished Al surface act as additional nucleation sites for the ice. This is witnessed in the smaller and more irregular grain structure seen on the polished Al substrates in Fig. 4(b), as opposed to the larger grains more closely resembling the classic hexagonal structure that ice assumes on the unpolished Al (Fig. 4(a)). The larger fraction of intersecting grain boundaries must lead to larger defect density at the interface, and in addition, provide sites for mechanical stress concentration. A more detailed discussion is outside the scope of the present investigation.

The lowering of adhesion strength by polishing the substrate surface was also found by Jellinek (1962), although his tests were performed under shear and on stainless steel substrates. In addition, Sonwalkar *et al.* (1993, found in shear experiments that the adhesion strength was proportional to the amount of the mechanical interlocking of ice on the substrate. Instead of varying the substrate surface roughness, they varied the actual substrates from stainless steel, copper, aluminum, titanium, to polytetrafluoroethylene (PTFE). The stainless steel, copper and aluminum showed the largest pit size, which allowed the ice to interlock on these substrates more than on titanium and PTFE. Similarly, the hills and valleys of the rough Al substrate (in the present investigation) provide a greater likelihood of interlocking and thus contributed to the increased adhesion strength over polished Al substrates, which have fewer anchoring sites.

5.3. *Addition of polymer coatings*

The addition of polymer coatings affected both the growth of the ice on the Al substrates and the measured adhesion strength. The surface of the polymers is relatively flat, with few pits, and therefore few nucleation sites for ice growth. This implies that ice growth will be quite random, as is evident from Fig. 5(a) and (b), which show the ice grain structure for substrates coated with PMMA and PI, respectively. The materials chosen for this investigation were done so because of their availability and their durability to repeated testing. For the present investigation, the two polymers exhibit slight polarity, yet not to the extent of Al_2O_3 , which is inevitably found on the Al surface. This provided few bonding sites for the ice on the coated substrates (compared with Al alone) which contributes to the rather low (for this study) adhesion strength values of 181 MPa and 190 MPa for ice on PMMA and PI, respectively. However, as discussed below, there is a potential to lower this strength further.

The structure of PI shows that there are many oxygen atoms available on both sides of its chain to which hydrogen atoms form the liquid-like layer can attach. In comparison, PMMA lacks the exposed oxygen that PI displays, but it does have a polar side group, COOCH_3 . Thus, even though the PMMA coatings on Al substrates provide fewer bonding sites to the liquid layer in comparison to the PI, the PMMA layer is by no means completely hydrophobic. Attempts to manufacture such coatings using the concepts of self assembled monolayers of polymeric material is currently in progress.

5.4. *Transverse cracking of ice columns*

Finally, using the simulation, the transverse tensile stress that led to the cracking of the grain boundaries was estimated to be 47.4 MPa from data obtained at -10°C . These cracks were observed to begin (Fig. 7) within the bulk of the ice away from the interface and the free surface. This value of the grain boundary strength is much smaller than the cleavage strengths across the prismatic planes of 1.3 GPa (Gupta and Tian, 1994).

6. CONCLUSIONS

A basic understanding of the nature and strength of this bond is crucial to solve the deicing problem from a fundamental standpoint. Motivated by such goals, a new strategy to measure the tensile strength of interfaces between ice and structural surfaces was developed and presented in this paper. Because the interface separation is accomplished at an ultra high strain rate (10^7 s^{-10}), all inelastic deformation during the interface separation process are essentially suppressed and the measured strength is the actual strength of the interface. The tensile strength of ice with the as-manufactured 6061 Al surfaces was measured as a function of temperature (-10 – -40°C), and the results indicated an exponential decrease in the bond strength with decrease in the temperature, 274 MPa at -10°C to 179 MPa at -40°C . The effect of polishing

the aluminum surface was to reduce the adhesion dramatically, from 274 MPa for the as-manufactured surfaces to 181 MPa for surfaces polished on a metallographic wheel using α -alumina powder of sizes 1.0 μm , 0.3 μm and 0.05 μm . This was also consistent with results of other investigators (Jellinek, 1962; Sonwalkar *et al.*, 1993). The same holds true with the experiments on Al substrates coated with polymer films. As in other investigations (Jellinek, 1957a, Jellinek *et al.*, 1978), polymer coated substrates exhibited lower adhesion strengths when compared with untreated metal substrates. The interface between polymer and ice was the weakest, and for polyimide and PMMA, tensile strength values of 190 and 181 MPa were recorded. This result shows the promise of developing better hydrophobic coatings with no outstanding polar groups.

An understanding of the fundamental adhesion is only one step in resolving the overall ice/adhesion engineering problem. In any deicing or mechanical ice removal process, the energy consumed in propagating a crack along an ice/structure interface or in its vicinity is much larger than what is required to overcome the intrinsic tensile strength of the interfacial bonds, and often termed as the *total roughness G* of the interface. This depends upon many extrinsic parameters including the specimen geometry, loading rate, creep effects, temperature, roughness and adsorbed impurities on structural surfaces, interface flaw density, and the ratio of the tensile to shear stress ratio at the interface. Experiments that can sort out the role played by each of these process variables separately are vital for a complete understanding of the ice adhesion process. The results of such a study should be also useful in designing efficient ice removal strategies.

ACKNOWLEDGEMENTS

This work was funded via the Army Research Office Contract Nos. DAAL03-92-G-0250 and DAAH04-96-1-0010, and the Office of Naval Research Grant No. N00014-93-1-1106 for which we are grateful to Drs Russell Harmon, Tom Swain, Y. D. S. Rajapakse, Tom Curtin, Robert Reeber and Wilbur Simmons of these agencies.

REFERENCES

- Amery, B. (1976) Wide range velocity interferometer, in *Sixth Symposium on Detonation*, (Arlington, Virginia), pp. 673–681, Office of Naval Research-Department of the Navy, August 24–27.
- Archer, P. (1996) Investigation of the adhesion strength of ice to aluminum using a laser spallation experiment. Master's thesis, Thayer School of Engineering, Dartmouth College, Hanover, New Hampshire, U.S.A.
- Barker, L. M. (1972) Laser interferometry in shock-wave research. *Experimental Mechanics* **12**, 5, 209–215.

- Brandes, E. and Brook, G. ed. (1992) *Smithells Metals Reference Book*. London: Butterworth-Heinemann, seventh edn.
- Faraday, M. (1859) On regelation, and on the conservation of force. *Philosophical Magazine* **17**, 162–169.
- Gupta, V., Argon, A. S., Parks, D. M. and Cornie, J. A. (1992) Measurement of interface strength by a laser spallation technique. *Journal of the Mechanics and Physics of Solids* **40**, **1**, 141–180.
- Gupta, V., Yuan, J. and Pronin, A. (1994) Recent developments in the laser spallation technique to measure the interface strength and its relationship to interface toughness with applications to metal/ceramic, ceramic/ceramic and ceramic/polymer interfaces. *Journal of Adhesion Science and Technology* **8**, **6**, 712–747.
- Gupta, V. and Yuan, J. (1993) Measurement of interface strength by the modified laser spallation technique. II. Applications to metal/ceramic interfaces. *Journal of Applied Physics* **74**, **4**, 2397–2404.
- Gupta, V. and Tian, X. (1994) Measurement of cleavage strength in ice crystals by a laser spallation technique. *Journal of Offshore Mechanics and Arctic Engineering* **116**, 35–42.
- Gupta, V., Argon, A. S., Cornie, J. A. and Parks, D. M. (1990) Measurement of interface strength by a laser-pulse-induced spallation. *Materials Science and Engineering A126*, 105–117.
- Hobbs, P. (1974) *Ice Physics*. Clarendon Press.
- Hosler, C., Jensen, D. and Goldshlak, L. (1957) On the aggregation of ice crystals to form snow. *Journal of Meteorology* **14**, 415–420.
- Jellinek, H. (1962) Ice adhesion. *Canadian Journal of Physics* **40**, 1294–1309.
- Jellinek, H. (1957a) Tensile strength properties of ice adhering to stainless steel. *Research Report 23*, U.S. Army Snow Ice and Permafrost Research Establishment.
- Jellinek, H. (1957b) Adhesive properties of ice. *Research Report 38*, U.S. Snow Ice and Permafrost Research Establishment.
- Jellinek, H. (1960) Adhesive properties of ice, Part II. *Research Report 62*, U.S. Snow Ice and Permafrost Research Establishment.
- Jellinek, H. (1967) Liquid-like transition layer on ice. *Journal of Colloid and Interface Science* **25**, 192–205.
- Jellinek, H., Kachi, H., Kittaka, S., Lee, M. and Yokoto, R. (1978) Ice releasing block-copolymer coatings. *Colloid and Polymer Science* **256**, 544–551.
- Landy, M. and Freiburger, A. (1967) Studies of ice adhesion I. Adhesion of ice to plastics. *Journal of Colloid and Interface Science* **25**, 231–244.
- Mittal, K. (1978) Adhesion measurement: recent progress, unsolved problems, and prospects, in *Adhesion measurements of thin films, thick films, and bulk coatings*, STP-640 ed. K. Mittal, (Philadelphia), pp. 5–17, ASTM.
- Nickolayev, O. and Petrenko, V. (1995) SRM studies of the surface morphology of ice, in *MRS Symposium Proceedings*, ed. B. G. Demczyk, *et al.*, (Pittsburg), pp. 221–226, MRS.
- Petrenko, V. (1994) The surface of ice. *Special Report 94-22*, U.S. Army Corps of Engineers, CRREL.
- Picu, C. R. and Gupta, V. (1995a) Crack nucleation in Columnar ice due to elastic anisotropy and grain boundary sliding. *Acta Metallurgica et Materialia* **43**, **10**, 3798–3805.
- Picu, C. R. and Gupta, V. (1995b) Observations of crack nucleation in columnar ice due to grain boundary sliding. *Acta Metallurgica et Materialia* **43**, **10**, 3791–3797.
- Pronin, A. and Gupta, V. (1993) Interferometry on diffuse surfaces in high-velocity measurements. *Review of Scientific Instruments* **64**, **8**, 2233–2236.
- Rice, J. R. and Sih, G. C. (1965) Plane problems of cracks in dissimilar media. *Journal of Applied Mechanics* **32**, 418–423.
- Sonwalkar, N., Sunder, S. S. and Sharma, S. (1993) Ice/solid adhesion analysis using low-temperature Raman microprobe shear apparatus. *Applied Spectroscopy* **47**, **10**, 1585–1593.
- Weyl, W. (1951) Surface structure of water and some of its physical and chemical manifestations. *Journal of Colloid and Interface Science* **6**, **5**, 389–405.

- Yuan, J., Gupta, V. and Pronin, A. (1993) Measurement of interface strength by modified laser spallation technique. III. Experimental optimization of the stress pulse. *Journal of Applied Physics* **74**, **4**, 2405–2410.
- Yuan, J. and Gupta, V. (1993) Measurement of interface strength by the modified laser spallation technique. I. Experiment and simulation of the spallation process. *Journal of Applied Physics* **74**, **4**, 2388–2396.
- Yuan, J. and Gupta, V. (1995) The effect of microstructure and chemistry on the tensile strength of Nb/sapphire interfaces with and without interlayers of Sb and Cr. *Acta Metallurgica et Materialia* **43**, **2**, 781–794.



Pergamon

J. Mech. Phys. Solids, Vol. 46, No. 10, pp. 1773–1787, 1998
© 1998 Elsevier Science Ltd. All rights reserved
Printed in Great Britain
0022-5096/98 \$—see front matter

PII: S0022-5096(98)00047-7

INITIATION AND PROPAGATION TOUGHNESS OF DELAMINATION CRACK UNDER AN IMPACT LOAD

PRASHANT KUMAR* AND N. N. KISHORE

Department of Mechanical Engineering, Indian Institute of Technology, Kanpur—208 016, India

(Received 20 December 1997; in revised form 23 February 1998)

ABSTRACT

A combined experimental and finite element method is developed to determine the interlaminar dynamic fracture toughness. An interlaminar crack is propagated at very high speed in a double cantilever beam (DCB) specimen made of two steel strips with a precrack. A special fixture is designed to apply impact load to one cantilever and determine the deflection of the cantilever-end, initiation time and crack propagation history. The experimental results are used as input data in a FE code to calculate J -integral by the gradual release of nodal forces to model the propagation of the interlaminar crack. The initiation fracture toughness and propagation fracture toughness are evaluated for interlaminar crack propagating between 850 and 1785 m/s. The initiation and propagation toughness were found to vary between 90–200 J/m² and 2–13 J/m² respectively. The technique is extended to study initiation and propagation toughness of interlaminar crack in unidirectional FRP laminates. © 1998 Elsevier Science Ltd. All rights reserved.

Keywords: A. delamination, A. dynamic fracture, A. fracture toughness, B. fibre-reinforced composite material, C. finite elements.

1. INTRODUCTION

Laminates of fibre reinforced plastic (FRP) are increasingly used as structural members because they offer many attractive properties such as high specific strength, high specific stiffness and environmental stability.

A laminate is commonly made by stacking prepregs over each other and curing them at high temperature and pressure. High strength man made fibres (carbon, kevlar, glass) impart stiffness and strength in the plane of a ply but the plies are bonded to each other with the help of comparatively low strength matrix material; high strength fibres do not reinforce the laminate through the thickness. However, interlaminar strength is usually adequate for an FRP structure loaded under quasi-static loading conditions.

When an FRP laminate is impacted by a foreign body at subsonic velocity an intense damage is observed at the centre of the impact with fibre breakage, matrix cracking and fibre pull out. Also the damage spreads laterally to a considerably large area mainly through interlaminar separation even if the impacting body is of low mass (10–30 g) (Kumar and Badri, 1993).

* To whom correspondence should be addressed. Fax: 0091 512 59 7408; E-mail: prkumar@iitk.ernet.in

On the other hand, when a foreign body impacts a metallic surface, material at the impact point yields, usually with workhardening in most engineering materials, resulting in formation of a small dent. FRP laminates are less tough as a result, in comparison to conventional metals. Furthermore, in opaque composite laminates (e.g. carbon fibre laminates) delamination damage occurring on interfaces between various plies is not visible from outside and may not be detected easily. Interlaminar cracks are observed to propagate at very high speeds that are comparable to shear wave velocities. The speed of expanding fronts of delamination cracks, as measured by high speed cameras, is as high as 200–500 m/s (Takeda *et al.*, 1982). When glass fibre reinforced epoxy laminates are impacted it was found that if the total delamination area between various plies is multiplied by the quasi-static energy release rate, the net energy exceeds the energy of the impacting mass [Kumar and Narayanan, 1993]. This suggests that delamination cracks at high speeds propagate at lower toughness resulting in a fairly large damage area. Therefore the characterization of the interlaminar fracture toughness under dynamic crack propagation is of utmost concern for composite laminates.

Experiments to determine dynamic fracture toughness have been mostly done on large metal plates having a crack through the thickness. Schardin (1959) introduced the method of caustics that was further developed by Mannog (1966) and Theocaris (1970) and discussed in detail by Popadopoulos (1993). Ravi Chandar and Knauss (1982, 1984a, 1984b, 1984c, 1984d) conducted exhaustive studies through the method of caustics for Homolite-100. Rosakis, Duffy and Freund (1984) performed a dynamic crack propagation experiment using wedge loading. Zehnder and Rosakis (1990) used the optical method of reflected caustics, combined with high speed photography, to investigate the dynamic fracture initiation and propagation in a 4340 steel specimen.

A special technique was developed by Ravichandran and Clifton (1989) to study the initiation and propagation of crack in a steel disc containing a prefatigued edge-crack in the midplane. The disc was plate impacted by a thin flyer of the same material. The resulting compressive pulse propagates through the specimen and reflects from the rear surface as a tensile pulse of a submicron duration. The motion of the rear surface was monitored using a laser interferometer system.

Berger and Dally (1990a) used a series of strain gauges ahead of the crack tip at a certain predetermined location to monitor the strain and crack propagation. Berger, Dally and Sanford (1990b) also used strain gauges ahead of the crack tip to determine the dynamic stress intensity factor associated with a propagating crack.

Although a considerable amount of work has been done to study the fracture phenomena through numerical methods, only large rectangular double cantilever beams were given attention. Owen and Shantaram (1977) introduced the use of finite element method to study dynamic crack growth. Nishioka and Atluri (1982a, 1982b) investigated the crack propagation and arrest in a high strength steel DCB specimen using moving singular dynamic finite element procedure. Crouch and Williams (1987) used a dynamic mode finite element program to analyse different geometries. Aminpour and Holsapple (1991) developed a finite element procedure to provide the state of stress, displacement and stress intensity factors of a propagating crack at the interface of the two dissimilar anisotropic materials. Crack propagation is accomplished by moving the crack tip inside the singular element according to a

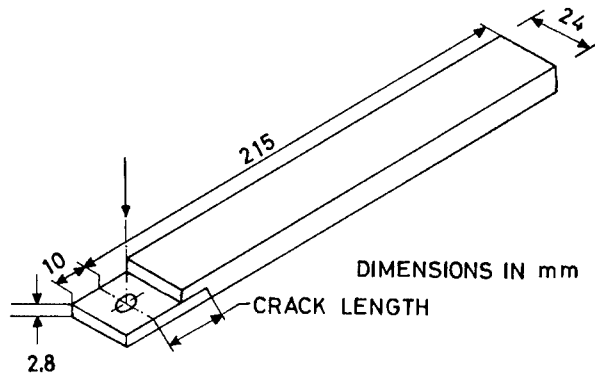


Fig. 1. DCB specimen.

prescribed crack tip history. A local redefinition of the finite element is required when the crack tip reaches an extreme position inside the singular element. Thesken and Gudmundson (1991) worked with an elasto-dynamic moving element formulation incorporating a variable order singular element to enhance the local crack tip description. Wang and Williams (1994) investigated high speed crack growth in a thin double cantilever beam specimen using finite element method. The strain release rate obtained by FEM was compared with the quasi-static solution based on beam theory, for various loading conditions.

The study of fast moving delamination cracks in a laminate, whose thickness is usually less than 5–7 mm, is complex from an experimental and numerical point of view. It was felt that, to determine dynamic interlaminar toughness, a combined technique should be developed, which would make use of numerical simulation using experimental data from an instrumentation that is not too sophisticated and expensive. The technique is initially developed on a double cantilever beam (DCB) specimen made from hardened steel strips bonded together with epoxy. One of the cantilevers is impacted and with the help of experimental data a FE code is developed to simulate the wave propagation in the DCB specimen and to determine the initiation and propagation toughness of the interlaminar crack. The experimental theoretical technique is then extended to determine initiation and propagation toughness of delamination crack in a DCB specimen made of unidirectional glass fibre reinforced epoxy laminates.

2. EXPERIMENTAL DETAILS

2.1. Steel and FRP specimen

The DCB specimen is made by bonding two thin strips of steel each of 2.8 mm thickness and of 24 mm width with a precrack as shown in Fig. 1. The cantilevers are made of hardened 4340 steel and ground flat. For bonding the sheets together, epoxy LY 556, hardener HT 976, and accelerator XY 73 are mixed in the mass ratio of

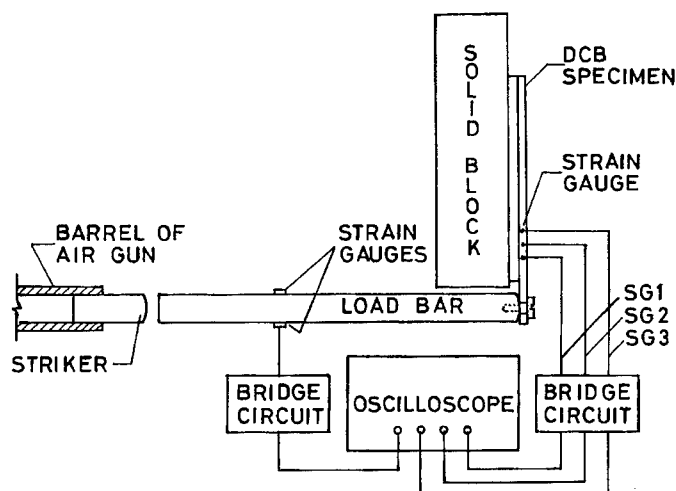


Fig. 2. Schematic diagram of the experimental setup.

100:35:2 (purchased from Ciba-Geigy Limited, Bombay). The curing is carried out at 140°C for four h under a pressure of 0.5 MPa. It is then cooled to room temperature at the same pressure. The precrack, introduced in the DCB specimen during bonding by placing a thin (18 μm BOPP sheet is sharpened through a specially designed fixture (Verma, 1995).

The unidirectional FRP laminate specimen is made from glass fibre preregs by stacking 32 plies with a thin teflon film (20 μm) placed at the midthickness of the laminate to introduce a precrack. It is cured at 120°C with 0.7 MPa for one h and then at higher temperature of 140°C maintaining the same pressure for six h. The specimen is 7 mm thick (each cantilever is 3.5 mm thick) and 25 mm wide; its length ranges from 190–220 mm. The as-cast crack tip is sharpened with the special arrangement designed for steel specimen.

2.2. Experimental setup

The schematic diagram of the experimental setup is shown in Fig. 2. In this technique a stress pulse is generated in the cylindrical load bar by impacting it with a striker propelled from an airgun. The load bar and the striker are made of the same material and are of the same diameter. The end of the rear cantilever beam is screwed to the load bar and the end of the load bar is made spherical to facilitate the rotation of the rear cantilever. The face of the front cantilever is bonded to a rigid block of mild steel (50 mm \times 50 mm \times 150 mm) which is clamped further to a rigid base plate.

Two strain gauges, at diametrically opposed locations, are mounted in the longitudinal direction on the surface of the load bar to record the incident and the reflected pulses. When this incident pulse reaches the specimen, part of it is transmitted to the cantilever, thus dynamically loading the specimen. The remaining energy of the incident pulse is reflected into the load bar. Responses of the strain gauges are recorded

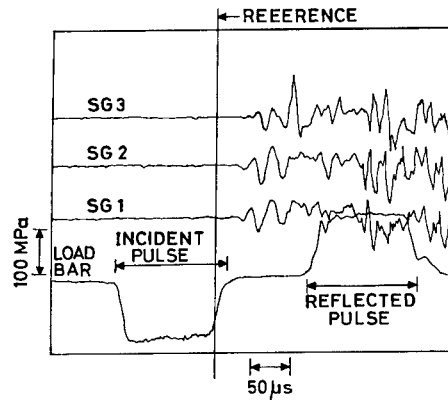


Fig. 3. Oscilloscope traces (Experiment S-1 of steel specimen).

on a four channel digital oscilloscope (Model 1624, Gould Inc., U.K.). The length of load bar and the location of its strain gauges are suitably chosen to separate the incident and reflected pulses.

To measure the interlaminar crack velocity, three strain gauges (0.2 mm length, 1.4 mm width, $120 \pm 0.3 \Omega$) are bonded to the side face of the rear cantilever. These gauges were supplied by Tokyo Sokki Kinkyuju Ltd., Japan. The first strain gauge (SG1) is bonded very close to the already sharpened crack tip (within 2–3 mm, and the distance between the strain gauges (SG1, SG2 and SG3) is approximately 5 mm. The locations of the strain gauges are measured accurately with the help of a travelling microscope, prior to loading the specimen in the experimental setup. As the crack advances and approaches a strain gauge, the strain increases and reaches a maximum value due to the singular stress field. By recording the time at which the maximum strain is reached in all three gauges, growth of the crack length with time is determined. Figure 3 shows the four oscilloscope traces of an experiment; the lowest trace shows incident and reflected pulses in the load bar and the other three traces are the outputs of the small strain gauges attached to the specimen. By applying one dimensional wave propagation theory to the incident and reflected pulses in the elastic load bar one obtains particle velocity at the cantilever-end which is integrated to determine deflection history of the cantilever-end.

Thus the experiment provides the following data for numerical simulation of wave propagation in the specimen and building up of the *J*-Integral at the tip of interlaminar crack :

- (a) the deflection of the cantilever-end with time,
- (b) the crack initiation time, and
- (c) the crack propagation history.

3. NUMERICAL SIMULATION

The system of finite element equations governing the linear dynamic response of an elastic body can be expressed as

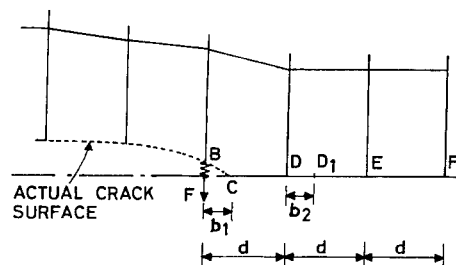


Fig. 4. Crack opening scheme.

$$[M]\{\ddot{U}\} + [K]\{U\} = \{R\} \quad (1)$$

where $[M]$ and $[K]$ are the mass and stiffness matrices respectively and $\{R\}$ is the external load vector. $\{U\}$ and $\{\ddot{U}\}$ are displacement and acceleration vectors of finite element assemblage respectively. In the present analysis the damping is neglected and Newmark Integration Method for time variables is used (Bathe, 1990). To simulate the crack propagation, the crack tip jumps from one node to the next if a simple node release procedure is used. To overcome such difficulties, several algorithms exist in literature which release the nodes gradually. The various schemes available to decrease the nodal forces gradually to zero are due to Malluck and King (1978), Rydholm *et al.* (1978) and Kobayasi *et al.* (1978).

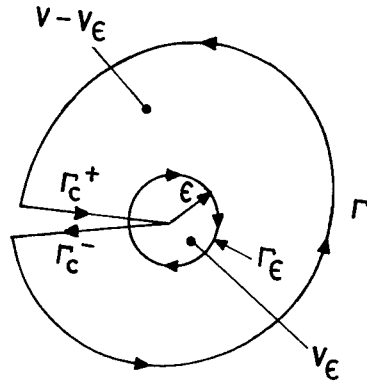
In the present work a modified method is adopted to achieve gradual and smooth propagation of interlaminar crack. The holding-back force at node B (Fig. 4) is decreased linearly in proportion to the distance of the crack tip from the end of the succeeding element (node E). Thus, when the crack tip is located between nodes B and D, the force F_B at node B is given by

$$\frac{F_B}{F_{BC}} = \left(1 - \frac{b_1}{2d}\right) \quad (2)$$

where b_1 is the crack extension beyond node B and F_{BC} is the internal force when the crack tip was located at node B. As the crack tip moves beyond node D by distance b_2 , internal force at the node B becomes

$$\frac{F_B}{F_{BC}} = \left(1 - \frac{d + b_2}{2d}\right) \quad (3)$$

Path independent \hat{J} -Integral is adopted to represent the fracture toughness. Similar to the J-Integral used for computing elasto-static fracture in mode I, path integrals are developed for elasto-dynamic crack propagation. This also involves the domain integral arising out of the kinetic energy term (Atluri, 1982; and Nishioka and Atluri, 1983). In the present work \hat{J}_1 given by Kishimoto, Aoki and Sakata (1980) is adopted which is defined as

Fig. 5. Contour of \hat{J} -Integral.

$$\hat{J}_I = \lim_{\epsilon \rightarrow 0} \int_{\Gamma_c^- + \Gamma + \Gamma_c^+} [W n_1 - t_i u_{i,1}] ds + \int_{V - V_\epsilon} \rho \ddot{u}_i u_{i,1} dV \quad (4)$$

where integration paths Γ_c^- , Γ and Γ_c^+ and the volumes V and V_ϵ are defined in Fig. 5; W represents the strain energy density, u_i the displacement and n_1 the component of unit normal in x_1 direction.

The computer code for crack simulation has been validated (Verma (1995)) against known problems, Parton and Boriskovsky (1989), Nishioka and Atluri (1986).

Higher order elements are not preferred for generating mesh in a DCB specimen; a simple four noded isoparametric element is employed. However, very fine mesh is used. Uniform mesh throughout the specimen is generated to avoid spurious reflections of stress waves. In the steel specimen four noded isoparametric elements of size 0.4 mm along the length and 0.28 mm in the direction of thickness were generated. Mesh size of 0.4 mm \times 0.35 mm was generated in the unidirectional FRP specimen.

In the initial stage of this study both cantilevers of the DCB specimen were modelled for evaluating \hat{J}_I . However, contribution of the front cantilever (Fig. 1) is only marginal because it is bonded to a very stiff block. Therefore only rear cantilever was analysed to minimize computations.

Bathe (1990) suggested guidelines to choose the proper time step (Δt) to satisfy the stability criterion. Δt should be smaller or equal to h/c where h is the spatial resolution and c is the highest wave velocity in the specimen. For the steel specimen, Δt should be less than 0.08 μs to meet the guidelines. However, it was found that \hat{J} obtained with $\Delta t = 0.2 \mu s$ was very close to \hat{J} determined through $\Delta t = 0.03 \mu s$. Thus to decrease computational time it was decided to use the time step of 0.2 μs .

4. RESULTS AND DISCUSSION

4.1. Steel DCB specimen

The stress waves propagating in the cantilever-end slowly build up the value of \hat{J} at the crack tip. Reference time ($t = 0$) corresponds to the arrival of the incident stress

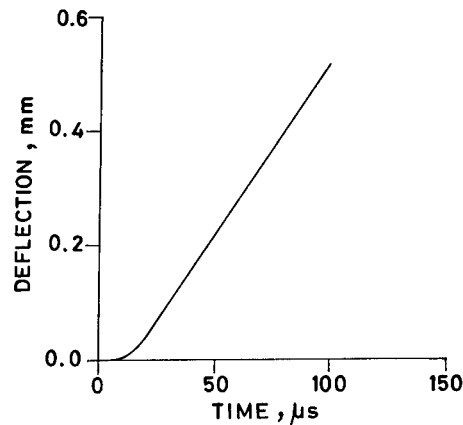


Fig. 6. Deflection of cantilever-end (Experiment S-1 of steel specimen).

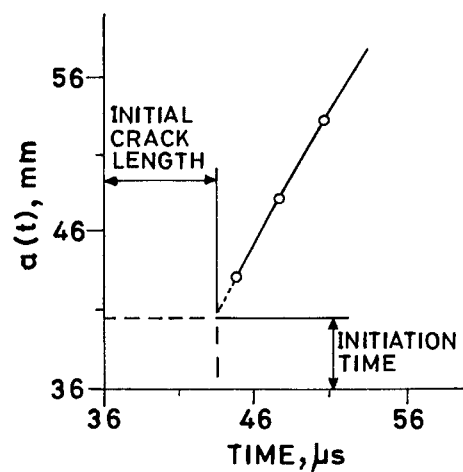


Fig. 7. Variation of crack length with time and determination of initiation time (Experiment S-1 of steel specimen).

pulse at the cantilever's end as shown in Fig. 3. The crack remains stationary until the interlaminar bond is able to resist the crack propagation.

Incident and reflected pulses of lower trace (Fig. 3) determine the variation of velocity of cantilever-end with time. The velocity is integrated to obtain displacement boundary condition of cantilever-end (Fig. 6).

The upper three traces of specimen-strain gauges (Fig. 3) determine the velocity of interlaminar crack propagation, as discussed earlier in section 2. The crack length as a function of time is plotted in Fig. 7, a second degree polynomial curve is fitted through these data points and is extrapolated to the initial crack length to find the crack initiation time. It is worthwhile to note that determination of the initial time

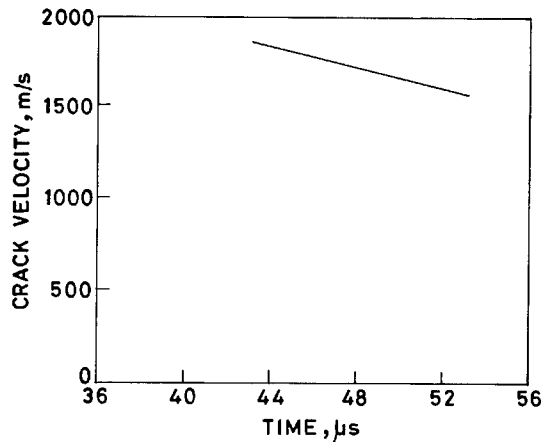


Fig. 8. Variation of crack propagation velocity. (Experiment S-1 of steel specimen).

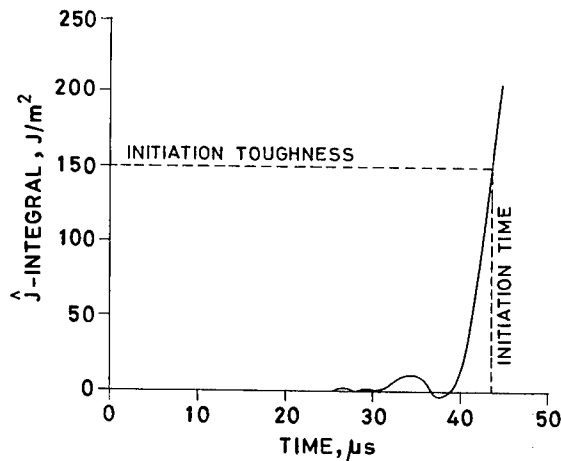


Fig. 9. Initiation toughness of Experiment S-1 of steel specimen.

through extrapolation is not expected to introduce much error because (i) crack velocity is extremely high at initiation time (≈ 1850 m/s of experiment S-1) and (ii) the distance between the location of initial crack tip and the first strain gauge is small. In fact, it is estimated that the crack tip takes only $1.3 \mu\text{s}$ to reach the first strain gauge, which is much smaller than the initiation of $43.51 \mu\text{s}$. Figure 8 shows the variation of the interlaminar crack velocity with time.

4.2. Interlaminar initiation fracture toughness

Displacement and stress fields for a stationary crack are determined through the FE computer program after each time step and variation of \hat{J}_I is shown in Fig. 9. Corresponding to the initiation time, interlaminar initiation toughness (\hat{J}_{ini}) is

Table 1. Initiation time and initiation toughness in steel DCB specimen

Expt. No.	Crack Length (mm)	SG1 from crack-tip (mm)	Time of Strain-gauge peak			Initiation time (μ s)	\hat{J}_{ini} (J/m^2)
			SG1	SG2	SG3		
S-1	40.9	2.3	44.8	47.6	50.6	43.51	150
S-2	40.8	1.0	43.4	47.0	49.8	42.64	90
S-3	42.1	2.3	46.5	50.0	54.0	45.20	160
S-4	41.1	1.3	45.0	48.5	52.7	44.32	200
S-5	39.3	1.5	44.3	49.6	55.6	42.76	125

determined. The details of initiation time and initiation toughness are given in Table 1 for all five experiments. Interlaminar toughness under quasi-static loading (J_{quas}) is $12 \text{ J}/\text{m}^2$. It is clear from the table that \hat{J} required to initiate the crack growth is at least one order higher.

4.3. Interlaminar propagation fracture toughness

The crack propagation simulation (eqns 2 and 3) is invoked as soon as the crack initiation takes place with available crack velocity history. The advancement of crack in each iteration is calculated and stress and displacement fields are determined. \hat{J}_I after the crack initiation is known as interlaminar propagation toughness (J_{prop}). Figure 10 shows that drop in \hat{J}_I is sharp and substantial.

The oscillatory behaviour of \hat{J}_{prop} may be due to several reasons. Firstly, the free surfaces of DCB specimen are close to the crack tip; in fact, propagation time of

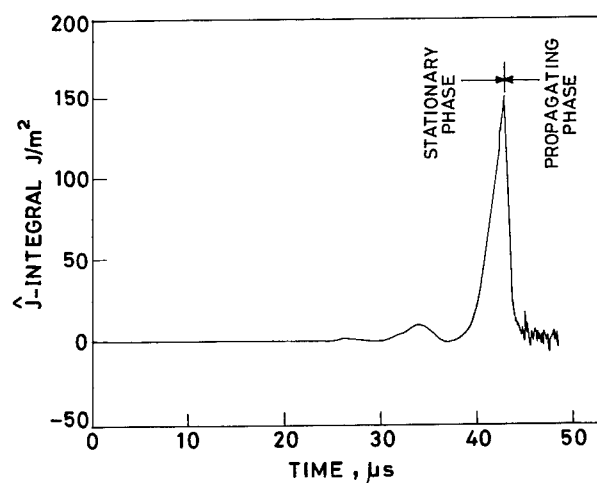


Fig. 10. Variation of \hat{J} with time for stationary and propagating crack (Experiment S-1 of steel specimen).

Table 2. Average crack velocity, initiation and propagation toughness in steel specimen

Expt. No.	Length of precrack (mm)	Average crack velocity		\hat{J}_{ini} (J/m ²)	\hat{J}_{prop} (J/m ²)
		\dot{a}_1^* (m/s)	\dot{a}_2^\dagger (m/s)		
S-1	40.9	1785	1700	150	3
S-2	40.8	1416	1607	90	2
S-3	42.1	1437	1300	160	3
S-4	41.1	1400	1190	200	8
S-5	39.3	925	850	140	13

* Average crack velocity between first and second strain gauge.

† Average crack velocity between second and third strain gauge.

stress waves to emanate from the crack tip, reach the free surface and then come back to the crack tip is 1–2 μ s only. The superposition of these waves and their effect on \hat{J}_{prop} cause fluctuations. Secondly, the crack tip which moves from one node to another in numerical simulation decreases the holding back force linearly. A better model for estimation of nodal forces at the node may decrease the fluctuations.

The details of average crack velocity, \hat{J}_{ini} and average \hat{J}_{prop} are given in Table 2 for all five experiments with the DCB specimen prepared from thin steel plates. At very high crack speeds \hat{J}_{prop} is much smaller than J_{quas} (12 J/m²). At relatively lower crack velocity (850–925 m/s of experiment S-5) \hat{J}_{prop} is 13 J/m² which is approximately the same as J_{quas} .

4.4. DCB specimen of FRP

The experimental numerical technique is being extended to unidirectional glass fibre epoxy laminate with specimen geometry described in section 2. Preliminary results are reported and discussed in this section.

Table 3 provides the initial crack length, average crack velocity, \hat{J}_{ini} and \hat{J}_{prop} for all five experiments with FRP specimens. The experimentally recorded incident and reflected pulses in the load bar and the responses of all the specimen strain gauges are shown through traces in Fig. 11 for experiment FRP-1. The computer simulation shows the variation of \hat{J}_I in Fig. 12. \hat{J}_{prop} can be seen better in the magnified view shown in Fig. 13.

Interlaminar toughness at quasistatic loading (\hat{J}_{quas}), in FRP laminate was found to vary between 344 and 478 J/m². Similar to the results of the steel DCB specimen, the drop in \hat{J}_{prop} is sharp and substantial. In fact, in experiment FRP-3, with very high average crack velocity, \hat{J}_{prop} takes very low values. Furthermore, \hat{J}_{ini} is smaller than \hat{J}_{quas} , but it has not decreased to very low values. The reduction of interlaminar toughness at high crack velocity of FRP laminates is similar to that of the steel DCB specimen except for the difference that in the steel specimen $\hat{J}_{ini} > \hat{J}_{quas}$ whereas in the FRP laminates $\hat{J}_{ini} < \hat{J}_{quas}$.

Table 3. Crack velocity, \dot{J}_{ini} and \dot{J}_{prop} of DCB specimen of FRP

Expt. No.	Initial crack length (mm)	Average crack velocity		\dot{J}_{ini} (J/m ²)	\dot{J}_{prop} (J/m ²)
		\dot{a}_1^* (m/s)	\dot{a}_2^\dagger (m/s)		
FRP-1	46.5	622	361	230	11-59
FRP-2	43.5	898	743	145	12-28
FRP-3	44.0	1016	751	102	0-26
FRP-4	30.0	730	572	118	3-28
FRP-5	34.0	734	543	90	1-20

* Average crack velocity between first and second strain gauge.

† Average crack velocity between second and third strain gauge.

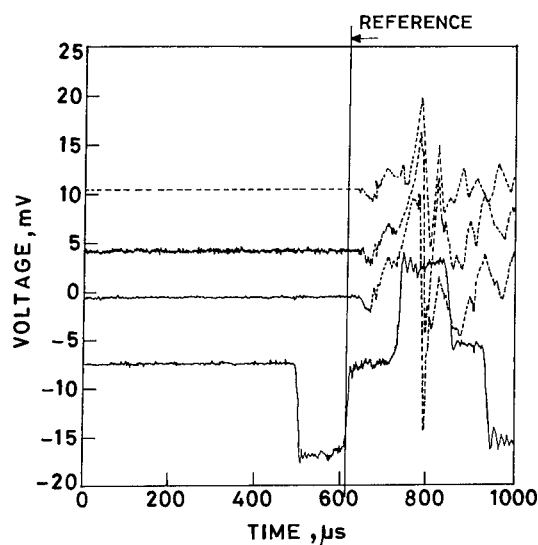
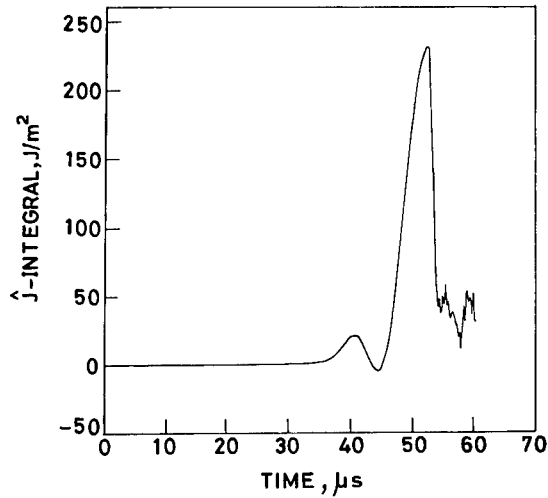
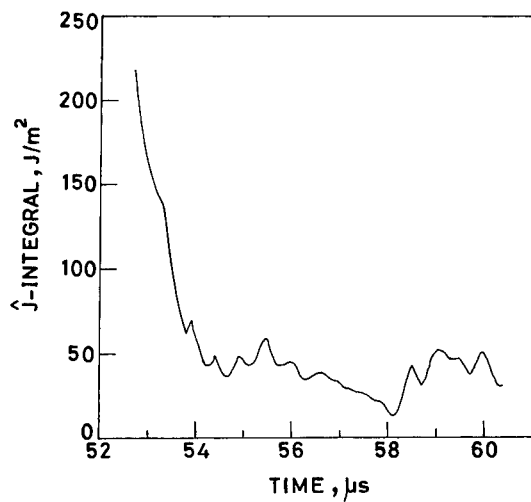


Fig. 11. Oscilloscope traces of Experiment FRP-1.

5. CONCLUSIONS

A combined technique has been developed, using experimental measurements and finite element analysis, to determine the initiation and propagation toughness of a DCB specimen, prepared by bonding two steel strips together with epoxy. It was found that \dot{J} builds up to a high value before the crack starts growing. Once the crack is initiated, it was observed to propagate at high velocity of 800–1700 m/s with low

Fig. 12. Variation of \hat{J} with time of Experiment FRP-1.Fig. 13. \hat{J}_{prop} vs time of Experiment FRP-1.

toughness. For a quasi-static toughness of 12 J/m^2 , the initiation toughness of the steel specimen was found to be in the range of $90\text{--}230 \text{ J/m}^2$, with propagation toughness decreasing sharply to $2\text{--}13 \text{ J/m}^2$. Preliminary experiments on unidirectional glass fibre composite materials showed initiation toughness of $90\text{--}230 \text{ J/m}^2$ against quasi-static toughness of $344\text{--}478 \text{ J/m}^2$. Propagation toughness of $0\text{--}50 \text{ J/m}^2$, was found for interlaminar crack propagation with velocity in the range of $622\text{--}1016 \text{ m/s}$.

ACKNOWLEDGEMENTS

The authors wish to thank Aeronautics Research and Development Board (Structures Panel) and the Ministry of Defence, Government of India, for sponsoring the project.

REFERENCES

- Aminpour, M. A. and Holsapple, K. A. (1991) Finite element solutions for propagating interface crack with singularity elements. *Engineering Fracture Mechanics* **39**, 451–468.
- Atluri Satya, N. (1982) Path independent integrals in finite elasticity and inelasticity with body forces, inertia and arbitrary crack-face conditions. *Engineering Fracture Mechanics* **16**, 341–364.
- Bathe, Klaus-Jürgen (1990) *Finite Element Procedure in Engineering Analysis*. Prentice Hall, India.
- Berger, J. R. and Dally, J. W. (1990a) A spatially overdetermined analysis for propagation toughness using strain gauges. *Mechanics Research Communications* **17**, 93–99.
- Berger, J. R., Dally, J. W. and Sanford, R. J. (1990b) Determining the dynamic stress intensity factor with strain gauges using a crack tip location algorithm. *Engineering Fracture Mechanics* **36**, 145–156.
- Crouch, B. A. and Williams, J. G. (1987) Application of dynamic solution to high speed fracture experiments-I. Analysis of experimental geometries. *Engineering Fracture Mechanics* **26**, 541–551.
- Kishimoto, K., Aoki, S. and Sakata, M. (1980) On the path independent integral-J. *Engineering Fracture Mechanics* **13**, 841–850.
- Kobayashi, A. S., Mall, S., Urabe, Y. and Emery, A. F. (1978) A numerical dynamic fracture analysis of three wedge load DCB specimen. In *Numerical methods in fracture mechanics*, ed. A. R. Luxmoore and D. R. J. Owen, pp. 673–684. University College, Swansea.
- Kumar Prashant and Narayanan, M. D. (1993) Energy dissipation of projectile impacted panels of glass fabric reinforced composites. *Composite structures* **15**, 75–90.
- Kumar Prashant and Rai Badri (1993) Delamination of barely visible impact damage in CFRP laminates. *Composite Structures* **23**, 313–318.
- Malluck, J. F. and King, W. W. (1978) Fast fracture simulated by finite element analysis which accounts for crack tip energy dissipation. In *Numerical Methods in Fracture Mechanics*, ed. A. R. Luxmoore and D. R. J. Owen, pp. 648–659. University College, Swansea.
- Manogg, P. (1966) Investigations of the rupture of a plexiglass plate by means of an optical method involving high speed filming of shadow originating around holes drilled in plate. *International Journal of Fracture* **2**, 604–613.
- Nishioka, T. and Atluri, S. N. (1982a) Numerical analysis of dynamic crack propagation: Generation and prediction studies. *Engineering Fracture Mechanics* **16**, 303–332.
- Nishioka, T. and Atluri, S. N. (1982b) Finite element simulation of fast fracture in steel DCB specimen. *Engineering Fracture Mechanics* **16**, 157–175.
- Nishioka, T. and Atluri, S. N. (1983) Path independent integrals, energy release rate and general solution of near-tip fields in mixed mode dynamic fracture mechanics. *Engineering Fracture Mechanics* **18**, 1–22.
- Nishioka, T. and Atluri Satya, N. (1986) *Computational Methods in Mechanics of Fracture*, ed. S. N. Atluri. Elsevier Science, New York.
- Owen, D. J. R. and Shantaram, D. (1977) Numerical study of dynamic crack growth by the finite element. *International Journal of Fracture* **13**, 821–837.
- Parton, V. Z. and Boriskovsky, V. G. (1989) *Dynamic Fracture Mechanics*, Vol. 1, pp. 203–204. Hemisphere Publishing Corporation.
- Popadopoulos, George A. (1993) *Fracture Mechanics: The Experimental Method of Caustics and The Det.-criterion of Fracture*. Springer-Verlag, London.

- Ravichandran, G. and Clifton, R. J. (1989) Dynamic fracture under plane wave loading. *International Journal of Fracture* **40**, 157–201.
- Ravi Chandar, K. and Knauss, W. G. (1982) Dynamic crack tip stresses under stress wave loading—A comparison of theory and experiment. *International Journal of Fracture* **20**, 202–222.
- Ravi Chandar, K. and Knauss, W. G. (1984a) An experimental investigation into dynamic fracture: I. Crack initiation and arrest. *International Journal of Fracture* **25**, 247–262.
- Ravi Chandar, K. and Knauss, W. G. (1984b) An experimental investigation into dynamic fracture: II. Microstructural aspects. *International Journal of Fracture* **26**, 65–80.
- Ravi Chandar, K. and Knauss, W. G. (1984c) An experimental investigation into dynamic fracture: III. On steady-state crack propagation and crack branching. *International Journal of Fracture* **26**, 141–154.
- Ravi Chandar, K. and Knauss, W. G. (1984d) An experimental investigation into dynamic fracture: IV. On interaction of stress waves with propagating cracks. *International Journal of Fracture* **26**, 189–200.
- Rosakis, A. J., Duffy, J. and Freund, L. B. (1984) The determination of dynamic fracture toughness of AISI 4340 steel by the shadow spot method. *Journal of the Mechanics and Physics of Solids* **4**, 443–460.
- Rydhom, G., Fredriksson, B. and Nilsson, F. (1978) Numerical investigation of rapid crack propagation. *Numerical Methods in Fracture Mechanics*, ed. A. R. Luxmoore and D. R. J. Owen, Univ. College, Swansea, 660–672.
- Schardin, H. (1959) *Velocity Effect in Fracture*, ed. B. L. Averbach, pp. 297–350. MIT Press, Cambridge.
- Takeda, N., Sierakowski, R. L., Ross, C. A. and Malvern, L. E. (1982) Delamination crack propagation in ballistically impact glass/epoxy composite laminates. *Experimental Mechanics* **22**, 19–25.
- Thesken, J. C. and Gudmundson, Peter (1991) Application of a moving variable order singular element to dynamic fracture mechanics. *International Journal of Fracture* **52**, 47–65.
- Theocaris, P. S. (1970) Local yielding around a crack tip in plexiglass. *Journal of Applied Mechanics* **37**, 409–415.
- Verma, S. K. (1995) Determination of Static and Dynamic Interlaminar Fracture Toughness—A combined Experimental and Finite Element Method. *Ph.D. thesis submitted to Indian Institute of Technology, Kanpur, India.*
- Wang, Y. and Williams, J. G. (1994) A numerical study of dynamic crack growth in isotropic DCB specimens. *Composites* **25**, 323–331.
- Zehnder, Alant T. and Rosakis, Ares J. (1990) Dynamic fracture initiation and propagation in 4340 steel under impact loading. *International Journal of Fracture* **43**, 271–285.



Pergamon

J. Mech. Phys. Solids, Vol. 46, No. 10, pp. 1789–1813, 1998

© 1998 Elsevier Science Ltd. All rights reserved

Printed in Great Britain

0022-5096/98 \$—see front matter

PII: S0022-5096(98)00036-2

INTERSONIC CRACK PROPAGATION IN BIMATERIAL SYSTEMS

ARES J. ROSAKIS,^{*,a} OMPRAKASH SAMUDRALA,^a RAMAN P. SINGH^a
and A. SHUKLA^b

^a Graduate Aeronautical Laboratories, California Institute of Technology, Pasadena CA 91125, U.S.A.; ^b Department of Mechanical Engineering, University of Rhode Island, Kingston, RI 02881, U.S.A.

(Received 20 December 1997; in revised form 13 February 1998)

ABSTRACT

This paper describes experimental observations of various phenomena characteristic of dynamic intersonic decohesion of bimaterial interfaces. Two separate but complementary optical methods are used in conjunction with high-speed photography to explore the nature of the large-scale contact and mach wave formation at the vicinity of running cracks in two different bimaterial systems. Theoretical predictions of crack tip speed regimes, where large-scale contact is implied, are confirmed. Also, the theoretically predicted mach wave emanating from the intersonically propagating crack tip is observed. Direct visual evidence is also obtained for another traveling mach wave emanating from the end of the intersonically moving contact zone. Subsequently, a physical model for intersonic crack propagation along bimaterial interfaces is presented and ratified in view of recent experimental observations and theoretical developments. Finally, the paper presents very recent experimental evidence that shows crack tip speeds exceeding the intersonic regime and becoming clearly supersonic. © 1998 Elsevier Science Ltd. All rights reserved.

Keywords: A. dynamic fracture, B. crack mechanics, layered material, D. optical interferometry.

INTRODUCTION

In homogeneous materials, the observations of crack growth speeds greater than the shear wave speed, $v > c_s$, is limited to the cases when the loading is applied directly to the propagating crack tip. For remotely loaded cracks, energy considerations make it impossible for the crack tip speed to exceed the Rayleigh wave speed of the material (Broberg, 1960; Freund, 1990). Thus, the only experimental observations of intersonic or supersonic crack tip speeds, $v > c_s$ or $v > c_r$, in a laboratory setting have been on crack growth along weak crystal planes in single crystals of potassium chloride, where the crack faces were loaded by laser induced expanding plasma (Winkler *et al.*, 1970; Curran *et al.*, 1970). Indirect observation of intersonic shear rupture ($c_s < v < c_r$) has also been reported for crustal earthquakes (Archuleta, 1982). These observations have motivated extensive theoretical work in the area of high-speed shear fracture in homogeneous materials. This has been primarily conducted with seismological

* To whom correspondence should be addressed. Tel.: 626 395 3690. Fax: 626 449 2677. E-mail: rosakis@atlantis.caltech.edu

applications in mind and includes the work of Burridge (1973), Burridge *et al.* (1979), Freund (1979), Broberg (1985, 1989), Georgiadis (1986), Bykovtsev and Kramarovskii (1989) and Aleksandrov and Smetanin (1990).

In bimaterial systems, however, it has been recently demonstrated (by the authors and their coworkers) that intersonic crack propagation along bimaterial interfaces is possible even under remote loading conditions (Liu *et al.*, 1993; Lambros and Rosakis, 1995a, b, c; Singh and Shukla, 1996). Indeed, it has been experimentally shown that if there exists a significant mismatch in the stress wave speeds across the bimaterial interface then the crack can propagate intersonically with respect to the material with the lower shear wave speed, while it remains subsonic with respect to the material with the higher wave speed. Under these conditions only a finite amount of energy has to be supplied to the crack tip to maintain extension as the propagational speed approaches the lower of the two Rayleigh wave speeds. This fact was analytically confirmed by Yang *et al.* (1991) on the basis of a subsonic analysis which removes the theoretical restriction for the attainment of intersonic crack tips speeds of the type that exist in homogeneous materials.

Despite these initial attempts, the phenomenon of intersonic crack propagation is still more or less unexplored. The experimental evidence is quite limited and still there does not exist a completely physically realistic theoretical model for the intersonically propagating interfacial crack. In view of these limitations, the current study presents valuable experimental observations on interface failure in the intersonic regime and interprets these observations based on currently available theory.

EXPERIMENTAL TECHNIQUES

The two techniques of coherent gradient sensing (CGS) and photoelasticity were employed independently to study intersonic crack propagation along a bimaterial interface subjected to impact loading. Both these optical techniques provide real-time full field information and are ideally suited to investigate dynamic fracture events when used in conjunction with high-speed photography. However, the two techniques have their own advantages and limitations and the information provided is complementary. Hence, employing both the techniques allows for a better understanding of the dynamic fracture process. This will become apparent when the two techniques are discussed in the following sections.

Coherent Gradient Sensing interferometer (CGS)

Figure 1 shows a schematic of the CGS setup in a transmission configuration. A coherent, monochromatic, collimated laser beam is incident on the bimaterial specimen. After transmission through the transparent side of the deforming specimen, it acquires an optical path difference and loses collimation. The optical path difference acquired is due to stress induced differences in refractive index and due to a non-uniform contraction in the thickness direction around the vicinity of the crack tip (Poisson's ratio effect for elastic solids). The resulting, non-collimated, beam passes through two line diffraction gratings G_1 and G_2 of fine pitch p (typically 40 lines/mm).

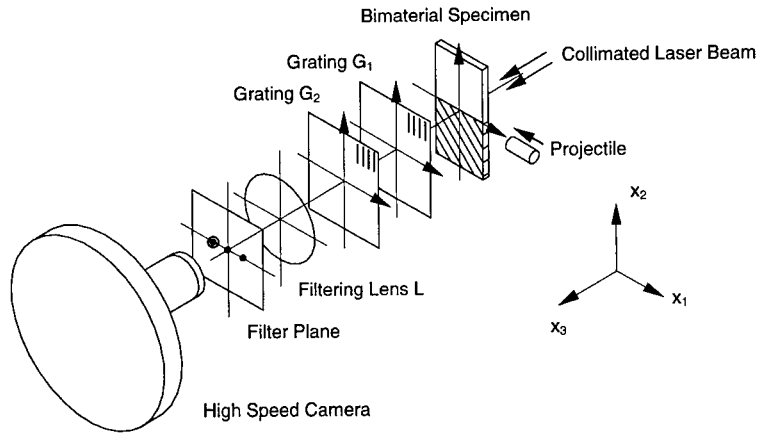


Fig. 1. Schematic of CGS setup in transmission. PMMA/steel bimaterial specimen is illustrated.

The gratings are situated a distance Δ (typically 30–50 mm) apart and perform a “shearing” of the incident wave front. The gratings’ output intensity is transmitted through a filtering lens L . A diffraction spot pattern is obtained on the filtering plane, which is located at the back focal plane of lens L . On this plane all but one diffraction orders are blocked. The one remaining diffraction spot (either of ± 1 orders), shown in Fig. 1 as the open circle on the filtering plane, is imaged to produce an interference pattern. For the case of a dynamic experiment the imaging device is a high-speed camera focused on the specimen.

The details of analyzing the CGS optical method can be found in several previous articles including Tippur *et al.* (1991) and Rosakis (1993) and will not be repeated here for the sake of brevity. The condition for formation of constructive CGS interference fringes on the image plane, for gratings with lines parallel to the x_2 -direction, is,

$$\frac{\partial(S(x_1, x_2))}{\partial x_1} = \frac{mp}{\Delta}, \quad m = 0, \pm 1, \pm 2, \dots \quad (1)$$

Where, $S(x_1, x_2)$ is the optical path change that is introduced due to specimen deformation at a certain location in the x_1 – x_2 plane. It has also been assumed that the diffraction gratings G_1 and G_2 are close enough and/or fine enough to obtain an interferogram that represents the x_1 -gradient of S , rather than an x_1 -finite difference of S . If the grating lines are parallel to the x_1 direction then it can be shown that the condition for constructive interference becomes

$$\frac{\partial(S(x_1, x_2))}{\partial x_2} = \frac{np}{\Delta}, \quad n = 0, \pm 1, \pm 2, \dots \quad (2)$$

For the case of plane stress and a transmission configuration the quantity $S(x_1, x_2)$ is related to the stress state in the deforming specimen as (Rosakis, 1993),

$$S(x_1, x_2) \approx c_\sigma h [\hat{\sigma}_{11}(x_1, x_2) + \hat{\sigma}_{22}(x_1, x_2)]. \quad (3)$$

Where c_σ is a stress optical coefficient for the material, h is the specimen thickness and $\hat{\sigma}_{11}$ and $\hat{\sigma}_{22}$ are thickness averages of the in-plane stress components in the plate.

For points outside the near tip three-dimensional region the CGS patterns assume a simple interpretation in terms of two-dimensional stress field approximations. In particular, eqns (1) and (2) in conjunction with eqn (3) now indicate that the fringes obtained from regions surrounding the three-dimensional zone can be related to the in-plane gradients of $\hat{\sigma}_{11} + \hat{\sigma}_{22}$ as follows,

$$c_\sigma h \frac{\partial(\hat{\sigma}_{11} + \hat{\sigma}_{22})}{\partial x_1} = \frac{mp}{\Delta}, \quad c_\sigma h \frac{\partial(\hat{\sigma}_{11} + \hat{\sigma}_{22})}{\partial x_2} = \frac{np}{\Delta}, \quad m, n = 0, \pm 1, \pm 2, \dots \quad (4)$$

Where, in the case of transmission, c_σ is the stress optical coefficient of the transparent material.

The CGS interferograms are imaged by a rotating mirror type high-speed camera (Cordin Co., model 330A). The camera records 80 frames of the dynamic event and is typically operated at an interframe time of $1.2 \mu\text{s}$ (about 840,000 frames/s). Individual frames are obtained by operating the laser light source (Spectra-Physics Argon-ion laser, model 166-09; operating wavelength $\lambda = 514.5 \text{ nm}$ light) in a pulsed mode. The exposure time used in all experiments (i.e., the laser pulse duration) is 30 ns and the image is recorded on 35-mm black and white film (Kodak TMAX-3200).

Note that in this case the CGS interferograms represent contours of constant gradients of the first stress invariant, $\hat{\sigma}_{11} + \hat{\sigma}_{22}$, of the thickness averaged stress tensor in plane stress, $\hat{\sigma}$. This invariant can also be expressed in terms of the principal stresses of $\hat{\sigma}$ as follows: $\hat{\sigma}_{11} + \hat{\sigma}_{22} = \hat{\sigma}_1 + \hat{\sigma}_2$, since $\hat{\sigma}_{33} = \hat{\sigma}_3 = 0$. Thus, the technique of CGS will not be sensitive to changes in the individual components of stress as long as the derivative of $\hat{\sigma}_1 + \hat{\sigma}_2$ remains a constant.

Photoelasticity

A schematic of the photoelastic setup in a transmission configuration is shown in Fig. 2. The specimen is placed in the optical bench of a high speed Cranz-Schardin spark-gap camera. The optical setup consists of two field lenses, F_1 and F_2 , and two circular polarizers, C_1 and C_2 . The first field lens, F_1 , collimates white light from the

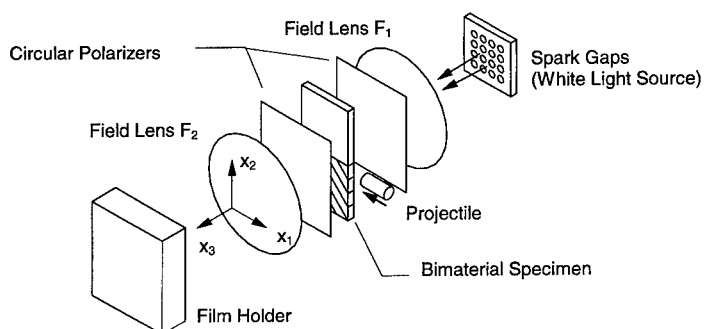


Fig. 2. Schematic of photoelasticity setup in transmission. Homalite-100/aluminum bimaterial specimen is illustrated.

spark-gaps that is incident on the specimen, while the second field lens, F_2 , focuses the light transmitted through the specimen onto the film plane of the high speed camera. Meanwhile, the two circular polarizers form a circular polariscope, which allow photoelasticity to be used to observe the state of stress in the specimen. The transparent side of the bimaterial specimen is specially chosen so that it exhibits stress induced birefringence, which is a fundamental requirement of this technique. A filter (Kodak Wratten filter no. 8) is placed before the film plane of the high speed camera, so that only fringes corresponding to a particular wavelength of light are recorded. The technique of photoelasticity is very well established for a variety of solid mechanics applications and the reader is referred to Dally and Riley (1991) for further details.

The generation of isochromatic fringe patterns is governed by the stress optic law. For the case of monochromatic light, the condition for the formation of fringes is expressed as,

$$\hat{\sigma}_1 - \hat{\sigma}_2 = \frac{Nf_{\sigma}}{h}, \quad (5)$$

where, $\hat{\sigma}_1 - \hat{\sigma}_2$ is the principal stress difference of the thickness averaged stress tensor, $\hat{\sigma}, f_{\sigma}$ is the material fringe value, h is the specimen thickness and N is the isochromatic fringe order. The isochromatic fringe patterns observed are contours of constant maximum shear stress, $\hat{\tau}_{\max} = (\hat{\sigma}_1 - \hat{\sigma}_2)/2$.

The photoelastic fringe patterns are imaged using a high speed Cranz-Schardin spark-gap camera. The camera provides a total of twenty images of the dynamic fracture event at an interframe time of $4 \mu\text{s}$ (250,000 frame/s). The spark-gaps serve as the light sources and the exposure time is typically 400 ns, as determined by the time duration of the sparks. The recording medium is once again black and white photographic film (Kodak Professional $8' \times 10'$ film no. 4127).

Bimaterial specimen and loading arrangement

The bimaterial specimens used in these experiments consisted of a transparent polymer bonded directly to a metal. The material combinations were chosen so that there would be a large mismatch in the mechanical properties across the interface and this would intensify the dynamic effects. The particular choice of the transparent polymer was also dictated by the particular needs of the experimental technique employed, i.e. CGS or photoelasticity. For the case of CGS, the transparent half was Plexiglas (Polymethylmethacrylate or PMMA) while the metal half was AISI 4340 steel. For the photoelastic experiments, the transparent half was Homalite-100, a polyester resin that exhibits stress induced birefringence, while the metal half was 6061 aluminum. Throughout this paper, the transparent polymer side of the specimen will be referred to as material-1 and the metal side as material-2.

Mechanical properties of the material constituents are listed in Table 1. Since both PMMA and Homalite-100 exhibit rate sensitivity their properties are listed for two extreme strain rates [$\dot{\epsilon} = 10^{-3} \text{ s}^{-1}$ and $\dot{\epsilon} = 10^3 \text{ s}^{-1}$ (glassy state)] that could be encountered by material elements in the vicinity of the propagating crack tip. In reality the material surrounding the propagating crack tip is not subject to any uniform value of strain rate. Instead there is a strain rate distribution around the crack tip, which

Table 1. *Mechanical properties and wave speeds of interface constituents*

Property	PMMA		Homalite-100 ¹				4340 Steel	6061 Aluminum
	$\dot{\epsilon} = 10^{-3} \text{ s}^{-1}$	$\dot{\epsilon} = 10^3 \text{ s}^{-1}$	$\dot{\epsilon} = 10^{-3} \text{ s}^{-1}$	$\dot{\epsilon} = 10^{-3} \text{ s}^{-1}$	$\dot{\epsilon} = 10^3 \text{ s}^{-1}$	$\dot{\epsilon} = 10^3 \text{ s}^{-1}$		
Young's modulus, E (GPa)	3.2	5.6	3.9	3.9	5.3	5.3	208	71
Poisson's ratio, ν	0.35	0.35	0.35	0.35	0.35	0.35	0.3	0.33
Density, ρ (kg/m ³)	1190	1190	1230	1230	1230	1230	7830	2770
Dilatational wave speed, c_l (m/s)	1760	2330	1890	1890	2220	2220	5400	5430
(plane-stress)								
Shear wave speed, c_s (m/s)	1000	1330	1080	1080	1270	1270	3195	3100
Rayleigh wave speed, c_R (m/s)	935	1243	1010	1010	1185	1185	2950	2890
Material fringe value, f_σ (kN/m)	—	—	—	—	23.7	23.7	—	—
$\epsilon^{\text{PMMA/steel}} = 0.1037$ $\epsilon^{\text{PMMA/rigid}} = 0.1073$ $\epsilon^{\text{Homalite-100/aluminum}} = 0.0912$ $\epsilon^{\text{Homalite-100/rigid}} = 0.1073$								

¹Manufactured by Homalite Inc., Delaware, U.S.A.

depends on the crack tip stress field. Thus, the material wave speeds at any given point of observation would depend on the effective strain rate at that point and would lie between the two extreme values listed in Table 1. It should be noted that neither 6061 aluminum nor 4340 steel exhibit any appreciable strain rate sensitivity for the strain rates in consideration.

As shown in Table 1, either of the PMMA/steel or the Homalite-100/aluminum combination results in a significant mismatch of mechanical properties and, most importantly for dynamics, wave speeds across the bimaterial interface. The values of the plane-stress quasi-static oscillatory index ε are also listed for PMMA/steel, PMMA/rigid, Homalite-100/aluminum and Homalite-100/rigid material combinations. As demonstrated by these values, both the material combinations behave very similar to an elastic/rigid bimaterial system. Thus, one can expect intensified interfacial effects during the dynamic fracture event.

The specimen preparation procedure for both the material combinations is the same in principle. The bonding is achieved using the monomer of the transparent polymer in conjunction with appropriate catalysts/hardening-agents. Bonding for the PMMA/steel interface is described by Tippur and Rosakis (1991) while that for the Homalite-100/aluminum interface by Singh and Shukla (1996). The issue of bond strength and toughness has also been addressed by the same authors.

The bimaterial specimens were subjected to one-point bend type impact loading as shown in Fig. 3. The impact was achieved by using a cylindrical steel projectile launched using a pressurized gas-gun. For the CGS experiments the projectile was 75 mm long and 50 mm in diameter, and the impact velocity was 20 m/s. Meanwhile, for the photoelastic experiments the projectile was 100 mm long and 12.5 mm in diameter, and the impact velocity was 30 m/s. As will be shown later, both these loadings result in essentially the same mode of bimaterial failure. It is apparent that the loading history experienced by the crack tip would depend on whether the specimen was impacted on the polymer side or the metal side of the interface. In all these experiments the specimen was impacted from the metal side of the interface, so that the energy to the propagating crack tip would be supplied from the side with the higher stress-wave speeds.

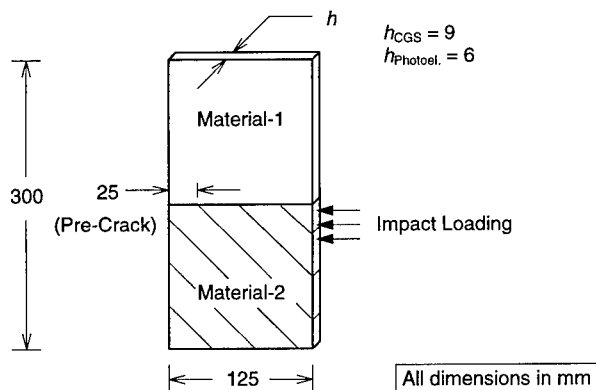


Fig. 3. Bimaterial specimen showing the one point bend impact geometry.

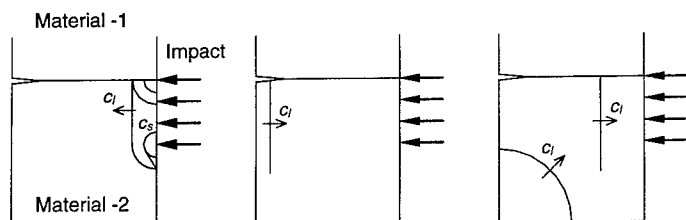


Fig. 4. Stress wave loading of the interfacial crack tip arising from the one point bend impact, (a) just after impact, (b) just before initiation and (c) during crack growth.

The nature of the loading arrangement results in the interface crack tip being loaded primarily in shear. The projectile impacting the metal side of the specimen generates stress wave fronts as shown in Fig. 4(a). The main compressive dilatational stress wave traverses the width of the metal specimen. When this wave passes by the pre-crack tip at the interface it loads the crack tip primarily in shear. This compressive dilatational stress wave then reflects from the opposite free surface as a tensile wave and again propagates by the crack-tip on the interface going in the opposite direction. Doing so it enhances the state of shear that exists around the crack tip (doubles the particle velocity in the negative x_1 -direction), resulting in crack initiation and crack extension. The acoustic mismatch across the bimaterial interface greatly impedes the transfer of stress waves from the metal to the polymer. Hence, the interface crack is driven from the metal side and primarily in a state of shear. Note that at later times other reflections from the specimen boundaries will also impinge upon the interface, as shown in Fig. 4(c), and will change the nature of loading. However, these effects occur later on in the time history of the fracture process.

RESULTS AND DISCUSSION

Observation of contact and shear mach wave

A typical selected sequence of CGS interferograms from a one point bend experiment on a PMMA/steel specimen is shown in Fig. 5 (Lambros and Rosakis, 1995a). Note that the CGS fringes are observed only in the transparent side (i.e. the PMMA side) of the specimen. The instantaneous location of the crack tip is known from each frame and this was used to determine the history of the crack tip speed. A typical crack tip speed history obtained from one such experiment is plotted in Fig. 6. The shear wave speed of PMMA, c_s^{PMMA} , is also plotted in the same figure for two extreme loading rates [$\dot{\epsilon} = 10^{-3} \text{ s}^{-1}$ and $\dot{\epsilon} = 10^3 \text{ s}^{-1}$ (glassy state)] that may be typically expected in the region surrounding the propagating crack tip. The effective shear wave speed at a given point of observation would depend on the effective strain rate at that point and thus would lie between the two extreme values shown in Fig. 6. After initiation the crack tip accelerated very rapidly to beyond the upper extreme of the shear wave speed of PMMA. Then the crack tip speed oscillated between the upper and lower extremes of c_s^{PMMA} for about $15 \mu\text{s}$, after which it accelerated even

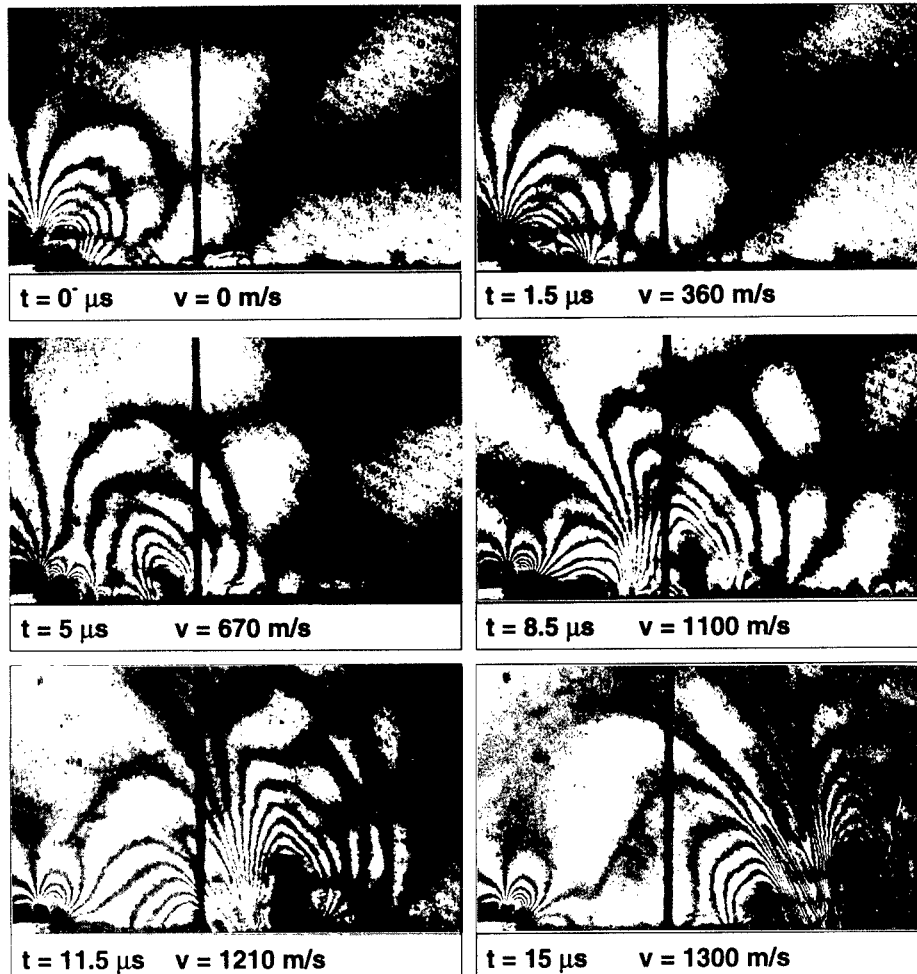


Fig. 5. Typical set of CGS interferograms obtained for dynamic crack growth along a PMMA/steel bimaterial interface subjected to impact loading.

further. Crack tip accelerations were of the order of 10^8 m/s^2 , which establishes the highly unstable nature of this crack tip event. This dynamic and highly repeatable variation of the crack tip speed was first observed by Lambros and Rosakis (1995a) and explained by Lambros and Rosakis (1995c) and Liu *et al.* (1995).

Tests conducted with Homalite-100/aluminum specimens, using the technique of photoelasticity, yield similar observations despite the fact that now different materials constitute the bimaterial interface. Figure 7 shows a typical set of isochromatic fringe patterns obtained for dynamic crack propagation along a Homalite-100/aluminum bimaterial surface (Singh and Shukla, 1996). The history of the crack tip speed typically observed for these experiments is plotted in Fig. 8. As observed for the PMMA/steel case the crack tip accelerated very rapidly after initiation to beyond the

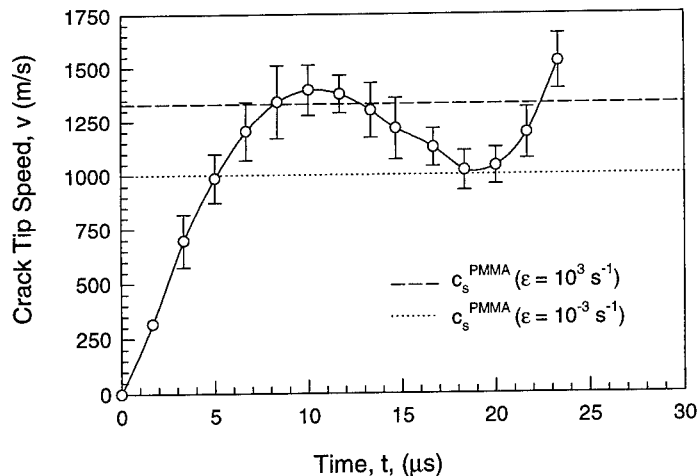


Fig. 6. Typical crack tip speed history for dynamic crack growth along a PMMA/steel bimaterial interface subjected to impact loading.

upper extreme of the shear wave speed of material-1 (Homalite-10). Thereafter, the crack tip speed stayed at this value for about 20 μs , after which it accelerated even further.

The terminal crack tip speeds that have been observed for these experiments were about 140% of the upper extreme of c_s^{PMMA} for the PMMA/steel bimaterial interface and about 130% of the upper extreme of $c_s^{\text{Homalite-100}}$ for the Homalite-100/aluminum bimaterial interface. Nevertheless, the dilatational wave speed of material-1 (PMMA or Homalite-100) was not exceeded in either case. Crack growth in this speed regime is termed as being intersonic.

Crack propagation in the intersonic regime has a direct effect on the nature of the fringe patterns observed. At first the fringes are smooth and continuous, while the crack tip is still subsonic, as shown in the first few frames in Figs 5 and 7. Moreover, the forward and rear fringe loops focus at a single point along the interface, which is the crack tip. In subsequent frames, however, the fringes become squeezed and elongated normal to the interface. Finally, in the intersonic crack growth regime, the fringes in the center of the two lobed fringe pattern do not seem to focus to a single point along the interface. Instead they intercept the bond line over a finite area between the two main lobes, which is evident in the last frame in Fig. 5 and the last three frames in Fig. 7. This effect is seen clearly in Fig. 9, in which the length of the area between the front and back lobes is identified as l . The fringe pattern in this particular frame is caused by large scale contact of the crack faces along l , as the crack is propagating in the intersonic regime. This large-scale contact of crack faces was first observed by Lambros and Rosakis (1995c), theoretically confirmed by Liu *et al.* (1995), and also observed by Singh and Shukla (1996). From the numerical simulation point of view, Xu and Needleman (1996) have confirmed the existence of a contact zone area when the crack tip speed exceeds the lower of the two Rayleigh wave speeds.

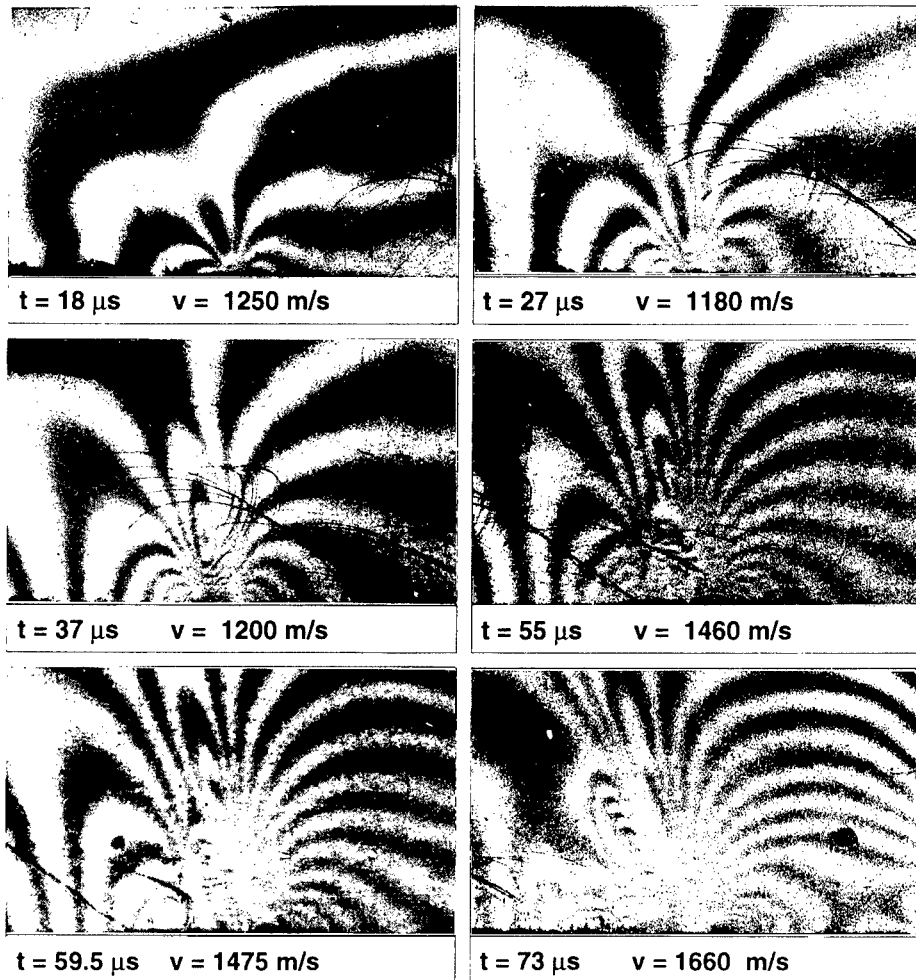


Fig. 7. Typical set of isochromatic fringe patterns obtained for dynamic crack growth along a Homalite-100/aluminum bimaterial interface subjected to impact loading.

Another direct consequence of intersonic crack propagation is the formation of a mach wave (or line-of-discontinuity) in the stress field surrounding the moving crack tip. The propagating crack tip acts as a source of shear and dilatational stress waves, which radiate out into the material and establish the stress field that surrounds the crack tip. If this source (the crack tip) propagates faster than the shear wave speed then the spreading out of the shear waves is limited and a mach wave (or line-of-discontinuity) forms. The existence of such mach waves was predicted by the analysis of Liu *et al.* (1995) but could not be confirmed by the earlier CGS experiments. Note that by the very nature of the technique, CGS would not be sensitive to these discontinuities in the stresses and hence the mach wave would not show up in the

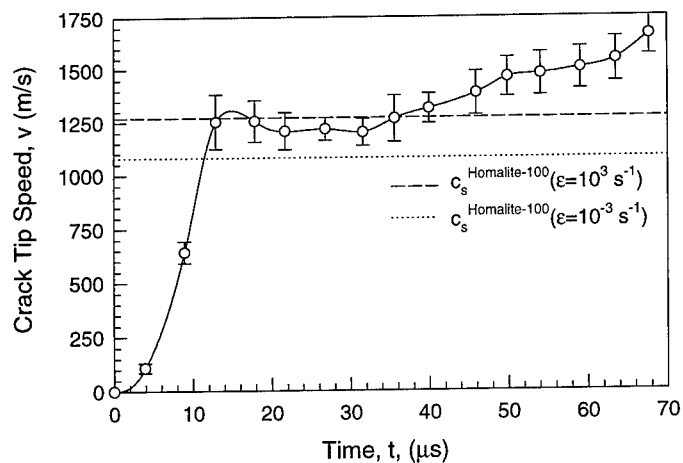


Fig. 8. Typical crack tip speed history for dynamic crack growth along a Homalite-100/aluminum bimaterial surface interface subjected to impact loading.

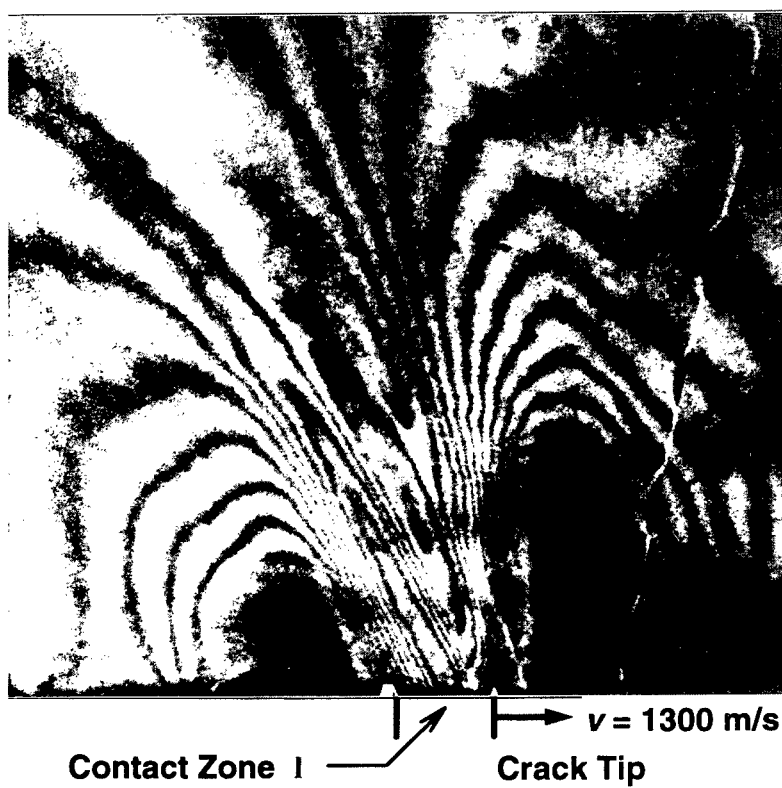


Fig. 9. Enlarged view of CGS fringes in the intersonic crack growth regime showing the area of crack face contact.

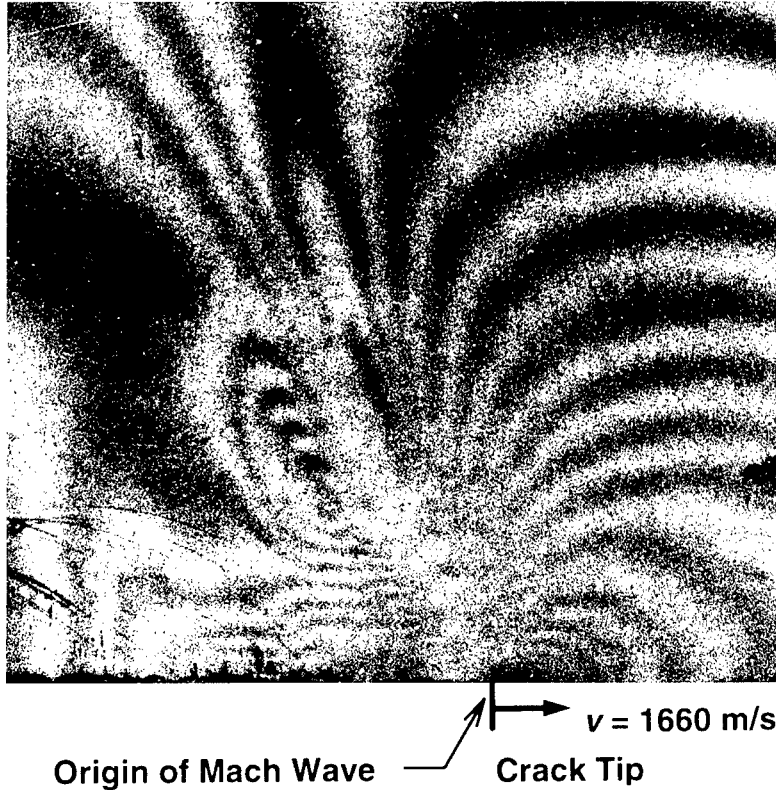


Fig. 10. Discontinuities of isochromatic fringe contours representing the formation of a mach wave.

CGS interferograms. Experimental evidence of the mach wave is observed in the photoelasticity experiments in the form of discontinuous isochromatic fringe contours as shown in Fig. 10. The line originates at the crack tip and radiates out into the material. To the authors' knowledge this is the first direct observation of mach wave formation resulting from intersonic crack propagation along a bimaterial interface.

Intersonic crack growth along an elastic/rigid interface

It was noted earlier that both the PMMA/steel and Homalite-100/aluminum bimaterial systems can be modeled very well by an elastic/rigid approximation. Now, consider a crack propagating intersonically along an elastic/rigid interface, as shown in Fig. 11. Using an asymptotic analysis Liu *et al.* (1995) have shown that the stress field around the crack tip can be expressed as,

$$\sigma_{ij} = \frac{\mu A_0}{1 + \alpha_l^2 \alpha_s^2} \left\{ \frac{\Sigma_{ij}^a}{r_l^q} + \frac{\Sigma_{ij}^b}{(\eta_1 + \hat{\alpha}_s \eta_2)^q} H(\eta_1 + \hat{\alpha}_s \eta_2) + \frac{\Sigma_{ij}^c}{(-\eta_1 - \hat{\alpha}_s \eta_2)^q} H(-\eta_1 - \hat{\alpha}_s \eta_2) \right\}, \quad (6)$$

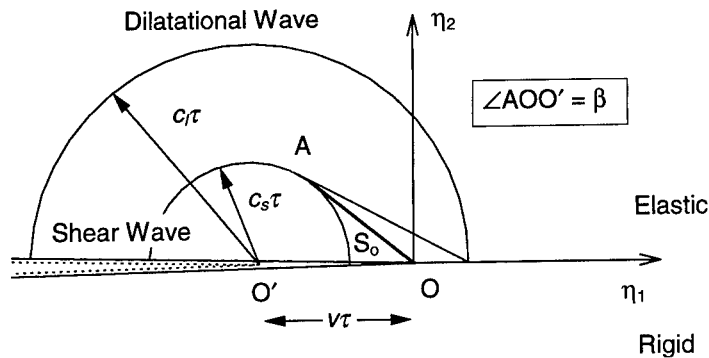


Fig. 11. A crack propagating intersonically along an elastic/rigid interface.

$$\alpha_l^2 = 1 - \frac{v^2}{c_l^2}, \quad \alpha_s^2 = \frac{v^2}{c_s^2} - 1. \quad (7)$$

Where, v is the crack tip speed; μ , c_l and c_s are the shear modulus, dilatational wave speed and shear wave speed, respectively, of material-1 and $H(\cdot)$ is the Heaviside unit step function. Also, the functions Σ_{ij}^a , Σ_{ij}^b and Σ_{ij}^c are functions of θ , the crack tip speed, v , and the wave speeds of material-1, c_l and c_s . The scaled polar coordinates are defined as,

$$r_l = \sqrt{\eta_1^2 + \alpha_l^2 \eta_2^2}, \quad \theta_l = \arctan \left(\frac{\alpha_l \eta_2}{\eta_1} \right). \quad (8)$$

Finally, the strength of the crack tip singularity is given as,

$$q(v) = \frac{1}{\pi} \arctan \left\{ \frac{\alpha_l \alpha_s [4 - (1 - \alpha_s^2)^2]}{4 \alpha_l^2 \alpha_s^2 + (1 - \alpha_s^2)^2} \right\}. \quad (9)$$

The variation of the singularity exponent, $q(v)$, with crack tip speed, v , is plotted in Fig. 12 for different values of the Poisson's ratio of the elastic material. The exponent starts at a value of $q(v) = 0$ at $v = c_s$ and increases monotonically with crack tip speed till it reaches a maximum value at $v = \sqrt{2}c_s$. With further increase in the crack tip speed the exponent decreases monotonically back to the value $q = 0$. Note that $q(v)$ remains less than 0.5 for the entire speed range considered. This limit on the maximum value of $q(v)$ implies that energy flux into the moving crack tip is always zero irrespective of the crack tip speed in the intersonic crack growth regime.

The asymptotic analysis is very useful in explaining several key features of intersonic crack propagation along bimaterial interfaces. The first result is that across the head wave front S_0 , see Fig. 11, the components of stress and particle velocity are discontinuous. Therefore, unlike subsonic crack growth where only one singular point is present at the crack tip, for the case of intersonic crack growth, an entire singular line of infinite jumps in stress and particle velocity appears in the body. The singularity across this line is the same as that at the crack tip. The line originates from the

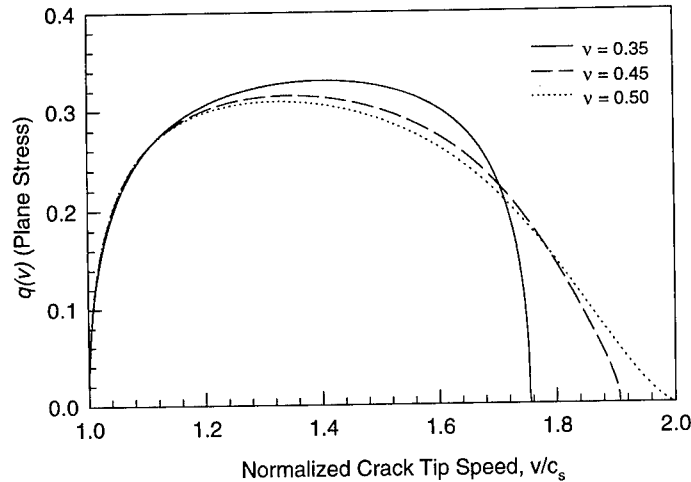


Fig. 12. Variation of the singular exponent $q(v)$ as a function of crack tip speed v for different values of Poisson's ratio (Liu *et al.*, 1995).

propagating crack tip and radiates out into the elastic solid. The existence of such a discontinuity is evident by inspection of eqn (6) shown above. This is the line-of-discontinuity that appears in the isochromatic fringe patterns obtained in the photoelastic experiments. The equation of the moving line of discontinuity is given by,

$$\eta_1 + \alpha_s \eta_2 = 0. \quad (10)$$

Thus, the angular orientation of this line, with respect to the interface, can be expressed in terms of the crack tip speed, v , and the shear wave speed of the elastic material (or material-1), c_s , as,

$$\tan \beta = \frac{1}{\sqrt{\frac{v^2}{c_s^2} - 1}}. \quad (11)$$

The orientations of the line-of-discontinuity determined from the experimental isochromatic fringe patterns were compared with the angles predicted by the above equation and are listed in Table 2. The correspondence between the experimentally observed and theoretically predicted angles is excellent and substantiates the fact that the experimentally observed line-of-discontinuity is indeed the theoretically predicted mach wave. Further evidence of the line-of-discontinuity is presented in the numerical simulations of Xu and Needleman (1996). Liu *et al.* (1995) also showed that there is no energy dissipation when the singular line S_0 moves through the elastic material.

Consider the normal tractions along the interface at an arbitrary distance a ahead of the moving crack tip, $\sigma_{22}(a, 0^+, t)$, and the crack opening displacement at the distance a behind the moving crack tip, $u_2(-a, 0^+, t)$. Then it can be shown (Liu *et al.*, 1995) that if the crack tip speed is in the range $c_s < v < \sqrt{2}c_s$, $\sigma_{22}(a, 0^+, t)$ and

Table 2. Comparison of experimentally measured and theoretically predicted orientations of the line-of-discontinuity

Frame number	$v/c_s^{\text{Homalite-100}}$	β_{Theory} ($^{\circ}$)	$\beta_{\text{Experiment}}$ ($^{\circ}$)
13	1.16	59.5	63
14	1.19	57.5	55
15	1.21	55.7	53
16	1.30	50.3	48

$u_2(-a, 0^+, t)$ have opposite signs. This implies that when the normal traction ahead of the crack tip is positive, crack face penetration into the rigid substrate is predicted. Now, positive normal tractions ahead of the crack tip are required to facilitate interface rupture and crack face penetration is physically impossible. Hence, in the crack tip speed range $c_s < v < \sqrt{2}c_s$ the crack faces would come into contact behind the propagating crack tip. This accounts for the large-scale contact of crack faces observed experimentally in the CGS interferograms when the crack tip speed was indeed in the range $c_s^{\text{PMMA}} < v < \sqrt{2}c_s^{\text{PMMA}}$. When the crack tip speed is in the range $\sqrt{2}c_s < v < c_t$, a positive normal traction ahead of the crack tip results in crack face opening behind the moving crack tip and no contact of the crack faces should be observed asymptotically. However, up to date, no observations of crack tip speeds greater than $\sqrt{2}c_s$ have been made.

It should be noted at this point that in the intersonic regime the asymptotic crack tip field does not have the oscillatory nature characteristic of all subsonic crack growth solutions. In the subsonic cases it is this oscillatory nature that accounts for contact and interpenetration. As discussed by Rice (1988), in most cases, this "small scale" contact is of the order of $10^{-8}L$, where L is a characteristic length of the problem. The situation here is very different. The observed and predicted contact zones are large scale ($l \approx 1-5$ mm) and are not a result of an oscillatory nature of the field. In the present scenario contact is related to the intersonic motion of the crack tip disturbance. Indeed this phenomenon is reminiscent of the intersonic motion of a line load on an elastic half-space. In this problem when the speed of the moving load exceeds the Rayleigh wave speed of the half-space the direction of surface displacements, under the load, is in opposition to the direction of loading as discussed by Georgiadis and Barber (1993).

When crack face contact does indeed occur, the asymptotic solution is no longer valid and the problem must be revisited under different crack face boundary conditions. Nevertheless, despite this limitation the solution does provide considerable conceptual insight into the intersonic crack growth phenomenon.

Same qualitative observations as above have been made for a more realistic elastic/elastic analysis for intersonic bimaterial crack growth (Huang *et al.*, 1996). Here again traveling mach waves have been predicted. Also, for certain crack tip speed range large-scale contact was implied by the solution. However, the details of the

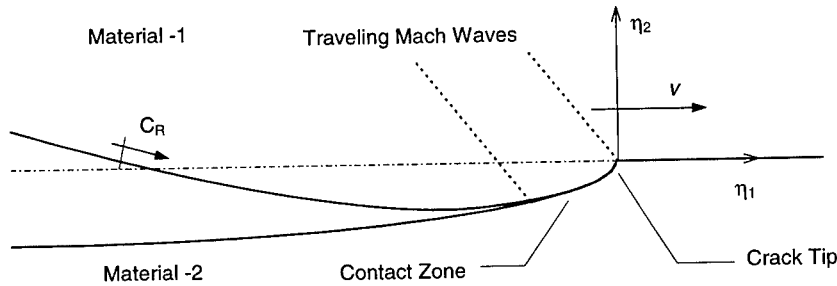


Fig. 13. Schematic of crack face openings for an intersonically propagating interface crack.

speed range where contact is predicted is slightly modified depending on the relative magnitudes of wave speed mismatch of the two elastic solids.

Given the experimental observations presented in the previous section and the asymptotic analyses of Liu *et al.* (1995) and Huang *et al.* (1996) it is believed that when the crack tip is propagating in the regime $c_s < v < \sqrt{2}c_s$, with respect to material-1, the crack faces behind the moving crack tip would be in contact. This contact zone would propagate along with the moving crack tip as illustrated in Fig. 13. Finite contact behind the propagating crack tip raises the possibility of two mach waves being generated at the moving crack tip and at the end of the contact zone. Indeed, most recent experimental observations based on photoelasticity clearly show the existence of two such mach waves when the crack propagates in the regime $c_s < v < \sqrt{2}c_s$ with respect to the more compliant material (Singh *et al.*, 1997). Figure 14 shows the two shock waves observed using dynamic photoelasticity for intersonic crack propagation along a homalite-100/aluminum interface. In addition, the experiments also show that the two shock waves are equally inclined to the interface and indeed propagate with the same speed for substantial time periods throughout the experiments.

Very recently, Huang *et al.* (1997) have employed an asymptotic analysis to determine the stress field around crack tip propagating intersonically along a bimaterial interface accounting for frictional, finite crack face contact (as shown in Fig. 15). They have shown that the stress field around the crack tip is given as

$$\begin{aligned} \sigma_{11} = & \frac{\mu A_0}{1 + \alpha_l^2 \alpha_s^2} \left\{ \frac{1 + 2\alpha_l^2 + \alpha_s^2}{r_1^{q_1} r_2^{q_2}} (\alpha_l \alpha_s \cos \beta + \sin \beta) \right. \\ & - \frac{2\alpha_l \alpha_s}{|R_1|^{q_1} |R_2|^{q_2}} \{ H(R_1) + (\cos q_1 \pi - \alpha_l \alpha_s \sin q_1 \pi) [H(R_2) - H(R_1)] \} \\ & \left. + \frac{\alpha_s^2 - 1}{|R_1|^{q_1} |R_2|^{q_2}} [(\alpha_l \alpha_s \cos(q_1 + q_2)\pi + \sin(q_1 + q_2)\pi) H(-R_2)] \right\} \quad (12a) \end{aligned}$$

$$\sigma_{22} = \frac{-\mu A_0}{1 + \alpha_l^2 \alpha_s^2} \left\{ \frac{1 - \alpha_s^2}{r_1^{q_1} r_2^{q_2}} (\alpha_l \alpha_s \cos \beta + \sin \beta) \right.$$

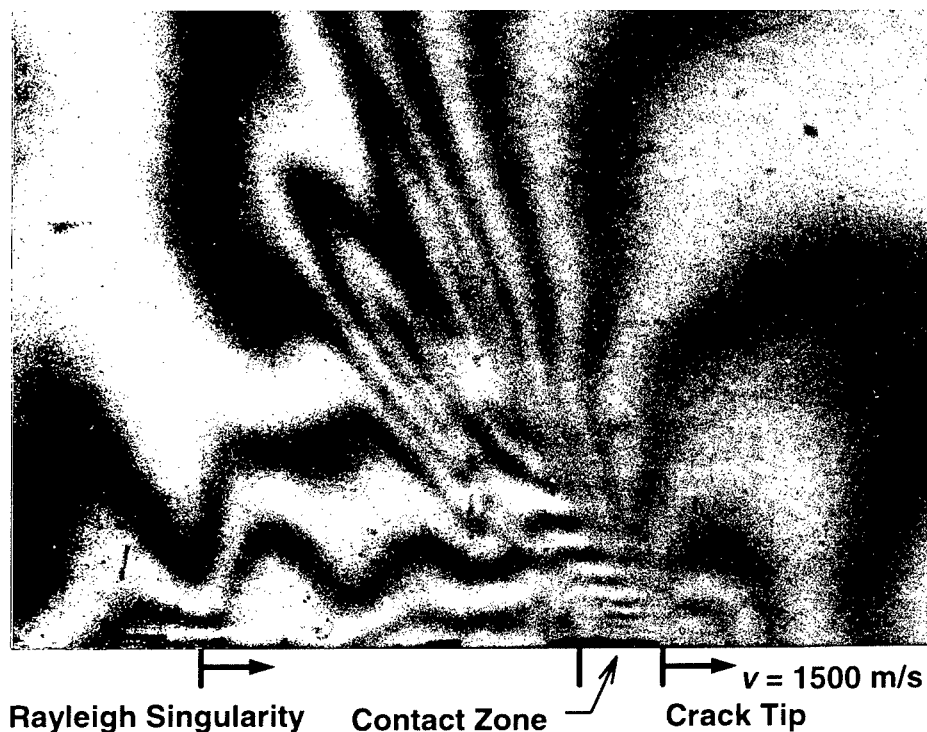


Fig. 14. Details of the isochromatic fringe patterns around the intersonically propagating crack tip showing the primary and secondary mach waves as lines-of-discontinuity, the dynamically moving contact zone, and the Rayleigh disturbance.

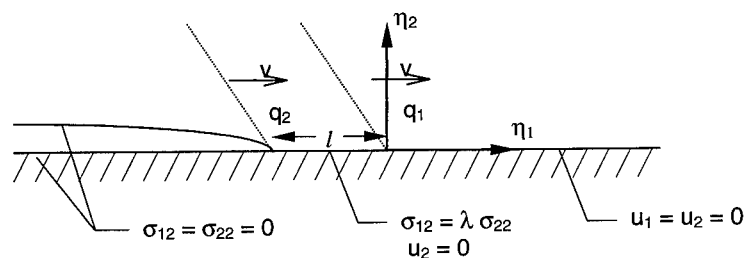


Fig. 15. An interface crack propagating intersonically between an elastic solid and a rigid substrate, with a finite contact zone of length l trailing the crack tip.

$$\begin{aligned}
 & - \frac{2\alpha_i \hat{\alpha}_s}{|R_1|^{q_1} |R_2|^{q_2}} \{ H(R_1) + (\cos q_1 \pi - \alpha_i \hat{\alpha}_s \sin q_1 \pi) [H(R_2) - H(R_1)] \} \\
 & + \frac{\hat{\alpha}_s^2 - 1}{|R_1|^{q_1} |R_2|^{q_2}} [(\alpha_i \hat{\alpha}_s \cos(q_1 + q_2) \pi + \sin(q_1 + q_2) \pi) H(-R_2)] \} \quad (12b)
 \end{aligned}$$

$$\begin{aligned} \sigma_{12} = & \frac{-\mu A_0}{1 + \alpha_l^2 \hat{\alpha}_s^2} \left\{ \frac{2\alpha_l}{r_1^{q_1} r_2^{q_2}} (\cos \beta - \alpha_l \hat{\alpha}_s \sin \beta) \right. \\ & - \frac{\alpha_l (1 - \hat{\alpha}_s^2)}{|R_1|^{q_1} |R_2|^{q_2}} \{ H(R_1) + (\cos q_1 \pi - \alpha_l \hat{\alpha}_s \sin q_1 \pi) [H(R_2) - H(R_1)] \} \\ & \left. + \frac{(\hat{\alpha}_s^2 - 1)^2}{2\hat{\alpha}_s |R_1|^{q_1} |R_2|^{q_2}} [(\alpha_l \hat{\alpha}_s \cos(q_1 + q_2)\pi + \sin(q_1 + q_2)\pi) H(-R_2)] \right\}. \quad (12c) \end{aligned}$$

Where, λ is the friction coefficient, l is the contact length, $H(x)$ is the Heaviside function, and

$$\eta_1 = x - vt \quad \eta_2 = y \quad (13)$$

$$\begin{aligned} r_1 &= \sqrt{\eta_1^2 + \alpha_l^2 \eta_2^2}, \quad \theta_1 = \arctan \left(\frac{\alpha_l \eta_2}{\eta_1} \right) \\ r_2 &= \sqrt{(\eta_1 + l)^2 + \alpha_l^2 \eta_2^2}, \quad \theta_2 = \arctan \left(\frac{\alpha_l \eta_2}{\eta_1 + l} \right) \end{aligned} \quad (14)$$

$$\alpha_l = \sqrt{1 - \frac{v^2}{c_l^2}}, \quad \hat{\alpha}_s = \sqrt{\frac{v^2}{c_s^2} - 1} \quad (15)$$

$$R_1 = \eta_1 + \hat{\alpha}_s \eta_2, \quad R_2 = \eta_1 + \hat{\alpha}_s \eta_2 + l \quad (16)$$

$$\begin{aligned} q_1 &= \frac{1}{\pi} \tan^{-1} \left[\frac{\alpha_l (1 + \hat{\alpha}_s^2) (1 + \lambda \hat{\alpha}_s)}{\alpha_l^2 \hat{\alpha}_s (1 + \hat{\alpha}_s^2 + 2\lambda \hat{\alpha}_s) + \lambda (1 - \hat{\alpha}_s^2)} \right] \\ q_2 &= \frac{1}{\pi} \tan^{-1} \left[\frac{\alpha_l (1 - \hat{\alpha}_s^4) [2\lambda \hat{\alpha}_s - (1 - \hat{\alpha}_s^2)]}{4\alpha_l^2 \hat{\alpha}_s (1 + \hat{\alpha}_s^2 + 2\lambda \hat{\alpha}_s) + \lambda (1 - \hat{\alpha}_s^2)^3} \right] \end{aligned} \quad (17)$$

$$\beta = q_1 \theta_1 + q_2 \theta_2. \quad (18)$$

The functions q_1 and q_2 represent the singularity strengths at the crack tip and at the end of the contact zone. For a far-field observer located at $r = L \gg l$ the crack tip and the end of the contact zone appear as one and have a stress singularity given as

$$q = q_1 + q_2. \quad (19)$$

Where, the coefficient q is the same as defined by eqn (9) and plotted in Fig. 12.

The solution features a large-scale contact zone and predicts two distinct traveling mach waves, one emanating from the crack tip and the other from the end of the contact zone. Moreover, it also predicts a non-zero energy dissipation rate due to frictional dissipation associated with the contact region. Figure 16 shows representative isochromatic fringe patterns generated using the crack tip stress fields given in eqn (12). Here the crack tip is propagating with velocity $v = 1.2c_s$ as for the experimental case shown in Fig. 14. The theoretically generated fringe patterns show

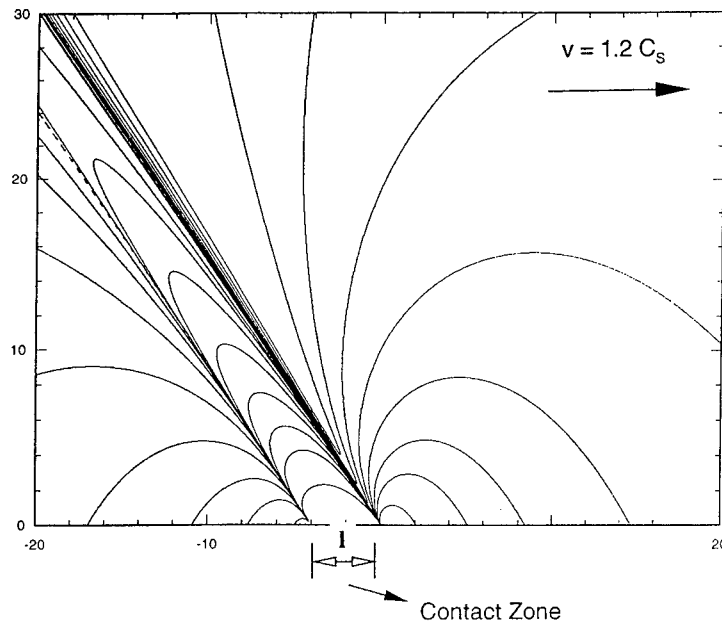


Fig. 16. Representative isochromatic fringe patterns generated using the asymptotic crack-tip stress fields (Yang *et al.*, 1997).

the existence of two distinct mach waves, one emanating from the crack tip and the other from the trailing edge of the contact zone.

Future directions

Motivated by the critical crack opening and shearing displacement criterion for subsonic crack growth along a bimaterial interface (Lambros and Rosakis, 1995b) a fracture growth criterion has also been proposed for the case of intersonic crack growth along a bimaterial interface (Huang *et al.*, 1997). In the absence of opening displacements in the contact zone for intersonically growing interface cracks (as depicted in Fig. 15) it is postulated that intersonic crack growth will take place in the presence of a critical sliding displacement evaluated at the end of the contact zone (Huang *et al.*, 1997),

$$u_1(\eta_1 = -l, \eta_2 = 0^+) = \delta_c. \quad (20)$$

Where, δ_c is the critical value of the sliding displacement and depends only on bimaterial and bond properties. Based upon eqn (20) it is possible to express the normalized energy dissipation rate associated with the propagating crack as a function of the crack tip speed. Figure 17 shows the variation of the normalized energy dissipation rate as a function of crack tip speed for the case of a positive coefficient of contact friction, λ . For this specific case it is found that the energy dissipation rate has a large but finite value at c_s . This suggests that there exists a finite energy barrier

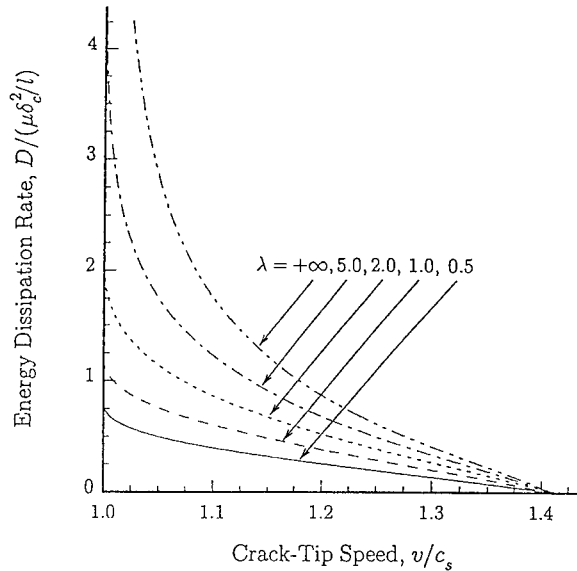


Fig. 17. Normalized energy dissipation rate for intersonic crack propagation along an elastic/rigid interface (Yang *et al.*, 1997).

at the velocity c_s , which is consistent with experimental observations (Liu *et al.*, 1993; Lambros and Rosakis, 1995c; Singh *et al.*, 1997). In these experiments it was observed that the crack seemed to favor growth at $v = c_s$ and stayed at this speed for a substantial period of time before accelerating further in an unstable fashion. Indeed, the unstable acceleration of the crack tip beyond $\sqrt{2}c_s$ is consistent with the decreasing energy dissipation rate, as shown in Fig. 17.

Very recent experiments conducted on the PMMA/Aluminum bimaterial system have demonstrated that it is possible for bimaterial cracks to propagate at speeds even greater than $\sqrt{2}c_s$ of the more compliant material (i.e. PMMA). These experiments employed the same specimen geometry and loading arrangement as before. However, the time window of observation was extended to observe more of the fracture process. A typical selected sequence of CGS interferograms from such an experiment is shown in Fig. 18. Note that, as before, the CGS fringes are observed only in the PMMA side of the specimen. The history of the crack tip speed obtained from this experiment is plotted in Fig. 19. It can be seen that the crack propagates for some time in the regime $c_s^{\text{PMMA}} < v < \sqrt{2}c_s^{\text{PMMA}}$ before accelerating further in a rapid unstable fashion. Terminal crack tip speeds in this case have exceeded not only the plane wave speed of PMMA, c_l^{PMMA} , but also the Rayleigh wave speed of aluminum. Thus, this is the case of crack growth being truly supersonic with respect to the compliant half of the bimaterial interface. Note that once $\sqrt{2}c_s^{\text{PMMA}}$ has been exceeded there is no further requirement for crack face contact and the model depicted in Fig. 15 must be revisited and suitably modified.

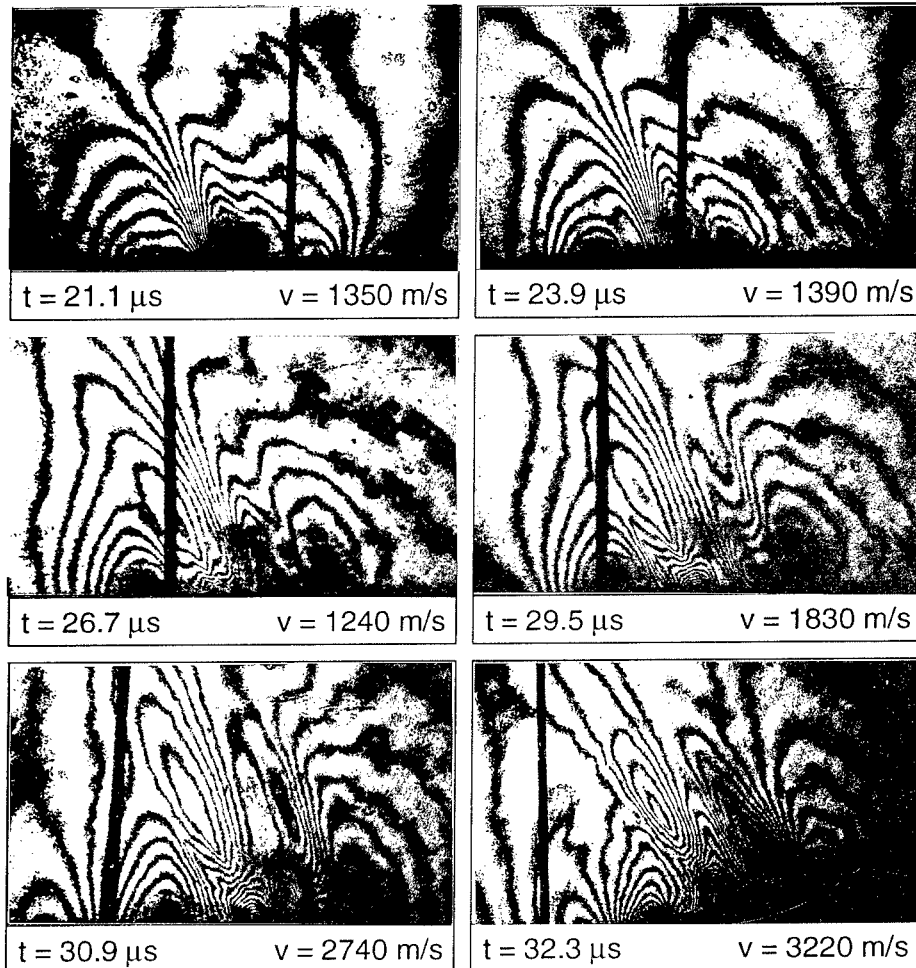


Fig. 18. Typical set of CGS interferograms obtained for dynamic crack growth along a PMMA/aluminum bimaterial interface subjected to impact loading. (Extended time window of observation.)

CLOSURE

This paper describes experimental observations of various phenomena characteristic of dynamic intersonic decohesion of bimaterial interfaces. The optical techniques of coherent gradient sensing (CGS) interferometry and photoelasticity, were employed in conjunction with high speed photography, in separate yet complementary experiments, to explore intersonic interfacial crack propagation in two different bimaterial systems, namely, PMMA/steel and Homalite-100/aluminum.

Using the two techniques the nature of large-scale contact and mach wave formation at the vicinity of running cracks in the two bimaterial systems is explored. It is confirmed that large-scale contact does indeed occur when the crack tip speed is in

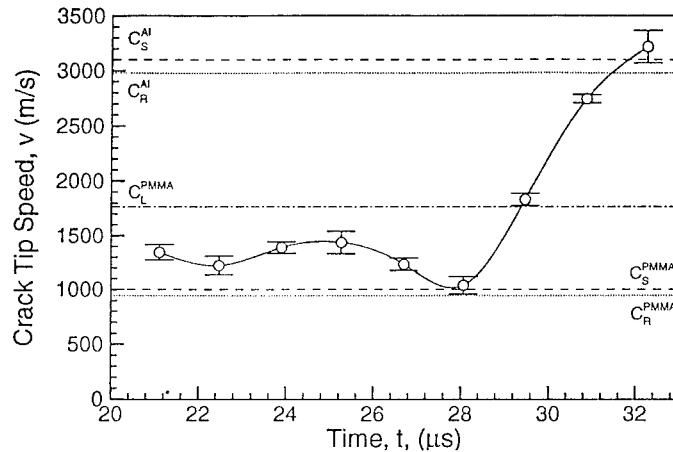


Fig. 19. Crack tip speed history of dynamic crack growth along a PMMA/aluminum bimaterial interface.

the $c_s < v < \sqrt{2}c_s$ regime, as implied theoretically. Also, direct visual evidence is obtained for mach waves emanating from the intersonically moving crack tip and the end of the intersonically moving contact zone. In view of these experimental observations, a physical model for intersonic crack propagation along bimaterial interfaces was presented and ratified in view of recent theoretical developments. Finally, very recent experimental evidence was presented to demonstrate the possibility of super-sonic crack growth along a bimaterial interface.

ACKNOWLEDGEMENTS

The authors would like to acknowledge the support of the National Science Foundation through a joint Grant No. CMS-9424113 to the University of Rhode Island and the California Institute of Technology (Dr O. Dillon, Scientific Officer). A. J. Rosakis would also like to acknowledge the support of the Office of Naval Research under Grant No. N00014-95-1-0453 (Dr Y. Rajapakse, Scientific Officer).

REFERENCES

- Aleksandrov, V. M. and Smetanin, B. I. (1990) Supersonic cleavage of an elastic strip. *PMM U.S.S.R.* **54**(5), 677–682.
- Archuleta, R. J. (1982) Analysis of near-source static and dynamic measurements from the 1979 Imperial Valley earthquake. *Bull. Seismological Soc. Am.* **72**(6), 1927–1956.
- Broberg, K. B. (1960) The propagation of a Griffith crack. *Ark. Fys.* **18**, 159.
- Broberg, K. B. (1985) Irregularities at earth-quake slip. *J. Tech. Phys.* **26**(3–4), 275–284.
- Broberg, K. B. (1989) The near-tip field at high crack velocities. *International Journal of Fracture* **39**(1–3), 1–13.

- Burridge, R. (1973) Admissible speeds for plane-strain shear cracks with friction by lacking cohesion. *Geophys. J. R. Soc. Lond.* **35**, 439–455.
- Burridge, R., Conn, G. and Freund, L. B. (1979) The stability of a rapid mode II shear crack with finite cohesive traction. *J. Geophys. Res.* **85**(B5), 2210–2222.
- Bykovtsev, A. S. and Kramarovskii, D. B. (1989) Non-stationary supersonic motion of a complex discontinuity. *PMM U.S.S.R.* **53**(6), 779–786.
- Curran, D. R., Shockey, D. A. and Winkler, S. (1970) Crack propagation at supersonic velocities, II. Theoretical model. *Int. J. Fract.* **6**(3), 271–278.
- Dally, J. W. and Riley, W. F. (1991) *Experimental Stress Analysis*. McGraw-Hill.
- Freund, L. B. (1979) The mechanics of dynamic shear crack propagation. *J. Geophys. Res.* **84**(B5), 2199–2209.
- Freund, L. B. (1990) *Dynamic Fracture Mechanics*. Cambridge University Press, Cambridge.
- Georgiadis, H. G. (1986) On the stress singularity in transonic shear crack propagation. *International Journal of Fracture* **30**(3), 175–180.
- Georgiadis, H. G. and Barber, J. R. (1993) Steady-state transonic motion of a line load over an elastic half-space: the corrected Cole/Huth solution. *Journal of Applied Mechanics* **60**, 772–774.
- Huang, Y., Liu, C. and Rosakis, A. J. (1996) Transonic crack growth along a bimaterial interface: an investigation of the asymptotic structure of near-tip fields. *International Journal of Solids and Structures* **33**(18), 2625–2645.
- Huang, Y., Wang, W., Liu, C. and Rosakis, A. J. (1997) Intersonic interfacial crack growth in a bimaterial: an investigation of crack face contact. *Journal of the Mechanics and Physics of Solids*, in press.
- Lambros, J. and Rosakis, A. J. (1995a) Dynamic decohesion of bimaterials: experimental observations and failure criteria. *International Journal of Solids and Structures* **32**(17/18), 2677–2702.
- Lambros, J. and Rosakis, A. J. (1995b) On the development of a dynamic decohesion criterion for bimaterials. *Proceedings of the Royal Society of London*.
- Lambros, J. and Rosakis, A. J. (1995c) Shear dominated transonic interfacial crack growth in a bimaterial—I. Experimental observations. *Journal of the Mechanics and Physics of Solids* **43**(2), 169–188.
- Liu, C., Huang, Y. and Rosakis, A. J. (1995) Shear dominated transonic interfacial crack growth in a bimaterial—II. Asymptotic fields and favorable velocity regimes. *Journal of the Mechanics and Physics of Solids* **43**(2), 189–206.
- Liu, C., Lambros, J. and Rosakis, A. J. (1993) Highly transient elastodynamic crack growth in a bimaterial interface: higher order asymptotic analysis and experiments. *Journal of the Mechanics and Physics of Solids* **41**(12), 1887–1954.
- Rice, J. R. (1988) Elastic fracture mechanics concepts for interfacial cracks. *Journal of Applied Mechanics* **55**, 98–103.
- Rosakis, A. J. (1993) Two optical techniques sensitive to gradients of optical path difference: the method of caustics and the coherent gradient sensor (CGS). *Experimental Techniques in Fracture*, pp. 327–425.
- Rosakis, A. J., Samudrala, O. and Singh, R. P. (1997) Work in progress. Graduate Aeronautical Laboratories, California Institute of Technology, Pasadena, California.
- Singh, R. P. and Shukla, A. (1996) Subsonic and intersonic crack growth along a bimaterial surface. *Journal of Applied Mechanics* **63**, 919–924.
- Singh, R. P., Lambros, J., Shukla, A. and Rosakis, A. J. (1997) Investigation of the mechanics of intersonic crack propagation along a bimaterial interface using coherent gradient sensing and photoelasticity. *Proceedings of the Royal Society of London*, in press.
- Tippur, H. V. and Rosakis, A. J. (1991) Quasi-static and dynamic crack growth along bimaterial interfaces: a note on crack-tip field measurements using coherent gradient sensing. *Expt. Mech.* **31**(3), 243–251.
- Tippur, H. V., Krishnaswamy, S. and Rosakis, A. J. (1991) A coherent gradient sensor for crack tip measurements: analysis and experimental results. *International Journal of Fracture* **48**, 193–204.

- Winkler, S., Shockey, D. A. and Curran, D. R. (1970) Crack propagation at supersonic velocities, I. *International Journal of Fracture* **6**(2), 151–158.
- Xu, X.-P. and Needleman, A. (1996) Numerical simulations of dynamic crack growth along an interface. *International Journal of Fracture* **74**, 289–324.
- Yang, W., Suo, Z. and Shih, C. F. (1991) Mechanics of dynamic debonding. *Proceedings of the Royal Society of London* **A433**, 679–697.



Pergamon

J. Mech. Phys. Solids, Vol. 46, No. 10, pp. 1815–1833, 1998

© 1998 Elsevier Science Ltd. All rights reserved

Printed in Great Britain

0022-5096/98 \$—see front matter

PII: S0022-5096(98)00059-3

THE INFLUENCE OF CRACK TRAPPING ON THE TOUGHNESS OF FIBER REINFORCED COMPOSITES

G. XU,^{*a} A. F. BOWER^b and M. ORTIZ^b

^aDepartment of Mechanical Engineering, M.I.T., Cambridge, MA 02139, U.S.A.;

^bDivision of Engineering, Brown University, Providence, RI 02912, U.S.A.

(Received 20 December 1997; in revised form 18 March 1998)

ABSTRACT

Frictional crack bridging is the main mechanism of toughening in brittle fiber/brittle matrix composites. In addition, the fibers may have a second beneficial effect: they tend to trap cracks propagating through the solid, and may cause them to arrest. The effectiveness of crack trapping increases with the fracture toughness of the interface between fibers and matrix. In contrast, crack bridging tends to be more effective if the interface between fibers and matrix has a low fracture toughness. In this paper, we study the competing effects of crack trapping and bridging in a brittle fiber/brittle matrix composite. A numerical method is used to predict in three dimensions the path of a crack as it bypasses rows of fibers in an ideally brittle matrix. The results are used to deduce the influence of crack trapping on the toughness of the composite. In addition, a simple model of frictional crack bridging is used to compare the relative effects of crack trapping and bridging. It is shown that, in general, the influence of bridging greatly exceeds that of trapping. However, if the fibers have a low tensile strength and there is a large resistance to sliding between fibers and matrix, crack trapping can be significant: in this case, the best composite toughness is achieved by using a tough interface between fibers and matrix. © 1998 Elsevier Science Ltd. All rights reserved.

1. INTRODUCTION

Ceramics have a high specific stiffness and yield stress; they melt at high temperatures, and are resistant to wear, oxidation and corrosion. Materials with these properties are in demand for a number of applications, particularly where components are required to withstand high temperatures and a hostile environment. However, ceramics have a very low ductility and fracture toughness compared to metals. This severely limits their performance, and at present ceramics can only be used in components which are subjected to modest loads. There is therefore great interest in finding ways to improve their fracture toughness.

One promising approach is to add a second phase to the solid, in the form of particles, whiskers or fibers. Two general types of composite are made in this way. In one type, a tough, ductile material (such as a metal) is chosen for the second phase, and the reinforcing particles are strongly bonded to the matrix. In this case, the reinforcing particles have two beneficial effects: firstly, they trap the front of a crack as it propagates through the solid, and may cause the crack to arrest. Secondly, they

*To whom correspondence should be addressed. Terra Tek, University Research Park, 420 Wakara Way, Salt Lake City, UT 84108, U.S.A. E-mail: analysis@terratek.com

are left intact in the wake of the crack, pinning the crack faces and carrying part of the load. Both experiment and theory show that the combined effects of crack trapping and bridging can increase the toughness of a brittle matrix a factor of 10 (Krstic *et al.*, 1981; Krstic, 1983; Bower and Ortiz, 1991). The toughness of the composite increases with the toughness and volume fraction of the reinforcing phase.

The main disadvantage of reinforcing a ceramic with metal particles is that the high temperature performance of the composite is limited, due to oxidation and melting in the metal. For high temperature applications, it is common to reinforce ceramics with ceramic fibers: one example is an alumina matrix reinforced by silicon carbide fibers. In this case, the toughness of the fibers is comparable to that of the matrix. To strengthen the composite, the interface between fibers and matrix must have a low toughness. Then, as a crack propagates through the solid, it is deflected along the interface between fibers and matrix. Many fibers remain intact in the wake of the crack, and are progressively pulled free from the surrounding matrix as the crack faces separate. Energy is dissipated by frictional sliding, so the toughness of the composite may be considerably greater than that of its constituents.

Brittle matrix/brittle fiber composites must be designed with care. The strength of the composite is very sensitive to the properties of its constituents, and to the properties of the interface between fiber and matrix. Unless the combination of material properties is chosen correctly, the toughness of the composite may be little better than that of the matrix. Much effort has therefore been devoted to finding materials and interfaces that optimize the fracture resistance of composites.

To direct the development, it is helpful to predict the combination of material properties which should lead to the highest strength. A number of theoretical models have been developed for this purpose, (Rose, 1987; Budiansky, 1986; Budiansky *et al.*, 1988; Becher *et al.*, 1988; Budiansky and Amazigo, 1989; Nair, 1990). The standard approach is to assume that frictional crack bridging is the main mechanism which is responsible for improving the strength of the composite. The effect of the bridged zone in the wake of a crack is often idealized as a distribution of pressure $p(\delta)$ which acts on the crack faces. The relationship between the pressure p and the crack opening δ is found by calculating the force required to pull a single fiber free from the matrix. The pull-out force is determined by a number of factors, including the fracture toughness of the interface between fiber and matrix; the nature of the friction force acting between the sliding surfaces; the geometry of the fibers; and residual stresses in the solid. Once the function $p(\delta)$ has been found, one may calculate the toughness of the composite, the length of the bridging zone, and the crack opening displacements, as a function of the properties of the materials. Models of this type have successfully predicted many of the features of fracture in fiber reinforced composites.

There is no doubt that frictional crack bridging is the dominant toughening mechanism in brittle matrix/brittle fiber composites. However, the fibers have another important effect. Suppose that a semi-infinite crack propagates through a fiber reinforced solid, as illustrated in Fig. 1. One of several possible events may occur whenever the crack meets the fibers. If the fiber toughness exceeds that of the matrix, and the fibers are strongly bonded to the surrounding material, then the crack is trapped by the fibers. This process can significantly improve the strength of a brittle solid. However, for trapping to be effective, the fiber toughness must be at least three

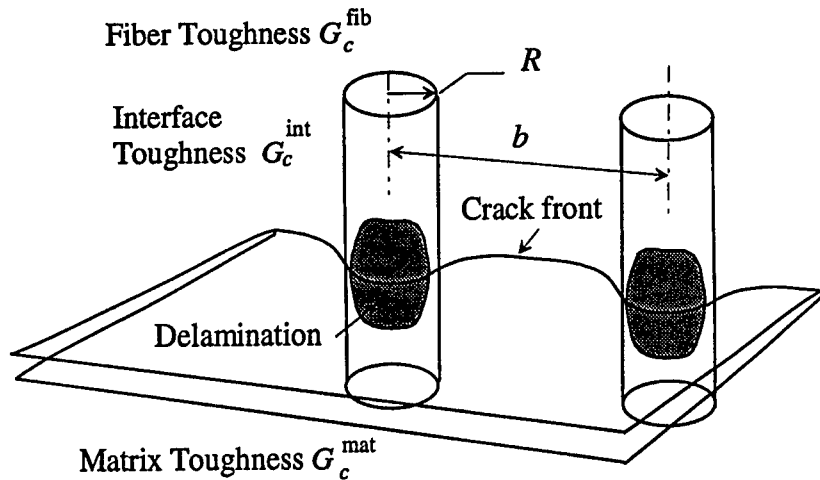


Fig. 1. Idealized model of a crack bypassing a row of fibers.

times that of the matrix. If the fibers have a low toughness, the semi-infinite crack breaks through them, and the toughness of the composite is little better than that of the matrix. One may prevent the fibers from breaking by bonding them only weakly to the surrounding solid. Then, the semi-infinite crack is deflected along the interface between fibers and matrix. The crack is effectively trapped within the interface: the semi-infinite crack bypasses the fibers, which are left intact in the crack wake, and toughen the solid by frictional crack bridging.

Although this form of crack trapping is not as effective as the trapping by strongly bonded, tough fibers, it nevertheless influences the toughness of the composite. If the interface between fiber and matrix is relatively strong, one might expect some improvement in toughness due to trapping, while if the interface has a low toughness, the solid may be weakened by the debonding. A detailed analysis of this process has not yet been attempted. Existing models of fracture in brittle fiber reinforced composites either neglect the effects of crack trapping altogether, or assume that fiber debonding reduces the strength of the matrix. In this paper, we present a detailed three dimensional analysis of crack trapping by fibers in a brittle matrix.

Figure 1 shows our model of fracture in a fiber reinforced composite. The matrix is taken to be an isotropic linear elastic solid, with Young's modulus E and Poisson's ratio ν . The matrix is assumed to be ideally brittle, with a mode I plane strain fracture toughness K_{IC}^{mat} or critical energy release rate G_c^{mat} . The solid is reinforced by a regular distribution of long, cylindrical fibers, with radius R and spacing b . For simplicity, we assume that the fibers have the same elastic properties as the matrix. The fibers are also assumed to be ideally brittle, with fracture toughness K_{IC}^{fib} and critical energy release rate G_c^{fib} . The interface between fibers and matrix is taken to be ideally brittle as well, with interface toughness G_c^{int} . For simplicity, we assume that the solid is stress free when unloaded.

To calculate the toughening due to crack trapping, we investigate the behavior of

a planar, semi-infinite crack as it propagates past a row of fibers. The shape of the crack is calculated in detail, and the toughening is estimated by computing the load required to bypass the row of fibers. The results are used to investigate the influence of the interfacial toughness and fiber volume fraction on the toughening due to crack trapping. Our results show that crack trapping can significantly improve the strength of a fiber reinforced solid, even if the interface between fibers and matrix has a low fracture toughness. The toughening due to trapping increases with the fracture toughness of the interface.

In contrast, several authors have shown that if one reduces the fracture toughness of the interface, the toughening due to frictional crack bridging tends to increase. This suggests that there may be an optimal value for the interface toughness, which leads to the greatest toughness for the composite. To investigate this possibility, we have estimated the combined effects of crack trapping and bridging on toughness. To find the effects of crack bridging, we have used the results of calculations by Charalambides and Evans (1989), Hutchinson and Jensen (1990), and Nair (1990). These models approximate the bridging region as a cohesive zone in the crack wake: the toughening is deduced by finding the work done to pull a fiber free from the matrix.

2. ANALYSIS OF CRACK TRAPPING

2.1. Assumptions

We begin by calculating the toughening due to crack trapping. For this purpose, we suppose that the composite contains a planar semi-infinite crack, whose plane is perpendicular to the fiber axes. The crack faces are assumed to be free of bridging fibers. We suppose that the crack front is initially straight, and lies just short of a row of fibers. The solid is subjected to remote loading so as to induce mode I stress intensity factors on the initial crack front. The magnitude of the external loading is parameterized by a remote stress intensity factor K_I^∞ . We now suppose that the remote load is progressively increased.

The remote load induces uniform mode I stress intensity factors on the initial crack front. When the remote load reaches a magnitude $K_I^\infty = K_{IC}^{\text{mat}}$, the crack begins to propagate. In all the calculations presented here, we have selected parameters so that the crack is either trapped at the fibers, or is deflected along the interface. The remainder of the crack bows out between the fibers. Our objective is to calculate the shape of the crack (including any crack growth along the interface), and to estimate the critical load required to bypass a row of fibers.

The shape of the crack is determined by an appropriate fracture criterion. The crack may adopt a complex three-dimensional shape, and generally propagates in mixed mode: one must therefore specify the influence of mode mixity on the fracture process. We have used a particularly simple fracture criterion in our analysis. A local energy release rate $G(s)$ is defined at each point on the crack front

$$G = \frac{1-\nu}{2\mu} \left(K_I^2 + K_{II}^2 + \frac{1}{1-\nu} K_{III}^2 \right) \quad (1)$$

At points where $G < G_c$, the crack is assumed to arrest. For crack growth to be possible, the condition $G = G_c$ must be satisfied. Situations in which $G > G_c$ are assumed to be physically inadmissible. Where the crack lies in the matrix, we assume that it grows in a direction so as to satisfy $K_{II}(s) = 0$. Cracks which are trapped in the fiber/matrix interface may propagate in fully mixed mode.

This approach has been shown to predict accurately both fracture loads and crack trajectories in homogeneous solids. However, it is likely to underestimate the strength of an interface. Experiments show that the toughness of an interface increases with the ratio of K_{II}/K_I (Evans *et al.*, 1989; Hutchinson and Suo, 1991; Shih, 1991): this is not predicted by the simple fracture criterion that we have adopted. Consequently, our calculations are likely to underestimate the toughening due to trapping.

2.2. Numerical procedure

To apply the fracture criterion, one must calculate distributions of stress intensity factor and energy release rate around the crack front. We have used a numerical procedure to do this. The method is described in detail by Xu and Ortiz (1993), so only a brief summary is given here. Consider a three-dimensional crack in an infinite, linear elastic solid. Let S denote the plane of the crack, and let $\mathbf{n}(\mathbf{x})$ be a unit vector normal to S at \mathbf{x} . Suppose that the solid is loaded by remote stress σ^∞ , which induces a displacement jump $\mathbf{u}(\mathbf{x})$ in direction $\mathbf{n}(\mathbf{x})$ across S at \mathbf{x} . Xu and Ortiz (1993) show that the potential energy of the solid Φ may be expressed as

$$\Phi[\mathbf{u}] = W[\mathbf{u}] - \int_S \mathbf{u} \cdot \sigma^\infty \cdot \mathbf{n} dS. \quad (2)$$

Here, $W[\mathbf{u}]$ represents the elastic strain energy due to introducing the displacement discontinuity $\mathbf{u}(\mathbf{x})$ into the solid. It may be computed by representing the crack as a distribution of dislocation loops which lie on the cracked plane. Xu and Ortiz (1993) give the following expression for W

$$\begin{aligned} W[\mathbf{u}] = & \frac{\mu}{4\pi} \int_S \int_S \frac{[\mathbf{e}_i \cdot (\mathbf{n}(\mathbf{x}) \times \nabla u_j(\mathbf{x}))][\mathbf{e}_j \cdot (\mathbf{n}(\xi) \times \nabla u_i(\xi))]}{R} dA_\xi dA_x \\ & - \frac{\mu}{8\pi} \int_S \int_S \frac{[\mathbf{e}_i \cdot (\mathbf{n}(\mathbf{x}) \times \nabla u_i(\mathbf{x}))][\mathbf{e}_j \cdot (\mathbf{n}(\xi) \times \nabla u_j(\xi))]}{R} dA_\xi dA_x \\ & + \frac{\mu}{8\pi(1-\nu)} \int_S \int_S \frac{[\mathbf{e}_i \times (\mathbf{n}(\mathbf{x}) \times \nabla u_i(\mathbf{x}))] \cdot \mathbf{T} \cdot [\mathbf{e}_j \times (\mathbf{n}(\xi) \times \nabla u_j(\xi))]}{R} dA_\xi dA_x \quad (3) \end{aligned}$$

Here, \mathbf{e}_i denote a set of Cartesian basis vectors; ∇ is the gradient operator; μ and ν are the shear modulus and Poisson's ratio of the solid; $R = |\mathbf{x} - \xi|$, and \mathbf{T} is a tensor with components

$$T_{ij} = \frac{\partial^2 R}{\partial x_i \partial x_j} \quad (4)$$

To calculate stress intensity factors for an arbitrarily shaped crack, one must find

the distribution of crack opening displacements which minimizes eqn (2). A numerical approximation is found by dividing the surface of the crack into a number of six-noded triangular elements, and using quadratic shape functions to interpolate the crack opening displacements within each element. For elements on the crack front, the mid-side nodes are relocated to quarter-point locations so as to approximate accurately the parabolic variation of opening displacements. By substituting the resulting expressions for the opening displacements into eqns (2) and (3), one finds a system of linear equations for the opening displacements at discrete points on the cracked surface. One advantage of this formulation is that the system of equations is symmetric. Finally, the stress intensity factors are deduced from the asymptotic variation of crack opening displacements near the crack front.

As the crack propagates around the fibers, the shape of the crack must be adjusted so as to satisfy the fracture criteria at all points on the crack front. We have used two procedures to do this. In simulations where there is no fiber debonding, we calculate the crack shape by integrating a pseudo-dynamic equation of motion for the crack tip. Freund (1990) has shown that the velocity of the tip of a semi-infinite crack under mode I loading is closely approximated by

$$\dot{a}(s) = \begin{cases} c_R[1 - G_c/G(s)], & G(s) \geq G_c, \\ 0 & G(s) < G_c \end{cases} \quad (5)$$

where \dot{a} is the rate of crack advance, and c_R is the Rayleigh wave speed for the material. We have used this expression to compute the rate of advance of each point on the crack front. The shape of the crack is then computed by integrating the rate of crack advance using a simple Euler time marching scheme. To ensure that $G(s) \sim G_c$ over all propagating regions of the crack, the remote load is increased slowly so that $\dot{a} \ll c_R$. In situations where the crack does not grow in a plane, one must also calculate the direction of growth. Here, we wish to enforce the condition $K_{II}(s) = 0$ over regions of the crack front in the matrix. For this purpose, we compute the kink angle $\omega(s)$ at each point on the crack front from the first-order estimate $\omega(s) = 2K_{II}(s)/K_I(s)$. Provided that the crack is advanced in small steps, we have found that this procedure ensures that $K_{II}(s) \ll K_I(s)$.

In situations where fiber debonding occurs, we have found it more convenient to satisfy the fracture criterion by iteration. Initial, approximate crack profiles are adopted at various stages of growth. The final profiles and remote loads are computed by repeatedly advancing regions of the crack front where the energy release rate exceeds the fracture toughness, and healing regions which have $G > G_c$. This process is continued until the fracture criterion is satisfied within a prescribed tolerance.

2.3. Results

To illustrate the general process of crack trapping by tough fibers in a brittle matrix, we first consider a planar crack as it bypasses tough fibers that are strongly bonded to the matrix. Similar analyses have been described by Fares (1989) and Bower and Ortiz (1991), so our results are presented mainly for comparison.

Suppose that a brittle matrix, fracture toughness K_{IC}^{mat} , is reinforced by a rectangular

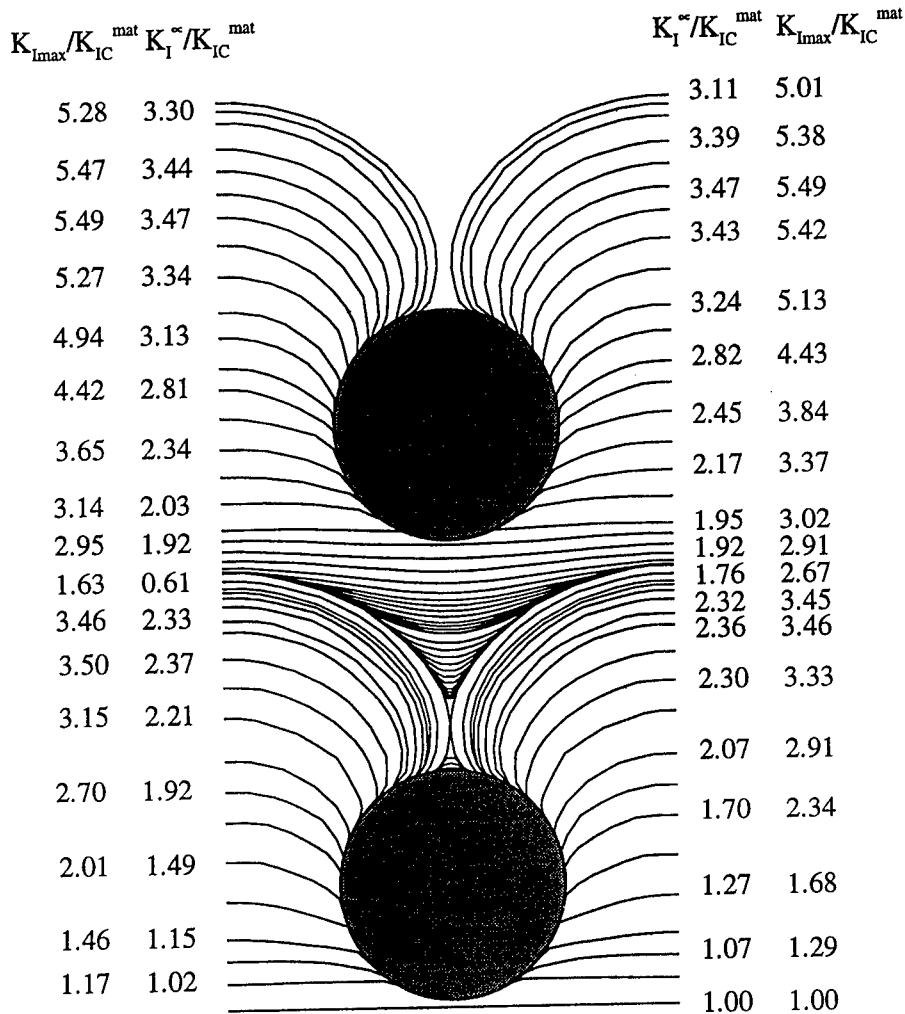


Fig. 2. Profiles of a semi-infinite crack as it bypasses two rows of impenetrable, strongly bonded fibers.

array of circular fibers, with radius R and spacing b . Assume that the toughness of the fibers greatly exceeds that of the matrix, and that the fibers are perfectly bonded to the matrix. We now consider the behavior of a planar, semi-infinite crack as it propagates through the matrix. Figure 2 shows a sequence of profiles of the crack front as it bypasses two successive rows of fibers. Results are shown for a ratio of fiber radius to spacing $R/b = 0.25$. Initially, the crack front is straight. When it meets a row of fibers, parts of the crack arrest: to drive the crack past the fibers, one must increase the remote stress. In Fig. 2, we have shown values of the remote load, parameterized by a remote stress intensity factor $K_I^{\infty}/K_{IC}^{\text{mat}}$, at various stages of crack growth. Also shown is the maximum value of stress intensity factor on the crack front $K_{I_{\max}}/K_{IC}^{\text{mat}}$. Eventually, the crack bows so far past the row of obstacles that parts of

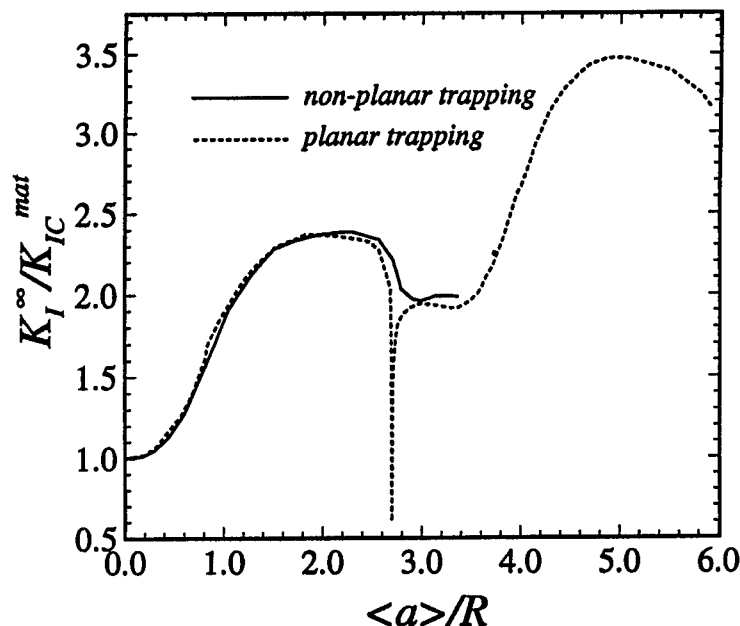


Fig. 3. Variation of remote stress intensity factor with mean distance advanced by the crack, as a crack bypasses two rows of tough fibers.

the crack front are attracted to one another: thereafter, the crack propagates under decreasing remote load, until it reaches and bypasses another row of obstacles.

Figure 3 shows the variation of remote load $K_I^\infty / K_{IC}^{\text{mat}}$ as a function of mean crack advance $\langle a \rangle / R$, where $\langle a \rangle$ is the square root of the area swept by the propagating crack and R is the particle radius. Evidently, the remote stress intensity factor must be increased to 2.4 times the matrix toughness to bypass a single row of fibers. We take this maximum value of K_I^∞ to be the effective toughness of the solid due to trapping, since this is the apparent toughness that one would deduce by measuring the load required to initiate unstable crack growth.

These results confirm earlier computations which predict substantial increases in strength due to crack trapping. Bower and Ortiz (1991) have conducted a detailed parametric study of crack trapping by tough, perfectly bonded fibers. For modest volume fractions of fibers, their numerical results are closely approximated by the expression

$$\frac{G_c^{\text{trap}}}{G_c^{\text{mat}}} = \left(\frac{K_{IC}^{\text{trap}}}{K_{IC}^{\text{mat}}} \right)^2 = 1 - 2 \frac{R}{b} + \left(2.1 + 4.8 \frac{R}{b} \right)^2 \frac{2R}{b} \quad (6)$$

where G_c^{trap} is the maximum remote energy release rate required to bypass a single row of fibers. This expression is valid in the range $0 < R/b < 0.35$.

Experiments conducted by Mower and Argon (1995) have confirmed many of the predicted features of crack trapping. In particular, they have shown that the pre-

dictions of eqn (6) agree with experiment; in addition, the measured profiles of the crack front match the theoretical predictions well. However, the experiments showed a striking feature that has not been predicted theoretically. Figure 2 shows the crack front coalescing with itself on the far side of a row of trapping fibers. Experiments show that this does not occur: instead, the two lobes of the crack front ahead of the fiber bypass one another and overlap.

We have investigated the cause of this phenomenon and its influence on the effective toughness of the solid. For this purpose, we suppose that the initial semi-infinite crack is not perfectly planar, but contains a small periodic geometrical perturbation which may promote non-planar crack growth. In the simulation we present here, assume that the height of the initial crack plane above $z = 0$ is given by

$$z(x, y) = \begin{cases} (x + a_0)\Omega \sin(2\pi y/b), & x \geq -a_0 \\ 0 & x \leq a_0 \end{cases} \quad (7)$$

with $\Omega = 2.5^\circ$ and $a_0 = b/2$. We then calculate the path of the crack as it bypasses a single row of fibers, as before. Figure 4 shows the predicted crack profiles after the

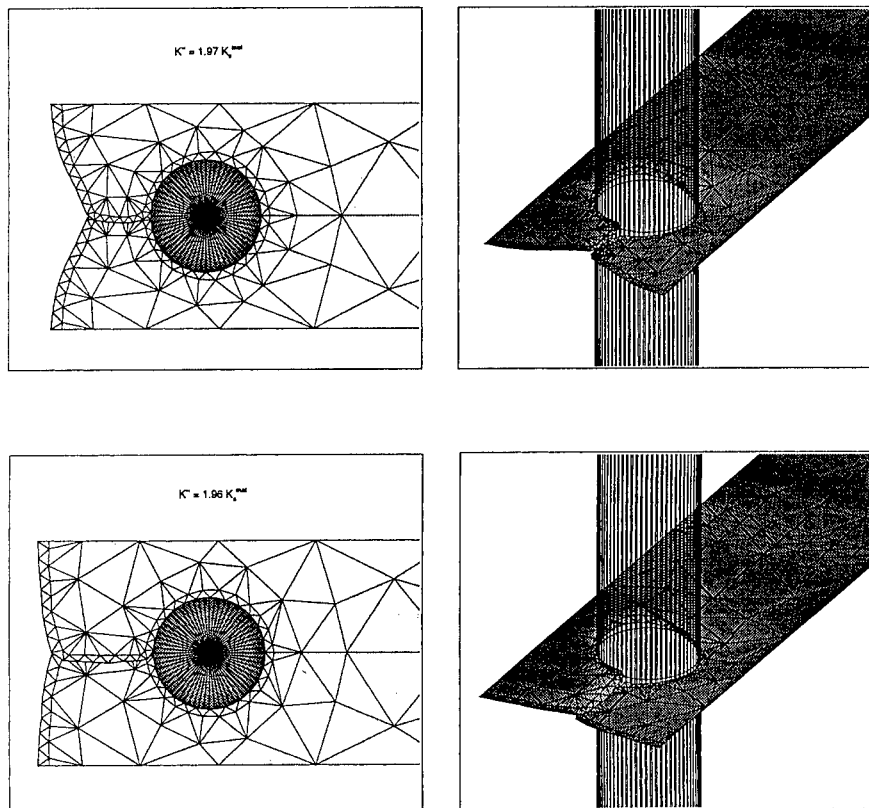


Fig. 4. The profiles of a semi-infinite crack as it asymmetrically bypasses perfectly bonded impenetrable fibers.

crack has bypassed the fibers. The two approaching crack tips avoid one another and overlap, as observed in the experiments. The variation of remote stress intensity factor as the crack grows has been added to Fig. 3. The results are very similar to those obtained for a perfectly planar crack, except that for the planar crack, the load drops precipitously while the crack coalesces with itself; this drop is not observed for the non-planar crack. However, the peak load required to bypass the fibers is not affected, so this phenomenon has no practical significance. Henceforth, we will assume that the initial semi-infinite crack in the solid is perfectly planar.

The simulations shown in Fig. 2 show that the fracture toughness of the fibers must be at least 3.5 times that of the matrix for the crack to bypass the fibers. More generally, Bower and Ortiz (1993) suggest that for bridging particles to form, the fiber toughness should exceed

$$G_c^{\text{fib}}/G_c^{\text{mat}} \geq (2.1 + 4.8R/b)^2 \quad (8)$$

If this is not the case, the semi-infinite crack cuts through the fibers: the maximum possible toughness of the composite is then (Rose, 1975)

$$\frac{G_c^{\text{eff}}}{G_c^{\text{mat}}} = 1 + \frac{2R}{b} \left(\frac{G_c^{\text{fib}}}{G_c^{\text{mat}}} - 1 \right) \quad (9)$$

If the fiber toughness G_c^{fib} is comparable to G_c^{mat} , very little improvement in toughness is observed.

If brittle fibers are to reinforce a brittle solid, the interface between fibers and matrix should have a low fracture toughness. Then, if a semi-infinite crack meets the fibers, it is deflected along the interface, so that bridging fibers may remain intact in the crack wake. He and Hutchinson (1989) have shown that crack deflection will occur if the interface toughness is sufficiently low, $G_c^{\text{int}} < 0.25G_c^{\text{fib}}$. Our objective is to investigate the influence of crack trapping in a composite where this condition is satisfied.

Figure 5 shows a typical sequence of crack profiles as a semi-infinite crack bypasses a single row of fibers. In the simulation shown, the fiber radius $R/b = 0.25$, and the interface toughness $G_c^{\text{int}} = 0.25G_c^{\text{mat}}$. We have also assumed that $G_c^{\text{fib}} \geq G_c^{\text{mat}}$: therefore, the crack deflects up the interface between fibers and matrix. The crack deflection retards the matrix crack, and one must increase the remote load to bypass the fibers. Figure 6 shows the variation of remote load, parameterized by the remote stress intensity factor K_I^∞ , as the crack bypasses the fibers. The angle α shown in Fig. 1 is used to characterize the extent of crack growth. Results are not shown for $\alpha > 120^\circ$, because at this point the crack faces come into contact at some points within the debonded region. Our numerical procedure is not yet able to account for crack face contact and friction. The results shown in Fig. 6 suggest that interfacial debonding considerably reduces the effectiveness of crack trapping. Nevertheless, we find some improvement in toughness due to trapping, even if the interface has a low fracture toughness.

Figure 7 shows the predicted variation of stress intensity factors around the crack front. The debond in the fiber/matrix interface evidently propagates under strongly mixed mode loading. This demonstrates that it is important to characterize the

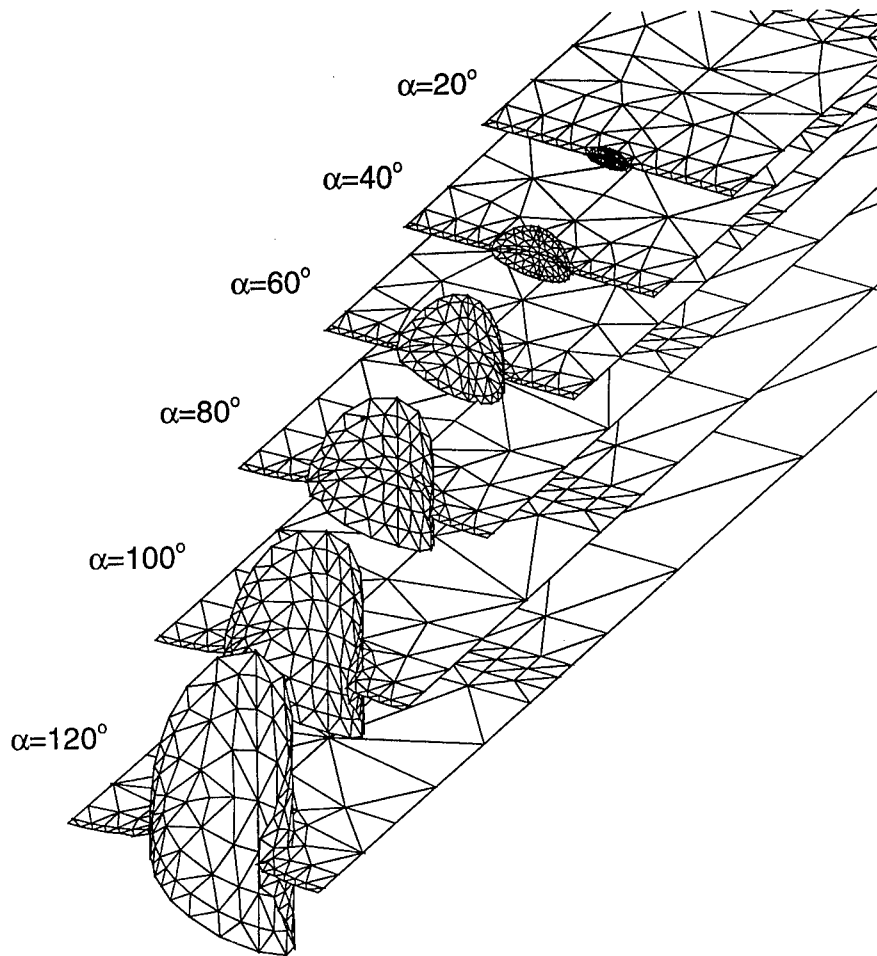


Fig. 5. Profiles of a semi-infinite crack as it bypasses weakly bonded fibers.

mixed mode fracture behavior of interfaces accurately. Several experiments have been conducted to measure the influence of mixed mode I/mode II loading on interfacial fracture (Cao and Evans, 1989; Wang and Suo, 1990; O'Dowd *et al.*, 1992). The effects of mode III loading are not as well understood.

For practical purposes, the influence of interfacial toughness and fiber volume fraction on the effective toughness are of particular interest. We have not been able to calculate the maximum load required to bypass a row of fibers, due to the difficulty in accounting for contact between the crack faces. Instead, we have used as a measure of effective toughness the load required to propagate the crack to a critical configuration, such that the angle $\alpha = 90^\circ$. The results shown in Figs 2 and 5 suggest that, for a weakly bonded interface, this is likely to underestimate the true effective toughness by about 10%; while for a perfectly bonded interface, this procedure would under-

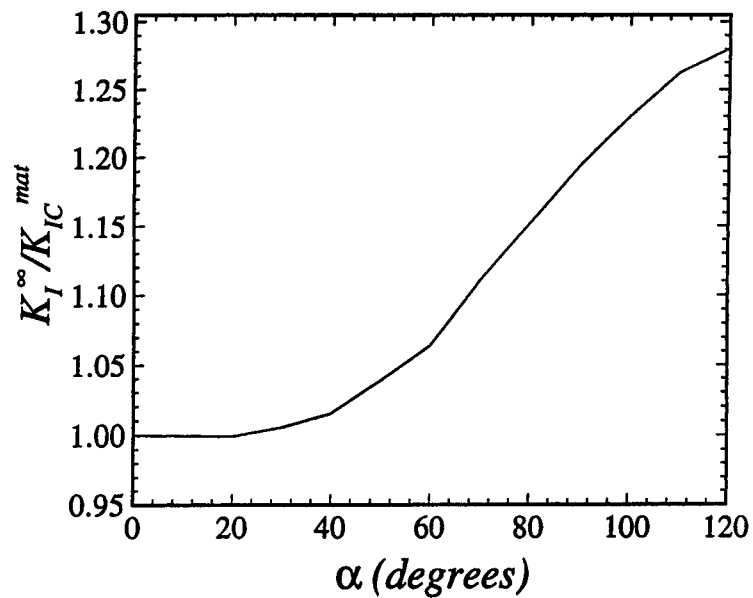


Fig. 6. Variation of remote stress intensity factor with mean distance advanced by the crack, as a crack bypasses a row of weakly bonded fibers.

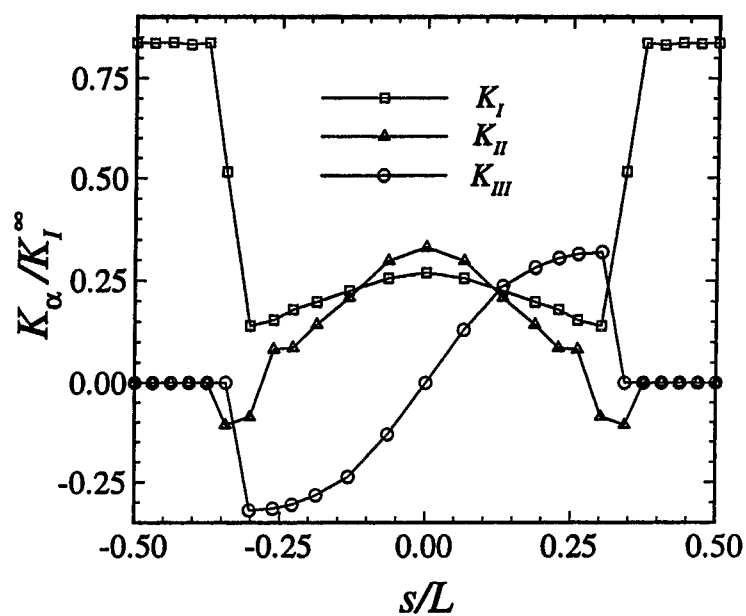


Fig. 7. Variation of stress intensity factors along the crack front shown in Fig. 5.

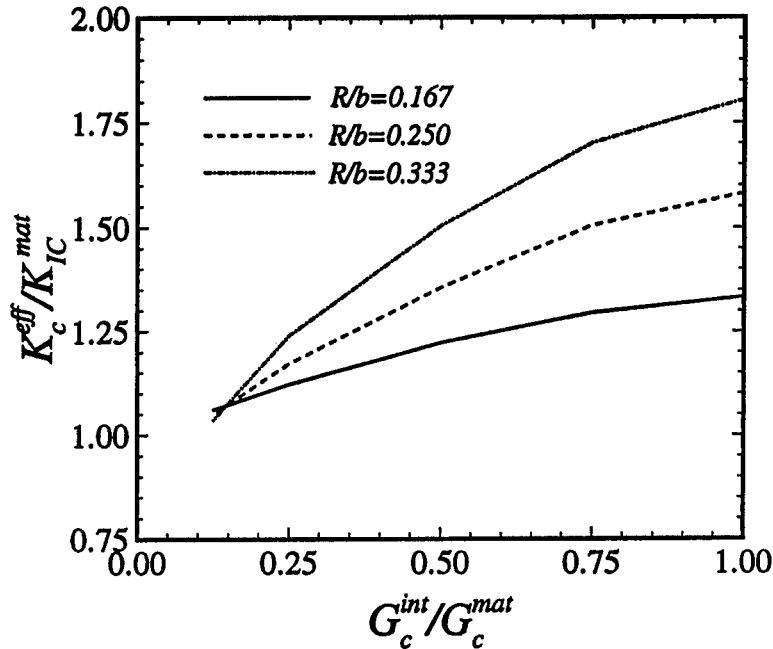


Fig. 8. Variation of effective toughness due to crack trapping.

estimate the toughening by approximately 30%. Nevertheless, it is likely to predict the trends accurately.

Using this procedure, we have plotted the predicted variation of toughness as a function of interface toughness in Fig. 8, for various fiber radii R/b . The strengthening caused by crack trapping increases with the toughness of the interface, and with the volume fraction of fibers. It is important to note that the predictions in Fig. 8 are valid only if the fiber is sufficiently tough for crack deflection to occur: this requires that $G_c^{fib} > 4G_c^{int}$. The toughening due to trapping will continue to increase with G_c^{int} until the interface is strong enough to prevent crack deflection, in which case the toughness may be computed from eqn (6).

3. ANALYSIS OF CRACK BRIDGING

Crack trapping is not the main mechanism of toughening in brittle fiber reinforced composites; the most important effect is frictional bridging in the wake of the crack. The analysis described in the preceding section shows how bridging fibers are formed: the crack repeatedly bypasses rows of fibers, leaving debonded fibers in its wake. Several hundred rows of bridging fibers may form in this way. A three-dimensional analysis of this process would be prohibitively expensive, so we have resorted to a simple two dimensional model to estimate the influence of bridging fibers. Our objective here is to assess the interaction between crack trapping and bridging in a fiber

reinforced composite, rather than to develop a new model of crack bridging. We therefore used results from Charalambides and Evans (1989), Hutchinson and Jensen (1990), and Nair (1990) to estimate the effects of crack bridging.

Following the standard approach, we idealize the bridging zone in the crack wake as a distribution of pressure $p(\delta)$ which acts on the crack faces. The variation of pressure p with crack opening displacement δ is estimated from the force required to pull a single fiber free from the matrix. It is then straightforward to find the toughness due to combined trapping and bridging. As before, we do so by considering the behavior of a semi-infinite crack as it bypasses a single row of fibers. We suppose that there is a fully formed bridging zone in the crack wake, whose length remains constant as the crack grows. Provided that the bridging zone is much longer than the spacing between fibers, the effect of the pressure acting on the crack faces is simply to reduce the energy release rate uniformly over the propagating crack front. One may calculate the reduction in $G(s)$ using the J integral, following the procedure outline by Rose (1987) and Budiansky and Amazigo (1989). The result is

$$\Delta G^{\text{bridg}} = \int_0^\infty p(\delta) d\delta. \quad (10)$$

To fracture the composite, the remote load must be increased until $G(s) = G^{\text{trap}}$, where G^{trap} is the critical energy release rate required to bypass a row of fibers, calculated in the preceding section. Thus, the effective toughness of the composite follows as

$$G_c^{\text{eff}} = G^{\text{trap}} + \Delta G^{\text{bridg}} \quad (11)$$

To find ΔG^{bridg} , one must find the cohesive law $p(\delta)$ which characterizes the bridged zone in the crack wake. For this purpose, we idealize the bridged region as shown in Fig. 9. The matrix is assumed to be reinforced by a volume fraction f of long,

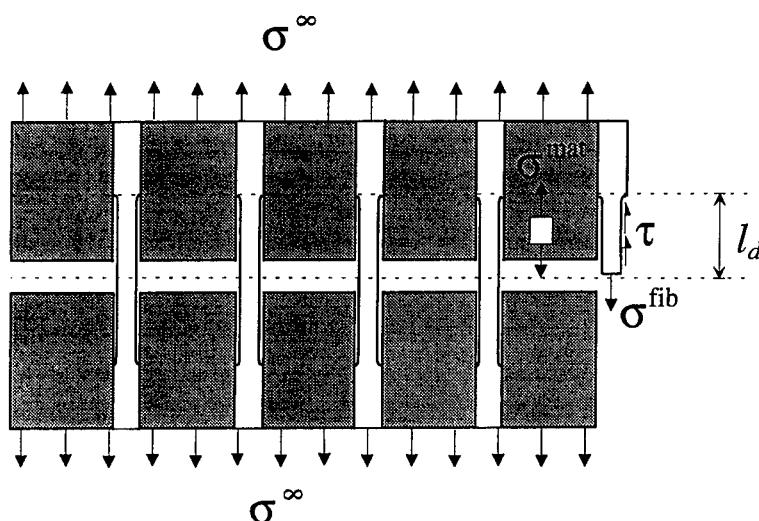


Fig. 9. Idealized model of fibers pulling out in the wake of a crack.

cylindrical fibers with radius R , which are progressively pulled free from the matrix. We suppose that both fibers and matrix have the same Young's modulus E and Poisson's ratio ν , and residual stresses are neglected. The fracture toughness of the interface between fibers and matrix is assumed to be sufficiently low that debonding is initiated while a crack bypasses the fibers, as described in the preceding section. Thereafter, the fibers continue to debond from the matrix due to a cylindrical crack which propagates up the interface. We assume that after debonding, a shear stress τ resists sliding between the fibers and the matrix (any tendency for the fiber to lose contact with the matrix is neglected, for simplicity).

Hutchinson and Jensen (1990) show that under these conditions, the longitudinal stress in the fiber σ_z^{fib} varies linearly in the debonded region of the fibers,

$$\sigma_z^{\text{fib}} = \frac{1}{f} \sigma^\infty - 2\tau \frac{z}{R} \quad (12)$$

where σ^∞ is the stress in both matrix and fibers some distance above the debonded region. This expression is valid for $z < l_d$, where l_d is the length of the debonded region

$$\frac{l_d}{R} = \frac{1-f}{2f} \frac{\sigma^\infty}{\tau} - \left\{ \frac{(1-f)EG_c^{\text{int}}}{(1-\nu^2)R\tau^2} \right\}^{1/2} \quad (13)$$

Evidently, the greatest stress in the fiber (apart from the stress singularity at the tip of the debond) occurs at $z = 0$. We suppose that the fibers continue to pull free from the matrix until the maximum fiber stress reaches a critical value, $\sigma_z^{\text{max}} = \sigma_{\text{fract}}$, whereupon the fibers break at $z = 0$. In practice, experiments show that many fibers fracture at the end of the debonded region, and are subsequently pulled free from the matrix. By assuming all fibers break at $z = 0$, we underestimate the toughness due to bridging.

To find the properties of the cohesive zone $p(\delta)$ required in eqn (10), we imagine the crack faces to be some distance above the debonded region of the fibers. Then, we identify the pressure p acting on the crack faces as $p \equiv \sigma^\infty$. The displacement of the crack faces δ is taken to be the additional relative displacement of material points above and below the debonded region due to fiber debonding. The additional displacement may be deduced by integrating the strain in the fibers

$$\delta = 2 \int_0^{l_d} (\sigma_z^{\text{fib}} - \sigma^\infty) / E \, dz = \frac{(1-f)}{f} \frac{\sigma^\infty}{E} l_d - \frac{\tau}{E} \frac{l_d^2}{R} \quad (14)$$

Substituting for l_d and using $p \equiv \sigma^\infty$, one may write the cohesive law in a simple form

$$\frac{p}{\sigma_{\text{fract}}} = 2 \left\{ \frac{k^2}{\beta^2} + \left(1 - \frac{k^2}{\beta^2} \right) \frac{\delta}{\delta_{\text{fract}}} \right\}^{1/2} \quad \delta < \delta_{\text{fract}}$$

$$\frac{p}{\sigma_{\text{fract}}} = 0 \quad \delta > \delta_{\text{fract}} \quad (15)$$

where δ_{fract} is the crack opening displacement at the point where the fibers break, and k, β are dimensionless constants, defined by

$$\delta_{\text{fract}} = \frac{R(1-f)^2 \sigma_{\text{fract}}^2}{4\tau E} \quad k = \sqrt{\frac{G_c^{\text{int}}}{G_c^{\text{mat}}}} \quad \beta = \frac{\sigma_f}{2} \sqrt{\frac{(1-\nu^2)(1-f)R}{EG_c^{\text{mat}}}} \quad (16)$$

Finally, evaluating the integral in (10), we conclude that

$$\frac{\Delta G_c^{\text{bridg}}}{G_c^{\text{mat}}} = \frac{4f(1-f)}{3(1-\nu^2)} \Lambda \beta^2 \left(1 - \frac{k^3}{\beta^3}\right) \quad (17)$$

where

$$\Lambda = \sigma_{\text{fract}}/\tau \quad (18)$$

Although we have described particularly simple analysis of crack bridging, Nair (1990) has shown that a very similar model predicts accurately many of the features of fracture in fiber reinforced composites. It is well suited for our purpose, to compare the relative importance of trapping and bridging in strengthening a fiber reinforced composite.

4. TOUGHENING DUE TO COMBINED TRAPPING AND BRIDGING

To combine the results of the preceding two sections, it is useful to note that

$$G_c^{\text{trap}}/G_c^{\text{mat}} = 1 + 4.23\sqrt{f(k^2 - 0.15)} \quad (19)$$

gives an adequate fit to the numerical data presented in Fig. 8. In fitting to our numerical results, we have assumed that $R/b \equiv \sqrt{f/\pi}$. Then, the effective toughness of the composite may be expressed as

$$G_c^{\text{eff}}/G_c^{\text{mat}} = 1 + 4.23\sqrt{f(k^2 - 0.15)} + \frac{4f(1-f)}{3(1-\nu^2)} \Lambda \beta^2 \left(1 - \frac{k^3}{\beta^3}\right) \quad (20)$$

Here, the first term represents the effects of trapping, while the second accounts for frictional crack bridging. It should be noted that this expression is valid only for a limited range of its parameters. The expression for the toughness due to trapping is valid only for $0.2 < k < 1$, $0 < f < 0.4$; while the expression of the toughness due to bridging is valid only if the length of the debonded region of the fibers is significantly greater than the fiber radius. This requires

$$\frac{1}{2} \Lambda (1-f) \left(1 - \frac{k}{\beta}\right) > 1$$

Finally, the fracture toughness of the fibers must be sufficiently large that cracks are deflected up the interface: this requires $G_c^{\text{fib}}/G_c^{\text{int}} > 4$.

Typical values for the parameters in our expression at $\Lambda = 60$, $\beta = 0.7$, $f = 0.25$ and $\nu \sim 0.25$ (Nair, 1990). As a representative case, we have plotted the predicted toughness of a fiber reinforced composite as a function of interface toughness par-

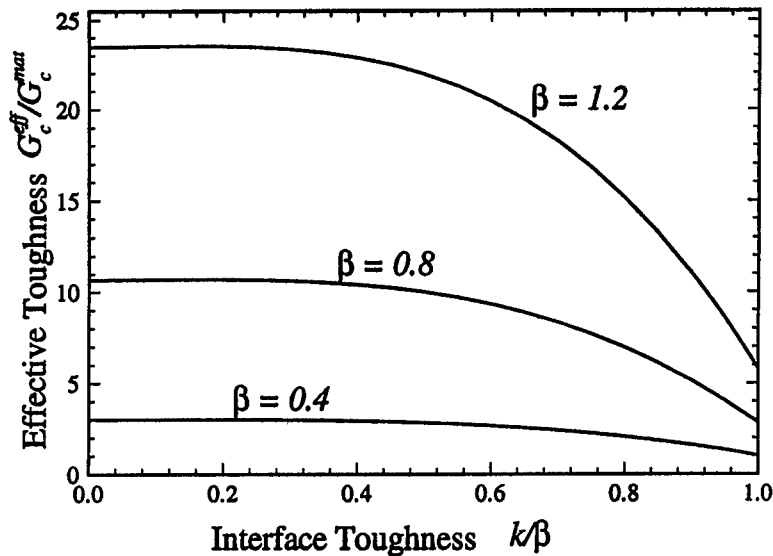


Fig. 10. Effective toughness of a fiber reinforced composite, as a function of interface toughness. $\Lambda = 60$, $\nu = 0.25$, $f = 0.25$.

ameter k/β in Fig. 10, for $\Lambda = 60$, $f = 0.25$. Results are shown for a range of values of the fiber strength parameter β . Under these conditions, the increasing the toughness of the interface between fibers and matrix tends to reduce the strength of the composite. This is because for large values of the parameter Λ , the influence of crack bridging greatly outweighs that of crack trapping.

Crack trapping is more significant if the ratio of fiber strength to interface sliding resistance Λ is small. To illustrate this, we have plotted the effective toughness of the composite as a function of k/β in Fig. 11, for various values of Λ . In each case, we have assumed that $\beta = 0.8$. Evidently, for low values of Λ , it is preferable to exploit the effects of crack trapping by using the largest possible value for interface toughness. For values of $\Lambda > 15$, crack bridging begins to dominate crack trapping, and better performance is achieved by using an interface with a low fracture toughness. The critical value of Λ appears to be insensitive to the value of β .

5. CONCLUSIONS

We have analyzed in detail the influence of crack trapping on the toughness of fiber reinforced composites. Two cases were considered. In the first instance, the fibers were assumed to be much tougher than the matrix, and were assumed to be strongly bonded to the surrounding solid. In this case, we found a substantial increase in toughness due to trapping: as an example, for aligned cylindrical fibers spaced four fiber radii apart, we found $G_c^{\text{trap}}/G_c^{\text{mat}} = 5.6$. Our calculations also showed that the ratio of fiber toughness to that of the matrix must exceed a critical value

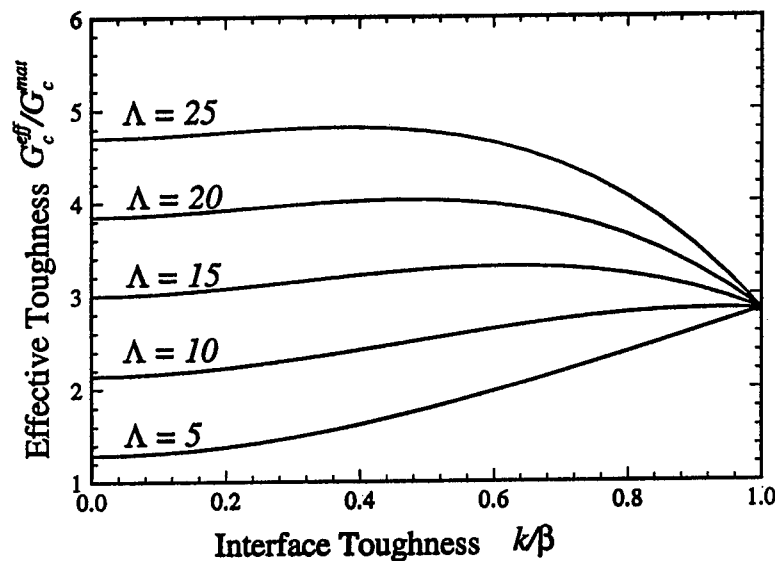


Fig. 11. Effective toughness of a fiber reinforced composite, as a function of interface toughness. $\beta = 0.8$, $\nu = 0.25$, $f = 0.25$.

($G_c^{\text{fib}}/G_c^{\text{mat}} > 12$) for trapping or bridging to be effective. If the fiber toughness is less than this critical value, it is preferable to bond them to the matrix with an interface that has a low fracture toughness, such that $G_c^{\text{int}}/G_c^{\text{fib}} < 4$ (He and Hutchinson, 1989). In this case, the crack is deflected up the interface between fibers and matrix when it meets the fibers. Under these conditions, we found that cracks may still be trapped by the fibers, but the strengthening effect of crack trapping is greatly reduced. Figure 8 summarizes the results. The increase in toughness due to trapping tends to increase with the fracture toughness of the interface. In contrast, it is known that the toughening effects of bridging decrease with interface toughness. We used a simple cohesive zone model of bridging to investigate this trade-off in detail. Our calculations show that if the fibers have a high fracture stress σ_{fract} and the resistance to slip between fibers and matrix τ is small ($\sigma_{\text{fract}}/\tau > 15$), it is preferable to maximize the effects of bridging by using an interface with low fracture toughness. If $\sigma_{\text{fract}}/\tau < 15$, the fibers strengthen the matrix more effectively if the interface toughness is as large as possible, within the constraint $G_c^{\text{int}}/G_c^{\text{fib}} < 4$.

ACKNOWLEDGEMENT

This work was supported by the Materials Research Group on Micromechanics of Failure Resistant Materials at Brown University, which is funded by the National Science Foundation under Grant No. DMR-9223683.

REFERENCES

- Becher, P. F., Hsueh, C.-H., Angelini, P. and Tiegs, T. N. (1988) Toughening behavior in whisker-reinforced ceramic matrix composites. *Journal of the American Ceramic Society* **71**(12), 1050.
- Bower, A. F. and Ortiz, M. (1991) A three-dimensional analysis of crack trapping and bridging by tough particles. *Journal of the Mechanics and Physics of Solids* **39**(6), 815.
- Bower, A. F. and Ortiz, M. (1993) The influence of grain size on the toughness of monolithic ceramics. *Journal of Engineering Materials and Technology* **115**, 228–236.
- Budiansky, B. (1986) *Micromechanics II, Proceedings of the 10th National U.S. Congress of Applied Mechanics*, ed. P. J. Lamb. Austin, Texas.
- Budiansky, B. and Amazigo, J. C. (1989) Toughening by aligned, frictionally constrained fibers. *Journal of the Mechanics and Physics of Solids* **37**(1), 93.
- Budiansky, B., Amazigo, J. C. and Evans, A. G. (1988) Small-scale crack bridging and the fracture toughness of particulate-reinforced ceramics. *Journal of the Mechanics and Physics of Solids* **36**(2), 167.
- Cao, H. C. and Evans, A. G. (1989) *Mechanics of Materials* **7**, 295–305.
- Charalambides, P. G. and Evans, A. G. (1989) Debonding properties of residually stressed brittle-matrix composites. *Journal of the American Ceramic Society* **72**(5), 746–53.
- Evans, A. G., Dalgleish, B. J., He, M. and Hutchinson, J. W. (1989) On crack path selection and the interface fracture energy in bimaterial systems. *Acta Metallurgica* **37**(12), 3249–3254.
- Fares, N. (1989) Crack fronts trapped by arrays of obstacles: numerical solutions based on surface integral representation. *Journal of Applied Mechanics* **56**, 837.
- Freund, L. B. (1990) *Dynamic Fracture Mechanics*. Cambridge University Press.
- He, M. Y. and Hutchinson, J. W. (1989) Kinking of a crack out of an interface. *Journal of Applied Mechanics* **56**, 270.
- Hutchinson, J. W. and Jensen, H. M. (1990) Models of fiber debonding and pullout in brittle composites with friction. *Mechanics of Materials* **9**, 139.
- Hutchinson, J. W. and Suo, Z. (1991) Mixed mode cracking in layered materials. In *Advances in Applied Mechanics*. Academic, New York.
- Kristic, V. D. (1983) On the fracture of brittle matrix/ductile-particle composites. *Philosophical Magazine A* **48**(5), 695.
- Kristic, V. D., Nicholson, P. S. and Hoagland, R. G. (1981) Toughening of glasses by metallic particles. *Journal of the American Ceramic Society* **64**(9), 499.
- Mower, M. T. and Argon, A. S. (1995) Experimental investigations of crack trapping in brittle heterogeneous solids. *Mechanics of Materials* **19**(4), 343.
- Nair, S. V. (1990) Crack-wake debonding and toughness in fiber- or whisker-reinforced brittle-matrix composites. *Journal of the American Ceramic Society* **73**(10), 2839–47.
- O'Dowd, N. P., Stout, M. G. and Shih, C. F. (1992) Fracture toughness of alumina-niobium interfaces: experiment and analysis. *Philosophical Magazine A* **66**(6), 1037–1064.
- Rose, L. R. F. (1975) Toughening due to crack front interaction with a second phase dispersion. *Mechanics of Materials* **6**, 11–15.
- Rose, L. R. F. (1987) Crack reinforcement by distributed springs. *Journal of the Mechanics and Physics of Solids* **35**(4), 383.
- Shih, C. F. (1991) Cracks on bimaterial interfaces: elasticity and plasticity aspects. *Materials Science and Engineering A* **143**, 77.
- Xu, G. and Ortiz, M. (1993) A variational boundary integral method for the analysis of 3-D cracks of arbitrary geometry modeled as continuous distributions of dislocation loops. *International Journal of Numerical Methods in Engineering* **36**, 3675–3701.
- Wang, J. S. and Suo, Z. (1990) Experimental determination of interfacial toughness using brazil nut sandwich. *Acta Metallurgica* **38**, 1279–1290.



Pergamon

J. Mech. Phys. Solids, Vol. 46, No. 10, pp. 1835–1844, 1998

© 1998 Elsevier Science Ltd. All rights reserved

Printed in Great Britain

0022-5096/98 \$—see front matter

PII: S0022-5096(98)00019-2

A SURFACE CHEMICAL POTENTIAL FOR ELASTIC SOLIDS

L. B. FREUND*

Division of Engineering, Brown University, Providence, RI 02912, U.S.A.

(Received 20 December 1997; in revised form 23 January 1998)

ABSTRACT

The surface chemical potential field represents the tendency for an elastic solid to lower its free energy by means of mass rearrangement. In a recent paper in this Journal, Wu [1996, *J. Mech. Phys. Solids* **44**, 2059–2077] pointed out that the commonly used definition of chemical potential for elastic solids is inconsistent with the change in free energy of the system associated with shape change at finite strain. The purpose here is to rederive Wu's main result by a direct rate calculation, rather than a variational approach, which appears to be simpler in implementation. In addition, the definition is generalized to include orientation dependence of surface energy. © 1998 Elsevier Science Ltd. All rights reserved.

Keywords: A. chemo-mechanical processes, A. diffusion, surface, A. surface tension.

INTRODUCTION

The concept of chemical potential enters the description of shape change in elastic solids in the following way. For a mechanical process under isothermal conditions, the total free energy of an elastic solid is the sum of the elastic strain energy and the surface energy. The time required for a perturbed system to reach mechanical equilibrium is typically very small compared to times characteristic of mass rearrangement mechanisms, so the mechanical fields are assumed to be in equilibrium at all times. However, systems can be far from chemical equilibrium, defined as a state of minimum free energy. According to the second law of thermodynamics, a system which is not in chemical equilibrium will tend to reduce its free energy if dissipative mechanisms are available for doing so. In the context of the present discussion, a consequence of activating any such mechanism is to add mass to the surface by condensation, remove mass by evaporation, or rearrange mass by surface diffusion; the possibility of bulk diffusion, which usually occurs much more slowly than surface diffusion, is not considered. The shape of the reference configuration of the body is altered by any of these modes. If there is no exchange of energy between the solid and its surroundings, then the change in free energy for a given change in shape represents the driving force for that shape change. The chemical potential at any point on the surface of the solid is then defined as this driving force per unit mass for addition for an infinitesimal amount of mass at that point. Recently, Wu (1996) has pointed out

* Fax: 001 401 863 2857. E-mail: freund@engin.brown.edu

inconsistencies between the commonly used definition of chemical potential and the actual variation in free energy with change in shape of an elastic solid, and the discussion of this point is continued here.

Gibbs introduced the concept of chemical potential in a two-part article concerned with the chemical equilibrium between a deformable solid in contact with a solution saturated with the same material in dissolved form; the article is reproduced in his *Collected Works* (Gibbs, 1928). During the past four or five decades, the concept has been further developed within the contexts of a range of applications. A few overview articles are cited here, and each includes many relevant references to work on the topic. For example, Herring (1953) was concerned with the processes by which highly compressed powders are converted into solids by curvature-driven mass transport at elevated temperature during sintering. In connection with studies of creep cavitation and rupture of materials in high temperature environments, Rice and Chuang (1981) added stress effects to Herring's curvature effects to broaden the applicability of chemical potential as a surface field driving mass transport. The fundamental interface problems of solidification and heat treatment of crystals, polycrystals and alloys are reviewed by Leo and Sekerke (1989) who focused on the effects of surface stress at finite strain on chemical equilibrium of interfaces. In recent years, the challenges of fabricating high quality material nano-structures, mainly for microelectronic applications, has generated broad interest in the equilibrium, stability and evolution of surfaces and interfaces. Some recent ideas are reviewed from the solid state physics perspective by Nozieres (1992) and from the mechanics of materials perspective by Suo (1997). Each of these sources includes many citations of relevant original work. The very recent contribution of Wu (1996) represents a significant step in resolving some inconsistencies in defining the chemical potential surface field, and Wu's (1996) insightful analysis is reexamined here from a different point of view but with the same general conclusions.

The principal assumptions underlying the development are summarized here:

- (i) Although Wu's (1996) calculation can be applied to three-dimensional deformation fields as well as two-dimensional, he limited consideration to the latter; the same restriction is adopted here for both convenience and clarity of central ideas.
- (ii) The possibility that deformation is finite is admitted and no restrictions are placed on the magnitudes of deformation gradients.
- (iii) As already suggested above, the process is assumed to be isothermal, so that the free energy is the isothermal Helmholtz free energy.
- (iv) No externally applied traction acts on S , the evolving part of the boundary of the solid.
- (v) The conditions of mechanical equilibrium are satisfied by the deformation field at each instant.
- (vi) There is no exchange of energy between the system and its surroundings. This condition can be satisfied, for example, if the fields are spatially periodic and the boundaries of the region considered are chosen to be boundaries on which conditions are periodic. It can also be satisfied if shape changes are spatially localized and fields on remote boundaries are not perturbed by these shape changes.

- (vii) All mass rearrangement is coherent. This condition ensures that no incompatible strains are introduced through mass transport, and that a well-defined stress free reference state always exists.

TOTAL FREE ENERGY

A portion of an elastic solid is shown in Fig. 1 in its natural reference configuration. For plane deformation, the material occupies the area R . The portion of the bounding surface with the potential for shape change is S . The remainder of the boundary (shown dashed) represents workless constraints. Material points are located in R with respect to a fixed rectangular basis \mathbf{e}_k by coordinates p_k . Arc length s along S is measured from some arbitrary origin. Local surface orientation is represented by a tangent unit vector \mathbf{m}_i in the direction of increasing s and by a corresponding outward normal unit vector \mathbf{n}_i . It is also useful to represent local surface orientation at any time t by means of the angle $\theta(s) = \sin^{-1}[\mathbf{e}_3 \cdot (\mathbf{e}_1 \times \mathbf{m})]$. In terms of this angle, the surface curvature is

$$\kappa(s) = \frac{\partial \theta}{\partial s} \quad (1)$$

at any time t .

The configuration shown in Fig. 1 is mapped into the current configuration at any time t by the continuous deformation

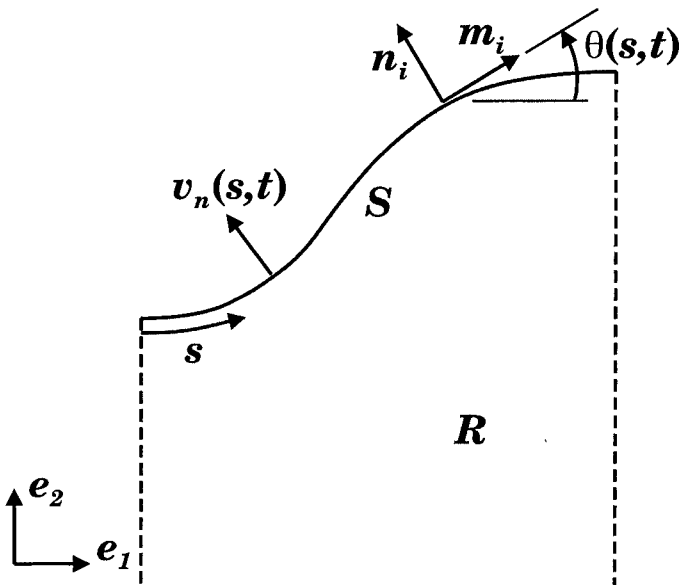


Fig. 1. Schematic diagram of a deformable body in its natural reference configuration, including a portion S of the surface which involves by mass transfer. The constraints acting on R are assumed to be workless.

$$x_k = \chi_k(p_1, p_2) \quad (2)$$

The deformation gradient throughout R is

$$F_{ij} = \frac{\partial \chi_i}{\partial p_j} \quad (3)$$

The deformation of the surface S associated with this bulk deformation is of particular interest. This is conveniently represented by the surface deformation gradient which is obtained from F_{ij} by restricting its domain to include only material line elements in the surface; its range is still the full two dimensional plane. In other words, the surface deformation gradient is the 2×1 tensor which carries line elements lying in S into vectors representing the length and orientation of the material elements in the current configuration, that is,

$$\tilde{F}_i = F_{ij} m_j \quad (4)$$

where F_{ij} in this expression is understood to be the limiting value of the deformation gradient on S upon approach from within R . Some special surface deformation tensors have been adopted in the past which have the convenient property of preserving the role as a transformation of three-dimensional vectors into three-dimensional vectors, in general (cf Leo and Sekerke, 1989). However, the calculation of rates of change of these tensors requires special attention so these tensors are not adopted here.

The change in shape of the reference configuration is specified by prescribing the normal velocity $v_n(s)$ along S . It is emphasized that v_n has no connection to deformation; it is due solely to local addition ($v_n > 0$) or removal ($v_n < 0$) of material from the surface. It is this feature that makes it preferable to describe the process in terms of the reference configuration rather than the current configuration. Chemical potential is defined as energy change per unit mass added and, in the reference configuration, the rate of material volume addition represented by v_n is equivalent to the rate of material mass added for a homogeneous material. This is a matter of convenience rather than necessity.

The bulk material in R is characterized by the strain energy function $U(F_{ij})$. The nominal stress in R is then

$$N_{ij} = \frac{\partial U}{\partial F_{ij}} \quad \text{in } R \quad (5)$$

and the condition of equilibrium requires that

$$N_{ij,j} = 0 \quad \text{in } R \quad (6)$$

The limiting traction on S from within R is denoted by T_i , so that

$$T_i = N_{ij} n_j \quad \text{on } S \quad (7)$$

The behavior of the two-dimensional surface material (which is one dimensional for plane strain deformation) is characterized by the surface energy $\tilde{U}(\tilde{F}_i, \theta)$. The first argument \tilde{F}_i reflects dependence of surface energy on deformation and the second argument θ reflects dependence on local orientation. The surface tension $\tilde{\Sigma}_i$ is represented through the constitutive property that

$$\tilde{\Sigma}_i = \frac{\partial \tilde{U}}{\partial \tilde{F}_i} \quad \text{on } S \quad (8)$$

The magnitude of $\tilde{\Sigma}_i$ is the surface tension in the current configuration (which is the same as the magnitude in the reference configuration because the length of surface material lines in the \mathbf{e}_3 direction are not affected by deformation) and the direction is the tangent line in the current configuration. Equilibrium of the surface requires that

$$\frac{\partial \tilde{\Sigma}_i}{\partial s} = N_{ij} n_j \quad \text{on } S \quad (9)$$

With the assumptions adopted and the definitions established, the total free energy of the system at any instant of time is

$$\mathcal{E}(t) = \int_R U(F_{ij}) dR + \int_S \tilde{U}(\tilde{F}_i, \theta) dS \quad (10)$$

The task is now to evaluate the rate of change of \mathcal{E} , denoted by $\dot{\mathcal{E}}$, and to cast the result into the form

$$\dot{\mathcal{E}} = \int_S \Phi (\text{deformation shape}) v_n dS \quad (11)$$

At any point s along the surface, the factor $v_n dS$ is essentially the rate of addition of material volume. It follows that the quantity Φ can be identified as the chemical potential field over S .

THE CHEMICAL POTENTIAL FIELD ON S

The free energy \mathcal{E} can change with shape for a number of reasons:

- (i) change in strain energy due to change in deformation in R
- (ii) change in strain energy due to addition/removal of deformed material
- (iii) change in surface energy due to change in deformation of surface
- (iv) change in surface energy due to change in orientation of surface
- (v) change in surface energy due to increase/reduction in amount of surface

The effects are evident in a direct evaluation of $\dot{\mathcal{E}}$. As tacitly implied in (11), a dot superimposed on a function of time denotes its derivative. In the expressions to follow, a superposed dot on any field depending on both t and p_k denotes the derivative with respect to time of that field at fixed p_k ; the operator d/dt is reserved to represent the total time derivative of such fields at a point convecting with the surface at speed v_n as it moves with respect to the material.

Application of the definition of a derivative to (10) yields

$$\dot{\mathcal{E}} = \int_R \frac{\partial U}{\partial F_{ij}} \dot{F}_{ij} dR + \int_S U v_n dS + \int_S \left[\frac{\partial \tilde{U}}{\partial \tilde{F}_i} \frac{d\tilde{F}_i}{dt} + \frac{\partial \tilde{U}}{\partial \theta} \dot{\theta} - \tilde{U} v_n \kappa \right] dS \quad (12)$$

The first, second and last terms on the right side correspond to items (i), (ii) and (v) above. By recalling the definition of the surface deformation gradient, the total time derivative appearing in (12) can be decomposed into

$$\frac{d\tilde{F}_i}{dt} = \left(\dot{F}_{ij} + v_n \frac{\partial F_{ij}}{\partial p_k} n_k \right) m_j + F_{ij} \dot{m}_j \quad (13)$$

The second term in (13) must be included because the point at which F_{ij} is to be evaluated in computing $d\tilde{F}_i/dt$ moves with respect to the material as time goes on. The rate of change of the tangent vector is

$$\dot{m}_i = \dot{\theta} n_i = \frac{\partial v_n}{\partial s} n_i \quad (14)$$

Similarly, the term involving rate of deformation evaluated on S is

$$\dot{F}_{ij} m_j = \dot{\chi}_{i,j} m_j = \frac{\partial \dot{\chi}_i}{\partial s} \quad (15)$$

If the right most forms in (14) and (15) are substituted into (13) and the rule for differentiation of a product is applied, then

$$\begin{aligned} \dot{\mathcal{E}} = & \int_R N_{ij} \dot{F}_{ij} dR + \int_S U v_n dS \\ & + \int_S \left[\tilde{\Sigma}_i \left(\dot{F}_{ij} m_j + v_n \frac{\partial F_{ij}}{\partial n} m_j + \frac{\partial v_n}{\partial s} F_{ij} n_j \right) + \frac{\partial \tilde{U}}{\partial \theta} \frac{\partial v_n}{\partial s} - \tilde{U} v_n \kappa \right] v_n dS \end{aligned} \quad (16)$$

where $\partial \tilde{F}_i / \partial n$ at any point on S is interpreted as the double inner product of the limiting boundary value of $\partial F_{ij} / \partial p_k$ with $m_j n_k$ at that point. If the divergence theorem is applied to the first term on the right side, the equilibrium equations are enforced, and the condition of workless boundary constraints is recalled, then (16) reduces to the form (11) with

$$\Phi(F_{ij}, \theta) = U + \tilde{\Sigma}_i \frac{\partial \tilde{F}_i}{\partial p_k} n_k - \frac{\partial}{\partial s} (\tilde{\Sigma}_i F_{ij} n_j) - \frac{\partial \tilde{\Sigma}_i}{\partial \theta} \frac{\partial \tilde{F}_i}{\partial s} - \kappa \left(\tilde{U} + \frac{\partial^2 \tilde{U}}{\partial \theta^2} \right) \quad (17)$$

as the chemical potential field. For isotropic surface energy, $\partial/\partial\theta \equiv 0$ and this result agrees with the result given in eqn (3.19) of Wu's article.

SOME INTERPRETATIONS AND OBSERVATIONS

While the interpretations of some terms in Φ are self-evident, this is not so for all. To gain further insight into the result, consider a portion of the boundary S in the

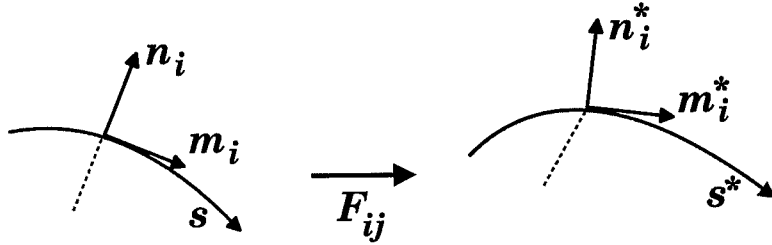


Fig. 2. A portion of the evolving free surface S in the reference configuration (left) and the current configuration (right); the configurations are related through the deformation gradient F_{ij} .

reference configuration and in the current configuration, as depicted in Fig. 2. Suppose that a material element on S aligned with m_i in the reference configuration has a stretch ratio $\lambda_{(m)}$; this element is aligned with the tangent unit vector m_i^* in the current configuration. Then

$$F_{ij}m_j = \lambda_{(m)}m_i^* \quad (18)$$

If s^* is arc length along the deformed surface in the current configuration then, for any surface field,

$$\frac{d}{ds} = \lambda_{(m)} \frac{d}{ds^*} \quad (19)$$

The unit vectors tangent to and normal to the surface in either configuration are related through the corresponding surface curvatures according to the differential relations

$$\frac{dm_i}{ds} = \kappa n_i, \quad \frac{dm_i^*}{ds^*} = \kappa^* n_i^* \quad (20)$$

where κ^* is the curvature of the surface in the current configuration. Denote the stretch ratio of a material element at the surface S , but aligned with the surface normal n_i in the reference configuration, by $\lambda_{(n)}$. Then it is noted that

$$F_{ij}n_j = \lambda_{(n)}v_i^* \neq \lambda_{(n)}n_i^* \quad (21)$$

where $v_i^*v_i^* = 1$, if there is any shear deformation between the normal and tangential directions. In general, this shear strain is given by the inner product

$$\lambda_{(m)}\lambda_{(n)}\cos\left(\frac{\pi}{2} - \gamma_{(mn)}\right) = F_{ik}m_k F_{ij}n_j \quad (22)$$

where $\gamma_{(mn)}$ is the decrease in angle between line elements aligned with m_i and n_i in the reference configuration as they are deformed into the current configuration. The connection between κ and κ^* can be established by forming the inner product of the terms shown as equal in (21) with m_i^* , and then differentiating with respect to arclength s . The result is

$$\kappa^* n_i^* v_i^* = \frac{1}{\lambda_{(n)}} \left\{ \kappa - \frac{1}{\lambda_{(m)}} n_k \frac{\partial \lambda_{(m)}}{\partial p_k} + \frac{1}{\lambda_{(m)}} m_k \frac{\partial}{\partial p_k} (m_i^* v_i^* \lambda_{(n)}) \right\} \quad (23)$$

Finally, if τ is the surface tension at a point on the surface in the deformed configuration then

$$\tilde{\Sigma}_i = \tau m_i^* \quad (24)$$

With these relationships and definitions in hand, it is clear that the second term in the definition of Φ can be reduced as

$$\tilde{\Sigma}_i \frac{\partial \tilde{F}_i}{\partial p_k} n_k = \tau m_i^* m_i^* \frac{\partial \lambda_{(m)}}{\partial n} = \tau \frac{\partial \lambda_{(m)}}{\partial n} \quad (25)$$

Strictly, the right side of this expression does not exist because $\lambda_{(m)}$ is defined only on the surface, whereas calculation of the normal derivative requires that it also be defined for points interior to R adjacent to S . This poses no difficulty, however. The stretch ratio of every material element in R is known through F_{ij} . To compute $\partial \lambda_{(m)} / \partial n$ at some point on S with tangent m_i , note that the stretch ratios of all material lines parallel to m_i along a line extending from the point of interest into R are known. Thus, this normal derivative can be calculated unambiguously.

The third term in (17) can also be reduced to the form

$$\frac{\partial}{\partial S} (\tilde{\Sigma}_i F_{ij} n_j) = \lambda_{(m)} \frac{\partial}{\partial S^*} (\tau F_{ik} m_k F_{ij} n_j) = \lambda_{(m)} \frac{\partial}{\partial S^*} \left[\tau \lambda_{(m)} \lambda_{(n)} \cos \left(\frac{\pi}{2} - \gamma_{(mn)} \right) \right] \quad (26)$$

The surface equilibrium equation (9) can also be written in a more interpretable form by applying the definitions and conventions introduced in this section. If the Cauchy stress in the current configuration is σ_{ij} , then $N_{ij} n_j = \lambda_{(m)} \sigma_{ij} n_j^*$ and the surface equilibrium equation becomes

$$\frac{\partial \tilde{\Sigma}}{\partial S} = \lambda_{(m)} \frac{\partial (\tau m_i^*)}{\partial S^*} = \lambda_{(m)} \left(\frac{\partial \tau}{\partial S^*} m_i^* + \tau \kappa^* n_i^* \right) = \lambda_{(m)} \sigma_{ij} n_j^* \quad (27)$$

If the term-by-term inner product of this equation with n_i^* is formed then the local form of the classical Laplace relationship involving surface tension, surface curvature, and internal pressure results, namely,

$$\tau \kappa^* = n_i^* \sigma_{ij} n_j^* \quad (28)$$

On the other hand, if the term-by-term inner product with m_i^* is formed then it follows that the tangential surface traction acting on the boundary of R is equal to the surface gradient of surface tension, that is,

$$\frac{\partial \tau}{\partial S^*} = m_i^* \sigma_{ij} n_j^* \quad (29)$$

It follows that the limiting tangential surface traction on the boundary of R is zero only when τ is a constant, say τ_0 , along the deformed surface. This is the case if

$$\tilde{U} = \tau_0 \sqrt{\tilde{F}_i \tilde{F}_i} = \tau_0 \lambda_{(m)} \quad (30)$$

which implies that $\partial\tilde{U}/\partial\theta = 0$. In this case, $\gamma_{(nm)}$ is also zero point-wise along the deformed surface.

The conceptual structure of this development, as introduced by Wu (1996) and as slightly extended here, can be carried over to three space dimensions and time without modification. However, the details of the calculation are more complex. In the case of two space dimensions, the advantages of using arc length as the independent variable for surface fields is fairly obvious. In general, the intrinsic surface geometry in three-dimensions is non-Riemannian, intrinsic surface coordinates may not have length dimensions, and the two-point tensor fields representing deformation of surface elements are more difficult to interpret.

The new features of chemical potential for elastic solids introduced by Wu, as well as those having to do with surface energy anisotropy introduced here, require further investigation to make their significance for surface diffusion and other mass transport phenomena clearer. It would seem that two paths would be pursued simultaneously in an effort to advance understanding of such phenomena. First, the relative contributions of the various terms in (17) to the value of chemical potential or chemical potential gradient must be understood for a range of processes. Are there any situations for which the additional features make a significant difference? Also, it must be recognized that the present level of development includes everything that local continuum mechanics has to offer. However, it should not be forgotten that the physical phenomena which motivate such developments arise from the discrete nature of real materials, and this gives rise to the second question. Are the mechanical features which emerge from such developments actually representative, in some average sense, of the behavior of surfaces of real materials?

ACKNOWLEDGEMENT

This work was supported in part by the Office of Naval Research under Contract N00014-95-1-0239, and in part by the MRSEC Program of the National Science Foundation under Award DMR-9632524. This support is gratefully acknowledged.

REFERENCES

- Gibbs, J. W. (1928) On the equilibrium of heterogeneous solids. In *The Collected Works of J. Willard Gibbs. Volume I, Thermodynamics*, pp. 55–373. Longmans, Green and Co., New York.
- Herring, C. (1953) The use of classical macroscopic concepts in surface energy problems. In *Structure and Properties of Solid Surfaces*, ed. R. Gomer and C. S. Smith, pp. 5–72. University of Chicago Press, Chicago.
- Leo, P. and Sekerka, R. F. (1989) The effect of surface stress on crystal–melt and crystal–crystal equilibrium. *Acta Metallurgica* **37**, 3119–3138.
- Nozieres, P. (1992) Shape and growth of crystals. In *Solids Far From Equilibrium*, ed. C. Godrech, pp. 1–54. Cambridge University Press, Cambridge.

- Rice, J. R. and Chuang, T. J. (1981) Energy variations in diffusive cavity growth. *J. Amer. Ceram. Soc.* **64**, 46–53.
- Suo, Z. (1997) Motions of microscopic surfaces in materials. In *Advances in Applied Mechanics*, ed. J. W. Hutchinson and T. Y. Wu, Vol. 33, pp. 193–293. Academic Press, San Diego.
- Wu, C. H. (1996) The chemical potential for stress-driven surface diffusion. *Journal of the Mechanics and Physics of Solids* **44**, 2059–2077.



Pergamon

J. Mech. Phys. Solids, Vol. 46, No. 10, pp. 1845–1867, 1998

© 1998 Elsevier Science Ltd. All rights reserved

Printed in Great Britain

0022-5096/98 \$—see front matter

PII: S0022-5096(98)00057-X

A NON-LOCAL FORMULATION OF THE PEIERLS DISLOCATION MODEL

RON MILLER,^a ROB PHILLIPS,^{*a} GLEN BELTZ^b and MICHAEL ORTIZ^c

^a Division of Engineering, Brown University, Providence, RI 02912, U.S.A. ^b Department of Mechanical and Environmental Engineering, University of California Santa Barbara, Santa Barbara, CA 93106-5070, U.S.A. ^c Graduate Aeronautical Laboratories, California Institute of Technology, Pasadena, CA 91125, U.S.A.

(Received 20 December 1997; in revised form 16 March 1998)

ABSTRACT

Cohesive zone models provide an illuminating and tractable way to include constitutive non-linearity into continuum models of defects. Powerful insights have been gained by studying both dislocations and cracks using such analyses. Recent work has shown that as a result of the locality assumption present in such cohesive zone models, significant errors can be made in the treatment of defect energies. This paper aims to construct a non-local version of the Peierls–Nabarro model in which the atomic level stresses induced at the slip plane depend in a non-local way on the slip degrees of freedom. Our results should be seen as a demonstration in principle of how microscopic calculations can be used to construct insights into constitutive nonlocality. The non-local interplanar kernel used here is computed directly from atomistics and is used to evaluate both the structure and energetics of planar dislocations. The non-local formulation does not significantly change the dislocation core structure from that obtained with the local model, but the new formulation leads to significant improvements in the description of dislocation energetics for dislocations with planar cores. © 1998 Elsevier Science Ltd. All rights reserved.

1. INTRODUCTION

The appropriate method to use in modeling the behavior of a material is often dictated by some intrinsic length scale in the problem. When considering atomic scale defects, atomistic models are often required. On the other hand, macroscopic models are concerned with bulk properties of specimens with dimensions on the micron scale or larger. In this regime, the assumptions of continuum mechanics are justified. Recently, there has been increased interest in modeling the so-called mesoscale regime, the range of length scales that are often too large for fully atomistic models but too small for discrete lattice effects to be ignored. In this regime, neither atomistic modeling nor continuum mechanics is entirely satisfactory, and new models which incorporate features from both approaches seem to be necessary.

One class of model which serves as a bridge between the microscopic and macroscopic approaches is that of cohesive zone models. Using a cohesive zone model allows bulk regions to be handled using conventional continuum mechanics, while

* To whom correspondence should be addressed. Fax: 001 401 863 1157. E-mail: phillips@alpha1.engin.brown.edu

atomistic effects are incorporated only at certain interfaces where it is deemed that they are important. Models of this type were first proposed by Peierls (1940) to describe dislocations, by Barenblatt (1962) to model fracture processes and by Dugdale (1959), and Bilby *et al.* (1962) to estimate plastic zone sizes ahead of cracks. A review of a number of examples of this approach may be found in Miller and Phillips (1996b), while this paper focuses on the specific example of the Peierls dislocation.

The Peierls dislocation model has received renewed interest of late, being used, for example, by Rice (1992) in his description of the brittle vs ductile behavior of crystals. The attractiveness of the Peierls framework is that it offers an analytically tractable (or at least numerically expedient) continuum model which incorporates nonlinear features resulting from the presence of the discrete lattice. The model assumes that the atomistic features of a dislocation are confined to a single atomic plane referred to as the slip plane. It is only at the slip plane that discontinuities in the displacement fields are assumed to take place, and a special constitutive law is used to account for them. Away from the slip plane, the remainder of the bulk crystal is treated as a linear elastic medium. In conventional treatments, the constitutive law at the slip plane is simplified by assuming that the energy and stress depend only locally on the slip distribution, despite the non-local nature of atomic interactions. In effect, while the Peierls model does incorporate a periodic length into the local relation between stress and slip, it does not define a length scale below which the non-local effects due to slip gradients become important.

In earlier work (Miller and Phillips, 1996b) it has been demonstrated that the various approximations inherent in the Peierls model can lead to serious error in the energetic description of a dislocation. One important source of error arises from the failure to incorporate non-local effects, since full atomistic calculations show that the gradients in the slip distribution that are present in realistic dislocation cores are often too large for non-local effects to be ignored. By postulating a new form for the energy of a slip distribution, we formulate a model which includes a non-local term while at the same time reduces to the original Peierls model in the limit where slip gradients become small. This new model includes non-locality in a simple way, allowing for an investigation of non-local effects alone. We do not consider the other sources of error in the Peierls model, as these have been addressed elsewhere (see, for example, Miller and Phillips, 1996b; Bulatov and Kaxiras, 1997).

Many examples exist where a certain model, derived under specific assumptions, is pushed to the extremes of its range of applicability and as a result must be corrected through inclusion of higher order terms. Anharmonic models of lattice vibrations (Duesbery *et al.*, 1973; DiVincenzo, 1986), recent work on gradient models (Fleck *et al.*, 1994; Aifantis, 1992), and several papers on non-local continuum theories (Eringen *et al.*, 1977; Eringen and Balta, 1979; Eringen, 1987) are but a few examples of this strategy. Similar extensions are made here in the context of the Peierls framework. Due to the inclusion of a new term in the expression for the energy of a slip distribution, the model is now able to capture non-local effects due to the presence of gradients in the slip distribution. This improvement is demonstrated via comparisons to fully atomistic calculations of slip plane energies, and is then used to model dislocation core structures. This work is undertaken not so much in the name of improving the Peierls–Nabarro model itself as to examine the interplay between

atomic level nonlocality and plausible constitutive models of extended defects in solids. The artificial confinement of the entirety of the constitutive complexity to a single plane reduces the computational difficulties substantially, while still allowing for substantive insights to be gained. Ultimately, for the treatment of generic dislocations, we advocate a less conservative approach in which constitutive nonlocality and nonlinearity are not restricted to any particular plane (see, for example, Tadmor *et al.*, 1996).

In Section 2 we begin with a brief description of the original Peierls framework and its breakdown in the limit of rapidly varying slip distributions. In Section 3, we present the details of our non-local formulation and describe how atomistic calculations are used to build the necessary non-local constitutive model. We then use the non-local Peierls model to compute the energetics of crystalline slip, and show that the non-local model is in better agreement with purely atomistic results than was the classical Peierls framework. Finally, in Section 4, the non-local model is used to obtain the core structure of a (100)[011] dislocation in fcc Al.

2. BREAKDOWN OF THE TRADITIONAL PEIERLS FRAMEWORK

In this section, we present a brief explanation of the Peierls model, but focus mainly on describing the breakdown of the local cohesive zone assumptions. For a complete description of the Peierls model, see Hirth and Lothe (1992).

The Peierls model assumes that a dislocation can be described as two elastic half-spaces joined at a common plane on which there is a discontinuous jump in the displacement fields. We adopt the convention that the slip plane is the x - y plane, with the dislocation line along the y -axis. The discontinuity in displacements due to the presence of the dislocation is referred to as the slip distribution, $\delta(x, y) = \mathbf{u}^+(x, y) - \mathbf{u}^-(x, y)$, where $\mathbf{u}^\pm(x, y)$ are the displacement fields just above and below the slip plane. We confine our discussion to the simple case of plane strain in the x - z plane, and to the situation where only one component of δ is non-zero. This allows us to write δ as a scalar, $\delta(x)$. Dealing with the more general case is a straightforward extension of the results presented below, while the simple case being discussed here is better suited to demonstrate our arguments. It is important to bear in mind that $\delta(x)$ is not constant as in rigid slip, nor is it a simple step function as in the Volterra model of a dislocation. Rather, the slip distribution varies from zero at a point on the slip plane far from the dislocation core to a full Burgers vector once the core is traversed. The slip distribution is assumed to lead to atomic level forces due to the interaction between the slipped surfaces, thus providing the tractions, $\tau(x)$, on the elastic regions. These tractions take a simple form that depends only on the local slip discontinuity

$$\tau(x) = \tau[\delta(x)], \quad (1)$$

and can be determined on the basis of atomistic calculations. Early work within the Peierls framework assumed a simple periodic form for eqn (1), with the periodicity tied to the Burgers vector (see, for example, Foreman *et al.*, 1951). More recently, highly accurate atomistic calculations have allowed for the direct calculation of $\tau(\delta)$,

improving the agreement between models built upon the Peierls framework and the results of direct atomistic simulation (see, for example, Sun *et al.*, 1993).

For the purposes of this paper, we find it more convenient to consider dislocation energetics rather than the resulting forces and tractions. According to the Peierls models, the energy of a dislocation is made up of two parts—the elastic energy contained in bulk regions and the misfit energy associated with the slip plane. The first component, the elastic energy, is fully defined once the elastic constitutive law for the bulk regions is specified, while the misfit energy is computed as an integral over the slip plane. While this is generally a surface integral, for the simplified geometry of a straight dislocation oriented along the y -axis, the integral reduces to

$$E_L = \int_{-\infty}^{\infty} \Phi[\delta(x)] dx, \quad (2)$$

where E_L is understood to be the local misfit energy per unit length along the dislocation line. This convention will be maintained throughout the paper. In eqn (2), $\Phi(\delta)$ is given by

$$\Phi(\delta) = \int_0^{\delta} \tau(\delta') d\delta'. \quad (3)$$

$\Phi(\delta)$ is referred to as the interplanar slip potential, and can be thought of as the energy cost associated with slipping one block of atoms over another by an amount δ . As with the tractions $\tau(\delta)$, the interplanar slip potential can also be obtained through simple atomistic calculations (see, for example, Sun *et al.*, 1993; Kaxiras and Duesbery, 1993).

The energetic description provided above introduces an important assumption that has been central to the Peierls framework and results in a formulation that is strictly local. Specifically, this assumption arises from the fact that the interplanar potential is computed on the basis of a purely uniform slip distribution, even though the actual slip distributions of interest are non-uniform. The energy of the non-uniform slip distribution is found using eqn (2), which effectively divides the slip distribution into infinitesimal slip steps, samples the interplanar potential for each of these steps, and sums the results. The tacit assumption of this approach is that despite the non-uniform nature of the slip distribution, the local environment at each point can be considered to be approximately uniform, allowing for the local slip energy to be determined from the interplanar slip potential. It is expected that as long as the gradients in the slip distribution are small, this approximation will be valid, but as the gradients become more severe, the approximation will break down. One result of interest is to quantify what the maximum acceptable gradients are, and to determine whether or not the slip gradients occurring in real dislocation core structures exceed these values.

These questions about the validity of the assumptions in eqn (2) were addressed by Miller and Phillips (1996b). The breakdown of the local assumptions was quantified by computing the energy of a number of idealized slip distributions in two ways, first using atomistics (considered “exact” in this context) and then using the approximation embodied in eqn (2). The parameters in the slip distribution were then selectively varied, allowing for control of the severity of the slip gradients and a direct comparison

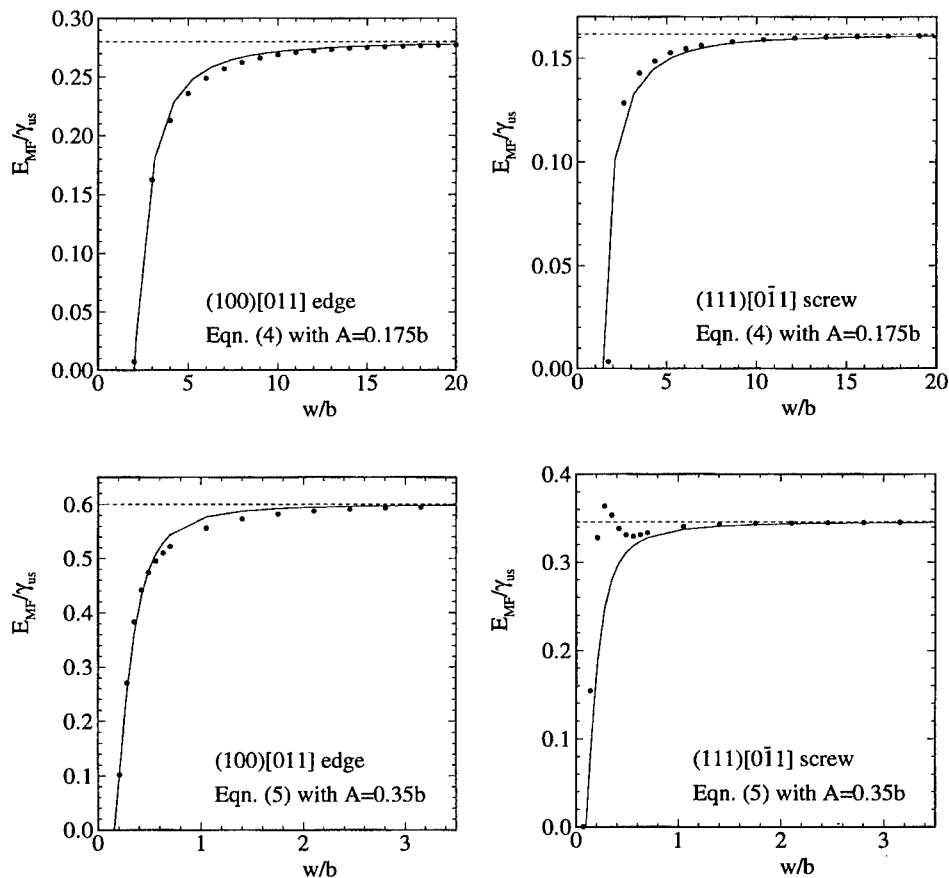


Fig. 1. Energy of idealized distributions as a function of the parameter w , which determines the gradients in the slip distribution. These results demonstrate the failure of the local slip approximation for small w . Exact atomistic energy (filled circles); local model (dashed line); non-local model (solid line).

of the two methods of obtaining the slip plane energy. These calculations demonstrated a clear breakdown in the locality assumption. Further, it was found that the gradients associated with the slip distributions for simulated core structures are of the same order of magnitude as those for which eqn (2) failed.

In Fig. 1, we reproduce the results of Miller and Phillips for the $\{001\}[110]$ slip system in fcc Al and include new results for the $\{111\}[\bar{1}\bar{1}0]$ slip system. The figure shows a plot of misfit energy per unit area of the slip plane for various slip distributions. For periodic distributions, this is computed by dividing the misfit energy per period by the periodic length. For slip distributions which are not periodic, an effective slip area was used, which is defined as the area over which the slip is greater than 1% of its maximum value. The following slip distributions were used,

$$\delta(x) = A \sin \frac{2\pi x}{w}, \quad (4)$$

$$\delta(x) = A \exp \left[-\frac{1}{2} \left(\frac{x}{w} \right)^2 \right]. \quad (5)$$

For these slip distributions, w can be varied in order to control the slip gradients. Small w corresponds to large gradients, and hence the regime in which we expect the local approximation to fail. To build these slip distributions for an atomistic calculation, one divides a crystal in two, and imposes a different deformation field in the upper and lower halves. Judicious choice of these deformations leads to the appropriate discontinuity at their common surface, and allows for the computation of the misfit energy due to that discontinuity. This is the exact atomistic energy which is compared to the results of eqn (2) in Fig. 1. Further detail of the atomistic calculation of misfit energy is given in Section 3.

Figure 1 includes two different types of slip deformation. In the slip distributions associated with straight dislocations, two types of gradient effects are possible. First, both the direction in which the slip distribution is changing and the direction of the slip discontinuity itself can be the same. This is characteristic of the slip distributions for pure edge dislocations, and therefore we refer to any slip distribution for which the δ vector and the $\nabla\delta$ vector are parallel as an "edge"-type distribution. The second type of gradient effect occurs when the direction of the slip discontinuity is perpendicular to the direction along which it is changing. This is characteristic of a pure screw dislocation, and therefore we refer to such an instance as a "screw"-type slip distribution. It is possible to mix these two effects, but for our present purposes we consider only the pure edge and pure screw cases. These two types of slip distributions are analogous to longitudinal and transverse phonons.

The results in Fig. 1 demonstrate the breakdown of the Peierls assumption for the slip distribution of eqns (4) and (5) for both the $\{001\}[110]$ edge distribution and the $\{111\}[\bar{1}\bar{1}0]$ screw distribution. The plots give the energy of the slip distributions as a function of the parameter w . In all of the plots, the prediction of the local slip approximation for the misfit energy is shown as the constant dashed line near the top of each graph, a striking manifestation of the lack of a characteristic length scale in the local cohesive zone approach. For periodic slip distributions, it is easy to see why the Peierls model approximation is independent of the parameter w . The plots of Fig. 1 are of the quantity

$$\frac{E_L^0}{w} = \frac{1}{w} \int_0^w \Phi[A \sin(2\pi x/w)] dx, \quad (6)$$

where E_L^0 is the energy of a single periodic length of the slip plane. The fact that this integral correctly represents the energy of a single periodic length is discussed in Section 3. By making the change of variables $y = x/w$, one can see that the expression is independent of w . The data points in Fig. 1 come from atomistic calculations of the same misfit energies. Note the divergence from the local estimate at small values of w . The significance of this divergence in the context of dislocations depends on the gradients found in their cores. Evidence that non-local effects are indeed important in real cores was presented in Fig. 4(b) of Miller and Phillips (1996b), which shows that non-local effects in an arctan slip distribution become important for core widths

$c/b < 0.5$ in the (100)[011] slip system. Actual core widths for this slip system have been found using lattice static core simulations by fitting slip distributions to the arctan function (Miller and Phillips, 1996a). Using a least squares fit to the entire core, a value of $c/b = 0.224$ was obtained, while fitting the slope at the center of the core resulted in a value of $c/b = 0.435$. Both of these values are in the regime where non-local effects become important.

The first mission of the non-local model will be to improve the agreement between the atomistic and continuum predictions for the slip energy shown in Fig. 1. The solid lines in this figure show the improvements made by using the non-local model, and will be discussed in more detail at the end of Section 3.

3. THE NON-LOCAL FORMULATION

The notion that any field variable (for example stress, strain or temperature) is known pointwise, and depends only on other state variables at that point is a natural starting point in the construction of constitutive models. The result is the assumption of locality—one of the basic tenets of the Peierls model, most other cohesive zone models, and classical continuum mechanics in general. However, on the atomic scale the state of each atom is influenced by a finite cluster of its neighbors, not only by the state at an individual atomic site. The non-local formulation of the Peierls model outlined in this section is proposed as a simple way to include the non-local nature of atomic interactions into cohesive zone models such as the Peierls framework.

The modification made to the Peierls model in going from the local to non-local formulation involves the inclusion of a non-local contribution to the misfit energy. The addition of this term has far-reaching implications, though it is the only conceptual change that is introduced. Clearly, this approach will confine all non-local effects to the slip plane, in the same way that the original Peierls framework confines the extent of non-linearity. It is recognized that this approach will only approximate the true non-local effects in the core, which could be more rigorously treated via non-local elasticity in the bulk regions. On the other hand, this simple approach leads to a tractable analysis that still allows for an explicit venue within which one may study the effect of non-local behavior.

Consider again the misfit energy of a dislocation as given in the local framework of eqn (2). Non-locality is incorporated by the addition of a term which should vanish for slowly varying slip distributions while at the same time capturing gradient effects when they are present. We confine ourselves to a discussion of a straight edge dislocation as a clear example of the underlying concepts. For a straight dislocation, we postulate the non-local misfit energy to be given by

$$E_{MF} = \int_{-\infty}^{\infty} \Phi[\delta(x)] dx + \int_{-\infty}^{\infty} \int_{-\infty}^{\infty} K(x-x')\delta(x)\delta(x') dx dx'. \quad (7)$$

The additional term contains the non-local interplanar kernel $K(x-x')$, which weights the non-local contributions to the total energy. On physical grounds, we assume that $K(x-x') = K(x'-x)$, or that the influence that one point has on another depends

only on the distance between these points. The new model requires only that we determine a suitable form for the non-local kernel $K(x-x')$. We propose to adopt a similar strategy to that used in obtaining $\Phi(\delta)$, whereby we extract a numerical reckoning of $K(x-x')$ from atomistic calculations and then fit these results to simple analytic forms. In the past, non-local expressions of this type have been advanced without the benefit of atomistic calculations to determine the influence function (Eringen *et al.*, 1977; Eringen and Balta, 1979; Eringen, 1987). It seems possible that the methods presented here can be adapted to those cases as well.

Given the non-local kernel, the traction at the slip plane can be written as the first variation of the misfit energy functional with respect to the slip distribution, yielding

$$\tau(x) = \frac{\partial E_{\text{MF}}}{\partial \delta} = \frac{\partial \Phi[\delta(x)]}{\partial \delta} + 2 \int_{-\infty}^{\infty} K(x-x') \delta(x') dx'. \quad (8)$$

Thus, for the non-local model, the traction τ at any point on the slip plane depends on the entire slip distribution, whereas in the local formulation the stress is determined pointwise. It is this additional feature of the new model which allows it to capture the gradient effects discussed earlier.

To determine the non-local kernel, we solve eqn (7) for $K(x-x')$ by imposing a number of special slip distributions, and use the non-local term to exactly fit the energies of these slip distributions to the atomistic result. This procedure amounts to the assumption that $K(x-x')$ is independent of the form of the slip distribution. While this may not be rigorously true, it is postulated that the non-local kernel obtained in this way will be reasonably effective for general slip distributions. Based on this assumption, it is convenient to choose slip distributions which allow for a determination of the Fourier components of $K(x-x')$. For the purposes of our calculation we place two demands on the slip distributions. First, that it be periodic with period l , and second, that the maximum amplitude of the distribution is small with respect to the lattice parameter of our material. The first requirement is one of computational convenience, allowing for the use of periodic boundary conditions when determining the exact atomistic energy of a slip distribution, while the second requirement is made in order to allow us to rewrite the interplanar potential, Φ , using its quadratic approximation. This step proves essential in determining $K(x-x')$ in much the same way that one uses the quadratic approximation to match the shear modulus in the case of the Frenkel sinusoid model. It simplifies the local term in the energy for the purpose of finding the non-local kernel, but once the kernel is computed the exact form of the local term will be reinstated. This ensures that the non-local model will still be applicable to large slip deformations.

The energy expression of eqn (7) yields the energy of the slip distribution over the entire slip plane. On the other hand, atomistic models naturally provide us with a way to compute the energy of only a finite section of the slip plane. If periodic boundary conditions are used in the atomistic model, as will be used here, then the energy obtained from atomistics is the energy of a single periodic length of the slip distribution. In order to make valid comparisons between the exact atomistic misfit energy and the energy obtained from the non-local model, we must find the non-local expression for the energy of a single periodic length of slip. Equation (7) can be rewritten in the form

$$E_{\text{MF}}(\delta) = \sum_{n=-\infty}^{\infty} \left[\int_{nL+\xi}^{(n+1)L+\xi} c\delta(x)^2 dx + \int_{nL+\xi}^{(n+1)L+\xi} \int_{-\infty}^{\infty} K(x-x')\delta(x)\delta(x') dx' dx \right], \quad (9)$$

where the constant c arises from the treatment of the interplanar potential via its quadratic approximation and ξ is some origin where $0 \leq \xi \leq L$. It is easy to show that for periodic slip distributions, the integrals inside this sum are independent of n and ξ , and hence each periodic length in the variable x contributes the same amount to the total misfit energy. We can then write the misfit energy of a single period of the slip plane, $E_{\text{MF}}^0(\delta)$, as

$$E_{\text{MF}}^0(\delta) = \int_0^L c\delta(x)^2 dx + \int_0^L \int_{-\infty}^{\infty} K(x-x')\delta(x)\delta(x') dx' dx, \quad (10)$$

and note that for a given slip distribution, $E_{\text{MF}}^0(\delta)$ is a quantity which can be computed directly from atomistics. For this purpose, it is convenient to take $\delta(x)$ to be

$$\delta(x) = \delta_q(x) = A \sin qx, \quad (11)$$

where $q = 2\pi/L$ and A is much smaller than the lattice constant of the crystal under consideration. We insert this form of $\delta(x)$ into the expression for E_{MF}^0 . Making a change of variables $z = x - x'$ and recalling that $K(z) = K(-z)$, the energy expression becomes

$$E_{\text{MF}}^0(\delta_q) = \frac{cA^2L}{2} + A^2 \int_0^L \sin qx \left[\int_{-\infty}^{\infty} K(z) \frac{e^{iq(z+x)} - e^{-iq(z+x)}}{2i} dz \right] dx, \quad (12)$$

where we have made use of the exponential form of the sine function. We recall the definition of the Fourier transform, $\hat{f}(k)$, of a function $f(x)$ as

$$\hat{f}(k) = \int_{-\infty}^{\infty} f(x) e^{-ikx} dx, \quad (13)$$

and also the inverse Fourier transform

$$f(x) = \frac{1}{2\pi} \int_{-\infty}^{\infty} \hat{f}(k) e^{ikx} dk, \quad (14)$$

and use eqn (13) to write the non-local energy expression in terms of the Fourier transform of the non-local kernel, $\hat{K}(q)$. Noting again that $K(z) = K(-z)$, we see that $\hat{K}(q) = \hat{K}(-q)$, and the expression for the total energy becomes

$$E_{\text{MF}}^0(\delta_q) = \frac{cA^2L}{2} + A^2 \hat{K}(q) \int_0^L \sin^2 qx dx. \quad (15)$$

Evaluating the integral leads to an explicit expression for the non-local interplanar kernel in Fourier space;

$$\hat{K}(q) = \frac{2E_{\text{MF}}^0(\delta_q)}{A^2L} - c. \quad (16)$$

At this point, the strategy is to obtain the energy dependence on the Fourier variable q numerically through an atomistic model.

3.1. Atomistic determination of the non-local interplanar kernel

The procedure for determining the energy of a given slip distribution was outlined in Section 2 and is described in detail by Miller and Phillips (1996b). Here, we use the same computational approach which is described briefly below.

We desire the energy of the slip distribution given by eqn (11) as a function of the parameter q . To make the computation, the crystal is divided into an upper and a lower half. By imposing the appropriate displacement fields on the two half spaces, we can create the desired slip distribution at their common interface. For example, consider the slip distribution of eqn (11). For the case of edge-type slip, the slip distribution can be obtained by imposing the following displacement fields on the crystal:

$$\mathbf{u}^+ = [(A/2) \sin qx, 0, 0], \quad (17)$$

$$\mathbf{u}^- = [(A/2) \sin qx, 0, 0], \quad (18)$$

where \mathbf{u}^+ represents the displacement field in the upper half of the crystal and \mathbf{u}^- is that in the lower half. This combination of displacement fields leads to a slip distribution of the form

$$\delta(x) = u_x^+ - u_x^- = A \sin qx \quad (19)$$

at the plane where the upper and lower half spaces meet.

Using any convenient atomistic model (we have used the embedded atom method (EAM), see Daw and Baskes, 1984 for example) it is then possible to compute the energy of this crystal. The result of such an atomistic calculation is an energy consisting of two parts, that due to the interface and an additional elastic strain energy due to the deformation in the bulk regions of the crystal. The elastic energy can be found directly by computing the energy of each half space separately, using a periodic computational cell containing no slip discontinuities. This energy can then be subtracted from the total energy of the configuration which includes the slip jump, leaving the misfit energy, E_{MF}^0 .

By repeating this procedure for a sequence of values of q , we obtain a discrete representation of the non-local kernel $\hat{K}(q)$ in Fourier space. Results of such calculations using the EAM potentials for Al of Ercolessi and Adams (1994) are presented in Fig. 2. The various slip systems are either edge, screw or "mixed", where edge and screw are as defined in Section 2. The "mixed" system is in this case the direction associated with the 30° Shockley partial. All of the curves are given in non-dimensional form using the constants given in Table 1, where γ_{us} is the unstable stacking fault energy for a given slip system. The values in the table are obtained by rigidly sliding two blocks of atoms with respect to one another and allowing relaxations in only the

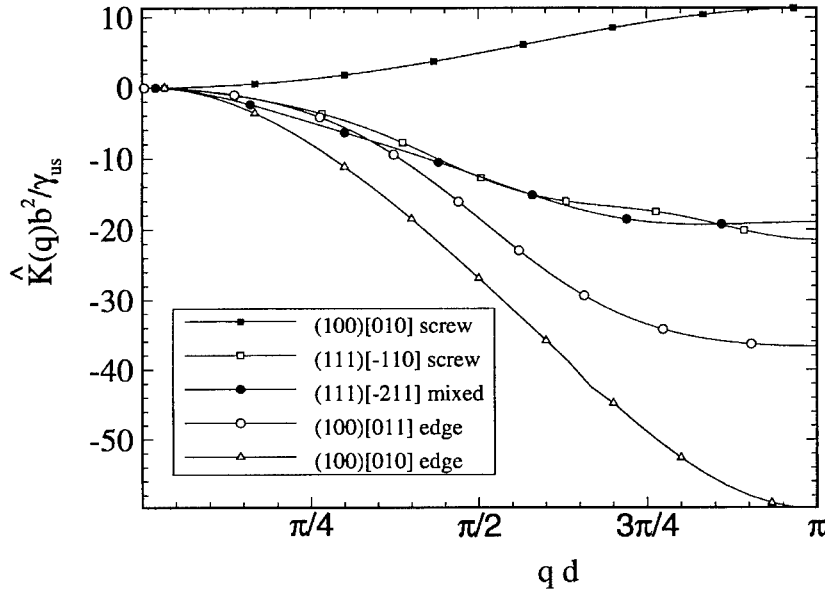


Fig. 2. Examples of the Fourier space representation of the non-local interplanar kernel, \hat{K} , for various slip systems in Al, as obtained using the EAM potentials of Ercolessi and Adams (1994). See Table 1 for normalization constants.

Table 1. *Burgers vector b , interplanar spacing d and unstable stacking fault energy γ_{us} for the slip systems considered in Fig. 2 as obtained from the EAM Al potentials of Ercolessi and Adams (1994)*

Slip system	$b(\text{\AA})$	d/b	$\gamma_{us} (\text{eV}/\text{\AA}^2)$
(100)[010] Screw	4.032	$1/2$	0.04065
(111)[$\bar{1}10$] Screw	2.851	$\sqrt{3}/6$	0.02705
(111)[$\bar{2}11$] Mixed	1.646	$\sqrt{3}/2$	0.008032
(100)[011] Edge	2.851	$1/2$	0.02521
(100)[010] Edge	4.032	$1/2$	0.04065

out-of-plane direction. The remaining constants in the table are b , the Burgers vector, and d , which is defined below. The representative examples in Fig. 2 demonstrate a number of the characteristics of the non-local interplanar kernel when constructed in Fourier space. All such functions are even and periodic, and therefore only the first half period of each is shown. The periodic length of \hat{K} depends on the slip system being considered, and is given by $2\pi/d$ where d is the distance between planes with normal parallel to the direction of the slip gradient vector. Note that these planes are a set of y - z planes, which are perpendicular to the x - y slip plane. Another characteristic feature of the \hat{K} function is that it is exactly zero at $q = 0$, which implies that in the

limit of very slowly varying slip distributions, the non-local correction vanishes and we recover the classical Peierls framework. It is also worth noting that while most of the \hat{K} functions are negative, we see that for the case of screw-type slip distributions on the $\{001\}[010]$ slip system \hat{K} is entirely positive. This suggests that there is no set rule about whether the non-local contribution to the misfit energy is positive or negative—it will depend on both the slip system being considered and on the Fourier components of the slip distribution itself. Comparing the various curves in this figure can help us to understand the relative importance of the non-local effect for various slip systems. Note that the strongest effect is associated with the $(100)[010]$ edge system. It is interesting that this same slip system, but in the screw orientation, shows the weakest non-local correction, and that the sign of this correction for the various Fourier components of the slip distribution is reversed. This is because the screw-type sinusoidal slip distribution represents a more severe misfit configuration than the edge-type for this slip system. Meanwhile, the local model predicts the same energy for either edge or screw slip due to the symmetries of the $\{100\}$ planes. For this slip system, the local prediction for misfit energy somewhat overestimates the edge energy, while somewhat underestimating its screw counterpart. The result is this seemingly anomalous behavior of the screw-type slip.

3.2. Approximate analytic form in real space

Numerical inversion of the Fourier representation of \hat{K} deduced above can be problematic due to the fact that \hat{K} is known only for a discrete set of points in Fourier space. Therefore, we propose to fit \hat{K} in Fourier space with a cosine series, which can be easily transformed into real space in the form of a sum of Dirac delta functions. Because $K(x-x')$ exists as part of an integrand over the entire slip plane, these Dirac deltas will have the effect of reducing the dimension of the integral in eqn (7). We have found that excellent fits of the numerical data can be obtained using only the first few terms of such a cosine series, and one can therefore write

$$\hat{K}(q) \cong \frac{a_0}{2} + \sum_{n=1}^N a_n \cos n dq, \quad (20)$$

where a_n are the fitting parameters and d is the distance between planes perpendicular to the slip plane, as described previously. The number of fitting parameters N will depend on the range of the atomistic potentials used in obtaining \hat{K} , but we have found that for the potentials and slip systems considered here, the value of N typically does not need to exceed five. This form for the non-local kernel allows for easy Fourier inversion, yielding

$$K(x-x') = \frac{a_0}{2} \delta_D(x-x') + \sum_{n=1}^N \frac{a_n}{2} (\delta_D(x-x'+nd) + \delta_D(x-x'-nd)), \quad (21)$$

where δ_D is the Dirac delta function. This expression for the non-local kernel can be used in the original definition for the misfit energy, as well as in the expression for the tractions on the slip plane. The results are

$$E_{MF} = \int_{-\infty}^{\infty} \Phi[\delta(x)] dx - \sum_{n=1}^N \int_{-\infty}^{\infty} a_n \left(\delta(x)^2 - \frac{\delta(x)\delta(x-nd) + \delta(x)\delta(x+nd)}{2} \right) dx, \quad (22)$$

$$\tau(x) = \frac{\delta\Phi[\delta(x)]}{\delta} - \sum_{n=1}^N a_n (2\delta(x) - \delta(x+nd) - \delta(x-bd)), \quad (23)$$

where we have eliminated a_0 from the expressions by using the fact that $\hat{K}(0) = 0$. The δ appearing in this expression is the slip distribution, and not the Dirac delta function δ_D . The computed values of a_n are plotted in Fig. 3 for the five slip systems considered here. In this figure, increasing n corresponds to sampling the slip distribution farther and farther from the point at which the energy and stress is being computed. It is clear that the non-local effects decays quite rapidly, and in all cases a_1 (corresponding to the near neighbor non-local influence) is by far the most important contribution. Non-local influence is felt as far as five neighbors away in some systems, but beyond a_5 , the coefficients are negligible.

Note that the expressions for the energy and stress are consistent with our intuition as to the nature of the non-local terms. First, in the limit when $\delta(x)$ is slowly varying, $\delta(x \pm nd) \rightarrow \delta(x)$ and the above expressions reduce to the conventional local formulation. Second, the non-local effects for a given point arise as a result of sampling a discrete set of points along the rest of the slip distribution. These points are spaced by a distance d , which coincides with the spacing of atomic planes in the direction of the slip gradient vector. The discreteness of this sampling, together with the physical significance of the spacing of the sampling points results in a sensible atomistic extension of the original constitutive assumptions of the local model.

Finally, it is interesting to note that the terms of the sum in eqn (23) can be viewed as a linear combination of approximations to the derivatives of the slip distribution. The symmetry of our non-local kernel in Fourier space means that only even order derivatives contribute to this correction, and therefore it is possible to re-write eqn (23) in the form

$$\tau(x) = \frac{\tau\partial\Phi[\delta(x)]}{\partial\delta} - \sum_{n=1}^N c_{2n} \delta^{(2n)}(x), \quad (24)$$

where the coefficients c_n are the weights associated with the n th derivative, and $\delta^{(n)}$ is the central difference approximation to the n th derivative of the slip distribution. The c_n are simply linear combinations of the a_n already introduced. For example, if we take $N = 2$ in eqns (23) and (24), and make use of the following central difference approximations for the second and fourth derivative of $\delta(x)$,

$$\frac{d^2\delta}{dx^2} = \frac{\delta(x+d) - 2\delta(x) + \delta(x-d)}{d^2}, \quad (25)$$

$$\frac{d^4\delta}{dx^4} = \frac{\delta(x+2d) - 4\delta(x+d) + 6\delta(x) - 4\delta(x-d) + \delta(x-2d)}{d^4}, \quad (26)$$

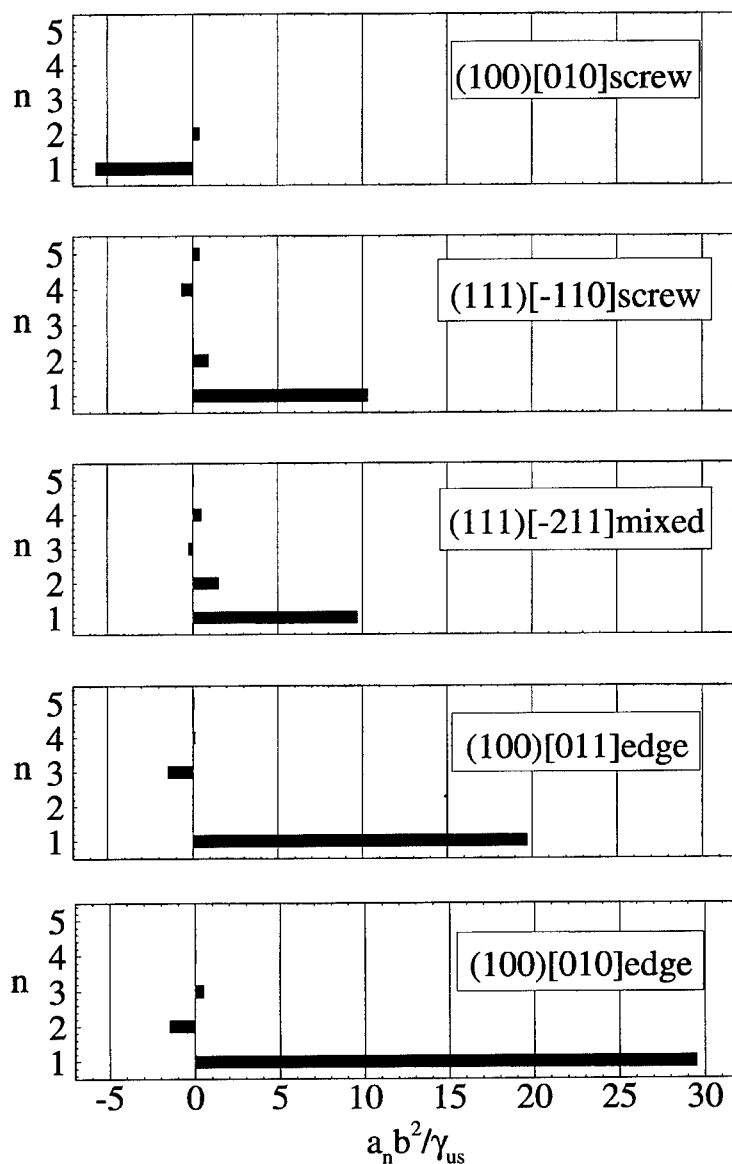


Fig. 3. Non-local influence coefficients, a_n , for the slip systems considered in Fig. 2.

then we can solve for the coefficients c_2 and c_4 . In this case, these are found to be

$$c_2 = -d^2(a_1 + a_2), \quad (27)$$

$$c_4 = -d^4 a_2. \quad (28)$$

This exercise highlights the parallels between our non-local approach and recent

gradient correction models (e.g., Fleck *et al.*, 1994; Aifantis, 1992), although in this paper we will not explore the gradient correction form of these equations further.

3.3. *Energy of crystalline slip within the non-local formulation*

The simplest test of the non-local model is to re-examine the energetics of idealized slip distributions as originally presented in Fig. 1. Recall that in this figure the predictions of the local model are given by the constant dashed line near the top of each graph, whereas the data points are exact calculations of the misfit energy as determined using atomistics. The solid curves are the results of using the non-local model, which are in significantly better agreement with the exact results than are the local results. In each case, the energetics using the non-local model exhibit the correct trend as a function of slip gradients, unlike the original model which does not capture gradient effects. The non-local model is not able to capture the anomalous upturn in the atomistic results for the $\{111\}[1\bar{1}0]$ screw orientation, a pathology of this particular slip deformation which results from putting atoms into highly unfavorable proximity across the slip plane. Nonetheless from the standpoint of purely energetic considerations, the non-local model shows a marked improvement over the local model, without any great cost in model complexity.

4. THE NON-LOCAL MODEL OF REALISTIC DISLOCATION CORES

As an example, we apply the non-local model to the determination of the core structure for a straight dislocation with a planar core. For this purpose we consider the Lomer dislocation in fcc Al, with a $\langle 110 \rangle$ line direction and Burgers vector $(a/2)\langle \bar{1}10 \rangle$.

We obtain the Lomer core structure using two schemes. The first makes use of a simplified form for local part of the interplanar potential $\Phi(\delta)$ that allows for a closed form analytic solution for the slip distribution in Fourier space. In the second determination of the Lomer core, the full-blown atomistic result for $\Phi(\delta)$ is used and the core structure is computed numerically. Each of these results is then compared to the slip distribution taken directly from the atomic positions resulting from full relaxation of the atomistic degrees of freedom. The first scheme, which admits of an analytic solution, is of interest as a method for testing the numerical procedures used in the second scheme. At the same time, it demonstrates that considerable analytical progress can be made with the non-local formulation. The second, fully numerical solution demonstrates that stable core structures are readily obtainable within the non-local formulation. We will see that while the effect of the non-local terms on the slip distribution and core structures are subtle to the eye, they represent a significant improvement when quantified in terms of the predicted misfit energy of the dislocation core.

4.1. *Eigenstrains solution for δ within the quadratic well approximation*

In this section, we describe the procedure used in determining an analytic result for the core structure of the Lomer dislocation. The important approximation in this

procedure in relation to the results of the subsequent section is the simplified form used for the interplanar potential $\Phi(\delta)$.

Within the Peierls framework, the determination of $\delta(x)$ is equivalent to finding the core structure of the dislocation. Once $\delta(x)$ is found, the elastic displacement fields away from the slip plane can be computed from an integral of the Volterra kernel over the entire slip plane. As well, the misfit and elastic energy are then fully specified by the slip distribution. Therefore, we seek the slip distribution $\delta(x)$ which minimizes the total energy functional. The energy associated with the dislocation, which is a functional of the slip distribution $\delta(x)$, can be expressed as the sum of three parts

$$E_{\text{tot}} = E_L + E_{\text{NL}} + E_B. \quad (29)$$

E_L is the misfit energy as determined within the traditional local model and given in eqn (2), E_{NL} is the non-local correction term added to the misfit energy in eqn (7), and E_B is the elastic energy of the bulk region. The elastic term is obtained by superimposing the elastic interaction energy for a distribution of infinitesimal dislocations with Burgers vector density $-\text{d}\delta/\text{d}x$,

$$E_B = \frac{1}{2} \int_{-\infty}^{\infty} \int_{-\infty}^{\infty} B \log \left(\frac{R}{|x-x'|} \right) \frac{\text{d}\delta(x)}{\text{d}x} \frac{\text{d}\delta(x')}{\text{d}x'} \text{d}x \text{d}x'. \quad (30)$$

In this equation, R is a measure of the size of the bulk region. Making use of integration by parts, it is possible to eliminate the constant R from the analysis. B is defined as

$$B = 2C_{ij}s_i s_j \quad (31)$$

where s_i is the i th component of the slip direction for the dislocation of interest and C_{ij} is the prelogarithmic energy tensor, discussed in detail, for example, in Bacon *et al.* (1979). In the case of an isotropic solid B reduces to

$$B_{\text{iso}} = \frac{\mu}{2\pi(1-\nu)}. \quad (32)$$

For the purposes of obtaining an analytic solution we use the method of eigenstrains (Mura, 1984). We make the approximation that the local interplanar potential $\Phi(\delta)$ takes the form of a periodic array of quadratic wells as shown in Fig. 4(a). This approximation is clearly not an accurate representation of the full interplanar potential, but does capture one of the real potentials most significant features, namely, its convexity, and is a standard tool in the method of eigenstrains. The full interplanar potential will be incorporated in Section 4.2. Now, we employ the method of eigenstrains as described by Mura to minimize the energy functional with respect to the slip distribution for a dislocation dipole with spacing r . The dipole configuration is used so that the slip distribution goes to zero at $x = \pm\infty$. By making r large, the dipole becomes two isolated dislocations of opposite sign. This approach allows us to rewrite the local contribution to the energy as

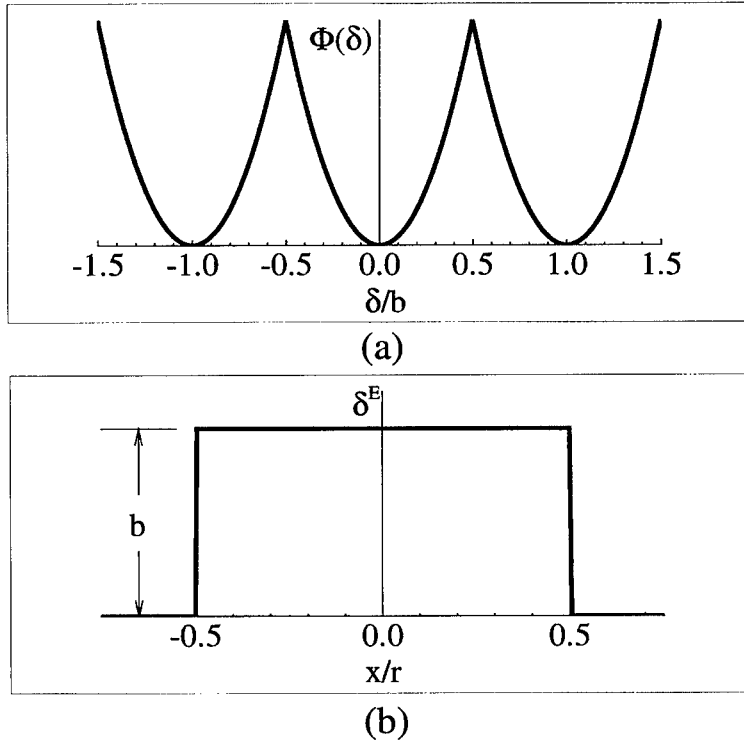


Fig. 4. (a) Quadratic well approximation to the local interplanar potential. (b) Eigenslip, $\delta^E(x)$ for the dipole configuration.

$$E_L = \int_{-\infty}^{\infty} c(\delta(x) - \delta^E(x))^2 dx. \quad (33)$$

In this equation the constant c is determined by fitting the quadratic wells to linear elasticity at small values of $\delta - \delta^E$. This leads to $c = \mu/2a$ where a is the spacing between slip planes and μ is the relevant shear modulus for the slip system of interest. δ^E in this expression is the "eigenslip" which ensures that the dipole slip configuration is enforced during the energy minimization. $\delta^E(x)$ is shown in Fig. 4(b), where b is the Burgers vector and r is the dipole spacing. We will need the Fourier transform of this eigenslip, which is found to be

$$\hat{\delta}^E = \int_{-r/2}^{r/2} b e^{-ikx} dx = \frac{2b}{k} \sin \frac{kr}{2}. \quad (34)$$

Making use of eqn (14), we can replace δ , δ^E and K with their Fourier transforms, allowing for a Fourier space representation of the total energy. Integrating by parts on the bulk energy terms and assuming that the order of integrations can be switched allows us to simplify the energy expression to

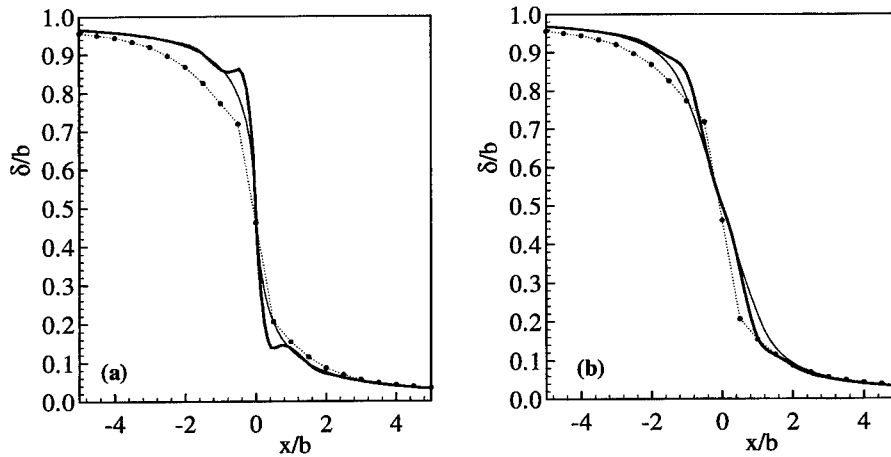


Fig. 5. Comparison of core structures for the Lomer dislocation in Al as obtained from the continuum model with exact atomistic results. (a) Structure obtained using the quadratic well model of the interplanar potential and (b) with the full numerical solution to the Peierls-Nabarro equation. The filled circles represent the atomistic result, the thin line is the local model result, and the thick line is the non-local model result.

$$E_{\text{tot}} = \int_{-\infty}^{\infty} \left[\hat{\delta}(k) \hat{\delta}(-k) \left(\frac{c}{2\pi} + \frac{\hat{K}(k)}{2\pi} + \frac{B}{4} |k| \right) - \frac{c}{\pi} \hat{\delta}(k) \hat{\delta}^E(-k) + \frac{c}{2\pi} \hat{\delta}^E(k) \hat{\delta}^E(-k) \right] dk. \quad (35)$$

Note that at this point, our solution is predicated upon a knowledge of the Fourier space features of the interplanar kernel. Taking variations with respect to $\hat{\delta}$ and setting $\delta E_{\text{tot}} = 0$ we find

$$\hat{\delta}(k) = \frac{2b \sin \frac{kr}{2}}{k \left[1 + \frac{\hat{K}(k)}{c} + \frac{\pi B}{2c} |k| \right]} \quad (36)$$

where we have made use of the fact that $\hat{K}(k)$ is an even function and used eqn (34) to replace the Fourier transform of the eigenslip. This expression gives us the Fourier transform of the slip distribution for the dislocation dipole. Although it cannot be transformed into real space explicitly, the transformation integral is straightforward to perform numerically once the form of \hat{K} is known. Thus we numerically compute the slip distribution from the expression

$$\delta(x) = \frac{2b}{\pi} \int_0^{\infty} \frac{\sin \frac{kr}{2} \cos kx}{k \left[1 + \frac{\hat{K}(k)}{c} + \frac{\pi Bk}{2c} \right]} dk. \quad (37)$$

This result is plotted in Fig. 5 for the case of $\hat{K} = 0$ (which corresponds to the local

Peierls model solution) and with \hat{K} from Fig. 2 for the (100)[011] edge (Lomer) slip system. Only one member of the dimple pair is shown because of the symmetry of the distribution. For comparison, we have included the slip distribution obtained from a lattice statics energy minimization of the same dislocation core. Note that in making such comparisons, care must be taken to insure that the method used in extracting the slip distribution from the atomic coordinates is consistent with the definition of $\delta(x)$ used in the continuum model. A discussion of this distinction can be found, for example, in Miller and Phillips (1996b) or Rice (1992).

We see in Fig. 5(a) that the effect of the non-local correction is to introduce small oscillations in the slip distribution and increase its slope slightly at the dislocation core. At first, the oscillations may appear to be unphysical, but recall that this continuous curve is really a representation of the slip for a discrete set of lattice sites. Therefore, only the values at the lattice sites are germane for the atomic positions implied by the solutions. It is interesting to note that this analytic model provides a reasonable approximation to the dislocation core, although the differences between the local and non-local results are hard to quantify. It seems that the quadratic well approximation used in obtaining this result leads to an overestimate of the lattice restoring force, as evidenced by the narrowness of the Peierls model cores when compared to the atomistic result. In the next section, we will see the improved representation of these forces when the full interplanar potential is used. We should not expect the quadratic well model to accurately capture subtle details of the atomic core, but it is encouraging that the model does lead to a stable core configuration that is similar to the exact result.

4.2. Numerical solution for the slip distribution

It is now of interest to see what effect the non-local correction has on the dislocation core structure when the correct atomistically obtained $\Phi(\delta)$ is used. In this case, it is necessary to resort to a full numerical solution of the governing equation.

The numerical approach for finding $\delta(x)$ follows closely the approach of Beltz and Freund (1994), to which we refer the interested reader for more details. We begin with the well-known Peierls–Nabarro equation (Hirth and Lothe, 1992)

$$\tau[\delta(x)] = -\frac{\mu}{2\pi(1-\nu)} \int_{-\infty}^{\infty} \frac{d\delta(x')/dx'}{x-x'} dx', \quad (38)$$

into which we can substitute eqn (23) for $\tau[\delta(x)]$. By an appropriate change of variables, the domain of integration can be collapsed onto the finite domain $(-1, 1)$. This domain can be discretized and the integration carried out by making use of the Gauss–Chebyshev integration techniques described in Erdogan and Gupta (1972). This approach reduces the problem to a set of nonlinear algebraic equations which can be solved iteratively via the Newton–Raphson method, leading to a discrete representation of the slip distribution $\delta(x)$. The results of such a calculation for the Lomer core structure are presented in Fig. 5(b). Again, we note that the resulting core structure is not changed dramatically relative to the local model as a result of adding the non-local correction. Note that neither of the two continuum models can capture the slight asymmetry of the atomistic core which arises due to discrete lattice effects.

One important improvement in the non-local model is a slight increase in the slope at the core center, which brings the narrowness of the core into better agreement with that of the atomistic result.

The fact that the structural differences between the local and non-local models are small does not imply that the non-local effect is unimportant. Another quantity to compare between the two models is their predictions for the total energy of the dislocation. The elastic energy is computed in the same way for the two models, and the highly similar cores implies that the value of the elastic energy for the two models will be about the same. On the other hand, the misfit energy is computed differently, and even identical core structures will lead to different misfit energies by virtue of the non-local energy term.

Using the method described in Miller and Phillips (1996b) to isolate the misfit energy from the strain energy in the bulk regions, we can compute the exact atomistic misfit energy of the Lomer dislocation to be $0.1362 \text{ eV}/\text{\AA}$. This is accomplished by representing the atoms in the upper and lower bulk regions by nodes in a finite element mesh, and computing the strains (and consequent strain energy) in this mesh via the Cauchy–Born rule (Erickson, 1984). On the other hand, we can compute this energy using the local and non-local models from eqns (2) and (22), respectively. The local model predicts an energy of $0.1979 \text{ eV}/\text{\AA}$, about 45% greater than the exact energy. The non-local result is $0.1471 \text{ eV}/\text{\AA}$, only 8% greater than the atomistic result. This result demonstrates that although the core structures in the local and non-local formulations are very similar, the non-local treatment of the core energies is significantly more accurate. We would expect similar adjustments to the cohesive zone model estimate of the Peierls stress.

5. CONCLUSIONS

Motivated by previous work which demonstrated a failure of the local Peierls framework to accurately describe the energy of interplanar slip for the types of slip distributions found in real dislocation cores, we proposed a non-local formulation of this framework. We then proceeded to outline a set of simple atomistic calculations whereby one can obtain the non-local interplanar kernel required in the formulation of the model. To demonstrate that the model improved estimates of the slip energy, we compared these results to purely atomistic calculations and showed that the non-local model improves the agreement between the cohesive zone model energies and explicit atomistic energies.

Given that the non-local model leads to better energetic descriptions of slip distributions, we proceeded to demonstrate the model by computing the structure of a straight dislocation with a planar core, namely, the Lomer dislocation in Al. It was found that the differences between the local and non-local results, and between either of them and the atomistic core, were subtle and difficult to quantify when considering only the spatial structure of the dislocation. However, an alternative measure of the performance of the models is the energy they imply, which the local model predicted to be 45% larger than the exact atomistic result. The non-local model significantly improved the energetic description of the core, overestimating the exact result by only

8%. Nevertheless, the negligible changes in the non-local description of the core structure serve as a reminder that the cohesive zone approach appears to lack the flexibility to really serve as a generic basis for mixed atomistic and continuum studies of dislocations. Even in its non-local form, this framework restricts the slip, all non-linearity and all non-locality to a particular slip plane, thus forbidding the emergence of complex cores such as those found in bcc metals.

Future work in the context of cohesive zone models could include an attempt to integrate non-local effects into other models of the mechanical behavior of materials. One example of interest is the model of Rice (1992) and the numerous related works that describe dislocation emission from crack tips. Preliminary investigations in this area suggest that the concepts outlined here can be used for such problems (Miller *et al.*, 1997). The basic equation to be solved in the case of a dislocation near a crack tip is a modified version of the Peierls–Nabarro equation with additional terms due to the presence of the crack. Any realistic solution of this equation requires a numerical procedure, and the simple form of the non-local corrections in eqns (22) and (23) mean that the additional computational cost in the non-local formulation is small. The most serious obstacle in this case seems to be the proper treatment of the boundary conditions in the non-local setting, and most importantly the stress free boundaries at the crack faces. However, the fact that non-locality plays an important role at the atomic level means that a correct non-local treatment of the atomistically sharp crack may be an important contribution to our understanding of crack tip phenomena.

One important approximation of the Peierls model not discussed in this work is the treatment of the inherently discrete slip distribution as a continuous function $\delta(x)$. Another possible direction for this work is the integration of the non-local formulation into the recently proposed “semi-discrete Peierls framework” of Bulatov and Kaxiras (1997), which correctly treats the slip distribution as a discrete function. Results using the semi-discrete version of the Peierls model show significant improvement to the conventional Peierls framework, but some error remains. It is possible that including non-local effects into this model may further improve its agreement with atomistics while retaining its tractability.

A third future direction for this research should be an effort to compute other non-local kernels analogous to $K(x-x')$. For example, it may be possible to directly compute from atomistics the non-local elastic moduli introduced by Eringen *et al.* (1977) for bulk crystals. This would eliminate guesswork about their appropriate form and base them solidly on their atomistic underpinnings. Other recent work (Tadmor *et al.*, 1996a, b) substantiates our belief in the critical role played by constitutive non-locality in the description of atomic scale defects and calls for continued efforts to put such models on a clear analytic footing.

ACKNOWLEDGEMENTS

This work was supported by the Natural Sciences and Engineering Research Council of Canada, by NSF Grants CMS-9414648 and CMS-9502020 and by the National Science Foundation under the Materials Research Group Grant No. DMR-9223683. We are grateful to S. Foiles and M. Daw for the use of their code Dynamo. Finally, it is a pleasure to acknowledge

useful conversations with V. Bulatov, A. Carlsson, M. S. Duesbery, J. R. Rice, V. Shenoy and E. Tadmor.

REFERENCES

- Aifantis, E. C. (1992) On the role of gradients in the localization of deformation and fracture. *Int. J. Engng Sci.* **30**(10), 1279–1299.
- Bacon, D. J., Barnett, D. M. and Scattergood, R. O. (1979) Anisotropic continuum theory of lattice defects. *Prog. Mat. Sci.* **23**, 51–262.
- Barenblatt, G. I. (1962) The mathematical theory of equilibrium cracks in brittle fracture. *Adv. Appl. Mech.* **7**, 55.
- Beltz, G. E. and Freund, L. B. (1994) Analysis of the strained-layer critical thickness concept based on a Peierls–Nabarro model of a threading dislocation. *Phil. Mag. A* **69**, 183–202.
- Bilby, B. A., Cottrell, A. H. and Swinden, K. H. (1962) The spread of plastic yield from a notch. *Proc. Roy. Soc. Lond. A* **272**, 304.
- Bulatov, V. and Kaxiras, E. (1997) Semidiscrete variational Peierls framework for dislocation core properties. *Phys. Rev. Lett.* **78**(22), 4221–4224.
- Daw, M. S. and Baskes, M. I. (1984) Embedded-atom method: derivation and application to impurities, surfaces, and other defects in metals. *Phys. Rev. B* **29**, 6443–6453.
- DiVincenzo, D. P. (1986) Dispersive corrections to continuum elastic theory in cubic crystals. *Phys. Rev. B* **34**(8), 5450–5465.
- Duesbery, M. S., Taylor, R. and Glyde, H. R. (1973) Anharmonic lattice dynamics in K. *Phys. Rev. B* **8**, 1372–1378.
- Dugdale, D. S. (1959) Yielding of steel sheets containing slits. *J. Mech. Phys. Sol.* **8**, 100.
- Ercolossi, F. and Adams, J. B. (1994) Interatomic potentials from first-principles calculations—the force-matching method. *Europhys. Lett.* **26**, 583.
- Erdogan, F. and Gupta, G. D. (1972) On the numerical solution of singular integral equations. *Q. Appl. Math.* **29**, 525–534.
- Ericksen, J. L. (1984) *Phase Transformations and Material Instabilities in Solids*, pp. 61–77. Academic Press, New York.
- Eringen, A. C. (1987) Theory of nonlocal elasticity and some applications. *Res. Mech.* **21**, 313–342.
- Eringen, A. C. and Balta, F. (1979) Edge dislocation in nonlocal hexagonal elastic crystals. *Crystal Lattice Defects* **8**, 73–80.
- Eringen, A. C., Speziale, C. G. and Kim, B. S. (1977) Crack-tip problem in non-local elasticity. *J. Mech. Phys. Sol.* **25**, 339–355.
- Fleck, N. A., Muller, G. M., Ashby, M. F. and Hutchinson, J. W. (1994) Strain gradient plasticity: theory and experiment. *Acta Met. et Mat.* **42**, 475–487.
- Foreman, A. J., Jawson, M. A. and Wood, J. K. (1951) Factors controlling dislocation widths. *Proc. Roy. Soc. Lond. A* **64**, 156–163.
- Hirth, J. P. and Lothe, J. (1992) *Theory of Dislocations*. Krieger, Malabar, Florida.
- Kaxiras, E. and Duesbery, M. S. (1993) Free energies of generalized stacking faults in silicon and implications for the brittle–ductile transition. *Phys. Rev. Lett.* **70**(24), 3752–3755.
- Miller, R. and Phillips, R. (1996a), unpublished.
- Miller, R. and Phillips, R. (1996b) Critical analysis of local constitutive models for slip and decohesion. *Phil. Mag. A* **73**(4), 803.
- Miller, R., Phillips, R., Beltz, G. and Ortiz, M. (1997), unpublished.
- Mura, T. (1984) *Micromechanics of Defects in Solids*, 2nd edn. Kluwer Academic, The Netherlands.
- Peierls, R. E. (1940) The size of a dislocation. *Proc. Phys. Soc. Lond.* **52**, 34.
- Rice, J. R. (1992) Dislocation nucleation from a crack tip: an analysis based on the Peierls concept. *J. Mech. Phys. Sol.* **40**, 239.

- Sun, Y., Beltz, G. E. and Rice, J. R. (1993) Estimates from atomic models of tension-shear coupling in dislocation nucleation from a crack tip. *Mat. Sci. Eng. A* **170**, 67–85.
- Tadmor, E. B., Ortiz, M. and Phillips, R. (1996a) Quasicontinuum analysis of defects in solids. *Phil. Mag. A* **73**(6), 1529–1563.
- Tadmor, E. B., Phillips, R. and Ortiz, M. (1996b) Mixed atomistic and continuum models of deformation in solids. *Langmuir* **12**(19), 4529–4534.



Pergamon

J. Mech. Phys. Solids, Vol. 46, No. 10, pp. 1869–1886, 1998
© 1998 Published by Elsevier Science Ltd. All rights reserved
Printed in Great Britain
0022-5096/98 \$—see front matter

PII: S0022-5096(98)00056-8

SOME NEW DATA ON DEFORMATION AND FRACTURE OF SOLIDS UNDER SHOCK-WAVE LOADING

G. I. KANEL*

High Energy Density Research Center, IVTAN, Izhorskaya 13/19, Moscow, 127412, Russia

(Received 20 December 1997; accepted 16 March 1998)

ABSTRACT

The topics considered are poorly understood aspects of the high-rate deformation and fracture under shock-wave loading, and some new kinds of shock-wave experiments. A high mobility of the crystal lattice behind the shock front as a result of formation of many stacking faults, unexpectedly high dynamic yield strength of metals at elevated temperatures as a result of viscous dislocation drag and spontaneous nucleation of point defects, spall strength of metals at temperatures up to the melting point, use of the line imaging interferometer technique to study a relationship between trans-granular and inter-granular dynamic strength of a polycrystalline metal, and inelastic deformation and fracture of glasses under impact loading are discussed. © 1998 Published by Elsevier Science Ltd. All rights reserved.

1. INTRODUCTION

Since the shock wave and high-strain-rate phenomena are involved to broad technological and other applications, we are interested in understanding the time-dependent mechanical properties under these non-trivial conditions. On the other hand, the shock-wave technique provides a powerful tool for studying material properties at extremes of strain rates. Since then the modern high-resolution methods of monitoring of the stress and particle velocity histories in shock waves have been created, numerous investigations of mechanical properties of different classes materials were performed, and numerous phenomenological as well as microscopical models were developed. However, in spite of a quite sufficient general understanding, experiments, theory, and material models do not agree in details. Mechanical yielding and strength behavior in shock waves show complexities that are not understood yet.

There are reasons for concern that unidentified processes and phenomena occur. One of the goals of the paper is to attract an attention to some such unidentified aspects of high-rate deformation and fracture of solids in conditions of shock-wave loading. Another goal of the paper is to discuss some new kinds of experiments that, we hope, can provide important interesting data. Examples and possible mechanisms of a fast stress relaxation in ductile crystalline materials will be discussed in Chapter

* E-mail: kanel@icp.ac.ru

2. Chapter 3 is devoted to discussion of anomalous temperature effects on the dynamic yield strengths of metals. The high-temperature effect on the spall strength of metals as well as new possibilities to study the spall phenomena are discussed in Chapter 4. Chapter 5 presents some last results on the failure waves in glasses.

2. A FAST STRESS RELAXATION IN METALS

It is usually recognized that mechanical behavior of metals and alloys is well understood and is well described by modern advanced phenomenological and dislocation models. Nevertheless, there is a series of observations which point out that the high rate of strain of metals in shock waves is accompanied by a specific change in their properties. Let us consider examples.

Figure 1 shows the stress histories in the armco iron and steel samples loaded successively by two compression pulses (Kanel *et al.*, 1978). Measurements were done with the insulated manganin pressure gauges. The insulating films decreased the time resolution at low stresses in the elastic precursor wave, but at stresses of around 4–5 GPa and more the time resolution (~ 50 ns) is good enough. The initial parts of stress profiles shown in Fig. 1 are typical for metals at low peak shock pressures. The first load pulses include the elastic-plastic compression and unloading waves. The amplitude of elastic precursor of the first compression wave is the Hugoniot elastic limit (HEL). There is no indication of a finite purely elastic stress range in the release part of stress profiles. For the elastic-plastic solids, the stress decrease in the elastic portion of the unloading wave should be twice the HEL, however the experimental

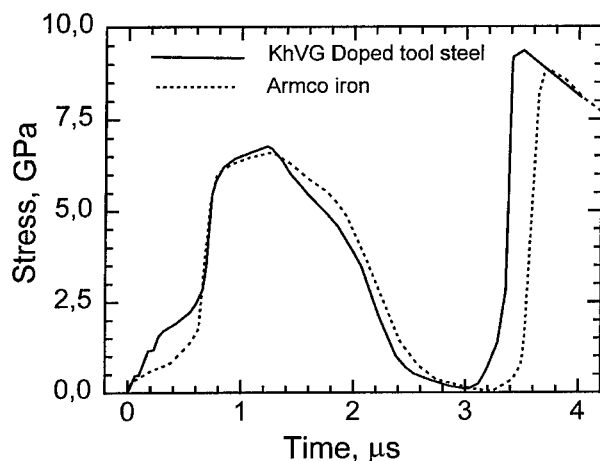


Fig. 1. Stress profiles in the armco iron and steel samples loaded successively by two compression pulses. Measurements were done with manganin gauges embedded on a distance of 15 mm from the impact surface. Low time resolution at small stresses in vicinity of the Hugoniot elastic limit is a result of the gauges insulations.

data show that only the very start of the release could be indicative of purely elastic behavior, the plastic strain starts almost immediately behind the wavefront rarefaction. The stress history also exhibits the change in character, and drop in the amplitude, of the elastic compression precursor in the second load pulse. Similar behavior was observed also for titanium (Kanel *et al.*, 1978) and molybdenum (Furnish *et al.*, 1992). It looks like materials become softer or transition from the elastic-viscous-plastic to elastic-viscous response occurs after the shock compression.

Another example of this series is related to the unloading and reloading of shock-compressed metals (Dremin and Kanel, 1976; Asay and Lipkin, 1978; Asay and Chhabildas, 1981). In contrary to the purely elastic-plastic model, the initial unloading or reloading from the shocked state is determined to be elastic in both cases. Furthermore, the difference between increments in the deviatoric stress in compression and rarefaction waves is not much less than the magnitude of the increments, i.e. the stressed state of matter immediately behind the shock front is almost isotropic.

Finally, until now it has not been clear how the polymorphous transformations occur so rapidly under shock-wave conditions. The basic mechanisms driving and controlling the shock transitions are still uncertain.

From these observations we may conclude that shock waves appear to have a specific effect on matter: relatively high mobility of the crystal lattice and the fast relaxation of shear stresses become possible. For explanation of the phenomenon, observations of the microscopic structure in the shock-compressed state should be attracted. One such technique involves the study of X-ray diffraction during shock wave compression of crystalline solids (Johnson *et al.*, 1970; Egorov *et al.*, 1972). It has been shown (Zaretsky *et al.*, 1991a, 1991b; Zaretsky 1992) that, whereas for bcc metals the ratio of the diffraction peak angles of the initial and shock-compressed states is proportional to the ratio of the lattice constants, this obvious relationship is not maintained for fcc metals. The discrepancy has been explained by Zaretsky *et al.* in terms of formation of the stacking faults. This disturbance of the crystal symmetry leads to a shift of the diffraction peaks in the case of fcc structure, while for bcc lattice the stacking faults produce only broadening of the diffraction peaks and does not produce their shift (Warren, 1959). During the plastic flow, the stacking faults arise as a result of a splitting of complete dislocation in the (111) planes into two partial dislocations in the same planes. Simulations of the weak-shock induced plasticity by the molecular dynamics methods (Mogilevsky and Mynkin, 1978; Holian, 1995) confirm generation of the partial dislocations.

At the maximum concentration of stacking faults, the fcc lattice transforms into a hcp lattice which is not stable. Estimations (Zaretsky, 1992) show that the whole or almost whole plastic strain has to be produced by the partial dislocations to provide the observed anomalous shift of the diffraction peaks. As a result, the stacking faults concentration reaches few percents in shock waves of several GPa peak stress. The large concentration of the stacking faults means that a remarkable amount of metastable phase is produced during the shock compression. Thus, a possible base for the physical description of the observed time-dependent shear stress response is that the lattice becomes unstable and, due to that, the fast stress relaxation becomes possible during disappearing of the metastable phase.

3. RESISTANCE TO PLASTIC DEFORMATION OF METALS AT ELEVATED TEMPERATURES

The effect of strain rate on the plastic flow behavior of metals has been successfully rationalized in terms of the dynamics of dislocations (Kumar and Kumble, 1969). For low rates of mechanical loading, the dislocation motion is aided by thermal fluctuations. The dislocations are obstructed at barriers and a combination of thermal agitation and applied stress field is required to activate the dislocation over the obstacles. At some point (10^3 – 10^4 s⁻¹) between intermediate strain rates and the higher strain rates, the plastic deformation process makes a transition from being dominated by stress-assisted thermal activation to being controlled by the time it takes a mobile dislocation to get from one barrier to the next; this latter time depends on the effective stress and viscous-drag force provided by the perfect lattice. At very high strain rates the applied stress is high enough to overcome instantaneously the usual dislocation barriers without any aid from thermal fluctuations and viscous phonon drag becomes dominant. Clifton (1971) has given the earliest and most complete discussion of transition from thermal activation to dislocation drag in shock-loaded solids; modern state of the question was discussed recently by Johnson and Tonks (1992).

In order to evaluate conditions of the transition from the thermal activation mode to athermal mechanisms of the plastic deformation, measurements over a wide temperature range are necessary. There were just few observations of the mechanical yielding and strength behavior in shock waves at elevated temperatures. Rhode (1969) studied the dynamic yield behavior of iron over a temperature range of 76–573°K. The dynamic yield stress at strain rate of $\sim 10^5$ sec⁻¹ was found to be independent of the temperature in contrast to the highly temperature sensitive quasi-static yield stress which decreased by a factor of 2.5 between 76 and 298°K. It was concluded that the motion of twinning dislocations is the mechanisms of dynamic yielding of iron. According to Asay (1974), the elastic precursor amplitude in bismuth is independent of temperature almost up to 523°K while the melting temperature is 544.4°K. Unlike to that, Duffy and Ahrens (1994) have found the HEL amplitude of molybdenum is reduced by 26–46% relative to its room temperature value reported by Furnish and Chhabildas (1992), but there is not assurance that the tested molybdenum specimens were of the same incident structure.

Figure 2 shows examples of the free-surface velocity profiles in aluminium AD1 (analogous to the Al 1100 alloy) and cast magnesium Mg95 measured with VISAR techniques (Kanel *et al.*, 1996b). The initial temperature of samples was varied from room temperature to near the melting point.

In the profiles presented in Fig. 2, the elastic-plastic compression wave initially accelerates the sample surface. The unloading wave originating from the back of the impactor plate subsequently begins to decrease the free-surface velocity. Interaction of the reflected compression pulse from the free surface and the unloading wave creates tensile stresses within the sample and causes internal spall fracture. Relaxation of tensile stresses at the spall interface produces the subsequent second acceleration wave which appears in the free-surface velocity profile as a spall signal.

Experiments performed at high initial temperature have yielded unexpected

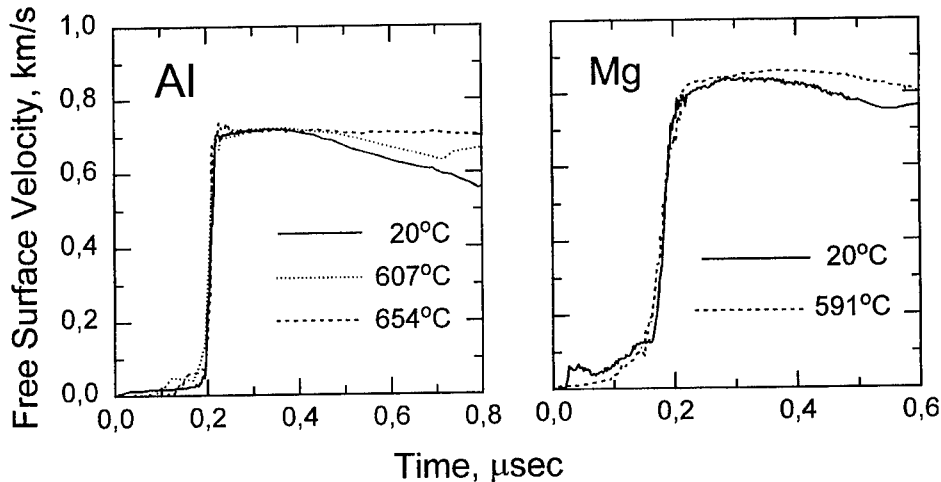


Fig. 2. Examples of the free surface velocity profiles measured in experiments with aluminium and magnesium samples at normal and elevated incident temperature.

behavior: the amplitude of elastic precursor wave, and hence the Hugoniot elastic limit, as temperature approaching melt is achieved becomes substantially larger than the value at ambient temperature. Since the precursor amplitude is determined not only by the yield stress but also by the elastic modules, the result observed does not mean that the dynamic yield stress is growing with increasing temperature. Isoentropic elastic modules of metals as a function of the temperature from 20°C to 640°C have been published by Simmons (1965), and Tallon and Wolfenden (1979). Using these values and the free surface velocity profiles, the stress-strain diagrams were reconstructed by Utkin *et al.* (1997) in a frame of the simple wave approach. Figure 3 presents the results for aluminium. The plastic strain, ε_p , was calculated from the relationship $\varepsilon_p = \varepsilon - \sigma_x / (K + 4/3G)$, where the total strain $\varepsilon = (V_0 - V)/V_0$.

It is difficult to say now whether the observed temperature effect is related to the initial yield strength or the increase in flow stress can be observed over the whole cycle of deformation. We are continuing now these investigations with single-crystalline metal samples and, in general, preliminary results are in agreement with the data discussed here.

Since the high strain rate is controlled by the viscous phonon drag, it is natural to suppose that the growth of phonon viscosity with increasing temperature is a main reason of the observed high dynamic yield strength at elevated temperature. Another explanation is based on spontaneous nucleation of point defects. At high temperatures, some atoms achieve energies sufficient to leave their positions in the lattice and to occupy interstitial positions (Frenkel, 1926) or free positions at surfaces or internal imperfections (voids, grain boundaries, dislocations) (Wagner and Shottky, 1930). It is argued (Kraftmakher and Strelkov, 1970; Goland, 1976), that the equilibrium concentration of vacancies can reach $\sim 0.1\%$ at the melting point. The point defects create additional drag forces for the dislocations. Since only initial magnitudes of the

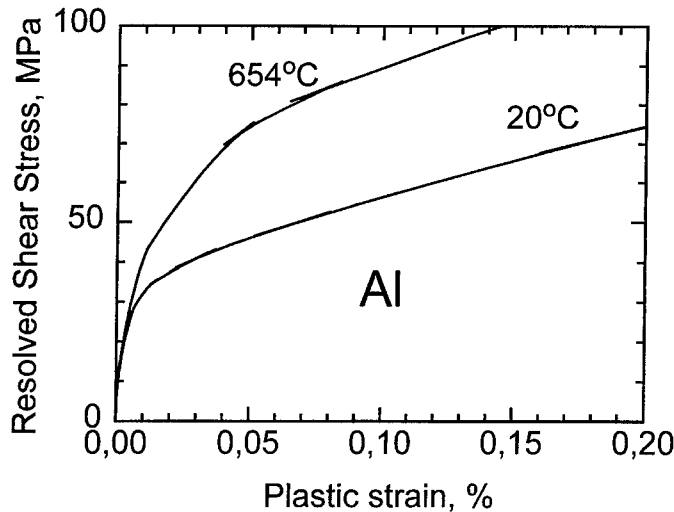


Fig. 3. Deviator stress as a function of the plastic strain in elastic precursor in aluminium at normal and elevated temperatures.

dynamic yield stress were measured, we cannot exclude that the growth of this value is a consequence of condensation of vacancies on pre-existing dislocations. Formation of clouds of vacancies creates an obstacle resisting the activation and motion of dislocations.

If the growth of the dynamic yield strength near melting point will be confirmed for other metals, we will need to revise interpretation of the adiabatic shear bands mechanisms which is treated as a result of deformation instability at a high level of strain and strain rates (Zurek and Meyers, 1996).

4. NEW STUDIES OF THE SPALL FRACTURE PROCESSES

The dynamic tensile strength of materials at load durations of microseconds or less is studied by analyzing spall phenomena under shock pulse action (Davison *et al.*, 1996). Spalling is the process of internal rupture of a body due to tensile stresses generated as a result of compression pulse reflection from the surface. During the dynamic fracture process, many microvoids or microcracks, more or less simultaneously, undergo nucleation, growth, and coalescence in a volume of material to form a failed or spalled region (Curran *et al.*, 1987). Large overstresses even near the ultimate theoretical tensile strength can be reached under these conditions due to the high rate of stress application (Kanel *et al.*, 1994). The amount of activated damage nucleation sites sharply increases with increasing tensile stress because smaller defects get involved.

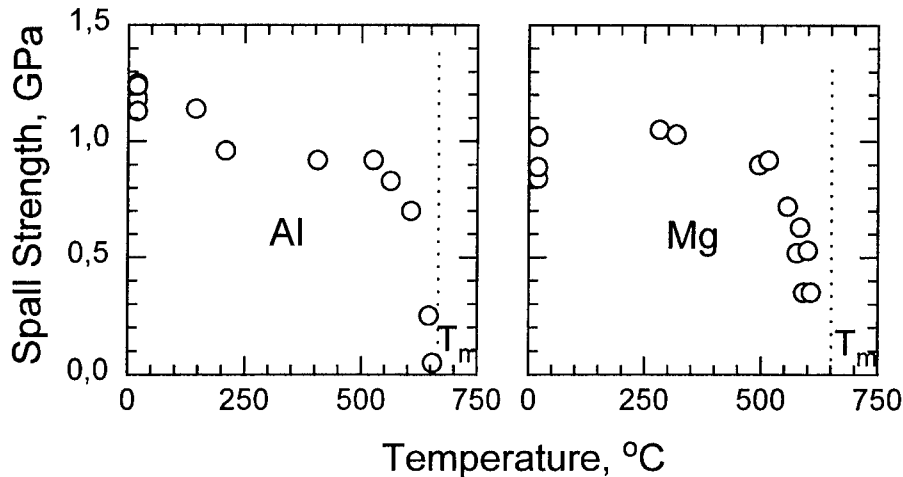


Fig. 4. Spall strength of aluminium AD1 and magnesium Mg95 as a function of the initial temperature.

Figure 4 shows the dependence of the spall strength on the initial temperature for aluminium and magnesium (Kanel *et al.*, 1996). In general, the spall strength decreases with initial temperature but this decrease occurs much slower than it takes a place for the quasistatic tensile strength. A larger drop in the spall strength is associated with heating above ~ 0.9 of the melting temperature in the absolute scale. A theoretical description of the dependence should be still developed.

As a rule, kinematic parameters of shock-wave loads are monitored in one point of the sample. Since the fracture is a process of nucleation and growth of cracks or voids, it is often important to know a space picture of the phenomenon. It seems, a first step in this direction has been done by Ravichandran and Clifton (1989) and Prakash and Clifton (1992) when they investigated a crack propagation under conditions of plane strain. In these experiments, the rear surface motion was monitored at four pre-determined points. The recently developed line imaging interferometer technique (Baumung *et al.*, 1996a) provides capability to record simultaneously the velocity histories in many points along a line on the sample surface. With this technique, we can hope to construct a strength map and to see some new details of dynamics of the fracture initiation and growth.

Figure 5 presents the line imaging ORVIS interferogram of an experiment with a 0.82 mm thick magnesium sample (Baumung *et al.*, 1997). It is clear, we may be able to see any variations in the fracture only in tests with a scale close to that of nonuniformity of the material. Because of this, experiments were carried out at a small load durations using a pulse ion beam (Baumung *et al.*, 1996b) as a shock-wave generator. Each point of vertical sections in the interferogram corresponds to a separate point of the measuring line on the sample surface. A vertical displacement of the interference fringes is proportional to velocity increments. The amplitude of the initial velocity jump in the shock front is not resolved, however, exact knowledge of the velocity peak is not so important for the spall strength measurements.

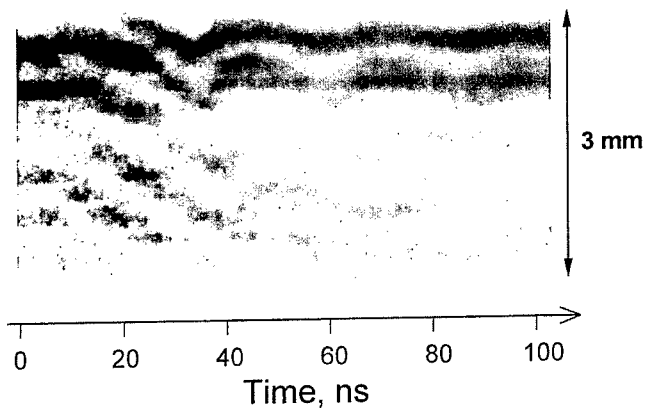


Fig. 5. Line imaging ORVIS interferogram of experiment with 0.82 mm thick cast magnesium Mg95 sample.

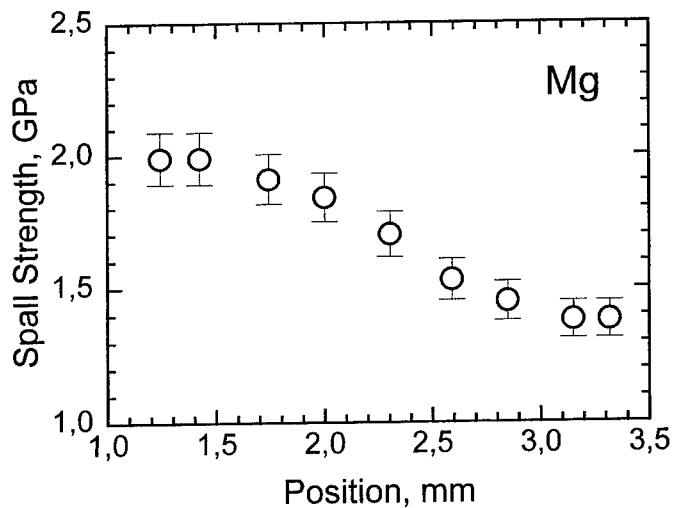


Fig. 6. The spall strength distribution in magnesium calculated from the interferogram presented in Fig. 5.

The original cast magnesium Mg95 has a grain size in the order of 1–2 mm. The field of view of the velocimeter included two large grains that are visible on the interferogram due to the different reflectivity. Results of evaluations presented in Fig. 6 indicate that the spall strength is changing from point to point in the sample, but, despite of the grain boundary in the ORVIS field of view, there is no sharp jump in the strength distribution. It is necessary to mention that, under conditions of one-dimensional shock loading of metals with low yield strength, the stress tensor is nearly spherical. In other words, there is no large anisotropy of the loading, and there is no

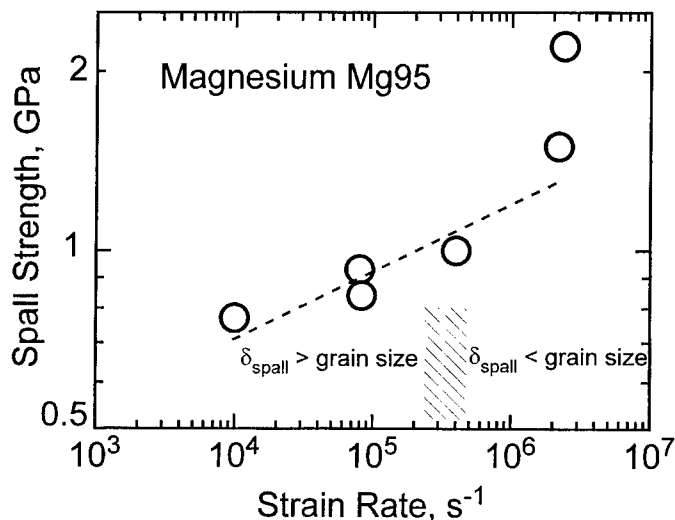


Fig. 7. Spall strength of magnesium as a function of strain rate at unloading in the incident compression pulse. δ_{spall} is the spall plate thickness. Two upper points show the spall strength range covered by the data presented in Fig. 6.

strength jump between grains of different orientation of their crystal structure. Of course, the inter-granular boundary in the ORVIS field of view has to be a site of easier nucleation of fracture, but it seems such fine details can be observed only at much larger magnifications.

Figure 7 shows result of measurements in comparison with the resistance to spall fracture of the same magnesium at lower strain rates. In many previous investigations, such dependences are well approximated by a power function over a wide range of strain rate. The new data at highest strain rate are deflected from the power dependence to larger values of the spall strength. The spall thickness in this shot varied between ~ 60 and $\sim 80 \mu m$, that is much smaller than the grain size. This means the spall crack had to cross the grains and the measured spall strength should correspond to that of crystals. It has been found earlier (Kanel *et al.*, 1994, 1996a) that the spall strength of copper and molybdenum single crystals exceeds that of polycrystalline samples by a factor of ~ 2 for molybdenum and ~ 3 for copper. Since the deviation of the new data from the extrapolated dependence, in average, is not so large, we may suppose that, in this experiment, the main spall crack at least partly coincides with the inter-granular boundary below the sample surface. Thus, both intra-granular and inter-granular strength were observed, and the intra-granular strength is as much as twice the strength on inter-granular boundaries.

The preliminary data presented here show that the line-imaging interferometry of free-surface velocity profiles is a way to analyze uniformity of strength properties of materials. In the following, we are planning similar measurements at increased space resolution to see the fracture initiation in visible grain boundaries.

5. INELASTIC DEFORMATION AND FRACTURE OF GLASSES UNDER IMPACT LOADING

The dynamic fracture of brittle materials occurs through a formation of multiple cracks. The impact loading of a glass and, probably, other brittle materials can be accompanied by an appearance of failure wave. The failure wave is a network of cracks that are nucleated on the surface and propagate into the stressed body. We may hope that the investigations of failure wave in glasses provide information about the mechanisms and general rules of nucleation, growth and interactions of the multiple cracks and will help us to interpret better the experiments with other hard brittle materials, like ceramics and rocks.

The failure wave was observed under the planar shock-wave compression below the Hugoniot elastic limit. In experiments described by Razorenov *et al.* (1991) and Kanel *et al.* (1992), the shock pulse was introduced into the glass sample through a copper baseplate. When the peak stress of the shock pulse was far below the elastic limit, a short negative velocity pullback appeared in the free-surface velocity profile as a result of the re-reflection of the rarefaction wave at the sample-baseplate interface. In contrast, however, no re-reflected tensile pulses were observed in experiments near the elastic limit. Instead, a small velocity rise was indicated on the free surface profile and the moment of this velocity rise was earlier than the elastic wave reverberation in the sample. This modification of the wave process was explained in terms of the formation of a failed layer near the sample-baseplate interface under the uniaxial compression. An expansion of the failed layer was interpreted as a failure wave propagation.

Brar *et al.* (1991, 1992) have shown by direct measurements on a soda lime glass that behind the failure wave the tensile strength drops to zero, or almost to zero, and the transverse stress increases, indicating a decrease in shear strength. Raiser and Clifton (1994a, 1994b) have found that the surface roughness of the aluminosilicate glass between 0.04 and 0.52 μm does not appear to play a significant role in the formation of a failure wave. Independently on the surface roughness, they observed a high spall strength of the glass when the compressive stress was around 3.5 GPa while at the peak stresses of 7.5–8.4 GPa the spall strength was high ahead of the failure front and was low behind of it. They have also got evidence of increasing of the failure wave velocity with increasing impact stress. Dandekar and Beaulieu (1995) have found that failure wave is initiated in a soda lime glass at an impact stress between 4.7 GPa and 5.2 GPa. The propagation velocity of the failure wave is determined to be 1.56 km/s and it remains constant with the thickness of glass sample between 3.1 and 9.4 mm at the impact stress of 5.2 GPa. Espinosa *et al.* (1997) observed a progressive reduction in normal stress behind the failure wave close to the impact surface. They have concluded that the inelastic process responsible for the reduction in shear strength has well defined kinetics. While much work has concentrated around relatively open structure, lower density glasses, Bourne *et al.* (1996b) observed the failure wave in a higher density filled lead glass which has a density of 5180 kg/m³.

The failure wave was visualized by Brar and Bless (1992), Bourne and Rosenberg (1996a) and Senf *et al.* (1995). Most interesting results were obtained in experiments

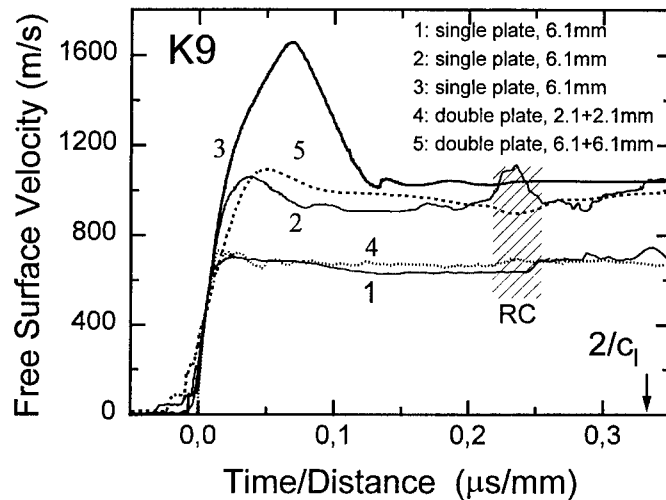


Fig. 8. Results of measurements of the free-surface velocity profiles for K9 glass samples below and above the Hugoniot elastic limit. The area of recompression pulse appearance is marked as RC.

with large specimens of the optical glass K5 impacted by blunt steel cylinders (Senf *et al.*, 1995). The experiments demonstrated several modes of the fracture nucleation. Around the edges of projectile many cracks are initiated by the propagating surface wave, which form the conical shaped fracture zone. In the central part, the damage zone exhibits a planar front that propagates with velocity equalling the terminal crack velocity of 1550 m/s in this type of glass. Besides the fracture nucleation on the sample surface, separate crack nucleation sites were also activated on the microdefects inside the stressed glass target. As a result, several spherical or nearly spherical failure waves were formed ahead of the main front.

Figure 8 shows the free-surface velocity profiles measured in experiments with Chinese K9 crown glass. In more detail, these experiments will be described in a separate paper (Kanel *et al.*, 1997). The targets were composed of one or two glass plates 2–6 mm thick. In the diagram, the time, t , has been normalized as t/h , where h is the sample thickness in the case of single-plate sample or the second piece thickness in the case of two-plate sample. A few weak velocity steps before the main front in some shots are the result of shock waves in the residual and infiltrated gas between the impactor plate and the sample. In the shot 3 at maximum peak stress, the inelastic deformation in the compression wave is starting in vicinity of 1200 m/s of the free-surface velocity that corresponds to the Hugoniot elastic limit (HEL) of about 9 GPa and the compressive yield strength, $Y = \sigma_{\text{HEL}}(1 - 2\nu)/(1 - \nu)$, of ~ 6.6 GPa. The free-surface velocity profiles of this shot contains the unloading part of the incident shock pulses that exhibit a high dynamic tensile strength of the material above the HEL.

When the peak stress does not exceed the Hugoniot elastic limit, the wave reflection inside the sample is recorded in the vicinity of 0.22–0.25 $\mu\text{s/mm}$ of the normalized time both for single-plate and composed targets. This confirms formation

of the failure wave under shock compression below the HEL. Estimations have given the average propagation velocity of the failure wave of 0.91 km/s at 5.2 GPa and 1.25 km/s at 7.8 GPa in the K9 glass. Comparison of experimental data for one-piece and two-piece targets shows that the failure wave were nucleated on the piece surfaces, independently on whether it is the impact surface or the surface of piece inside the composed sample. Similar results have been obtained for a dense flint glass also. Since the failure waves are nucleated on the internal interfaces of two-plate targets, we may certainly confirm that, unlike to phase transitions or elastic-plastic responses, the failure wave is a non-local phenomenon in the sense that response of each elementary volume in the body depends not only on its local state, but also on whether the failure wave has approached to this point or not.

Silicate glasses exhibit a high yield strength at shock compression. The very high yield strength of glasses is associated with their amorphous state because the dislocation slip is impossible in the irregular structure. When the peak stress exceeds the Hugoniot elastic limit, brittle glasses become ductile. Ductility of glasses is caused by a loose structure with a large amount of molecular-sized microvoids. It is known that glasses show gradual structural changes resulting in increased density (Arndt and Stoffer, 1969). Since the densification occurs under Vickers indentation, it is supposed (Ernsberger, 1968) that the irreversible densification and compaction in the silicate structure are responsible for the plastic flow properties of glasses under high pressure. This densification, the degree of which can be varied to some extent by variation of pressure, temperature, and shear strain, remains irreversible at normal conditions. Once the plastic flow started, the stress relaxation reduces the stress concentration at the crack tip and, by this way, stops propagation of cracks. Thus, the inelastic deformation of glasses under compression above the HEL may occur without cracking. Unlike to cracks, the plastic flow is not associated with formation of free surfaces inside the body and, respectively, does not destroy the cohesive strength.

A microscopic examination of the deformed zone in glass under pyramidal indentations (Hagan, 1980) shows that inelastic deformation is concentrated in shear faults of negligible thickness produced by genuine shear displacements without cracking. Under dynamic conditions, localization of inelastic deformation is accompanied by a temperature rise within the shear bands that, in turn, should decrease the densification threshold and provide the ductility under unloading. The high spall strength revealed in the stress range above the HEL means that the ductility is preserved even at following tension.

Below the HEL, inelastic deformation may occur by cracking. A mechanism of inelastic deformation in the failure wave is not quite clear yet. Clifton (1993) expressed the fundamental doubts about extensive cracking under the uniaxial strain compression. However, it is known that applied stress is locally modified by a crack, and may become tensile at certain points on the crack surface, even when applied stress is wholly compressive (Griffith, 1924; McClintock and Argon, 1966), so the cracks may grow in response to this local tensile stress. The growth of cracks in glass under compression was observed by Brace and Bombolakis (1963). They have found that the most severely stressed cracks are inclined at about 30° to the axis of compression.

Our previous investigations (Kanel and Molodets, 1976) of behavior of the K8

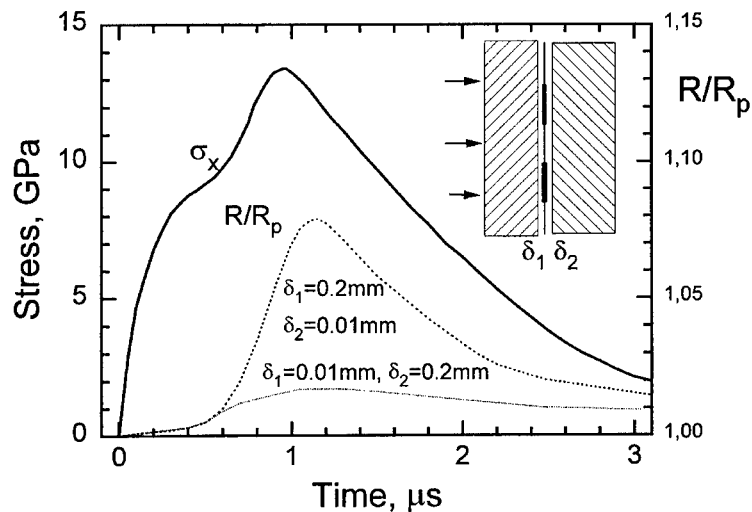


Fig. 9. Stress history in the K8 glass target impacted by a PMMA flyer plate (6 mm thickness, 3.15 km/s impact velocity). Measurements were carried out at the distance of 10.5 mm from the impact surface with manganin and constantan gauges insulated by teflon films with thickness of δ_1 and δ_2 , where δ_1 is the thickness of film placed toward the impact side, δ_2 is the film thickness toward the sample rear surface. Dotted lines show the component of gauge resistance increase that is provided by the gauge elongation.

crown glass under shock compression and unloading brings to conclusion that there is a mutual influence of the cracking and densification. In this study, a distortion of internal interfaces of the two-piece glass targets was revealed at the uniaxial compression above the HEL. The distortion appeared in elongation of the manganin piezoresistant foil gauges used for recording the stress profiles. Figure 9 presents, simultaneously with the stress history, the component of gauge resistance increase that is provided by the gauge elongation. The foil gauges feel the surface distortion if the nonuniformity size is comparable or larger than the foil thickness. Obviously, the finding is a result of localization of deformation which forms blocks bounded by cracks or shear bands. According to the observations, the peak distortion increases, as the ramping of the compression wave grows. This observation may be interpreted in terms of different concentration of activated cracks or shear bands and respectively different size of the blocks. It seems, ultimate amount of the shear faults is activated when the large stress is applied suddenly. When the stress grows with some limited rate, the larger faults provide relaxation of the shear stresses and, by this way, prevent activation of smaller faults which need higher stresses to activate them.

Figure 9 shows that, at stresses above the HEL, the distortion of the surface through which the compression wave goes out from the first piece of the target is much less than the distortion of surface through which the wave enters into the second plate. In other words, larger blocks are formed when the cracks grow in the direction of loading. We may conclude also that the ductile shear strain is concentrated in continuation of the cracks that have been activated first in the elastic deformation phase. Very

surprisingly is the reversibility of surface distortion which means that the unloading strain occurs along the same shear faults as the strain at compression. Another important observation is that the maximum of the surface distortion is delayed relatively to the stress maximum. Obviously, mutual shifting of blocks and, correspondingly, the shear stress relaxation are continuing until the shear stresses will not be reduced to zero.

It would be important to explain peculiarities of the free-surface velocity profiles when the failure wave is formed. In most of the experiments, the free-surface velocity profiles contain smooth maxima immediately behind the front. Computer simulation of the phenomena performed by Kanel *et al.* (1992) showed that the "rounding" of top of the compression wave can be formed as a result of decreasing propagation velocity of the failure wave, or increasing yield strength of comminuted material, or increasing relaxation time with increasing propagation distance. Brace and Bombolakis (1963), in their study of the growth of cracks in glass under compression, have found that the cracks grow along a curved path which becomes parallel with the direction of compression. When this direction is attained, growth stops. This observation may explain the decreasing velocity of the failure wave or increasing relaxation time. Unfortunately, low reproducibility of the wave profiles does not permit to make certain conclusions on the wave dynamics of the phenomenon.

6. CONCLUSION

Investigations of material properties under shock-wave loading are carried out with a main goal to predict their response to a high-velocity impact, explosion, or to impulsive laser and particle beams. In this regard, it seems that relatively simple empirical or semiempirical constitutive models are quite sufficient for most practical applications. Nevertheless, more careful examination of accumulated experimental data displays the complexities of physical and mechanical processes active in the shock-wave event. The unidentified shock-wave properties of solids are fascinating researches and can be expected to challenge the experimenters and theorists for a long time to come. New prospects are created by the development of new experimental technique.

In the present review, possible mechanisms of a fast stress relaxation in ductile crystalline materials, anomalous temperature effect on the yield and tensile strength of metals, new studies of the dynamic fracture, and the failure waves in glasses were discussed.

From observations of the stress profiles in metals at various ways of shock loading and anomalous X-ray diffraction pattern shifts, we have concluded that a large amount of the stacking faults is produced in shock waves. As a result, the lattice becomes unstable and, due to that, the fast stress relaxation becomes possible. Probably, such behavior can be described in terms of models of multicomponent media with variable concentrations of components.

Unexpected growth of the dynamic yield strength as the melting temperature is approached, still needs confirmation and deeper interpretation. The viscous dislocation drag and spontaneous nucleation of point defects can be a possible base for

mechanisms of the phenomenon. If the growth can be confirmed, we probably should reconsider the nature of adiabatic shear band at high-speed deformation. Measurements showed a precipitous drop in the spall strength of preheated samples as temperatures approached the melting point while at temperatures up to $\sim 0.9 T_m$ the spall strength decreased very slowly. A nature of the precipitous drop still needs an explanation.

The recently developed line imaging interferometer technique provides the capability to construct a strength map along the sample surface. With this technique, experiments on coarse-grain cast magnesium have been performed. Both in-granular and inter-granular strength were observed and in-granular strength exceeds that on inter-granular boundaries by as much as a factor of two.

Silicate glasses exhibit a high yield strength at shock compression. When the peak stress exceeds the Hugoniot elastic limit, brittle glasses become ductile that appears in their high spall strength at large peak stresses. The irreversible densification is responsible for the plastic flow properties of glasses under high pressure. Below the HEL, inelastic deformation may occur by cracking. The multiple crack network forms the failure wave that is initiated on the impact surface, as well as on any internal surfaces, and propagates into the stressed body with subsonic speed. In both cases deformation is localized with the formation of blocks bounded by cracks or shear bands. As a result, a distortion of internal interfaces of the two-piece glass targets can be observed. A mathematical description of the failure wave should account a non-local nature of the phenomenon.

ACKNOWLEDGEMENT

This study was supported by International Science Foundation, grant numbers MAH000 and MAH300, and by the Russian Foundation for Basic Research Grant number 97-02-17701.

REFERENCES

- Arndt, J. and Stoffer, D. (1969) Anomalous changes in some properties of silica glass densified at very high pressure. *Phys. and Chem. of Glasses*, **10**(3), 117–134.
- Asay, J. R. and Chabildas, L. C. (1981) Determination of the shear strength of shock-compressed 6061-T6 aluminium. In *Shock Waves and High-Strain-Rate Phenomena in Metals*, ed. Meyers, M. M. and Murr, L. E. Plenum Publishing Corp., New York, NY.
- Asay, J. R. and Lipkin, L. (1978) A self-consistent technique for estimating the dynamic yield strength of a shock-loaded material. *J. Appl. Phys.* **49**, 4242.
- Asay, J. R. (1974) Shock-induced melting in bismuth. *J. Appl. Phys.* **45**, 4441–4452.
- Baumung, K., Kanel, G. I., Razorenov, S. V., Rusch, D., Singer, J. and Utkin, A. V. (1997) Investigations of the dynamic strength variations in metals, *J. Phys.*, IV France, **7**, C3–927.
- Baumung, K. *et al.* (1996a) Shock-wave physics experiments with high-power proton beams. *Laser and Particle Beams*, **14**, 181–209.
- Baumung, K., Singer, J., Razorenov, S. V. and Utkin, A. V. (1996b) Hydrodynamic proton beam-target interaction experiments using an improved line-imaging velocimeter. In *Shock Compression of Condensed Matter—1995*, eds. S. C. Schmidt and W. C. Tao, pp. 1015–1018. AIP Conference Proceedings 370, Woodbury, New York.

- Bourne, N. K., Millett, J. C. F. and Rosenberg, Z. (1996) Failure in a shocked high-density glass. *J. Appl. Phys.* **80**(8), 4328–4331.
- Bourne, N. K. and Rosenberg, Z. (1996a) The dynamic response of soda-lime glass. In *Shock Compression of Condensed Matter—1995*, eds. S. C. Schmidt and W. C. Tao, pp. 567–572. AIP Conference Proceedings 370.
- Brace, W. F. and Bombolakis, E. G. (1963) A note on brittle crack growth in compression. *J. Geophys. Res.* **68**(12), 3709–3713.
- Brar, N. S. and Bless, S. J. (1992) Failure waves in glass under dynamic compression. *High Pressure Research*, **10**, 773–784.
- Brar, N. S., Rosenberg, Z. and Bless, S. J. (1991) Spall strength and failure wave in glass. *J. de Physique IV*, Coll. C3, Suppl. au. J. de Physique III, 1, C3-639-644.
- Clifton, R. J. (1971) Plastic waves: theory and experiment. In *Shock Waves and the Mechanical Properties of Solids*, eds. J. J. Burke and V. Weiss. pp. 73–116. Syracuse University Press.
- Clifton, R. J. (1993) Analysis of failure waves in glasses. *Appl. Mech. Review*, **46**(12), 540.
- Curran, D. R., Seaman, L. and Shockey, D. A. (1987) Dynamic failure of solids. *Phys. Rept.* **147**, 253–388.
- Dandekar, D. P. and Beaulieu, P. A. (1995) Failure wave under shock wave compression in soda lime glass. In *Metallurgical and Material Applications of Shock-Wave and High-Strain-Rate Phenomena*, eds. L. E. Murr, K. P. Staudhammer and M. A. Meyers pp. 211–218. Elsevier Science B. V.
- Davison, L., Grady, D. E. and Shahinpoor, M. (1996) *High Pressure Shock Compression of Solids—II. Dynamic Fracture and Fragmentation*. Springer-Verlag New York, Inc.
- Dremin, A. N. and Kanel, G. I. (1976) Compression and rarefaction waves in shock-compressed metals. *J. Appl. Mech. Tech. Phys.* **2**, 146–153.
- Duffy, T. S. and Ahrens, T. J. (1994) Dynamic response of molybdenum shock compressed at 1400 C. *J. Appl. Phys.* **76**(2), 835–842.
- Egorov, L. A., Nitochkina, E. V. and Orekin, Y. K. (1972) Recording of debyegram of aluminium compressed by a shock wave. *Sov. Phys.-JETP Lett.* **16**, 4–6.
- Ernsberger, F. M. (1968) Role of densification in deformation of glasses under point loading. *J. Amer. Ceram. Soc.* **51**(10), 545–547.
- Espinosa, H. D., Xu, Y. and Brar, N. S. (1977) Micromechanics of failure waves in glass. Part I: experiments. *J. Am. Cer. Soc.* **80**(8), 2061–2073.
- Frenkel, J. I. (1926) *Z. Phys.* **35**, 652.
- Furnish, M. D., Chhabildas, L. C., Steinberg, D. J. and Gray III, G. T. (1992) Dynamic behavior of fully dense molybdenum. In *Shock Compression of Condensed Matter 1991*, eds. S. C. Schmidt, *et al.*, pp. 419–422. Elsevier Science Publishers B.V.
- Goland, A. N. (1976) In *Struttura Atomica e Proprieta Meccaniche dei Metalli* (Rendiconti della Scuola Internazionale di Fisica “Enrica Fermi”, LXI Corso), Societa Italiana di Fisica, Bologna, Italy.
- Griffith, A. A. (1924) Theory of rupture. *Intern. Congr. Appl. Mech.*, ed. J. Waltman, pp. 55–63. Delft.
- Hagan, J. T. (1980) Shear deformation under pyramidal indentations in soda-lime glass. *J. Mat. Sci.* **15**, 1417–1424.
- Holian, B. L. (1995) Atomistic computer simulations of shock waves. *Shock Waves* **5**, 149–157.
- Johnson, J. N. and Tonks, D.L. (1992) Dynamic plasticity in transition from thermal activation to viscous drag. In *Shock Compression of Condensed Matter 1991*, eds. S. C. Schmidt, *et al.*, pp. 371–378. Elsevier Science Publishers B.V.
- Johnson, Q., Mitchell, A. C., Keeler, R. N. and Evans, L. (1970) X-ray diffraction during shock wave compression. *Phys. Rev. Lett* **25**, 1099–1101.
- Kanel, G. I. and Molodets, A. M. (1976) Behavior of the K8 glass under dynamic compression and following unloading. *Sov. Phys.—Tech. Phys.*, **XLVI**(2), 398–407.
- Kanel, G. I., Molodets, A. M. and Dremin, A. N. (1978) Change of the strength properties of metals in shock wave. *Phys. Met. Metall.* **46**(1), 201–203.
- Kanel, G. I., Razorenov, S. V. and Fortov, V. E. (1992) The failure waves and spallations in

- homogeneous brittle materials. In *Shock Compression of Condensed Matter 1991*, eds. S. C. Schmidt, *et al.*, pp. 451–4554.
- Kanel, G. I., Razorenov, S. V. and Utkin, A. V. (1996a) Spallation in solids under shock-wave loading: analysis of dynamic flow, methodology of measurements, and constitutive factors. In *High Pressure Shock Compression of Solids—II. Dynamic Fracture and Fragmentation*, eds. L. Davison, D. E. Grady and M. Shahinpoor. pp. 1–24. Springer-Verlag New York, Inc.
- Kanel, G. I., Razorenov, S. V., Bogatch, A., Utkin, A. V., Fortov, V. E. and Grady, D. E. (1996b) Spall fracture properties of aluminium and magnesium at high temperatures. *J. Appl. Phys.* **79**(11), 8310–8317.
- Kanel, G. I., Razorenov, S. V., Utkin, A. V., Baumung, K., Karow, H. U. and Licht, V. (1994) Spallation near the ultimate strength of solids. In *High-Pressure Science and Technology—1993*, eds. S. C. Schmidt, J. W. Shaner, G. A. Samara and M. Ross. pp. 1123–1126. AIP Press, NY.
- Kanel, G. I., Razorenov, S. V., Utkin, A. V., Hongliang He, Xianming Zhou, Xiaogang Jin (1998) Influence of the load conditions on the failure wave in glasses. To be published in *High Pressure Research*.
- Kraftmakher, Ya. A. and Strelkov, P. G. (1970) In *Vacancies and Interstitials in Metals*, ed. A. Seeger, D. Schumacher, W. Schilling and J. Diehl, p. 59. North-Holland, Amsterdam.
- Kumar, A. and Kumble, R. G. (1969) Viscous drag on dislocations at high strain rates in copper. *J. Appl. Phys.* **40**(9), 3475–3480.
- McClintock, F. A. and Argon, A. S. (1966) *Mechanical behavior of materials*. Addison-Wesley Publ.
- Mogilevsky, M. A. and Mynkin, I. O. (1978) Effect of the point defects on one-dimensional compression of a lattice. *Combust. Explo. Shock Waves* **14**(5), 159–163.
- Prakash, V. and Clifton, R. J. (1992) Experimental and analytical investigation of dynamic fracture under conditions of plane strain. In *Fracture Mechanics: Twenty-second Symposium* (Volume 1), ASTM STP 1131, eds. H. A. Ernst *et al.*, pp. 412–444. American Society for Testing and Materials, Philadelphia.
- Raiser, G. and Clifton, R. J. (1994a) Failure waves in uniaxial compression of an aluminosilicate glass. In *High Pressure Science and Technology—1993*, eds. S. C. Schmidt, *et al.*, AIP Conference Proceedings 309, 1039–1042.
- Raiser, G., Wise, J. L., Clifton, R. J., Grady, D. E. and Cox, D. E. (1994b) Plate impact response of ceramics and glasses. *J. Appl. Phys.* **75**(8), 3862–3869.
- Razorenov, S. V., Kanel, G. I., Fortov, V. E. and Abasehov, M. M. (1991) The fracture of glass under high-pressure impulsive loading. *High Pressure Research* **6**, 225–232.
- Ravichandran, G. and Clifton, R. J. (1989) Dynamic fracture under plane wave loading. *Int. J. of Fracture*, **40**, 157–201.
- Rhode, R. W. (1969) Dynamic yield behavior of shock-loaded iron from 76 to 573 K. *Acta Metallurgica*, **17**, 353–363.
- Senf, H., Strauburger, E. and Rothenhausler, H. (1995) Visualization of fracture nucleation during impact in glass. In *Metallurgical and Material Applications of Shock-Wave and High-Strain-Rate Phenomena*, eds. L. E. Murr, K. P. Staudhammer and M. A. Meyers, pp. 163–170. Elsevier Science B.V.
- Simmons, G. (1965) Single crystal elastic constants and calculated aggregate properties. *J. Grad. Res. Centr.* **34**, 1–269.
- Tallon, J. L. and Wolfenden, A. (1979) Temperature dependence of the elastic constants of aluminium. *J. Phys. Chem. Solids* **40**(11), 831–837.
- Utkin, A. V., Kanel, G. I., Razorenov, S. V., Bogach, A. A. and Grady, D. E. (1998) Elastic modulus and dynamic yield strength of metals near the melting temperature. To be published in *Shock Compression of Condensed Matter—1997*.
- Wagner, C. and Schottky, W. Z. (1930) *Phys. Chem.* **11**, 163.
- Warren, B. E. (1959) X-ray studies of deformed metals. *Prog. Metal. Phys.* **8**, 379–396.
- Zaretsky, E. B. (1992) X-ray diffraction evidence for the role of stacking faults in plastic deformation of solids under shock loading. *Shock Waves* **2**, 113–116.

- Zaretsky, E. B., Mogilevsky, P. A., Kanel, G. I. and Fortov, V. E. (1991a) Installation for X-ray diffraction studies of shock-compressed materials. *High. Temp.* **29**, 1002–1008.
- Zaretsky, E. B., Mogilevsky, P. A., Kanel, G. I. and Fortov, V. E. (1991b) X-ray diffraction study of phase transition mechanism in shock-compressed KCl single crystal. *Dokl. AN SSSR* (Soviet Physics—Doklady) **318**, 111–115.
- Zurek, A. K. and Meyers, M. A. (1996) Microstructural aspects of dynamic fracture. In *High-Pressure Shock Compression of Solids II: Dynamic Fracture and Fragmentation* eds. L. Davison, M. Shahinpoor and D. Gray. pp. 25–70. Springer-Verlag New York, Inc.



Pergamon

J. Mech. Phys. Solids, Vol. 46, No. 10, pp. 1887–1908, 1998

© 1998 Elsevier Science Ltd. All rights reserved

Printed in Great Britain

0022-5096/98 \$—see front matter

PII: S0022-5096(98)00046-5

ON THE SHOCK INDUCED FAILURE OF BRITTLE SOLIDS

NEIL BOURNE*†, JEREMY MILLETT‡, ZVI ROSENBERG‡
and NATALIE MURRAY†

† Shock Physics, PCS, Cavendish Laboratory, Madingley Road, Cambridge, CB3 0HE, UK.

‡ Raftael, PO Box 2250, Haifa, Israel

(Received 20 December 1997; in revised form 21 February 1998)

ABSTRACT

The response of brittle materials to uniaxial compressive shock loading has been the subject of much recent discussion. The physical interpretation of the yield point of brittle materials, the Hugoniot elastic limit (HEL), the dependence of this threshold on propagation distance and the effect of polycrystalline microstructure remain to be comprehensively explained. Evidence of failure occurring in glasses behind a travelling boundary that follows a shock front has been accumulated and verified in several laboratories. Such a boundary has been called a failure wave. The variations of properties across this front include complete loss of tensile strength, partial loss of shear strength, reduction in acoustic impedance, lowered sound speed and opacity to light. Recently we have reported a similar behaviour in the polycrystalline ceramics silicon carbide and alumina. It is the object of this work to present our observations of these phenomena and their relation to failure and the HEL in brittle materials. © 1998 Elsevier Science Ltd. All rights reserved.

Keywords: dynamic fracture, shock waves, ceramic material, glass material, plate impact.

1. INTRODUCTION

The dynamic response of brittle materials to impact results primarily from an interest in their possible use as armour materials or as engine turbine blades. The early literature (Ahrens and Linde, 1968; Graham and Brooks, 1971; Gust *et al.*, 1973; Gust and Royce, 1971) showed ceramic materials to exhibit very high dynamic compressive strengths (HELs). Munson and Lawrence (1979) used the velocity interferometry system for any reflector (VISAR) to obtain accurate figures for the HEL and generated renewed interest in ceramics in impact situations. Further studies have extended the range of materials characterised, a review of which appears in Rosenberg (1992). The most comprehensive recent review of the field is that of Grady (1996).

In recent years there has been some controversy over whether the HEL of polycrystalline ceramics displays precursor decay. Early work by Gust and Royce (1971) showed that both hot pressed alumina and boron carbide exhibit a decay in elastic precursor amplitude with thickness but they could find no consistent trend in the other materials studied. Rosenberg *et al.* (1988) reported a steady HEL only for tile thickness greater than 10 mm in both 76 and 99% purity aluminas. Much interest has

* To whom correspondence should be addressed. E-mail: nkb10@phy.cam.ac.uk

centred on the testing of higher purity aluminas with Bourne *et al.* (1994a) showing precursor decay in 96% pure aluminas and Stachler *et al.* (1994) observing this effect in a 99.99% pure material. Cagnoux and Longy (1988) and Grady (1994a) observe no influence upon the value of the HEL for their high purity aluminas, although Grady defines his HEL at a different point in the loading history. The effect can also manifest itself as an increase in amplitude of the elastic precursor with increasing driving stress as was noted in several works (Bourne *et al.*, 1994b; Munson and Lawrence, 1979; Murray *et al.*, 1996).

There has also been extensive research over the last three decades into the response of various glasses to impact loading (Abou-Sayed and Clifton, 1976; Ananine *et al.*, 1974a,b; Barker and Hollenbach, 1970; Bless *et al.*, 1988; Cagnoux, 1982; Grady *et al.*, 1975; Kane *et al.*, 1977; Kondo *et al.*, 1983; Kondo *et al.*, 1981; Wackerle, 1962). The materials investigated have varied from the more open-structure materials such as fused silica and borosilicate, through the partially filled soda-lime, to the highly filled lead glasses. The open structure glasses show high Hugoniot elastic limits (HELs) in the range 6–9 GPa (Bourne *et al.*, 1996d; Holmquist *et al.*, 1995) and spall strengths (over 4 GPa) resulting from their amorphous silicate network structure (Rosenberg *et al.*, 1985). This structure also gives rise to the possibility of densification during compression and this manifests itself in leading ramps on the rising edge of the wave (for comparison of three types of glass used in this study see Bourne *et al.*, 1996c). The highly filled glasses on the other hand exhibit fast rising elastic waves and have similar wave profiles to polycrystalline ceramics (Bourne *et al.*, 1996b). Such materials have lower HELs in the 4–5 GPa range since the network structure is disrupted by the presence of the large lead atoms which fill the matrix. All of the glasses show pronounced elastic precursor decay with target thickness (Bourne *et al.*, 1996a). This effect has been shown to be reduced by lowering temperature (Dremin *et al.*, 1992).

Rasorenov *et al.* (1991) were the first to observe the phenomenon of delayed failure behind the elastic wave in glass, across a front which has been called a fracture or more lately a failure wave. Such a wave was proposed by Nickolaevskii (1981) who used the concept of a wave of fracture passing through a brittle material to explain the elastic limit. Later work (Brar and Bless, 1992; Brar *et al.*, 1991a,b) confirmed the existence of these waves by measuring spall and shear strength strengths ahead of and behind the failure wave, using manganin stress gauges.

Grady (1996) and Grady *et al.* (1977) have presented the most comprehensive model for the failure of a generic brittle material. The model incorporates time-dependent fracture and rate-dependent plasticity. Two nested and independent yield surfaces (see Fig. 1) are hypothesised, the inner of which identifies a fracture limit at which a flaw or system of flaws is activated by the load. Dynamic loads may exceed this surface because of the time dependence of fracture. In shock loading, the very high strain-rates may allow the stress to reach the outer surface with the accrual of negligible fracture damage. When the surface is reached, a transition to shear failure is achieved. It is this outer surface that is associated with the HEL of the material.

We have conducted a matrix of plate impact experiments on several brittle materials including glasses, aluminas and silicon carbides using embedded stress and strain gauges, velocity interferometry and high-speed photography. Some of these results are presented below to contrast the brittle failure behaviour of a range of materials.

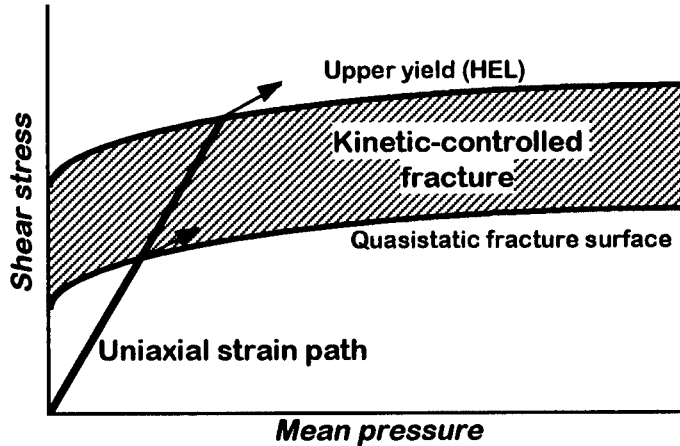


Fig. 1. Schematic of the model of Grady (1996) for the response of polycrystalline ceramics to shock loading.

More detailed accounts of the responses of individual materials may be found in papers referred to in the text. We will address specifically their compressive failure in this paper leaving the spall response to other publications. We show that a wave of fracture passes through glasses and that this determines their HEL. On the other hand, the fracture is localised in polycrystalline ceramics to a failed zone at the impact face.

2. EXPERIMENTAL

Plate impact experiments were carried out on the 50 mm bore gun at the University of Cambridge, (Bourne *et al.*, 1995b). Stress profiles were measured with commercial manganin stress gauges both embedded, or placed on the rear face of the specimens and supported with thick polymethylmethacrylate (PMMA) blocks. These gauges (Micromasurements type LM-SS-125CH-048) were calibrated by Rosenberg *et al.* (1980). In some experiments the backsurface configuration was used for longitudinal stress measurements since it is superior to the fully embedded gauge as the impedance mismatch between gauge package and specimen is removed leading to a faster response from the gauge. Stresses in the specimen are inferred from the measured signals in the PMMA using the well-known impedance correction factor

$$\alpha = \frac{Z_1 + Z_2}{2Z_1} \quad (1)$$

where Z_1 and Z_2 are the shock impedances of specimen and PMMA respectively. The signals were recorded using a fast (1 GS^{-1}) digital storage oscilloscope and transferred onto a micro-computer for data reduction. Impact velocity was measured to an accuracy of 0.5% using a sequential pin-shorting method and tilt was fixed to be

less than 1 mrad by means of an adjustable specimen mount. Impactor plates were made from lapped tungsten alloy, copper and aluminium discs and were mounted onto a polycarbonate sabot with a relieved front surface in order that the rear of the flyer plate remained unconfined. Targets were flat to within five fringes across the surface. Lateral stresses were also measured using manganin stress gauges, this time of type J2M-SS-580SF-025 (resistance 25 Ω). The data collected cannot be used directly to infer the lateral stress and were thus reduced using a new analysis requiring no knowledge of the longitudinal stress (Millett *et al.*, 1996). The gauges had an active width of 240 μm and were placed at varying distances from the impact face. The lateral gauges were mounted using Hysol 0151 clear epoxy and a special clamping fixture which holds the two halves of the sectioned target during its curing time (about 8 h). A 25 Ω resistor was added in series to the lateral gauge leads in order to produce 48 Ω across the input to the power supply. The gauge mounting positions and sample configurations are shown in Fig. 2a.

The lateral stress, σ_y , was used along with measurements of the longitudinal stress, σ_x to calculate the shear strength τ of the material using the well-known relation

$$\tau = \frac{1}{2}(\sigma_x - \sigma_y). \quad (2)$$

This quantity has been shown to be a good indicator of the ballistic performance of the material (Meyer *et al.*, 1990). Our method of determining the shear strength has the advantage over previous calculations of being direct since no computation of the hydrostat is required.

In one of the experiments, a target was constructed from soda lime glass to investigate the effect of an inner interface on the response. Two stress gauges were sandwiched between the faces of two tiles in order to measure the lateral component of the stress (see Fig. 2b). The sample was constructed from two identical targets, both faces of which were ground flat with 25 μm alumina (removing at least seven times the average surface flaw size) and then polished to an optical finish using jeweller's rouge. After these targets were prepared, they were bonded together with a low viscosity epoxy to form a single assemblage containing two orthogonal cuts, with the

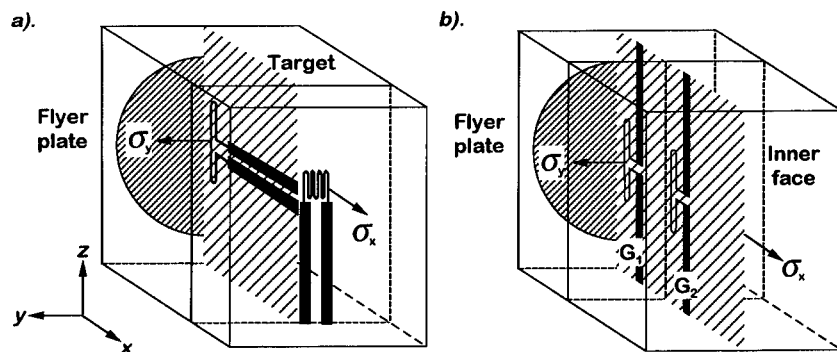


Fig. 2. Experimental arrangement used in the experiments showing sectioning of the target and the insertion of gauges.

gauges now placed along the plane oriented in the direction of shock propagation at 2 and 12 mm from the impact face. A second target was constructed from a monolith of thickness 25 mm which was sectioned in the direction of shock propagation and then reconstructed with two lateral gauges embedded at 2 and 12 mm from the impact face. The impact surface of the block was lapped with a 25 μm alumina paste. The samples were then subjected to the same impact conditions from a copper flyer plate of thickness 10 mm to ensure no longitudinal unloading from the flyer plate and inducing a longitudinal stress of around the HEL of the glass (further details in Bourne *et al.*, 1997b).

Each of the materials used in the study was characterised in several tests at lower strain-rate. These results are summarised in the table of material properties (Table 1). The alumina had its grain size determined by a linear intercept method to be 4 ± 4 μm . The material was 97.5% pure and had a porosity of 3.5%. The silicon carbide was produced by a pressureless sintering process with carbon added as a sintering aid. The three glasses used in the study were of varying density. The chemical composition of the glasses is given in Table 2. Microstructural examination of the glasses

Table 1. *Materials' data for the brittle materials studied*

	Borosilicate	Soda-lime	DEDF	Alumina	SiC
$\rho(\pm 0.05 \text{ g cm}^{-3})$	2.23	2.49	5.18	3.80	3.16
$E(\text{GPa})$	73.1	73.3	52.8	346	422
$\mu(\text{GPa})$	30.4	29.8	21.1	140	181
Poisson's ratio ν	0.20	0.23	0.25	0.23	0.16
$c_L(\pm 0.01 \text{ mm } \mu\text{s}^{-1})$	6.05	5.84	3.49	10.30	11.94
$c_s(\pm 0.01 \text{ mm } \mu\text{s}^{-1})$	3.69	3.46	2.02	6.07	7.57
Quasi-static $Y(\pm 0.4 \text{ GPa})$	1.2	1.0	—	3.4	5.2
SHPB $Y(\pm 0.4 \text{ GPa})$	—	—	—	54.1	7.3
HEL ($\pm 0.5 \text{ GPa}$)	8.0	6.0	4.5	7.7	13.5

Table 2. *Composition of the glasses used in this study*

	Soda-lime	DEDF	Borosilicate
SiO_2	72.6	27.3	80.6
Al_2O_3	1.0		2.2
Na_2O	13		4.2
K_2O	0.6	1.5	
PbO		71.0	
MgO	3.94		0.05
CaO	8.4		0.1
Fe_2O_3	0.11		0.05
As_2O_3		0.1	
B_2O_3			12.6
$\rho(\text{kg m}^{-3})$	2490	5180	2230

indicated randomly distributed flaws of three types. Sub-micron bubbles of average separation ca 10 μm , larger bubbles of radius of order 50 μm and conchoidal cracks of size ca 50 μm . Both these larger flaws were separated by 5–10 mm.

3. RESULTS

3.1. *The brittle failure of glasses*

The three glass types described above have all been characterised in uniaxial strain impacts so that their Hugoniot might be measured (Bourne *et al.*, 1996b,d; Bourne and Rosenberg, 1996a). Several interesting features of the longitudinal stress histories were noted, of which two are presented here. Whilst the ramping behaviour of borosilicate glasses is well-known, the detail of the rising part of pulses in soda-lime glass has not received so much attention.

Figure 3 shows longitudinal stress histories obtained using embedded gauges placed 5 mm from the impact face in soda-lime glass. The lower trace shows a flat plateau typical of the lower stress levels. The highest stress achieved shows a ramping rise to a stress of 7 GPa over ca 700 ns. This trace is above 6 GPa which is normally regarded as the HEL of this material. The middle stress history achieved a stress of 4.5 GPa before relaxing over a period of a few hundred ns back to a stress of 4 GPa. Such relaxations are always observed for soda-lime glass in our experiments, in the range of longitudinal stresses between 4 and 6 GPa, most noticeably at the lower end of this range. A second feature (noted in Bourne *et al.*, 1996c) is that of a break to a shallower ramp at ca 4 GPa observed primarily in backsurface traces, where details of the rise

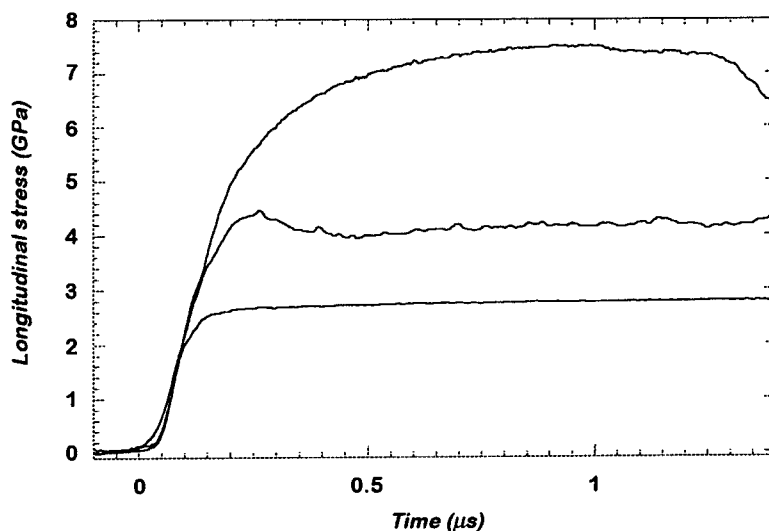


Fig. 3. Three traces showing impacts upon soda-lime glass taken with embedded gauges. Note the stress relaxation in the centre stress history.

are clearer. This can be seen in our experiments and also those of others (for instance Dandekar and Beaulieu, 1995). The importance of such longitudinal stress relaxations is that they occur only in the stress range above 4 GPa which has been determined by the authors and by Brar and Bless (1992) as the threshold for the onset of the failure wave. Such stress relaxations are believed to result from fracture behind the shock front.

The response of the filled lead glass DEDF is shown in Fig. 4 where a series of backsurface measurements of stress at varying positions from the impact face for a pulse of amplitude ca 6 GPa is presented. Thicknesses of tile ranging from 2–15 mm were impacted by a 6 mm thick copper flyers travelling at nominally 535 m s^{-1} . The gauge was mounted between the rear of the tile and a PMMA backing so as to give maximum temporal resolution. In each of the traces the elastic wave jumps very rapidly over 40–60 ns followed by a concave ramp as the plastic wave rises. This behaviour is often seen in ceramics (such as the aluminas of Murray *et al.*, 1996) where the rapid rise of the wave often leads to an electrical ringing at the HEL as seen in these traces. This ringing is not a mechanical effect and can be suppressed by moving the gauge back into the PMMA (Bourne and Rosenberg, 1996b). The form of the plastic rise suggests that the Hugoniot has a section that is concave downwards just above the HEL before rising as normal. It is apparent that the break between the elastic and plastic rises decays as the tile thickness increases. In this glass, the precursor amplitude decays from 1.9–1.4 GPa (as measured in PMMA) at ca 12 mm at which value it becomes steady. This represents a reduction of the order 25% of the initial value. The decay mechanism is assumed to result from micro-cracking. Fracture relieves stresses behind the shock front at stresses in excess of the HEL. Release waves

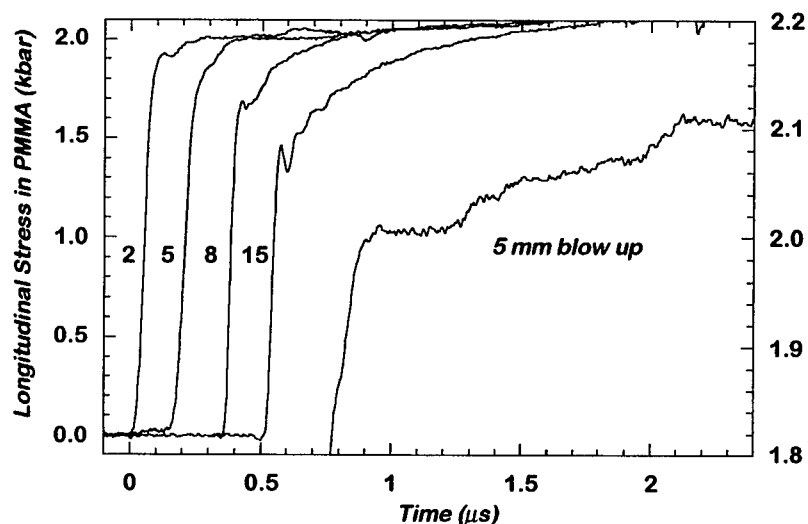


Fig. 4. Precursor decay in the filled glass DEDF. The precursor amplitude can be seen decreasing from 2–15 mm. On the right hand side of the figure a blow up of the upper section of the 5 mm trace shows steps on the plateau.

sent forward from the rear catch the shock front and slow stress increments above the HEL back down to this value.

The top of the 5 mm trace is blown up on the right hand side of Fig. 4. It will be noted that none of the traces have smooth, flattened tops in this stress range. As an example we show the stress history at 5 mm which has a stepped appearance. The stress range viewed for this trace is shown on the right-hand axis. These steps are believed to result from reflections of the release from the PMMA block at the failure front returning as a compression and then ringing between the travelling failure front and the PMMA interface. Such features have been noted previously for soda-lime glass most typically in VISAR measurements (see Kanel *et al.*, 1992 for example).

In Fig. 5 we present results of an experiment in which a soda-lime monolith containing lateral gauges at 2 and 12 mm was compared with an equivalent sample in which gauges were placed at the same position, but in which a highly polished interface had been added at 10 mm. The form of the traces for the monolith, which are represented by solid lines, is typical of lateral stress measurements across failure waves. The initial lateral stress is ca 2 GPa rising to 4 GPa across a front travelling behind the shock wave. The gauge at 12 mm sees much the same stresses in the case of the monolith. The longitudinal stress for this impact is very close to the quoted HEL of 6 GPa giving values of the shear strength of the order of 2 GPa ahead of the failure front. The expected value of shear strength can be calculated within the elastic range using the well-known relations.

$$\sigma_y = \frac{\nu}{1-\nu} \sigma_x \text{ and thus } 2\tau = \frac{1-2\nu}{1-\nu} \sigma_x, \quad (3)$$

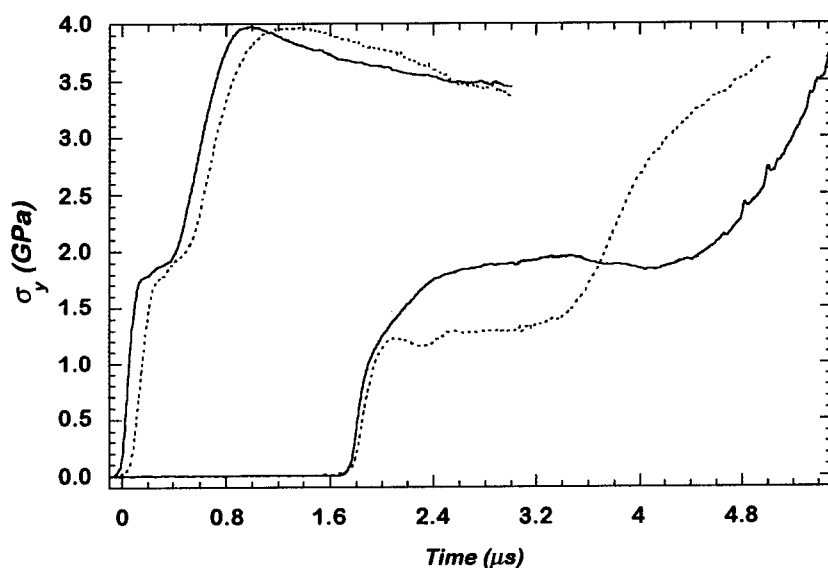


Fig. 5. Lateral stress histories taken at 2 and 12 mm from the impact face of soda-lime glass targets shot to a stress of 6 GPa. The solid traces represent histories measured in a monolith. The dotted represent those where an interface was introduced 10 mm from impact.

which (when Poisson's ratio $\nu = 0.23$ is substituted) leads to an expected value of 2τ ahead of the failure front of 4 GPa. This may be applied to this case since we are at the quoted HEL and the agreement is good. The second pair of traces show the effect of a polished interface in the centre of the target on the propagation of the failure wave. The first gauge sees much the same trace as the monolith even though this tile had been specially polished to an optical finish to remove surface flaws. This provides confirmation of the result of Raiser *et al.* (1994) who showed that surface finish had no effect on failure wave speed. However, at 12 mm the initial strength of target, ahead of failure propagating from the new interface, is higher than that on the impact face by ca 0.6 GPa. This remarkable result means that the second tile behaves as if it is stronger, as a result of the wave having crossed an inner interface before reaching it. The wave nevertheless arrives sooner at this gauge than was the case for a monolith, indicating that a second failure was nucleated at the interface.

The ability to place multiple gauges in glass targets allows one to build up a picture of the velocity at which the failure front passes through the tile at given impact stresses. We have noted that the wave travels at approximately constant speed through glasses and that the wave velocity can be made to travel fast enough so that failure can occur within the shock front itself (Bourne *et al.*, 1996a). This occurs at ca 10 GPa for soda-lime glass, and at ca 8 GPa for the filled glass DEDF. Nevertheless, in the region below this threshold we have calculated the velocity of the wave corrected by the particle velocity to give a Lagrangean value and these data are plotted in Fig. 6. The top curve, B, is for the borosilicate glass, the central one, SL, is for soda-lime glass and the lower, D is for DEDF. It will be seen that the lowest density material B, shows the most rapid failure with the DEDF the slowest. All three glasses show an increased failure wavespeed with stress which is to be expected.

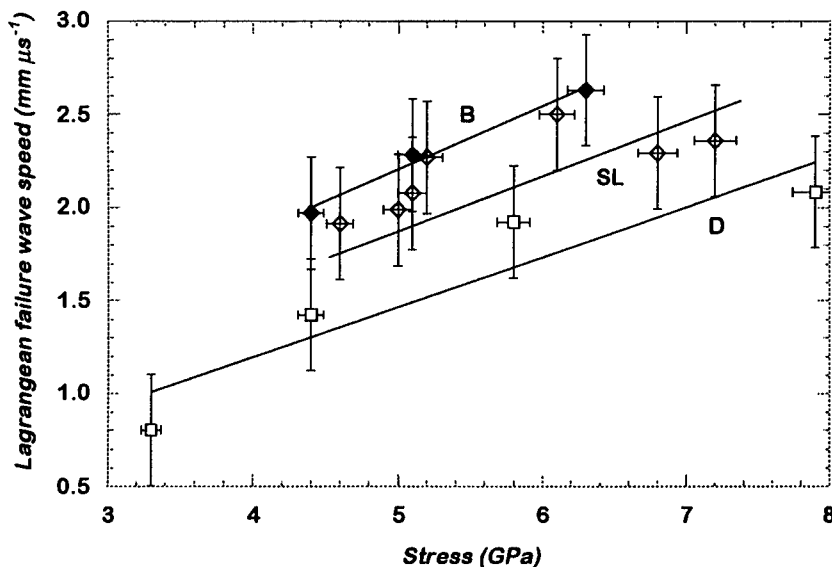


Fig. 6. Failure wavespeed plots for the three glasses tested. The speed is represented after particle velocity has been subtracted.

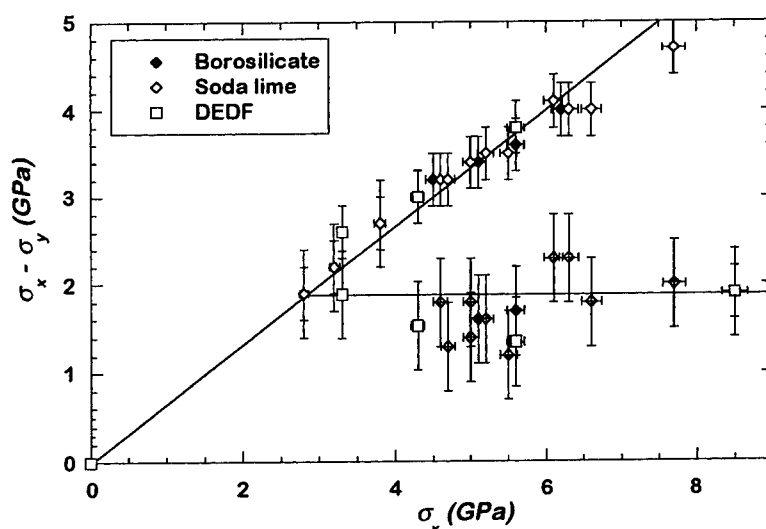


Fig. 7. Deviatoric response of three glasses constructed from lateral stress measurements.

The deviatoric behaviour of the three glasses can be summarised by plotting the value measured for twice the shear stress at increasing longitudinal stress. These data are presented in Fig. 7 for the three glasses. The diagonal line is at a slope of two-thirds as calculated from eqn (3). Note the remarkable uniformity of the response with the initial values of the strength all lying on the upper elastic (or extension of the elastic) line and the failed strengths lying along the lower horizontal line. It should be noted that even above the HEL the materials are found to exhibit a strength which lies on an extension of the elastic curve beyond the yield point. It is a puzzling feature of the response of the three glasses that their deviatoric behaviour should be described by a single curve since their Hugoniot are different from one another. No explanation is as yet offered but it may be noted that all three glasses contain a silica network microstructure.

3.2. The brittle response of an alumina

The response of aluminas has been a topic of great interest for many laboratories over the last 20 years. One feature of the response that has always attracted controversy has been the question as to whether the amplitude of the elastic precursor decays with travel of the shock pulse through the target. In other studies we have presented evidence of the decay of the precursor in aluminas for 88, 97 and 99% purity (Murray *et al.*, 1996). Further features of the stress histories will be highlighted here in order to provide support for the lateral stress measurements which follow. We present the results of precursor decay measurements for the 97% pure alumina in Fig. 8. The histories were measured using gauges embedded at the rear surface of the tile in a PMMA block. The precursor decays in value from ca 10–8 GPa over the range of thicknesses studied when correction has been made for the measurement having been

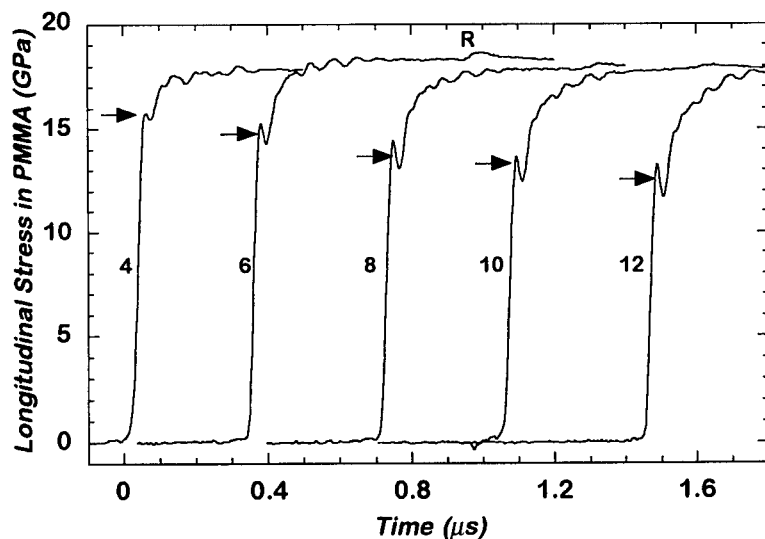


Fig. 8. Precursor decay in the alumina taken at various tile thicknesses. Note the reload signal R seen on the 6 mm trace.

made in PMMA. The major part of this decay is seen over the region up to 6 mm from the impact face. We note that all of the traces, except that at 4 mm, show an interesting structure on the top plateau which is reminiscent of that seen in the DEDF. This is a reload signal which comes from the surface failed zone. Detail of the 6 mm trace is provided in the figure to illustrate the reload signal, *R*, which is a reflected release off a low impedance region near the impact face. We identify this region as containing a failure wave using lateral stress measurements below. The relative positions of these signals on each trace confirm that the failed zone is of limited extent confined at the front surface.

Figure 9 presents the results of three lateral gauge experiments in the same alumina. The tiles were 25 mm thick and were sectioned to allow gauges to be introduced at 2 mm from the impact face. All were then impacted with 10 mm thick copper flyers travelling as 350, 480 and 650 m s⁻¹. This induced longitudinal stresses of ca 6, 9 and 12 GPa respectively. The three traces clearly show the failure wave behaviour noted previously in glasses. There is an initial plateau which lasts for up to 0.5 μs in the lower of the traces before delayed failure occurs. It should be noted that this is much longer than the plastic wave risetime of the pulse from the HEL to the Hugoniot stress. By the uppermost trace, the stress is sufficient to fail the material in the shock front itself as noted early for the glasses. Note that this delayed failure is occurring below the HEL for the material (which is ca 9 GPa) for the lower of the stress histories.

The same experiment was repeated at a stress of 9 GPa in the target. This is incidentally, around the value of the HEL in the material. In a series of experiments the lateral stress histories at 2, 4, 5, 6, and 8 mm from the impact face were recorded. The traces at 2 and 4 mm (shown as dotted curves) show evidence of the same failure

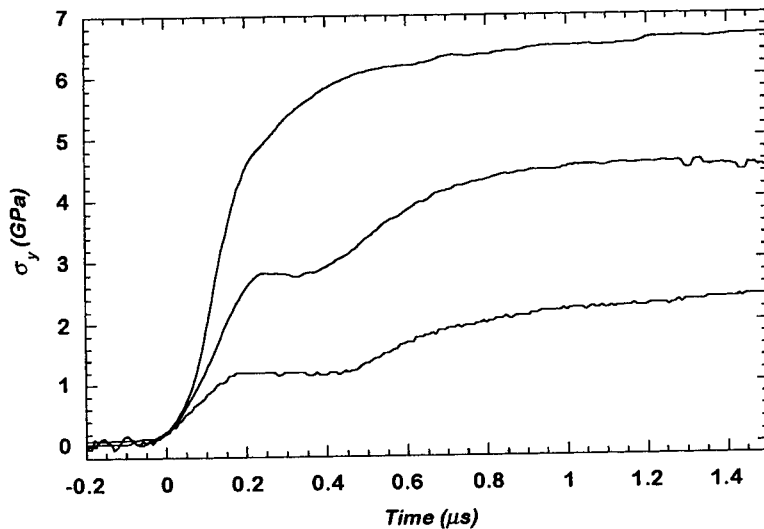


Fig. 9. Lateral stress measurements at 2 mm in alumina shot with a 10 mm copper flyer plate inducing longitudinal stresses of 6, 9 and 12 GPa.

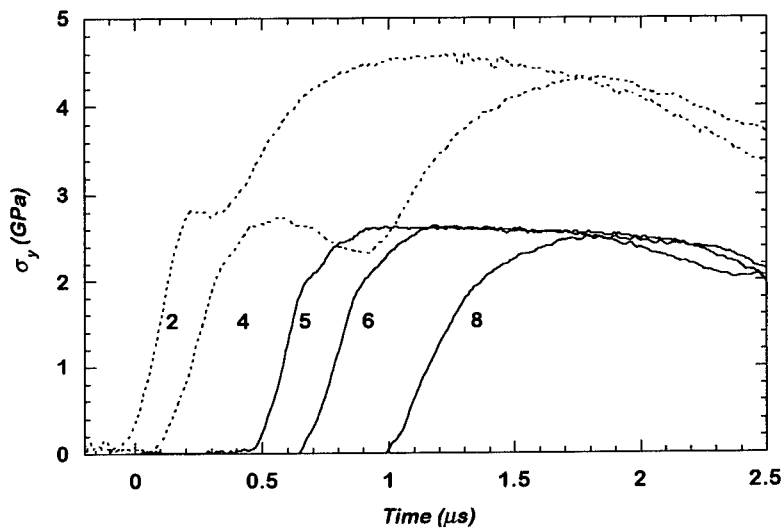


Fig. 10. Lateral stress histories recorded at various distances from the impact face after impact with copper flyers of thickness 10 mm. Longitudinal stress is 9 GPa.

seen earlier. However, at 5 mm and beyond no failure wave was seen to arrive for the duration of the experiment. These observations indicate that contrary to the glasses, the failure process swept into the target from the interface in alumina does not reach beyond the first 5 mm of the target. This distance is approximately that over which

the majority of the precursor decay is observed to occur indicating that the precursor decay is a real effect governed by the delayed failure swept in from the surface. Interestingly, the initial value of 2τ which is ca 6 GPa reduces to ca 4 GPa in the surface zone but remains at its initial value in the bulk. The expected value of 2τ calculated using eqn (3) is close to 6 GPa in agreement with our measurements of the bulk strength. The dip in the lateral stress seen before the arrival of the failure front in the 4 mm trace is reproduced in many others. It may indicate a relaxation in the amplitude of the first wave due to the fracture process.

We summarise the response of the alumina in Fig. 11 where we plot the strength data for alumina as we have done previously for the glasses. The dark points are for the experiments of Figs 9 and 10 whilst the open diamonds are data for AD85 taken from Rosenberg *et al.* (1987). It will be seen that the agreement between the strengths measured for the two aluminas is good considering that the AD85 has lower alumina content and higher porosity. Note also that the materials have differing HEL (6 and 8 GPa respectively). That they show similar strength behaviour may indicate that the shear strength depends principally upon the alumina grains rather than the glassy phase. A feature of our curve is the failed curve which extends from ca 6 to 10 GPa. Several aspects of this curve are worthy of note. Firstly it does not extend beyond 10 GPa, since by this point the failure is nucleated and remains within the shock. It is thus clear that the surface failure process determines the magnitude of what we have been calling the HEL up to this point. Secondly, this failed zone has a strength which is lower than the bulk which contrasts with the measurements in glass where the strength of material before failure could rise up the elastic line beyond the HEL until the failure could occur behind the shock. The figure represents a cut through a three dimensional surface where distance from the impact face is the third axis. We have

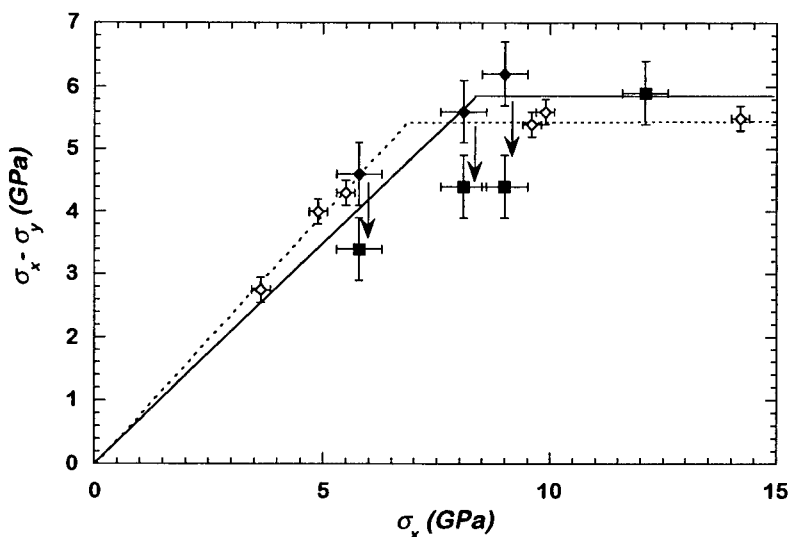


Fig. 11. Deviatoric response of the alumina at 2 mm from the impact face constructed from lateral stress measurements.

shown that the failed surface only exists up to ca 5 mm and that beyond that only the upper curve is measured (which would have been the case in the AD85 experiments due to the position of the gauge in that work).

3.3. The response of silicon carbide

Finally, we show equivalent experiments for a silicon carbide material further details of which appear in Bourne *et al.* (1997a). The measured HEL was 13.5 ± 0.3 GPa as reported in that paper. Experiments were carried out to measure the lateral stress histories at 2 mm from the impact face at five different stress levels; ca 9, 14, 16, 19, and 21 GPa. An additional experiment was carried out in which the gauge was placed 4 mm from the impact face in order to assess the size of the failed surface zone. Again the impactor was a 10 mm thick copper flyer plate to ensure that longitudinal release did not enter the gauge region until after the compressive failure processes had occurred. The histories are presented in Fig. 12. Similar behaviour was observed in this material as that seen in the alumina. At the lower stresses, delayed failure was observed whilst at the highest it occurred within the shock front itself. The dotted, 4 mm trace shows that the delay time increases to nearly $1 \mu\text{s}$ from its previous value at 2 mm of 400 ns. This means that the failure wave is slowing rapidly. It thus appears that as in the case of the aluminas, the failed zone does not propagate more than a few mm into the target. Note again that the lowest stress is below the HEL and shows similar behaviour to histories recorded at much higher stresses.

The deviatoric response of this SiC at 2 mm is summarised in Fig. 13. The solid line represents elastic behaviour up to the HEL. The delayed failure is indicated by the arrows from an upper unfailed to a failed surface. By the highest stress, 21 GPa,

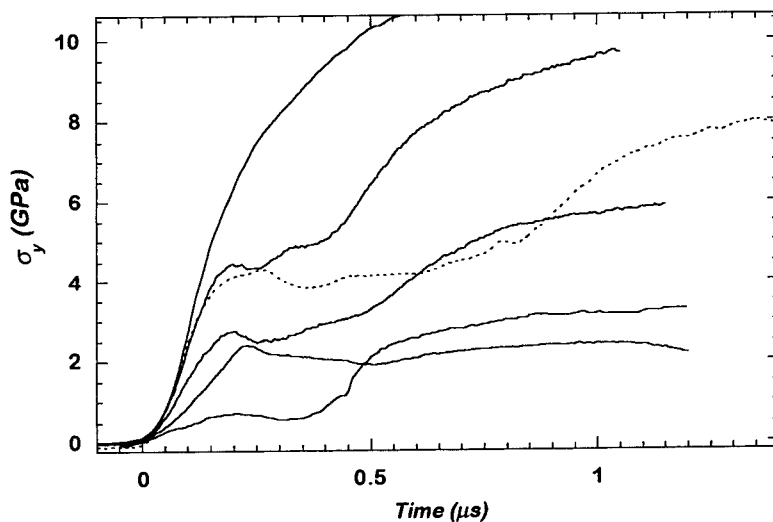


Fig. 12. Lateral stress measurements at 2 mm in silicon carbide shot with a 10 mm copper flyer plate inducing longitudinal stresses of 9, 14, 16, 19 and 21 GPa. The dotted trace is at 19 GPa but the gauge was placed at 4 mm from the impact face.

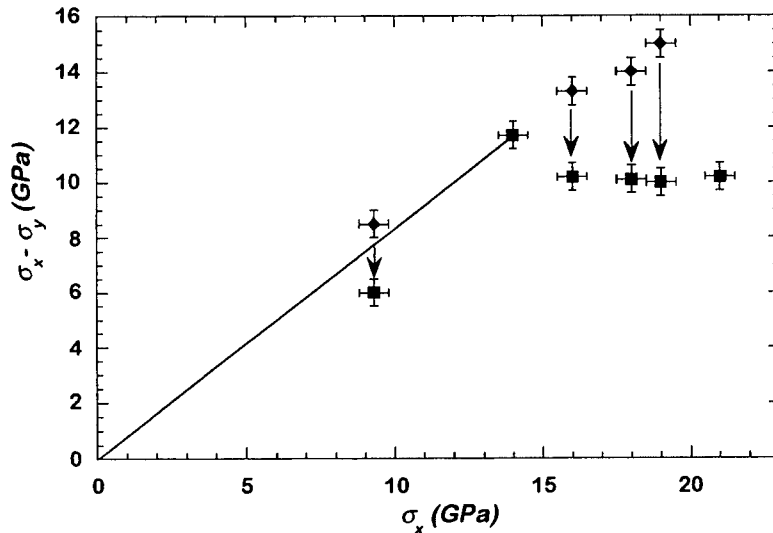


Fig. 13. Deviatoric response of silicon carbide at 2 mm from the impact face constructed from lateral stress measurements.

the material is failing in the shock front. Whereas alumina never exceeds the strength at the HEL, SiC does so in the region where it exhibits delayed failure. It does ultimately, however, fail to a strength less than that at the HEL. Again the measured and calculated strengths at the HEL agree well. We emphasise again that this represents a single set of measurements at one distance from the impact face. We have shown in Fig. 12 that the failure wave is slowing rapidly and is confined to a failed surface zone so that this response will only be seen in impact surfaces.

4. DISCUSSION

The results presented above have highlighted both similarities and differences in the behaviour of these five materials. The failure wave and its consequences control the response of the glasses, particularly their shear strength, whilst the wave is less important in this respect in the polycrystalline materials. In these, its primary effect is to control the magnitude of the elastic precursor.

Let us first consider the magnitude of the strengths measured for our materials. The deviatoric response of all those mentioned above is plotted on the same axes in Fig. 14. This curve represents the strength of material close to the impact face as we have shown.

The failed strengths of the materials rank in order of ballistic performance with the glasses showing 2τ of 2 GPa, alumina, 6 GPa and silicon carbide 11 GPa. It will be seen that the surface region can support shear stresses up to ca 8 GPa transiently in silicon carbide. This ability to display strengths in excess of those measured at the HEL is a feature shared in common with the glasses.

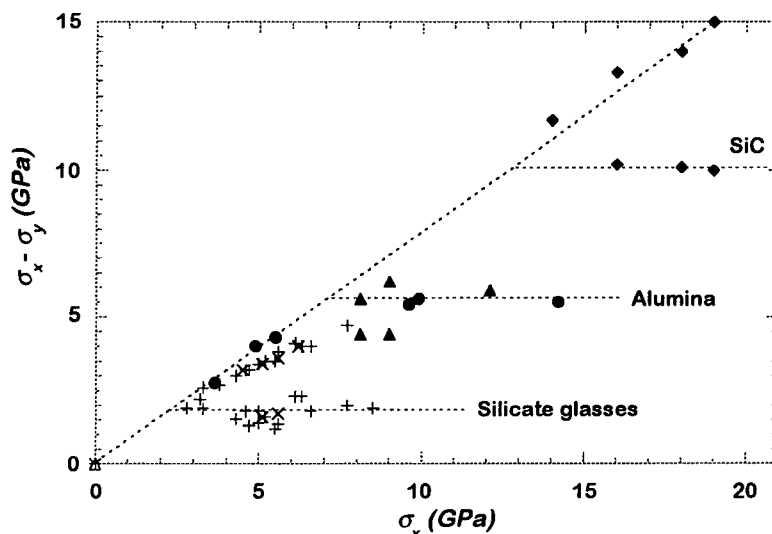


Fig. 14. Deviatoric response at 2 mm from the impact face of all classes of material presented collated from Figs 6, 12 and 14.

The evidence presented above may be summarised as follows. Brittle materials appear to fail as a result of a fracture wave propagating into the material from the impact face. This wave crosses the entire target in the case of the glasses, but in polycrystalline materials the failure wave does not penetrate into more than a surface region of the tile. This behaviour has been observed directly by lateral gauges monitoring strength loss at different locations from the impact face. Importantly, these findings have been confirmed by independent measures such as reflected waves picked up by gauges monitoring longitudinal stresses in the backsurface configuration. It is thought that the failure wave is fracture propagating from the impact face. In glasses, embedded gauges have observed relaxations in the longitudinal stress which are seen at stresses exceeding the failure wave threshold. Additionally, high-speed photography has shown cracks propagating from the impact face behind the shock (Bourne *et al.*, 1995a). In all the brittle materials observed, the failure wave has been observed to propagate at a stress below the steady value of the HEL of the material. We estimate this stress to be 3 GPa for DEDF, 4 for soda-lime and 5 for borosilicate. Similar thresholds are found in ceramics but have not been accurately determined as yet. The threshold may correspond to that at which the spall strength begins to decrease as the stress amplitude increases. A feature of this failed zone in alumina is that its extent is precisely that determined for precursor decay in other experiments (Murray *et al.*, 1996).

The Rayleigh wave speed is generally accepted as the threshold velocity for the propagation of a single crack and is close to $0.9 c_s$ for the materials tested. It is probable that some failure is also triggered at bulk flaw sites by the shock and this may allow some regions of locally failed material that could in principle give failure speeds in excess of the Rayleigh wavespeed. The data of Fig. 6 show that in the case

of soda-lime and borosilicate the maximum speeds measured do not reach this limit. On the other hand, DEDF, where the failure wave was driven into the front, appears to show speeds that asymptote to ca $2 \text{ mm } \mu\text{s}^{-1}$ consistent with the Rayleigh wavespeed. Clearly this evidence suggests that the failure is propagating faster than would be possible for shear cracking alone since this, although propagating at c_s , would be travelling at 45° to the applied stress which would give a resolved velocity in the direction of the shock of $0.7 c_s$ giving $1.4 \text{ mm } \mu\text{s}^{-1}$ as an upper limit. The situation in the polycrystalline materials is more revealing. Here we see two differing behaviours which may be explained by noting that alumina fails faster than silicon carbide (as noted in Grady, 1996). This may be due to the glassy phase present in the alumina. The slower failure of silicon carbide allows it to load substantially above the shear strength at the HEL (along the elastic curve) before failure drops it to the lower failure surface. Alumina on the other hand does not display this type of behaviour.

It is believed that the principal reason why the failure is localised to the surface in the polycrystalline materials is that the grain boundaries act to impede the fracture front eventually stopping it. Similar effects were observed at the inner interface in the experiment described above. The presence of a weaker layer in the material acts to stop or filter out the smaller cracks whilst the larger ones can reform across the boundary. This effect may operate in polycrystalline materials where many internal interfaces exist.

We have discussed the failure wave in some depth but have not as yet mentioned other possible inelastic deformation mechanisms that might be occurring in the materials. It is known that open structure glasses such as soda-lime and borosilicate became more dense during the shock process and this masks some of the features of the failure wave propagation although clear evidence of its effects are seen in the lateral gauge measurements. The filled glass DEDF provides the model brittle material in which to study the effects of brittle failure. In the case of both alumina and silicon carbide there is compelling evidence of plasticity within the grains as evidenced from recovery and Hopkinson bar experiments. It is apparent that this provides the mechanism for the shear failure of the bulk of these materials. We schematically represent the deviatoric response of the glasses and polycrystalline materials in Fig. 15.

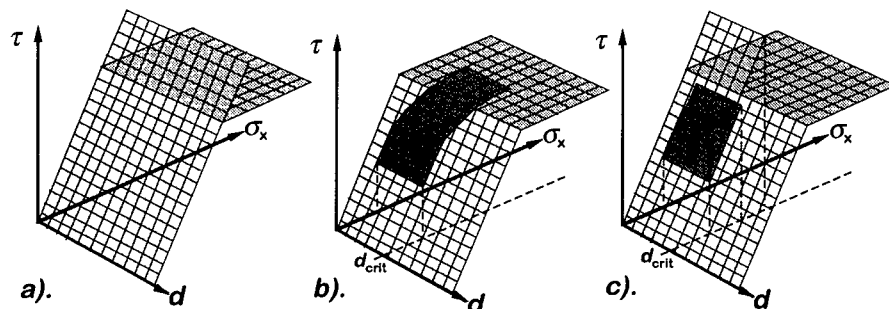


Fig. 15. Schematic representation of the variation of deviatoric response with distance from the impact face in (a) glass, (b) alumina, (c) silicon carbide.

In Fig. 15(a), (b) and (c) we show surfaces representing the schematic response of glasses, alumina and silicon carbide respectively. The elastic and failed surfaces are represented as planes extending outward as a function of the distance from the impact face. The response of glass can be represented by these surfaces at any position in the sample as shown in (a). The stress loads up the elastic surface and then drops after some time to the failed plane. At high impact stresses the final strength lies directly on the failed surface. At low stresses it remains on the elastic surface. Only the presence of an interface alters this representation by moving the failed surface upwards at that position. In (b) we represent the behaviour of alumina. In a surface zone up to a critical distance d_{crit} from the impact face, the stress follows the elastic or the upper surface, which is always horizontal, and fails to a lower surface over a limited range of stresses lying from below the HEL to some way above it. At positions in the bulk beyond the critical distance, the fracture does not penetrate and the failure beyond the HEL is directly onto the horizontal surface. In (c) we note the differing response of silicon carbide. At stresses below the HEL a lower failed surface appears to lie below the elastic one up the critical distance where the surface fracture can penetrate. Above the HEL, the behaviour is more reminiscent of the glasses in that the stress can load up the elastic surface and then drops to the failed surface below it. The differences between (b) and (c) are believed to result from the different times to failure discussed above.

Clearly the failure wave does have effects in polycrystalline materials. Even though it does not penetrate far into the bulk it nevertheless determines the amplitude of the elastic precursor and determines the pulse shape since releases can travel forward to relieve stresses from the rear. In glasses, the wave is not apparently stopped and the precursor amplitude in DEDF for instance, where densification is not possible due to the filled microstructure, will decrease as the wave travels and damage accrues.

Other features of the response of polycrystalline materials may now be explained with the knowledge that a damaged surface zone is present. Spall strength measurements can be seen to be highly geometry dependent. We are not, it should be noted, suggesting that the spall strength is reduced completely to zero in the failed surface zone. The state of the strength will depend upon the time at which the material is sampled and whether or not the crack network can interconnect. It is thus plausible that some tiles may be recovered only partly cracked at twice the HEL if the samples were pure and thick (Longy and Cagnoux, 1990). Additionally, it becomes vital to know the region from which samples where recovery analyses have been done were taken, since their microstructural features will be determined by their position.

We can apply these ideas to the response of other polycrystalline materials. Several ceramics have been regarded as showing anomalous responses, for instance titanium diboride which shows two cusps in its Hugoniot and boron carbide which shows pronounced precursor decay and retains little or no shear strength with its response rapidly collapsing to the hydrostat (Grady, 1994b). The two yields in TiB_2 may correspond to the onset of the failure process and the onset of grain plasticity respectively. The visibility of the lower cusp may be similar to the situation in soda-lime glass where the lower threshold for the failure wave is manifested by a kink on the longitudinal stress history. The behaviour is entirely brittle and a failure wave may propagate with little slowing through the material hence the pronounced precursor

decay and loss of strength determined almost entirely by fracture processes. Finally, we note that in many ceramics a volume of material ahead of a penetrating long rod is seen to be comminuted (Shockey *et al.*, 1990). This region, known as the Mescall zone, may now be explained in terms of the fracture wave described above.

5. CONCLUSIONS

We have presented experimental results showing details of the response of several brittle materials to plate impact loading. The materials chosen were glasses and polycrystalline ceramics and many common features were observed. The low density glasses showed behaviour dominated by fracture and by densification in the shock front. The highest density glass showed behaviour which was determined by brittle fracture in its response.

The polycrystalline materials, on the other hand, showed evidence of both brittle failure and plasticity. The surface responds to impact by driving a failure wave into the bulk which is rapidly slowed and eventually halted as it encounters grain boundaries. This means that a layer near the impact face shows delayed failure occurring behind the propagating shock. This surface zone is characterised by several features. Firstly, its size corresponds with that over which elastic precursor decay is observed. Secondly, the precursor amplitude steadies to a constant value above a threshold stress when tiles of a fixed thickness are shocked to different levels. This threshold stress corresponds with that required to fail the material immediately within the shock front. The failure communicates its effects to the shock front via waves which travels forward from the failed zone. In the bulk of the material in contrast the steady elastic limit is determined by a second, rate independent yield surface on which the controlling deformation mechanism is grain plasticity.

The glasses show several interesting features. The failure wave does not reach the Rayleigh wave speed in the open structure glasses but appears to saturate at this value in the filled glass. Secondly, the failure wave itself must restart at inner interfaces which results in the apparent strength of a second tile being higher than the facing one. The mechanism by which this operates may be removal of the smaller fractures by the weaker interlayer material.

Further experiments are in progress to elucidate these mechanisms further and these will be published in future papers.

ACKNOWLEDGEMENTS

N.K.B. acknowledges funding from EPSRC, DERA Fort Halstead and Chertsey and Pilkingtons plc. We thank Professor J. E. Field for many useful discussions and Mr D. L. A. Cross, Mr G. Stevens and Mr R. P. Flaxman for technical support.

REFERENCES

- Abou-Sayed, A. S. and Clifton, R. J. (1976) Pressure shear waves in fused silica. *Journal Appl. Phys.* **47**, 1762–1770.
- Ahrens, T. J. and Linde, R. K. (1968) Response of brittle solids to shock compression. In *Behaviour of Dense Media Under High Dynamic Pressures: IUTAM Symposium H.D.P.*, pp. 325–336. Gordon and Breach, New York.
- Ananin, A. V., Breusov, O. N., Dremine, A. N., Pershin, S. V., Rogacheva, A. I. and Tatsii, V. F. (1974a) Action of shock waves on silicon dioxide. II: Quartz glass. *Combust. Explos. Shock Waves* **10**, 504–508.
- Ananin, A. V., Breusov, O. N., Dremine, A. N., Pershin, S. V. and Tatsil, V. F. (1974b) The effect of shock waves on silicon dioxide. I: Quartz. *Combust. Explos. Shock Waves* **10**, 372–379.
- Barker, L. M. and Hollenbach, R. E. (1970) Shock-wave studies of PMMA, fused silica, and sapphire. *Journal Appl. Phys.* **41**, 4208–4226.
- Bless, S. J., Brar, N. S. and Rosenberg, Z. (1988) Strength of soda lime glass under shock compression. In *Shock Waves in Condensed Matter 1987*, ed. S. C. Schmidt and N. C. Holmes, pp. 309–312. North Holland, Amsterdam.
- Bourne, N. K., Millett, J. C. F. and Pickup, I. (1997a) Delayed failure in shocked silicon carbide. *Journal Appl. Phys.* **81**, 6019–6023.
- Bourne, N. K., Millett, J. C. F. and Rosenberg, Z. (1996a) Failure in a shocked high-density glass. *Journal Appl. Phys.* **80**, 4328–4331.
- Bourne, N. K., Millett, J. C. F. and Rosenberg, Z. (1996b) The shock wave response of a filled glass. *Proc. Royal Soc. London A* **452**, 1945–1951.
- Bourne, N. K., Millett, J. C. F. and Rosenberg, Z. (1997b) On the origin of failure waves in glass. *Journal Appl. Phys.* **81**, 6670–6674.
- Bourne, N. K. and Rosenberg, Z. (1996a) The dynamic response of soda-lime glass. In *Shock Compression of Condensed Matter 1996*, ed. S. C. Schmidt and W. C. Tao, pp. 567–572. American Institute of Physics, Woodbury, New York.
- Bourne, N. K. and Rosenberg, Z. (1996b) Fractoemission and its effect upon noise in gauges placed near ceramic interfaces. In *Shock Compression of Condensed Matter 1995*, ed. S. C. Schmidt and W. C. Tao, pp. 1053–1056. American Institute of Physics, Woodbury, New York.
- Bourne, N. K., Rosenberg, Z., Crouch, I. G. and Field, J. E. (1994a) The effect of microstructural variation upon the dynamic compressive and tensile strengths of aluminas. *Proc. Royal Soc. London A* **446**, 309–318.
- Bourne, N. K., Rosenberg, Z. and Field, J. E. (1995a) High-speed photography of compressive failure waves in glasses. *Journal Appl. Phys.* **78**, 3736–3739.
- Bourne, N. K., Rosenberg, Z., Field, J. E. and Crouch, I. G. (1994b) Wave steadiness in aluminas. *Journal Phys. IV France Colloq. C8 (DYMAT 94)* **4**, 269–274.
- Bourne, N. K., Rosenberg, Z. and Ginzburg, A. (1996c) The ramping of shock waves in three glasses. *Proc. Royal Soc. London A* **452**, 1491–1496.
- Bourne, N. K., Rosenberg, Z., Johnson, D. J., Field, J. E., Timbs, A. E. and Flaxman, R. P. (1995b) Design and construction of the UK plate impact facility. *Meas. Sci. Technol.* **6**, 1462–1470.
- Bourne, N. K., Rosenberg, Z. and Millett, J. C. F. (1996d) The plate impact response of three glasses. In *Structures under Shock and Impact IV*, ed. N. Jones, C. A. Brebbia and A. J. Watson, pp. 553–562. Computational Mechanics Publications, Southampton.
- Brar, N. S. and Bless, S. J. (1992) Failure waves in glass under dynamic compression. *High Press. Res.* **10**, 773–784.
- Brar, N. S., Bless, S. J. and Rosenberg, Z. (1991a) Impact-induced failure waves in glass bars and plates. *Appl. Phys. Letts* **59**, 3396–3398.
- Brar, N. S., Rosenberg, Z. and Bless, S. J. (1991b) Spall strength and failure waves in glass. *Journal Phys. IV France Colloq. C3 (DYMAT 91)* **1**, 639–644.
- Cagnoux, J. (1982) Shock-wave compression of a borosilicate glass up to 170 kbar. In *Shock*

- Waves in Condensed Matter*—1981, ed. W. J. Nellis, L. Seaman and R. A. Graham, pp. 392–396. American Institute of Physics, New York.
- Cagnoux, J. and Longy, F. (1988) Spallation and shock wave behaviour of some ceramics. *Journal Phys. France Colloq. C3 (DYMAT 88)* **49**, 3–10.
- Dandekar, D. P. and Beaulieu, P. A. (1995) Failure wave under shock wave compression in soda lime glass. In *Metallurgical and Materials Applications of Shock-Wave and High-Strain-Rate Phenomena*, ed. L. E. Murr, K. P. Staudhammer and M. A. Meyers, pp. 211–218. Elsevier, Amsterdam.
- Dremin, A. N., Orlov, A. V. and Molodets, A. M. (1992) Temperature influence on glass shock wave inelastic strain rate. In *Proc. 2nd Int. Symp. on Intense Dynamic Loading and its Effects*, ed. Z. Guanren and H. Shihui, pp. 415–420. Sichuan University Press, Chengdu, China.
- Grady, D. E. (1994a) Precursor attenuation in ceramics. Sandia National Laboratories, TMDG0694.
- Grady, D. E. (1994b) Shock-wave strength properties of boron carbide and silicon carbide. *Journal Phys. IV France Colloq. C8 (DYMAT 94)* **4**, 385–391.
- Grady, D. E. (1996) Shock-wave properties of brittle solids. In *Shock Compression of Condensed Matter 1995*, ed. S. C. Schmidt and W. C. Tao, pp. 9–20. American Institute of Physics, Woodbury, New York.
- Grady, D. E., Hollenbach, R. E., Schuler, K. W. and Callender, J. F. (1977) *Journal Geophys. Res.* **71**, 1325–1333.
- Grady, D. E., Murri, W. J. and de Carli, P. S. (1975) Hugoniot sound velocities and phase transformations in two silicates. *Journal Geophys. Res.* **80**, 4857–4861.
- Graham, R. A. and Brooks, W. P. (1971) Shock-wave compression of sapphire from 15 to 420 kbar. The effects of large anisotropic compressions. *Journal Phys. Chem. Solids* **32**, 2311–2330.
- Gust, W. H., Holt, A. C. and Royce, E. B. (1973) Dynamic yield, compressional, and elastic parameters for several lightweight intermetallic compounds. *Journal Appl. Phys.* **44**, 550–560.
- Gust, W. H. and Royce, E. B. (1971) Dynamic yield strengths of B_4C , BeO , and Al_2O_3 ceramics. *Journal Appl. Phys.* **42**, 276–295.
- Holmquist, T. J., Johnson, G. R., Grady, D. E., Lopatin, C. M. and Hertel Jr., E. S. (1995) High strain rate properties and constitutive modeling of glass. In *Proc. 15th Int. Symp. on Ballistics*. Vol. 1, ed. M. Mayseless and S. R. Bodner, pp. 237–224. Jerusalem.
- Kanel, G. I., Molodets, A. M. and Dremin, A. N. (1977) Investigation of singularities of glass strain under intense compression waves. *Combust. Explos. Shock Waves* **13**, 772–777.
- Kanel, G. I., Rasorenov, S. V. and Fortov, V. E. (1962) The failure waves and spallations in homogeneous brittle materials. In *Shock Compression of Condensed Matter—1991*, ed. S. C. Schmidt, R. D. Dick, J. W. Forbes and D. G. Tasker, pp. 451–454. Elsevier, Amsterdam.
- Kondo, K., Ahrens, T. J. and Sawaoka, A. (1983) Shock induced radiation spectra of fused quartz. *Journal Appl. Phys.* **54**, 4382–4385.
- Kondo, K., Sawaoka, A. and Ahrens, T. J. (1981) Electrical measurements on fused quartz under shock compression. *Journal Appl. Phys.* **52**, 5084–5089.
- Longy, F. and Cagnoux, J. (1990) Plate impact recovery experiments of ceramics. In *Shock Compression of Condensed Matter—1989*, ed. S. C. Schmidt, J. N. Johnson and L. W. Davidson, pp. 441–444. Elsevier, Amsterdam.
- Meyer, L. W., Behler, F. J., Frank, K. and Magness, L. S. (1990) Interdependencies between the dynamic mechanical properties and the ballistic behavior of materials. In *Proc. 12th Int. Symp. Ballistics*, pp. 419–428.
- Millett, J. C. F., Bourne, N. K. and Rosenberg, Z. (1996) On the analysis of transverse gauge data from shock loading experiments. *Journal Phys. D: Appl. Phys.* **29**, 2466–2472.
- Munson, D. E. and Lawrence, R. J. (1979) Dynamic deformation of polycrystalline alumina. *Journal of Appl. Phys.* **50**, 6272–6282.
- Murray, N. H., Bourne, N. K. and Rosenberg, Z. (1996) Precursor decay in several aluminas. In *Shock Compression of Condensed Matter 1995*, ed. S. C. Schmidt and W. C. Tao, pp. 491–494. American Institute of Physics, Woodbury, New York.

- Nickolaevskii, V. N. (1981) Limit velocity of fracture front and dynamic strength of brittle solids. *International Journal Engng. Sci.* **19**, 41–56.
- Raiser, G. F., Wise, J. L., Clifton, R. J., Grady, D. E. and Cox, D. E. (1994) Plate impact response of ceramics and glasses. *Journal Appl. Phys.* **75**, 3862–3869.
- Rasorenov, S. V., Kanel, G. I., Fortov, V. E. and Abasehov, M. M. (1991) The fracture of glass under high pressure impulsive loading. *High Press. Res.* **6**, 225–232.
- Rosenberg, Z. (1992) The response of ceramic materials to shock loading. In *Shock Compression of Condensed Matter—1991*, ed. S. C. Schmidt, R. D. Dick, J. W. Forbes and D. G. Tasker, pp. 439–446. Elsevier, Amsterdam.
- Rosenberg, Z., Brar, N. S. and Bless, S. J. (1988) Elastic precursor decay in ceramics as determined with manganin stress gauges. *Journal Phys. France Colloq. C3 (DYMAT 88)* **49**, 707–712.
- Rosenberg, Z., Yaziv, D. and Bless, S. J. (1985) Spall strength of shock-loaded glass. *Journal Appl. Phys.* **58**, 3249–3251.
- Rosenberg, Z., Yaziv, D. and Partom, Y. (1980) Calibration of foil-like manganin gauges in planar shock wave experiments. *Journal Appl. Phys.* **51**, 3702–3705.
- Rosenberg, Z., Yaziv, D., Yeshurun, Y. and Bless, S. J. (1987) Shear strength of shock-loaded alumina as determined with longitudinal and transverse manganin gauges. *Journal Appl. Phys.* **62**, 1120–1122.
- Shockey, D. A., Marchand, A. H., Skaggs, S. R., Cort, G. E., Burkett, M. W. and Parker, R. (1990) Failure phenomenology of confined ceramic targets and impacting rods. *International Journal Impact Engng.* **9**, 263–275.
- Stachler, J. M., Predebon, W. W. and Pletka, B. J. (1994) The response of a high purity alumina to plate impact testing. In *High Pressure Science and Technology 1993*, ed. S. C. Schmidt, J. W. Shaner, G. A. Samara and M. Ross, pp. 745–748. American Institute of Physics, New York.
- Wackerle, J. (1962) Shock-wave compression of quartz. *Journal Appl. Phys.* **33**, 922–937.



Pergamon

J. Mech. Phys. Solids, Vol. 46, No. 10, pp. 1909–1942, 1998

© 1998 Elsevier Science Ltd. All rights reserved

Printed in Great Britain

0022-5096/98 \$—see front matter

PII: S0022-5096(98)00027-1

A FINITE DEFORMATION CONTINUUM/DISCRETE MODEL FOR THE DESCRIPTION OF FRAGMENTATION AND DAMAGE IN BRITTLE MATERIALS

HORACIO D. ESPINOSA,* PABLO D. ZAVATTIERI and
SUNIL K. DWIVEDI

School of Aeronautics and Astronautics, Purdue University, West Lafayette, IN 47907-1282, U.S.A.

(Received 20 December 1997; accepted 29 January 1998)

ABSTRACT

A dynamic finite element analysis of large displacements, high strain rate deformation behavior of brittle materials is presented in total Lagrangian coordinates. A continuum/discrete damage model capable of capturing fragmentation at two size scales is derived by combining a continuum damage model and a discrete damage model for brittle failure. It is assumed that size and distribution of potential fragments are known a priori, through either experimental findings or materials properties, and that macrocracks can nucleate and propagate along the boundaries of these potential fragments. The finite deformation continuum multiple-plane microcracking damage model accounts for microcracks within fragments. Interface elements, with cohesive strength and reversible unloading before debonding, between potential fragments describe the initiation of macrocracks, their propagation, and coalescence leading to the formation of discrete fragments. A surface-defined multibody contact algorithm with velocity dependent friction is used to describe the interaction between fragments and large relative sliding between them. The finite element equations of motion are integrated explicitly using a variable time step. Outputs are taken at discrete time intervals to study material failure in detail.

The continuum/discrete damage model and the discrete fragmentation model, employing interface elements alone, are used to simulate a ceramic rod on rod impact. Stress wave attenuation, fragmentation pattern, and overall failure behavior, obtained from the analyses using the two models, are compared with the experimental results and photographs of the failing rod. The results show that the continuum/discrete model captures the stress attenuation and rod pulverization in agreement with the experimental observations while the pure discrete model underpredicts stress attenuation when the same potential fragment size is utilized. Further analyses are carried out to study the effect of potential fragment size and friction between sliding fragments. It is found that compared with the continuum/discrete damage model, the discrete fragmentation model is more sensitive to the multi-body discretization. © 1998 Elsevier Science Ltd. All rights reserved.

Keywords: A. dynamic fracture, A. grain boundaries, A. microcracking, B. crack mechanics, C. finite elements.

This paper is dedicated to Professor Rodney Clifton, a pioneer in the study of failure and damage of advanced materials. It is our hope that the reader will recognize the influence of Professor Clifton in two major features presented in this paper. Firstly, the formulation of failure models capable of analyzing real and complex field applications

* To whom correspondence should be addressed. Fax: 001 765 494 0307.

through a combined experimental/computational approach. Secondly, the role of specially designed wave propagation experiments in the identification of rate and temperature effects in brittle failure. Fundamental contributions within these lines are envisioned in years to come.

1. INTRODUCTION

The study of ceramics under high velocity impact and penetration has gained prominence over the years owing to their high compressive strength and low density which make them more suitable for armor applications when compared to other conventional materials. There have been attempts to determine the fracture characteristics and threshold conditions for dynamic fragmentation of ceramics through particle impact experiments (Evans, 1978; Field, 1988; Shockey *et al.*, 1990a; Andrews and Kim, 1997). Also, there have been numerous experimental studies to evaluate and characterize the performance of ceramics under various impact and boundary conditions (Shockey *et al.*, 1990b; Espinosa *et al.*, 1992; Hauver *et al.*, 1993, 1994; Woodward *et al.*, 1994; Espinosa, 1995; Orphal and Franzen, 1996, 1997a; Orphal *et al.*, 1997b; Espinosa *et al.*, 1997a; Xu and Espinosa, 1997; Brar *et al.*, 1997). The outcome of these experiments has been that ceramics can be extremely efficient in defeating long rod penetrators as long as they are properly confined. In this case, high compressive strength and friction between fragmented pieces, in the comminuted zone, is achieved. The more efficient the confinement, the better the resistance of ceramics to penetration. However, many phenomena observed during deformation of the material under such high strain rate still remain unanswered, e.g., the effect of material processing route and grain size on penetration resistance, coupling between structural design and ceramic response, etc. These issues are expected to play a significant role in deriving useful design criteria and scaling experimental results to field application. Achieving these objectives by experiments alone is a difficult if not impossible task. Hence, recourse is sought to a combined experimental and numerical study.

The use of finite element analyses to determine the performance of ceramic targets under high velocity impact and penetration is relatively recent. The majority of the efforts up to now have been devoted to modeling the complicated response of ceramics in the post-failure regime, i.e., in the presence of cracks. Brittle failure in ceramics is the result of initiation and propagation of cracks, marked by fragmentation and stress attenuation. The various models available until now to describe this behavior can be categorized into two classes; those based on a continuum approach, and those based on a discrete approach. The continuum approach (Johnson and Cook, 1985; Addessio and Johnson, 1989; Curran *et al.*, 1990; Steinberg, 1992; Johnson and Holmquist, 1992; Rajendran and Grove 1992a; Rajendran, 1992b, etc.) is based on homogenizing the cracked solid and finding its response by degrading the elasticity of the material. The fundamental assumption in these models is that the inelastic strains are caused by microcracks whose evaluation during loading degrades the strength of the material. This degradation is defined in terms of damage moduli whose evaluation under compressive, as well as tensile loading, is formulated using the generalized Griffith

criterion. In addition, some of these models account for the initiation of cracks, coalescence, friction between fragments in the comminuted zone, etc. However, some of these phenomenological models have shortcomings in that they cannot describe damage induced anisotropy and also, that their parameters are difficult to measure experimentally. To overcome these limitations, Espinosa (1992, 1995) derived a multiple-plane microcracking model based on the micromechanics of solids. In this model, the constitutive response of the material is obtained from fundamental quantities that can be determined experimentally such as grain size and fracture toughness. In addition, since the dynamic growth of microcracks is described independently on each orientation, damage induced anisotropy and rate effects are naturally incorporated in the model. The model has been used extensively (Espinosa *et al.*, 1996, 1997, 1998) to study the high velocity impact response of ceramics under various conditions. In spite of these developments, continuum models have been criticized because they require assumptions on the size and distribution of microcracks to start with, and because they cannot describe the growth of dominant cracks leading to failure, which are not suitable for homogenization. Computationally, continuum models possess the problem of very large deformation under high strain rates, specially for higher order elements. As a result, elements distort and integration time step reduces below an acceptable level. One of the possible means to circumvent this problem is to use adaptive meshing (Camacho and Ortiz, 1996; Espinosa *et al.*, 1996, 1998) by which the elements in the highly deformed zone are remeshed into regular shaped elements.

On the contrary, models based on a discrete approach (Needleman, 1988; Biner, 1994; Lawn, 1994; Gong, 1995; Xu and Needleman, 1995; Camacho and Ortiz, 1996, etc.) nucleate cracks, and follow their propagation and coalescence during the deformation process. In this respect, the Camacho and Ortiz (1996) model is one of the most elaborate and powerful models currently available. In their model, conical and longitudinal cracks can nucleate at any node in a finite element mesh when the resolved normal or shear stress at the node exceeds an effective fracture stress. Cracks are nucleated by duplicating nodes and propagated, along the element boundary, by opening further nodes. Adaptive remeshing is used to provide a reach enough set of possible fracture paths around the crack tip. The forces at the cracked surfaces are brought to zero in accordance with the Griffith criterion accounting for unloading, if any, before reaching the critical fracture opening. Following this procedure, fragments are generated as cracks coalesce in a closed path. Thereafter, the model accounts for contact and friction between fragments. Realizing the computer resources required for carrying out three dimensional analyses, they carry out two dimensional axisymmetric analyses accounting for radial cracks based on a continuum approach. The major disadvantages of the discrete models are that they are extremely computer intensive and become infeasible as the number of cracks increases. At the limit, meshes with element size of the order of the grain size are required to capture all possible crack nucleating sites.

Besides all these developments, a fact remains that the experimental and numerical work have been carried out more or less independently of each other. There have been very few attempts (Espinosa *et al.*, 1998) to use meaningful experimental results to motivate the numerical modeling and vice versa. The experimental evidence (Simha *et al.*, 1995; Espinosa and Brar, 1995; Espinosa *et al.*, 1998; Brar *et al.*, 1997) is used

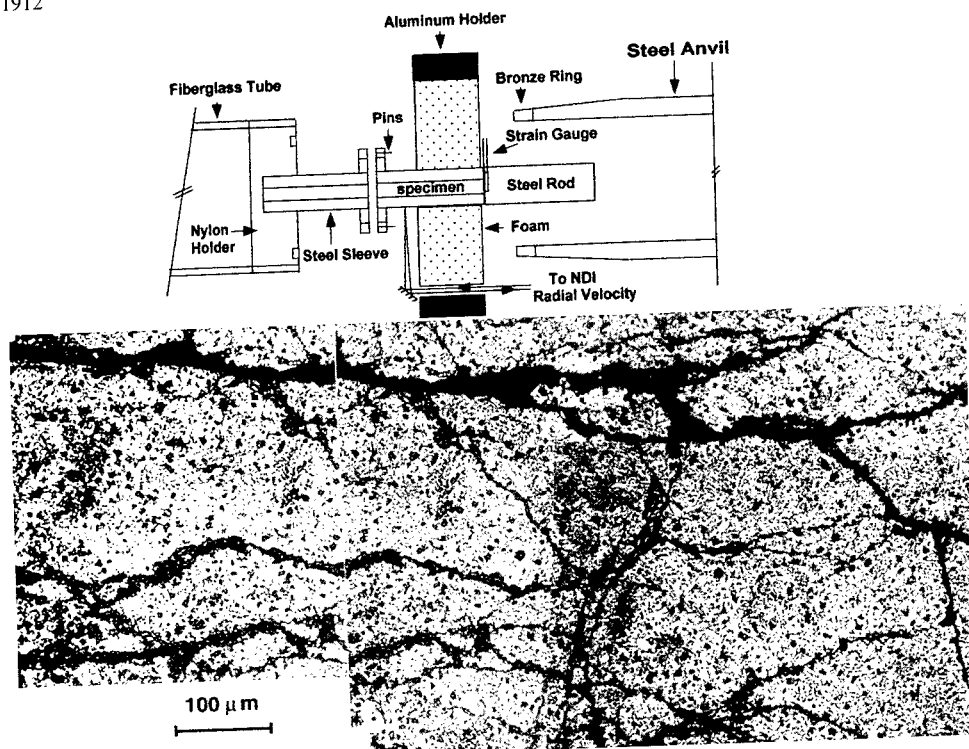


Fig. 1. Damaged end of the ceramic rod recovered after experiment.

herein in an attempt to simplify the modeling procedure while preserving all the physics of the problem. It is known that numerous cracks get generated inside grains and at grain boundaries in ceramics during the early stage of impact and penetration. Only a fraction of them grow and finally propagate, mostly along the grain boundaries, to form major flaws (henceforth referred to as macrocracks), while the rest of them get arrested during the deformation. The coalescence of these macrocracks in a closed path gives rise to fragments. This phenomenon is evident in Figs 1–4.

Figure 1 shows the schematic arrangement of ceramic rod on rod impact together with an optical photograph of the damaged end of the rod. The figure shows fragments, bounded by cracks, whose average size has been measured to be more than $100\text{ }\mu\text{m}$. In some cases, the major dimension of the fragments exceeds $400\text{ }\mu\text{m}$. An SEM micrograph of the ceramic microstructure within a fragment is shown in Fig. 2. The micrograph confirms that each fragment contains numerous microcracks of length about $10\text{--}20\text{ }\mu\text{m}$. Figure 3 shows a schematic of yet another experiment carried out to investigate interface defeat in ballistic experiments. Figure 4 shows a photograph of the cross-section obtained after cutting the penetrated TiB_2 ceramic sample. The fragment size measured from the center line is found to vary in the range of $200\text{--}500\text{ }\mu\text{m}$.



Fig. 2. Micrograph showing microcracks between grains and within glassy phase of ceramic rod.

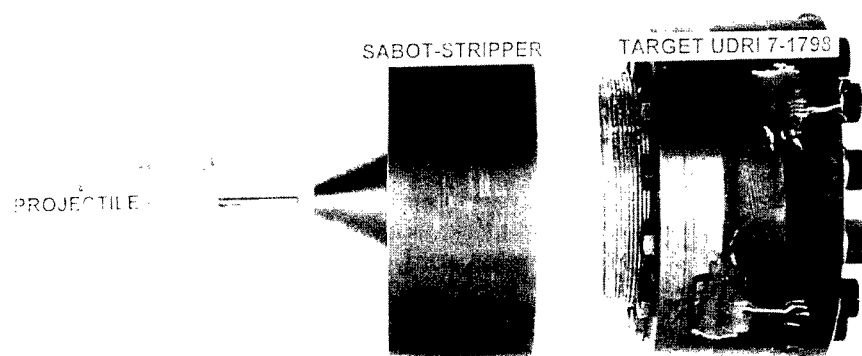


Fig. 3. Schematic of the interface defeat experiment.



Fig. 4. Micrograph showing fragmentation in T_1B_2 target plate.

Microcracks that are not able to propagate and transform into a major crack can be modeled using a continuum approach so that the resulting degradation in the strength of the material is accounted for. A discrete approach can be used simultaneously to model crack coalescence and formation of fragments. To this effect, one simplification is made in the present analyses, based on the above experimental findings, by assuming that the macrocracks initiate only at potential fragment boundaries, i.e., the microcracks inside fragments do not propagate to the fragment boundaries and transform into macrocracks. This assumption makes it possible to model individual ceramic fragments with a continuum approach, and their boundaries by a discrete approach. The contact-interface element of Espinosa *et al.* (1997b) inserted along fragment boundaries can further eliminate the computation overheads in creating the microcracks and the remeshing to provide the crack path. The above assumption of macrocracks only along fragment boundaries and the existence of fragments containing a large number of microcracks, allows the analyst to consider a cluster of grains as a single fragment. Hence, analyses can be carried out with few hundreds to few thousands of fragments instead of millions of grains. The size and distribution of fragments can be determined from the initial grain structure of ceramics, distribution of macrocracks in recovered samples after shock and validation of the analysis results with the experimental results. This further concretizes the concept of a combined experimental-numerical study for such complex problems.

The following sections briefly describe the multiple-plane microcracking model of Espinosa (1995) extended to a large deformation formulation and the contact-interface model of Espinosa *et al.* (1998) including rate and temperature effects followed by the analyses of the ceramic rod on rod impact carried out based on discrete as well as continuum-discrete models. The comparison of the analyses results with the experimental results clearly marks the advantages and disadvantages of the two approaches and the effect of size of fragments and friction between fragments.

2. EQUATIONS OF MOTION

In our formulation, the field equations describing the material response of a body use a total Lagrangian approach. Considering a solid with volume B_0 in the reference configuration, and a deformation process characterized by the mapping $\mathbf{x}(\mathbf{X}, t)$, a material point initially at \mathbf{X} will be located at $\mathbf{x} = \mathbf{X} + \mathbf{u}$ after deformation, in which \mathbf{u} is the displacement vector, as shown in Fig. 5. A displacement based finite element formulation is obtained from the weak form of the momentum balance or dynamic principle of virtual work. At time t , the weak form is given by

$$\int_{B_0} [\nabla_0 \mathbf{T}^0 + \rho_0 (\mathbf{b}_0 - \mathbf{a})] \cdot \boldsymbol{\eta} \, dB_0 = 0 \quad (1)$$

$$\int_{B_0} \mathbf{T}^0 : \nabla_0 \boldsymbol{\eta} \, dB_0 - \int_{B_0} \rho_0 (\mathbf{b}_0 - \mathbf{a}) \cdot \boldsymbol{\eta} \, dB_0 - \int_{S_{0\sigma}} \mathbf{t} \cdot \boldsymbol{\eta} \, dS_0 = 0 \quad (2)$$

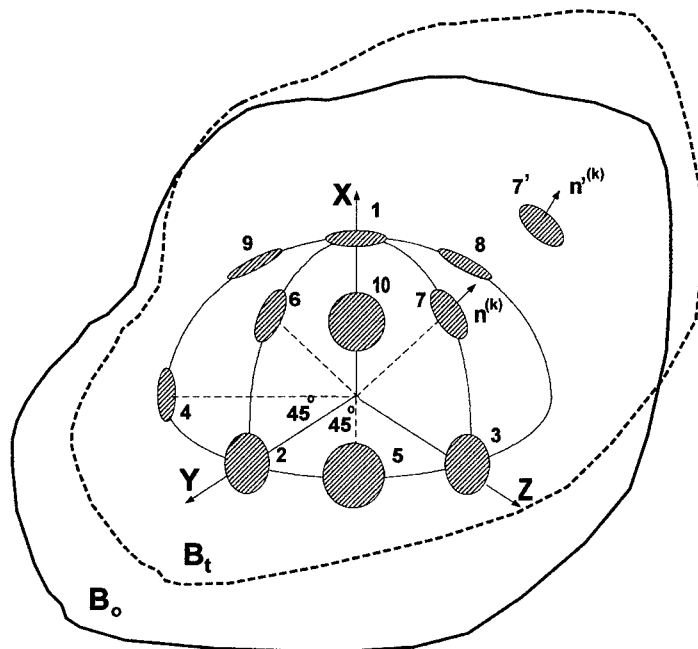


Fig. 5. Reference and current configurations. Orientations 11, 12 and 13 are hidden.

where \mathbf{T}^0 is the first Piola–Kirchhoff stress tensor at time t ; \mathbf{b}_0 , \mathbf{a} , and \mathbf{t} are the body force vector, acceleration vector, and boundary traction vector on volume B_0 and boundary $S_{0\sigma}$, respectively. Virtual displacement field η is assumed to be admissible, and ρ_0 represents the material density per unit volume in the reference configuration. The symbol ∇_0 denotes the material gradient with respect to the reference configuration, and ‘ \cdot ’ is used to denote the inner product between second order tensors, e.g., $\mathbf{A}:\mathbf{B} \equiv A_{ij}B_{ji}$, where the summation convention on repeated indices is implied. Another form of the weak form of the momentum balance, in terms of spatial quantities, is given by

$$\int_{B_0} \tau : \nabla^s \eta \, dB_0 - \int_{B_0} \rho_0 (\mathbf{b}_0 - \mathbf{a}) \cdot \eta \, dB_0 - \int_{S_{0\sigma}} \mathbf{t} \cdot \eta \, dS_0 = 0 \quad (3)$$

in which superscript s stands for the symmetric part of the tensor, τ is the Kirchhoff stress and ∇ is the spatial deformation tensor. The Kirchhoff’s stress is related to first Piola–Kirchhoff stress \mathbf{T}^0 and second Piola–Kirchhoff stress tensor \mathbf{S} by $\tau = \mathbf{F}\mathbf{T}^0 = \mathbf{F}\mathbf{S}\mathbf{F}^T$, where \mathbf{F} is the deformation gradient at time t .

The discretization of eqn (3) defines a system of nonlinear ordinary differential equations which can be solved for the updated deformation \mathbf{x}_{n+1} . A displacement-based finite element formulation is obtained by expressing field variables at any point in an element as a function of nodal quantities and the element shape functions in the

reference configuration. For the two dimensional analyses considered herein, they are given as:

$$\begin{aligned} u_{ia} &= \sum_{a=1}^{\text{NEN}} N_a(\xi, \eta) u_i^a \\ v_{ia} &= \sum_{a=1}^{\text{NEN}} N_a(\xi, \eta) v_i^a \\ a_{ia} &= \sum_{a=1}^{\text{NEN}} N_a(\xi, \eta) a_i^a \end{aligned} \quad (4)$$

where u_{ia} , v_{ia} , and a_{ia} are the displacement, velocity, and acceleration at the point of interest. $N_a(\xi, \eta)$ are the shape functions relating nodal quantities u_i^a , v_i^a , and a_i^a to the point of interest and the summation is taken over the number of nodes in the element, i.e., NEN. The vector ξ, η contains the natural coordinates of the point of interest in the isoparametric master element. For the triangular elements, these natural coordinates are related to the area coordinates as $L_1 = \xi$, $L_2 = \eta$ and $L_3 = 1 - \xi - \eta$.

Substitution of the discretized variables into eqn (3) leads to the following system of ordinary differential equations,

$$M_{iajb} \dot{a}_{jb} = f_{ia}^{\text{ext}} - f_{ia}^{\text{int}} \quad (5)$$

where,

$$\begin{aligned} f_{ia}^{\text{int}} &= \sum_c \int_{B_o^c} n_{a,j} \tau_{ij} \, dB_0 = \sum_c \int_{B_o^c} \mathbf{B}^T \boldsymbol{\tau} \, dB_0 \\ f_{ia}^{\text{ext}} &= \sum_c \int_{B_o^c} \rho_0 b_{oi} N_a^c \, dB_0 + \int_{\partial S_o^c} \bar{t}_i N_a \, dS_0 \\ M_{iajb} &= \sum_c \int_{B_o^c} \delta_{ij} \rho_0 N_b^c N_a^c \, dB_0 \end{aligned} \quad (6)$$

in which f_{ia}^{int} , f_{ia}^{ext} , and M_{iajb} are the internal nodal forces, the external nodal forces, and the lumped mass matrix, respectively. In the above equations, summation is taken over all the elements in the mesh according to their nodal connectivities.

3. FINITE DEFORMATION CONTINUUM MICROCRACKING MODEL

The large deformation continuum response of ceramics in the presence of cracks is described through a microcracking multiple-plane model based on a dilute approximation (Taylor model). The formulation is an extension of the small deformation multiple-plane microcracking model given in Espinosa (1995), assuming that the displacements and rotations are large while the strains are moderate. This assumption allows us to adopt the rate form of the work conjugate second Piola–Kirchhoff stress

tensor and Green–Lagrangian strain tensor with an additive decomposition of the later into an elastic and inelastic part, i.e.,

$$\dot{\mathbf{E}}_{ij} = \dot{\mathbf{E}}_{ij}^e + \dot{\mathbf{E}}_{ij}^c \quad (7)$$

where $\dot{\mathbf{E}}^e$ is the elastic part of the Lagrangian strain rate, and $\dot{\mathbf{E}}^c$ is the inelastic part arising from the presence of microcracks within the solid. Based on this decomposition, the elasticity law can be formulated as;

$$\dot{\mathbf{S}}_{ij} = \mathbf{L}_{ijkl} \dot{\mathbf{E}}_{kl}^e \quad (8)$$

in which \mathbf{L}_{ijkl} is the fourth order material stiffness tensor.

The basic assumption in the microcracking multiple-plane model is that microcracking and/or slip can occur on a discrete number of orientations (see Fig. 5) Slip plane properties (friction, initial size, density, etc.) and their evolution are independently computed on each plane. In contrast to scalar representations of damage, the present formulation is broad enough to allow the examination of damage induced anisotropy and damage localization in the interpretation of impact experiments.

For a representative volume B_0 , in the underformed configuration, of an elastic solid containing penny-shaped microcracks with a density $N^{(k)}$, the average Lagrangian inelastic strain rate tensor can be written as;

$$\dot{\mathbf{E}}_{ij}^c = \sum_{k=1}^{13} N^{(k)} \pi (a^{(k)})^2 \frac{1}{2} (\dot{\bar{b}}_i^{(k)} n_j^{(k)} + n_i^{(k)} \dot{\bar{b}}_j^{(k)}) + \sum_{k=1}^{13} N^{(k)} \pi a^{(k)} \dot{a}^{(k)} (\bar{b}_i^{(k)} n_j^{(k)} + n_i^{(k)} \bar{b}_j^{(k)}) \quad (9)$$

where the subindex k is used to label the orientations, $a^{(k)}$ denotes the radius of a microcrack on orientation k , $n^{(k)}$ the corresponding unit normal, and $\bar{b}^{(k)}$ the average displacement jump vector across $A^{(k)}$.

If the resolved normal traction acting on the microcracks on orientation k is tensile, the average displacement jump vector resulting from an applied second Piola–Kirchhoff stress field \mathbf{S} is given by

$$\bar{b}_i^{(k)} = \frac{1}{A^{(k)}} \int_{A^{(k)}} b_i^{(k)} dA = \frac{16(1-\nu^2)}{3E(2-\nu)} a^{(k)} (2S_{ij}n_j^{(k)} - \nu S_{jj}n_j^{(k)}n_i^{(k)}), \quad (10)$$

in which E and ν are the Young's modulus and Poisson's ratio of the uncracked solid, and a^k is the radius of the penny-shaped microcracks on orientation k . By contrast, if the normal traction is compressive, the microcracks are closed and the average displacement jump is given by

$$\bar{b}_i^k = \frac{32(1-\nu^2)}{3\pi E(2-\nu)} a^k f_i^k \quad (11)$$

where \mathbf{f}^k is the effective shear traction vector on orientation k given by

$$f_i^k = (S_\tau^k + \mu S_n^k)(n_\tau)_i^k. \quad (12)$$

In the above equation, μ is the friction coefficient of the microcrack faces, S_τ^k and S_n^k are the resolved shear stress and the normal stress acting on microcracks with orien-

tation k , respectively, and n_c^k is the unit vector in the direction of the resolved shear traction. Embodied in eqn (12) is the notion that \mathbf{f}^k provides the effective driving force for the sliding of the microcracks. If $\tau^{(k)} \leq \mu \sigma_n^{(k)}$ a sticking condition occurs. Hence, irreversible displacement jumps develop making the deformation process strongly nonlinear and history dependent.

In order to compute the inelastic strain tensor at all times, it becomes necessary to follow the evolution of the microcrack radius, a^k , in the selected orientations. Following Freund (1990), an equation of evolution for a in the case of mixed mode loading can be derived, Espinosa *et al.* (1992), Espinosa (1995), viz.,

$$\dot{a}^k = m^\pm c_R [1 - (K_{IC}/K_{\text{eff}}^k)^{n^\pm}] \geq 0 \quad (13)$$

in which n^\pm and m^\pm are phenomenological material constants which may have different values in tension and compression, c_R is the Rayleigh wave speed, K_{IC} is the material toughness, and $K_{\text{eff}}^k(\mathbf{S}, a^k)$ is an effective stress intensity factor which is a function of the stress state \mathbf{S} and the microcrack size $a^{(k)}$. For mixed mode conditions, K_{eff}^k is derived by considering an average energy release rate associated with an increase in radius of the microcracks, namely,

$$\mathcal{G}^k = \frac{1}{2\pi} \int_0^{2\pi} \frac{1-v^2}{E} [K_I^2 + K_{II}^2 + K_{III}^2/(1-v)] d\theta \quad (14)$$

from which the following expression for K_{eff}^k is obtained,

$$K_{\text{eff}}^k = \sqrt{\frac{\mathcal{G}^k E}{1-v^2}}. \quad (15)$$

The general structure of these constitutive equations corresponds to that of a solid with a damage-induced anisotropic stress-strain relation with elastic degradation. In particular, the effective behavior of the solid is predicted to be rate dependent due to crack kinetics effects. From a computational standpoint, this insures numerical reliability and mesh independence, according to Needleman (1988), and Espinosa (1989). This is in contrast to quasi-static formulations of damage for which the governing equations become ill-posed in the softening regime, as in Sandler & Wright (1984). Details about the stress update algorithm, assuming the above additive decomposition of strain rates into an elastic and cracking part, can be found in Espinosa (1995).

It should be pointed out that this inelastic model is a continuum model in which material damage results from microcracking. If the material is subjected to a predominantly tensile stress state, microcracks along orientations perpendicular to the direction of maximum tensile stresses will grow according to eqns (10) and (13). In this case, significant dilation is expected due to mode I crack opening. If a predominantly compressive state of stress with shear is imposed, then crack opening is inhibited but inelasticity is manifested by the growth of penny-shaped cracks in modes II and III (shear modes).

4. CONTACT/INTERFACE LAW WITH FINITE-KINEMATICS

The continuum model is integrated with a dynamic contact/interface model for predicting the discrete response of the material with regard to the cracks initiating at and propagating along the fragment boundary. A versatile multi-body contact model for explicit dynamic analysis has been developed. The contact algorithm is based on predicting accelerations assuming no contact and later correcting the accelerations of the surface nodes so that the surfaces do not interpenetrate. In addition, a velocity dependent friction model is included. This surface-based contact algorithm allows contact between bodies that undergo large relative displacements as they move. It also allows the easy incorporation of a velocity-dependent friction model where the friction coefficient is made a function of pressure and temperature. A detailed description of the contact algorithm can be found in Espinosa *et al.* (1996, 1998).

The contact algorithm is augmented with interface elements to simulate the initiation of cracks and subsequent large sliding, opening and closing of the cracked surfaces. The model is based on the interface model proposed by Tvergaard (1990) for quasi-static calculations. It assumes that a perfect interface between two surfaces carries forces that oppose separation and shear between them until debonding. After debonding, the two surfaces will behave as distinct identities. The propagation of a crack can thus be simulated as the consecutive failure of interface elements between *potential* fragments. The magnitude of the opposing forces before debonding is a function of the relative normal and shear displacement jumps between the two surfaces. The normal and tangential tractions are given as,

$$T_n = \frac{u_n}{\delta_n} F(\lambda_c), T_t = \alpha \frac{u_t}{\delta_t} F(\lambda_c) \quad (16)$$

$$F(\lambda_c) = \frac{27}{4} T_{\max} (1 - 2\lambda_c + \lambda_c^2), \quad \text{for } 0 \leq \lambda_c \leq 1 \quad (17)$$

where, T_{\max} is the maximum interface traction and λ_c is a non-dimensional parameter representing an effective normalized displacement jump given by,

$$\lambda_c = \sqrt{\left(\frac{u_n}{\delta_n}\right)^2 + \left(\frac{u_t}{\delta_t}\right)^2}. \quad (18)$$

In the above equation, u_n and u_t are the normal and tangential displacement jumps at the interface. δ_n and δ_t are critical displacement jump values at which the interface breaks, i.e., crack initiation. T_{\max} , δ_n and δ_t can be easily determined from energy arguments based on the mode I critical strain energy release rate of the interface. It is evident that the value of λ_c varies from 0 to 1 with $\lambda_c = 1$ defining interface failure. Four node quadrilateral elements are embedded as the interface elements between fragments. The normal and tangential forces are computed depending upon the state of stress at the interface, as shown in Fig. 6 and Table 1.

As long as the value of λ_c remains less than unity, the interface normal traction is computed from the contact model in the case of compression-shear and from the interface model in the case of tension-shear. The shear traction is computed from the

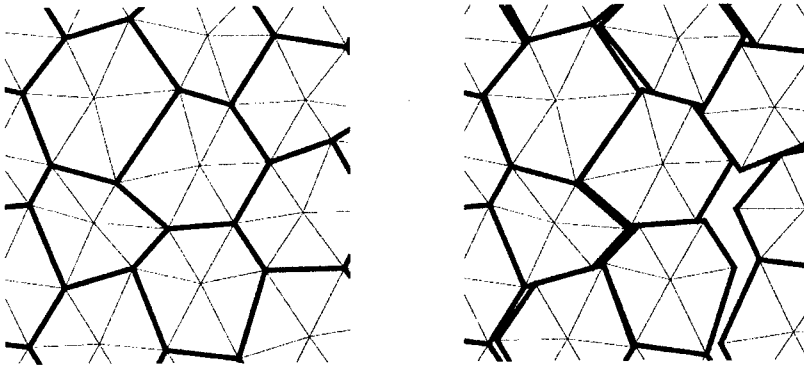


Fig. 6. Schematic of contact/interface law.

Table 1. *Contact and interface calculations based on interface traction*

Load	State	T_n	T_t
Tension-shear	$\lambda_c < 1$	Interface	Interface
	$\lambda_c \geq 1$	Contact	Open
Compression-shear	$\lambda_c < 1$	Contact	Interface
	$\lambda_c \geq 1$	Contact	Friction

interface model. These normal and tangential tractions contribute to the internal nodal forces so that the f_{ia}^{int} of eqn (6) gets modified as;

$$f_{ia}^{\text{int}} = \sum_e \int_{B_o^e} \mathbf{B}^T \tau dB_0 + f_{ia}^{\text{inte}} = \sum_e \int_{B_o^e} \mathbf{B}^T \tau dB_0 + \sum_{\text{inte}} \int_{S_c^{\text{inte}}} \mathbf{N}^T \mathbf{T} dS \quad (19)$$

where f_{ia}^{inte} is the force contributed by interface element to node i which is calculated by integrating the interface tractions over the midsurface of the element. For values of λ_c larger than unity, signifying initiation of crack, only the contact model is used to compute the interface tractions in both states. The dependence of the interface model on the materials properties and switching from interface to contact and vice versa make the approach realistic to simulate crack initiation, unloading if any before opening of cracks and subsequent large sliding at the newly created surfaces.

Two possibilities exist for the description of interface friction unloading. The first, based on the existence of a potential, describes unloading following the loading path. The second, based on an irreversible process, may describe unloading connecting the maximum displacement jump and the origin. The irreversible interface law (Pandolfi and Ortiz, 1997) could be used in problems where interface damage occurs. In this law, the maximum displacement jump is used to represent history effects. Both possible

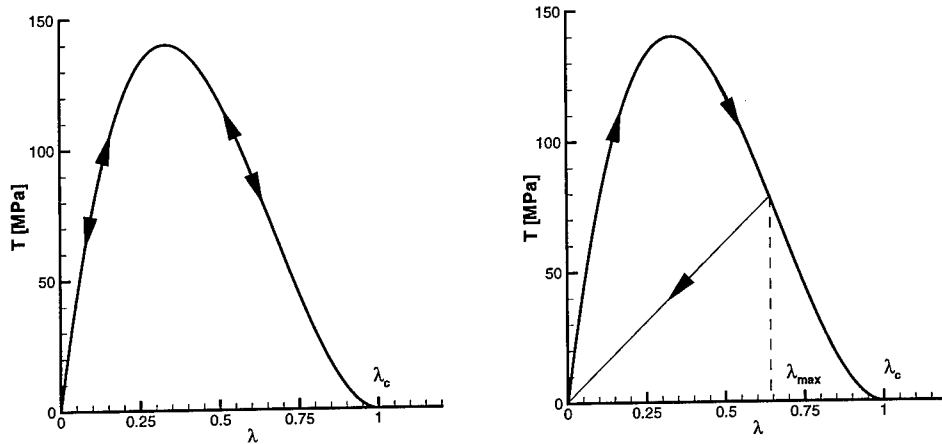


Fig. 7. Schematic representation of reversible and irreversible interface laws.

interface laws are schematically shown in Fig. 7. The reversible model is used in the calculations reported later.

Rate and temperature effects in the interface description can be easily incorporated in terms of the λ_c parameters as given by,

$$T_{\max} = T_{\max}^0 \left(1 + \beta \ln \left[\frac{\dot{\lambda}_c}{\dot{\lambda}_{c,0}} \right] \right) \left(1 - \frac{[T - T_0]}{[T_m - T_0]} \right)^x \text{ with } T_{\max}^0 = \frac{48G_c}{27\delta_n}. \quad (20)$$

In the above expression, T_{\max} is the maximum interface traction at the current displacement jump rate $\dot{\lambda}_c$ and current temperature T , T_{\max}^0 is the maximum interface traction at reference displacement jump rate $\dot{\lambda}_{c,0}$ and reference temperature T_0 , and T_m is the melting point of the material. The parameter β and x can be identified through specially designed experiments. Since there are three parameters and only one energy equation, a proper characterization requires impact experiments, i.e., spallation and compression shear, in which the cohesive law can be properly characterized. Similarly, the functional dependence of the interface traction on displacement jumps and temperature needs intensive experimental characterization.

5. DIRECT TIME INTEGRATION ALGORITHM

An explicit central-difference integration algorithm is being used to integrate the system of ordinary differential equations in time. The algorithm, accounting for acceleration corrections due to contact and equivalent nodal forces arising from

Table 2. *Explicit integration algorithm*

-
1. Initial conditions :

$$\begin{aligned} n &= 0 \\ \mathbf{u}_0 &= \bar{\mathbf{u}}_0 \\ \mathbf{v}_0 &= \bar{\mathbf{v}}_0 \\ \mathbf{a}_0 &= \mathbf{M}^{-1} (\mathbf{f}_0^{\text{ext}} - \mathbf{f}_0^{\text{int}}). \end{aligned}$$

2. Correction accelerations due to changes in boundary conditions :

$$\hat{\mathbf{a}}_n = \mathbf{M}^{-1} (\mathbf{f}_{n+1}^{\text{ext}} - \mathbf{f}_n^{\text{ext}}).$$

3. Compute displacement predictor :

$$\hat{\mathbf{u}}_{n+1} = \mathbf{u}_n + \Delta t \mathbf{v}_n + 1/2 \Delta t^2 \hat{\mathbf{a}}_n.$$

4. Modify accelerations due to surface contact based on $\hat{\mathbf{u}}_{n+1}$.

$$\mathbf{a}_n = \hat{\mathbf{a}}_n + \Delta \mathbf{a}_n$$

5. Update displacements :

$$\mathbf{u}_{n+1} = \mathbf{u}_n + \Delta t \mathbf{v}_n + 1/2 \Delta t^2 \mathbf{a}_n.$$

6. Update second Piola–Kirchhoff stress tensor \mathbf{S} at each element using material constitutive law

7. Compute the interface traction $\mathbf{T}(\lambda_c)$ for the intact interface elements

8. Compute internal force vector :

$$\mathbf{f}_{n+1}^{\text{int}} = \int_{B_0} \mathbf{B}^T \boldsymbol{\tau}_{n+1} dB_0 + \int_{S_c^{\text{int}}} \mathbf{N}^T \mathbf{T}(\lambda_c) dS; \quad \boldsymbol{\tau}_{n+1} = \mathbf{F}_{n+1}^c \mathbf{S}_{n+1} \mathbf{F}_{n+1}^{cT}.$$

9. Solve for accelerations :

$$\mathbf{a}_{n+1} = \mathbf{M}^{-1} (\mathbf{f}_{n+1}^{\text{ext}} - \mathbf{f}_{n+1}^{\text{int}}).$$

10. Update velocity vector :

$$\mathbf{v}_{n+1} = \mathbf{v}_n + \frac{\Delta t}{2} (\mathbf{a}_n + \mathbf{a}_{n+1}).$$

11. $n = n + 1$, if $n < n_{\text{max}}$ go to step (2), else stop.
-

interface elements, is summarized in Table 2. As in any initial boundary value problem, initial displacements and velocities \mathbf{u}^0 and \mathbf{v}^0 are required. Initial accelerations \mathbf{a}_0 are calculated from initial applied forces $\mathbf{f}_0^{\text{ext}}$, and initial internal forces $\mathbf{f}_0^{\text{int}}$ from the equation of motion at time t .

At each time step n , the nodal accelerations must first be corrected for any time-dependent changes in the traction boundary conditions. Then, a displacement predictor at time $n + 1$, is computed using the corrected acceleration, displacements and velocities at time step n . Modified accelerations at time n are computed based on the

corrected acceleration and changes in accelerations resulting from surface contact/interface determined from the displacement predictor at $n+1$. Updated displacements at $n+1$ are used in the update of stresses and the computation of internal forces. Lastly, accelerations and velocities at time $n+1$ are obtained completing the time integration scheme.

This explicit integration method is very useful for studies in which high rates of loading are expected. The time steps used by these explicit calculations are limited by stability, so care must be taken in finite deformation dynamic calculations to ensure that waves do not propagate through the mesh faster than the material wave speeds. To this end, the time step is calculated dynamically from the maximum element frequency in the mesh ω_{\max} , such that $\Delta t \leq 2/\omega_{\max}$. Flanagan and Belytschko (1984), derived the following estimate of ω_{\max} for an N -noded isoparametric element,

$$\omega_{\max}^2 \leq N \left(\frac{\hat{\lambda} + 2\hat{\mu}}{\rho} \right) \frac{B_{ii} B_{ii}}{A^2} \quad (21)$$

in which $B_{ii} B_{ii}$ is the trace of $[B][B]^T$, and the area A is found as $C_{IJ} X_I Y_J$, where

$$C_{IJ} = \iint_A \left(\frac{\partial N_I}{\partial \xi} \frac{\partial N_J}{\partial \eta} - \frac{\partial N_I}{\partial \eta} \frac{\partial N_J}{\partial \xi} \right) d\eta d\xi, \quad (22)$$

and N_I are the element shape functions.

6. CASE STUDY : ROD ON ROD IMPACT

6.1. Problem definition

After developing a finite element model for large deformation brittle failure, validation by simulating specially designed experiments is required. Moreover, accessing its ability to capture the observed material inelasticity and failure mechanisms is desirable. Espinosa and Brar (1995) and Simha *et al.* (1995) studied damage and fragmentation of AD-998 and AD-94 sintered alumina bars manufactured by Coors Porcelain Company, Golden, CO. The experiments consisted of the co-axial impact of a ceramic rod against another rod made of identical materials with diameter 12.7 mm. The length of the impactor rod was 80 mm, while that of the target rod was 170 mm. Moreover, in-material stress measurements were performed with manganin gauges (Type C-880113, Micro-Measurements, Raleigh, NC) embedded at 10 rod diameters from the impact surface. The gauges were backed by 25.4 or 50 mm rods of the same material as the front piece. The back pieces of the assembled bar targets were set in a lexan disk using epoxy in order to align the target for a planar impact. A coaxial trigger pin was also set through a hole in the lexan ring to trigger a manganin gauge bridge circuit and a high speed Imacon camera operated at 10^5 frames/s. The bars were painted black so that cracks and faults could be distinguished during the failure event. Measured stress profiles revealed the material remains elastic when the impact velocity is below about 100 m/s. By contrast, when the impact velocity reaches 304 m/s, the maximum compressive stress is sustained for only 200 μ s with a main

pulse duration of approximately $1.8 \mu\text{s}$ followed by a tail. Damage evolution was observed in a sequence of photographs taken every $10 \mu\text{s}$ with the Imacon camera. Well defined patterns of longitudinal cracks are also observed in a region approximately two bar diameters in size, symmetrically formed from the impact surface. A violent radial expansion with a debris of fine particles results from accumulated damage and pulverization of the material.

The results obtained from the rod on rod experiments are used to validate the numerical model described earlier. The model is further used to carry out parametric analyses and establish the adequacy of the proposed model. The dimensions of the two ceramic rods used in the analyses are the same as mentioned above. All the analyses are carried out at an impact velocity of 304 m/s.

6.2. *Multi-body discretization*

As stated earlier, it is important to measure the initial grain size of the ceramic material to estimate the smallest possible fragment size (cluster of grains) based on experimental observations. Based on this estimate, fragments are generated in the ceramic bars with random morphology. The application of the model to actual grain sizes and fragments is the subject of current research work. For discretization, it is assumed that potential fragments are of quasi-hexagonal shape with random size and their major axes are aligned parallel to the axis-of-symmetry. In order to minimize the computation time, potential fragments are generated only in a portion of the length of the two bars where severe fragmentation was observed. The rest of the bars length is discretized continuously without potential fragments.

A pre-processor has been developed and integrated in our version of FEAP (Zienkiewicz and Taylor, 1991a, b) for generating potential fragments and the interface elements between them. The bar radius, the axial length and the number of fragments to be generated along the two directions, i.e., X - and Y -, are given as input to the pre-processor. The pre-processor calculates the average fragment size based on the input and generates the hexagons. Subsequently, the vertices of the hexagon are displaced randomly maintaining the outer boundaries. The direction and the amount of displacement for each node are generated using a standard random number generator. Each hexagon is then discretized into six 6-noded quadratic triangular elements. On account of symmetry at the center and to maintain the continuity of the material, partial hexagons are generated at the boundaries which are discretized into two or three triangles. Four noded interface elements are embedded along the edges of hexagons by picking two edge nodes from the hexagon on the right side of an edge and remaining two nodes from the hexagon on the left side of the edge.

The quadratic triangular elements in the continuous region of the two bars are generated using a pre-processor already in-built in this version of FEAP. One additional module has been developed to connect the hexagons and continuous regions by embedding interface elements between them.

Two types of meshes have been used in the analyses. As shown in Fig. 8 with zooms centered at the impact plane, one is a coarse mesh having 100 hexagons, 2713 nodes, 923 triangular elements and 510 interface elements. A fine mesh shown in the same figure having 304 hexagons, 7464 nodes, 2564 triangular elements and 1656 interface elements was also used.

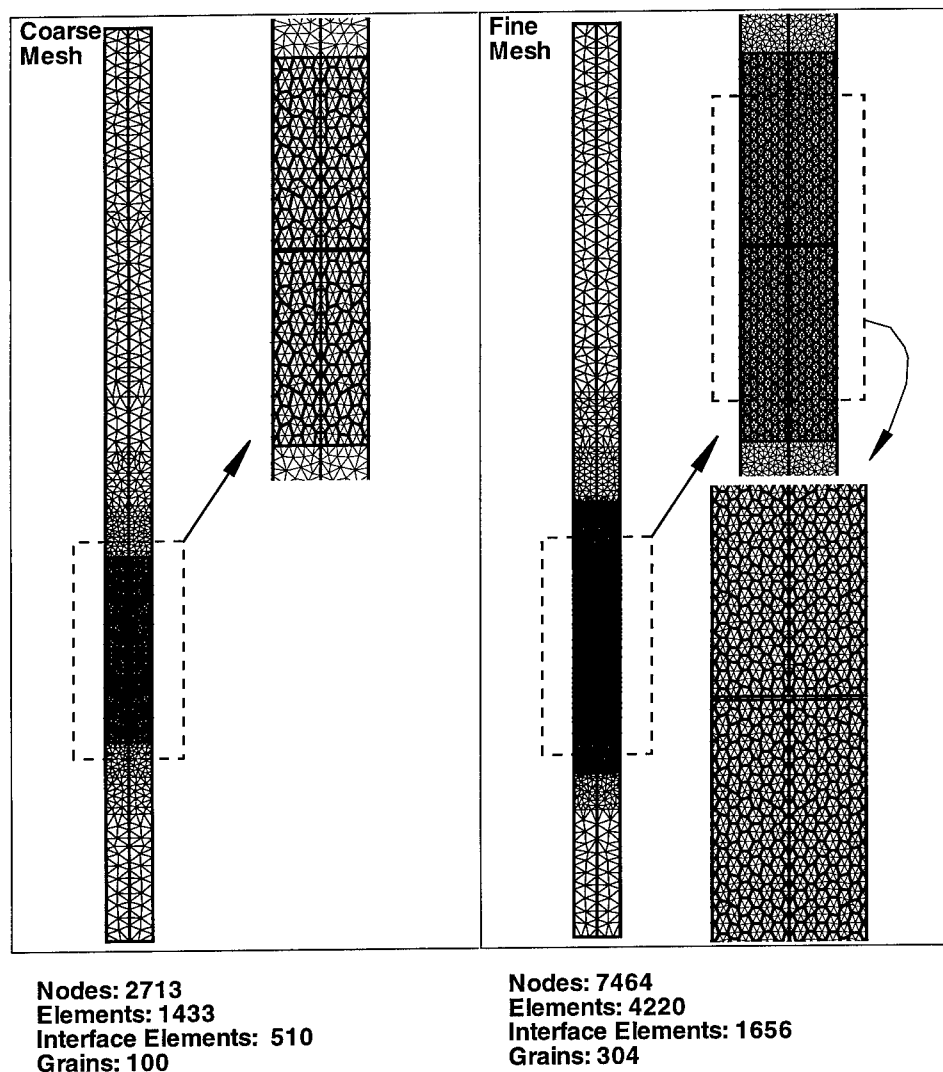


Fig. 8. Coarse and fine meshes.

6.3. *Materials properties*

The properties of the alumina ceramic and the parameters for the contact and interface elements used in the various analyses are given in Tables 3–5. The ceramic multiple-plane continuum damage model parameters are selected such that a damage threshold is properly captured and, at the same time, they are in agreement with values reported in the literature. As pointed out in Espinosa and Brar (1995), it should be noted that microstructural differences have an effect on model parameters. For instance, the existence of a second phase at the grain boundaries controls parameters

Table 3. *Material properties for alumina*

AD-99.5 Alumina ceramic	
Elastic Properties	
$E = 374 \text{ GPa}$	Young's modulus
$\nu = 0.22$	Poisson's ratio
$\rho_0 = 3890 \text{ kg/m}^3$	Density
Inelastic properties	
$\mu = 0.1$	Internal friction coefficient
$c_R = 5000 \text{ m/s}$	Wave speed
$K_{IC} = 1.7 \times 10^6 \text{ MPa } \sqrt{\text{m}}$	Critical stress intensity factor
$a_0 = 10 \text{ } \mu\text{m}$	Initial crack radius
$c_n^1 = 1.0 \times 10^{12} \text{ m}^{-3}$	Crack density for plane 1
$c_n^2 = 1.0 \times 10^{12} \text{ m}^{-3}$	Crack density for plane 2
$c_n^3 = 1.0 \times 10^{12} \text{ m}^{-3}$	Crack density for plane 3
$c_n^4 = 0.0$	Crack density for plane 4
$c_n^5 = 0.0$	Crack density for plane 5
$c_n^6 = 1.0 \times 10^{10} \text{ m}^{-3}$	Crack density for plane 6
$c_n^7 = 0.0$	Crack density for plane 7
$c_n^8 = 0.0$	Crack density for plane 8
$c_n^9 = 0.0$	Crack density for plane 9
$c_n^{10} = 0.0$	Crack density for plane 10
$c_n^{11} = 1.0 \times 10^{10} \text{ m}^{-3}$	Crack density for plane 11
$c_n^{12} = 0.0$	Crack density for plane 12
$c_n^{13} = 0.0$	Crack density for plane 13
$n^+ = 0.3$	Ratio 1 (tension)
$n^- = 0.1$	Ratio 2 (compression)
$m^+ = 0.3$	Power 1 (tension)
$m^- = 0.1$	Power 2 (compression)

Table 4. *Contact constants*
(Espinosa et al., 1998)

μ	0.0	0.2	0.5
μ_0	0.0	0.2	0.5
μ_∞	0.0	0.2	0.5
γ	0.0	0.0	0.0
β	0.5	0.5	0.5

$$\mu = \mu_\infty + (\mu_0 - \mu_\infty)e^{\gamma/\mu}.$$

μ , n^\pm , m^\pm and K_{IC} . The grain size controls the values of a_0 and maximum crack density of each orientation. The choice of different crack densities as a function of orientation is motivated by experimental data (Espinosa *et al.*, 1992) indicating that the density of active microcracks is a function of the mechanism responsible for crack nucleation. In the case of predominantly compressive stress states, glass at the grain boundaries

Table 5. *Interface element constants*

Interface properties	
$T_{\max} = 140.0 \text{ MPa}$	Maximum interfacial traction
$\delta_n = 1.0 \text{ } \mu\text{m}$	Critical normal opening
$\delta_t = 1.0 \text{ } \mu\text{m}$	Critical tangential slip
$\alpha = 0.5$	Interface mode coupling parameter

determines the early stages of inelasticity and acts as a precursor for the development of triple point microcracks. In the case of predominantly tensile stress states, cracks are mainly nucleated due to grain boundary decohesion at a much lower stress level. In the present axisymmetric calculations, plane 1 is a plane on which positive normal tractions result from unloading waves emanating from the bar surface. By contrast, planes 6 and 11 are mainly shear cracks.

The interface parameters were selected consistently with the assumed fracture toughness of the material, i.e., $K_{IC} = 1.7 \text{ MPa } \sqrt{\text{m}}$ or $G_c = 78.75 \text{ N/m}$. Assuming a $\delta_c = 1 \text{ } \mu\text{m}$, a quasi-static $T_{\max} = 140 \text{ MPa}$ is obtained. In the present analyses, a reversible law is used and no rate or temperature effects are included due to the limited experimental data available.

6.4. *Summary of analyses*

Two dimensional axisymmetric analyses for the rod on rod impact have been carried out to validate the model with the experimental results and to study the effect of various parameters. The continuum-discrete approach as mentioned earlier, as well as the discrete approach using the interface elements, are employed to analyze the hexagon region of the two bars, while only continuum damage is used to analyze the continuous region. The effect of fragment size is analyzed by carrying out analyses with two different mesh sizes as given earlier. Analyses have also been carried out with three different values of the friction coefficients between fragments to study their effect on the response during deformation. The various analyses carried out are summarized in Table 6.

As mentioned earlier, the continuum damage model possesses the problem of very large distortion of elements which has been circumvented before by adaptive meshing of the highly deformed zone. In the present case too, the fragments deform excessively when the continuum/discrete model is used. The remeshing of grains and reinsertion of interface elements between them due to mesh changes are under development. The problem has been circumvented for the present analyses by using erosion (Espinosa *et al.*, 1998). Fragments in which all elements attain a critical value of erosion parameter at their integration points are eroded. The value of 2.0 for the effective inelastic strain considered as erosion parameter has been used in all the analyses with the continuum/discrete model.

Table 6. *Summary of various analyses*

Analysis	Model	Mesh	Friction coef.
I	Continuum/discrete	coarse	0.0
II	Continuum/discrete	coarse	0.2
III	Continuum/discrete	coarse	0.5
IV	Discrete	coarse	0.0
V	Discrete	coarse	0.2
VI	Discrete	coarse	0.5
VII	continuum/discrete	fine	0.2
VIII	Discrete	fine	0.0
IX	Continuum	coarse	0.0

7. RESULTS AND DISCUSSION

As given below, the results obtained from various analyses are discussed in terms of the continuum-discrete vs discrete damage models, effect of fragment size and friction and the fracture patterns predicted with the two models. The results obtained from the analyses are compared with the experimental results in terms of the measured in-material stress histories and the recorded fragmentation pattern with high speed photography.

7.1. *Continuum/discrete vs discrete damage models*

As mentioned in the previous section, failure in ceramics is the result of initiation and propagation of cracks. As a result of which, stress attenuation and fragmentation take place. In general, stress attenuation can be described reasonably well by means of continuum models. However, due to the inherent assumptions, they cannot describe crack coalescence leading to discrete fragmentation. Hence, a complete description of brittle failure can be obtained either by means of discrete fragmentation models or continuum/discrete models.

In order to examine the features of continuum/discrete and discrete models in predicting the response during impact, analyses are carried out with a coarse as well as a fine mesh. The analyses with the coarse mesh have been carried out without friction between fragments, while a value of friction coefficient of 0.2 is used in the case of the fine mesh. The axial stress at 120 mm from the impact plane is retrieved from analyses results. This stress is compared with the experimentally measured stress and is plotted in Figs. 9 and 10 for the two types of meshes, respectively. An analysis has also been carried out with the continuum damage model alone for comparison purposes. Its stress history is also given in Fig. 9.

It is found that the discrete model reasonably predicts the stress increase and its peak value, but overpredicts the pulse duration and fails to capture the strong stress attenuation observed experimentally. By contrast, the pure continuum model provides a good overall fit for the set of parameters previously reported. However, the continuum/discrete model predicts the pulse duration and shock attenuation with reason-

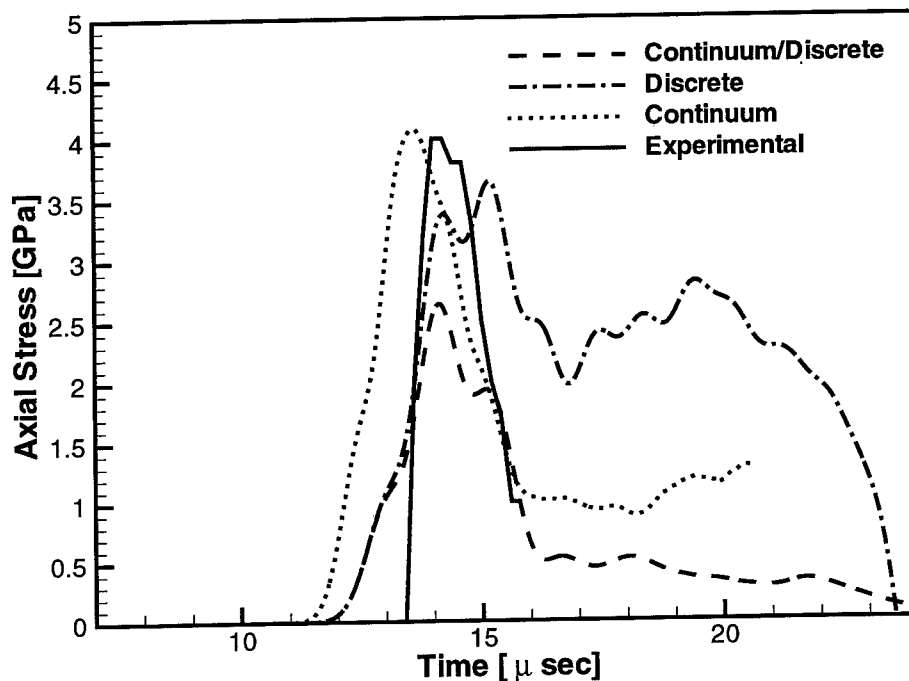


Fig. 9. Continuum/discrete and discrete models vs experimental data with coarse mesh.

able accuracy but underestimates the peak stress. It is not surprising that the continuum/discrete model results in a lower peak stress than the one obtained with a pure continuum damage model. In fact, since the same crack density is used in both cases, the continuum/discrete model possesses a larger crack surface area per unit volume in view of the point that, in addition to the microcrack density used in the multiple-plane model, macrocracks are allowed in the formation of fragments. It can be inferred from the plot that the continuum/discrete model can capture not only the measured stress profile, but also the pulverization observed experimentally in the impact region (see later discussion on fragmentation pattern and ceramic pulverization near the impact region).

7.2. *Effect of friction between fragments*

An important aspect of the failure of ceramics is the role of friction between fragments. It is known that the shear strength of comminuted ceramics is controlled by the friction properties between fragments. For this reason, confinement pressure also play a dominant role in the material shear resistance. In the case of rod on rod impact, the confinement pressure is generally low. However, friction between fragments is important at the early stages of damage.

In order to investigate the effect of friction between fragments, analyses have been

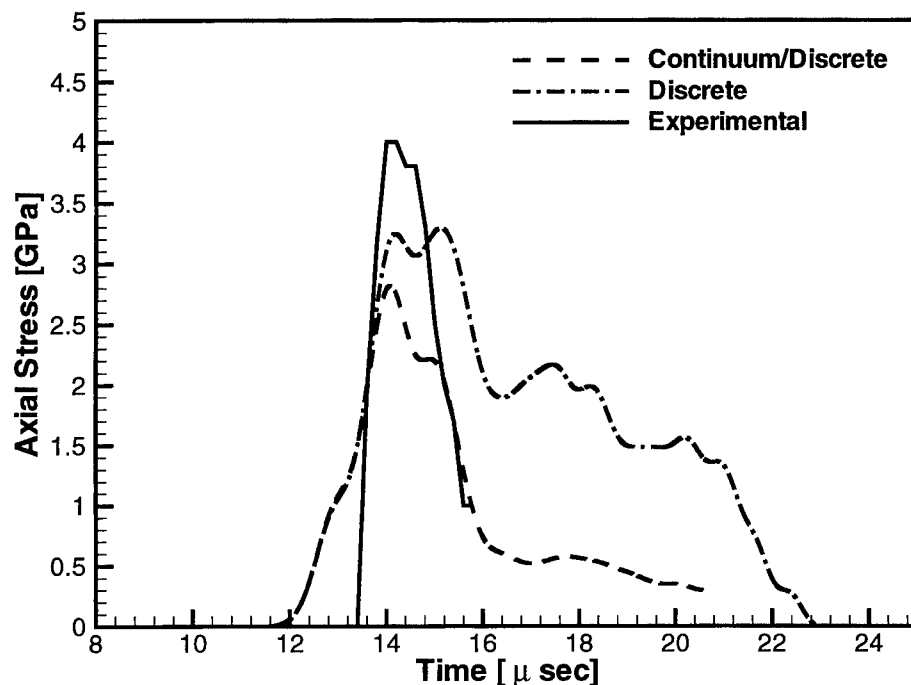


Fig. 10. Continuum/discrete and discrete models vs experimental data with fine mesh.

carried out with three values of the friction coefficient as 0.0, 0.2 and 0.5 using both the continuum/discrete and discrete models and the coarse mesh. Axial stress histories predicted by the two models with the 0.2 and 0.5 friction coefficients together with that obtained with the zero coefficient discussed above are plotted in Figs 11 and 12, respectively. The fragmented bars at 10, 20, 30 and 40 μ s are shown in Fig. 13 for the three coefficients obtained by the discrete model. A comparison with high speed photographs, at these times, taken during the experiment is also shown in the figure. The experimental photographs clearly show longitudinal cracks and an increasing radial expansion, near the impact surface, leading to the pulverization of the ceramic.

As observed in Figs 11 and 12, the friction coefficient has a lesser effect in the case of continuum/discrete model compared to the discrete model. The difference in the peak stress predicted by continuum/discrete model is about 0.8 GPa when the friction coefficient is increased from 0–0.5. But the pulse duration and stress attenuation are not altered significantly. In the case of the discrete model, the peak stress increases by about 2.2 GPa as the friction coefficient is increased to 0.5. Also, the pulse duration increases and the stress attenuation is reduced significantly. As the value of friction coefficient is definitely larger than zero, the response predicted by the discrete model is in sharp contrast to that obtained experimentally. It should be noted that in the case of the continuum/discrete damage model, a significant fraction of the total

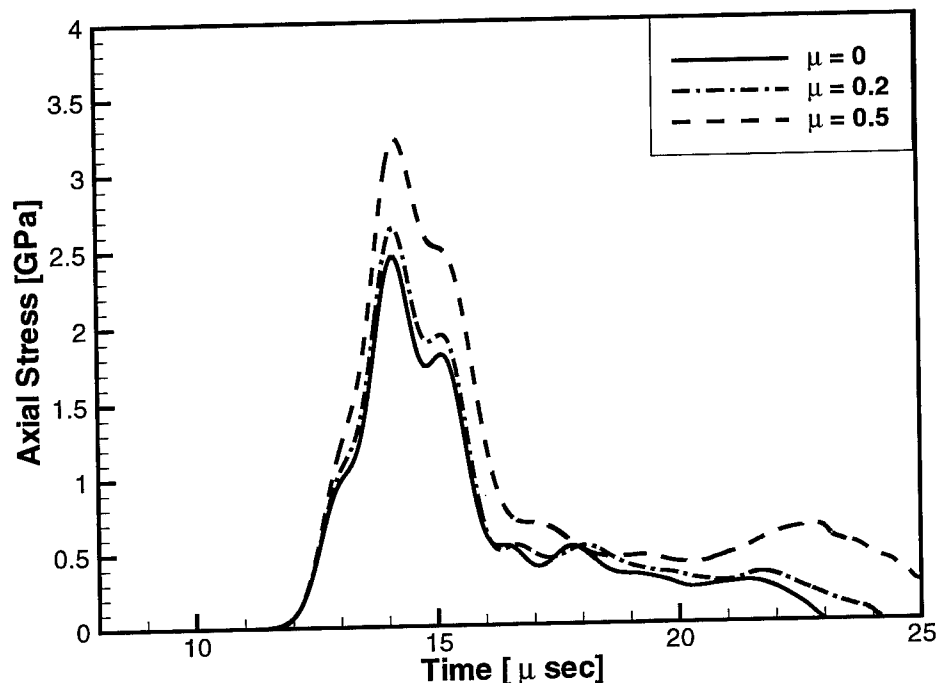


Fig. 11. Continuum/discrete model with $\mu = 0, 0.2$ and 0.5 .

dissipated energy occurs within the fragments due to the growth of a large density of penny-shaped cracks. In the calculations, the internal friction coefficient used in the description of the multiple-plane model was not modified.

It is observed in Fig. 13 that the discrete model predicts overall fragmentation consistently with the experimental results only at low values of μ . While the discrete model is more sensitive to the friction coefficient between fragments, it does not require fragment erosion to advance the calculation. As a result, a better understanding of the evolution of fragment initiation and evolution is attained. It is observed that the amount of radial expansion and rotation in the fragmented zone is very much reduced with the increase in friction coefficient. The response predicted by the model when the friction coefficient is set to 0.2 , matches reasonably well with the fragmentation progression as recorded by high speed photographs. Similar results have been obtained with the continuum/discrete model (not plotted here) with the difference that it requires a small amount of fragment's erosion to advance the solution.

7.3. Effect of model type on fracture patterns

It is also important for the model to predict fracture patterns leading to failure in agreement with the experimental findings. For this purpose in this subsection, the fracture pattern obtained from the discrete and continuum/discrete models are given in Figs 14–17, respectively, obtained with the coarse and fine meshes at the early

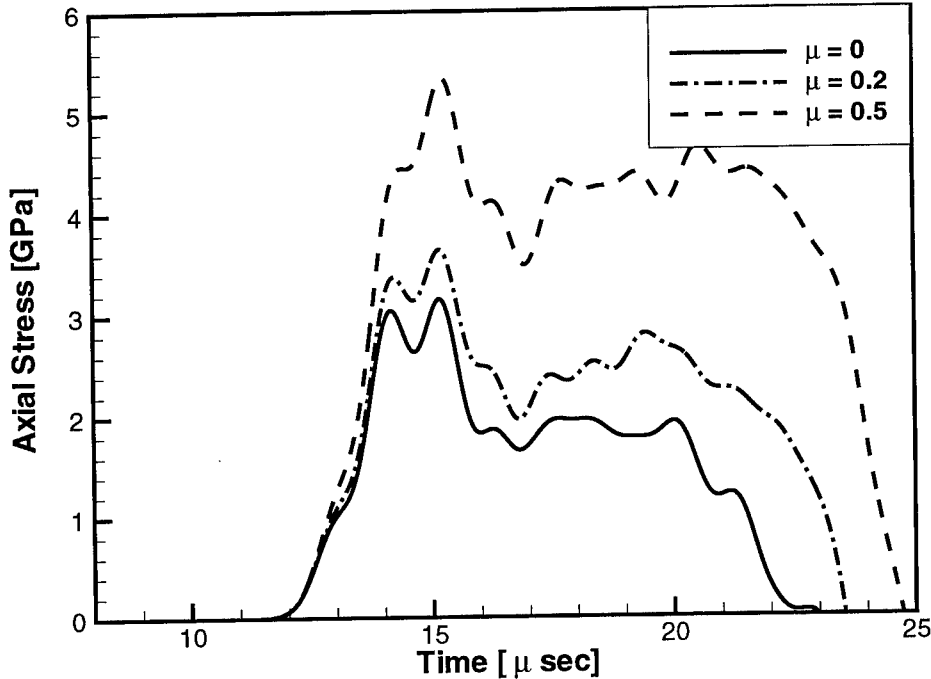
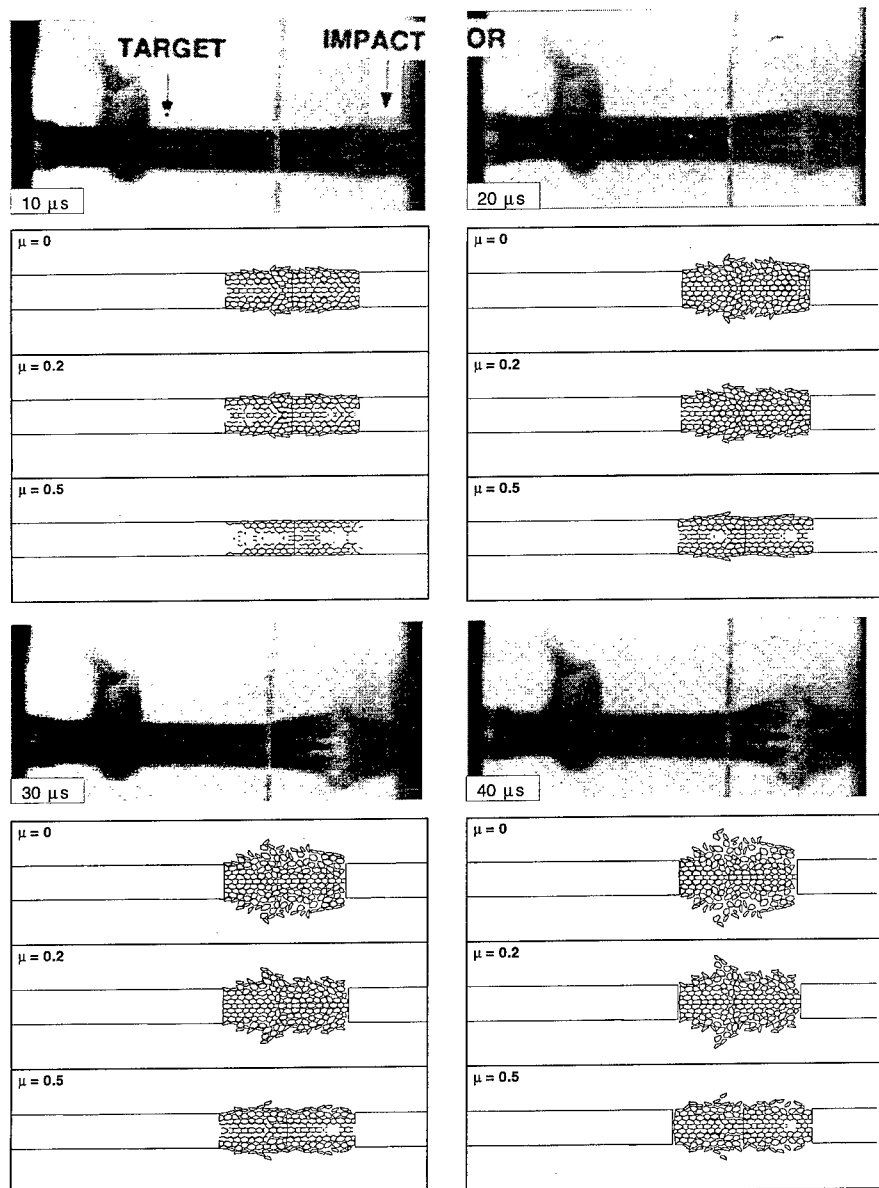


Fig. 12. Discrete model with $\mu = 0, 0.2$ and 0.5 .

stages of fragmentation, first $12 \mu\text{s}$. It is observed, in both models, that fracture of ceramic rods starts from the outer surface and propagates towards the core and away from the impact surface. This is consistent with the wave propagation theory in inelastic media. Together with the compressive shock wave generated at the impact surface, tensile rarefaction waves are generated at the rod free surface which tail the shock wave with the sound speed of the ceramic material. These rarefaction waves are primarily responsible for the initiation of cracks near the surface. So long as the rarefaction wave from the other end of the bars has not arrived to the hexagon region, failure of both bars, impactor and target, remains more or less similar in pattern. However, due to arrival of the unloading pulse, the core of the shorter impactor bar produces additional fragments in the impactor. These phenomena can be seen in the case of the coarse, as well as fine mesh, in Figs 14–17.

It is found that in both models, there is not excessive deformation and rotation of grains, in the failure zone, during the first $12 \mu\text{s}$. Fragments displace radially outward giving the step pattern of the failure surface at the boundary which is consistent with the experimental observation as evident from the high speed photographs. The photographs show that the crack density gradually diminishes away from the impact surface. This behavior is predicted to some approximation by both models, though the deformation and rotation of grains in the simulations are appreciable. A larger gradient in crack density is observed in the continuum/discrete damage model.

An important observation to be made from these plots is that there are distinct

Fig. 13. Damage validation at 10, 20, 30 and 40 μs .

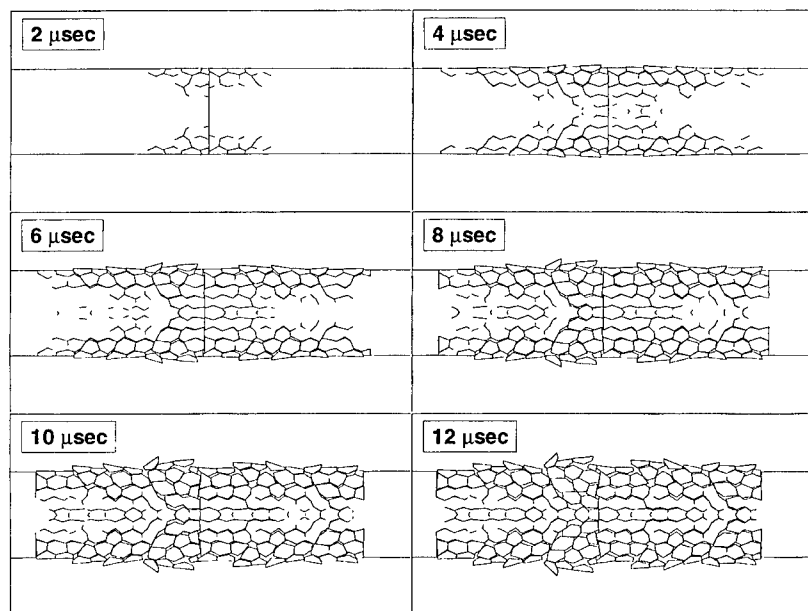


Fig. 14. Fracture pattern for discrete model with coarse mesh.

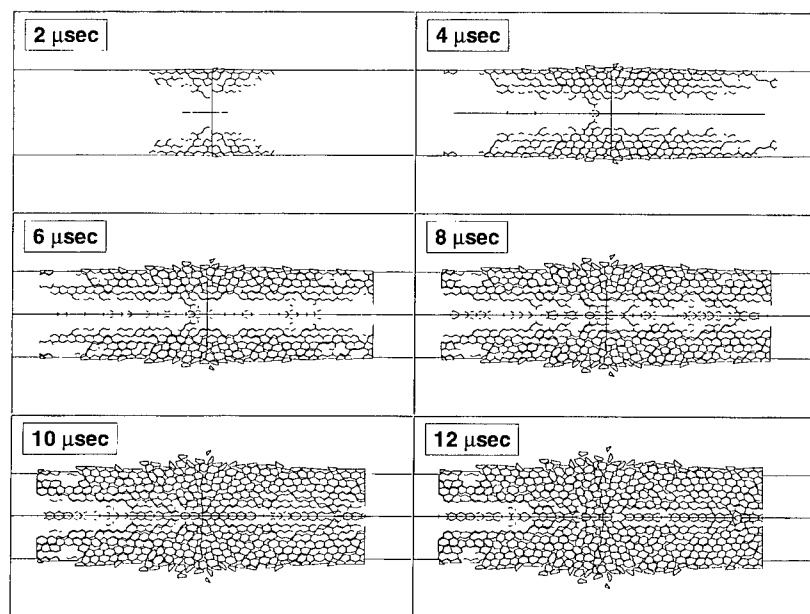


Fig. 15. Fracture pattern for discrete model with fine mesh.

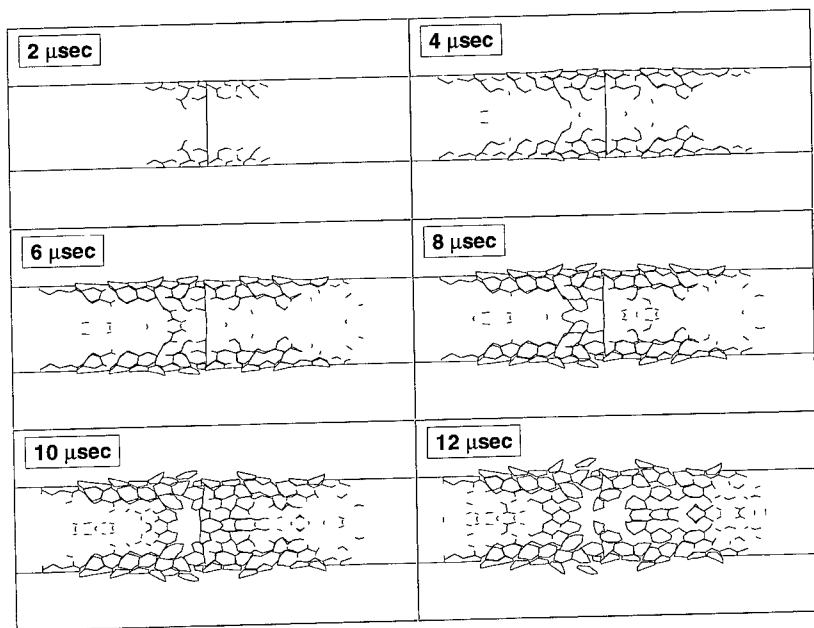


Fig. 16. Fracture pattern for continuum/discrete model with coarse mesh.

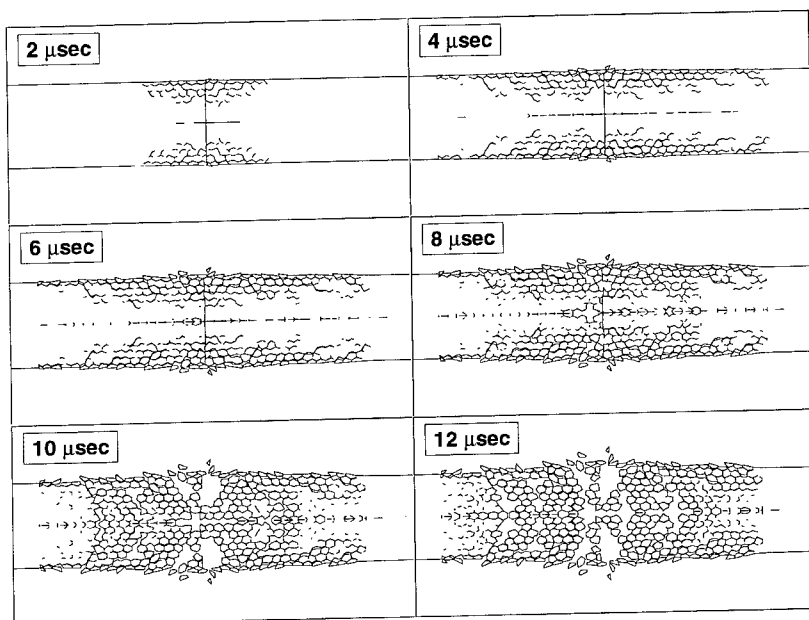


Fig. 17. Fracture pattern for continuum/discrete model with fine mesh.

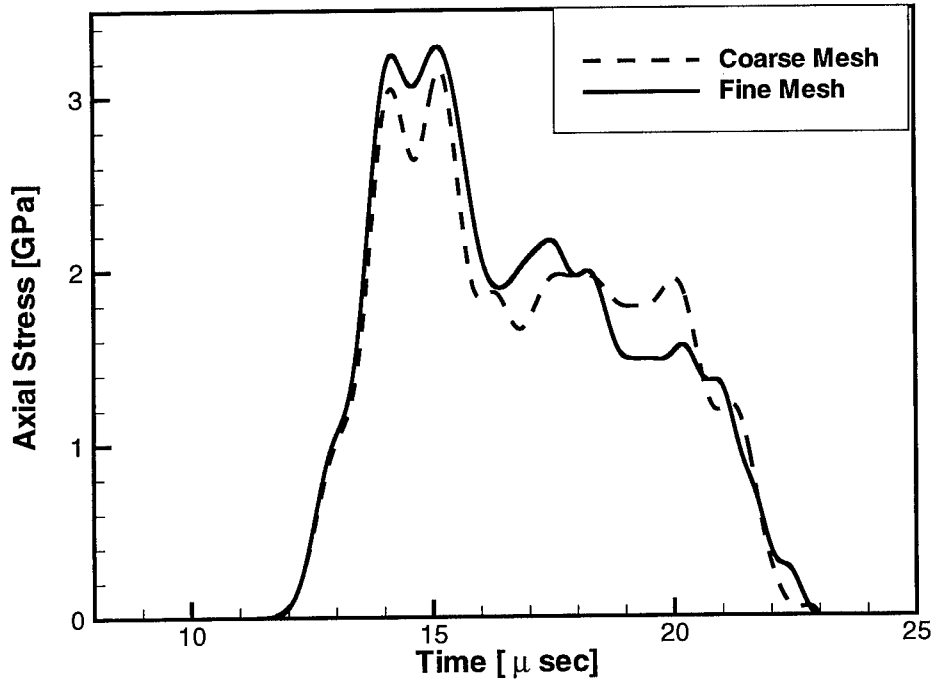


Fig. 18. Axial stress comparison between fine and coarse meshes for discrete model.

planes at which radial bulging is observed. The length interval at which this takes place is the same in the case of the coarse and fine meshes indicating the phenomena to be related to a material behavior. One possible reason for this may be the attenuation of the tensile rarefaction radial waves due to release of energy in crack initiation and enlargement. Additional failure can take place only by the new rarefaction wave generated down the length of the bars. This observation is important from the experiment at viewpoint in deciding the location of the gauge for stress and radial velocity measurement. The constant length interval in the case of coarse and fine meshes indicates that the pulse duration and the attenuation of waves appear independent of the mesh size.

7.4. Effect of potential fragment/mesh size

As mentioned earlier, one of the objectives of the present research is to develop a model which minimizes the run-time and yields results consistent with experimental observations. Figures 18 and 19 compare the axial stress obtained from coarse and fine meshes with the discrete and continuum/discrete models, respectively. The friction coefficient in the case of continuum/discrete model is 0.2 while the discrete model uses zero friction coefficient. It is observed that there is not appreciable difference in the peak stress, pulse duration and stress attenuation predicted by both models for a given value of friction coefficient, between fragments, as the mesh is refined. Hence, the two models are predicted to be almost mesh independent for the two fragment

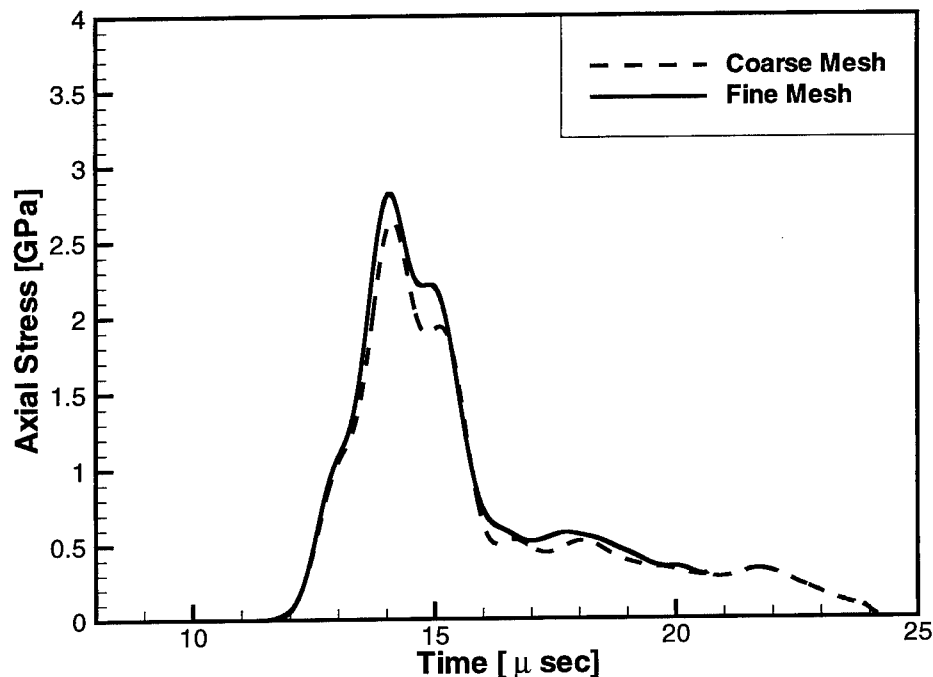


Fig. 19. Axial stress comparison between fine and coarse meshes for continuum/discrete model.

sizes considered in the present analyses. This shows that the assumption of fragments containing a large number of grains is not far from realism in computational analyses.

It can be argued that it is surprising that not much mesh sensitivity is observed in the case of the pure discrete fragmentation model. In fact, it is expected that as the number of potential fragments in the mesh is increased, the stress history would approach the experimentally measured stress history. A possibility for the lack of significant increase in stress attenuation behind the wave front, with fragment size reduction, (see Fig. 18), may be due to the fact that an extremely fine mesh, with potential fragment sizes of the order of the material grain size is required to capture the initiation of all possible microcracks. Certainly, in the present analyses, the reduction in the fragment size in the case of fine mesh is far from achieving the actual grain size of the material.

8. CONCLUDING REMARKS

A novel way of predicting structural response of ceramics during impact capable of capturing brittle failure features has been presented by combining two classes of damage models, viz., continuum and discrete damage models. The model so arrived, and named continuum/discrete model, is able to predict the response of ceramics in agreement with experimental observations. The concept of arriving at meaningful

finite element simulations of such highly nonlinear class of problems, in a reasonable time, may be well served as established by comparing simulation results with experimental results. The simulations presented here establish the advantages of the continuum/discrete damage model over the discrete damage model in terms of the structural response of ceramics, e.g., deformation, stress history, fracture pattern, etc. The arguments in favor of the two classes of damage models may be applied simultaneously to the continuum/discrete model. However, one argument against the model may be related to the assumption of the initial fragment size and interface elements between them providing pre-determined crack paths. The discrete damage model with the capability of initiating as many cracks as required with their propagation in the correctly predicted direction, or the continuum/discrete damage model with the fragment size of the order of actual grain size may seem to be scientifically more accurate. However, such analyses would be so computer intensive that they may prove to be far from realism for field design applications. Also, such analyses would be carried out omitting useful experimental findings. On the contrary, potential fragment shape and size can be reasonably chosen based on experimental findings as discussed in the introduction. This further concretizes the concept of combined experimental/numerical investigation for such highly nonlinear and complex class of problems. The concept of choosing a random pattern of potential fragments, a priori, and embedding interface elements between them, i.e., prefixing the direction for crack propagation, may find application readily in many other problems for which the position of crack initiation and propagation are more or less well defined, e.g., machining of ceramics, delamination in fiber reinforced composite materials (Lu, 1998), etc.

The interface law plays a significant role in the continuum/discrete model. In principle, any interface law can be used after experimental determination of its parameters through well designed experiments, viz., plate impact experiments and Kolsky bar experiments (see contributions by Clifton and Klopp (1985); Duffy, 1980). The rate effect included in our interface formulation is expected to eliminate the need for regularization through nonlocal analyses, thus making the prediction of dynamic failure mesh independent.

One disadvantage of the continuum/discrete model is that with the accumulation of damage, element distortion within fragments may become excessive. In such case, remeshing of elements within each fragment is required if erosion is not desirable. Such remeshing with a consistent mesh transfer operator can be easily implemented. Hence, it may be concluded that the present methodology provides a powerful tool for predicting the structural response of brittle materials in agreement with experimental measurements and observations.

ACKNOWLEDGEMENTS

This research was supported by the National Science Foundation through grants MSS-9309006, MSS 9311289, CMS-9523113, the Army Office of Scientific Research through Grant No DAAH04-96-1-0142, and ARO-MURI Grant No. DAAH04-96-1-0331.

REFERENCES

- Addessio, F. L. and Johnson, J. N. (1989) A constitutive model for the dynamic response of brittle materials. LA-UR-89-2651, Los Alamos National Laboratory, Los Alamos, NM, U.S.A.
- Andrews, E. W. and Kim, K. S. (1997) Threshold conditions for dynamic fragmentation of ceramic particles. *International Journal of Solids and Structures*, to appear.
- Biner, S. B. (1994) Numerical analysis of crack growth in microcracking ceramic and ceramic composites. *Proc. Symp. Materials Research Society* **365**, 165–170.
- Brar, N. S., Yuan, G., Espinosa, H. D. and Zavattieri, P. D. (1997) Experimental study of interface defeat in confined ceramic targets. *Proceedings of 97 APS Topic Conference of Shock Compression of Condensed Matter*, 27 July–1 August, Amherst, MA.
- Camacho, G. T. and Ortiz, M. (1996) Computational modeling of impact damage in brittle materials. *International Journal of Solids and Structures* **33**, 2899–2938.
- Clifton, R. J. and Klopp, R. W. (1985) Pressure-shear plate impact testing, In *Metals Handbook: Mechanical Testing* 8, 9th edn, p. 230.
- Curran, D., Seaman, L., Cooper, T. and Shockey, D. (1990) Micromechanical model for comminution and granular flow of brittle material under high strain rate application to penetration of ceramic targets. *International Journal Impact Engineering* **13**, 53–83.
- Duffy, J. (1980) The Dynamic Plastic Deformation of Metals: A Review, AFML-TR-82-4024, Wright-Patterson Air Force base, OH.
- Espinosa, H. D. (1989) *Finite element analysis of stress induced damage in ceramics*. MSc thesis, Brown University, Providence, RI.
- Espinosa, H. D. (1992) *Micromechanics of the dynamic response of ceramics and ceramic composites*. Ph.D. thesis, Brown University, Providence, RI.
- Espinosa, H. D., Raiser, G., Clifton, R. J. and Ortiz, M. (1992) Experimental observations and numerical modeling of inelasticity in dynamically loaded ceramics. *J. Hard Mat.* **3**, 285–313.
- Espinosa, H. D. (1995) On the dynamic shear resistance of ceramic composites and its dependence on applied multiaxial deformation. *International Journal of Solids and Structures* **32**, 3105.
- Espinosa, H. D. and Brar, N. S. (1995) Dynamic failure mechanisms of ceramic bars: experiments and numerical simulations. *Journal of the Mechanics and Physics of Solids* **43**(10), 1615.
- Espinosa, H. D., Emore, G. L. and Zavattieri, P. D. (1996) Computational modeling of geometric and material nonlinearities with an application to impact damage in brittle materials. In *Advances in Failure Mechanism in Brittle Materials*, ed. R. J. Clifton and H. D. Espinosa. MD-75, AMD-219, pp. 119–161.
- Espinosa, H. D., Yuan, G., Dwivedi, S. and Zavattieri, P. D. (1997) Numerical study of penetration in ceramic targets with a multiple-plane model. *Proceedings of 97 APS Topic Conference of Shock Compression of Condensed Matter*, 27 July–1 August, Amherst, MA.
- Espinosa, H. D., Lu, H.-C. and Xu, Y. (1998) A novel technique for penetrator velocity measurement in ballistic penetration studies. *Journal of Composite Materials* **32**(8), 722–743.
- Espinosa, H. D., Dwivedi, S., Zavattieri, P. D. and Yuan, G. (1998) Numerical investigations of penetration in multilayered material/structure systems. *International Journal of Solids and Structures* **35**(2), 2975–3001.
- Espinosa, H. D., Zavattieri, P. D. and Emore, D. (1998) Adaptive FEM computation of geometric and material nonlinearities with application to brittle failure. *Mechanics of Materials*, to appear.
- Evans, A. G. (1978) Impact damage in ceramics. *Fracture Mechanics of Ceramics*, ed. R. C. Bradt, D. P. H. Hasselman and F. F. Lange, Vol. 3, pp. 303–331. Plenum Press.
- Field, J. E. (1988) Investigation of the impact performance of various glass and ceramic systems. Technical report USARDSG-UK ARO-R DAJA45-85-C-0021. Cavendish Laboratory, University of Cambridge.
- Flanagan, D. P. and Belytschko, T. (1984) Eigenvalues and stable time steps for the uniform

- strain hexahedron and quadrilaterals. *Transactions of A.S.M.E., Journal of Applied Mechanics* **51**, 35.
- Freund, L. B. (1990) *Dynamic Fracture Mechanics*. Cambridge University Press, Cambridge.
- Gong, S. X. (1995) On the micromechanics modeling of microcrack toughening in ceramic materials. *Trans. Cand. Sc. Mech. Engr.* **19**(3), 317–329.
- Gurson, A. L. (1977) Porous rigid-plastic materials containing rigid inclusions-yield function, plastic potential and void nucleation. In *Adv. Res. Strength Fract. Matls.* ed. D. M. R. Tablin. Pergamon Press, NY, U.S.A.
- Hauver, G., Netherwood, P., Benck, R. and Kecskes, L. (1993) Ballistic performance of ceramic Targets. *Proceedings of the Army Symposium on Solid Mechanics*, 17–19 August, Plymouth, MA, Orlando, FL, U.S.A.
- Hauver, G., Netherwood, P., Benck, R. and Kecskes, L. (1994) Enhanced ballistic performance of ceramics. *19th Army Science Conference*, 20–24 June, Orlando, FL, U.S.A.
- Johnson, G. R. and Cook, W. H. (1985) Fracture characteristics of three metals subjected to various strains, strain rates, temperature and pressure. *Eng. Frac. Mech.* **21**, 31–48.
- Johnson, G. R. and Holmquist, T. J. (1992) A computational constitutive model for brittle materials subjected to large strains, high strain rates and high pressures. In *Shock-Wave and High Strain Rate Phenomena in Materials*, ed. M. A. Meyers, L. E. Murr and K. P. Staudhammer, pp. 1075–1081. Marcel Dekker, New York.
- Lawn, B. R. (1994) Model for microcrack initiation and propagation beneath Hertzian contacts in polycrystalline ceramics. *Acta. Met. et Mat.* **42**(5), 1683–1693.
- Lu, H.-C. (1998) Ballistic penetration of GRP composites: identification of failure mechanisms and modeling. Ph.D. thesis, Purdue University, IN.
- Needleman, A. (1988) Material rate dependence and mesh sensitivity in localization problems. *Comput. Meth. App. Mech. Engg.* **67**, 69–85.
- Orphal, D. L. and Franzen, R. R. (1996) Penetration of confined aluminum nitride targets by tungsten long rod at 1.5–4.5 km/s. *International Journal of Engineering* **18**, 355–368.
- Orphal, D. L. and Franzen, R. R. (1997a) Penetration of confined silicon carbide targets by tungsten long rods at impact velocities from 1.5–4.6 km/s. *International Journal of Impact Engineering* **19**, 1–13.
- Orphal, D. L., Franzen, R. R., Charters, A. C. *et al.* (1997b) Penetration of confined boron carbide targets by tungsten long rods at impact velocities from 1.5–5.0 km/s. *International Journal of Impact Engineering* **19**, 15–29.
- Pandolfi, A. and Ortiz, M. (1997) A Class of Cohesive Elements for the Simulation of Three-Dimensional Crack Propagation, presented at ASME International Mechanical Engineering Congress and Exposition, 16–21 November, Dallas, TX.
- Rajendran, A. M. and Grove, D. J. (1992a) Modeling the impact behavior of AD85. In *Proceedings, 24th Int. SAMPE Tech. Conf.* Allied-Signal Inc.
- Rajendran, A. M. (1992b) High strain rate behavior of metals, ceramics and concrete. Air Force Report WL-TR-92-4006, Wright-Patterson Air Force Base, OH, U.S.A.
- Sandler, I. S. and Wright, J. P. (1984) Strain softening. In *Theoretical Foundations for Large Scale Computations of Nonlinear Materials Behavior*, ed. Nemat-Nasser *et al.*, p. 285.
- Shockey, D. A., Rowcliffe, D. W., Dao, K. C. and Seaman, L. (1990a) Particle impact damage in silicon nitride. *Journal of the American Ceramics Society* **73**, 1613–1619.
- Shockey, D. A., Marchard, A. H., Skaggs, S. R. *et al.* (1990b) Failure phenomenology of confined ceramic targets and impacting rods. *International Journal of Impact Engineering* **9**(3), 263–275.
- Simha, C. H., Bless, S. J. and Porar, N. S. (1995) Dynamic failure of AD-99.5 alumina. In *Metallurgical and Materials Applications of Shock-Wave and High-Strain-Rate Phenomena*, ed. L. E. Murr, K. P. Staudhammer and M. A. Meyers. Elsevier, New York, pp. 195–202.
- Steinberg, D. (1992) *Shock Compression of Condensed Matter*–1992, pp. 447–450. Elsevier Science Pub., B.V.
- Tvergaard, V. (1990) Effect of fibre debonding in a whisker-reinforced material. *Materials Science and Engineering* **A125**, 203.
- Woodward, R. L., Gooch, W. A., O'Donnell, R. G., Perciballi, W. J., Baxter, B. J. and Pattie,

- S. D. (1994) A study of fragmentation in the ballistic impact of ceramics. *International Journal of Impact Engineering* **15**, 605–618.
- Xu, Y. and Espinosa, H. D. (1997) Damage quantification in confined ceramics. *Proceedings of 97 APS Topic Conference of Shock Compression of Condensed Matter*, 27 July–1 August, Amherst, MA.
- Xu, X.-P. and Needleman, A. (1995) Numerical simulation of dynamic interfacial crack growth allowing for crack growth away from the bond line. *International Journal of Fractures* **74**, 253–275.
- Zienkiewicz, O. C. and Taylor, R. L. (1991a) *The Finite Element Method*, 4th edn. Vol. **1**. McGraw Hill.
- Zienkiewicz, O. C. and Taylor, R. L. (1991b) *The Finite Element Method*, 4th edn. Vol. **2**. McGraw Hill.
- Zukas, J. A. (1990) *High Velocity Impact Dynamics*. John Wiley and Sons, Inc., New York.



Pergamon

J. Mech. Phys. Solids, Vol. 46, No. 10, pp. 1943–1967, 1998

© 1998 Elsevier Science Ltd. All rights reserved

Printed in Great Britain

0022-5096/98 \$—see front matter

PII: S0022-5096(98)00031-3

DYNAMIC FRACTURE TOUGHNESS VERSUS CRACK TIP SPEED RELATIONSHIP AT LOWER THAN ROOM TEMPERATURE FOR HIGH STRENGTH 4340VAR STRUCTURAL STEEL

YOUNGSEOG LEE AND VIKAS PRAKASH*

Department of Mechanical and Aerospace Engineering, Case School of Engineering, Case Western
Reserve University, Cleveland, OH 44106

(Received 20 December 1997; accepted 17 February 1998)

ABSTRACT

A transient finite element analysis is carried out to provide insight into the low temperature dynamic material toughness versus crack tip relationship for high strength structural steels under intense stress pulse loading. The problem analyzed here is plane strain fracture of an edge cracked specimen under plane wave loading conditions. The finite element formulation employed accounts for the effects of finite geometry changes, material inertia, and heat conduction. The material is characterized as an isotropically hardening and thermally softening elastic-viscoplastic von-Mises solid. To model crack initiation and crack advance various crack-tip equations of motion based on elastodynamic modelling of crack growth are used. In particular, relatively simple forms for the crack tip equation of motion corresponding to crack growth at either constant energy release rate, or a constant stress intensity factor, or a constant crack tip speed, along with more complicated forms involving a sharp upturn in fracture resistance at a limiting crack tip speed are employed. The results of these models emphasize the existence of a sharp upturn in dynamic fracture toughness in high strength structural steels at a material characteristic limiting crack tip speed at test temperatures as low as -80°C and with crack tip loading rates of the order of $\dot{K}_I \approx 10^8 \text{ MPa } \sqrt{\text{m/s}}$.
© 1998 Elsevier Science Ltd. All rights reserved.

Keywords: A. dynamic fracture, A. fracture toughness, B. elastic-viscoplastic material, C. finite elements, C. plate impact.

1. INTRODUCTION

In the present study, results of plate impact fracture experiments (Prakash, 1993), conducted on AISI 4340VAR steel at lower than room temperature, are used to examine several crack initiation and crack propagation models under nominally brittle fracture conditions. The objective is on understanding the primary features of the low temperature dynamic material toughness versus crack tip speed relationship for

* To whom correspondence should be addressed. E-mail: vxp18@po.cwru.edu

dynamically propagating cracks in high strength structural steels. The plate impact fracture experiments (Prakash, 1993) are designed to subject a pre-cracked disk to a large amplitude tensile pulse with a sharp wave-front. The loading results in the onset of crack extension in less than a microsecond. Significant inertial effects can arise under these conditions due to rapidly applied loading on the cracked solid and/or from rapid crack propagation (Freund, 1990). Strain rate effects have generally been regarded as making elastic-viscoplastic materials to appear more brittle. This increased propensity for brittle failure can be attributed to the elevation in the material's flow stress, due to its strain rate sensitivity, to a critical level required for initiating cleavage failure before significant plastic strains can accumulate and mitigate the effects of the otherwise sharp crack tip. At the same time, dynamic loading with sustained elevated plastic strain rates is capable of inducing significant levels of plastic strains in a very short time, leading to blunting of the crack tip and hence crack growth by primarily deformation controlled mechanisms.

In order to ascertain the validity of the various crack propagation models it is desirable to compare the target free surface motion obtained from the aforementioned plate impact fracture experiments with predictions of target free-surface particle velocity history obtained by employing various crack propagation models into an elastic-viscoplastic material framework. Analytical solutions for crack-tip quantities such as the history of the stress intensity factor, under the assumptions of small scale yielding, are available for a semi-infinite crack in an infinite isotropic body under plane wave loading (Achenbach and Nuismer, 1971 ; Freund, 1973). However, such solutions are not available for far-field quantities such as particle velocities and stresses for cracks propagating non-uniformly under stress-wave loading conditions. Thus, in the present investigation, a numerical solution for the far field quantities of interest is sought by employing a transient finite element analysis in conjunction with various crack initiation and propagation models.

The finite element formulation employed accounts for the effects of finite geometry changes, material inertia, and heat conduction. The material is characterized as an isotropically hardening and thermally softening elastic-viscoplastic von Mises solid. To model crack initiation and crack advance various crack tip equation of motion based on the elastodynamic modelling of crack growth are employed. These crack tip equations of motion are obtained by assuming various functional forms for the dynamic fracture toughness versus crack-tip speed relationship for the particular 4340VAR steel under investigation. In particular, relatively simple forms for the crack tip equation of motion corresponding to crack growth at either a constant energy release rate, or a constant stress intensity factor, or a constant crack tip speed, along with more realistic forms involving the sharp upturn in fracture resistance at the limiting crack tip speed characteristic of the material (Rosakis, Duffy and Freund, 1984), are employed.

The paper is presented as follows: in Section 2.1 a brief description of the experimental configuration and appropriate theoretical background is provided. Section 2.2 provides a summary of the experimental results. The problem formulation for the computational analysis along with its finite element implementation is provided in Section 3. Section 4 outlines the various crack growth criteria employed to obtain the crack tip equation of motion. Section 5 provides the results and discussion.

2. PLATE IMPACT FRACTURE EXPERIMENTS

2.1. Experimental configuration and theoretical background

The experiment involves the plane strain loading of a plane crack by a step tensile pulse with duration of approximately $1 \mu\text{s}$. The loading is achieved by impacting a disk shaped specimen containing a mid-plane crack by a thin flyer plate fabricated from the same material as the specimen, in a plate impact loading device as shown in Fig. 1. The specimen is machined from a notched cylindrical bar in which a fatigue crack has been grown by subjecting the bar to cyclical bending (Ravichandran, 1983). Impact occurs in a vacuum chamber that has been evacuated to a pressure of 60 to $80 \mu\text{m}$ of Hg and is part of a single stage gas-gun assembly. Upon impact, compressive waves of uniaxial strain are generated; one that propagates in the specimen and another that propagates in the flyer. The wave propagating through the specimen reflects from the rear surface of the specimen as a plane tensile pulse, and it is this wave which loads the crack in tension. Details of experimental procedure used for specimen preparation and executing the plate impact fracture experiments are provided in Ravichandran and Clifton (1989) and Prakash and Clifton (1992).

The time-distance diagram for the wave fronts that traverse the specimen and the flyer plate is shown in Fig. 2. The compressive wave that propagates through the specimen reaches the rear surface of the specimen at time, t_1 . The compressive wave that travels in the flyer reflects from the rear surface of the flyer as a plane tensile wave-front and propagates back towards the specimen. This unloading wave from the flyer removes the pressure that was imposed on the crack plane by the initial compressive pulse, leaving the crack-faces traction free. The velocity of the free surface of the specimen remains constant at the impact velocity V_0 , until the unloading wave reflected from the rear surface of the flyer arrives at the rear surface of the target plate

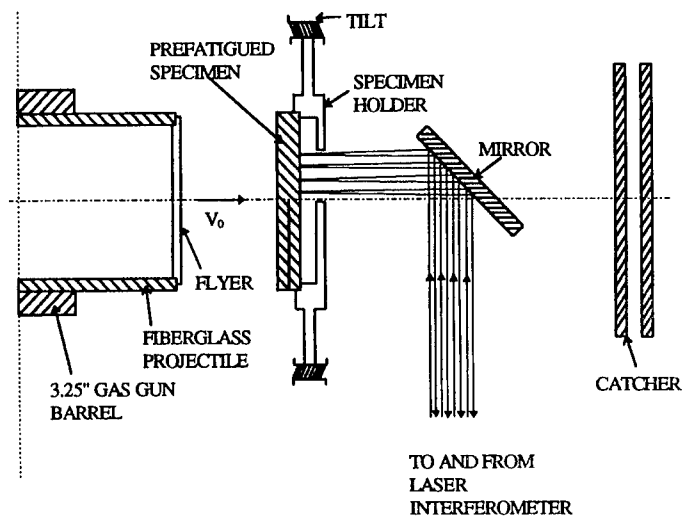


Fig. 1. Schematic of the experimental configuration.

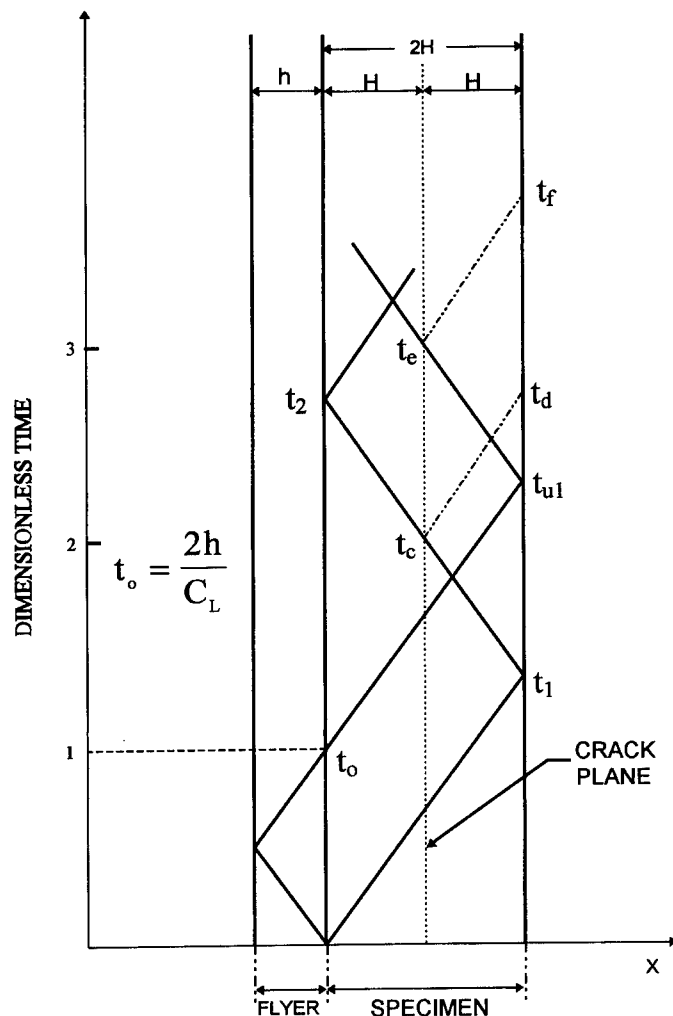


Fig. 2. Wave propagation in the flyer and the specimen.

at time, t_{u1} . This unloading wave brings the rear surface velocity of the specimen to zero. During this time interval, the compressive wave reflected from the rear surface of the specimen plate arrives at the traction-free crack plane as a tensile pulse at time, t_c . The cylindrically diffracted longitudinal wave arrives at the rear surface of the specimen plate at a point directly opposite the crack tip at time, t_d . Tensile loading of the crack plane continues until the time, t_e when the end of the tensile pulse arrives. The corresponding diffracted longitudinal wave arrives at the rear surface of the specimen plate at time, t_f . Thus, the time interval (t_d, t_f) is the interval of primary interest in this experiment.

A four point normal displacement interferometer is used to measure the rear surface motion of the specimen. With this interferometer, the motion of four different points on the specimen surface can be measured simultaneously during the experiment. This is important, since unlike the conventional plate impact experiments where the rear surface motion is independent of in plane coordinates, a two-dimensional field is generated by the diffraction of the plane wave by the crack. Details of the four point laser interferometer employed in the experiments for measuring the target rear surface motion can be found in Mello, Prakash and Clifton (1991).

In the design of the experiments, the dimensions of the specimen plate are adjusted such that the unloading waves from the lateral surface of the target plate arrives at the monitoring points after the time, t_f . This condition ensures that the loading conditions for the dynamic fracture experiment are essentially exactly those of plane strain, at-least until the diffracted waves from the lateral boundary reach the centre of the specimen. This feature greatly facilitates the detailed correlation of theory and experiment, since for two-dimensional fracture dynamics, numerical solutions can be obtained with acceptable levels of computational effort.

The loading pulse has a duration $t_0 = 2h/C_L$, where h is the thickness of the flyer plate, and C_L is the speed of propagation of longitudinal waves in 4340VAR steel. The tensile stress of loading pulse, σ^* , is given by

$$\sigma^* = \frac{1}{2} \rho C_L V_0, \quad (1)$$

where ρ is the mass density and V_0 is the projectile velocity measured during the experiment.

For a loading of pulse of duration t_0 , the transient stress intensity factor for the present model problem is given by Freund (1990) as

$$K_I(t) = n(v) \sigma^* C_L^{1/2} [t^{1/2} - (t - t_0)^{1/2} H(t - t_0)]. \quad (2)$$

In eqn (2) $H(t)$ is the Heaviside unit step function, and $n(v)$ is given by

$$n(v) = \frac{2}{(1-v)} \left(\frac{1-2v}{\pi} \right)^{1/2}, \quad (3)$$

where v is the Poisson's ratio. The crack-tip stress intensity factor, for the stationary crack increases in proportion to \sqrt{t} for $0 < t < t_0$. For $t > t_0$, the stress intensity factor decreases due to the unloading term in proportion to $\sqrt{t - t_0}$. The largest value of the stress intensity factor reached is $n(v) \sigma^* \sqrt{C_L t_0}$ so that the crack will initiate only if $n(v) \sigma^* \sqrt{C_L t_0} > K_{Id}$, the critical value of the dynamic stress intensity factor for the material.

Subsequently, the crack initiation time, τ , is given by

$$\tau = \frac{1}{n^2(v) C_L} \left(\frac{K_{Id}}{\sigma^*} \right)^2. \quad (4)$$

Knowing τ and using eqn (2), the dynamic fracture toughness, K_{Id} and the crack tip loading rate, \dot{K}_I , can be expressed as

$$K_{Id} = n(v)C_L^{1/2}\sigma^*\tau^{1/2} \quad \text{and} \quad \dot{K}_I = \frac{K_{Id}}{2\tau}, \text{ respectively.} \quad (5)$$

The crack arrest time, t_a , assumed to take place when the stress intensity factor reduces to the value K_{Id} , can be obtained from eqns (2) and (4) as

$$t_a = \frac{\tau}{4} \left(1 + \frac{t_0}{\tau} \right)^2. \quad (6)$$

2.2. Experimental results

The material used in the present study is AISI 4340VAR steel. This material is a high strength, low ductility, structural alloy having reduced levels of phosphorus and sulfur to enhance the fracture toughness. The material is heat treated by normalizing at 900°C for 2 h austenizing at 850°C for 2 h, and then rapidly quenching in an ice brine solution. The heat treatment ensures a hardness of 55 to 56 on the Rockwell C scale.

Table 1 summarizes the experiment described in the present manuscript. It gives the impact velocity, V_0 , the applied normal tensile stress, σ_0 , and the duration of the pulse, t_0 . The low temperature of the test (-80°C) ensures fracture in a primarily brittle or cleavage mode. The magnitude of the applied normal stress corresponds to approximately 47% of the Hugoniot elastic limit for 4340VAR steel.

The solid lines in Fig. 3 correspond to the experimentally recorded velocity-time profiles at the four monitoring points on the target free surface. The data shown corresponds to the time interval of primary interest, which is between t_d and t_f on the time-distance diagram (Fig. 2). The closest monitoring point is 0.6 mm ahead of the crack tip. The remaining three monitoring points are spaced at 0.7 mm intervals. The zero of the time scale corresponds to the first arrival of the longitudinal wave at the closest monitoring point. The curves with the lowest (Curve A) and the highest (Curve D) velocity-time profiles correspond to the farthest (Point A) and the closest (Point D) monitoring points, respectively. The delay times between the traces correspond closely to the difference in arrival times of waves diffracted from the crack tip. The dashed curves correspond to the numerical simulation using a temperature dependent elastic-viscoplastic material model, and assuming that the crack remains stationary (details of the finite element method employed to obtain the diffracted free surface particle velocity field are provided in Section 3.0). Agreement between the computed and experimentally obtained velocity-time profiles is observed to be good up to

Table 1. Summary of the experiment on 4340 VAR steel

Impact velocity (m/s)	Stress pulse amplitude (MPa)	Pulse duration (μs)	Crack growth (mm)	Test temp. (°C)
59.0	1342.0	1.01	1.3	-80

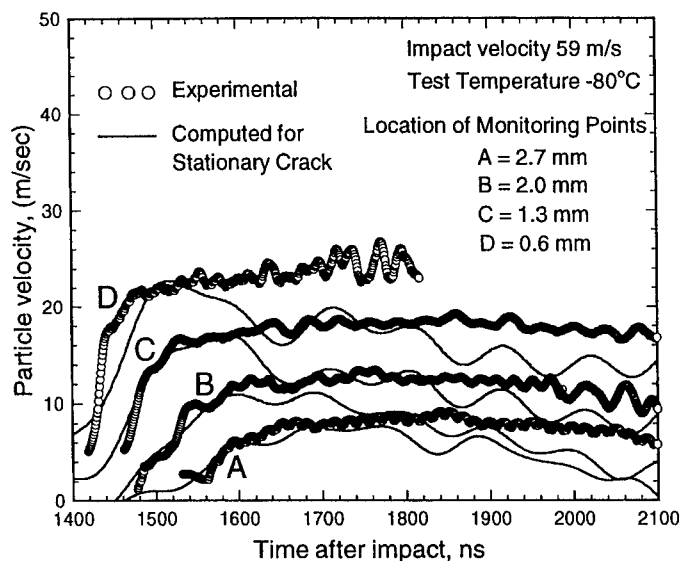


Fig. 3. Experimental target free surface particle velocity and the predicted target free surface particle velocity history for a stationary crack at the four monitoring points (A–D).

a certain time. Thereafter, the experimental and computed profiles separate. This separation point is understood to be related to the time of crack initiation during the experiment. The experimental record after the separation point corresponds to crack propagation phase of the experiment. From Fig. 2 the crack initiation time can be inferred to be 116 ns. This corresponds to a dynamic initiation fracture toughness of $36 \text{ MPa} \sqrt{\text{m}}$. The crack tip loading rate can be estimated by using eqn (5) to be $1.5 \times 10^8 \text{ MPa} \sqrt{\text{m/s}}$.

Figure 4 shows a fractograph representative of the region in the vicinity of the crack initiation site. The predominant mode of crack initiation is cleavage. The multifaceted surface is typical of cleavage in a crystalline material; each facet corresponds to a single grain. The river patterns on each facet are also typical of cleavage fracture. The crack growth region contains many cleavage facets, often surrounded by a narrow dimpled region, and appreciable areas of decohesion between grains and/or phases. Presumably the cleavage facets are cross grains that have been favourably oriented for cleavage with the crack front and hence cleaved. Since the grains are not always favourably oriented to the fracture path, the fracture propagates in a tortuous path and is accompanied by some plastic flow. From the modes of failure depicted in the fractographs it is expected that besides the energy required for the cleavage of the favourably oriented cleavage grains a substantial fraction of the fracture energy is consumed in the necking down of the ductile ligaments left behind as the brittle fracture front advances through the material. Moreover, the presence of voids at the grain boundaries, suggest that inelastic processes involving the initiation, growth and coalescence of voids must accompany the dynamic fracture process. Thus, in the continuum sense, the failure mechanisms can be regarded as quasi-cleavage and any analysis pertaining to the experiment must include inelastic effects.

3. COMPUTATIONAL ANALYSIS

One of the objectives of the present study is to critically examine the applicability of various fracture criteria for sustained cleavage crack growth in high strength ferritic steels, by comparing the computed time history of the target free surface motion with that measured experimentally. To accomplish this a transient finite element analysis which accounts for the effects of finite geometry changes, material inertia, material rate sensitivity and heat conduction, is employed. The material is characterized as an isotropically hardening, and thermally softening elastic-viscoplastic von Mises solid. A combined power-law and exponential plastic strain-rate relation (Clifton, 1990), that gives rise to enhanced strain-rate hardening at ultra-high strain rates, e.g. Cambell and Ferguson (1970), and Klopp *et al.* (1985), is also employed.

3.1. Problem formulation

The analysis is based on a convected Lagrangian formulation of field equations with the initial undeformed body configuration as the reference. Convected coordinates y^i are introduced which serve as particle labels. Relative to a fixed Cartesian frame, the position of a material point in the reference configuration is given by $\mathbf{X}(y^i)$. The corresponding material particle in the current configuration is located by a position vector $\mathbf{x}(y^i)$. The base vectors for the reference and the current configuration of the body are denoted by \mathbf{g}_i and $\tilde{\mathbf{g}}_i$, respectively, with

$$\mathbf{g}_i = \frac{\partial \mathbf{X}}{\partial y^i} \quad \text{and} \quad \tilde{\mathbf{g}}_i = \frac{\partial \mathbf{x}}{\partial y^i}. \quad (7)$$

The displacement vector, \mathbf{u} , and the deformation gradient tensor, \mathbf{F} , are defined as

$$\mathbf{u} = \mathbf{x} - \mathbf{X} \quad \text{and} \quad \mathbf{F} = \frac{\partial \mathbf{x}}{\partial \mathbf{X}} \quad (8)$$

The dynamic principle of virtual work can be written in the integral form as

$$\int_V \tau^{ij} \delta E_{ij} dV = \int_S f^i \delta u_i dS - \int_V \rho_0 \frac{\partial^2 u^i}{\partial t^2} \delta u_i dV, \quad (9)$$

where V , S , and ρ_0 are the volume, surface area and mass density, respectively, of the body in the reference configuration, and τ is the Kirchoff stress defined by $\tau = \det(\mathbf{F})\sigma$. The traction vector component f^i on a surface with unit normal vector component n_j in the reference configuration is given by

$$f^i = (\tau^{ij} + u_{,k}^i \tau^{kj}) n_j. \quad (10)$$

The Lagrangian strain tensor in the reference configuration is

$$E_{ij} = \frac{1}{2}(u_{i,j} + u_{j,i} + u_{,i}^k u_{k,j}), \quad (11)$$

where $(\cdot)_{,i}$ represents the covariant partial differentiation in the reference frame.

With body forces and external heat energy source being absent, the balance of energy can be expressed as integrals over the reference configuration

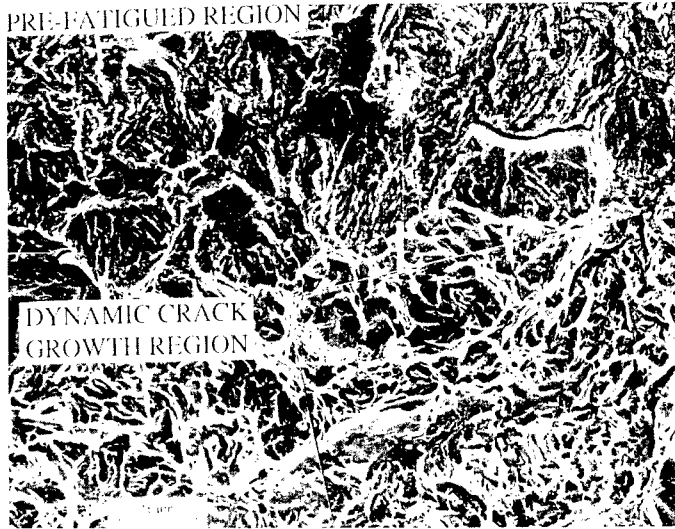


Fig. 4. Fractograph indicating quasi-cleavage fracture.

$$\int_V \rho_0 \dot{e} dV + \frac{d}{dt} \int_V \frac{1}{2} \rho_0 \dot{\mathbf{u}} \cdot \dot{\mathbf{u}} dV = \int_S \mathbf{f} \cdot \dot{\mathbf{u}} dS - \int_S J \mathbf{n} \cdot \mathbf{F}^{-1} \cdot \bar{\mathbf{q}} dS, \quad (12)$$

where e is the specific internal energy, d/dt is the material time derivative, J is the Jacobian of the deformation, and $\bar{\mathbf{q}}$ is heat-flux vector normal to the surface in the current configuration.

The formulation of the energy balance and the equation of heat conduction follows Povirk, Needleman and Nutt (1990) except for the inclusion of the kinetic energy term. Assuming that the heat capacity at constant stress can be approximated by the specific heat at constant pressure c_p , and assuming small elastic strains ($J = \det|\mathbf{F}| \approx 1$ hence $\tau = \sigma$), the balance of energy can be expressed in terms of integrals over the reference configuration as

$$\int_V \rho_0 c_p \dot{T} dV = \int_V \chi \tau : \mathbf{D}^p dV + \int_V J k \nabla_0 \cdot (\mathbf{F}^{-1} \cdot \mathbf{F}^{-T} \cdot \nabla_0 T) dV, \quad (13)$$

where the gradient operator in the reference configuration is denoted by

$$\nabla_0 = \mathbf{g}^K \frac{\partial}{\partial y^K},$$

and χ represents the fraction of plastic work rate converted to heat: χ is taken to have the value of 0.9, which is typical for metals (Taylor and Quinney, 1934).

The material is characterized as an isotropically hardening viscoplastic solid for which \mathbf{D}^p can be expressed using J_2 flow theory as

$$\mathbf{D}^p = \dot{\epsilon} \mathbf{p} \quad \text{where } \mathbf{p} = \frac{3\tau'}{2\bar{\sigma}}. \quad (14)$$

In eqn (14) $\dot{\bar{\epsilon}}$ is the equivalent plastic strain rate function: the deviatoric stress τ' and the equivalent flow stress $\bar{\sigma}$ are given by

$$\tau' = \tau - \frac{1}{3}(\tau : \mathbf{I})\mathbf{I} \quad \text{and} \quad \bar{\sigma}^2 = \frac{3}{2}\tau' : \tau'. \quad (15)$$

The material properties used in the present simulations are representative of hardened AISI 4340VAR steel. The plastic strain rate, $\dot{\bar{\epsilon}}$, is taken to be of the form

$$\dot{\bar{\epsilon}} = \frac{\dot{\epsilon}_1 \dot{\epsilon}_2}{\dot{\epsilon}_1 + \dot{\epsilon}_2}, \quad (16)$$

where

$$\dot{\epsilon}_1 = \dot{\epsilon}_0 \left[\frac{\bar{\sigma}}{g(\bar{\epsilon}, T)} \right]^m, \quad \dot{\epsilon}_2 = \dot{\epsilon}_m \exp \left[-\frac{ag(\bar{\epsilon}, T)}{\bar{\sigma}} \right] \quad (17)$$

and

$$g(\bar{\epsilon}, T) = \sigma_0 (1 + \bar{\epsilon}/\epsilon_0)^N \{1 - \beta[(T/T_0)^k - 1]\}. \quad (18)$$

Here,

$$\bar{\epsilon} = \int_0^t \dot{\bar{\epsilon}} dt$$

is the equivalent plastic strain, $\dot{\epsilon}_m$ is a reference strain rate, m and a are the rate sensitivity parameters, respectively, σ_0 is a reference stress, ϵ_0 is a reference strain, N is the strain hardening exponent, T_0 is a reference temperature, and β and k are the thermal softening parameters. The function $g(\bar{\epsilon}, T)$ represents the stress-strain relation at quasi-static strain rate of $\dot{\epsilon}_0$ and at temperature T . Equation (16), provides a smooth transition between the measured response $\dot{\bar{\epsilon}} = \dot{\bar{\epsilon}}_1(\bar{\sigma}, \bar{\epsilon}, T)$ at strain rates less than 10^3 s^{-1} , and the limiting behaviour $\dot{\bar{\epsilon}} = \dot{\bar{\epsilon}}_2(\bar{\sigma}, \bar{\epsilon}, T)$ at strain rates greater than, say, 10^5 s^{-1} .

The material response of 4340VAR steel is shown in Figs 5(a) and 5(b) along with the plastic strain rate and the temperature dependence of the flow stress. The material parameters used in the model are listed in Table 2.

3.2. Finite element implementation

As discussed by Budiansky (1969), the principle of virtual work eqn (9) can be used as the variational principle for a solid continuum undergoing arbitrarily large displacements and deformations. Moreover, the variational equation governing the thermo-mechanical energy balance can be obtained from the balance of energy, eqn (13), as

$$\begin{aligned} \int_V \rho_0 c_p \dot{T} \delta T dV = & \int_V \chi \tau : \mathbf{D}^p \delta T dV - \int_V Jk(\mathbf{F}^{-1} \cdot \mathbf{F}^{-T} \cdot \nabla \cdot T) \nabla \cdot \delta T dV \\ & + \int_S Jk \mathbf{N} \cdot \{(\mathbf{F}^{-1} \cdot \mathbf{F}^{-T} \cdot \nabla \cdot T)\} \delta T dS. \end{aligned} \quad (19)$$

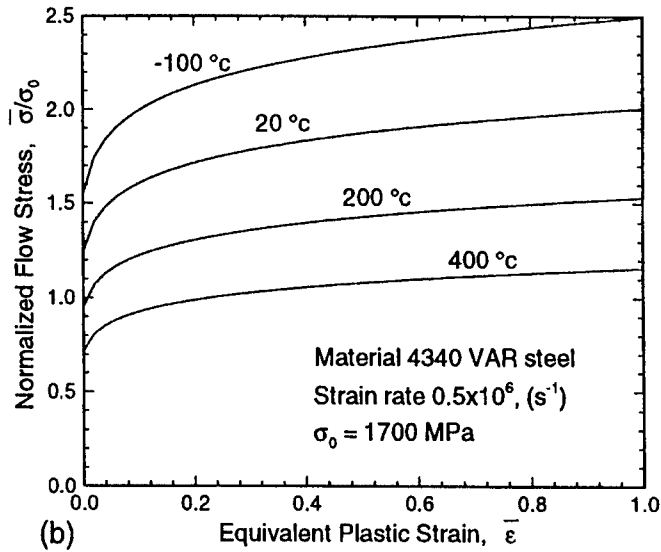
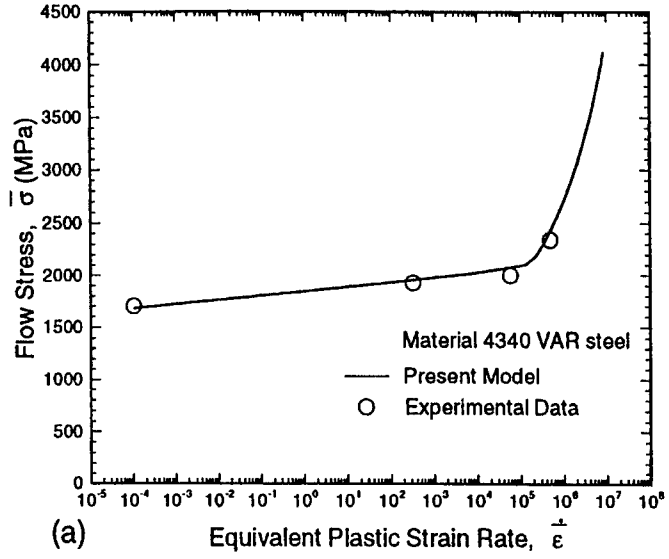


Fig. 5. Elastic-viscoplastic response of 4340 VAR steel, (a) Enhanced plastic strain rate sensitivity of flow stress for $\dot{\epsilon} > 10^5/s$, (b) Temperature dependence of the flow stress as a function of the plastic strain at a fixed plastic strain rate.

When the finite-element approximations for the displacement and temperature fields are substituted into eqns (9) and (19), the resulting equations take the form

$$\mathbf{M} \frac{\partial^2 \mathbf{U}}{\partial t^2} = \mathbf{R}, \quad (20)$$

Table 2. *Material parameters used to describe the present model for AISI 4340 VAR steel (200°C temper, $R_c = 55$)*

$E = 202 \text{ GPa}, \sigma_0 = 1895 \text{ MPa}$
$m = 100.0, \beta = 3.19$
$c_p = 465 \text{ J/(Kg} \cdot \text{K)}, \alpha = 1.0 \times 10^5 \text{ 1/K}$
$a = 10.0, \dot{\epsilon}_0 = 1.0 \times 10^{-4} \text{ s}^{-1}$
$\dot{\epsilon}_m = 5.0 \times 10^8 \text{ s}^{-1}, \epsilon_0 = \sigma_0/E$
$k = 100.0 \text{ W/m} \cdot \text{K}, T_0 = 293 \text{ K}$
$\kappa = 1.0, N = 0.1, \nu = 0.3$

$$\mathbf{C} \frac{\partial \mathbf{T}}{\partial t} = -\mathbf{K}\mathbf{T} + \mathbf{H}, \quad (21)$$

where \mathbf{U} is the vector of nodal displacements, \mathbf{T} is the vector of nodal temperatures, \mathbf{M} , \mathbf{C} , \mathbf{K} , are, respectively, the mass, heat capacitance, and heat conductance matrices, and \mathbf{R} and \mathbf{H} are the mechanical and thermal force vectors. A lumped mass matrix is used in eqn (20) instead of the consistent mass matrix; the lumped mass matrix has been found preferable for explicit time integration procedures from the point of view of computational efficiency and accuracy (Krieg and Key, 1973). Additionally, a lumped heat capacitance matrix is used in the eqn (21).

An explicit time integration scheme based on the Newmark β -method, with $\beta = 0$, and $\gamma = 0.5$ (Belytschko *et al.*, 1976) is used to integrate the equations of motion to obtain the nodal velocities and nodal displacements via

$$\frac{\partial^2 \mathbf{U}^{n+1}}{\partial t^2} = \mathbf{M}^{-1} \mathbf{R}^{n+1}. \quad (22)$$

$$\frac{\partial \mathbf{U}^{n+1}}{\partial t} = \frac{\partial \mathbf{U}^n}{\partial t} + \frac{1}{2} \Delta t_n \left(\frac{\partial^2 \mathbf{U}^n}{\partial t^2} + \frac{\partial^2 \mathbf{U}^{n+1}}{\partial t^2} \right). \quad (23)$$

$$\mathbf{U}^{n+1} = \mathbf{U}^n + \Delta t_n \frac{\partial \mathbf{U}^n}{\partial t} + \frac{1}{2} (\Delta t_n)^2 \frac{\partial^2 \mathbf{U}^n}{\partial t^2}, \quad (24)$$

where $()^{-1}$ denotes the matrix inverse.

The plastic dissipation rate, $\tau : \mathbf{D}^p$, is calculated and its contribution to the thermal force vector, \mathbf{H}^n , is determined. The nodal temperature at t_{n+1} are obtained via

$$\frac{\partial \mathbf{T}^{n+1}}{\partial t} = \mathbf{C}^{-1} (-\mathbf{K}^n \mathbf{T}^n + \mathbf{H}^n) \quad (25)$$

and

$$\mathbf{T}^{n+1} = \mathbf{T}^n + \Delta t_n \frac{\partial \mathbf{T}^{n+1}}{\partial t}. \quad (26)$$

The rate tangent modulus expansion method (Peirce *et al.*, 1984) is used to update the contravariant components of the convected Kirchhoff stress tensor, i.e.

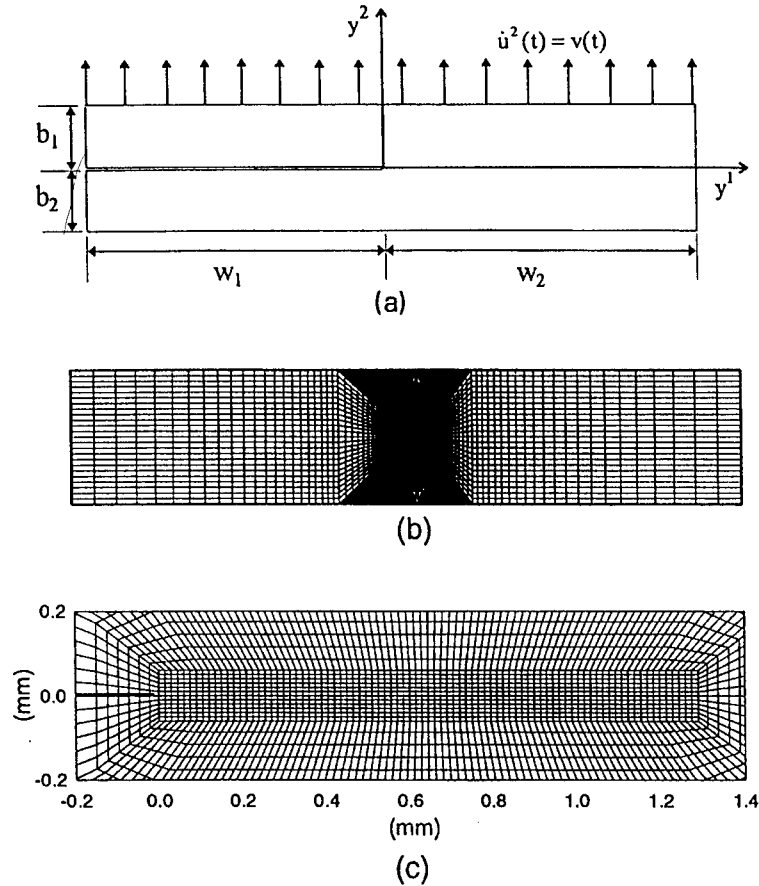


Fig. 6. (a) Geometry of the edge cracked specimen used in finite element discretization, (b) Quadrilateral elements consisting of four "crossed" triangles, the location of the initial crack tip, and the process zone.

$$\tau^{n+1} = \tau^n + \dot{\tau}^c \Delta t_n. \quad (27)$$

The computations are carried out for an edge cracked specimen as shown in Fig. 6(a). Plane strain conditions are assumed to prevail and a Cartesian coordinate system is used as a reference, with the y^1 - y^2 plane being the plane of deformation. The specimen dimensions are taken as $w_1 = w_2 = 20.0$ mm and $b_1 = b_2 = 4.0$ mm. To save computational time the initial conditions corresponding to a plane tensile pulse propagating towards the crack plane from the specimen rear-surface are prescribed. With origin of the coordinate system at the initial crack tip, the boundary conditions can be written as

$$\begin{aligned} f^1 &= 0, \quad f^2 = 0 \quad \text{on} \quad y^1 = -w_1, \\ f^1 &= 0, \quad f^2 = 0 \quad \text{on} \quad y^1 = w_2, \end{aligned}$$

$$\begin{aligned}
 f^1 &= 0, \quad f^2 = 0 \quad \text{on} \quad y^2 = 0 \quad \text{and} \quad y^1 < 0, \\
 f^1 &= 0, \quad f^2 = 0 \quad \text{on} \quad y^2 = -b_2, \\
 u_2 &= \int_0^t V(t) dt \quad \text{and} \quad f^1 = 0 \quad \text{on} \quad y^2 = b_1.
 \end{aligned} \tag{28}$$

The function $V(t)$ in eqn (28) is taken to be

$$V(t) = \begin{cases} V_0 t/t_{\text{nse}}, & \text{for } t \leq t_{\text{rise}}, \\ V_0, & \text{for } t_{\text{nsc}} < t \leq t_{\text{fall}}. \end{cases} \tag{29}$$

The finite element discretization is based on linear displacement triangular elements that are arranged in a 'crossed-triangle' quadrilateral pattern. In these constant strain triangular sub-elements the displacements and temperature are taken to vary linearly over the triangular elements. Nagtegaal *et al.* (1974) have shown that an element of this type can accommodate isochoric deformations. This is of significance since plastic strain is volume preserving, so that the total deformation at large strains is nearly isochoric.

In presenting computational results, the quadrilateral is regarded as the basic element, and when reporting values of field quantities the average value of the four triangles is associated with the centroid of the quadrilateral. The full finite element mesh used in the computations is shown in Fig. 6(b). In front of crack tip, a uniform mesh also referred to as the process zone, consists of 50 quadrilaterals in the y^1 direction and 10 quadrilaterals placed symmetrically about the y^2 direction. Each quadrilateral element in the process zone has a dimension $16 \mu\text{m} \times 10 \mu\text{m}$. The entire finite-element mesh consists of 3980 quadrilateral elements with 19,882 degrees of freedom.

4. MODELLING OF DYNAMIC CRACK INITIATION AND PROPAGATION

4.1. Crack tip equation of motion based on elastodynamic modelling of crack growth

In the study of dynamic propagation of a crack through a continuum solid, the field equations can be solved for any motion of the crack edge, in principle. That is, if the motion of the crack edge is specified, along with the configuration of the body and the details of the loading, then the resulting mechanical fields can be determined. However, in order to specify an acceptable crack tip equation of motion, dynamic crack initiation and crack growth criterion is required. For crack growth processes in materials which fail in a predominantly brittle manner, or in which any inelastic crack tip zone is completely contained within the surrounding elastic crack tip zone, the most common crack growth criteria are the generalizations of Griffith's critical energy release rate criterion (Griffith, 1920) and Irwin's critical stress intensity factor criterion (Irwin, 1957; 1960). According to the generalized Griffith criterion, a crack must grow in such a way that the crack tip dynamic energy release rate is always equal to

the dynamic fracture energy of the material. A similar statement can be made concerning the generalization of Irwin's stress intensity factor criterion to the case of dynamic crack propagation. In this criterion, the material specific resistance to crack advance is the dynamic fracture toughness. Consequently, if either the Griffith's or the Irwin's criterion is considered to provide an acceptable postulate for describing crack growth, then either the specific fracture energy or the dynamic fracture toughness characterizes the resistance of the material to crack growth and must be specified.

In general, the crack tip stress intensity factor represents the effect of the applied loading, the geometrical configuration of the body, and the bulk material parameters of the material in the crack tip region for any motion of the crack tip. For the case of non-uniform crack growth these parameters depend on time, the crack length and the crack tip speed. For the model problem considered here it has been shown, e.g. Freund (1990), that the instantaneous value of the crack tip stress intensity factor for an arbitrary motion of the crack tip depends on crack motion only through the instantaneous value of the crack tip speed, \dot{a} , and time. Moreover this dependence has a separable form

$$K_p(t, \dot{a}) = k(\dot{a})K(t; 0), \quad (30)$$

where K_p is the instantaneous dynamic stress intensity factor for crack propagation, $K(t; 0)$ is a functional given by (2), and $k(\dot{a})$ is a universal function of crack speed and can be approximated as

$$k(\dot{a}) \approx \frac{1 - \dot{a}/c_R}{1 - 0.5 \dot{a}/c_R}. \quad (31)$$

Analogously, the instantaneous energy release rate for propagating cracks, G_p , can be expressed as

$$G_p(t, \dot{a}) = g(\dot{a})G(t; 0), \quad (32)$$

where $g(\dot{a})$ is a universal function of crack speed and can be approximated by

$$g(\dot{a}) \approx 1 - \frac{\dot{a}}{c_R}. \quad (33)$$

Moreover, the instantaneous dynamic energy release rate for crack propagation, $G_p(t, \dot{a})$, is related to the instantaneous stress intensity $K_p(t, \dot{a})$ via the relationship

$$G_p(t; \dot{a}) = \frac{1 - \nu^2}{E} A(\dot{a}) K_p^2(t; \dot{a}). \quad (34)$$

where $A(\cdot)$ is a universal function of the instantaneous crack tip speed, \dot{a} . The function A has the properties that $A(\dot{a}) \rightarrow 1$ as $\dot{a} \rightarrow 0$, $A'(\dot{a}) \rightarrow 0$ as $\dot{a} \rightarrow 0$, and $A(\dot{a}) \rightarrow \infty$ as $\dot{a} \rightarrow c_R$.

Results of several dynamic fracture experiments on tough structural metals which do not undergo a transition in fracture mode with increasing crack tip speed and show relatively low strain hardening characteristics in the plastic range, indicate that the material's level of resistance to crack advance may depend on the instantaneous crack tip speed (see, e.g. Rosakis, Duffy and Freund, (1984); Rosakis and Zhender

(1990); and Kobayashi and Dally (1979)). The most significant feature of this dependence is the increasing sensitivity of dynamic fracture toughness to crack tip speed with increasing speed. Although this sensitivity might be attributed, at least in part, to strain rate dependence of the material response, it is noteworthy that the feature persists even for materials which appear to exhibit little strain rate dependence in their bulk response. Furthermore, the feature cannot be attributed entirely to crack speed dependence of the elastic field surrounding the crack tip plastic zone. The surrounding elastic field shows little dependence on crack speed for speeds less than about 50–60% of the shear wave speed, whereas the sharp upturn in the variation of toughness with speed has been observed for speeds in the range of 25–30% of the shear wave speed. Theoretical/numerical investigations of dynamic fracture in elastic ideally-plastic materials (Lam and Freund, 1985) have shown that this upturn in the material's fracture resistance can be attributed to inertial effects within the crack tip plastic zone. Furthermore, it has been demonstrated that for ductile solids, the inertia effects become important at much lower crack tip speeds as compared to those in brittle solids.

Experimental data (Rosakis, Duffy and Freund, (1984)), relating the dynamic fracture toughness to the crack tip velocity (from here onwards referred to as the K_{ID} versus \dot{a} relationship) can be correlated by the heuristic experimental relation suggested by Kanninen and Popelar (1985)

$$K_{ID}(t, \dot{a}) = \frac{K_{Ic}}{1 - \left(\frac{\dot{a}}{V_L}\right)^m}, \quad (35)$$

where K_{Ic} is the crack initiation toughness under dynamic loading conditions, V_L is the limiting crack tip speed, and m is a dimensionless shape factor. Using eqn (35), the K_{ID} vs \dot{a} curve for 4340 steel (heated to 843°C, oil quenched and tempered at 316°C for 1 h, and with $\sigma_0 = 1300$ MPa and $K_{Ic} = 60$ MPa \sqrt{m}), can be effectively represented by $V_L = 1100$ m/s and $m = 2$.

In view of the aforementioned possibilities, the crack growth criterion that is required to specify the equation of motion of the crack tip is assumed to be governed by any one of the following criteria

$$G_p(t, \dot{a}) = G_{Ic}(\text{constant energy release rate criterion}), \quad (36)$$

$$K_p(t, \dot{a}) = K_{Ic}(\text{constant stress intensity factor criterion}), \quad (37)$$

$$\dot{a} = \text{constant}(\text{constant crack velocity criterion}). \quad (38)$$

According to eqns (36) and (37), the crack must propagate in such a way that either the dynamic energy release rate, G_p , or the dynamic stress intensity factor, K_p , is always equal to its material characterizing value at crack initiation, i.e., G_{Ic} or K_{Ic} , respectively.

Using eqns (30) to (38), the average crack growth, Δa , corresponding to each of the three crack growth criterion can be expressed as,

$$\Delta a = \int_{\tau}^{t_a} \left(1 - \frac{K_{Ic}^2}{K_I^2(t)} \right) dt \quad (\text{for constant energy release rate criterion}), \quad (39)$$

$$\Delta a = C_R \int_{\tau}^{t_a} \left(1 - \frac{0.5K_{Ic}/K_I(t)}{1 - 0.5K_{Ic}/K_I(t)} \right) dt \quad (\text{for constant stress intensity factor criterion}), \quad (40)$$

$$\Delta a = \dot{a}(t_a - \tau) \quad (\text{for constant crack velocity criterion}). \quad (41)$$

To model crack propagation, material failure is implemented via the element vanishing technique Tvergaard (1982). When the crack tip passes a material point occupied by an element in the process zone ahead of the initial crack tip, the element is assumed to vanish and its contribution to the virtual work is neglected. The magnitude of reduction of the nodal forces is taken to be proportional to their initial values, with the proportionality factor depending instantaneously on the fraction of the length that the crack tip has traversed in the failed element.

5. RESULTS AND DISCUSSION

The computed and the experimental particle velocity-time profiles based on crack tip equation of motion (36), (37) and (38) are shown in Fig. 7. Early separation between the experimental and the computed profiles for the case of a stationary crack indicate that the cracks begin to propagate during the early part of the tensile pulse. Good agreement is obtained between measured velocity time profiles and predictions of a constant velocity crack propagation ($\dot{a} = 1300$ m/s) model. Predictions of the constant energy release rate model, and to a lesser extent, of the constant stress intensity factor model tend to overestimate the acceleration of the free surface over much of the time interval and especially the latter times.

The success of the constant crack velocity model in predicting the experimental free surface particle velocity provides a strong indication for the existence of a dynamic fracture toughness versus crack tip speed relationship similar to eqn (35) for the 4340VAR steel ($R_C = 55$) employed in the present investigation. In view of this the following particular form for the dependence of dynamic fracture toughness versus the crack speed is sought

$$K_{ID}(\dot{a}, t) = \frac{K_{Ic}}{\left[1 - \left(\frac{\dot{a}}{\xi c_r} \right)^p \right]^q}, \quad (42)$$

where ξ , p and q are empirical constants to be evaluated iteratively by comparing the experimental and the computed free-surface particle velocity history corresponding to eqn (42). Using eqn (42) in eqn (30), the governing equation for the crack tip motion takes the form

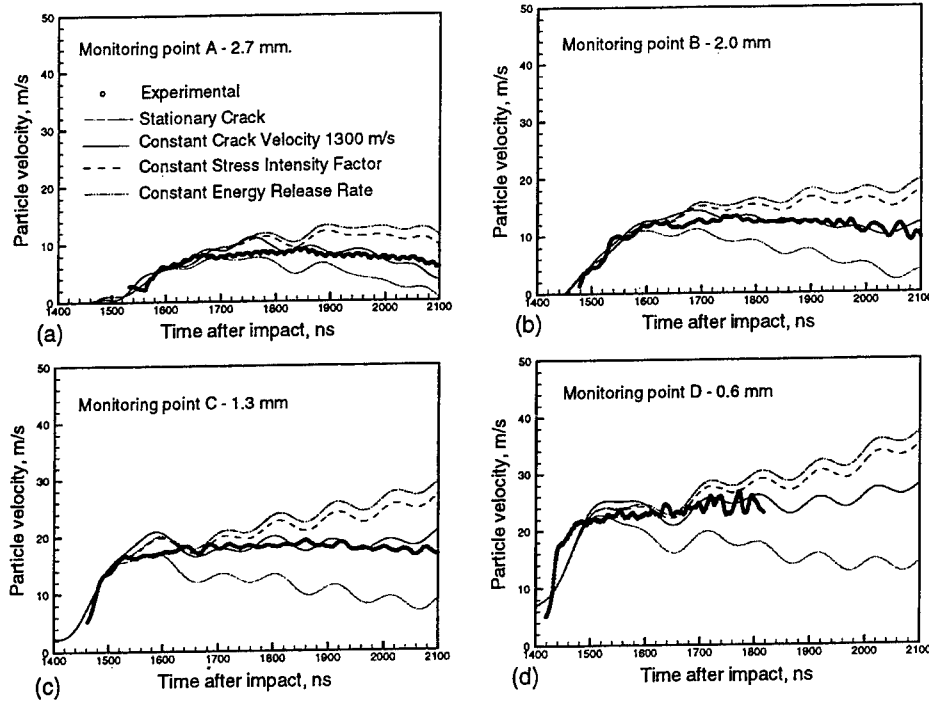


Fig. 7. Experimental and the predicted target free surface particle velocity profiles at the four monitoring points (A–D), corresponding to the constant energy release rate model, the constant stress intensity factor model, the constant crack velocity model (1300 m/s) and the case for the stationary crack.

$$K_{ID}(\dot{a}, t) = \frac{K_{Ic}}{\left[1 - \left(\frac{\dot{a}}{\xi c_r}\right)^p\right]^q} = k(\dot{a})K(t; 0). \quad (43)$$

Furthermore, by employing eqns (2) and (31) in eqn (43) yields the following ordinary differential equation

$$\left(\frac{1 - \dot{a}/c_R}{1 - 0.5\dot{a}/c_R}\right) \left[1 - \left(\frac{\dot{a}}{\xi c_r}\right)^p\right]^q = \frac{\tau^{1/2}}{(t^{1/2} - (t - t_0)^{1/2} H(t - t_0))}. \quad (44)$$

To obtain the history of the crack tip motion $a(t)$, eqn (44) can be solved for the crack tip velocity \dot{a} , at times t and $t + \Delta t$ by using the Newton-Raphson method. Further, by employing the mean value theorem of integral calculus the instantaneous crack tip position at $t + \Delta t$ can be expressed in terms of crack tip position at time t , as

$$a(t + \Delta t) = a(t) + \frac{\dot{a}(t + \Delta t) - \dot{a}(t)}{\Delta t} \Delta t + h.o.t. \quad (45)$$

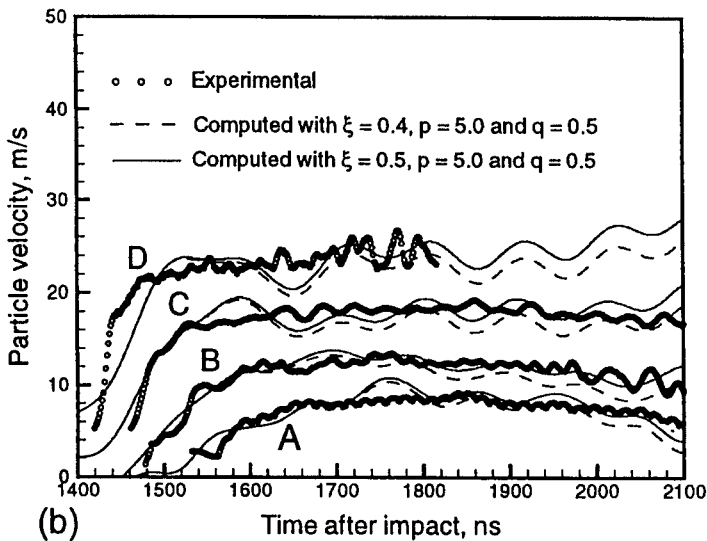
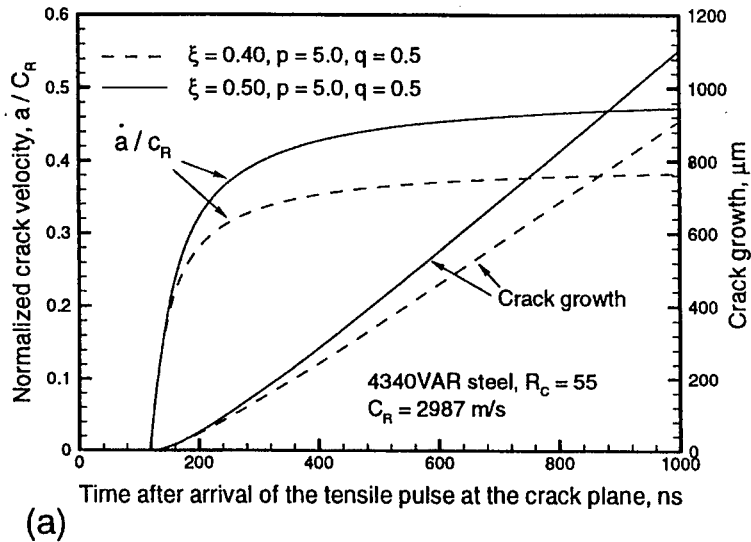


Fig. 8. (a) Crack tip position and the crack tip velocity as a function of time corresponding to two different values of the parameter ξ , i.e. $\xi = 0.4$ and $\xi = 0.5$ with $p = 0.5$ and $q = 5.0$, (b) Experimental and computed target free surface particle velocity history for $\xi = 0.4$ and $\xi = 0.5$ with $p = 0.5$ and $q = 5.0$.

Figure 8(a) depicts the corresponding solution for the crack tip position and the crack tip velocity as a function of time for $p = 5.0$, $q = 0.5$ and two different values of the parameter ξ , i.e. $\xi = 0.4$ and $\xi = 0.5$. The crack tip accelerates quickly during the initial 100 ns after the arrival of the loading pulse at the crack plane before reaching a plateau. Figure 8(b) compares the experimental and the computed target

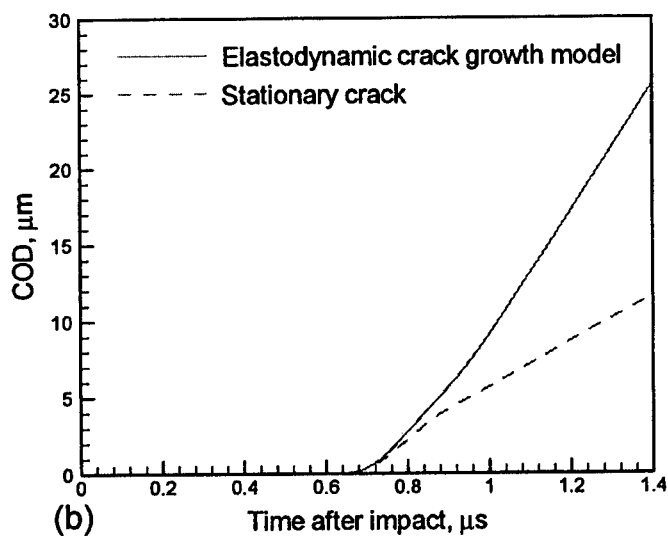
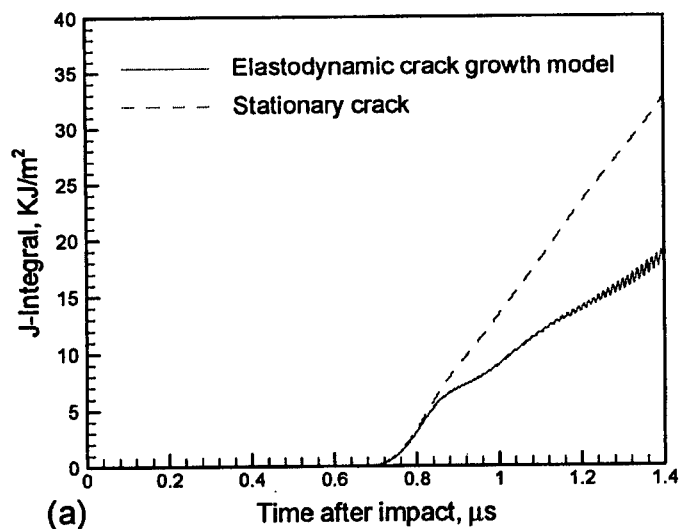


Fig. 9. (a) J -integral versus time profile, (b) COD versus time profile.

free surface particle velocity history obtained by employing eqn (42). The comparison between the experimental and the computed profiles is observed to be in good agreement for all times at the four monitoring points by using the model parameters with $\xi = 0.5$. Using this model parameter the crack tip velocity reaches a plateau of approximately 1400 m/s.

Figures 9(a) and 9(b) show the computed profiles for the J -integral (energy release

rate) and COD (crack opening displacement) versus time for the elastodynamic modelling of crack growth based on eqn (44). Along with these curves, the J -integral and the COD profiles for the case of the stationary crack are also shown for comparison purposes. The J -integral employed is the generalization of Rice's J -integral (Rice, 1968) to dynamic conditions, which involves a contour integral as well as an integral over the area inside the contour (Moran and Shih, 1987; Nakamura *et al.*, 1985)

$$J = \int_{\Gamma} [(W + L) dy^2 - T^i u_{i,1} ds] + \int_A \left[\alpha \tau_k^k T_{,1} + \rho \frac{\partial^2 u^i}{\partial t^2} u_{i,1} - \rho \frac{\partial u^i}{\partial t} \left(\frac{\partial u^i}{\partial t} \right)_{,1} \right] dA, \quad (46)$$

where A is the area of the contour Γ and

$$W = \int_0^{E_{ij}} \tau^{ij} dE_{ij} - \alpha \int_0^T \tau_k^k dT, \quad L = \frac{1}{2} \rho \frac{\partial u^i}{\partial t} \frac{\partial u_i}{\partial t}. \quad (47)$$

Using eqn (46), J was calculated on several contours outside the uniformly spaced mesh region, with any contribution of the cohesive surface ignored. The deviation on all paths away from the uniform mesh was within 7%, with the deviation being less in the early stages of crack growth. Prior to the onset of crack growth the curves of COD and the J -integral increase regularly as predicted by the elastodynamic solution for a half plane crack subjected to plane tensile pulse. With the onset of crack extension the COD grows linearly and exceeds the COD level for the case of stationary crack. The J -integral also increases with the crack growth but its value is always lower than that obtained for the case of the stationary crack. This is to be expected since the universal function for the energy release rate decreases monotonically with the increase in crack tip speed. The oscillations in J integral are a consequence of wave effects associated with the creation of new free surface using the element vanishing technique, which affects J -integral values computed for remote contours because of the area integral term in eqn (46).

Contours of Mises effective stress in the vicinity of the crack tip, are shown in Figs 10(a) to 10(d) for four different time intervals after the arrival of the tensile wave at the crack plane. For the contour plots at $t = 200$ ns and $t = 400$ ns the contours of effective Mises stress are similar in shape and level to those for the elastic material. At higher crack tip speeds (contour plots at $t = 600$ ns and $t = 750$ ns), leads to noticeable plastic deformation in the near crack tip region. This is also observed from the shape of the Mises effective stress contours which show a region of enhanced Mises effective stress behind the crack tip.

Figures 11(a)–11(d) show the contour plots for the effective plastic strain $\bar{\epsilon}^p$, in the vicinity of the crack tip at four different time intervals after the arrival of the tensile wave at the crack plane. The equivalent plastic strain in the vicinity of the crack tip increases as the crack growth occurs (to a maximum of 5% plastic strain), and the plastic strain profile shows decreasing plastic strain in the wake region behind the crack tip as the distance from the crack tip increases. This is consistent with the J -integral calculations which show an increase in toughness as the crack growth occurs. The limited but non-zero plastic strains at the crack tip aid in increasing the fracture

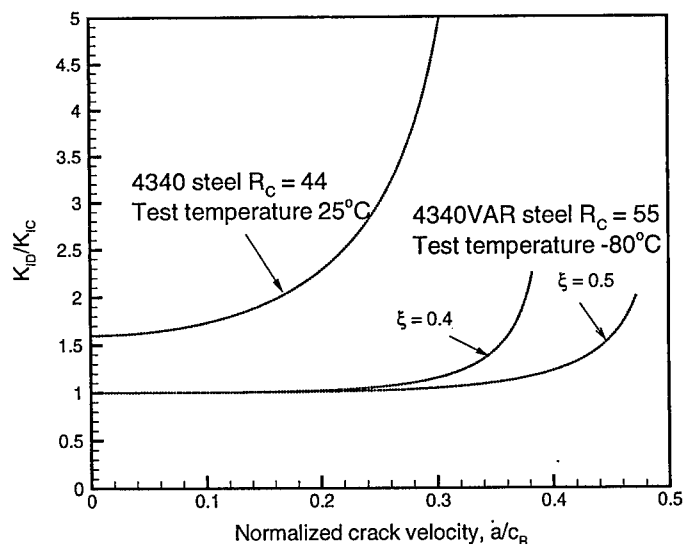


Fig. 10. Contour plots for the flow stress in the vicinity of the propagating crack at time $t = 200, 400, 600$ and 750 ns after the arrival of the tensile wave tip at the crack plane.

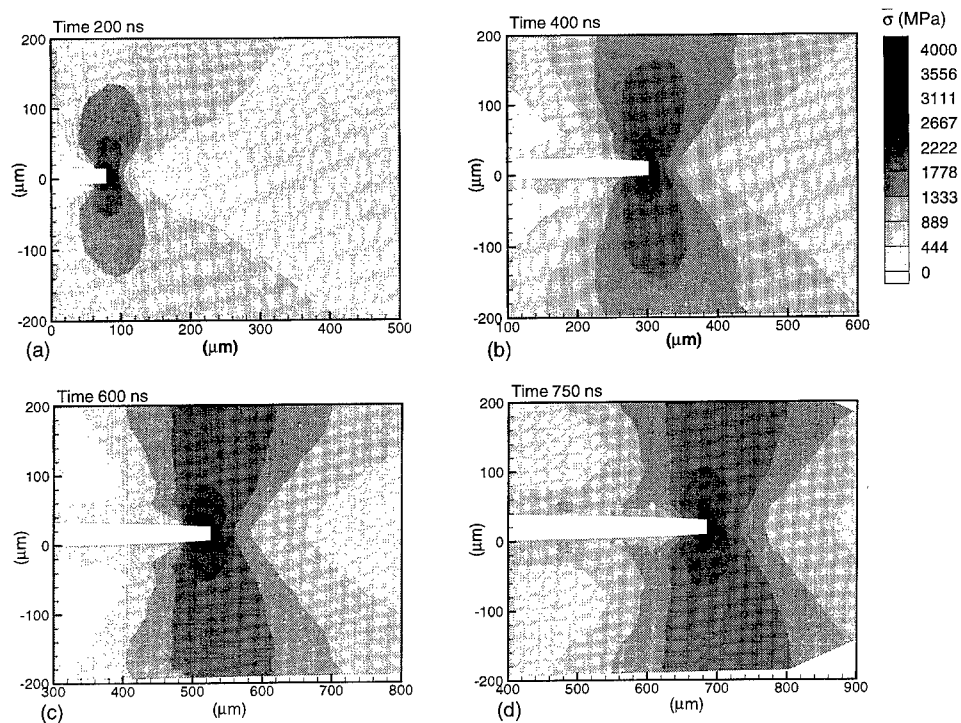


Fig. 11. Contour plots for the equivalent plastic strain in the vicinity of the propagating crack at time $t = 200, 400, 600$ and 750 ns after the arrival of the tensile wave tip at the crack plane.

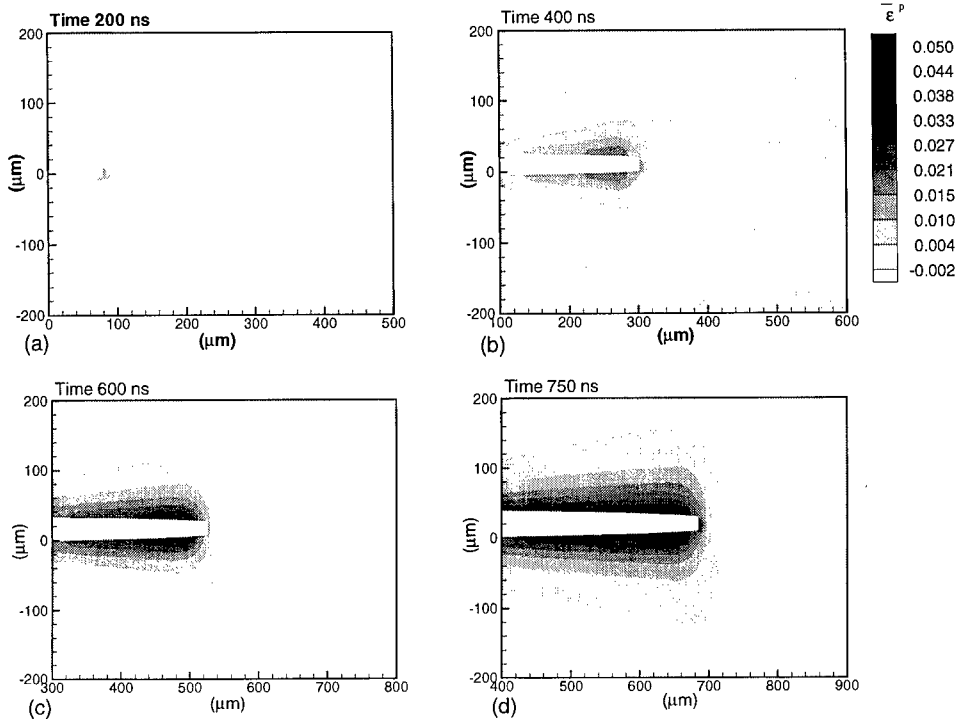


Fig. 12. Normalised dynamic fracture toughness versus dimensionless crack tip speed for the room temperature dynamic fracture of 4340VAR steel ($R_c = 45$), and the low temperature dynamic fracture of 4340 VAR steel ($R_c = 55$).

resistance of the dynamically propagating crack due to material inertia and the strain rate sensitivity of flow stress for 4340VAR steel. The local temperature change in the vicinity of the crack tip is also small. It increases from -80°C to a maximum of -50°C during the entire duration of crack growth. The temperature contours, which are similar to the equivalent plastic strain profiles, indicate that the heating extends in a narrow region around the crack tip and the deformation remains essentially adiabatic in the wake region behind the crack tip.

Figure 12 shows the normalized dynamic fracture toughness versus dimensionless crack tip speed for the room temperature dynamic fracture of 4340 steel ($R_c = 45$) and the low temperature dynamic fracture of 4340VAR steel ($R_c = 55$), obtained by using eqns (42)–(45). Both steels show a monotonically increasing fracture toughness versus crack velocity relationship which takes on large values for moderate values of \dot{a}/c_R ratio. Although there is no unambiguous way to associate a terminal velocity with these results, the plot suggests a maximum attainable velocity well below the Rayleigh wave speed of the material. The intercept value of fracture toughness at $\dot{a}/c_R = 0$ corresponds to the so-called steady state toughness value of the theory of stable crack growth. The spread of intercepts on the $\dot{a}/c_R = 0$ results because of the normalization factor (K_{Ic} corresponding to the 4340VAR steel ($R_c = 55$) at -80°C)

used to normalize all data shown on the plot. As discussed by Lam and Freund (1985), the variation of fracture toughness with crack speed for 4340 steel with $R_c = 45$ is primarily due to inertial effects. It is anticipated that if the inertial effects were neglected, the calculated toughness would be completely independent of speed (Siegmond and Needleman, 1997). As discussed in Section 2.2, the low temperature (-80°C) fracture of 4340 steel ($R_c = 55$), occurs essentially by a quasi-cleavage mechanism involving a limited amount of inelastic deformation. Moreover, as compared to the room temperature experiments, the flow stress of the 4340 steel ($R_c = 55$) in the vicinity of the crack tip (within the plastic zone region) would be significantly higher due to the lower than room test temperature and the relatively higher rate sensitivity of the steel employed in the present investigation. This results in relatively smaller levels of plastic deformation and hence to a smaller plastic zone size. The relatively smaller levels of inelastic deformation for the low temperature experiments, leads to smaller particle velocities and hence to lower particle accelerations in the vicinity of the crack tip region as compared to the room temperature experiments on 4340 steel in a much more ductile condition ($R_c = 44$). The smaller particle accelerations lead to a smaller inertial resistance, thus delaying the upturn in the fracture toughness to relatively higher crack tip speeds. This observation is also consistent with the analysis of Mataga *et al.* (1987), who, using a strain-based crack growth criterion, have shown that for tough structural materials requiring higher critical strains for failure, and thus with larger plastic zone sizes, show lower crack tip speeds at which the upturn in the material fracture resistance occurs.

REFERENCES

- Achenbach, J. D. and Nuismer, R. (1971) Fracture generated by dilatational wave. *Int. J. Fract.* **7**, 77–88.
- Belytschko, T., Chiapetta, R. L. and Bartel, H. D. (1976) Efficient large scale non-linear transient analysis by finite elements. *Int. J. Numer. Meth. Engng.* **10**, 579–596.
- Budiansky, B. (1969) Remarks on theories of solid and structural mechanics: Problems of hydrodynamics and continuum mechanics, ed. M. A. Lavrent'ev *et al.*, pp. 77–83., *SIAM*.
- Campbell, J. D. and Ferguson, W. G. (1990) The temperature and strain rate dependence of the shear strength of mild steel. *Phil. Mag.* **21**, 63–82.
- Clifton, R. J. (1990) High strain rate behavior of metals. *Appl. Mech. Rev.* **43**, S10–S22.
- Freund, L. B. (1973) Crack propagation in an elastic solid subjected to general loading. III. Stress wave loading. *J. Mech. Phys. Solids* **21**, 47–61.
- Freund, L. B. (1990) *Dynamic fracture mechanics*. Cambridge University Press, Cambridge, UK.
- Griffith, A. A. (1920) The phenomenon of rupture and flow in solids, *Phil. Mag.*, A221, 163–198.
- Irwin, G. R. (1957) Analysis of stresses and strains near the end of a crack traversing a plate. *J. Appl. Mech.* **24**, 361–364.
- Irwin, G. R. (1960) Fracture mechanics. In *Structural mechanics*, ed. J. N. Goodier and N. J. Hoff, pp. 557–591. Elmsford, Pergamon.
- Kannien, M. F. and Popelar, C. H. (1985) *Advanced Fracture Mechanics*. Oxford University Press, New York, Oxford.
- Klopp, R. W., Clifton, R. J. and Shawki, T. G. (1985) Pressure-shear impact and the dynamic plastic response of metals. *Mech. Mater.* **4**, 375–385.
- Kobayashi, T. and Dally, J. W. (1979) Crack arrest methodology and applications, *ASTM*

- STP 711, ed. G. T. Hahn and M. F. Kanninen, pp. 189–210. American Society of Testing and Materials, Philadelphia.
- Krieg, R. D. and Key, S. W. (1973) Transient shell response by numerical time integration. *Int. J. Numer. Meth. Engng.* **7**, 273–286.
- Lam, P. S. and Freund, L. B. (1985) Analysis of dynamic growth of a tensile crack in elastic-plastic material. *J. Mech. Phys. Solids* **33**, 253–167.
- Mataga, P. A., Freund, L. B. and Hutchinson, J. W. (1987) Crack tip plasticity in dynamic fracture. *J. Phys. and Chem. Solids* **48**, 985–1005.
- Mello, M. C., Prakash, V. and Clifton, R. J. (1991) Multi-point interferometry for monitoring two-dimensional wave motions, in shock compression of condensed matter. Proc. American Physical Society Topical Conference, Williamsburg, VA, pp. 763–767.
- Moran, J. and Shih, C. H. (1987) General treatment of crack tip contour integrals. *Int. J. Frac.* **35**, 295–310.
- Nakamura, T., Shih, C. F. and Freund, L. B. (1985) Computational methods based on an energy integral in dynamic fracture. *Int. J. Frac.* **27**, 229–243.
- Nagtegaal, J. C., Parks, D. M. and Rice, J. R. (1974) On numerically accurate finite element solutions in the fully plastic range. *Comp. Meth. Appl. Mech. Engng.* **4**, 153–175.
- Peirce, D., Shih, C. F. and Needleman, A. (1984) A tangent modulus method for rate dependent solids, *Comp. and Struc.* **18**, 875–887.
- Povirk, G. L., Needleman, A. and Nutt, S. R. (1990) An analysis of residual stress in whisker-reinforced Al-SiC composites. *Mater. Sci. and Engng.* **A125**, 129–140.
- Prakash, V. and Clifton, R. J. (1992) Experimental and analytical investigations of dynamic fracture under conditions of plane strain. In *Proc. 22nd Mat. Symp. Fracture mechanics 1*, ASTM STP 1131, ed. H. A. Ernst, A. Saxena and D. L. Dowell, Philadelphia, pp. 412–444.
- Prakash, V. (1993) Ph.D dissertation, Brown University, Providence, Rhode Island.
- Ravichandran, G. (1983) A plate impact experiment for studying crack initiation at loading rates $\dot{K}_I \approx 10^8$ MPa $\sqrt{\text{m/s}}$. Sc.M. thesis, Brown University, Providence, Rhode Island.
- Ravichandran, G. and Clifton, R. J. (1989) Dynamic fracture under plane wave loading. *Int. J. Fract.* **40**, 157–201.
- Rice, J. R. (1968) A path independent integral and the approximate analysis of strain concentration by notches and cracks. *J. Appl. Mech.* **35**, 379–386.
- Rosakis, A. J., Duffy, J. and Freund, L. B. (1984) The determinism of dynamic fracture toughness of AISI 4340 steel by the shadow spot method. *J. Mech. Phys. Solids* **32**, 443–460.
- Rosakis, A. J. and Zhender, A. T. (1990) Dynamic fracture initiation and propagation in 4340 steel under Impact loading. *Int. J. Fract.* **43**, 271–285.
- Siegmund, T. and Needleman, A. (1997) A numerical study of dynamic crack growth in elastic-viscoplastic solids. *Int. J. Solids and Struc.* **34**, 769–785.
- Taylor, G. I. and Quinney, H. (1934) The latent energy remaining in a metal after cold working. *Proc. Royal Soc. London* **A143**, 307–326.
- Tvergaard, V. (1982) Influence of void nucleation on ductile shear fracture at a free surface. *J. Mech. Phys. Solids* **30**, 399–425.



Pergamon

J. Mech. Phys. Solids, Vol. 46, No. 10, pp. 1969–1980, 1998

© 1998 Elsevier Science Ltd. All rights reserved

Printed in Great Britain

0022-5096/98 \$—see front matter

PII: S0022-5096(98)00045-3

APPLICATION OF THE COSSERAT SPECTRUM THEORY TO VISCOELASTICITY

XANTHIPPI MARKENSCOFF,^{†‡} WENSEN LIU,^{‡§}
and MICHAEL PAUKSHTO[¶]

[‡] University of California, San Diego, Department of Applied Mathematics and Engineering Sciences,
La Jolla CA 92093, U.S.A. [§] San Diego State University, College of Engineering, San Diego CA 92182,
U.S.A. [¶] Saint Petersburg State University, Institute of Mathematics and Mechanics, Saint
Petersburg, Russia

(Received 20 December 1997; in revised form 21 February 1998)

ABSTRACT

The Cosserat Spectrum theory is applied in the theory of linear viscoelasticity. The solution for the Laplace transform of the displacement of the viscoelastic problem is expressed in a series of the Cosserat eigenfunctions, which are dependent only on position, and the coefficients are expressed as convolutions of the time dependent body force or surface loading provided that the inverse Laplace transforms of the viscoelastic moduli are known. This renders the Cosserat Spectrum theory advantageous for the solution of viscoelastic problems. Several examples are shown. © 1998 Elsevier Science Ltd. All rights reserved.

Keywords: A. creep, B. viscoelastic material. C. Cosserat Spectrum.

1. INTRODUCTION

The homogeneous Navier equations $\Delta \vec{u} + \omega \nabla \nabla \cdot \vec{u} = 0$, [$\omega = (\lambda + \mu)/\mu = (1/(1 - 2\nu))$, λ and μ being the Lamé's constants, ν the Poisson's ratio], with homogeneous boundary conditions of displacement or traction admit nontrivial solutions when ω takes values in a set of points lying outside the physical range of Poisson's ratio called the Cosserat Spectrum. The Cosserat Spectrum theory was introduced by Cosserat and Cosserat (1898) and then fully developed by Mikhlin (1973), who proved the completeness and orthogonality of the Cosserat eigenfunctions and represented the displacement field \vec{u} as summation of the Cosserat eigenfunctions for the boundary value problems of displacement or traction. Pobedria (1970) applied the Cosserat Spectrum theory to 2-D viscoelastic problems. In a recent paper, Markenscoff and Paukshto (1998) applied it to problems in elasticity and thermoelasticity. They also developed a variational principle in thermoelasticity within the frame of the Cosserat Spectrum theory.

In the present article we develop a theory of linear viscoelasticity based on the Cosserat Spectrum theory. We show that in the Laplace transformed space the Navier equations hold and the Cosserat Spectrum theory can be applied. The solution for

[†] To whom correspondence should be addressed. E-mail: xmarkens@ames.ucsd.edu

the Laplace transform of the displacement function of viscoelastic problems is expressed in series of the Cosserat eigenfunctions, which are functions of geometry only (and not the transform variable s), and the coefficients are functions of s that can be easily inverted for rational functions, which is the case in the commonly used viscoelastic models (Christensen, 1971). Thus, once the inverse Laplace transforms of these functions that depend on the viscoelastic moduli are known, the solution may readily be expressed as convolutions of the time dependent body force or surface loading. In this respect, this method of solution has an advantage over the standard methods as in Lee (1955), Radok (1957), and Lee *et al.* (1959).

2. FORMULATION OF THE GOVERNING EQUATIONS OF VISCOELASTICITY IN TERMS OF THE COSSERAT SPECTRUM THEORY

The equations of quasi-static equilibrium are given by

$$\sigma_{ij,j}(t) + F_i(t) = 0 \quad \text{in } \Omega \quad (1)$$

with boundary conditions of displacement

$$\tilde{u} = \tilde{u}(t) \quad \text{on } \partial\Omega \quad (2a)$$

or traction

$$\tilde{t}^n(t) = \tilde{\sigma}(t) \cdot \tilde{n} \quad \text{on } \partial\Omega \quad (2b)$$

while the stress $\sigma_{ij}(t)$ and strain

$$\varepsilon_{ij}(t) = \frac{1}{2}[u_{i,j}(t) + u_{j,i}(t)] \quad (3)$$

are related by the constitutive equations (Christensen, 1971)

$$\sigma_{ij}(t) = \int_0^t [2\mu(t-t') d\varepsilon_{ij}(t') + \lambda(t-t') \delta_{ij} d\varepsilon_{kk}(t')] \quad (4)$$

with $\mu(t)$ and $\lambda(t)$ being the time dependent Lamé's moduli.

By applying the Laplace transform on the above equations, denoting by “ $\hat{\cdot}$ ” the transformed quantities, and combining the transformed eqns (1), (3) and (4), we obtain the Navier equations for the transformed displacements

$$\hat{u}_{i,jj} + \hat{\omega} \hat{u}_{j,ji} = -\frac{\hat{F}_i}{\hat{\mu}} \quad \text{in } \Omega \quad (5)$$

where

$$\hat{\omega} = \frac{\hat{\lambda} + \hat{\mu}}{\hat{\mu}} \quad (6)$$

with boundary conditions of displacement

$$\hat{\tilde{u}} = \hat{\tilde{u}}_b \quad \text{on } \partial\Omega \quad (7a)$$

or traction

$$\hat{\vec{t}} = \hat{\vec{\sigma}} \cdot \vec{n} \quad \text{on } \partial\Omega \quad (7b)$$

We now observe that the displacement $\hat{\vec{u}}$ satisfying eqns (5) and (7) may be expressed in terms of a series of the Cosserat eigenfunctions, which satisfy the homogeneous Navier equations

$$\nabla^2 \tilde{u}_n + \tilde{\omega}_n \nabla \nabla \cdot \tilde{u}_n = 0 \quad \text{in } \Omega \quad (8)$$

with homogeneous boundary conditions of displacement

$$\tilde{u}_n = 0 \quad \text{on } \partial\Omega \quad (9a)$$

or traction

$$\vec{\tau}'(\tilde{u}_n) = \vec{\sigma}(\tilde{u}_n) \cdot \vec{n} = 0 \quad \text{on } \partial\Omega \quad (9b)$$

As presented by Mikhlin (1973), the Cosserat eigenfunctions are complete in the Sobolev space H^1 , and thus, the solutions of the inhomogeneous eqn (5) with boundary conditions of displacement [eqn (7a)] or traction [eqn (7b)] admit the Mikhlin (1973) representation theorems as follows:

The solution for the boundary value problem of displacement

$$\Delta \hat{\vec{u}} + \hat{\omega} \nabla \nabla \cdot \hat{\vec{u}} = - \frac{\hat{\vec{F}}}{\hat{\mu}} \quad \text{in } \Omega \quad (10a)$$

$$\hat{\vec{u}} = 0 \quad \text{on } \partial\Omega \quad (10b)$$

admits the representation

$$\hat{\vec{u}} = \frac{1}{\hat{\mu}} \sum_{n=1}^{\infty} \left\{ \frac{(\hat{\vec{F}}, \tilde{u}_n^{(-1)})}{1 + \hat{\omega}} \tilde{u}_n^{(-1)} + (\hat{\vec{F}}, \tilde{u}_n^{(\infty)}) \tilde{u}_n^{(\infty)} + \frac{\tilde{\omega}_n}{\tilde{\omega}_n - \hat{\omega}} (\hat{\vec{F}}, \tilde{u}_n) \tilde{u}_n \right\} \quad (11a)$$

where

$$(\hat{\vec{F}}, \tilde{u}) \equiv \int \hat{\vec{F}} \cdot \tilde{u} \, dV \quad (11b)$$

The solution of

$$\Delta \hat{\vec{u}} + \hat{\omega} \nabla \nabla \cdot \hat{\vec{u}} = 0 \quad \text{in } \Omega \quad (12a)$$

$$\hat{\vec{u}} = \hat{\vec{u}}_b \quad \text{on } \partial\Omega \quad (12b)$$

admits the representation

$$\hat{\vec{u}} = \hat{\vec{u}}_0 + \sum_{n=1}^{\infty} \frac{\hat{\omega} \tilde{\omega}_n}{\hat{\omega} - \tilde{\omega}_n} (\text{div } \hat{\vec{u}}_0, \text{div } \tilde{u}_n) \tilde{u}_n \quad (13a)$$

where $\hat{\vec{u}}_0$ satisfies

$$\Delta \hat{\vec{u}}_0 = 0 \quad \text{in } \Omega \quad (13b)$$

$$\hat{u}_0 = \hat{u}_b \quad \text{on } \partial\Omega \quad (13c)$$

The solution for the boundary value problem of traction

$$\Delta \hat{u} + \hat{\omega} \nabla \nabla \cdot \hat{u} = - \frac{\hat{F}}{\hat{\mu}} \quad \text{in } \Omega \quad (14a)$$

$$\hat{\sigma}(\hat{u}) \cdot \vec{n} = \hat{t} \quad \text{on } \partial\Omega \quad (14b)$$

can be represented as

$$\hat{u} = \frac{1}{\hat{\mu}} \sum_{n=1}^{\infty} \left\{ \frac{2(\hat{f}, \hat{u}_n^{(-1)})}{1 + \hat{\omega}} \hat{u}_n^{(-1)} + (\hat{f}, \hat{u}_n^{(\infty)}) \hat{u}_n^{(\infty)} + \frac{1 - \hat{\omega}_n}{\hat{\omega} - \hat{\omega}_n} (\hat{f}, \hat{u}_n) \hat{u}_n \right\} \quad (15a)$$

where

$$(\hat{f}, \hat{u}) \equiv \int \hat{F} \cdot \hat{u} \, dV + \int \hat{t} \cdot \hat{u} \, dS \quad (15b)$$

By $\hat{u}_n^{(-1)}$ in the above equations is indicated the infinite orthogonal subspace of eigenfunctions corresponding to the eigenvalue of infinite multiplicity $\hat{\omega} = -1$, by $\hat{u}_n^{(\infty)}$ is indicated the infinite orthogonal subspace of eigenfunctions corresponding to the eigenvalue of infinite multiplicity $\hat{\omega} = \infty$, while by \hat{u}_n is indicated the orthogonal subspace of eigenfunctions corresponding to the eigenvalues of finite multiplicity of the discrete spectrum $\hat{\omega}_n$. We may note here that the Cosserat eigenfunctions are functions of the space variables only (and not the transform variable s).

3. INVERSION OF THE LAPLACE TRANSFORMS

An advantage of expressing the solutions of the viscoelastic problem in terms of the Cosserat eigenfunctions is that the inversion of the Laplace transform may be obtained by convolution, provided that inverse Laplace transforms of the terms involving the viscoelastic moduli can be easily obtained.

Let us consider the representation eqn (11) for the boundary value problem of displacement with homogeneous boundary conditions and denote

$$\hat{G}^{(-1)}(s) = \frac{1}{\hat{\mu}(1 + \hat{\omega})} \quad (16a)$$

$$\hat{G}^{(\infty)}(s) = \frac{1}{\hat{\mu}} \quad (16b)$$

$$\hat{G}(\hat{\omega}_n, s) = \frac{\hat{\omega}_n}{\hat{\mu}(\hat{\omega}_n - \hat{\omega})} \quad (16c)$$

If for a given viscoelastic material, eqn (16) can be inverted to obtain $G^{(-1)}(t)$, $G^{(\infty)}(t)$ and $G(\hat{\omega}_n, t)$, then the solution of the viscoelastic problem in the time domain may be obtained by convolution as follows

$$\begin{aligned} \bar{u}(t) = & \sum_{n=1}^{\infty} \int_0^t [\bar{F}(t'), \bar{u}_n^{(-1)}] G^{(-1)}(t-t') dt' \bar{u}_n^{(-1)} + \sum_{n=1}^{\infty} \int_0^t [\bar{F}(t'), \bar{u}_n^{(\infty)}] G^{(\infty)}(t-t') dt' \bar{u}_n^{(\infty)} \\ & + \sum_{n=1}^{\infty} \int_0^t [\bar{F}(t'), \bar{u}_n] G(\bar{\omega}_n, t-t') dt' \bar{u}_n \quad (17a) \end{aligned}$$

where

$$[\bar{F}(t), \bar{u}] \equiv \int \bar{F}(t) \cdot \bar{u} dV \quad (17b)$$

Similarly, the inversion of the representation eqn (13) for the boundary value problem of displacement with inhomogeneous boundary conditions, and eqn (15) for the boundary value problem of traction may be obtained. Thus for any time dependent body force loading or boundary loading, the solution of viscoelastic problems may be written immediately in the form of eqn (17) if the Cosserat eigenfunctions are known for the geometry of the problem. The functions $G^{(-1)}(t)$, $G^{(\infty)}(t)$ and $G(\bar{\omega}_n, t)$ for the commonly used viscoelastic models are presented in the Appendix.

4. APPLICATIONS AND EXAMPLES

(1) Time dependent temperature loading

We consider viscoelasticity problems with thermal loading that may, in addition, be time dependent. As shown by Markenscoff and Paukshto (1998), the temperature loading is equivalent to a body force loading that results in the representation of the displacement field in terms of a series of the Cosserat eigenfunctions according to

$$\bar{u} = (3\omega - 1)\alpha \sum_{n=1}^{\infty} \frac{\bar{\omega}_n}{\bar{\omega}_n - \omega} (T, \text{div } \bar{u}_n) \bar{u}_n \quad (18)$$

for the boundary value problem of displacement with zero boundary displacement, and

$$\bar{u} = (3\omega - 1)\alpha \sum_{n=1}^{\infty} \left\{ \frac{2}{\omega + 1} (T, \text{div } \bar{u}_n^{(-1)}) + \frac{1 - \bar{\omega}_n}{\omega - \bar{\omega}_n} (T, \text{div } \bar{u}_n) \bar{u}_n \right\} \quad (19)$$

for the boundary problem of traction with traction free boundary condition. The displacement field in the Laplace transform space s in thermoviscoelasticity is, accordingly, represented by the series

$$\hat{\bar{u}} = (3\hat{\omega} - 1)\alpha \sum_{n=1}^{\infty} \frac{\hat{\omega}_n}{\hat{\omega}_n - \hat{\omega}} (\hat{T}, \text{div } \bar{u}_n) \bar{u}_n \quad (20)$$

for the boundary value problem of displacement with zero boundary displacement, and by

$$\hat{u} = (3\hat{\omega} - 1)\alpha \sum_{n=1}^{\infty} \left[\frac{2}{\hat{\omega} + 1} (\hat{T}, \text{div } \tilde{u}_n^{(-1)}) \tilde{u}_n^{(-1)} + \frac{1 - \tilde{\omega}_n}{\hat{\omega} - \tilde{\omega}_n} (\hat{T}, \text{div } \tilde{u}_n) \tilde{u}_n \right] \quad (21)$$

for the boundary value problem with traction free boundary condition.

By applying the convolution theorem, according to the analysis of the previous section, we have the representation of the displacement for the solution of the thermoviscoelastic problem

$$\tilde{u} = \sum_{n=1}^{\infty} \int_0^t [T(t'), \text{div } \tilde{u}_n] G(\tilde{\omega}_n, t - t') dt' \tilde{u}_n \quad (22a)$$

where

$$G(\tilde{\omega}_n, t) = \tilde{\omega}_n \alpha L^{-1} \left[\frac{3\hat{\omega} - 1}{\tilde{\omega}_n - \hat{\omega}} \right] \quad (22b)$$

for the boundary value problem of displacement, and

$$\begin{aligned} \tilde{u} = \sum_{n=1}^{\infty} \left\{ \int_0^t [T(t'), \text{div } \tilde{u}_n^{(-1)}] G^{(-1)}(t - t') dt' \tilde{u}_n^{(-1)} \right. \\ \left. + \int_0^t [T(t'), \text{div } \tilde{u}_n] G(\tilde{\omega}_n, t - t') dt' \tilde{u}_n \right\} \quad (23a) \end{aligned}$$

where

$$\begin{aligned} G^{(-1)}(t) &= 2\alpha L^{-1} \left[\frac{3\hat{\omega} - 1}{\hat{\omega} + 1} \right] \\ G(\tilde{\omega}_n, t) &= (1 - \tilde{\omega}_n) \alpha L^{-1} \left[\frac{3\hat{\omega} - 1}{\hat{\omega} - \tilde{\omega}_n} \right] \quad (23b) \end{aligned}$$

for the boundary value problem of traction. If the material is initially undisturbed and the temperature T is not time dependent, then the convolution integrals are easily performed.

(2) The Lamé problem under time dependent loading

This is the problem of a spherical, viscoelastic shell under time dependent internal and external pressure p_1 and p_2 , respectively. The classical elastic solution (Luré, 1964) is

$$\begin{aligned} u_r &= -\frac{1}{\mu(3\omega - 1)} \frac{(p_2 r_2^3 - p_1 r_1^3)r}{r_2^3 - r_1^3} - \frac{1}{4\mu} \frac{(p_2 - p_1)r_1^3 r_2^3}{(r_2^3 - r_1^3)r^2} \\ u_\theta &= u_\varphi = 0 \quad (24) \end{aligned}$$

where r_1 and r_2 are the internal and external radius, respectively. It can be verified that the first term in eqn (24) is an eigenfunction corresponding to $\hat{\omega} = 1/3$, and the

second term is an eigenfunction corresponding to $\tilde{\omega} = \infty$. In the Laplace transform space s , the displacement field will be

$$\begin{aligned}\hat{u}_r &= -\frac{1}{\hat{\mu}(3\hat{\omega}-1)} \frac{(\hat{p}_2 r_2^3 - \hat{p}_1 r_1^3)r}{r_2^3 - r_1^3} - \frac{1}{4\hat{\mu}} \frac{(\hat{p}_2 - \hat{p}_1)r_1^3 r_2^3}{(r_2^3 - r_1^3)r^2} \\ \hat{u}_\theta &= \hat{u}_\phi = 0\end{aligned}\quad (25)$$

If the viscoelastic material is Hookean solid in dilatation and Kelvin solid in distortion, the material parameters represented by eqns (A3)–(A5) in the Appendix are now substituted into eqn (25)

$$\begin{aligned}\hat{u}_r &= -\frac{(\hat{p}_2 r_2^3 - \hat{p}_1 r_1^3)r}{3k(r_2^3 - r_1^3)} - \frac{1}{2(q_0 + q_1 s)} \frac{(\hat{p}_2 - \hat{p}_1)r_1^3 r_2^3}{(r_2^3 - r_1^3)r^2} \\ \hat{u}_\theta &= \hat{u}_\phi = 0\end{aligned}\quad (26)$$

The inverse Laplace transform of eqn (26) gives the solution for any general time dependent loading

$$\begin{aligned}u_r &= -\frac{[p_2(t)r_2^3 - p_1(t)r_1^3]r}{3k(r_2^3 - r_1^3)} \\ &\quad - \frac{r_1^3 r_2^3}{2q_1(r_2^3 - r_1^3)r^2} \int_0^t [p_2(t) - p_1(t)] \exp\left(-\frac{q_0(t-t')}{q_1}\right) dt' \\ u_\theta &= u_\phi = 0\end{aligned}\quad (27)$$

(3) The gravitating sphere

Let the body force acting on a viscoelastic sphere be gravity according to the Newton's law of gravitation. It is known from potential theory that the resultant attraction is directed along the radius to the center of the sphere and that its magnitude is proportional to radial distance. Consequently the body force is given by

$$\vec{F} = -\frac{\rho g \vec{r}}{r_0} \quad (28)$$

where ρ is density, g the gravitational acceleration, r_0 the radius of the sphere and \vec{r} position vector measured from the center of the sphere. The displacement field of an elastic gravitating sphere is presented by Lur  (1964). We rewrite it as follows

$$\begin{aligned}u_r &= -\frac{\rho g r_0}{10\mu} \left[\frac{1}{\omega + 1} \left(r - \frac{r^3}{r_0^2} \right) + \frac{2r}{3\omega - 1} \right] \\ u_\theta &= u_\phi = 0\end{aligned}\quad (29)$$

so that the first part is an eigenfunction corresponding to $\tilde{\omega} = -1$, and the second part is an eigenfunction corresponding to $\tilde{\omega} = 1/3$. If the spherical shell is of viscoelastic material, then the Laplace transform of the displacement field will be

$$\begin{aligned}\hat{u}_r &= -\frac{\rho g r_0}{10s\hat{\mu}} \left[\frac{1}{\hat{\omega}+1} \left(r - \frac{r^3}{r_0^2} \right) + \frac{2r}{3\hat{\omega}-1} \right] \\ \hat{u}_\theta &= \hat{u}_\varphi = 0\end{aligned}\quad (30)$$

Suppose that the material behaves as a Hookean solid in dilatation and Maxwell fluid in distortion, then the material parameters are represented by eqns (A14)–(A16). The inverse Laplace transform of eqn (30) will be

$$\begin{aligned}u_r &= -\frac{\rho g r_0}{10} \left[\frac{1}{k} + \frac{2q_1}{3k^2\tau_m} \exp\left(-\frac{t}{\tau_m}\right) \right] \left(r - \frac{r^3}{r_0^2} \right) - \frac{\rho g r_0 r}{15k} \\ u_\theta &= u_\varphi = 0\end{aligned}\quad (31)$$

where $\tau_m = [(3kp_1 + 2q_1)/3k]$. When $t \rightarrow \infty$, eqn (31) reduces to

$$\begin{aligned}u_r &= -\frac{\rho g r_0}{10k} \left(r - \frac{r^3}{r_0^2} \right) - \frac{\rho g r_0 r}{15k} \\ u_\theta &= u_\varphi = 0\end{aligned}\quad (32)$$

It is interesting to note that u_r is finite as $t \rightarrow \infty$. We have verified that both eigenfunctions satisfy $\nabla \times \vec{u} = 0$, that is, both are distortion-free vector. Furthermore, the second eigenfunction associated with $\hat{\omega} = 1/3$ produces uniform normal stress components and no shear components. Physically, since both eigenfunctions are of zero distortion, the displacement field remains finite even though the material is of the Maxwell fluid type in distortion.

(4) *Heat flow past a thermally insulated spherical cavity*

Suppose the material behaves as a Hookean solid in dilatation and a Maxwell fluid in distortion, then the material parameters are represented by eqns (A14)–(A16).

The temperature field is given by

$$T(t) = T_1(t) + T_2(t) \quad (33a)$$

where $T_1(t)$ is a linear function of position $z = r \cos \theta$, i.e.,

$$T_1(t) = \tau(t)r \cos \theta, \quad T_2(t) = \frac{\tau(t)r_0^2}{2r^2} \cos \theta \quad (33b)$$

where r_0 is the radius of the spherical cavity. The thermoelastic solution to this problem was given by Florence and Goodier (1959) who treated the temperature field with constant τ . Here we view this problem in thermoviscoelasticity with arbitrary $\tau(t)$.

The Laplace transform of the displacement field corresponding to free thermal expansion caused by $T_1(t)$ is given by

$$\begin{aligned}\hat{u}_r &= \frac{1}{2}\alpha\hat{\tau}r^2\cos\theta \\ \hat{u}_\theta &= \frac{1}{2}\alpha\hat{\tau}r^2\sin\theta\end{aligned}\quad (34)$$

The inverse Laplace transform of eqn (34) is given by

$$\begin{aligned}u_r &= \frac{1}{2}\alpha\tau(t)r^2\cos\theta \\ u_\theta &= \frac{1}{2}\alpha\tau(t)r^2\sin\theta\end{aligned}\quad (35)$$

The Laplace transform of the displacement caused by the temperature field $T_2(t)$ is a Cosserat eigenvector corresponding to the eigenvalue $\hat{\omega} = -1$, i.e.,

$$\begin{aligned}\hat{u}_r &= \frac{(3\hat{\omega}-1)\alpha\hat{\tau}r_0^2}{2(\hat{\omega}+1)}\left(-\frac{r_0^3}{3r^3}\right)\cos\theta \\ \hat{u}_\theta &= \frac{(3\hat{\omega}-1)\alpha\hat{\tau}r_0^2}{2(\hat{\omega}+1)}\left(\frac{r_0}{2r}-\frac{r_0^3}{6r^3}\right)\sin\theta\end{aligned}\quad (36)$$

The inverse Laplace transform of eqn (36) gives

$$\begin{aligned}u_r &= \frac{r_0^2}{4}\left(-\frac{r_0^3}{3r^3}\right)\cos\theta\int_0^t\tau(t')G^{(-1)}(t-t')dt' \\ u_\theta &= \frac{r_0^2}{4}\left(\frac{r_0}{2r}-\frac{r_0^3}{6r^3}\right)\sin\theta\int_0^t\tau(t')G^{(-1)}(t-t')dt'\end{aligned}\quad (37a)$$

where $G^{-1}(t)$ defined by eqn (23b) is written as

$$G^{(-1)}(t) = 2\alpha\left[\frac{3p_1}{\tau_m}\delta(t) + \frac{2q_1}{k\tau_m^2}\exp\left(-\frac{t}{\tau_m}\right)\right]\quad (37b)$$

If $\tau = \tau_0 H(t)$, then eqn (37) becomes

$$\begin{aligned}u_r &= \frac{\alpha\tau_0 r_0^2}{2}\left[3 - \frac{2q_1}{k\tau_m}\exp\left(-\frac{t}{\tau_m}\right)\right]\left(-\frac{r_0^3}{3r^3}\right)\cos\theta \\ u_\theta &= \frac{\alpha\tau_0 r_0^2}{2}\left[3 - \frac{2q_1}{k\tau_m}\exp\left(-\frac{t}{\tau_m}\right)\right]\left(\frac{r_0}{2r}-\frac{r_0^3}{6r^3}\right)\sin\theta\end{aligned}\quad (38)$$

where $\tau_m = [(3kp_1 + 2q_1)/3k]$ is the relaxation time of the viscoelastic material.

When $t \rightarrow \infty$, eqn (38) reduces to

$$\begin{aligned}u_r &= \frac{3\alpha\tau_0 r_0^2}{2}\left(-\frac{r_0^3}{3r^3}\right)\cos\theta \\ u_\theta &= \frac{3\alpha\tau_0 r_0^2}{2}\left(\frac{r_0}{2r}-\frac{r_0^3}{6r^3}\right)\sin\theta\end{aligned}\quad (39)$$

It is interesting to note that u_r is finite when $t \rightarrow \infty$. We have verified that the

eigenfunction satisfies $\nabla \times \tilde{u}^{(-1)} = 0$. Physically, since the eigenfunction is of zero distortion, the displacement field remains finite even though the material is of the Maxwell fluid type in distortion.

5. CONCLUSIONS

The Cosserat Spectrum theory is applied to the linear theory of viscoelasticity. The Mikhlin representation theorems in the form of Laplace transform are written in such forms that the inverse Laplace transforms are easily carried out for some frequently used viscoelastic models in terms of convolutions. Also the physical meaning associated with the Cosserat eigenfunctions corresponding to the eigenvalues $\tilde{\omega} = -1$ (distortion free) and $\tilde{\omega} = \infty$ (divergence free) ties naturally with viscoelastic behavior that may differ in the dilatation and distortion part of the constitutive relation.

ACKNOWLEDGEMENT

The support of the National Science Foundation through the Institute of Mechanics and Materials at University of California, San Diego to Michael Paukshto is gratefully acknowledged.

REFERENCES

- Christensen, R. M. (1971) *Theory of Viscoelasticity an Introduction*. Academic Press, New York.
- Cosserat, E. and Cosserat, F. (1898) Sur les equations de la theorie de l'elasticite. *C. R. Acad. Sci. Paris* **126**, 1089–1091.
- Florence, A. L. and Goodier, J. N. (1959) Thermal stress at spherical cavities and circular holes in uniform heat flow. *Journal of Applied Mechanics* **26**, 293–294.
- Lee, E. H. (1955) Stress analysis in viscoelastic bodies. *Quarterly of Applied Mathematics* **13**, 183–190.
- Lee, E. H., Radok, J. R. M. and Woodward, W. B. (1959) Stress analysis for linear viscoelastic materials. *Transactions of the Society of Rheology* **3**, 41–59.
- Lur , A. I. (1964) *Three-dimensional Problems of the Theory of Elasticity*. Interscience, New York.
- Markenscoff, X. and Paukshto, M. V. (1998) The Cosserat spectrum in the theory of elasticity and applications. *Proceedings of the Royal Society of London* **A454**, 147–154.
- Mikhlin, S. G. (1973) The spectrum of a family of operators in the theory of elasticity. *Russian Math. Surveys* **28**, 45–88.
- Pobedria, B. E. (1970) On solution of contact-type problems in the linear theory of viscoelasticity. *Doklady Akad. Nauk SSSR* **190**, 297–300.
- Radok, J. R. M. (1957) Viscoelastic stress analysis. *Quarterly of Applied Mathematics* **15**, 198–202.

APPENDIX

The functions of $G^{(-1)}(t)$, $G^{(\infty)}(t)$ and $G(\tilde{\omega}_n, t)$ for the commonly used viscoelastic models are as follows.

Model 1—Hookean solid in dilatation and Kelvin solid in distortion

The constitutive equations take the form

$$\sigma_{kk}(t) = 3k\varepsilon_{kk}(t) \quad (\text{A1})$$

$$s_{ij}(t) = \int_0^t [q_0 + q_1 \delta(t-t')] de_{ij}(t') \quad (\text{A2})$$

where k is the buck modulus in dilatation and q_1/q_0 the retardation time in distortion, s_{ij} and e_{ij} are the stress deviator and strain deviator, respectively. The complex Lamé moduli $\hat{\mu}$, $\hat{\lambda}$ and the spectrum parameter $\hat{\omega}$ are

$$\hat{\mu} = \frac{1}{2}(q_0 + q_1 s) \quad (\text{A3})$$

$$\hat{\lambda} = \frac{1}{3}(3k - q_0 - q_1 s) \quad (\text{A4})$$

$$\hat{\omega} = \frac{6k + q_0 + q_1 s}{3(q_0 + q_1 s)} \quad (\text{A5})$$

The functions of $G(t)$ for the boundary value problem of displacement, described by eqn (10), are now written as

$$G^{(-1)}(t) = \frac{3}{2q_1} \exp\left(-\frac{2q_0 + 3k}{2q_1} t\right) \quad (\text{A6})$$

$$G^{(\infty)}(t) = \frac{2}{q_1} \exp\left(-\frac{q_0}{q_1} t\right) \quad (\text{A7})$$

$$G(\tilde{\omega}_n, t) = \frac{6\tilde{\omega}}{(3\tilde{\omega}_n - 1)q_1} \exp\left(-\frac{(1 - 3\tilde{\omega}_n)q_0 + 6k}{(1 - 3\tilde{\omega}_n)q_1} t\right) \quad (\text{A8})$$

The functions of $G(t)$ for the boundary value problem of traction, described by eqn (14), are now written as

$$G^{(-1)}(t) = \frac{3}{q_1} \exp\left(-\frac{2q_0 + 3k}{2q_1} t\right) \quad (\text{A9})$$

$$G^{(\infty)}(t) = \frac{2}{q_1} \exp\left(-\frac{q_0}{q_1} t\right) \quad (\text{10})$$

$$G(\tilde{\omega}_n, t) = \frac{6(\tilde{\omega}_n - 1)}{(3\tilde{\omega}_n - 1)q_1} \exp\left(-\frac{(1 - 3\tilde{\omega}_n)q_0 + 6k}{(1 - 3\tilde{\omega}_n)q_1} t\right) \quad (\text{A11})$$

Model 2—Hookean solid in dilatation and Maxwell fluid in distortion

The constitutive equations take the form

$$\sigma_{kk}(t) = 3k\varepsilon_{kk}(t) \quad (\text{A12})$$

$$s_{ij}(t) = \int_0^t \frac{q_1}{p_1} \exp\left(-\frac{t-t'}{p_1}\right) de_{ij}(t') \quad (\text{A13})$$

where k is the buck modulus in dilatation, p_1 the relaxation time and q_1 the viscosity in distortion. The complex Lamé moduli $\hat{\mu}$, $\hat{\lambda}$ and the spectrum parameter $\hat{\omega}$ are

$$\hat{\mu} = \frac{q_1 s}{2(1 + p_1 s)} \quad (\text{A14})$$

$$\hat{\lambda} = \frac{3k + (3kp_1 - q_1)s}{3(1 + p_1 s)} \quad (\text{A15})$$

$$\hat{\omega} = \frac{6k + (6kp_1 + q_1)s}{3q_1 s} \quad (\text{A16})$$

The functions of $G(t)$ for the boundary value problem of displacement, described by eqn (10), are now written as

$$G^{(-1)}(t) = \frac{3p_1}{3kp_1 + 2q_1} \left[\delta(t) + \frac{2q_1}{p_1(3kp_1 + 2q_1)} \exp\left(-\frac{3kt}{3kp_1 + 2q_1}\right) \right] \quad (\text{A17})$$

$$G^{(\infty)}(t) = \frac{2p_1}{q_1} \left[\delta(t) + \frac{1}{p_1} \right] \quad (\text{A18})$$

$$G(\tilde{\omega}_n, t) = \frac{6\tilde{\omega}_n p_1}{(3\tilde{\omega}_n - 1)q_1 - 6kp_1} \times \left[\delta(t) + \frac{(3\tilde{\omega}_n - 1)q_1}{p_1[(3\tilde{\omega}_n - 1)q_1 - 6kp_1]} \exp\left(-\frac{6kt}{(1 - 3\tilde{\omega}_n)q_1 + 6kp_1}\right) \right] \quad (\text{A19})$$

The functions of $G(t)$ for the boundary value problem of traction, described by eqn (14), are now written as

$$G^{(-1)}(t) = \frac{6p_1}{3kp_1 + 2q_1} \left[\delta(t) + \frac{2q_1}{p_1(3kp_1 + 2q_1)} \exp\left(-\frac{3kt}{3kp_1 + 2q_1}\right) \right] \quad (\text{A20})$$

$$G^{(\infty)}(t) = \frac{2p_1}{q_1} \left[\delta(t) + \frac{1}{p_1} \right] \quad (\text{A21})$$

$$G(\tilde{\omega}_n, t) = \frac{6(\tilde{\omega}_n - 1)p_1}{(3\tilde{\omega}_n - 1)q_1 - 6kp_1} \left[\delta(t) + \frac{(3\tilde{\omega}_n - 1)q_1}{p_1[(3\tilde{\omega}_n - 1)q_1 - 6kp_1]} \exp\left(-\frac{6kt}{(1 - 3\tilde{\omega}_n)q_1 + 6kp_1}\right) \right] \quad (\text{A22})$$



Pergamon

J. Mech. Phys. Solids, Vol. 46, No. 10, pp. 1981–1995, 1998

© 1998 Elsevier Science Ltd. All rights reserved

Printed in Great Britain

0022-5096/98 \$—see front matter

PII: S0022-5096(98)00037-4

STRAIN INHOMOGENEITY AND DISCONTINUOUS CRACK GROWTH IN A PARTICULATE COMPOSITE

JAVIER GONZALEZ and W. G. KNAUSS*

Graduate Aeronautical Laboratories, California Institute of Technology, Pasadena CA 91125, U.S.A.

(Received 20 December 1997; in revised form 7 February 1998)

ABSTRACT

A full field method for visualizing strain fields around a crack tip under large strains is developed. Digital image correlation is used to compute strains and displacements incrementally between consecutive images in a process of large deformations. Values of strain and displacements for these consecutive deformations are added such that convergence of the DIC algorithm is assured. The method is used to investigate the strain distribution in a globally homogeneously strained particulate composite (solid propellant) as well as in a zone close to (~ 2 mm) the crack tip in such a material by using a microscope. It is found that maximal strain variations deviate by as much as a factor of three from the average strain; additionally, observations on the interaction of strain inhomogeneities with the tip of a macroscopic crack are discussed. © 1998 Elsevier Science Ltd. All rights reserved.

Keywords: A. fracture, A. strain localization, B. inhomogeneous material, B. viscoelastic material, C. digital image correlation.

1. INTRODUCTION

Particulate composites are widely used in engineering. In the automotive industry, for example, carbon black filled rubbers are used in tires. Many injection molded materials are filled with small particles, while other rigid polymers are toughened through the addition of rubber particles. Solid propellant rocket fuels are physical mixtures of mostly ammonium perchlorate and aluminum powder, often in a multi-modal size distribution, bonded together by a rubber phase called the matrix. Failure in all these materials is heavily dependent upon the interaction between the particles and the matrix, specifically on the separation of particles and binder. Failure also depends on the volume ratio of particles to matrix, which is typically close to 75% in solid propellant materials, but only in the range of 15–40% in structural polymers. In the sequel we examine the failure progression in a solid propellant (Thiokol TPH 1011). Application of continuum mechanics to the stress/strain analysis of structures made of these types of materials typically invoke macroscopically homogeneous material performance, even though deformations are anything but homogeneous at the size scale of the particles. We shall see that inhomogeneous deformations occur at a size scale that is significantly larger than the largest particle, and that the failure

*To whom correspondence should be addressed. E-mail: wkg@atlantis.caltech.edu

process is directly related to the micro-structural deformations associated with these inhomogeneities.

Measuring large strains over small domains of tens to hundreds of microns is not a trivial matter. Imprinted grids tend to serve well at a size scale just above what is required here. Determining the micromechanical deformation with the aid of optical microscopy, e.g. at the tip of a macroscopic crack, implies the need to extend the presently available tools of strain measurements. In principle the digital image correlation method (Sutton *et al.*, 1983, 1985, 1986, 1989; Vendroux and Knauss, 1994) is ideal for this purpose except that it is not suitable if the deformations are so large that convergence of the correlation algorithm is no longer guaranteed: we shall see that deformations involving strains much in excess of 10% cause convergence failure of the DIC algorithm. On the other hand, strains on the order of 50–100% are typical for crack propagation problems in the materials of interest here. Accordingly we develop an incremental application of the DIC method that is capable of analyzing large deformation histories. This development is first addressed in Section 2, and followed, in Section 3, by a discussion of the experimental setup for two sets of experiments: the first experiment addresses, in Section 4, locally inhomogeneous deformations in a globally homogeneous deformation field, and the second examines the deformation field around the tips of a (slowly growing) crack in Section 5, with particular interest centering on the inhomogeneity of the material response in the immediate crack tip region. The paper is summarized with concluding remarks in Section 6.

2. DIGITAL IMAGE CORRELATION

Developed by Sutton and his colleagues (1983, 1985, 1986, 1989) and improved by Vendroux and Knauss (1994), the digital image correlation (DIC) program is used to measure the displacement field and its gradients from images of an undeformed and deformed body. These are gray level images consisting of a grid of pixels (typically 640×480) with eight-bit gray levels (0–255 levels). In the sequel we discuss problems arising with large deformations and a remedy to the situation through a step-wise method we call Large Deformation Digital Image Correlation (LD-DIC).

2.1. *Effect of strain level in code convergence*

The problem in applying the DIC program to compute strain distributions in a large deformation process is, essentially, the failure of the DIC algorithm to converge from an initial solution estimate. The reasons for non-convergence may be diverse. The two major ones are changes of shadows from a fixed light source coupled with large motions of the surface, and, in the present case, possibly an inhomogeneous evolution of the deformation images. If one considers that the (rate of) convergence depends on the closeness of an initial estimate for the result (see the study on the radius of convergence by Vendroux and Knauss (1997)) it becomes reasonable that failure can occur at even moderate strains. Clearly, more definitive rules for code failure or success depend on the specific experimental conditions.

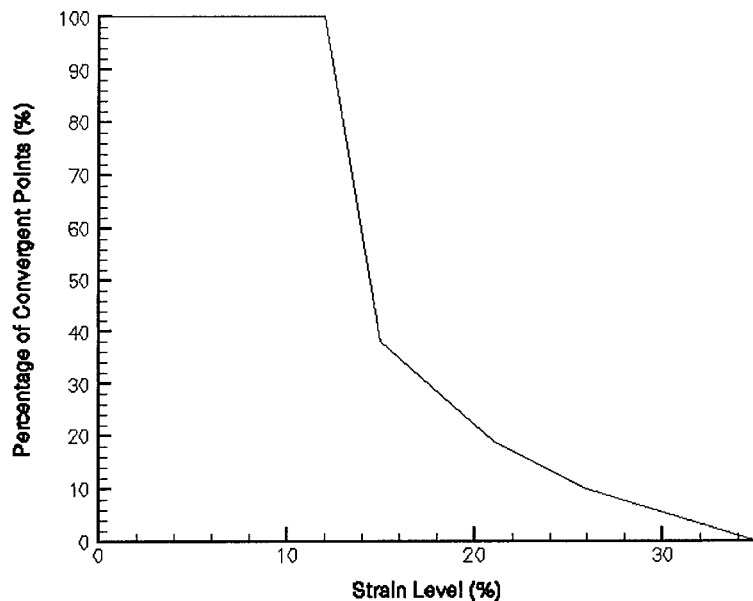


Fig. 1. Successful convergence of the DIC algorithm as a function of (Lagrangian) strain level.

To assess the effect of the strain level on the convergence of the DIC code, consider a test on a homogeneous silicone rubber sheet stretched uniaxially, for which the resultant undeformed and deformed images associated with stretches from 0–40% are compared with the aid of DIC. For each deformation the strains and displacements were computed at 300 points. The fraction of points at which the numerics for the correlation optimization converged is presented in Fig. 1 as a function of the Lagrangian strain.

It is apparent that for deformations in excess of 10% a pronounced decrease occurs in the number of points with successful convergence. For the purpose of studying cracked solid propellants, where typically strains in excess of 30% need to be measured, the applicability of the standard DIC method is thus seriously compromised and a new or extended analysis tool is required.

2.2. The Large Deformation Digital Image Correlation method

To illustrate a proposed Large Deformation Digital Image Correlation (LD-DIC), consider a sequential deformation process on a body: initially undeformed, the body undergoes a continuous deformation, called the “global deformation”. Consider three configurations of the body at three different instants during this global deformation. The first configuration describes the undeformed state of the body and the second a deformed state under a set of changed surface (and body) forces. Call this first segment of the global deformation “deformation A”. Next, an increment in the surface and body forces deforms the body further, this next incremental deformation being designated by “B”. The state of the body after deformation B is represented by the third

configuration. Each configuration corresponds to an experimentally determined and temporally ordered set of images, say, the first, second and third. We select load parameters such that, by assumption, the DIC code can converge successfully to the proper increments of displacements and displacement gradients for the two separate deformations. However, the strains between configurations 1 and 3 (global deformation) are presumed larger than those that cause convergence failure. The LD-DIC method computes the deformation for the third state from the deformations in the two separate steps. To this end compute the global deformation gradient tensor $\mathbf{F}_{\text{global}}$ as the product of the individual deformation gradients

$$\mathbf{F}_{\text{global}} = \mathbf{F}_B \mathbf{F}_A \quad (1)$$

The DIC program determines the displacements of deformation A and their gradients for a discrete set of points G_i defined on a rectangular grid with respect to the first (reference) configuration. For demonstration purposes, these points are represented in configuration 1 in Fig. 2 as a coarse rectangular grid. At the end of deformation A, material particles of the body at the grid points have moved to the points \tilde{G}_i in configuration 2 as signified by the non-orthogonal grid. By comparing the position of the points G_i and \tilde{G}_i in configurations 1 and 2 the DIC program yields the displacements u_i^A and v_i^A , and the associated gradients u_{xi}^A , v_{yi}^A , u_{yi}^A and v_{xi}^A where the index "i" signifies the individual initial positions of the G_i .

The displacements and displacement gradients are computed in a Lagrangian refer-

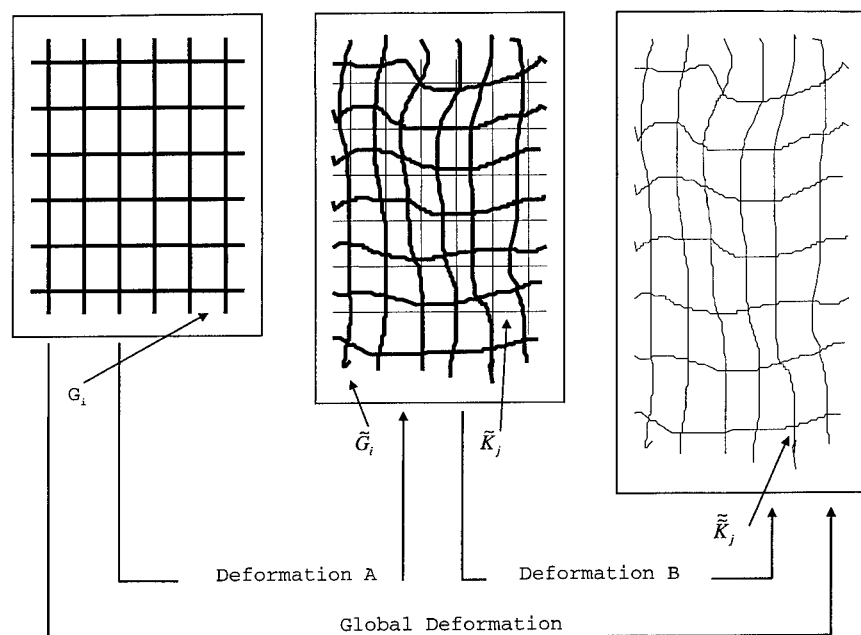


Fig. 2. The interpolation process.

ence frame, the coordinates of which are $\mathbf{X} = \{X_{1i}, X_{2i}\}$. Upon denoting the displacement components as \mathbf{u}_i^A motions of the material points are represented by

$$\tilde{G}_i(\mathbf{X}_i) = G_i(\mathbf{X}_i) + \mathbf{u}_i^A(\mathbf{X}_i) \quad (2)$$

During the second deformation (B), the displacements and their gradients are computed for a different set of material particles which are located in configuration 2 at the grid points \tilde{K}_j of an orthogonal grid, shown in Fig. 2 as the fine grid. In deformation B these points are mapped onto the set $\tilde{\tilde{K}}_j$ in configuration 3. $\tilde{\tilde{K}}_j$ is again represented in the Lagrangian reference frame $\mathbf{Y}_i = \{T_{1i}, T_{2i}\}$ of configuration 2 as

$$\tilde{\tilde{K}}_j(\mathbf{Y}_i) = \tilde{K}_j(\mathbf{Y}_i) + \mathbf{u}_j^B(\mathbf{Y}_i) \quad (3)$$

To obtain the global deformation (A + B) it is necessary to assure that the material points of the first deformation are the same as for the second one. It is thus necessary to interpolate the results from the DIC for deformation B onto the locations of the material particles or grid points of the first (reference) configuration to obtain the displacements and their gradients u_i^B , v_i^B , u_{xi}^B , v_{yi}^B , u_{yi}^B and v_{xi}^B relative to configuration 1. The interpolation of the coordinates \tilde{G}_i is achieved by constructing a set of piecewise continuous surfaces from bilinear patches (plane surfaces). These are determined from the coordinates \tilde{K}_j of configuration 2 so that the displacements and displacement gradients of the initial set of material points are now known.

Using the subscript "gl" to denote global variables, one finds the global displacement components as

$$\begin{aligned} \mathbf{u}_{\text{gl}} &= \mathbf{u}^A + \mathbf{u}^B \\ \mathbf{v}_{\text{gl}} &= \mathbf{v}^A + \mathbf{v}^B \end{aligned} \quad (4)$$

and their gradients are, upon invoking the tensorial relation (1),

$$\begin{aligned} [u_x]_{\text{gl}} &= u_x^A + u_x^B + u_x^A u_x^B + u_y^B v_x^A \\ [v_y]_{\text{gl}} &= v_y^A + v_y^B + v_y^A v_y^B + v_x^B v_y^A \\ [u_y]_{\text{gl}} &= u_y^A + u_y^B + u_y^A u_x^B + u_y^B v_y^A \\ [v_x]_{\text{gl}} &= v_x^A + v_x^B + u_x^A v_x^B + v_y^B v_x^A \end{aligned} \quad (5)$$

From which the (global) two-dimensional Lagrangian strain tensor derives, by definition, as

$$\begin{aligned} 2E_{xx} &= 2[u_x]_{\text{gl}} + \{[u_x]_{\text{gl}}^2 + [v_x]_{\text{gl}}^2\} \\ 2E_{yy} &= 2[v_y]_{\text{gl}} + \{[u_y]_{\text{gl}}^2 + [v_y]_{\text{gl}}^2\} \\ 2E_{xy} &= \{[u_y]_{\text{gl}} + [v_x]_{\text{gl}}\} + \{[u_x]_{\text{gl}}[u_y]_{\text{gl}} + [v_x]_{\text{gl}}[v_y]_{\text{gl}}\} \end{aligned} \quad (6)$$

Here the displacement gradients of the displacement "w" normal to the surface have been neglected. This is permissible (even) for this situation of "plane stress" since under these large deformations the propellant material voids considerably so that the effective Poisson ratio is rather small, thus giving rise to only small gradients. For a global deformation requiring more than two steps the same is applied con-

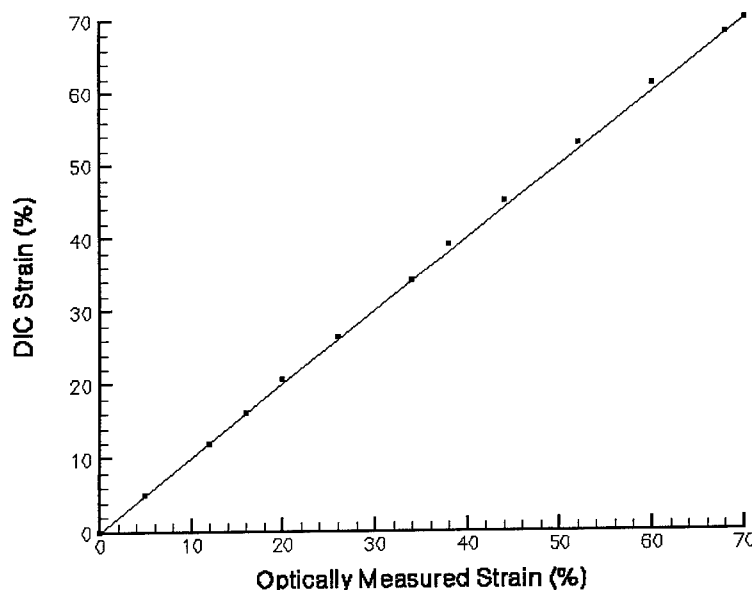


Fig. 3. Comparison of strains determined optically and by the LD-DIC method; the solid line is the ideal relation.

secutively such that the second-to-the last increment is treated like the first one in the two-step example outlined here.

When more than two steps are needed for field evaluations there arises a loss of information at the boundary. This is the result of interpolating information near and internal to the boundary. As more and more steps are required the information near the boundary becomes increasingly corrupted due to the interpolation process and thus information is lost here. This loss is evident in the field images presented later on as apparent white-out regions along a boundary, including the flanks of a crack. Minimization of this feature still requires future attention.

2.3. *Verification of the scheme for addition of fields*

In order to check the efficacy of the proposed multi-step scheme we examine experimentally a specimen of homogeneous silicone rubber without a crack and coated with microscopic speckles, stretched sequentially and uniaxially to a minimum (Lagrangian) strain of 0.70 in a sequence of 12 deformation steps of 3–4% strain each (13 images). These strains were recorded (optically) with the aid of a microscope by keeping track of special markers (\equiv prescribed strain). Also, by using the information generated by the DIC program for every sub-deformation and the Large Deformation DIC method, the strains corresponding to images 1 and 2, images 1 and 3, etc., were computed, up to the deformation of image 13 relative to image 1.

Figure 3 shows the result as a comparison of the (optically) prescribed strain and the Large Deformation DIC computed (Lagrangian) strains. The maximum deviation occurs at a strain of 40%, amounting to only a 1% difference between the strain

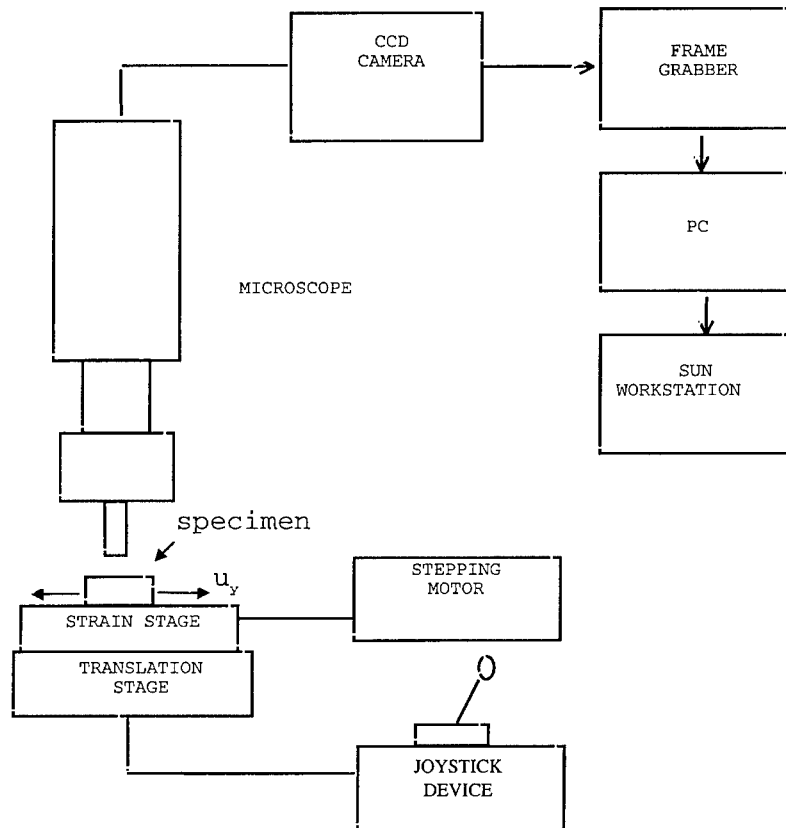


Fig. 4. Schematic of the experimental setup.

determined through the microscope and by the large deformation DIC method, a precision that is very acceptable for experimental mechanics investigations.

3. EXPERIMENTAL SETUP FOR DEFORMATION STUDIES

The equipment used for the experimental work on the particulate composite (solid propellant) has been described elsewhere in detail by Gonzalez (1997). It includes a straining stage driven by a stepping motor through a flexible cable. The straining stage is, in turn, mounted on a positioning stage, for which a joy-stick controller allows the positioning of the straining stage under the objective of a Nikon microscope (Measurescope MM-22), a CCD camera and a personal computer with a frame grabber unit. The images from the experiment are processed on a Sun workstation. A schematic of the experimental setup is shown in Fig. 4.

4. LOCALLY INHOMOGENEOUS DEFORMATIONS IN A GLOBALLY HOMOGENEOUS DEFORMATION FIELD

Before considering the problem of the strain distribution around the tip of a crack we examine the inhomogeneity of strains in a solid propellant sample subjected to uniform deformations at the specimen boundary (globally homogeneous deformation). To this end a sheet sample of propellant ($5 \times 2 \times 0.3$ cm) is strained uniformly in the direction parallel to the 2 cm dimension; after normalization by the 2 cm dimension, that boundary displacement is called the "applied strain". In Fig. 5 we show a 2.5×2.5 mm field from the center region of the specimen as resolved through a microscope and deduced with the aid of the LD-DIC algorithm. The false color scheme clearly identifies the inhomogeneous character of the strain field, and from this map it is quite clear that the variations in the strain values are not only very significant, but that the "material properties" vary to a like degree in these regions.

It is of interest to dwell briefly on the scale of the inhomogeneous regions. While the latter are not sharply defined, it is, nevertheless, clear that these domains are measured in terms of millimeters and not microns. One might argue that a variation in properties in a small region (a hole or a hard, well-bonded particle) embedded in a homogeneous field renders deviation from that field several times larger than the defect itself. The reference problem of a circular hole in an elastic infinite sheet suggests that a noticeable perturbation in its vicinity is on the order of three times its diameter. While it is not our purpose to analyze in detail here the precise origin of every inhomogeneity, be it one of larger strain than the average or of a smaller value, it appears clear that these inhomogeneities are produced either by clusters of particles or by the presence or absence of individual ones.

To quantify the inhomogeneity of the strain field further, consider a plot of the strain along the line in Fig. 5 as shown in Fig. 6. The magnitude of these strains vary by as much as a factor of three, although the average of the strain in Fig. 6 represents closely the applied global strain of 1.5%.

The distribution of these inhomogeneities defines a macroscopic size scale below which the assumption of homogeneous material properties is not justified. Stated alternately, in order to be able to assign homogeneous properties to such a composite it is necessary to deal with a size scale that is several times larger than the spacing between the regions of inhomogeneity. That region is, however, at least on the order of 5 mm or more.

We shall see that this size scale is important in the analysis of the failure/fracture process considered next, since in this context this size limitation emphasizes the dependence of the fracture process on the statistical nature of the medium.

5. THE STRAIN FIELD NEAR THE TIP OF A CRACK

Having examined the distribution of strains in a globally homogeneous deformation field we turn next to examining the deformations in the close vicinity of a crack tip. We describe first the experimental set-up and then proceed to the analysis of the results.

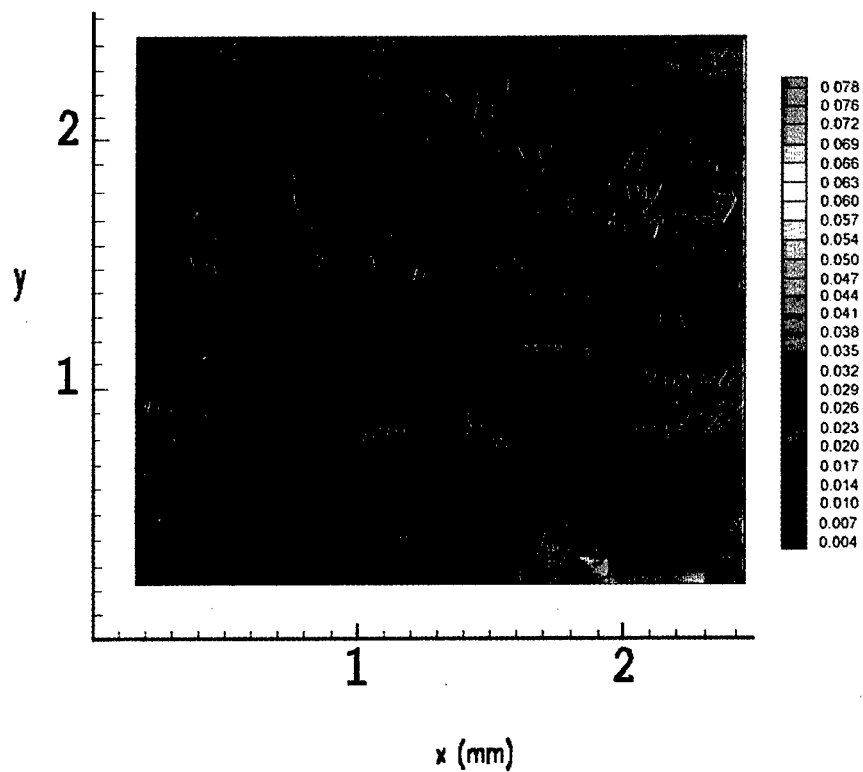


Fig. 5. Inhomogeneous strain distribution in an integral specimen "homogeneously" deformed to 1.5% global strain.¹

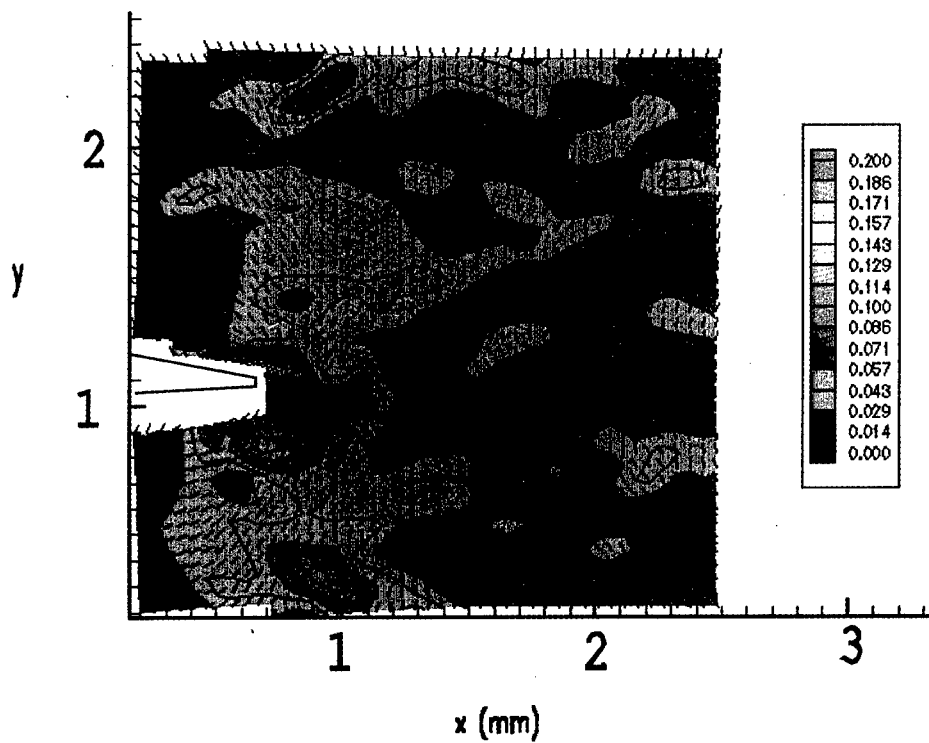


Fig. 8. Maximum principal strain distribution for 2% global strain.

¹ Note that the red domains surrounding the (green) high strain regions are the result of clustering of the red contour lines, not strain concentrations in themselves.

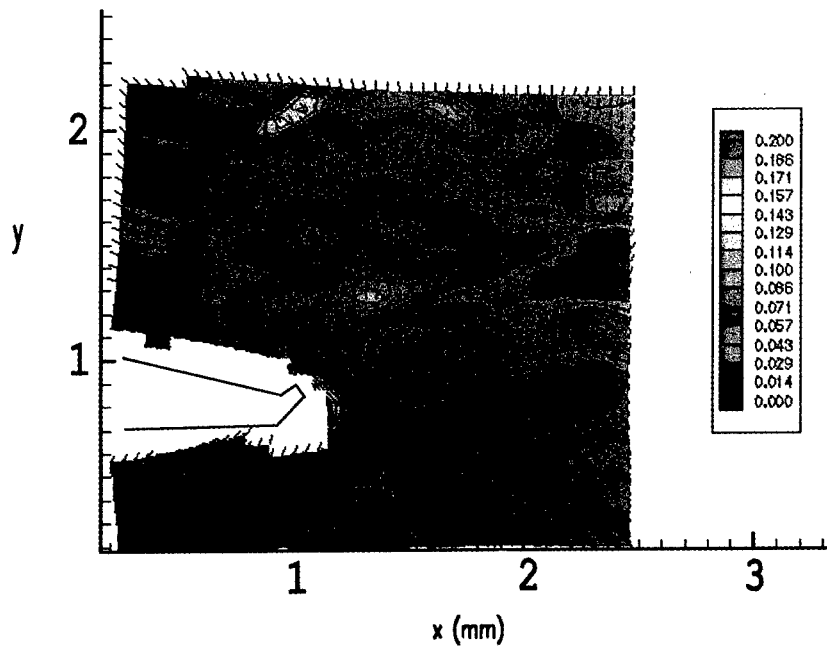
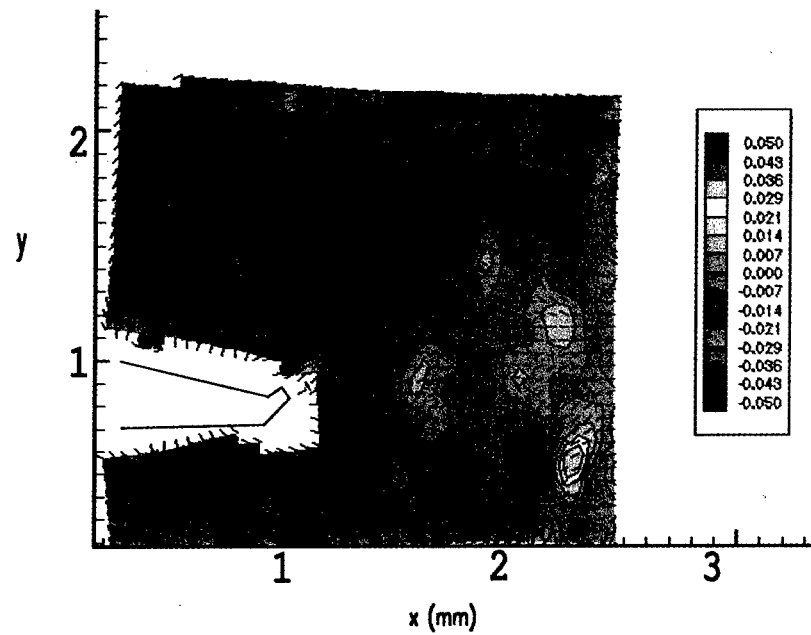


Fig. 9. Principal strain distribution for a far field strain of 4%. (a) Minimum principal strain (upper). (b) Maximum principal strain (lower).

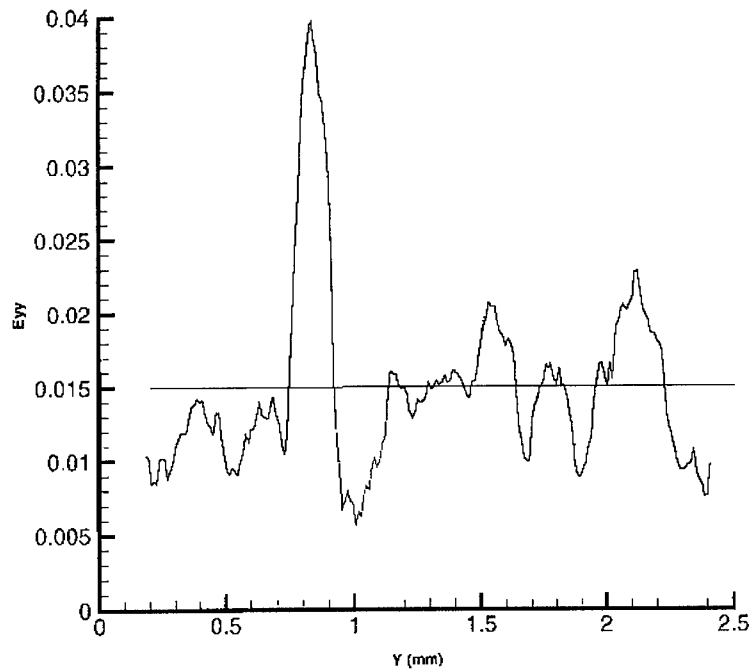


Fig. 6. E_{yy} distribution along the trace $x = 1.4$ mm in Fig. 5, parallel to the tension axis.

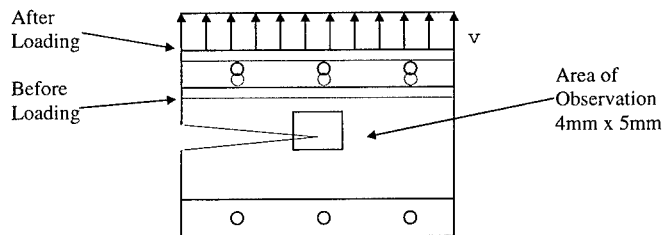


Fig. 7. Specimen geometry and straining of a specimen.

5.1. Experimental aspects

A cracked specimen of solid propellant TPH 1011 is deformed globally at a constant strain rate 0.001 $1/s$ in the direction perpendicular to the crack. The crack, cut initially with a razor blade, opens commensurately. Its opening process is monitored through a microscope at $25\times$ power. Five digital images of 640×480 pixels, representing 4×5 mm of the specimen surface were acquired every 10 s, corresponding to global (Lagrangian) strains of $E_{yy} = 0, 1, 2, 3$ and 4% .

Although each of the images, excepting the first, is associated with different deformations we select here only two loads or deformation levels for illustrative purposes. Application of the (multi-step) LD-DIC code renders deformation maps as shown in Figs 8 and 9.

Recall that because the multi-step method loses information at the boundary in each step the crack appears wide open and as having a very blunt tip. This appearance is the consequence of the multi-step method, so that Figs 8 and 9 do not represent the crack opening shape correctly; instead the shape has been sketched in as outlines.

5.2. Results

We demonstrate results for the global strain of 2 and 4%. While deformations at higher load levels can be obtained, their interpretation is more troublesome since it involves (more) motion of the crack tip. As an example we present (false color) plots of the maximum principal strain at 2% global deformation in Fig. 8 and both the maximum and minimum principal strains for 4% in Figs 9(a) and (b). The two strain levels are presented primarily to afford a comparison for two progressively larger strains. By comparing Figs 8 and 9(a) one can readily see how the inhomogeneities develop early and essentially grow in intensity with the global strain. In passing from 2–4% of global strain, a small amount of crack growth has taken place as is evident from comparing Figs 8 and 9(a).

As before, the amplitude of the (Lagrangian) strain is represented by colors and contours and the small lines represent the orientation of the corresponding principal axes. Note that although the maximum principal axes should be basically parallel to the applied global displacement(s), at least in the region ahead of the crack tip, there are numerous locations where marked differences occur from this orientation. These differences are associated with the material strain inhomogeneities discussed in Section 4. The same observation applies to the map of the minimum principal strain in Fig. 9(b) for which the orientations (small line segments) are generally orthogonal to those for the maximum principal strain. Also, compare the scale associated with the inhomogeneities and the distance of the high strain region relative to the crack tip. It is clear that the strain inhomogeneities cannot be separated from or submerged in the strain field of the crack tip: the crack tip strains are intimately connected with the scale of the material inhomogeneity. We note in particular that at this size of the viewing field the lobes that are part of the typical crack tip strain field for isotropic and homogeneous material are absent in the domain of observation or at most apparent in vestigial form; they are present only outside of the 2.5×2.5 mm observation area.

One feature of interest and identifiable in Figs 8 and 9 is the localization of high strain within a roughly circular area of 0.5 mm radius around the crack tip. Figure 8, which shows the maximum principal strains and directions for 2% far field strain, shows deformation localization around the crack tip in two locations. One, partially visible, is centered on the current crack tip (at $x = 0.7$ mm, $y = 1$ mm) and about 150 μ m in radius. The other concentration is centered on the position (0.7 mm, 0.8 mm), where it reaches a maximum principal strain of about 11%. However, that location does not become a part of the crack propagation process as is evident by its persistence in Fig. 9(a). Adjacent to these strain concentrations is a domain of about 5% local strain which includes the position (1.1 mm, 1 mm) where the orientation of the maximum principal strains is nearly aligned with the crack rather than being normal

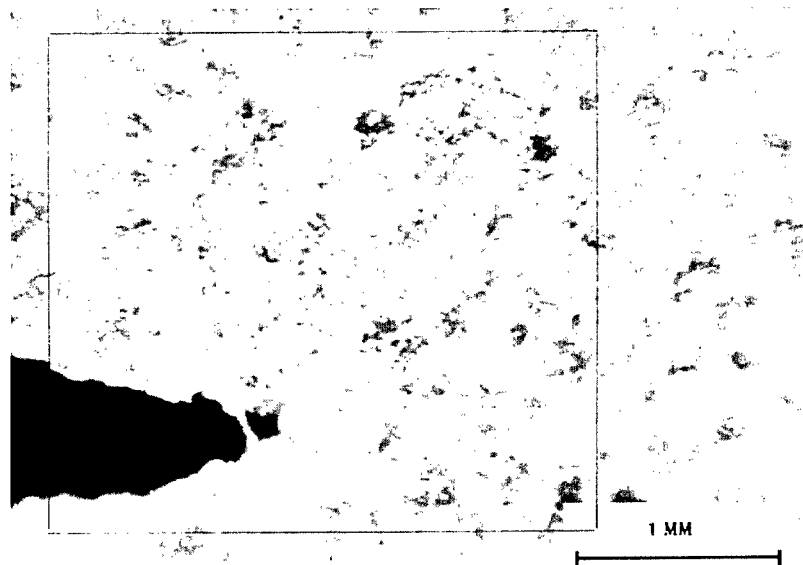


Fig. 10. Micrograph of the crack tip region at a global strain of 5%. The "void" at the crack tip was a region of "small" ($\sim 5\%$) surface strain in Fig. 8.

to it.² At this position a void develops under subsequently increased deformation. This void is visible in Fig. 10, which represents the image of the specimen for a 5% global deformation.

We have dwelt on these details to some extent in order to demonstrate that the observation of the surface of the failing material is not always indicative of how and where the crack is likely to propagate. Because one identifies strain inhomogeneities on the surface, it stands to reason that similar distributions exist through the thickness of the specimen. Thus, the observations offered here point to a truly three-dimensional process. However, it is quite clear that the domain in which the failure process is prominently operative is confined to a domain on the order of half, but not more than one millimeter. This observation agrees with the results of Liu (1997) who observed a similar confinement of the process zone to a very small region. So much is clear from these studies, only portions of which are reported here, namely that crack propagation occurs by opening up voids which are typically high strain regions, distributed statistically throughout the material, and through joining of these voids with the main crack.

6. CONCLUDING REMARKS

The method of digital image correlation has been extended to large deformations by dividing the strain range into intervals within each of which DIC converges. The

² Similar situations prevail in Fig. 7 at locations (1.6 mm, 0.9 mm), (2.1 mm, 1.1 mm) and (2.2 mm, 1.6 mm). In these regions the strains remain small, indicating that they are associated with rigid domains inside the specimen and under the surface.

sequential extension renders satisfactory results with deviations not exceeding 1% from the prescribed strain field. This method has allowed resolution of highly inhomogeneous deformations embedded in a globally homogeneous deformation field. It is then demonstrated that this method can be applied to the analysis of strains around the tip of a crack in a particulate composite (solid propellant rocket fuel).

The, perhaps, most striking result of that investigation is the surprisingly large, inhomogeneous variations in the local strain field in a globally homogeneously deformed solid propellant material. It is apparent that the inherent heterogeneity of the material plays a key role for distribution of strains around the crack tip and its propagation. A second important observation is the fact that most of the deformation related to the crack propagation process localizes in a region around the crack tip of only about 0.5 mm radius. Although there exist strain concentration domains outside of this small region on or close to the specimen surface, these deformations are insufficiently high to cause void formation of the strain concentrations so that they do not become sources of coalescence with the macroscopic crack. There is evidence, however, that the three-dimensional distribution of strain inhomogeneities through the thickness of the specimen plays a role that mimics their in-plane distribution. There is no reason to suppose otherwise for this kind of particulate solid. Certainly some of the features visible on the surface are the consequence of single particles and particle agglomerations buried just beneath the surface.

ACKNOWLEDGEMENTS

This work was performed under Grant AFOSR F49626-94-1-0253 from the Air Force Office of Scientific Research, with Dr Walter F. Jones and Major Brian Sanders as monitors. Also the frequent interaction with Dr C. T. Liu of the Air Force Phillips Laboratory (Edwards Air Force Base) is gratefully acknowledged.

REFERENCES

- Bruck, H. A., McNeil, S. R., Sutton, M. A. and Peters, W. H. (1989) Digital image correlation using Newton-Raphson method of partial differential correlation. *Experimental Mechanics* **29**, 261-267.
- Chu, T. C., Ranson, W. F., Sutton, M. A. and Peters, W. H. (1985) Applications of digital image correlation techniques to experimental mechanics. *Experimental Mechanics* **25**, 232-244.
- Farris, R. J. (1968) The character of the stress-strain function for highly filled elastomers. *Trans. Soc. Rheol.* **12**, 303-314.
- Farris, R. J. and Schapery, R. A. Development of a solid rocket propellant nonlinear viscoelastic constitutive theory. Technical Report AFRPL-TR-73-50, Air Force Rocket Propulsion Laboratory, Edwards, CA.
- Gonzalez, J. (1997) Full field study of strain distribution near the crack tip in fracture of solid propellant via large deformation digital image correlation and optical microscopy. Aeronautical Engineers's thesis, California Institute of Technology.
- Liu, C. T. (1991) Evaluation of damage fields near crack tips in a composite solid propellant. *Journal of Spacecrafts and Rockets* **28**, 64-72.

- Liu, C. T. (1997) The effect of micro damage on the time-dependent crack growth in a composite solid propellant. *Mech. Time-Dependent Materials* **1**, 123–136.
- Ravichandran, G. and Liu, C. T. (1995) Modeling constitutive behavior of particulate composites undergoing damage. *International Journal of Solids and Structures* **32**, 979–990.
- Sutton, M. A., Walters, W. J., Peters, W. H., Ranson, W. F. and McNeil, S. R. (1983) Application of an optimized digital image correlation method to planar deformation analysis. *Image Vision Computing* **4**, 143–150.
- Sutton, M. A., Cheng, M., Peters, W. H., Chao, Y. J. and McNeill, S. R. (1986) Application of an optimized digital correlation method to planar deformation analysis. *Experimental Mechanics* **4**, 143–150.
- Vendroux, G. and Knauss, W. G. (1994) Submicron deformation field measurements: II. Improved digital image correlation. GALCIT SM Report 94-5. *Experimental Mechanics*, to appear.
- Vratsanos, L. and Farris, R. (1993) A predictive model for the mechanical behavior of particulate composites. Part II: Comparison of the model predictions to literature data. *Polymer Engineering and Science* **33**, 1466–1474.
- Zhong, X. and Knauss, W. G. (1997) Analysis of interfacial failure in particulate filled elastomers. *ASME J. Eng. Materials and Tech.*, submitted.



DYNAMIC CRACK INITIATION IN DUCTILE STEELS

P. R. GUDURU, R. P. SINGH, G. RAVICHANDRAN and A. J. ROSAKIS†

Graduate Aeronautical Laboratories, California Institute of Technology, Pasadena CA 91125, U.S.A.

(Received 20 December 1997; in revised form 13 February 1998)

ABSTRACT

The goal of the work presented here is to study dynamic crack initiation in ductile steels (Ni–Cr steel and 304 stainless steel) at different loading rates and to establish appropriate dynamic failure criteria. A variety of infrared and visible optical methods and high-speed photography are used in this study. Precracked steel specimens are subjected to dynamic three-point bend loading by impacting them in a drop weight tower. During the dynamic deformation and fracture initiation process the time history of the transient temperature in the vicinity of the crack tip is recorded experimentally using a high-speed infrared detector. The dynamic temperature trace in conjunction with the HRR solution is used to determine the time history of the dynamic J -integral $J^d(t)$, and to establish the dynamic fracture initiation toughness, J_I^d . The measurements made using high-speed thermography are validated through comparison with determination of $J^d(t)$ by dynamic optical measurements of the crack tip opening displacement (CTOD). Finally, the micromechanisms of fracture initiation are investigated by studying the fracture surface using scanning electron microscopy. © 1998 Elsevier Science Ltd. All rights reserved.

Keywords: A. fracture toughness, dynamic fracture, B. elastic–plastic material, C. electron microscopy

1. INTRODUCTION

To aid in the design and vulnerability analysis of impact loaded structures and energy systems (e.g., pressure vessels, pipelines and reactors), it is necessary to quantify the mechanical behavior and failure modes of materials used in such systems under carefully controlled conditions. Because of design constraints and safety issues, these energy systems are typically fabricated with corrosion resistant and highly ductile metallic alloys such as stainless and Ni–Cr steels. Yet, relatively little is known regarding dynamic crack initiation and growth in such ductile metals. A major stumbling block in this area is the measurement of relevant fracture parameters, such as the J -integral, under a combination of large scale yielding conditions and dynamic loading. Considerable effort has been made towards the analytical and computational characterization of fracture parameters in highly ductile metals (Hutchinson, 1968; Rice and Rosengren, 1968; Needleman and Tvergaard, 1987; Nakamura and Parks, 1990; Narasimhan and Rosakis, 1990; Duffy and Chi, 1992; Cho *et al.*, 1993). Recently, several researchers have presented detailed analyses of ductile fracture using higher order expansions of the deformation fields within the plastic zone (Li and

† To whom correspondence should be addressed. Tel.: 626 395 3690. Fax: 626 449 2677. E-mail: rosakis@atlantis.caltech.edu

Wang, 1986; Sharma and Aravas, 1991; O'Dowd and Shih, 1991, 1992; Yang *et al.*, 1993).

To date relatively little experimental work has been done on determining fracture parameters, such as $J^d(t)$, for ductile fracture under dynamic loading conditions. Limited cases exist where careful choice of specimen geometry and loading histories allow for the measurement of J^d based on the use of dynamic boundary value measurements interpreted on the basis of quasi-static formulae for J (Costin *et al.*, 1977). Also, Douglas and Suh (1988) and Sharpe *et al.* (1988) have developed an alternate method based on comparing a dynamic finite element analysis with experimental observations to provide the critical value of CTOD (crack tip opening displacement) and thus the critical value of J , corresponding to crack initiation. The only direct measurements of the dynamic value of the J -integral, $J^d(t)$, have been made using the optical technique of caustics in conjunction with high-speed photography (Rosakis *et al.*, 1988; Zehnder *et al.*, 1990). However, even this approach employs a procedure using calibration of J vs the caustic diameter, D , under quasi-static loading conditions and then extends the same to dynamic loading conditions. Hence, this technique is limited to rate-insensitive materials and requires calibration for all combinations of specimen material and specimen geometry.

The current study introduces a technique for measurement of temperature variation in the vicinity of the dynamically loaded crack tip using a high speed infrared detector to determine the time history of the dynamic value of the J -integral, $J^d(t)$. The dynamic temperature trace is also employed to establish the dynamic fracture initiation toughness, $J^d(t_c) = J_i^d$, where t_c is the time of fracture initiation. The measurements made using high-speed thermography are validated through comparison with determination of $J^d(t)$ by dynamic optical measurements of the crack tip opening displacement (CTOD). Both these techniques provide a direct measurement of the time history of the dynamic J -integral and are not restricted by specimen geometry, rate of loading, or rate-sensitivity of the material.

2. EXPERIMENTAL SETUP

In this investigation high-speed infrared measurements of temperature and optical measurements of crack tip opening displacements were employed to study dynamic crack initiation in precracked ductile steel specimens. In the former, the temperature increase ahead of the crack tip during dynamic deformation is measured and is related to the dynamic J -integral. In the latter, the dynamic J -integral is estimated by relating it to the measured crack opening displacement history.

2.1. Specimen configuration, loading arrangement and material properties

The experiments employed edge cracked specimens in a three point bend configuration. The specimens were fabricated out of 2.3Ni-1.3Cr steel (will be referred to as Ni-Cr steel here onwards) and 304 stainless steel, whose compositions are listed

Table 1. *Composition for Ni-Cr steel and 304 stainless steel*

	C	Mn	Cu	Si	Ni	Cr	Mo	Co
Ni-Cr	0.17	0.30	0.13	0.22	2.35	1.32	0.25	—
304 Stainless	0.024	1.77	0.28	0.33	8.16	18.33	0.35	0.1

Table 2. *Material properties for Ni-Cr steel and 304 stainless steel*

Properties	Ni-Cr	304 Stainless
Young's modulus, E (GPa)	205	193
Density, ρ (kg/m ³)	7910	7900
Specific heat, c_p (J/Kg-K)	460	500
Yield Stress, σ_0 (MPa) ($\dot{\epsilon} = 10^{-3} \text{ s}^{-1}$)	750	510
Hardening exponent, n ($\dot{\epsilon} = 10^{-3} \text{ s}^{-1}$)	8	7

in Table 1. The relevant material properties for these two steels are listed in Table 2. Both the steels are relatively low to medium strength steels and fail in a ductile fashion under the given test conditions. Ni-Cr steel is strain rate sensitive as demonstrated by the uniaxial compression stress-strain behavior shown in Fig. 1. There was a significant elevation in the yield stress, σ_0 , as the strain rate was increased from 10^{-3} –

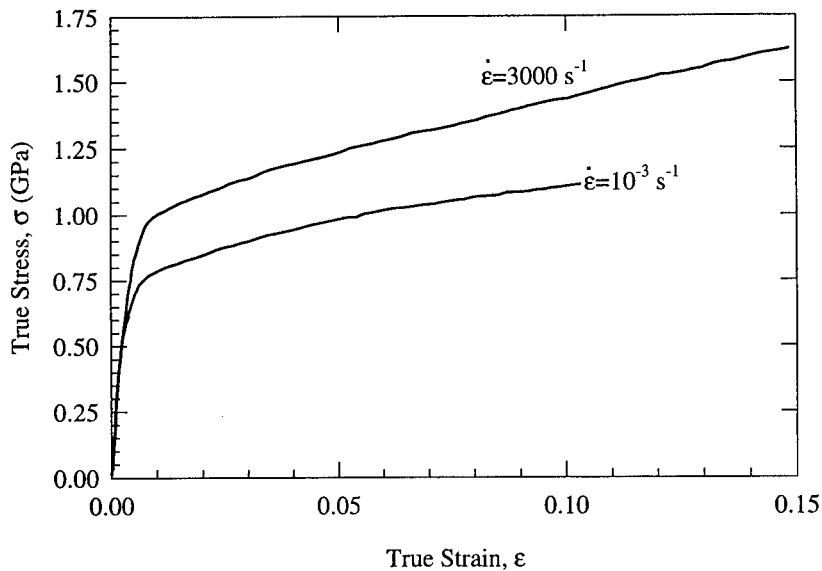


Fig. 1. Stress-strain behavior for Ni-Cr steel under uniaxial compression.

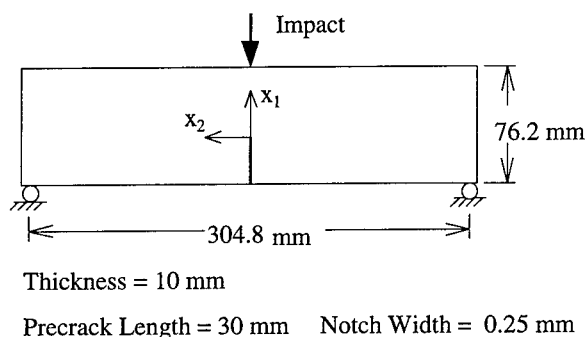


Fig. 2. Schematic of three-point bend impact loading of a precracked steel specimen.

10^3 s^{-1} . However, no appreciable change in the hardening exponent, n , was observed. On the other hand, 304 stainless steel is relatively rate insensitive and does not demonstrate any appreciable change in yield properties for the same change in strain rate. Dimensions for the edge-cracked specimen are shown in Fig. 2. An initial crack length of 30 mm was machined using a wire electric discharge machining (EDM) that resulted in a notch 0.25 mm wide.

The test specimens were dynamically loaded in a three-point bend configuration by subjecting them to impact in a Dynatup 8100A drop weight tower. A schematic of the loading configuration is shown in Fig. 2. A tup mass of 200 kg and an impact velocity of 5 m/s were employed for all the experiments conducted. This dynamic impact of the precracked steel specimens results in deformation followed by fracture initiation. The dynamic deformation and fracture initiation process were monitored using high-speed infrared measurement of temperature and optical measurement of crack tip opening displacements. Details of the two experimental techniques are presented in the following sections.

2.2. Infrared temperature measurements

In this first series of experiments high-speed infrared diagnostics were introduced to study dynamic crack initiation for the first time in precracked ductile steel specimens impact loaded in a three point bend configuration. As the specimen was loaded, a high-speed HgCdTe infrared detector was employed to record the evolution of the temperature trace at a pre-determined location from the crack tip, as shown in Fig. 3. A Newtonian optical arrangement, illustrated in Fig. 3(a), employs a collecting mirror M_1 in conjunction with a plane mirror M_2 to map the area of interest on the specimen on to the infrared detector element. This results in a focused system such that there is a one-to-one mapping between the detector element and the area of interest on the specimen. Moreover, varying the object and image distances allows the magnification to be changed so that any desired area from the specimen can be mapped onto the detector element, which has a fixed size of $100 \times 100 \mu\text{m}$ square. The location of the area of interest on the specimen, which is essentially the area of temperature measurement, is situated well within the plastic zone that engulfs the

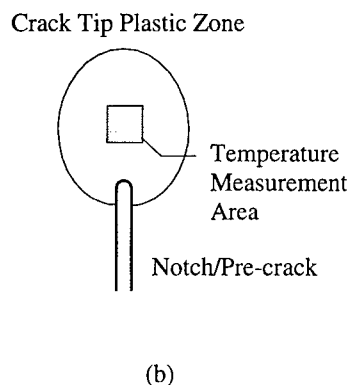
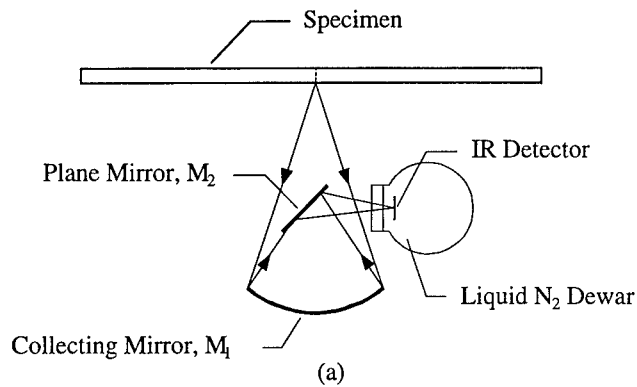


Fig. 3. Measurement of temperature variation in the vicinity of the dynamically loaded crack tip using an infrared detector. (a) Top view of specimen showing the infrared optical arrangement and (b) location of temperature measurement area on the specimen.

dynamically loaded crack tip, as shown in Fig. 3(b). If this temperature measurement is made at an appropriate location within the crack tip plastic zone surrounding the dynamically loaded crack tip, then, as it will be shown later, the history of the temperature trace can be directly related to the evolution of the dynamic value of the J -integral, $J^d(t)$.

2.3. Optical measurements of the crack tip opening displacement (CTOD)

In order to corroborate and evaluate the accuracy and applicability of the infrared temperature measurement technique to determine $J^d(t)$, optical measurements of the crack tip opening displacement (CTOD) were performed to measure the time history of the dynamic value of the J -integral, $J^d(t)$. The optical arrangement for the CTOD measurement, as illustrated in Fig. 4, employs a cavity dumped pulsed laser as the illumination source and a high-speed camera as the imaging system. A collimated laser beam is incident on the steel specimen, passes through the crack opening and is

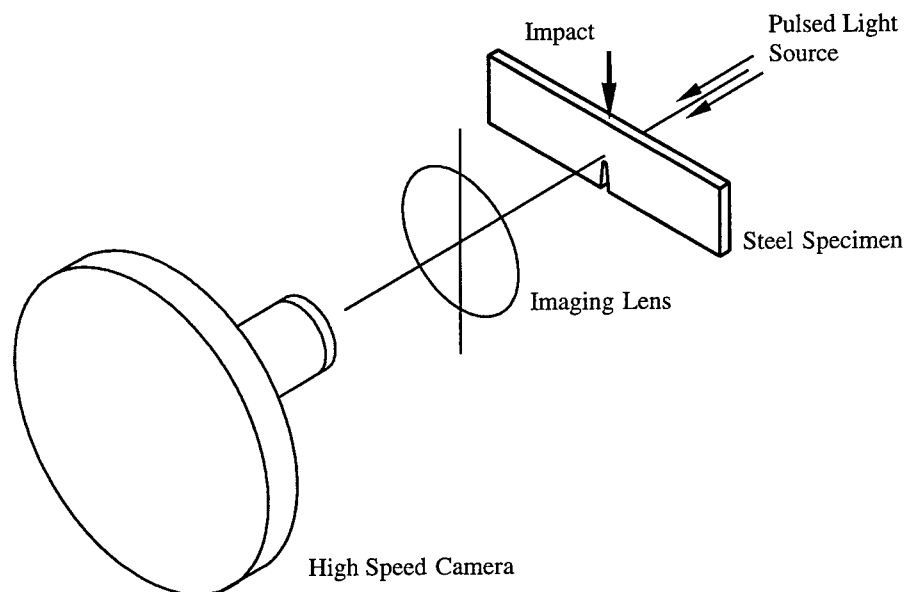


Fig. 4. Optical measurement of crack tip opening displacement (CTOD) using high speed photography.

imaged on to the film track of a rotating mirror type high-speed camera (Cordin Co., model 330A) with a maximum framing rate of 2 million/s. This results in the crack opening profile being photographed by the high-speed camera as the specimen undergoes dynamic deformation. The crack tip opening displacement is later measured directly from the recorded crack opening profiles. The camera recorded 80 frames of the dynamic event and was operated at an interframe time of $8.33 \mu\text{s}$ (120,000 frame/s). Individual frames were obtained by pulsing the laser light source (Spectra-Physics Argon-Krypton-ion laser, model 166-09; operating wavelength $\lambda = 514.5 \text{ nm}$ light) in a pulsed mode. The exposure time used in all experiments (i.e., the laser pulse duration) was 8 ns and the image was recorded on 35-mm black and white film (Kodak TMAX-400).

3. ANALYSIS PROCEDURE

The temperature measurements made in the vicinity of the dynamically loaded crack tip and the optical measurements of the crack tip opening displacement were analyzed to determine the time history of the dynamic value of the J -integral, $J^d(t)$. The analysis procedure involves the application of an appropriate asymptotic field that describes the crack tip stresses in an elastic-plastic material. The details of the analysis procedure are discussed in the following sections.

3.1. Asymptotic elastic-plastic crack tip field

Hutchinson (1968) and Rice and Rosengren (1968), collectively referred to as HRR, considered the case of a monotonically loaded stationary crack in a material described by a J_2 -deformation theory of plasticity and a power hardening relationship between the plastic strain ε_{ij}^p and stress σ_{ij} , and showed that the strain components in the crack tip region scale with the value of the J -integral. Within a small strain assumption, asymptotic solution of the elastic-plastic field equations in the crack tip region has the form

$$\varepsilon_{ij} \rightarrow \varepsilon_0 \left[\frac{J}{\sigma_0 \varepsilon_0 I_n r} \right]^{n/(n+1)} E_{ij}(n, \sigma) \quad (1)$$

$$\sigma_{ij} \rightarrow \sigma_0 \left[\frac{J}{\sigma_0 \varepsilon_0 I_n r} \right]^{1/(n+1)} \Sigma_{ij}(n, \theta) \quad (2)$$

as $r \rightarrow 0$. σ_0 is the tensile yield stress, ε_0 is the equivalent tensile yield strain, n is the hardening exponent, and the angular factors Σ_{ij} and E_{ij} depend on the mode of loading and the hardening exponent. The dimensionless quantity I_n is defined by Hutchinson (1968). The amplitude factor J is the value of Rice's J -integral (Rice, 1968). It has been suggested that, provided a one parameter representation of the crack tip fields remains valid, a condition for onset of crack growth is the attainment of a critical value of J .

3.2. Temperature rise associated with the HRR singular field

Consider an elastic-plastic isotropic homogeneous material with constant thermal conductivity. The heat conduction equation can be written as

$$k \nabla^2 \Theta - \alpha(3\lambda + 2\mu) \Theta_0 \dot{\varepsilon}_{kk}^e + \beta \sigma_{ij} \dot{\varepsilon}_{ij}^p = \rho c \dot{\Theta} \quad (3)$$

where, k is the thermal conductivity, Θ is the absolute temperature, α is the coefficient of thermal expansion, λ and μ are Lamé elastic constants, Θ_0 is the initial temperature, ε_{ij} and σ_{ij} are the Cartesian components of the strain and stress tensors, ρ is the mass density, and c is the specific heat. The quantity β is the fraction of plastic work rate density, $\dot{W}^p = \sigma_{ij} \dot{\varepsilon}_{ij}^p$, dissipated as heat. For the case of dynamic fracture in an elastic-plastic material we can neglect the thermo-elastic term, since $\dot{\varepsilon}_{kk}^e \ll \dot{\varepsilon}_{ij}^p$. Moreover, we can also assume the process to be sufficiently dynamic so that it can be approximated as being adiabatic. Hence, the heat conduction eqn (3) becomes

$$\frac{\beta}{\rho c} \sigma_{ij} \dot{\varepsilon}_{ij}^p = \dot{\Theta} \quad (4)$$

Substituting eqns (1) and (2) into eqn (4) we have

$$\dot{J}^d(t) = \frac{\rho c I_n}{\beta} \left(\frac{n+1}{n} \right) \frac{r}{\Sigma_{ij}(\theta, n) E_{ij}(\theta, n)} \dot{\Theta}(r, \theta, t) \quad (5)$$

On integrating eqn (5) with respect to time, t , we obtain

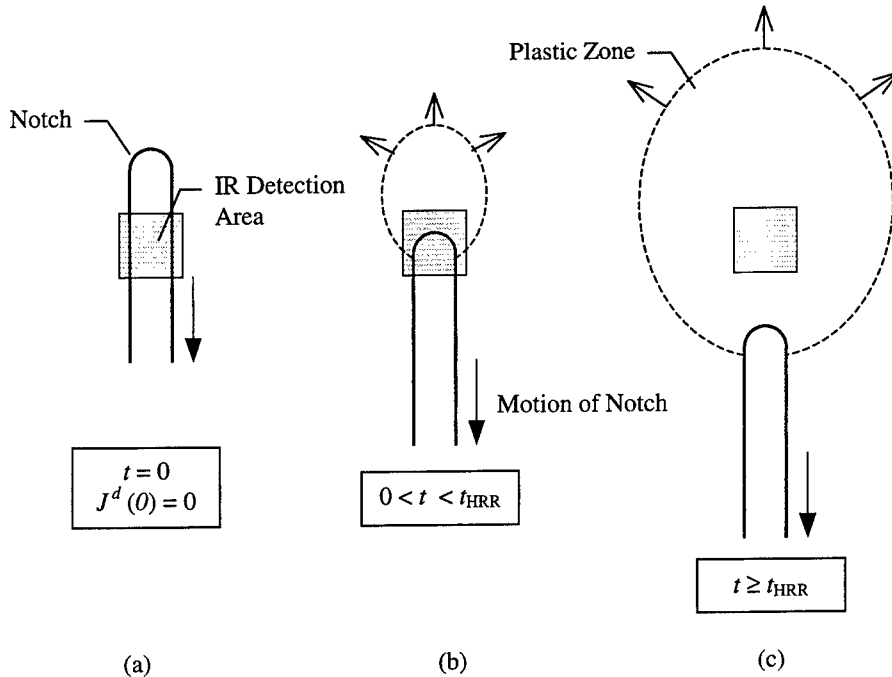


Fig. 5. Motion of the temperature sensing area relative to the crack tip as a function of time.

$$J^d(t) = \frac{\rho c I_n}{\beta} \left(\frac{n+1}{n} \right) \frac{r}{\Sigma_{ij}(\theta, n) E_{ij}(\theta, n)} [\Theta(r, \theta, t) - \Theta_0(r, \theta, t_0)] + J_0^d(t_0) \quad (6)$$

where $J_0^d(t_0)$ is the value of the J -integral at time $t = t_0$ and represents the integration constant. Equation (6) relates the time history of the dynamic value of the J -integral, $J^d(t)$, to the dynamic temperature rise in the vicinity of the crack tip.

It should be noted however that during the impact loading of the specimen the crack tip moves downward along with the motion of the impacting tup. This causes a relative motion between the crack tip and the area where the infrared temperature detector is focussed. This process is illustrated in Fig. 6. At the beginning of the

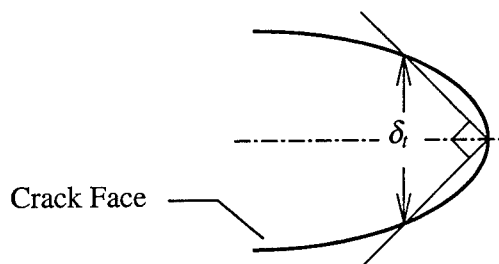


Fig. 6. Crack tip opening displacement defined on the basis of 90° intercepts (Shih, 1981).

experiment (pre-impact) the temperature detector is focussed at an area below the crack tip. During the post-impact loading and deformation process the crack tip moves downwards while the location of infrared temperature detection remains stationary, as shown in Fig. 5. Thus, it is only at some finite time, $t = t_{\text{HRR}}$, that the infrared detection area is well within the crack tip plastic zone and temperature is sensed in a zone characterized by the HRR singular field. This implies that eqn (6) is strictly valid only for, $t \geq t_{\text{HRR}}$, and hence is expressed as,

$$J^d(t) = \frac{\rho c I_n}{\beta} \left(\frac{n+1}{n} \right) \frac{r(t)}{\Sigma_{ij}(\theta, n) E_{ij}(\theta, n)} [\Theta(r, \theta, t) - \Theta_0(r, \theta, t_0)] + J^d(t_{\text{HRR}}), \quad t \geq t_{\text{HRR}} \quad (7)$$

The value of the dynamic J -integral at time $t = t_{\text{HRR}}$ is estimated, as a first approximation, by assuming a linear variation of $J^d(t)$ from $t = 0$ to $t = t_{\text{HRR}}$. It should also be noted that now the radial distance between the temperature detection area and the crack tip is given as a function of time, $r = r(t)$, which is experimentally determined using high speed photography.

3.3. Crack tip opening displacement (CTOD) associated with the HRR singular field

Consider crack face opening as shown in Fig. 6. Then the CTOD is defined using the intersection of a 90° vertex with the crack flanks. This definition of CTOD was invoked by Shih (1981) to relate the J -integral to the value of the crack tip opening displacement using the HRR singularity field as

$$J = \frac{\sigma_0}{d_n(\varepsilon_0, n)} \delta \quad (8)$$

where, δ is the CTOD, J is the value of the J -integral, σ_0 is the yield stress and d_n is a material dependent dimensionless constant as defined by Shih (1981). For the case of a dynamically loaded crack eqn (8) becomes

$$J^d(t) = \frac{\sigma_0}{d_n(\varepsilon_0, n)} \delta^d(t) \quad (9)$$

where, $J^d(t)$ is the dynamic value of the J -integral and $\delta^d(t)$ is the dynamic value of the CTOD.

4. EXPERIMENTAL OBSERVATIONS AND RESULTS

4.1. Measurement of $J^d(t)$

Typical variations of temperature measured in the vicinity of the crack tip for a dynamically loaded Ni-Cr steel specimen are shown in Fig. 7. Traces from two nominally similar experiments are plotted. There are a few features in the temperature traces that merit elucidation. The initial oscillations in the signal are due to the fact that the temperature detection area is moving past the crack tip (as in Fig. 5(b)) while

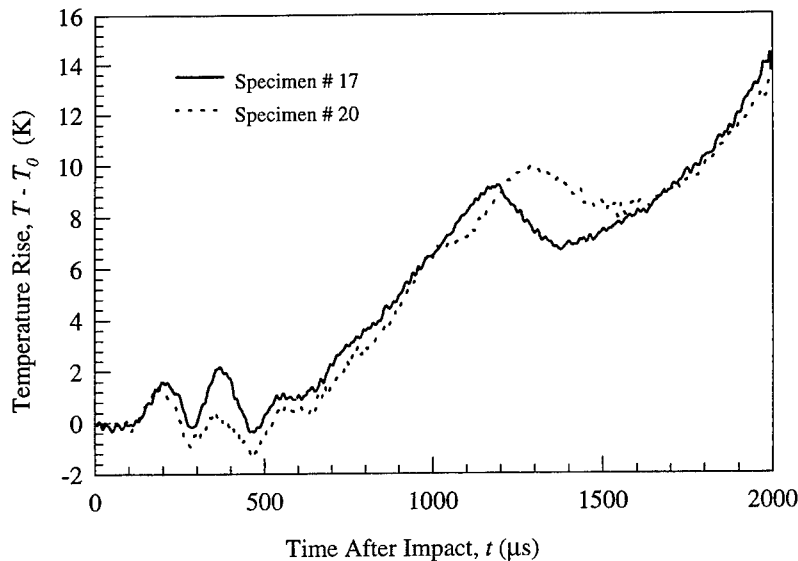


Fig. 7. Time history of the temperature variation in the vicinity of the dynamically loaded crack tip for a precracked Ni-Cr steel specimen subjected to three-point bend impact loading.

the specimen is undergoing initial structural oscillations resulting from impact. At about $550 \mu\text{s}$ after impact the temperature detection area is completely engulfed by the crack tip plastic zone and the transient temperature signal starts to increase steadily in a monotonic fashion. This increase remains steady until about $1200\text{--}1300 \mu\text{s}$ when a dip occurs in the temperature trace. It will be shown later, using strain gage instrumentation, that this dip corresponds to dynamic fracture initiation. Fracture initiation causes the specimen compliance to increase and thus results in a momentary decrease in the rate at which $J^d(t)$ increases, and possibly a drop in the value of $J^d(t)$. It should be noted that if the crack tip were stationary with respect to the temperature sensing area a decrease in the value of $J^d(t)$ would lead to elastic unloading and hence to thermoelastic cooling only. This would not cause any significant change in the temperature signal. However, in the present case the temperature detection area is continually moving away from the crack tip due to specimen motion. Therefore, since the temperature distribution exhibits r^{-1} dependence [eqn (6)], even a decrease in the rate at which $J^d(t)$ increases could lead to a drop in the temperature signal.

The transient temperature traces discussed above were analyzed using eqn (7) to determine the evolution of the instantaneous value of the J -integral, $J^d(t)$. The analysis procedure accounted for the relative motion of the temperature detection area with respect to the crack tip, $r = r(t)$, using high-speed photographic measurements of specimen (and crack tip) motion during the impact loading. Figure 8 shows a typical variation of $J^d(t)$ determined from infrared measurement of temperature in the vicinity of a dynamically loaded crack tip. This was the first time that a non-contact temperature measurement has been used to determine the time history of the dynamic J -integral, $J^d(t)$. Note that the values of $J^d(t)$ as shown in Fig. 8 will be valid only until

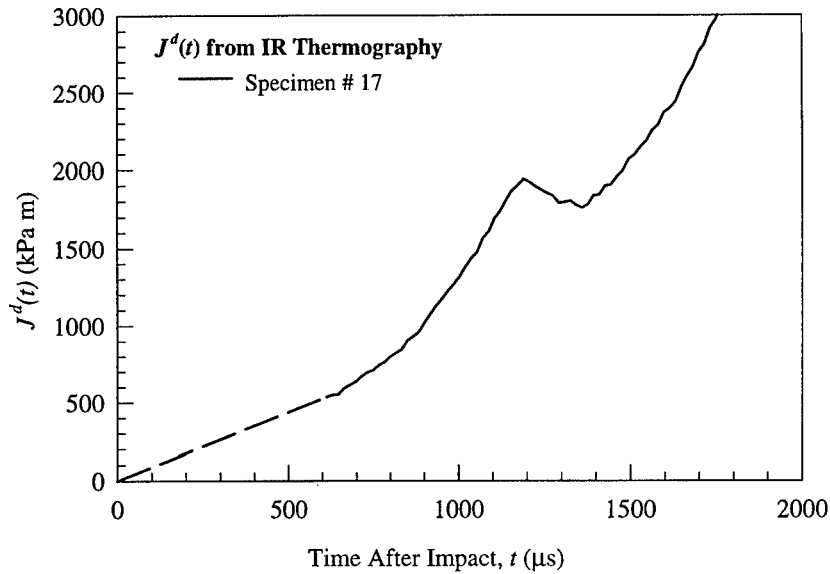


Fig. 8. Variation of the dynamic value of the J -integral as a function of time for Ni-Cr steel, as obtained from temperature measurement.

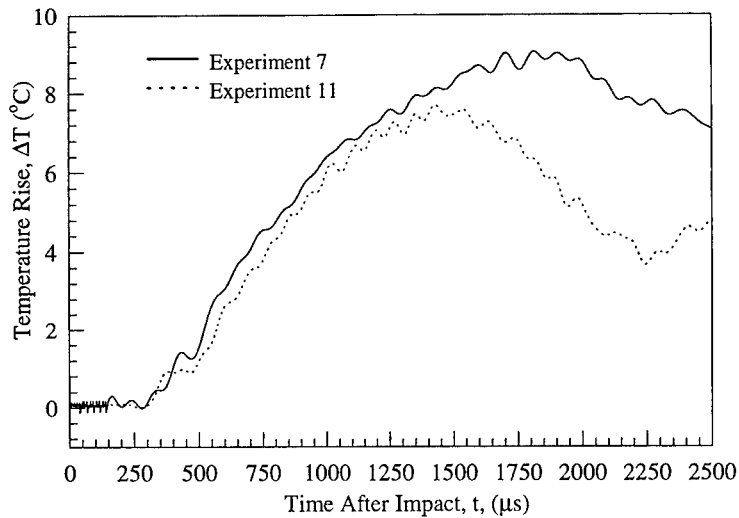


Fig. 9. Time history of the dynamic temperature variation in the vicinity of the dynamically loaded crack tip for a precracked 304 stainless steel specimen subjected to three-point bend impact loading.

the time of crack initiation, i.e. until the HRR asymptotic fields remain a good approximation of the crack tip fields.

Infrared thermography was also employed to study ductile failure of edge-cracked 304 stainless steel specimens subjected to three-point bend impact loading. Figure 9

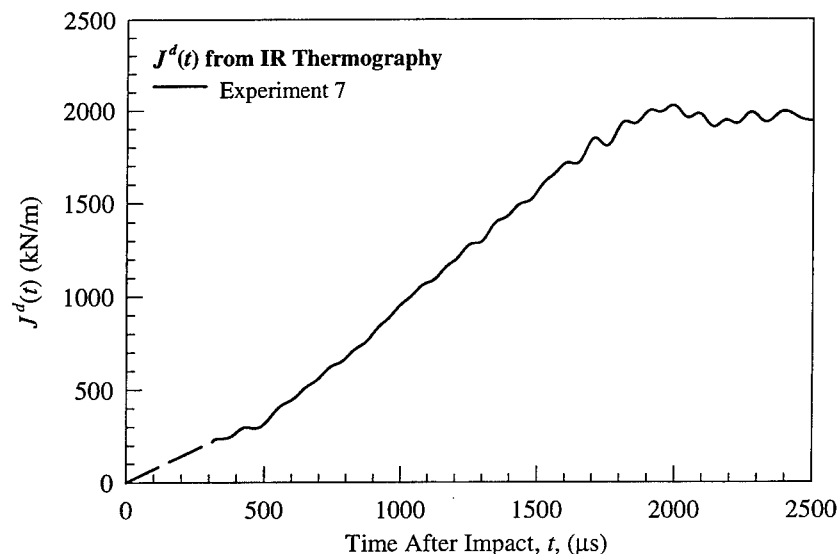


Fig. 10. Variation of the dynamic value of the J -integral as a function of time for 304 stainless steel, as obtained from temperature measurement.

shows typical variations of temperature measured in the vicinity of the dynamically loaded crack tip for a 304 stainless steel specimen. Traces from two nominally similar experiments are plotted. As shown in Fig. 9, the temperature traces begin to rise only after about 300 μs after impact, which coincides with the arrival of the plastic zone at the location where the temperature was being measured. A dip in the temperature traces occurred around 1500–1700 μs , which is associated with crack tip initiation. A typical time history of the dynamic J -integral, $J^d(t)$, as determined from the infrared temperature measurements is plotted in Fig. 10.

As discussed earlier, optical measurements of the crack tip opening displacements were made using a high-speed imaging system in order to validate the infrared thermography measurements of $J^d(t)$. Figure 11 shows a selected set of crack opening profiles obtained for three-point bend impact loading of an edge-cracked Ni–Cr steel specimen. The dynamic value of the CTOD, $\delta^d(t)$, was measured directly from these photographs using the 90° vertex intercept definition. Thereafter, time history of the dynamic value of the J -integral, $J^d(t)$, was determined from the CTOD variation in accordance with eqn (9). Figure 12 plots the time history of the dynamic J -integral, $J^d(t)$, as determined from measurements of the dynamic CTOD, $\delta^d(t)$. The figure also shows the variation of $J^d(t)$ as determined from infrared measurements of temperature. The excellent degree of correspondence between the two establishes the validity and accuracy of the infrared thermography technique to determine $J^d(t)$.

Optical measurements of the crack tip opening displacement were employed to determine the dynamic J -integral, $J^d(t)$, also for edge-cracked 304 stainless steel specimens subjected to three-point bend impact loading. Figure 13 shows the variation of $J^d(t)$ as determined from measurements of the dynamic CTOD, $\delta^d(t)$. Results

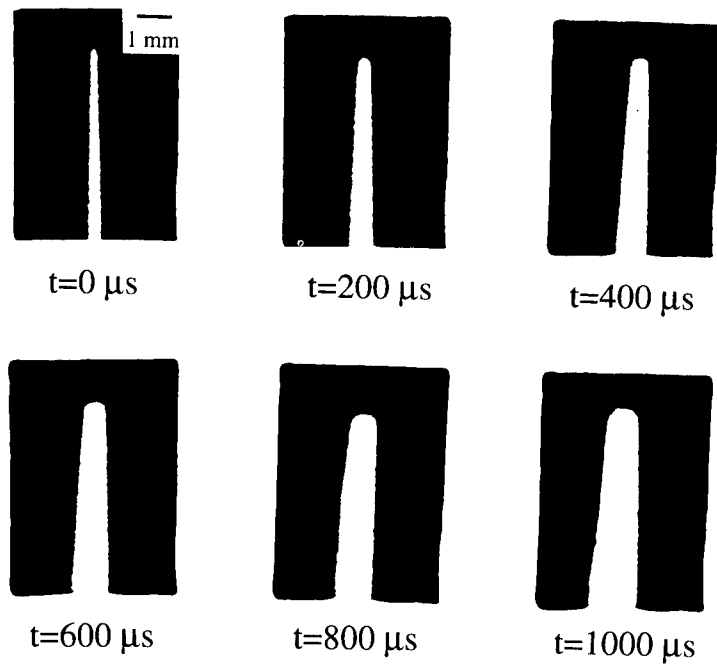


Fig. 11. Typical set of crack opening profiles obtained for a precracked Ni-Cr steel specimen subjected to three-point bend impact loading.

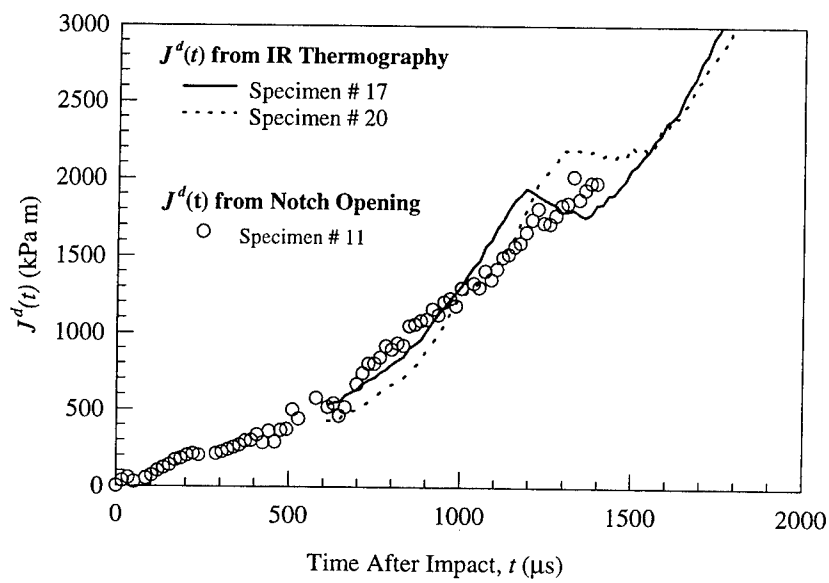


Fig. 12. Time history of the dynamic value of the J -integral as obtained from optical measurement of crack tip opening displacement and infrared measurement of temperature (Ni-Cr steel).

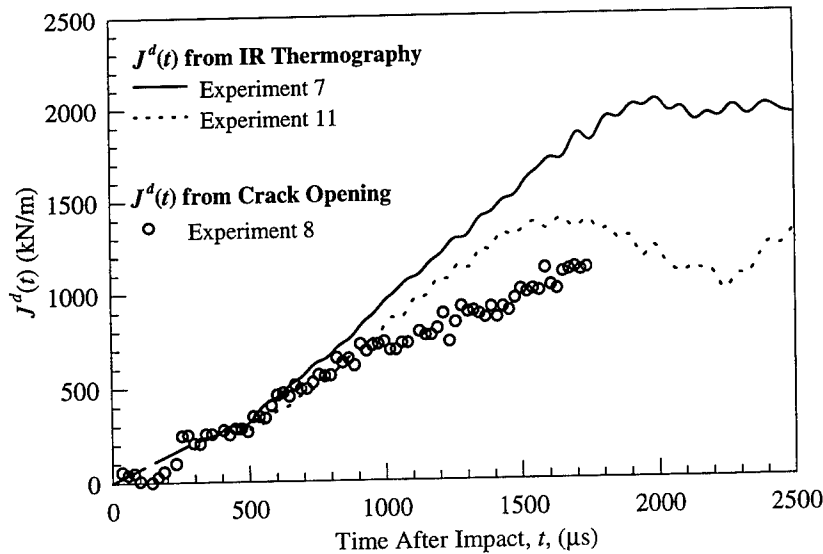


Fig. 13. Time history of the dynamic value of the J -integral as obtained from infrared measurement of temperature and optical measurement of crack tip opening displacement (304 stainless steel).

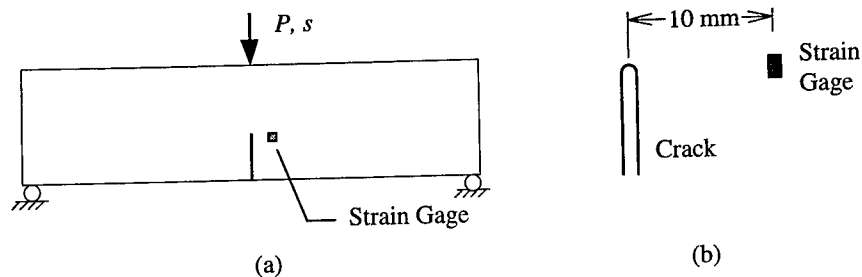


Fig. 14. Determination of fracture initiation during quasi-static loading of a precracked steel specimen. (a) Three-point bending loading configuration. (b) Location of strain gage with respect to crack tip.

obtained from infrared measurements of temperature are also plotted. There is excellent agreement between the two measurements for low values of $J^d(t)$. However, unlike the Ni-Cr case this correspondence breaks down for higher values of $J^d(t)$. This is due to the much higher deformations observed for the 304 stainless steel specimens. Equation (9), which relates the dynamic J -integral to the dynamic CTOD, is strictly valid only if the HRR singular field is an accurate representation of the stress and strain fields very close to the crack tip. However, for very large crack tip deformations this would not be the case and CTOD could not be expected to give an accurate estimation of the dynamic J -integral value. Nevertheless, away from the immediate vicinity of the crack tip the HRR singular field is still expected to hold and

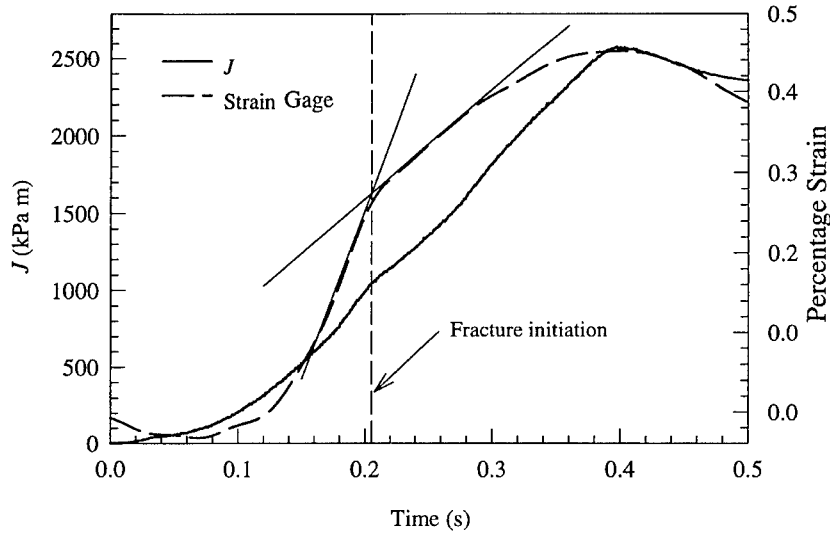


Fig. 15. Variation of the J -integral and strain gage signal during quasi-static three point bend loading of an edge cracked Ni-Cr specimen.

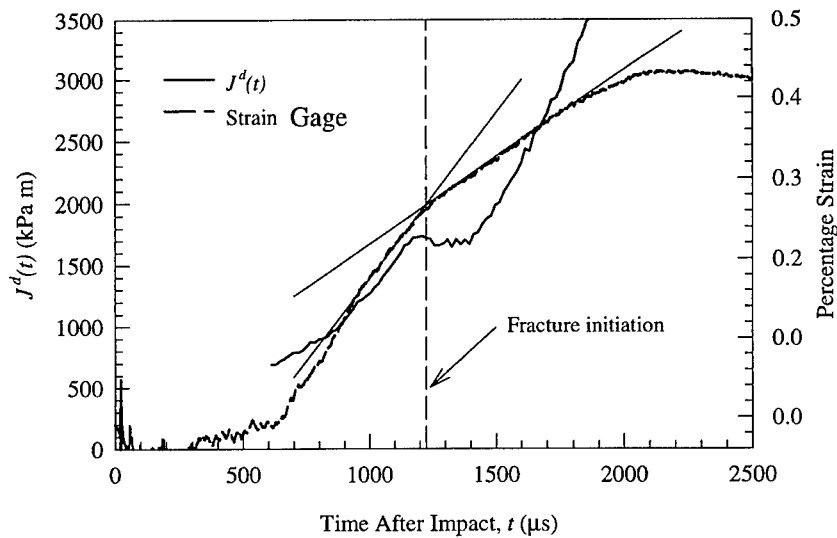


Fig. 16. Variation of the dynamic J -integral and strain gage signal during impact three-point bend loading of an edge cracked Ni-Cr specimen.

thus the infrared measurements of temperature would still provide a reasonable estimate of the dynamic J -integral value.

4.2. Identification of time of crack initiation

Identification of fracture initiation is a crucial step required to establish the dynamic fracture initiation toughness, $J^d(t_c) = J_c^d$, where $t = t_c$ is the time of fracture initiation.

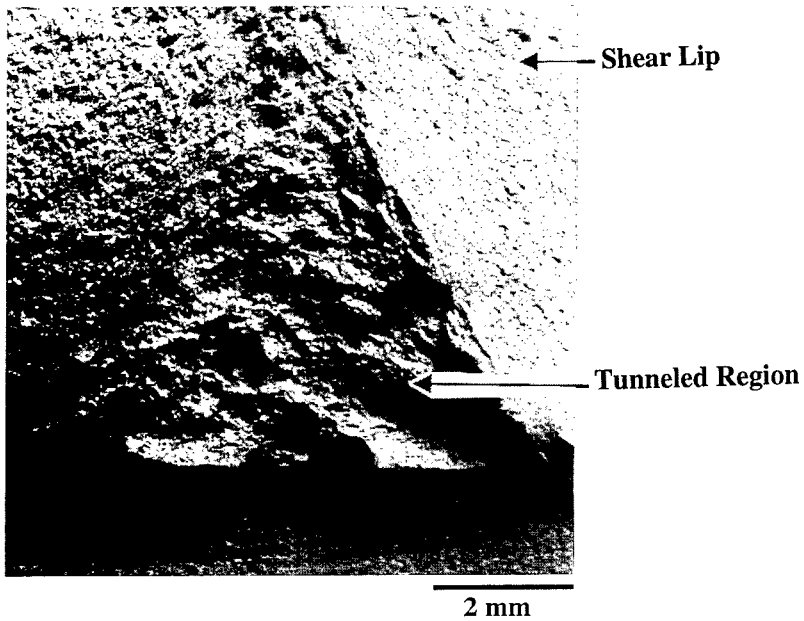


Fig. 17. A scanning electron micrograph of the fracture surface of Ni-Cr steel showing the tunneled region and the shear lip regions.

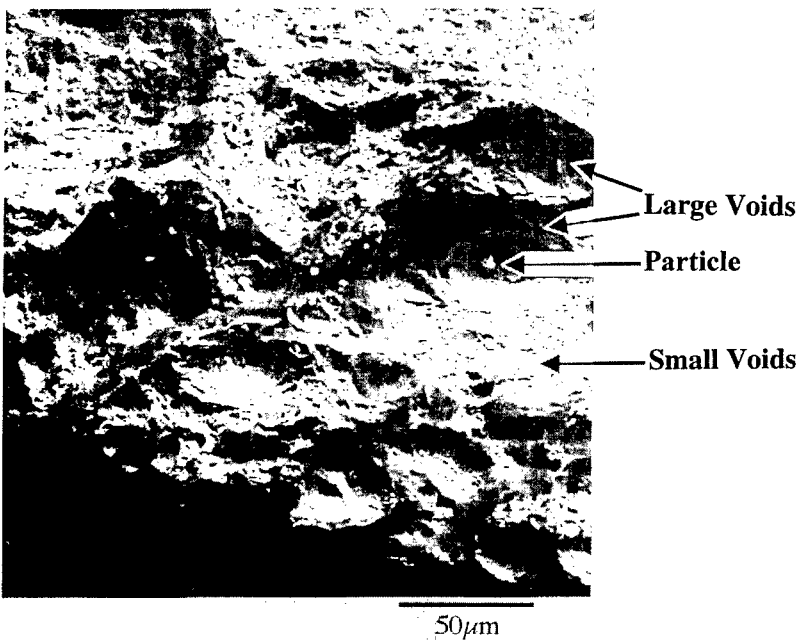


Fig. 18. SEM image of the tunneled region showing dual population of voids.

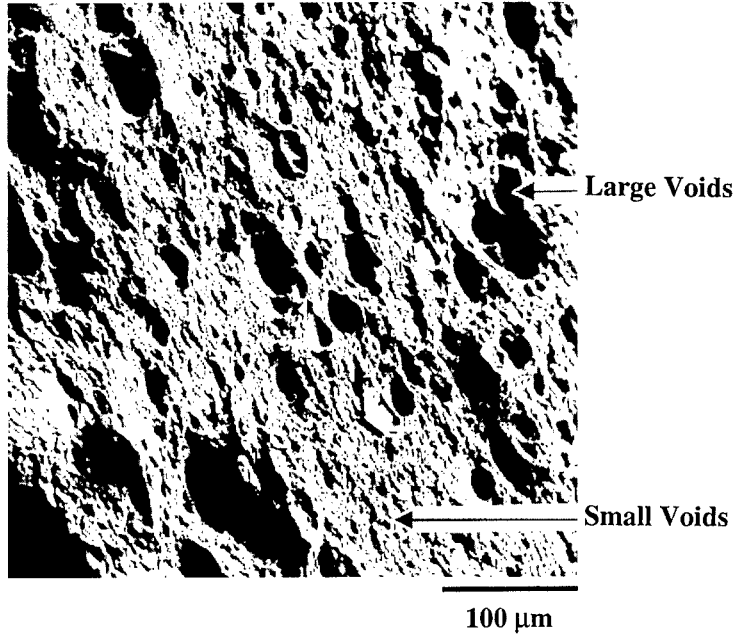


Fig. 19. SEM image of the shear lip region showing dual population of voids.

Strain gage instrumentation was employed to identify the fracture initiation event during dynamic deformation of the precracked steel specimens subjected to three-point bend impact loading (Couque, 1994). A strain gage located in the vicinity of the crack tip was employed to detect the change in specimen compliance that accompanies the fracture initiation event. The change in specimen compliance was reflected as a change in the rate at which the strain signal increases. As a first step, the strain gage technique was applied to identify the fracture initiation event in an edge-cracked specimen loaded quasi-statically in a three-point bend configuration. The advantage of quasi-static loading conditions is that the identification of fracture initiation can be corroborated with direct visual observation of the crack tip root. A schematic showing the loading arrangement and the strain gage location is given in Fig. 14. For this loading arrangement the value of the J -integral can be determined provided the load, P , and load point displacement, s , are known. Rice *et al.* (1973) have shown that

$$J = \frac{2}{tb} \int_0^\delta P ds \quad (10)$$

where b is the length of the uncracked ligament, t is the specimen thickness and δ is the load point displacement due to the presence of the crack. A typical variation of the value of the J -integral for quasi-static loading of an edge-cracked Ni-Cr steel specimen is shown in Fig. 15. The figure also shows the strain monitored by the strain gage employed to identify fracture initiation. The sudden change in slope of the

Table 3. *Fracture toughness as a function of loading rate for Ni–Cr steel and 304 stainless steel*

Ni–Cr steel		304 Stainless steel	
\dot{J}_{crit}^d	J_{crit}^d	\dot{J}_{crit}^d	J_{crit}^d
10 kN m ⁻¹ s ⁻¹	1080 kN m ⁻¹	8 kN m ⁻¹ s ⁻¹	1300 kN m ⁻¹
2500 kN m ⁻¹ s ⁻¹	1750 kN m ⁻¹	1300 kN m ⁻¹ s ⁻¹	1600 kN m ⁻¹

strain gage signal was identified as the fracture initiation event. This was confirmed simultaneously by direct visual observation of the crack tip root.

As a subsequent step, strain gages were employed to determine the fracture initiation event for dynamic three-point bend impact loading of a precracked Ni–Cr specimen. The strain gage location was selected to be the same as the quasi-static loading case. Figure 16 shows the variation of the strain as function of time during the impact loading of a precracked Ni–Cr steel specimen. The time history of the value of the dynamic J -integral, as determined by infrared thermography, is also shown in the same figure. As demonstrated in the figure, the fracture initiation event is clearly identified by the change in slope in the strain gage signal.

Table 3 lists the values of fracture initiation toughness, $J(t_c) = J_c$, obtained for quasi-static loading conditions and for dynamic loading. Fracture toughness values for both the steels are listed. The rate of loading at the time of fracture, $t = t_c$, is quantified in terms of the value of the rate of change of the J -integral. As can be seen from this data there is a significant increase in the value of the fracture toughness with increasing rate of loading for Ni–Cr steel. No such significant rise is observed for the 304 stainless steel.

4.3. *Micromechanisms of fracture initiation*

Ductile fracture in Ni–Cr and 304 stainless steels initiated in the form of tunneling in the center of the crack front followed by shear lip formation at the free surfaces. The failure process is dominated by void nucleation, growth and coalescence at the microstructural level. Figure 17 shows a scanning electron micrograph of the Ni–Cr fracture surface of a specimen loaded under dynamic conditions with tunnel and shear lip regions identified. Void formation begins in the center of the specimen due to the high constraint resulting from the prevailing plane strain conditions there, which leads to fracture initiation in the form of tunneling. These voids are nucleated at second phase particles in the microstructure. During the fracture process, these voids grow under the high crack tip stresses and eventually coalesce with each other and with the main crack. Figure 18 shows the voids and the particles that initiated these voids. Figure 18 also shows a much smaller void population filling up the regions between the larger voids. This points to the mechanism where the void coalescence takes place through the formation of void sheets consisting of a smaller void population. A similar mechanism appears to dominate the fracture process in the shear lip regions.

Figure 19 shows a detailed micrograph of the shear lip region. The elongated voids suggest that two mechanisms operated simultaneously in this region, i.e., void nucleation and growth and shear deformation. The distribution of smaller void population between the larger voids indicates that final failure again took place through the formation of void sheets.

5. SUMMARY

This study focuses on the development of a non-contact experimental technique to measure the history of the J -integral for dynamically loaded cracks in ductile solids. This technique utilizes infrared thermography for the first time to measure the temperature increase ahead of the dynamically deforming crack, which is subsequently related to the J -integral through HRR singular fields. The accuracy of this method is verified through an independent measurement of the dynamic J -integral, where high speed photography was used to measure the crack tip opening displacement (CTOD). A preliminary attempt has been made at understanding the micromechanisms of dynamic fracture initiation in ductile solids using scanning electron microscopy.

ACKNOWLEDGEMENTS

The authors would like to acknowledge the support of the Office of Naval Research under Grant No. N00014-95-1-0453 (Dr G. Yodder and Dr Y. D. S. Rajapakse, Scientific Officers) and of the Department of Energy under Grant No. De-FG03-95 ER14560 (Dr R. Goulard, Project officer). The authors are grateful to Dr D. M. Owen, Caltech, for his help in conducting the scanning electron microscopy and for other useful discussions.

REFERENCES

- Cho, K., Lee, S., Nutt, S. R. and Duffy, J. (1993) Adiabatic shear band formation during dynamic torsional deformation of an HY-100 steel. *Acta Metallurgica et Materialia* **41**, 923–932.
- Costin, L. S., Duffy, J. and Freund, L. B. (1977) Fracture initiation in metals under stress wave loading conditions. *Fast Fracture and Crack Arrest*. ASTM STP 627, American Society of Testing and Materials, pp. 301–318.
- Couque H. (1994) Effects of loading rate on the plane stress fracture toughness properties of an aluminum alloy. *Journal de Physique IV*, Colloque C8, Supplement au Journal de Physique III **4**, C8.747–C8.752.
- Douglas, A. S. and Suh, M. S. (1988) Impact fracture of a tough ductile steel. *Proceedings of the 21st ASTM National Fracture Symposium*. Annapolis, MD.
- Duffy, J. and Chi, Y. C. (1992) On the measurement of local strain and temperature during the formation of adiabatic shear bands. *Materials Science and Engineering A* **157**, 195–210.
- Hutchinson, J. W. (1968) Singular behavior at the end of a tensile crack in a hardening material. *Journal of Mechanics and Physics of Solids* **16**, 13–31.
- Li, Y. and Wang, Z. (1986) Higher order asymptotic field of tensile plane strain nonlinear crack problems. *Scientia Sinica (Series A)* **29**, 941–955.
- Nakamura, T. and Parks, D M. (1990) Three-dimensional crack tip fields in a thin ductile plate. *Journal of the Mechanics and Physics of Solids* **38**, 787–812.

- Narasimhan, R. and Rosakis, A. J. (1990) Three-dimensional effects near a crack tip in a ductile three-point bend specimen. I. A numerical investigation. *Journal of Applied Mechanics* **57**, 607–617.
- Needleman, A. and Tvergaard, V. (1987) An analysis of ductile rupture modes at a crack tip. *Journal of the Mechanics and Physics of Solids* **35**, 151–183.
- O'Dowd, N. P. and Shih, C. F. (1991) Family of crack tip fields characterized by a triaxiality parameter. I. Structure of fields. *Journal of the Mechanics and Physics of Solids* **39**, 989–1015.
- O'Dowd, N. P. and Shih, C. F. (1992) Family of crack tip fields characterized by a triaxiality parameter. II. Fracture applications. *Journal of the Mechanics and Physics of Solids* **40**, 939–963.
- Rice, J. R. (1968) A path independent integral and the approximate analysis of strain concentration by notches and cracks. *Journal of Applied Mechanics* **35**, 379–386.
- Rice, J. R. and Rosengren, G. F. (1968) Plane strain deformation near a crack tip in a power-law-hardening material. *Journal of the Mechanics and Physics of Solids* **16**, 1–12.
- Rice, J. R., Paris, P. C. and Merkle, J. G. (1973) Some further results on J -integral analysis and estimates. *Progress in Flaw Growth and Fracture Toughness Testing*. ASTM-STP 536, pp. 231–245.
- Rosakis, A. J. (1993) Two optical techniques sensitive to gradients of optical path difference: the method of caustics and the coherent gradient sensor (CGS). *Experimental Techniques in Fracture* pp. 327–425.
- Rosakis, A. J., Zehnder, A. T. and Narasimhan, R. (1988) Caustics by reflection and their application to elastic-plastic and dynamic fracture mechanics. *Optical Engineering* **27**(8), 596–610.
- Sharma, S. M. and Aravas, N. (1991) Determination of higher order terms in asymptotic elastoplastic crack tip solutions. *Journal of the Mechanics and Physics of Solids* **39**, 1043–1072.
- Sharpe Jr, J. R., Douglas, A. S. and Shapiro, J. M. (1988) Dynamic fracture toughness evaluation by measurement of C.T.O.D. Johns Hopkins Mechanical Engineering Report WNS-ASD-88-02.
- Shih, C. F. (1981) Relationships between the J -integral and the crack tip opening displacement for stationary and extending cracks. *Journal of the Mechanics and Physics of Solids* **29**, 305–326.
- Tippur, H. V., Krishnaswamy, S. and Rosakis, A. J. (1991) A coherent gradient sensor for crack tip measurements: analysis and experimental results. *International Journal of Fracture* **48**, 193–204.
- Yang, S., Chao, Y. J. and Sutton, M. A. (1993) Complete theoretical analysis for higher-order asymptotic terms and the HRR zone at a crack tip for mode I and mode II loading of a hardening material. *Acta Mechanica* **98**, 79–98.
- Zehnder, A. T., Rosakis, A. J. and Krishnaswamy, S. (1990) Dynamic measurement of the J -integral in ductile metals: comparison of experimental and numerical techniques. *International Journal of Fracture* **42**, 209–230.



Pergamon

J. Mech. Phys. Solids, Vol. 46, No. 10, pp. 2017–2032, 1998

© 1998 Elsevier Science Ltd. All rights reserved

Printed in Great Britain

0022-5096/98 \$—see front matter

PII: S0022-5096(98)00015-5

SCATTERING AS A MECHANISM FOR STRUCTURED SHOCK WAVES IN METALS

DENNIS GRADY*

Applied Research Associates, 4300 San Mateo, Blvd., A-220, Albuquerque, NM 87110, U.S.A.

(Received 20 December 1997; in revised form 15 January 1988)

ABSTRACT

The scattering of wave energy during shock propagation through heterogeneous media is examined as an alternative to visco-plasticity as the physics underlying the formation of structured steady shock waves in polycrystalline metals. A theory based on a quasi-harmonic representation of scattered acoustic energy in solids is pursued and used to develop continuum constitutive relations to describe nonlinear wave propagation in heterogeneous solids. Resulting constitutive models are compared with shock wave profile data for metals. © 1998 Elsevier Science Ltd. All rights reserved.

Keywords: A. shock waves, B. stress waves, B. inhomogeneous material, C. plate impact.

INTRODUCTION

Barker (1968) reported on experimental measurements of structured shock waves in aluminum providing one of the first demonstrations of the excellent temporal resolution of the velocity interferometry diagnostic methods in shock wave physics. Early theoretical work (e.g., Band and Duvall, 1961) referred to an underlying solid viscosity as the property responsible for the observed finite rise-time in steady structured shock waves. The early Russian literature also attributed effects observed in the shock wave environment to viscous characteristics of solids (e.g. Mineev and Savinov, 1967). From the aluminum data of Barker (1968) it was noted that this viscosity lessened with the shock amplitude giving rise to a very strong increase in the steepness of the shock wave with shock amplitude. In fact if a strain rate $\dot{\epsilon}$ was identified at the fastest rising portion of the structured steady wave it was found that the strain rate increased with the shock amplitude p according to $\dot{\epsilon} \sim p^4$ while the viscosity η was observed to lessen as $\eta \sim \dot{\epsilon}^{-1/2}$ (Grady, 1981). Structured steady-wave data on a range of metals were subsequently reported by Swegle and Grady (1985) and showed the same fundamental trends with variation in shock amplitude suggesting a universal behavior in the nature of structured steady waves in metals.

These structured shock-wave data for metals have led to a number of efforts to develop descriptive constitutive models (e.g., Johnson, 1992, Swegle and Grady, 1985; Rubin, 1990; Partom, 1990). Such models were generally based on formalisms of

* E-mail: dgrady.ara.com

visco-plasticity and have been reasonably successful in describing the trends in the experimental data. These previous modeling efforts tacitly assumed, of course, that the underlying physics of time-dependent plasticity processes (dislocations, twinning, etc.) are responsible for the dissipation and wave dispersion leading to observed structured shocks in metals. Visco-plasticity may, in fact, be the responsible physics but there are other viable physical mechanism which could account for the observed results that have not been adequately discounted.

An alternative mechanism, for example, which could account for the observed structured shock waves in metals is suggested by ultrasonic experiments of Mason and McSkimin (1947) on aluminum. Their work shows that the attenuation of ultrasonic waves above a frequency of about several megahertz is dominated by scattering within the grain structure of the polycrystalline metal. Acoustic scattering would lead to wave dispersion at any amplitude and could also counterbalance the shock-up tendency of nonlinear solids accounting for observed structured shock waves.

There can be little doubt that scattering plays a role in the propagation of large amplitude shock waves in metals. Whether scattering is principally responsible for the observed shock wave structure is the critical question.

With these brief remarks serving to introduce the nature of the topic of interest the remaining portion of the introduction will outline the objectives and briefly summarize the results of the present paper. It is suggested first that wave scattering may be responsible for the finite width structuring of shock waves in polycrystalline solids. Earlier ultrasonic data on wave scattering in metals are then summarized and serve to motivate ideas of wave scattering when material is subjected to large amplitude shock waves. Such ideas have received only the briefest of attention in earlier shock wave literature. Consequently, a substantial portion of the paper focuses on identifying the physics and developing a model descriptive of the processes by which shock waves scatter acoustic energy and which accounts for the subsequent representation of that energy. It is found that a quasi-harmonic theory of matter previously used to develop equilibrium thermal properties of solids can be extended to the problem of acoustic scattering, providing both a vehicle for clarifying the physics and a framework for modeling the phenomena.

This physics-based model is found to lead to continuum constitutive relations which are formally the same as governing relations arrived at by Barker (1971) and by Kanel' *et al.* (1995) on a more intuitive basis. It is shown that such relations based on the physics of acoustic wave scattering quite adequately model the structured steady shock-wave data for metals.

The results therefore leave open the question of whether visco-plasticity or wave scattering provides the dominate underlying physics responsible for observed behavior of structured steady waves in metals. Single-shock steady-wave data are not sufficient to discern between the constitutive models resulting from the two physical theories.

This observation opens the question of whether more complex large amplitude wave profile data would provide the test for distinguishing between the theories. It is noted that some two-step steady shock data exists for selected metals, providing an interesting alternative loading path for testing the models. Such data for aluminum are examined and it is found that the continuum models based on the physics of wave scattering which satisfactorily predicted the single-step steady shock data are unable

to predict the two-step data. It is noted, however, that the visco-plasticity models would also fail in this task.

The paper concludes at this indecisive point. An alternative physical mechanism underlying structured waves in metals is offered. A substantial physics-based modeling effort is pursued resulting in continuum governing relations for large amplitude wave propagation in materials exhibiting scattering-induced dispersion. The underlying physics of structured waves in metals is at present uncertain, however.

SCATTERING OF ACOUSTIC WAVES IN GRANULAR MATTER

Rayleigh (1929) investigated the scattering of wave energy from a single particle and derived the relation,

$$\frac{A_s}{A_i} = \frac{\pi v}{r\lambda^2} \left(\frac{\Delta E}{E} + \cos \theta \frac{\Delta \rho}{\rho} \right), \quad (1)$$

in the limit of the wave length λ long relative to the particle dimension. On the left of eqn (1) is the ratio of the scattering amplitude relative to the incident amplitude of the wave. On the right v is the particle volume, $\Delta E/E$ is a relative measure of the elasticity difference between particle and medium, $\Delta \rho/\rho$ is the relative density difference, while r and θ are the distance from particle to observation point, and the angle between this distance and the direction of the incident wave, respectively.

Mason and McSkimin (1947) surmised that Rayleigh's relation should apply to the scattering of acoustic wave energy by a single grain within a polycrystalline material because of the projected impedance difference of an arbitrarily oriented grain with respect to its neighbors. By integrating the scattered energy determined from eqn (1) over a sphere and accounting for the average contribution from all grains they arrive at the following expression for the acoustic attenuation factor due to scattering,

$$\alpha = \frac{4\pi^3 v}{\lambda^4} \left\langle \left(\frac{\Delta E}{E} \right)^2 \right\rangle_{\text{ave}}. \quad (2)$$

The expression exhibits the classic fourth power dependence on wave length of Rayleigh scattering. Subsequent analysis by Knopoff and Hudson (1964) showed that scattering of acoustic waves in polycrystalline media resulted in both incident dilatation and shear waves scattering predominantly into shear wave energy.

Experiments performed by Mason and McSkimin (1947) on several aluminum samples revealed an acoustic attenuation component proportional to the fourth power of the frequency. Calculated scattering losses based on the Rayleigh scattering relation [eqn (2)] agreed quite well with experiments. The fourth power scattering behavior was observed until the wave length approached about three grain dimensions. For higher frequencies attenuation increased more nearly with the square of the frequency—a not unexpected trend since scattering for very short wave lengths is predicted to be frequency independent.

STRUCTURED FINITE-AMPLITUDE WAVES IN HETEROGENEOUS MEDIA

Wave propagation in a homogeneous linear elastic continuum is well understood. In contrast wave propagation in a heterogeneous and nonlinear elastic media is considerably more complex. Elastic pulse wave transmission in heterogeneous solids exhibit similarities to wave propagation in dissipative media. Pulse wave shapes will evolve and attenuate, while energy is lost from the pulse as the wave propagates. Nonlinear elastic heterogeneous media can support steady structured shock waves and account for the prerequisite entropy production in the compressive shock process. The underlying cause is related to wave dispersion brought about by scattering within the heterogeneous microstructure.

Finite amplitude compression waves in nonlinear solids will become steeper as the wave propagates. Wave dispersion can counter the steepening process leading to structured steady shock waves. Heterogeneities within a solid body contribute to wave dispersion and can account for the structured steady shock waves. To understand the underlying physics responsible for structured steady shock waves in heterogeneous solids consider the following hypothetical situation: the material of concern is a nonlinear thermoelastic heterogeneous solid. Curves of elastic uniaxial strain loading corresponding to isothermal conditions, isentropic conditions and steady shock (Hugoniot) conditions for this solid are identified in Fig. 1. When subjected to shock compression through a steady structured shock the continuous stress versus strain compression path experienced by an appropriately averaged material element departs for the thermodynamic surface, following a straight Rayleigh line from the state in front of the shock to the compressed thermodynamic state behind the shock.

The following questions concerning shock compression of this elastic heterogeneous solid are relevant: first, what physically supports the excess nonequilibrium stress (the vertical distance between the Rayleigh line and the equilibrium thermodynamic

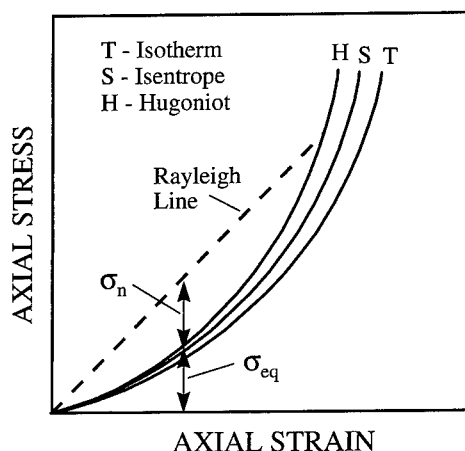


Fig. 1. Steady structured shock wave loading in a thermal-elastic solid.

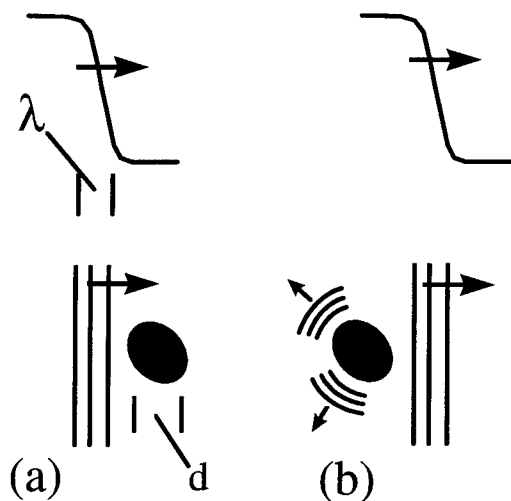


Fig. 2. Shock wave stimulated scattering at sites of heterogeneity in a solid.

surface) experienced during the shock transition process? Second, what are the underlying physical mechanisms responsible for the structure of the compression shock wave? Third, how is entropy production accounted for in the elastic shock process?

In pursuing answers to the questions posed consider the aspect of a heterogeneous solid illustrated in Fig. 2 by the single inclusion in an otherwise continuous solid. A region of the body including this inclusion compressed quasi-statically would achieve some level of lattice strain energy. That same region compressed by a finite amplitude shock wave would, in addition to the equilibrium lattice strain energy, include a dynamic or acoustic energy component associated with wave scattering as the shock wave passed over the inclusion. In fact, as the characteristic wave length λ of the shock approached the characteristic dimension d of the inclusion scattering would be expected to amplify markedly.

Thus, when a finite amplitude shock wave passes through a heterogeneous solid the energy residing in the material behind the shock wave will include both a component due to the lattice strain energy and a kinetic component corresponding to a field of acoustic phonon energy caused by wave scattering within the heterogeneous microstructure.

Such acoustic phonon energy can be characterized through a quasi-harmonic normal mode representation of anelastic solid. Although more commonly applied in the description of perfect crystals in which lattice waves and normal modes are the same (Klemans, 1965), heterogeneous elastic solids can, in principal, also be described by normal mode coordinates. A property of a normal mode coordinate is a decoupling from the other coordinates such that energy introduced into that coordinate persists. In nonlinear solids the elastic constants depend on distortion (dilation and shear). These anharmonic properties of the material will lead to a coupling of normal mode coordinates and thus energy introduced into a single coordinate would ultimately diffuse throughout the system of normal coordinates until an equilibrium controlled

by statistical mechanical principals is achieved. Acoustic phonon energy will also contribute to the global stress state if anharmonicity is a property of the media.

The inducement of a component of kinetic or acoustic phonon energy during the dynamics of the shock compression process as outlined in the brief comments above offer answers to the questions posed. During passage of the structured shock, wave scattering leads to the production of acoustic phonon energy within a limited spectrum of normal mode coordinates within the shock front. This nonequilibrium acoustic phonon energy would account for the excess stress on the Rayleigh line during passage of the shock wave. Diffusion of this energy to an equilibrium configuration throughout the acoustic normal modes is achieved as the final shock state is approached. Ultimately diffusion throughout the full thermal spectrum occurs until complete thermo-elastic equilibrium is achieved. The latter accounts for entropy production within the elastic shock process in the heterogeneous solid. Details of the steady shock wave profile structure are determined by characteristic relaxation times associated with specific acoustic energy diffusion processes.

NORMAL MODE DESCRIPTION OF SCATTERED ENERGY IN HETEROGENEOUS SOLID

The foregoing description of large-amplitude wave dispersion resulting from acoustic scattering in heterogeneous solids can be modeled through a quasi-harmonic representation of the shock compressed matter. As noted, the dynamic state of an elastic heterogeneous solid can be characterized by a normal mode system of coordinates.

Accordingly, consider a decomposition of the energy into that due strictly to lattice compression $U_0(\epsilon)$ and that due to the acoustic phonon energy, $U_k = \sum n_i h\nu_i$, such that,

$$U = U_0(\epsilon) + \sum_i n_i h\nu_i. \quad (3)$$

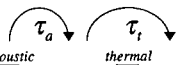
The current nominal axial strain state is ϵ while n_i is the number of phonons with energy $h\nu_i$. The normal mode frequency is ν_i and h is Planck's constant. Although a quantum representation of the acoustic phonon energy may appear superfluous to what is clearly a classical issue, the approach offers a particularly transparent framework for developing the appropriate relations and has been productively used in other common theoretical solid state concepts such as the Debye theory of specific heat and Gruneisen's theory of thermal pressure.

To proceed U_k in eqn (3) will be decomposed into acoustic and thermal normal modes,

$$U = U_0(\epsilon) + \sum_i^{acoustic} n_i h\nu_i + \sum_i^{thermal} n_i h\nu_i, \quad (4)$$

where the acoustic-to-thermal transition in vibrational frequency will be of the order 10^{10} – 10^{11} hertz while the upper cutoff is of the order of the Debye frequency ($\sim 10^{15}$

hertz). In equilibrium each normal coordinate would have an energy of $u_i = kT$ where T is the temperature. Because the density of vibrational frequencies increases like ν_i^2 , energies in the acoustic modes under equilibrium conditions are ordinarily negligible. In the present application, however, where energy is initially introduced into a limited spectrum of acoustic modes through scattering within the heterogeneous microstructure, the acoustic portion of the normal mode spectrum is critical to the physical processes. Equilibration throughout the acoustic spectrum and ultimately over the full thermal spectrum can be abstractly depicted in the following way;

$$U = U_o(\epsilon) + \sum_i^{\text{acoustic}} n_i h \nu_i + \sum_i^{\text{thermal}} n_i h \nu_i, \quad (5)$$


where τ_a and τ_t represent relaxation times over acoustic modes and over the thermal spectrum, respectively. The processes identify a diffusion of phonons into the under populated acoustic modes and, ultimately, the higher frequency thermal modes.

Recognizing the focus on the acoustic normal mode spectrum we will return to eqn (3) written in the form,

$$U = U_o(\epsilon) + \sum_i n_{i0} h \nu_i + \sum_i (n_i - n_{i0}) h \nu_i, \quad (6)$$

where n_{i0} represents the set of equilibrium population numbers. Combining the first two terms on the right as the equilibrium thermoelastic equation of state $U_{eq}(\epsilon, s)$ of the heterogeneous solid gives,

$$U = U_{eq}(\epsilon, s) + \sum_i (n_i - n_{i0}) h \nu_i. \quad (7)$$

The second term on the right in eqn (7) is then the nonequilibrium acoustic phonon energy induced in the shock-wave scattering process. The strain derivative of U provides the stress,

$$\sigma = \sigma_{eq} + \sum_i (n_i - n_{i0}) h \nu'_i, \quad (8)$$

also composed of an equilibrium component and a contribution due to the nonequilibrium acoustic phonon energy.

The anharmonic character of the respective normal modes is determined by the strain dependence of the normal mode vibration frequencies ν'_i . The time dependence of eqn (8) yields,

$$\dot{\sigma} = \dot{\sigma}_{eq} + \sum_i \frac{dn_i}{dt} h \nu'_i. \quad (9)$$

The second term on the right will be identified as $\dot{\sigma}_n$ the time rate of the nonequilibrium component of the stress due to the acoustic phonon field stimulated in the heterogeneous solid. Ignored in the step leading to eqn (9) is a nonzero time-dependent term resulting from the strain dependence of the normal mode frequency. Assumed

small in the present derivation this term could alternatively be included in the $S(\cdot)$ term defined in eqn (12) below.

The expression dn_i/dt is fundamental in modeling the rate of stimulation and relaxation of the phonon population within the acoustic normal modes. A reasonable governing equation would be,

$$\frac{dn_i}{dt} = s_i(\cdot) + \frac{1}{\tau_i}(n_i - n_{i0}), \quad (10)$$

where $s_i(\cdot)$ represents a phonon stimulation function dependent on the dynamics of the wave interaction with the heterogeneous microstructure. The second term provides for relaxation of the normal mode energy levels toward an equilibrium population n_{i0} with a characteristic relaxation time τ_i . Equations (9) and (10) combine to provide,

$$\dot{\sigma} = \dot{\sigma}_{eq} + \sum_i s_i h v'_i - \sum_i \frac{1}{\tau_i} (n_i - n_{i0}) h v'_i. \quad (11)$$

If one assumes that a common relaxation time $\tau \approx \tau_i$ sensibly describes all normal modes, eqn (11), with eqn (8), yields,

$$\dot{\sigma} = \dot{\sigma}_{eq} + S(\cdot) - \frac{1}{\tau}(\sigma - \sigma_{eq}). \quad (12)$$

Equation (12) resulted from a quasi-harmonic description of dispersive wave scattering in heterogeneous media is recognized as the functional form for a continuum nonlinear anelastic constitutive relation. In the following section phenomenological constitutive models of the form of eqn (12) proposed by earlier authors to describe dispersive wave propagation in heterogeneous media are examined.

MODELING DISPERSIVE WAVE PROPAGATION IN HETEROGENEOUS SOLIDS

The physical issues of nonlinear large-amplitude wave dispersion introduced in the earlier sections suggest a material response model initiating with the decomposition of stress,

$$\sigma = \sigma_{eq} + \sigma_n. \quad (13)$$

This decomposition is not an assumption. It is a recognition that on the most fundamental level forces of interaction in condensed matter are a composition of lattice potential and kinetic (momentum exchange) terms. The first term on the right will determine the equilibrium thermoelastic response of the heterogeneous solid. That this term may also include the equilibrium component of the acoustic phonon stress, as suggested by eqns (6) and (7), is not inconsistent with the fundamental stress decomposition of eqn (13). The second term on the right accounts for stresses brought about by the nonequilibrium acoustic phonon energy induced in the heterogeneous microstructure by the transient wave. The assumed time dependence is of the general form,

$$\dot{\sigma}_n = S + R, \quad (14)$$

where the terms S and R account, respectively, for the stimulation and relaxation of nonequilibrium acoustic phonon energy. Within these terms lies the opportunity to model a rich variety of responses exhibited by heterogeneous solids subjected to finite-amplitude transient stress wave propagation. The general model framework identified by eqns (13) and (14), and the specific models to be considered presently which fall within this framework, will be recognized as continuum anelastic representations of the stress vs strain response of solid matter.

Knopoff (1965) was perhaps one of the first to recognize the potential of continuum anelasticity models to describe wave dispersion brought about by scattering in heterogeneous media. He realized that heterogeneities within the earth's interior contributed to the dispersion and attenuation of sonic waves and explored the applicability of a linear Maxwell model to describe the wave propagation. The linear Maxwell model within the framework of eqns (13) and (14) is written,

$$\dot{\sigma} = \dot{\sigma}_n = M\dot{\epsilon} - \frac{1}{\tau}\sigma_n, \quad (15)$$

$$\dot{\sigma}_{eq} = 0. \quad (16)$$

In this most fundamental of anelasticity models transient stresses are stimulated through a modulus M and relax over a characteristic time τ . Knopoff (1965) found that dispersion characteristics predicted by eqn (15) were not in accord with observed attenuation of sound waves in the earth.

Barker (1971) proposed use of a general nonlinear Maxwell model in the form,

$$\dot{\sigma} + \varphi(\epsilon)\dot{\epsilon} = -\frac{1}{\tau}(\sigma - \sigma_{eq}), \quad (17)$$

to describe finite amplitude wave propagation in composite solids. This approach reasonably modeled available experimental data and was consistent with fundamental computer solutions of wave propagation in composites. Barker's model has been examined in some detail recently by Johnson *et al.* (1994). The stress decomposition of eqns (13) and (14) is readily reproduced,

$$\dot{\sigma}_n = M(\epsilon)\dot{\epsilon} - \frac{1}{\tau}\sigma_n, \quad (18)$$

$$\dot{\sigma}_{eq} = \vartheta(\epsilon)\dot{\epsilon}. \quad (19)$$

Equation (18) explicitly displays the stimulation and relaxation terms identified in eqn (14). Stimulation of nonequilibrium stress is accomplished through the modulus $M(\epsilon) = \varphi(\epsilon) - \vartheta(\epsilon)$. Relaxation is governed by a linear relation proportional to the nonequilibrium stress.

Barker's relation nicely models a theory of Zel'dovich (1946) on shock waves in relaxing media in which the normal mode coordinates are considered to be divided into two categories: those which are excited instantly and those which are stimulated only after some characteristic relaxation time. The modulus M then determines the difference in compression paths of the media under the conditions of restricted (non-

equilibrium) and unrestricted (equilibrium) stimulation of the normal mode degrees of freedom.

More recently Kanel' *et al.* (1995) have proposed another continuum anelasticity model to describe wave propagation in solid composites. In the same framework the model can be written,

$$\dot{\sigma}_n = k\dot{\epsilon}^m - \frac{1}{\tau}\sigma_n, \quad (20)$$

$$\dot{\sigma}_{eq} = \mathcal{G}(\epsilon)\dot{\epsilon}. \quad (21)$$

Although quite similar to Barker's model (the models differ only in the stimulation term) the physical implications in the stimulation term for $m \neq 1$ are fundamentally different. Rather than modeling a dichotomous (instantaneous and equilibrium) response of the material, the stimulation term implies a continuously increasing scattered energy (and hence nonequilibrium stress) with increasing strain rate within the shock wave. The modeled behavior can be likened, for example, to the Rayleigh scattering of sound waves in heterogeneous media as has been observed experimentally in the acoustic limit by Mason and McSkimin (1947) as discussed earlier.

STRUCTURED-STEADY WAVES

The relations put forth by Barker (1971) and by Kanel' *et al.* (1995) are intended to provide continuum models to describe the additional stress brought about by the scattering of acoustic wave energy resulting from shock wave propagation in heterogeneous media. The present theory based on a statistical normal-mode quasi-harmonic representation of this acoustic energy provides qualitative support for the general character of these models.

Written in the form,

$$\dot{\sigma} = \sigma'_{eq}(\epsilon)\dot{\epsilon} + k(\epsilon)\dot{\epsilon}^m - \frac{1}{\tau}(\sigma - \sigma_{eq}(\epsilon)), \quad (22)$$

summarizes both models with $k(\epsilon) = \text{const}$, for the Kanel' *et al.* equation, while $m = 1$ captures the Barker equation.

Structured steady-wave solutions require the stress-vs-strain path to traverse a straight Rayleigh line path connecting lower and upper points on the equilibrium curve. Consequently, the constraint $\dot{\sigma} = \rho U^2 \dot{\epsilon}$, where U is the steady-wave shock velocity, yields, with eqn (22), the ordinary nonlinear differential equation,

$$k(\epsilon)\dot{\epsilon}^m + (\sigma'_{eq}(\epsilon) - \rho U^2)\dot{\epsilon} - \frac{1}{\tau}(\rho U^2 \epsilon - \sigma_{eq}(\epsilon)) = 0, \quad (23)$$

for the time history of the strain through the structured steady wave. Directly solving eqn (23) for the strain rate may reveal regions in the domain where $\dot{\epsilon}$ is negative, indicating the occurrence of shock segments within the structured wave. Solutions of the differential equation for the $\epsilon(t)$ history through the steady wave applies then only to those regions in which continuous flow occurs.

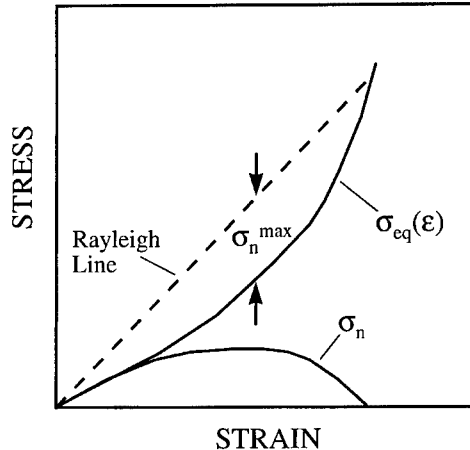


Fig. 3. Stress decomposition into equilibrium and nonequilibrium components in steady structured shock waves.

NATURE OF THE NONEQUILIBRIUM STRESS

From eqn (22) the nonequilibrium stress stimulated by the scattered acoustic energy during passage of the steady wave within the framework of the continuum models proposed by Barker, and by Kanel' *et al.*, is given by,

$$\dot{\sigma}_n = k(\epsilon)\dot{\epsilon}''' - \frac{1}{\tau}\sigma_n. \quad (24)$$

A maximum in σ_n occurs at $\dot{\sigma}_n = 0$ providing,

$$\sigma_n^{max} = \tau k(\epsilon)\dot{\epsilon}''', \quad (25)$$

where both ϵ and $\dot{\epsilon}$ are evaluated at the point of σ_n^{max} . Equation (25) is appropriate in corresponding closely to the conditions in which experimental results for structured steady waves have been presented in past work. Namely, $\dot{\epsilon}$ is determined at the fastest rising point in the wave and correlated with the maximum nonequilibrium stress as identified in Fig. 3 (e.g., Swegle and Grady, 1985).

COMPARISONS WITH STRUCTURED-STEADY WAVES IN METALS

Structured steady shock-wave data for metals have become available following development of high-resolution wave profile diagnostic techniques such as velocity interferometry (e.g. Swegle and Grady, 1985). It has become common to characterize the structure of the plastic shock through a correspondence of the stress jump with the maximum strain rate during the rise of the wave. Equivalently, a comparable correspondence between the maximum stress difference separating the Rayleigh line and the Hugoniot within this region can also be made as alluded to in closing the

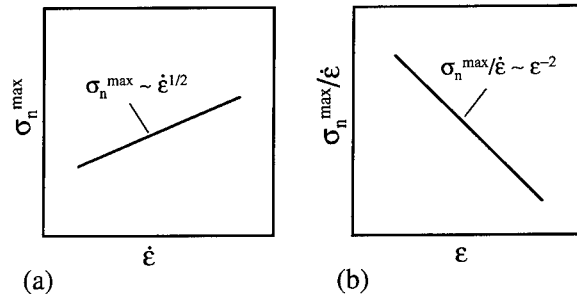


Fig. 4. Experimentally observed behavior of steady structured shock waves in metals (e.g., Sweigle and Grady, 1985).

previous section. A preponderance of these data indicate the trend shown on the left side of Fig. 4.

An alternative representation of the steady wave data follows through identification of a viscosity as the ratio of τ_{\max} and $\dot{\epsilon}$ compared with the amplitude of the strain within the structured wave. This is shown on the right in Fig. 4. Shock data on metal as indicate a reduction of this viscosity measure with the second power of the strain.

It is clear from the form of the structured wave data in Fig. 4 and the relation for the maximum nonequilibrium stress in eqn (25) that the models of Barker and of Kanel' *et al.* can both adequately fit the experimental data—at least to this first order representation of the steady shock profiles. For Barker's model $k(\epsilon) \sim \epsilon^{-2}$ while for the Kanel' *et al.*, model $k(\epsilon) = \text{const}$ and $m = 1/2$. Abilities to fit the full profile structure will differ, however, and this should be pursued.

COMPLEX SHOCK LOADING DATA

It should be reasonably clear at this point that the ability of the models proposed by Barker and Kanel' *et al.* to reasonably describe the shape and the trend of the observed character of structured steady shock waves in metals does not provide very strong support for acoustic scattering as the underlying physics structuring shock waves. In the present study this alternative physical explanation for structured shock waves in metals has been proposed and used as a stimulus for investigating a method of modeling the generation and effects of acoustic scattering energy in large amplitude wave propagation. This development has been accomplished and continuum anelastic models of the form proposed by Barker (1971) and by Kanel' *et al.* (1995) are found to be natural representations of such behavior and adequately describe observed steady shock waves in metals. Therefore, we can conclude that acoustic scattering is not inconsistent with the theory and must be considered as a viable mechanism.

Models similar to (although not precisely the same as) those of Barker and of Kanel' *et al.* emerge in consideration of a visco-plastic description of structured shocks in metals. For example the visco-plastic model developed by Sweigle and Grady (1985)

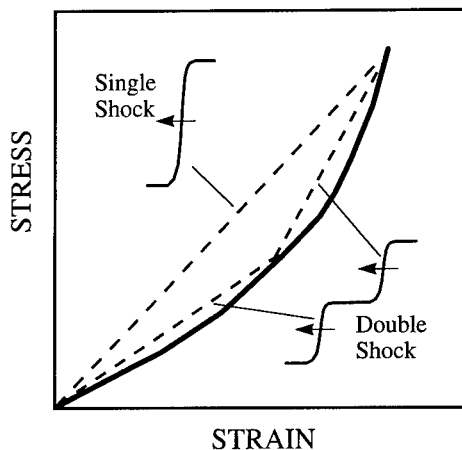


Fig. 5. Rayleigh line loading paths in single and double steady shock processes.

proposed a law whereby the plastic strain rate is related to the viscous stress according to $\dot{\gamma}_p \propto \tau_v^2$. That model also adequately described the structure shock data.

The stress-vs-strain-rate data or viscosity-vs-strain data described in Fig. 4 are related to a very special loading path. Namely, that of the Rayleigh line followed in a steady structured shock wave. As noted earlier the models of Barker (1971), of Kanel *et al.* (1995), and those based on visco-plasticity theories adequately described these data. Whether such models could successfully describe more general dynamic loading has not been seriously pursued.

Useful data exist for undertaking such a pursuit. Tests have been performed in which metal samples were subjected to structured steady shocks, allowed to dwell at the shock state for some period (typically about one microsecond), and then subjected to further compression through a subsequent second steady shock wave. The test methods are illustrated in Fig. 5 showing loading through both a single structured steady shock in contrast to loading through two structured steady shock waves. In the latter test loading is along separate Rayleigh line segments in contrast to a single Rayleigh line path in achieving the final compression state. Double shock experiments have been performed on several metals including and aluminum alloy (Asay and Chhabildas, 1981), copper (Chhabildas and Asay, 1982) and beryllium (Chhabildas *et al.*, 1982).

The models previously discussed, if sufficiently general, should predict the nature of the second shock as well as that of the principal shock. Thus, for the model of Kanel *et al.* (1995) a plot of the maximum nonequilibrium stress vs the strain rate for the second shock should lie on that of the principal shock data if the model is predictive. Similarly, for the model of Barker (1971) the viscosity vs strain data should overlie that of the principal shock.

Second shock data for 6061-T6 aluminum alloy (Asay and Chhabildas, 1981) are compared in this way in Fig. 6. As is readily seen, neither model survives this simplest of test generalizations. It is suspected that previous visco-plastic models developed to

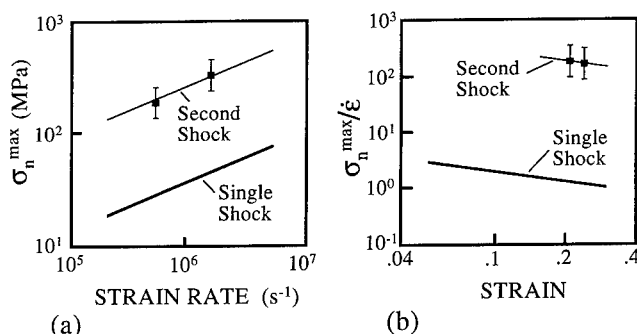


Fig. 6. Single and second shock states for aluminum alloy (Asay and Chhabildas, 1981).

describe steady shock data would also fail this comparison, although such an analysis has not been pursued in detail.

The second shock is considerably thicker (lower peak strain rate) than would be predicted from the principal structured shock data. Equivalently, the effective viscosity is substantially higher in the second shock than would be inferred from the principal shock data.

CONCLUSIONS

The physics underlying transient wave propagation, in which scattering of wave energy brought about by interaction of the wave with the heterogeneous substructure of a solid, has been explored in the present study. This feature of heterogeneous matter can lead to wave dispersion, wave attenuation and steady-structured waves not unlike wave propagation in dissipative media. A decomposition of energy into potential strain energy and vibrational energy was pursued where a normal mode quasi-harmonic representation of the latter is assumed. Key to the theoretical development is a recognition that transient wave interaction with the microstructure will lead to an initial highly nonequilibrium distribution of the vibrational energy. Statistical mechanical forces will drive the system toward an equilibrium distribution throughout the normal mode spectrum of the body. In application this energy will ultimately thermalize if it is not absorbed by intervening dissipative processes (i.e., damage, dislocation motions) as it percolates through the substructure degrees of freedom.

Relatively general assumptions in modeling the wave stimulation of the vibrational spectrum and the subsequent time-dependent relaxation toward equilibrium is found to lead to nonlinear continuum anelastic equations. Phenomenological equations developed and used by earlier workers (Barker, 1971; Kanel' *et al.*, 1995) to describe the wave propagation in heterogeneous matter are shown to be in accord with the theoretical results. Consequently, a firmer physical basis for such models has been established. More importantly, the theoretical methodology points toward a path

whereby the dynamics of more complex substructure physical processes can be modeled.

The underlying physics of scattering in nonlinear wave propagation in heterogeneous solids is then suggested as an alternative to visco-plastic processes in causing structured steady waves in polycrystalline metals. Models resulting from the scattering theory readily describe single shock steady-wave data for metals. Consequently the physics responsible for structured waves in metals must be regarded as uncertain.

The models are then compared with more complex two-step steady structured shock data in aluminum. The available models fail to predict these more general data raising serious concerns of current understanding of this fundamental shock phenomena.

REFERENCES

- Asay, J. R. and Chhabildas, L. C. (1981) Determination of the shear strength of shock compressed 6061-T6 aluminum. In *Shock Waves and High-Strain Rate Phenomena in Metals*, ed. M. A. Meyers and L. E. Murr, pp. 417–432. Plenum Press, New York.
- Band, W. and Duvall, G. E. (1961) Physical nature of shock propagation. *Amer. J. Phys.* **29**, 780–785.
- Barker, L. M. (1968) Fine structure of compressive and release wave shapes in aluminum measured by the velocity interferometer technique. In *Behaviour of Dense Media under High Dynamic Pressures*, pp. 483–505. Gordon and Breach, New York.
- Barker, L. M. (1971) A model for stress wave propagation in composite materials. *Journal of Composite Materials* **5**, 140–162.
- Chhabildas, L. C. and Asay, J. R. (1982) Time-resolved wave profile measurements in copper to megabar pressures. In *High Pressure in Research and Industry—Volume I*, ed. C. M. Backman, T. Johanson and L. Tegner, pp. 183–189. Arkicktkopia, Uppsala, Sweden.
- Chhabildas, L. C., Wise, J. L. and Asay, J. R. (1982) Reshock and release behavior of beryllium. In *Shock Waves in Condensed Matter—1981*, ed. W. J. Nellis, L. Seaman and R. A. Graham, pp. 422–426. American Institute of Physics, New York.
- Grady, D. E. (1981) Strain-rate dependence of the effective viscosity under steady-wave shock compression. *Appl. Phys. Lett.* **38**, 825–826.
- Johnson, J. N. (1992) Calculation of path-dependent shock-wave hardening. *Journal of Applied Physics* **72**, 797–799.
- Johnson, J. N., Hixson, R. S. and Gray, G. T. (1994) Shock-wave compression and release of metal/ceramic composites. *Journal of Applied Physics* **76**, 5706–5718.
- Kanel', G. I., Ivanov, M. F. and Parshikov, A. N. (1995) Computer simulations of the heterogeneous materials response to the impact loading. *International Journal of Impact Engineering* **17**, 455–464.
- Klemans, P. G. (1965) Effects of thermal and phonon process in ultrasonic attenuation. In *Physical Acoustics—IIIB*, ed. W. P. Mason, pp. 201–234. Academic Press, New York.
- Knopoff, L. (1965) Attenuation of elastic waves in the earth. *Physical Acoustics—IIIB*, ed. W. P. Mason, pp. 287–324. Academic Press, New York.
- Knopoff, L. and Hudson, J. A. (1964) Scattering of elastic waves by small inhomogeneities. *J. Acous. Soc. Am.* **36**, 338–343.
- Mason, W. P. and McSkimin, H. J. (1947) Attenuation and scattering of high frequency sound waves in metal and glasses. *J. Acous. Soc. Am.* **19**, 464–473.
- Mineev, V. N. and Savinov, E. V. (1967) Viscosity and melting point of aluminum, lead and sodium chloride subjected to shock compression. *Sov. Phys. JETP* **25**, 411–416.
- Partom, Y. (1990) Understanding the Swegle–Grady fourth power relation. In *Shock Waves*

- in Condensed Matter*—1989, ed. S. C. Schmidt, J. N. Johnson and L. W. Davison, pp. 317–320. American Institute of Physics, New York.
- Rayleigh (1929) *Theory of Sound*. The Macmillan Company, New York.
- Rubin, M. B. (1990) Analysis of weak shocks in 6061-T6 aluminum. In *Shock Waves in Condensed Matter*—1989, ed. S. C. Schmidt, J. N. Johnson and L. W. Davison, pp. 321–328. American Institute of Physics, New York.
- Swegle, J. W. and Grady, D. E. (1985) Shock viscosity and the prediction of shock wave rise times. *Journal of Applied Physics* **58**, 692–701.
- Zel'dovich, Ya. B. (1946) Propagation of shock waves in a gas in the presence of a reversible chemical reaction. *Zh. Eksperiment. i Teor. Fiz.* **16**, 365–368.



Pergamon

J. Mech. Phys. Solids, Vol. 46, No. 10, pp. 2033–2047, 1998
© 1998 Elsevier Science Ltd. All rights reserved
Printed in Great Britain
0022-5096/98 \$—see front matter

PII: S0022-5096(98)00017-9

ELASTIC WAVE PROPAGATION THROUGH A MATERIAL WITH VOIDS

THOMAS W. WRIGHT*

Army Research Laboratory, Aberdeen Proving Ground, MD 21005, U.S.A.

(Received 20 December 1997; accepted in revised form 23 January 1998)

ABSTRACT

An exact mathematical analogy exists between plane wave propagation through a material with voids and axial wave propagation along a circular cylindrical rod with radial shear and inertia. In both cases the internal energy can be regarded as a function of a displacement gradient, an internal variable, and the gradient of the internal variable. In the rod the internal variable represents radial strain, and in the material with voids it is related to changes in void volume fraction. In both cases kinetic energy is associated not only with particle translation, but also with the internal variable. In the rod this microkinetic energy represents radial inertia; in the material with voids it represents dilatational inertia around the voids. Thus, the basis for the analogy is that in both cases there are two kinematic degrees of freedom, the Lagrangians are identical in form, and therefore, the Euler–Lagrange equations are also identical in form. Of course, the constitutive details and the internal length scales for the two cases are very different, but insight into the behavior of rods can be transferred directly to interpreting the effects of wave propagation in a material with voids. The main result is that just as impact on the end of a rod produces a pulse that first travels with the longitudinal wave speed and then transfers the bulk of its energy into a dispersive wave that travels with the bar speed (calculated using Young's modulus), so impact on the material with voids produces a pulse that also begins with the longitudinal speed but then transfers to a slower dispersive wave whose speed is determined by an effective longitudinal modulus. The rate of transfer and the strength of the dispersive effect depend on the details in the two cases. © 1998 Elsevier Science Ltd. All rights reserved.

Keywords: voids and inclusions, porous material, stress waves, asymptotic analysis.

INTRODUCTION

The response of a material with voids has been a subject for research for many years. MacKenzie (1950) was perhaps the first to estimate the effective elastic moduli of a linearly elastic isotropic material that contains a random distribution of small voids. His approach was to consider a hollow sphere, made of the matrix material in question, that is embedded in a continuum of isotropic material with the average properties of the material with voids. The hole in the center of the sphere was of such a size that the void ratio for the sphere was the same as the void ratio for the complete material with voids. This approach, now known as the self-consistent method, was an adaptation of a method introduced by Fröhlich and Sack (1946), in estimating the viscosity of dispersions. The method has been extended to include composites gen-

* Tel.: 00410-278-6046; Fax: 00410-278-6952; E-mail: tww@art.mil

erally and has been used many times since as reported by Christensen and Lo (1979), for example. Other examples, as well as other approaches for estimating the overall properties of heterogeneous solids, can be found in a recent book by Nemat-Nasser and Hori (1993).

The approach described above is essentially static in nature. Carroll and Holt (1972), who also used the device of an embedded hollow sphere, initiated a dynamic version of this line of research. They investigated the dynamics of pore collapse due to an imposed pressure and used the results to supplement the so-called $P-\alpha$ model, due to Herrmann (1969), for shock compression of a porous material. The most notable effect was to add inertia and plastic flow, associated in a spherically symmetric way with the pores, but no effect from the gradient of porosity was included. The dynamics of pore collapse seemed to add rate dependence to the flow law for the material.

In the same year as Carroll and Holt's paper Goodman and Cowin (1972) published a general continuum theory for a fluid-like material with voids that was intended to be applied to flows of a granular material. In this paper they introduced the notions of equilibrated stress, equilibrated body force, and equilibrated inertia. These concepts all arise in a natural way once it is conceived that the energy in the material may depend on the porosity and its gradient, as well as on the usual kinematic variables. In effect, for purposes of constructing a constitutive theory, the porosity is allowed to have kinematic freedom that is on a par and completely independent of the average deformation. As a consequence, generalized forces and inertia must be introduced to develop a continuum theory that is unrestricted in scope *a priori*.

Subsequently, Nunziato and Cowin (1979) published a fully general theory for a nonlinearly elastic, porous solid, where the porosity and its gradient enter into the constitutive theory with the same kinematic independence as in the theory for granular materials. The resulting continuum theory is very elegant in its mathematical structure and generality, but it seems to have lost touch with the equally elegant ideas on composites that were developing contemporaneously with it. Intuitively it would seem to make sense that in the static limit of uniform stress the general continuum theory should coincide with the theory of effective properties for composites, a material with voids being one degenerate form of a composite, but this connection between the two lines of research does not seem to have been pursued.

Another line of research that on its face would seem to be completely independent of all of the preceding was developed by Wright (1982) in a paper describing the nonlinear dynamics of a circular cylindrical rod with radial inertia and shear. When the axial and radial motions are assumed to be kinematically independent, but still describable in a simple manner to be given later, the energetic structure of the theory is formally identical to a one dimensional version of the dynamical theory for a material with voids. Thus, the Euler-Lagrange equations for the theory of axial motions in a rod have the same mathematical structure as those for plane waves in a material with voids. This fact was noted by Wright (1982) for the linearized versions of the two theories. The linear equations for the rod were first given by Mindlin and Herrmann (1950) and for the material with voids by Nunziato and Walsh (1977).

In this paper a model linear problem is set up and examined in order to demonstrate the relationship between theories of effective moduli and the dynamical theory of

materials with voids. It will also be shown that previous work on the dynamics of rods can be used as an intuitive guide to understanding the nature of the generalized forces and the response of a material with voids.

WAVES IN A HOLLOW CYLINDER: A MODEL PROBLEM

Imagine a material that contains a large number of small voids with random sizes and locations such that on average there are a constant number of N voids per unit total volume. If the fraction of each element of spatial volume that is occupied by voids is denoted φ_R , where $0 \leq \varphi_R < 1$, then the solid fraction is $1 - \varphi_R$. Imagine further that the size distribution of voids in each unit of volume is clustered around an average size with volume equal to that of a sphere of radius \bar{a} . Then the void ratio must be proportional to the total number of voids per unit volume times the cube of the average radius. That is, $\varphi_R \propto N\bar{a}^3$. Since another length, \bar{b} , may be defined by the relationship $\varphi_R = (\bar{a}/\bar{b})^3$, then it is clear that $\bar{b} \propto N^{-1/3}$ and that \bar{b} may be thought of as approximately half the average spacing between void centers. The length \bar{b} will be regarded as a fundamental characteristic of the porous material for dynamical problems.

The usual determination of the effective elastic moduli would proceed from this point by considering deformations of a hollow sphere that is made entirely from the matrix material and so has known elastic moduli, that has inner radius \bar{a} and outer radius \bar{b} , and that is embedded in an infinite continuum that is characterized by the unknown effective moduli of the porous material. For present purposes only motions that are uniaxial on average will be considered so rather than examining an embedded sphere, imagine a hollow cylinder with inner radius a and outer radius b , where now the void volume ratio is given by $\varphi_R = (a/b)^2$. Since there is no unique way to map the voids into empty cylinders, for simplicity it will be assumed that the cylindrical and spherical characteristic lengths are approximately equal, $b \approx \bar{b}$ so that $b/\bar{b} = O(1)$. For example, if it is assumed that the characteristic sphere of radius \bar{b} is replaced by a characteristic right circular cylinder of equal volume, and that the cylinder has radius b and height $2b$, then it is easily worked out that $b/\bar{b} = (2/3)^{1/3}$. To maintain the same void volume ratio the cylinder must be pierced by a tube of radius $a/\bar{a} = (2/3)^{1/3} \varphi_R^{1/3}$. Whereas the characteristic length washes out in the determination of effective static moduli, it plays an important role in a dynamical theory, as will be seen, so it is necessary to retain it in some form even though the exact value is only known approximately.

If the void volume ratio is small, it is plausible to suppose that propagation of longitudinal waves through the material with voids should be essentially equivalent to propagation along the hollow tube, just described. Clearly the inner surface of the tube must be stress free, but for symmetry and to reflect the dominantly longitudinal motions that are contemplated here, the outer surface should be assumed to have mixed boundary conditions with vanishing normal displacements and shear tractions. The motion of the hollow tube will be treated in a way that is similar to the way Mindlin and Herrmann (1950) treated motion in a solid rod.

With cylindrical material coordinates and time (R, Z, t) , the kinematics for the hollow tube will be assumed to have the approximate form

$$\mathbf{r}(R, Z, t) = \left[R - B(Z, t) \left(R - \frac{b^2}{R} \right) \right] \mathbf{e}_R + [Z + w(Z, t)] \mathbf{e}_Z \quad (1)$$

where the bold face type indicates vectorial quantities (\mathbf{r} is the position vector, and $\mathbf{e}_R, \mathbf{e}_Z$ are unit vectors) and the functions B and w are the two allowed scalar degrees of freedom. The radial displacement has been assumed to take the correct form for the one-dimensional static problem with vanishing displacement at $R = b$. Note that the kinematic function B is proportional to the change in porosity since

$$\varphi - \varphi_R = \frac{2\pi a u_r(R=a)}{\pi b^2} = 2B \left(1 - \frac{a^2}{b^2} \right) \quad \text{or} \quad B = \frac{1}{2} \frac{\varphi - \varphi_R}{1 - \varphi_R}$$

Since there are only axial and radial motions allowed, the strain tensor ε , when eqn (1) is used, works out to be

$$\begin{aligned} \varepsilon &= \begin{Bmatrix} \frac{\partial u_r}{\partial R} & 0 & \frac{1}{2} \frac{\partial u_r}{\partial Z} \\ 0 & \frac{u_r}{R} & 0 \\ \frac{1}{2} \frac{\partial u_r}{\partial Z} & 0 & \frac{\partial u_z}{\partial Z} \end{Bmatrix} \\ &= \begin{Bmatrix} -B \left(1 + \frac{b^2}{R^2} \right) & 0 & -\frac{1}{2} B_Z \left(R - \frac{b^2}{R} \right) \\ 0 & -B \left(1 - \frac{b^2}{R^2} \right) & 0 \\ -\frac{1}{2} B_Z \left(R - \frac{b^2}{R} \right) & 0 & w_Z \end{Bmatrix} \end{aligned} \quad (2)$$

For an isotropic linearly elastic material the constitutive relation in Cartesian tensor notation is $\sigma_{ij} = \lambda e_{kk} \delta_{ij} + 2\mu e_{ij}$ or in terms of the assumed degrees of freedom

$$\begin{aligned} \sigma_{rr} &= \lambda w_Z - 2(\lambda + \mu)B - 2\mu \left(\frac{b}{R} \right)^2 B \\ \sigma_{\theta\theta} &= \lambda w_Z - 2(\lambda + \mu)B + 2\mu \left(\frac{b}{R} \right)^2 B \\ \sigma_{zz} &= (\lambda + 2\mu)w_Z - 2\lambda B \\ \sigma_{rz} &= -\mu \left(R - \frac{b^2}{R} \right) B_Z \end{aligned} \quad (3)$$

where λ and μ are the Lamé coefficients. There are only four nonzero components of the stress tensor, so the equations of motion in cylindrical components take the form

$$\begin{aligned}\frac{\partial \sigma_{rr}}{\partial R} + \frac{\partial \sigma_{rz}}{\partial Z} + \frac{\sigma_{rr} - \sigma_{\theta\theta}}{R} &= \rho \ddot{u}_r \\ \frac{\partial \sigma_{rz}}{\partial R} + \frac{\partial \sigma_{zz}}{\partial Z} + \frac{\sigma_{rz}}{R} &= \rho \ddot{u}_z\end{aligned}\quad (4)$$

Furthermore, since the displacement, strain, and stress relations will be approximate in the radial coordinate, except for the case of static uniaxial deformations, the equations of motion will only be required to hold in an appropriate average sense. Specifically eqn (4.2) will be averaged over the full cross sectional area of the hollow tube,

$$\frac{\partial}{\partial Z} \left(\frac{1}{\pi b^2} \int \sigma_{zz} dA \right) + \frac{1}{\pi b^2} \int_a^b 2\pi R \frac{1}{R} \frac{\partial}{\partial R} (R \sigma_{rz}) dR = \frac{\rho}{\pi b^2} \int \ddot{w} dA \quad (5)$$

and eqn (4.1) will first be multiplied by R and then averaged over the full cross section.

$$\frac{\partial}{\partial Z} \left(\frac{1}{\pi b^2} \int R \sigma_{rz} dA \right) + \frac{1}{\pi b^2} \int R \frac{1}{R} \frac{\partial}{\partial R} (R \sigma_{rr}) dA - \frac{1}{\pi b^2} \int \sigma_{\theta\theta} dA = \frac{\rho}{\pi b^2} \int R \ddot{u}_r dA \quad (6)$$

Equations (5) and (6) may be rewritten as

$$\begin{aligned}\frac{\partial S}{\partial Z} + 2 \frac{bZ_b - aZ_a}{b^2} &= \rho \left(1 - \frac{a^2}{b^2} \right) \ddot{w} \\ \frac{\partial Q}{\partial Z} - P + 2 \frac{b^2 R_b - a^2 R_a}{b^2} &= \frac{\rho b^2}{2} \left(1 - \frac{a^2}{b^2} \right)^2 \ddot{B}\end{aligned}\quad (7)$$

where S is the average stress over the whole tube, P is the average over the tube of the sum of radial and circumferential stresses, Q is the polar moment of radial shearing stress and $R_{a,b}$, $Z_{a,b}$ are radial and shear tractions on the inner and outer surfaces of the tube. That is

$$\begin{aligned}S &= \frac{1}{\pi b^2} \int \sigma_{zz} dA \\ P &= \frac{1}{\pi b^2} \int (\sigma_{rr} + \sigma_{\theta\theta}) dA \\ Q &= \frac{1}{\pi b^2} \int R \sigma_{rz} dA\end{aligned}\quad (8)$$

and $R_a = \sigma_{rr}(a, t)$, $Z_b = \sigma_{rz}(b, t)$, etc. Both components of traction have been assumed to vanish on the inner surface, and the shearing traction has been assumed to vanish on the outer surface, so that only the radial traction on the outer surface remains.

The surface tractions that appear in eqns (7.1) and (7.2) after integration by parts play the role of "equilibrated body forces" to use the language of Cowin and coworkers (e.g. see Nunziato and Cowin (1979)). A body force is usually thought of as being externally controlled, as would be the case in eqn (7) if the tractions were prescribed. But in the case considered here, three out of four possible components of traction have been assumed to vanish and the remaining one is a reaction that must take on the values necessary to prevent radial displacement on the outer surface. As shown by eqn (3.1) the radial stress that is compatible with vanishing radial displacement at $R = b$ depends on the strain in the tube as expressed by $w_z(Z, t)$ and $B(Z, t)$. Thus, in this case the "equilibrated body force" depends on constitutive information in the matrix material, but it is in the nature of a workless constraint for the tube. Equation (3.4) shows that the shear traction also vanishes on the outer surface, as required.

When the constitutive relations, as expressed approximately by eqn (3), are substituted into eqns (8) and (7), the displacement form of the equations of motion becomes

$$(\lambda + 2\mu)w_{zz} - 2\lambda B_z = \rho \ddot{w}$$

$$\mu B_{zz} + \frac{4}{(b^2 - a^2)^2} \{ \lambda a^2 w_z - 2[\lambda a^2 + \mu(a^2 + b^2)]B \} = \rho \ddot{B} \quad (9)$$

If the kinematical assumption had been $\mathbf{r}(R, Z, t) = R[1 + \psi(Z, t)]\mathbf{e}_R + [Z + w(Z, t)]\mathbf{e}_z$, rather than eqn (1), then the procedure described above would have produced the Mindlin-Herrmann (1950) equations of motion for a solid rod with traction free sides,

$$(\lambda + 2\mu)w_{zz} + 2\lambda\psi_z = \rho \ddot{w}$$

$$\mu\psi_{zz} - \frac{4}{b^2} \{ \lambda w_z + 2(\lambda + \mu)\psi \} = \rho \ddot{\psi} \quad (10)$$

The function $\psi(Z, t)$ has the interpretation of lateral strain in the solid rod. Clearly eqns (9) and (10) are very closely related, as is to be expected. (The relationship is clearer if B is replaced by $-B$ in eqn (9).)

The linearized continuum theory for longitudinal wave propagation in a solid material with voids, as given by Nunziato and Walsh (1977), takes the form

$$\bar{E}w_{zz} + \bar{\mu}\eta_z = \rho \ddot{w}$$

$$\alpha\eta_{zz} - (\bar{\mu}w_z + \rho\beta\eta) = \rho k \ddot{\eta} \quad (11)$$

and again the similarity to either eqns (9) or (10) is striking. In (11) $w(Z, t)$ is the translation of the matrix material in the Z direction, and $\eta(Z, t)$ is the change in void volume ratio. The coefficients \bar{E} and $\bar{\mu}$ are simply generic coefficients in a quadratic expansion of internal energy. Although they have the dimensions of *stress*, in the theory they are *a priori* unrelated to the Young's modulus or the shear modulus of

the matrix material. The modulus α has dimensions $\text{stress}(\text{length})^2$, and for consistency β and k must have dimensions $(\text{velocity})^2$ and $(\text{length})^2$, respectively. (In their original paper β , as used here, appears as $-\beta$. The change of sign is preferable for indicating stability of waves, as will be shown below.)

By cross differentiation each of the three systems of eqns (9), (10), or (11) may be put in the form

$$\mathcal{L}w = 0 \quad (12)$$

where \mathcal{L} is a linear operator,

$$\mathcal{L} = \left(c_1^2 \frac{\partial^2}{\partial Z^2} - \frac{\partial^2}{\partial t^2} \right) \left(c_2^2 \frac{\partial^2}{\partial Z^2} - \frac{\partial^2}{\partial t^2} \right) - \Gamma \left(c^2 \frac{\partial^2}{\partial Z^2} - \frac{\partial^2}{\partial t^2} \right) \quad (13)$$

and c_1 , c_2 , and c are all wave speeds.

All three systems have the same identical mathematical structure provided only that in each case the nondimensional coupling coefficient Γ has the same sign and the three wave speeds are ordered in the same way. From the form of eqn (13) it is clear that the characteristic speeds, that is, the speeds that can carry discontinuities, are $\pm c_1$ and $\pm c_2$. For the rod or the hollow tube $c_1^2 = (\lambda + 2\mu)/\rho$ and $c_2^2 = \mu/\rho$, which are the bulk longitudinal and shear speeds in the matrix material, but for the generic continuum with voids, $c_1^2 = \bar{E}/\rho$ and $c_2^2 = \alpha/\rho k$. The continuum theory does not indicate which wave speed is the greater, but it would also be reasonable to associate them with the bulk longitudinal and shear speeds. (Imagine a three-dimensional problem where a longitudinal wave passes through a material with distributed point scatterers. By Huygens' principle each scatterer would be the source of both longitudinal and shear waves, so it is natural to expect that a purely longitudinal pulse will generate secondary shear waves, and therefore, that the smaller characteristic speed in the reduced theories should be associated with the bulk shear speed.) Since eqn (11.1) indicates that c_1 should be associated with predominantly longitudinal motions, it will be assumed that in every case $c_1 > c_2$.

The wave operator (13) exhibits a hierarchy of wave speeds in Whitham's terminology, Whitham (1974). It was shown by Wu (1961) that for such a system to be stable, in the sense that no harmonic wave component can grow exponentially in time, it is required that $\Gamma > 0$ and $c > c_1$. (Whitham actually treated the stability of a slightly different wave system, and Wu extended the analysis to systems that include (13). The implications for the present case are as stated.) For the three cases

$$\Gamma = \begin{cases} \frac{8c_2^2}{(1-2\nu)b^2}; & \text{solid rod} \\ \frac{8(1-2\nu+\varphi_R)c_2^2}{(1-2\nu)(1-\varphi_R)^2b^2}; & \text{hollow rod} \\ \frac{\beta}{k}; & \text{continuum} \end{cases} \quad (14)$$

$$\rho c^2 = \begin{cases} 2\mu(1+v); & \text{solid rod} \\ 2\mu \frac{1-v+(1+v)\varphi_R}{1-2v+\varphi_R}; & \text{hollow rod} \\ \bar{E} - \frac{\bar{\mu}^2}{\rho\beta}; & \text{continuum} \end{cases} \quad (15)$$

where Poisson's ratio for the matrix material is given by $v = \lambda/2(\lambda + \mu)$. Wu's stability conditions are always met for the solid or the hollow rod. For the continuum they are met if $\beta > 0$ and $k > 0$, but for his theorem to apply at all, it is also required that $\bar{E} > \bar{\mu}^2/\rho\beta$. It will be assumed that this last condition holds, as well, since if it did not, disturbances with small enough wave numbers (long wavelengths) would have complex frequencies, implying exponential growth.

The lower wave speed, c , for the solid rod will be recognized as the bar speed, which is determined by Young's modulus, $E = 2(1+v)\mu$. For the hollow rod c depends on the void ratio φ_R , as is to be expected. As φ_R tends to zero, c tends to the bulk longitudinal speed, which is also reasonable. But as φ_R tends to one, c tends to the longitudinal speed for plane stress. This limit is reasonable for a thin walled tube whose outer surface cannot expand, but the thin walled tube itself is not a reasonable approximation for a material with a large void volume. Therefore, henceforward it will always be assumed that φ_R is small unless explicitly stated otherwise.

BEHAVIOUR OF SOLUTIONS TO $\mathcal{L}_W = 0$

Static solutions to eqn (12) are those that correspond to $S = \text{const}$, $P = \text{const}$, and $Q = 0$. (There are also static solutions where $Q \neq 0$, but these turn out to have boundary layers and will be ignored here.) Stated in another way, solutions are static when w_Z and either B , ψ , or η are constant. Then eqns (9.2), (10.2), or (11.2) may be solved for B , ψ , or η in terms of w_Z , and the effective static longitudinal modulus, L_S , may be found by examining the ratio S/w_Z . The result is

$$L_S = \begin{cases} \lambda + 2\mu + 2\lambda \frac{\psi}{w_Z} = 2\mu(1+v); & \text{solid rod} \\ \lambda + 2\mu - 2\lambda \frac{B}{w_Z} = 2\mu \frac{1-v+(1+v)\varphi_R}{1-2v+\varphi_R}; & \text{hollow rod} \\ \bar{E} + \bar{\mu} \frac{\eta}{w_Z} = \bar{E} - \frac{\bar{\mu}^2}{\rho\beta}; & \text{continuum} \end{cases} \quad (16)$$

The reader will immediately recognize that the lower order wave speed, or sub-characteristic wave speed, as it is also called, is determined by the static longitudinal modulus since the right-hand-sides of eqns (15) and (16) are identical. Wu's stability condition, $c < c_1$, corresponds to the physical statement that the effective longitudinal modulus is less than the longitudinal modulus of the matrix material. This is to be

expected, of course, because the presence of voids contributes some extra strain for the same applied stress and therefore increases the compliance. It will also be noted that the extra stability condition for the continuum, $\bar{E} > \bar{\mu}^2/\rho\beta$, is just the reasonable physical condition that the static longitudinal modulus should be positive.

It remains to describe the typical behavior of eqn (12) for a given typical disturbance. Let it be supposed that $c_1 > c > c_2$ (always true for eqns (9) and (10), and also expected to be true for (11) for small enough void volume ratios) and consider an initial boundary value problem where the medium is quiescent at $t = 0$. Let a step in longitudinal velocity be applied at time $t = 0$ to the boundary $Z = 0$, and calculate the response in the interior of the medium as a wave propagates off to infinity. Since the equations are linear, the interior response for other velocity histories at the boundary may then be calculated by convolution. Because of the exact mathematical analogy among the three physical problems, it is only necessary to consider one of them, say the case of the solid rod, where existing insight may be used to guide the analysis. Results for the rod may then be applied to the other cases directly, with only a change in interpretation of the physical constants.

Perhaps the most straightforward approach is to use the Laplace transform. Since this was worked out by Wright (1982), the details will not be repeated here, and only a brief summary follows. With boundary conditions $\dot{w}(0, t) = \dot{w}_0 h(t)$ and $\psi_Z(0, t) = 0$ ($h(t)$ is the Heavyside step function and \dot{w}_0 is an arbitrary constant), and with initial conditions $w(Z, 0) = \psi(Z, 0) = 0$, it was shown that an asymptotic representation for \dot{w} near the leading wavefront is

$$\frac{\dot{w}}{\dot{w}_0} \sim e^{-r_1 Z/b} + \frac{r_1 Z}{b} \int_b^\infty \frac{J_1(\gamma) d\gamma}{\sqrt{\gamma^2 - r_1^2} \sqrt{\gamma^2 + (r_1 Z/b)^2}}, \quad c_1 t \geq Z \quad (17)$$

where $r_1^2 = 8(c_1^2 - c^2)/c_1^2$. Equation (17) is shown plotted in Fig. 1. Note that the height of the step at the wave front remains constant, but that the magnitude of the particle velocity drops off rapidly behind the front, and the greater the distance from the origin, the more rapid the rate of decrease.

With the identity (e.g. see Bowman (1958))

$$\int_0^\infty \frac{J_1(\gamma) d\gamma}{\sqrt{\gamma^2 + \eta^2}} = \frac{1 - e^{-\eta}}{\eta} \quad (18)$$

and expansion of the Bessel function for small values of its argument, eqn (17) can be shown to give

$$\frac{\dot{w}}{\dot{w}_0} \sim 1 - 4 \left(1 - \frac{c^2}{c_1^2} \right) \frac{Z}{b} \frac{c_1 t - Z}{b} + \dots, \quad c_1 t - Z \geq 0 \quad (19)$$

Equation (19) shows the same trend as Fig. 1, and in addition it shows that the rate of decrease behind the front is greater as the ratio c/c_1 decreases. For the three cases the effect of the velocity ratio is given by

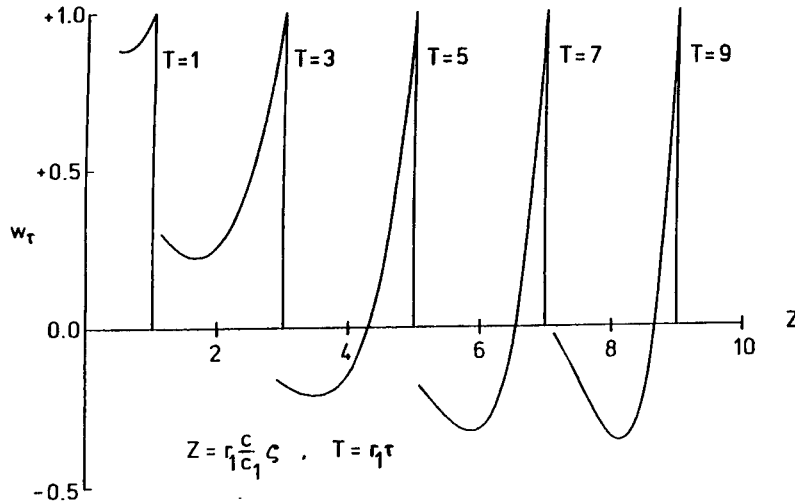


Fig. 1. Dispersion in the leading wave, as calculated from eqn (17). (Taken from Wright (1982). Reproduced with kind permission from Kluwer Academic Publishers.)

$$\frac{c_1^2 - c^2}{c_1^2} = \begin{cases} \frac{2v^2}{1-v}; & \text{solid rod} \\ \frac{2v^2 \varphi_R}{(1-v)(1-2v+\varphi_R)}; & \text{hollow rod} \\ \frac{\mu^2}{\rho \beta \bar{E}}; & \text{continuum} \end{cases} \quad (19a)$$

In an elastic bar, as is well known, the main pulse travels with the lower order wave speed that is determined by Young's modulus. The asymptotic response near $Z = ct$ can also be found from the Laplace transform (e.g. see Wright (1982)), but another, more intuitive approach, explained by Whitham (1974), may also be adapted for use here. Since a nondispersing and forward propagating wave with speed c can be described by the equation $(\partial/\partial Z + c^{-1}\partial/\partial t)\phi = 0$, as an approximation for the dispersive wave, set $\partial/\partial Z = -c^{-1}\partial/\partial t$ in all parts of eqn (13) except the forward wave operator with speed c itself. Then eqn (12) becomes

$$\left[\left(\frac{c_1^2}{c^2} - 1 \right) \left(\frac{c_2^2}{c^2} - 1 \right) \frac{\partial^3}{\partial t^3} + 2\Gamma \left(c \frac{\partial}{\partial Z} + \frac{\partial}{\partial t} \right) \right] \dot{w} = 0 \quad (20)$$

and with the change of variables $\phi = t - Z/c$ and $\xi = Z$ it finally becomes

$$\left(\frac{\partial^3}{\partial \phi^3} - r^3 c^3 \frac{\partial}{\partial \xi} \right) \dot{w} = 0, \quad \text{where } r^3 = \frac{2\Gamma c^2}{(c_1^2 - c^2)(c^2 - c_2^2)} \quad (21)$$

Note that $r^3 > 0$ by assumption concerning the ordering of the three wave speeds. Also since Γ has dimensions $(\text{time})^{-2}$, r^3 has dimensions $(\text{length})^{-2}$.

A similarity solution to eqn (21) may be found by setting $x = \phi \xi^{-1/3}$, which reduces it to Airy's equation

$$\left(\frac{d^2}{dx^2} + \frac{1}{3} r^3 c^3 x \right) \frac{d\dot{w}}{dx} = 0 \quad (22)$$

The solution to eqn (22) that vanishes as $\phi \rightarrow -\infty$ far ahead of the wave is

$$\frac{d\dot{w}}{dx} = CAi(-3^{-1/3} r c x) \quad (23)$$

where C is an arbitrary constant. After integration on x and adjustment of the constant, the solution is

$$\dot{w} = \dot{w}_0 \int_{-\infty}^{\psi} Ai(-\zeta) d\zeta, \quad \text{where } \psi = \frac{rc(t-Z/c)}{(3Z)^{1/3}} \quad (24)$$

Equation (24) is the same as the result given by asymptotic expansion of the solution by Laplace transform in Wright (1982) and is shown in Fig. 2. Note the familiar dispersive waveform with the Pochhammer-Chree ringing about the unit step. The scale of the risetime in the dispersive front is determined by $(3Z)^{1/3}/rc$, which is another familiar result for wave propagation in a bar. Although the exact numerical values of the constants here may vary somewhat from the three-dimensional result, the form is

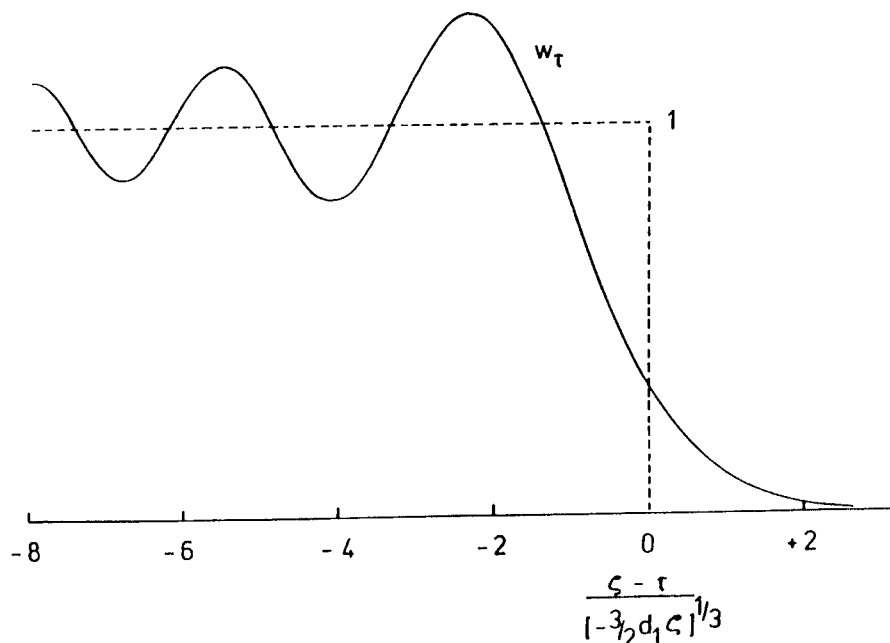


Fig. 2. Dispersion in the main pulse, as calculated from eqn (24). (Taken from Wright (1982). Reproduced with kind permission from Kluwer Academic Publishers.)

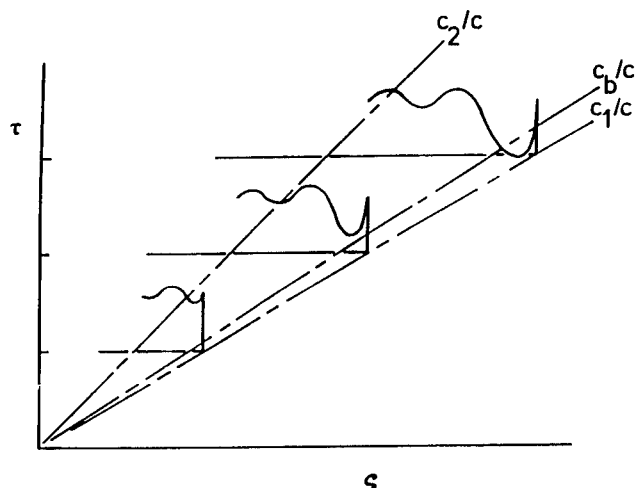


Fig. 3. Composite sketch showing expected separation of leading wave and main pulse. (Taken from Wright (1982). Reproduced with kind permission from Kluwer Academic Publishers.)

identical. Equation (24) may be rewritten so that b is the natural length scale for Z , just as it is in eqn (19). Figure 3 shows a composite sketch of the expected waveform when both (17) and (24) are taken into account. As time progresses, the discontinuous front and the main pulse should separate from one another, and the leading spike should become thinner and thinner. An example of this behavior, actually calculated for the continuum theory by Nunziato and Walsh (1977), is shown in Fig. 4. In their calculation the wave speeds satisfy the ratios $(c_2/c_1)^2 = 0.55$ and $(c/c_1)^2 = 0.81$ so the three speeds are ordered as assumed. Since $c = 0.9c_1$, the separation between the distinctive parts of the response does not occur very rapidly with distance of propagation, but the formation of the spike and the developing dispersive waveform are clearly evident.

Solutions for the hollow tube or the continuum with voids follow exactly the same pattern, but with differing numerical constants. Characteristic speeds were discussed following eqn (13), and the lower order or subcharacteristic speeds were given in eqn (15). The scaling parameter r^2 for the three cases works out to be

$$r^3 = \begin{cases} \frac{8}{b^2} \frac{1+v}{v^2(1+2v)}; & \text{solid rod} \\ \frac{8}{b^2} \frac{(1-2v+\varphi_R)^2}{v^2\varphi_R(1-\varphi_R)^2} \frac{1-v+(1+v)\varphi_R}{1+(1+2v)\varphi_R}; & \text{hollow rod} \\ \frac{(\rho\beta)^2}{k\bar{\mu}^2} \left(1 - \frac{\alpha/k\rho}{\bar{E} - \bar{\mu}^2/\rho\beta}\right)^{-1}; & \text{continuum} \end{cases} \quad (25)$$

Since risetime decreases as r increases, the dispersive wave reduces to a step pulse as $r \rightarrow \infty$. For both the solid and the hollow rods this happens when $v \rightarrow 0$, but then $c \rightarrow$

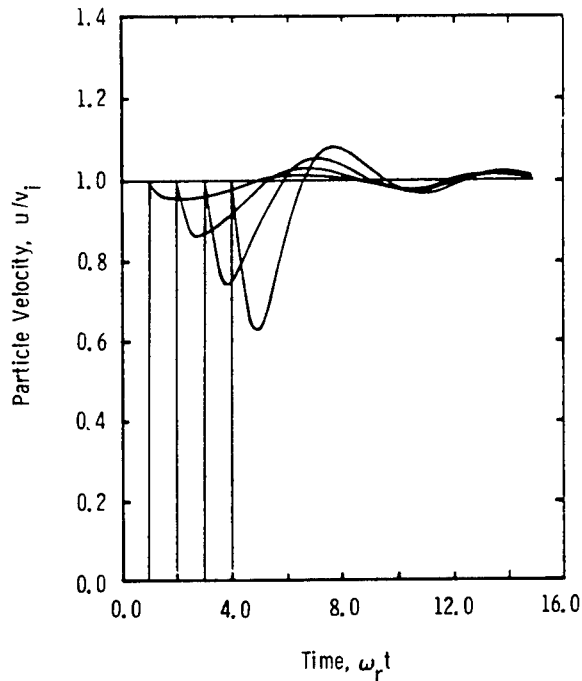


Fig. 4. Particle velocity vs time at four stations, as calculated by Nunziato and Walsh (1977). The cutoff frequency ω_r is calculated from $\omega_r^2 = \Gamma$ in present terminology. (Reproduced with kind permission from ASME.)

c_1 at the same time. For the hollow rod $c \rightarrow c_1$ also when $\phi_R \rightarrow 0$. For all of these cases the leading and dispersive waves coincide so the limiting behavior of the dispersive wave is to be expected. Similarly for the continuum, as $c \rightarrow c_2$, the term in parentheses vanishes, and the dispersive wave becomes a step wave.

DISCUSSION

Three physical systems have been shown to be described by the same linear partial differential equations. The case of the solid rod is well understood and can therefore be used as a guide to understanding the other two. The hollow rod, if regarded as a model problem that approximates the continuum with voids, shows how a small void volume fraction gives rise to a dispersive wave that is entirely analogous to the bar wave. Finally, the continuum theory of a material with voids shows that in general the analogy with the bar wave should hold true.

The main point to be recognized is that in systems of the kind described in this paper it is the lower order or subcharacteristic wave speed that carries the dominant energy pulse, but that it takes time and distance, possibly many characteristic lengths, for the dispersive wave to establish itself. The key parameters in determining the

decay of the leading spike are readily apparent in eqn (19). They are the relative difference between squares of wave speeds, given in eqn (19a), and the characteristic length scale. Obviously the porosity has a large influence on the rate of decay. Similarly the main features of the dispersive wave are determined by the parameters r , as determined from eqn (21) or (25), and the characteristic length scale. Again the porosity obviously has a large influence.

The wave profiles will be further modified if there is a finite rise time in the input velocity at the boundary. Since the solution in that case is a convolution with the response to a step load, the effect will be to clip the leading spike. The resulting wave profile may then be easily confused with a profile that results from a rate effect in the constitutive behavior of the material. To put it another way, when there are both rate and dispersive effects present, it may be extremely difficult in an experiment to separate the two without taking appropriate precautions.

Cowin and Nunziato (1983) suggested that with regard to the relationship between a continuum theory of a material with voids and the effective moduli calculations for porous materials, they are "... complementary, each being able to accomplish something the other cannot". Here it has been shown how the two approaches may be blended together so as to get the effects of both simultaneously. Although the model problem of the hollow rod, embedded in an equivalent continuum, has obvious limitations as a physical surrogate for a continuum with voids, it serves admirably to show the mathematical relationship between the solid rod and the continuum with voids.

REFERENCES

- Bowman, F. (1958) *Introduction to Bessel Functions*, p. 64, Dover, New York.
- Carroll, M. M. and Holt, A. C. (1972) Static and dynamic pore-collapse relations for ductile materials. *J. Appl. Phys.* **43**, 1626–1636.
- Christensen, R.M. and Lo, K.H. (1979) Solutions for effective shear properties in three phase sphere and cylinder problems. *J. Mech. Phys. Solids* **27**, 315–330.
- Cowin, S. C. and Nunziato, J.W. (1983) Linear elastic materials with voids. *J. Elasticity* **13**, 125–147.
- Fröhlich, H. and Sack, R. (1946) Theory of the rheological properties of dispersions. *Proc. Roy. Soc. Lond. Ser. A* **185**, 415–430.
- Goodman, M.A. and Cowin, S. C. (1972) A continuum theory for granular materials. *Arch. Rational Mech. Anal.* **44**, 249–266.
- Herrmann, W. (1969) Constitutive equation for the dynamic compaction of ductile porous materials. *J. App. Phys.* **40**, 2490–2499.
- MacKenzie, J.K. (1950) The elastic constants of a solid containing spherical holes. *Proc. Phys. Soc.* **B63**, 2–11.
- Mindlin, R. D. and Herrmann, G. (1950) A one-dimensional theory of compressional waves in an elastic rod. *Proc. 1st U.S. Nat. Cong. Appl. Mech.* 187–191.
- Nemat-Nasser, S. and Hori, M. (1993) *Micromechanics: Overall Properties of Heterogeneous Materials*. North-Holland, Amsterdam.
- Nunziato, J. W. and Cowin, S. C. (1979) A nonlinear theory of elastic materials with voids. *Arch. Rational Mech. Anal.* **72**, 175–201.
- Nunziato, J. W. and Walsh, E. K. (1977) Small-amplitude wave behavior in one-dimensional granular solids. *J. Appl. Mech.* **44**, 559–564.

- Whitham, G. B. (1974) *Linear and Nonlinear Waves*. Wiley, New York.
- Wright, T. W. (1982) Nonlinear waves in rods. In *Proc. of the IUTAM Symp. on Finite Elasticity*, ed. D. E. Carlson, and R. T. Shield, pp. 423–443. Martinus Nijhoff, The Hague.
- Wu, T. T. (1961) A note on the stability condition for certain wave propagation problems. *Comm. On Pure and Appl. Math.* **14**, 745–747.



Pergamon

J. Mech. Phys. Solids, Vol. 46, No. 10, pp. 2049–2068, 1998
© 1998 Elsevier Science Ltd. All rights reserved
Printed in Great Britain
0022-5096/98 \$—see front matter

PII: S0022-5096(98)00018-0

THE MECHANICS OF SIZE-DEPENDENT INDENTATION

MATTHEW R. BEGLEY^a and JOHN W. HUTCHINSON^{*,b}

^aDepartment of Mechanical Engineering, University of Connecticut, Storrs, CT 06269-3139, U.S.A.

^bDivision of Engineering and Applied Sciences, Harvard University, Cambridge, MA 02138, U.S.A.

(Received 20 December 1997; in revised form 23 January 1998)

ABSTRACT

Indentation tests at scales on the order of one micron have shown that measured hardness increases significantly with decreasing indent size, a trend at odds with the size-independence implied by conventional plasticity theory. In this paper, strain gradient plasticity theory is used to model materials undergoing small-scale indentations. Finite element implementation of the theory as it pertains to indentation modeling is briefly reviewed. Results are presented for frictionless conical indentations. A strong effect of including strain gradients in the constitutive description is found with hardness increasing by a factor of two or more over the relevant range of behavior. The results are used to investigate the role of the two primary constitutive length parameters in the strain gradient theory. The study indicates that indentation may be the most effective test for measuring one of the length parameters. © 1998 Elsevier Science Ltd. All rights reserved.

Keywords: A. indentation and hardness, B. elastic-plastic material, C. finite elements.

1. INTRODUCTION

Indentation tests have been used extensively to characterize the plastic properties of solids. Historically, one of the primary goals of indentation testing has been to estimate the yield stress by measuring the hardness, defined as the load on the indenter divided by the area of the resulting impression (e.g. Atkins and Tabor, 1965; Johnson, 1970; Rubenstein, 1981). Recently, hardness has been shown to be size-dependent when the width of the impression is below about fifty microns. Such small-scale experiments are often referred to as micro-indentation tests (or nano-indentation tests at the sub-micron scale) and have become a popular method of illustrating the size-dependence of plastic deformation (Gane and Cox, 1970; Pethica *et al.*, 1983; Doerner and Nix, 1986; Samuels, 1986; Stelmashenko *et al.*, 1993; Atkinson, 1995; Ma and Clark, 1995; Poole *et al.*, 1997). The measured hardness may double or even triple as the size of indent decreases from about fifty microns to one micron. In effect, the smaller the scale the stronger the solid. This is a large effect which almost certainly has significant implications for other applications of metal plasticity at the micron scale. A size-dependence of indentation hardness is not encompassed by conventional plasticity. Simple arguments, based on dimensional analysis, reveal that any plasticity

*To whom correspondence should be addressed. E-mail: hutchinson@husm.harvard.edu

theory which does not contain a constitutive length parameter will predict size-independent indentation hardness.

Recently, new plasticity theories containing constitutive length scales have been developed to characterize size-dependent plastic deformation (e.g. Fleck and Hutchinson, 1993, 1996; Acharya and Bassini, 1996, 1997). Micro-hardness tests are thought to provide an effective method for characterizing a material's flow response at small length scales. By correlating an indentation solution for a given theory with test data in the size-dependent range, one should be able to infer values of the constitutive length parameters, in much the same way as the macroscopic hardness test is used to measure flow stress.

In this paper, the Fleck–Hutchinson (1997) strain gradient plasticity theory has been used to determine the effect of the material length scale on predicted hardness for small indents. Prior to this work, only one attempt appears to have been made to analyze the size-dependence of micro-hardness tests with a continuum theory of strain gradient plasticity. Shu and Fleck (1996) applied an earlier version of the plasticity theory that accounts for contributions of rotation gradients to hardening but not of stretch gradients. They found that a version of the theory based on rotation gradients alone cannot account for the strong size-dependence observed experimentally. In part, their finding provides the motivation for the present work which extends the study to include the role of stretch gradients. In addition, contact will be made between the present results and predictions from dislocation-based models of micro-indentation size-dependence by Ma and Clarke (1995), Brown (1997) and Nix (1997).

The constitutive behavior and its finite element implementation are first briefly reviewed. Results are then presented for conical indentation without friction. The two primary goals of this paper are: (a) to assess the effectiveness of strain gradient plasticity theory in accounting for the strong size-dependence observed in indentation tests; and (b) to infer values of the constitutive length parameters via correlation of the mechanics results with experimental data available in the literature.

2. CONSTITUTIVE DESCRIPTION

The constitutive behavior of the material is described within the context of small strains and small rotations. A deformation theory version of strain gradient plasticity is used here in the form given by Fleck and Hutchinson (1997). The formulation is for a small strain, non-linear elastic solid, where both strain and strain gradients contribute to the strain energy density. It falls within the general class of solids considered by Toupin (1962) and Mindlin (1965). Interpretation of the strain gradient contribution to strain hardening in terms of the connection of strain gradients to the generation of geometrically necessary dislocations has been discussed by Fleck *et al.* (1994).

The strain tensor is defined in terms of the displacements u_i in the usual manner, that is $\varepsilon_{ij} = \frac{1}{2}(u_{i,j} + u_{j,i})$. The second gradient of the displacement vector is defined as $\eta_{ijk} = u_{k,ij}$; it can be expressed in terms of the strain gradients as $\eta_{ijk} = \varepsilon_{jk,i} + \varepsilon_{ik,j} - \varepsilon_{ij,k}$. The effective strain measure introduced below is taken to be a function of only the deviatoric parts of the strain and strain gradient tensors, defined as

$$\varepsilon'_{ij} = \varepsilon_{ij} - \frac{1}{3} \delta_{ij} \varepsilon_{kk} \quad (1a)$$

$$\eta'_{ijk} = \eta_{ijk} - \frac{1}{4} (\delta_{ik} \eta_{jpp} + \delta_{jk} \eta_{ipp}) \quad (1b)$$

such that $\eta'_{ikk} = 0$. Non-zero deviatoric strain gradients for the general axisymmetric case are given in terms of the displacements in the Appendix. Smyshlaev and Fleck (1995) showed that the deviatoric strain gradient tensor could be decomposed into three unique, mutually orthogonal third order deviatoric tensors according to $\eta'_{ijk} = \eta_{ijk}^{(1)} + \eta_{ijk}^{(2)} + \eta_{ijk}^{(3)}$, where $\eta_{ijk}^{(m)} \eta_{ijk}^{(n)} = 0$ for $m \neq n$ and each tensor preserves the properties $\eta_{ijk}^{(n)} = \eta_{jik}^{(n)}$ and $\eta_{ikk}^{(n)} = 0$. The steps required to carry out this decomposition are also given in the article by Fleck and Hutchinson (1997).

The effective strain measure used to define the deformation theory is taken to be the isotropic invariant

$$E_e^2 = \frac{2}{3} \varepsilon'_{ij} \varepsilon'_{ij} + l_1^2 \eta_{ijk}^{(1)} \eta_{ijk}^{(1)} + l_2^2 \eta_{ijk}^{(2)} \eta_{ijk}^{(2)} + l_3^2 \eta_{ijk}^{(3)} \eta_{ijk}^{(3)}. \quad (2)$$

The first term in (2), $\frac{2}{3} \varepsilon'_{ij} \varepsilon'_{ij}$, is the invariant used to form the classical J_2 deformation theory, and the strain gradient theory reduces to the classical theory in the limit in which the strain gradients are small. The three invariants of the strain gradients in (2) represent the most general dependence on the deviatoric strain gradient tensor that is isotropic and homogeneous of degree two. The contribution is positive definite when the three length quantities, l , are each non-zero. These lengths are the new constitutive parameters in the theory.

It is instructive to write the effective strain in a form which reveals more explicitly its dependence on rotation gradients. With the rotation as $\theta_i = \frac{1}{2} e_{ijk} u_{k,j}$, where e_{ijk} is the permutation tensor, define $\chi_{ij} = \theta_{i,j} = e_{ipk} e'_{kjp}$ as the rotation gradient. As Fleck and Hutchinson (1997) have noted, the second and third of the above strain gradient invariants depend only on the rotation gradients:

$$\eta_{ijk}^{(2)} \eta_{ijk}^{(2)} = \frac{4}{3} \chi_{ij} \chi_{ij} + \frac{4}{3} \chi_{ij} \chi_{ji} \quad \text{and} \quad \eta_{ijk}^{(3)} \eta_{ijk}^{(3)} = \frac{8}{5} \chi_{ij} \chi_{ij} - \frac{8}{5} \chi_{ij} \chi_{ji} \quad (3)$$

Thus, an equivalent alternative expression to (2) is

$$E_e^2 = \frac{2}{3} \varepsilon'_{ij} \varepsilon'_{ij} + l_1^2 \eta_{ijk}^{(1)} \eta_{ijk}^{(1)} + \frac{2}{3} l_{CS}^2 \chi_{ij} \chi_{ij} + \left(\frac{4}{3} l_2^2 - \frac{8}{5} l_3^2 \right) \chi_{ij} \chi_{ji} \quad (4)$$

where $l_{CS}^2 = (2l_2^2 + 12l_3^2/5)$. The invariant $\eta_{ijk}^{(1)} \eta_{ijk}^{(1)}$ depends on both stretch and rotation gradients. For deformations which are irrotational (i.e. $\chi_{ij} = 0$), only the first of the length parameters, l_1 , has any influence. It is through $l_1^2 \eta_{ijk}^{(1)} \eta_{ijk}^{(1)}$ that stretch gradients make their presence felt.

The first version of the strain gradient theory (Fleck *et al.*, 1994; Fleck and Hutchinson, 1994) assumed strain gradients enter only through the one invariant of the rotation gradients, $\chi_{ij} \chi_{ij}$, according to

$$E_e^2 = \frac{2}{3} \varepsilon'_{ij} \varepsilon'_{ij} + \frac{2}{3} l_{CS}^2 \chi_{ij} \chi_{ij}. \quad (5)$$

This is a special case of (4) with $l_1 = 0$, $l_2 = \frac{1}{2} l_{CS}$ and $l_3 = \sqrt{\frac{5}{24}} l_{CS}$. This class of solids falls within the framework of couple stress theory, a sub-set of Toupin–Mindlin theory. Fleck *et al.* (1994) analyzed wire torsion data for annealed copper wires ranging in radius from 7–60 microns using the version of the plasticity theory based

on (5). By fitting the theory to the data, they inferred that $l_{CS} \cong 4 \mu\text{m}$ for this material. The deformations in wire torsion are such that the two other invariants of the strain gradients in (4), $\eta_{ijk}^{(1)}\eta_{ijk}^{(1)}$ and $\chi_{ij}\chi_{ji}$, are identically zero (Fleck and Hutchinson, 1997). Thus, for this application, there is no loss in generality in using a theory based on (5) rather than (4). In other applications, however, contributions from stretch gradients through $l_1^2\eta_{ijk}^{(1)}\eta_{ijk}^{(1)}$ can be of dominant importance, particularly when deformations are nearly irrotational. Examples of this type discussed by Fleck and Hutchinson (1997) include void growth and cavitation, crack tip fields, and indentation.

No examples have been identified yet for which the third invariant of the strain gradients in (4), $\chi_{ij}\chi_{ji}$, plays a particularly important role. To reduce the set of length parameters from three to two, we will exclude any dependence on $\chi_{ij}\chi_{ji}$ in (4) by taking $l_2 = \sqrt{6/5}l_3$ (with $l_2 = l_{CS}/2$ and $l_3 = \sqrt{5/24}l_{CS}$) such that (4) becomes

$$E_e^2 = \frac{2}{3}\epsilon'_{ij}\epsilon'_{ij} + l_1^2\eta_{ijk}^{(1)}\eta_{ijk}^{(1)} + \frac{2}{3}l_{CS}^2\chi_{ij}\chi_{ij}. \quad (6)$$

From (2), it can be noted that this combination is positive definite if both l_1 and l_{CS} are non-zero. As mentioned above, l_{CS} controls the size effect in wire torsion, while the outcome of the present work will be that l_1 is by far the more important of the two parameters in micro-indentation. Thus, it seems likely that both length parameters, l_1 and l_{CS} , must be retained for general application of the theory. Moreover, unless it turns out that these two length parameters have fixed proportion for all metals, it would appear that experimental data from at least two different types of small scale tests will be required to separately determine l_1 and l_{CS} . Further discussion of this issue will be given at the end of the paper.

A strain energy density function is assumed in the form

$$W(E_e) = w(E_e) + \frac{E}{6(1-2\nu)}\epsilon_{ii}^2 \quad (7)$$

where E is Young's modulus and ν is Poisson's ratio. The dependence on deviatoric quantities $w(E_e)$ is chosen such that in uniaxial tension the stress-strain behavior derived from (7) reproduces the Ramberg-Osgood tensile relation

$$\epsilon = \frac{\sigma}{E} + \frac{3}{7} \frac{\sigma_y}{E} \left(\frac{\sigma}{\sigma_y} \right)^n. \quad (8)$$

The work increment per unit volume associated with an arbitrary variation of the displacements is

$$\delta W = \sigma_{ij}\delta\epsilon_{ij} + \tau_{ijk}\delta\eta_{ijk} \quad (9)$$

where the stress quantities, $\sigma_{ij} = \sigma_{ji}$ and $\tau_{ijk} = \tau_{jik}$, are obtained from W by

$$\sigma_{ij} = \frac{\partial W}{\partial \epsilon_{ij}} \quad \text{and} \quad \tau_{ijk} = \frac{\partial W}{\partial \eta_{ijk}}. \quad (10)$$

The principle of virtual work is given by

$$\int_V [\sigma_{ij}\delta\epsilon_{ij} + \tau_{ijk}\delta\eta_{ijk}] dV = \int_V f_i\delta u_i dV + \int_S [t_i\delta u_i + r_i n_j \delta u_{i,j}] dS \quad (11)$$

where dV and dS are the volume and surface elements, f_i is the body force per unit volume, t_i is the surface traction, r_i is the double stress traction, and n_i is unit surface normal. The equilibrium relationship derived from the principle is

$$\sigma_{ik,i} - \tau_{ijk,ij} = -f_k \quad (12a)$$

while the stress-traction relationships for a straight boundary aligned with the x_1 axis are

$$t_k = \sigma_{2k} - \tau_{2jk,j} - \tau_{21k,1} \quad (12b)$$

$$r_k = \tau_{22k}. \quad (12c)$$

Stress-traction relationships for arbitrarily oriented and shaped boundaries are given by Fleck and Hutchinson (1997).

3. FINITE ELEMENT FORMULATION AND INDENTATION MODEL

On the basis of the deformation strain gradient plasticity behavior outlined in the previous section, a finite element scheme was derived for the general axisymmetric case. The potential energy of the system is given by

$$\pi(u) = \int_V \left[w(E_v) + \frac{1}{2} \kappa \left(\frac{\epsilon_{ii}}{3} \right)^2 \right] dV - \int_S [t_k u_k + r_k D u_k] dS \quad (13)$$

where $\kappa = E/(3(1-2\nu))$ is the bulk modulus and S is the portion of the boundary on which tractions are prescribed. The principle of minimum potential energy applies in the usual manner, i.e. of all kinematically admissible displacement fields, the actual displacement field will render π a minimum. The governing equations are then found by taking the first variation of (14) in the usual manner. The finite element discretization of the result follows standard procedures, but is complicated by the dependence of w on strain gradients.

The finite element model is illustrated in Fig. 1. The contact radius is defined as a ; the depth of penetration of the indenter is δ . The half-angle of the indenter, β , was taken to be 72° , which corresponds to a Vickers indenter. The indenter is assumed to be rigid. Contact between the indenter and the substrate is assumed to be frictionless. Studies on conventional elastic-plastic solids indicate little difference between the hardness predicted for a frictionless indenter and that for an indenter-substrate system permitting no sliding. The material is modeled as being a semi-infinite half plane; the size of the mesh was chosen by decreasing the size relative to the contact radius until there was a negligible change in the calculated hardness.

3.1. Choice of element

It is important to note that admissibility requirements of the second gradient terms require C_1 continuity in displacements. Previous strain gradient modeling efforts have explored a variety of types of elements (Xia and Hutchinson, 1996) and have shown that element performance is strongly dependent on the constitutive behavior. Based

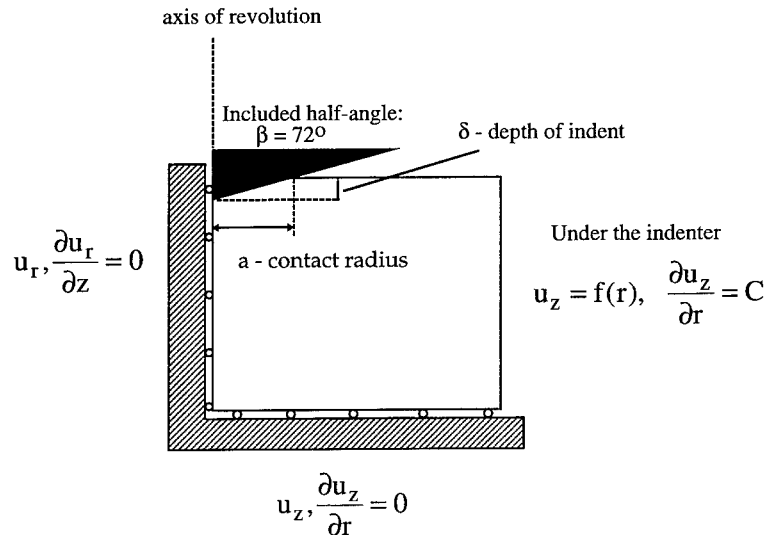


Fig. 1. Geometry of the axisymmetric indentation model and boundary conditions.

on this earlier work, an element similar to one initially derived for plate applications was chosen; problems in previous work (Xia and Hutchinson, 1996) with the element concerning adequate hydrostatic stress fields did not arise for the compressible material modeled here. More recently, C_0 elements with displacement gradients as nodal degrees of freedom have been investigated and performed admirably for linear elastic boundary value problems; these elements may prove more desirable for future efforts in strain gradient plasticity (Shu *et al.*, 1997).

The element is a three noded triangle with eighteen degrees of freedom. For each node, the nodal variables are

$$u_r, \frac{\partial u_r}{\partial r}, \frac{\partial u_r}{\partial z}, u_z, \frac{\partial u_z}{\partial r}, \frac{\partial u_z}{\partial z}. \quad (14)$$

Thus, the elements produce C_1 continuity at the nodes. The shape functions were derived by Specht (1988) and are outlined and discussed by Zienkiewicz and Taylor (1989). In general, the displacement gradients are not continuous across element boundaries, only at the nodes. However, the variation of displacement gradients along element faces are defined such that the element passes the patch test and can exactly reproduce constant strain gradient fields. This implies that there is no spurious energy contribution from jumps in displacement gradients across element boundaries.

The constitutive behavior and interpolation outline above were used in defining a general axisymmetric user element in the commercial code ABAQUS.

3.2. Boundary conditions

Axisymmetry dictates that u_r and $\partial u_r / \partial z$ are zero along the axis of symmetry. The vertical displacement along the bottom of the mesh was constrained to be zero,

while the radial quantities were unconstrained. Derivatives of displacements must be specified in addition to displacements, as they are additional nodal degrees of freedom.

For a frictionless indenter, the proper boundary condition underneath the indenter is a constraint between the radial and vertical displacements; the nodes in the contact region are constrained to fall on the indenter, with freedom to slide up and down the face of the indenter. For small strain theory and the shallow indenters considered here, this can be approximated by specifying the downward displacement and allowing the radial displacement to be free. The more shallow the indenter, the more accurate are these linearized boundary conditions. Thus, the following modified boundary conditions under the indenter were imposed:

$$(i) \quad u_z(r) = -\delta + \frac{r}{\tan \beta}, \quad \frac{\partial u_z}{\partial r} = \frac{1}{\tan \beta} \quad (15a)$$

$$(ii) \quad \text{no restriction on } u_r, \quad \frac{\partial u_r}{\partial r}, \quad \frac{\partial u_r}{\partial z}, \quad \frac{\partial u_z}{\partial z}. \quad (15b)$$

In addition to approximating zero shear traction under the indenter, (15b) results in a zero double stress traction [given by (12c)], enforced by the variational principle.

3.3. Determining the proper contact radius and indent depth

The contact between the indenter and the substrate was simulated by assuming a contact radius, a , and iterating to find the proper indentation depth, δ , for that size of indent. The proper indentation depth is defined as the depth at which the normal pressure between the indenter and material goes to zero at the edge of contact, i.e. at $r = a$. Using small strain theory for shallow indenters, the pressure is given by the traction in the vertical direction, given by (12b). The pressure under the indenter simplifies to

$$t_z = \sigma_{zz} - 2 \frac{\partial \tau_{rz}}{\partial r} - \frac{\partial \tau_{zz}}{\partial z}. \quad (16)$$

For the strain gradient solid, evaluating the tractions under the indenter using (16) and the finite element solution proved unreliable, due to the difficulty in evaluating the derivatives of the higher order stress quantities. To avoid this, the correct depth was assumed to be that at which the nodal forces went to zero at the edge of contact. Since the nodal forces represent the integrated average of the tractions over the element faces, this is consistent with the zero-traction criterion. The benchmark test results summarized below confirm the accuracy of this method.

3.4. Benchmark tests

The element performance and mesh geometry were tested by comparing predicted hardness values with an analytical solution for shallow conical indentation of an elastic half-space and some results based on conventional plasticity for the same problems which were presented by Shu and Fleck (1996). In general, the model was quite accurate. There was less than 2% error in the indentation load at a given indentation radius compared with the analytical solution for the elastic problem. The

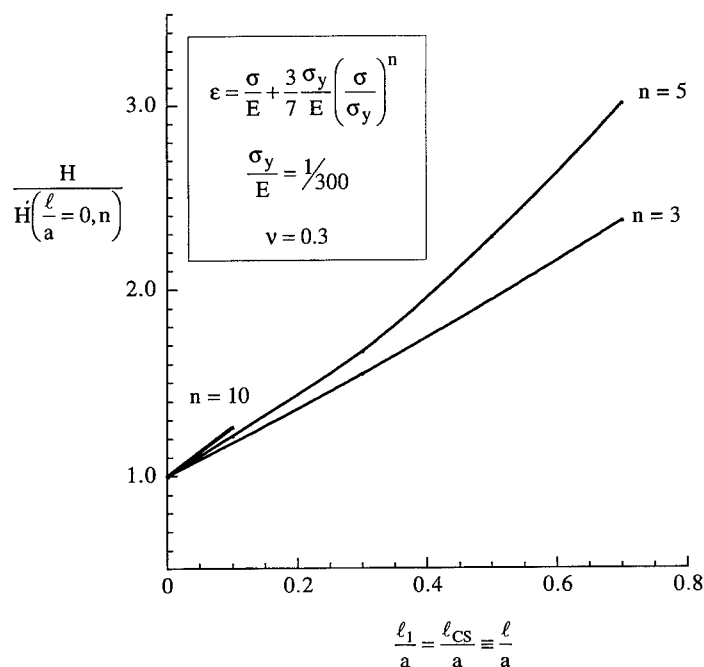


Fig. 2. Size-dependent hardness predictions as a function of material length scale over contact radius, for a frictionless conical indenter with a 72° half-angle.

hardness values (loads) for conventional plasticity were within 5% of the benchmark tests outlined by Shu and Fleck (1997).

The added computational expense of six degrees of freedom per node was partially compensated by the greater accuracy of the higher order element. The mesh density was chosen by examining the hardness values as the size of the smallest element (located adjacent to the contact radius) decreased. For both the conventional and strain gradient theories, the change in hardness was less than several percent when the minimum element size was decreased from $0.034a$ to $0.016a$; decreasing the minimum element size further by a factor of two led to even smaller changes in predicted hardness, although computation time increased significantly. The mesh used to generate the results was comprised of 1500 elements, with a minimum element size of $0.016a$.

4. NUMERICAL RESULTS

4.1. Size-dependent hardness

Computed size-dependent hardness for the conical indenter with a half-angle $\beta = 72^\circ$ is presented in Fig. 2, where the hardness H is defined as $P/(\pi a^2)$ with P as the load. These results are for the strain gradient solid with $l_1 = l_{CS} \equiv l$ for several

Table 1. *Values of the material length scale determined from least squares fits with several experiments from the literature*

	Orientation	Macroscopic hardness— H_0 MPa	$n = 3$ μm	$n = 5$ μm
Stelmashenko <i>et al.</i> (1993)	(100)[011]	3100	0.52	0.41
	(110)	3200	0.38	0.32
	(111)[011]	3300	0.25	0.22
Ma and Clarke (1995)	[100]	360	0.39	0.34
	[110]	375	0.22	0.19
Nix (1997)		566	0.60	0.42
Atkinson (1995)	Work-hardened		0.81	0.73
	Annealed		1.76	1.56

values of the hardening exponent n . The particular solid with $l_1 = l_{CS} \equiv l$ hardens in response to both stretch and rotation gradients. It was labeled an SG solid by Fleck and Hutchinson (1997) and was used in that paper to study the effect of strain gradients in several examples. Emphasis is on the variation of hardness with relative size of the indent as measured by the ratio of the indent radius to the material length parameter l . The results in this paper have been computed with $\sigma_y/E = 1/300$ and $\nu = 0.3$.

The hardness, H , in Fig. 2 has been normalized by the conventional plasticity result at the same value of n , i.e. the limiting result for $l/a \rightarrow 0$, which is given in Table 2 in the Appendix. The values for the conventional limit in Table 2 can be used with Fig. 2 to determine the actual hardness for a given length scale or size of indent. The plot thus represents the relative increase in hardness due to including strain gradients in the constitutive formulation. The abscissa in Fig. 2 is l/a , and it can be seen that size-dependent increases in hardness begin to become significant when a is less than about $10l$. Hardness is approximately doubled for indentation radii as small as about twice the length scale parameter l . The relative increase in hardness for $n = 5$ is greater than for $n = 3$, although the absolute increase in hardness at corresponding values of l/a are very nearly the same for the two strain hardening levels. In Section 5, the absolute value of the material length parameter will be estimated by comparison with experiments available in the literature.

4.2. Deformation characteristics

The deformed surface profiles under the indenter are shown in Fig. 3(a) for several indent sizes. In this figure, the radial and vertical locations have been normalized by the material length scale, which is assumed to be a material property. The values of the indent load (labeled in the figure) and displaced profiles accent the role of the normalizations used in calculating the hardness. The hardness, which is defined as the average stress under the indenter, is a function of the size of indent relative to the material property l , as already noted.

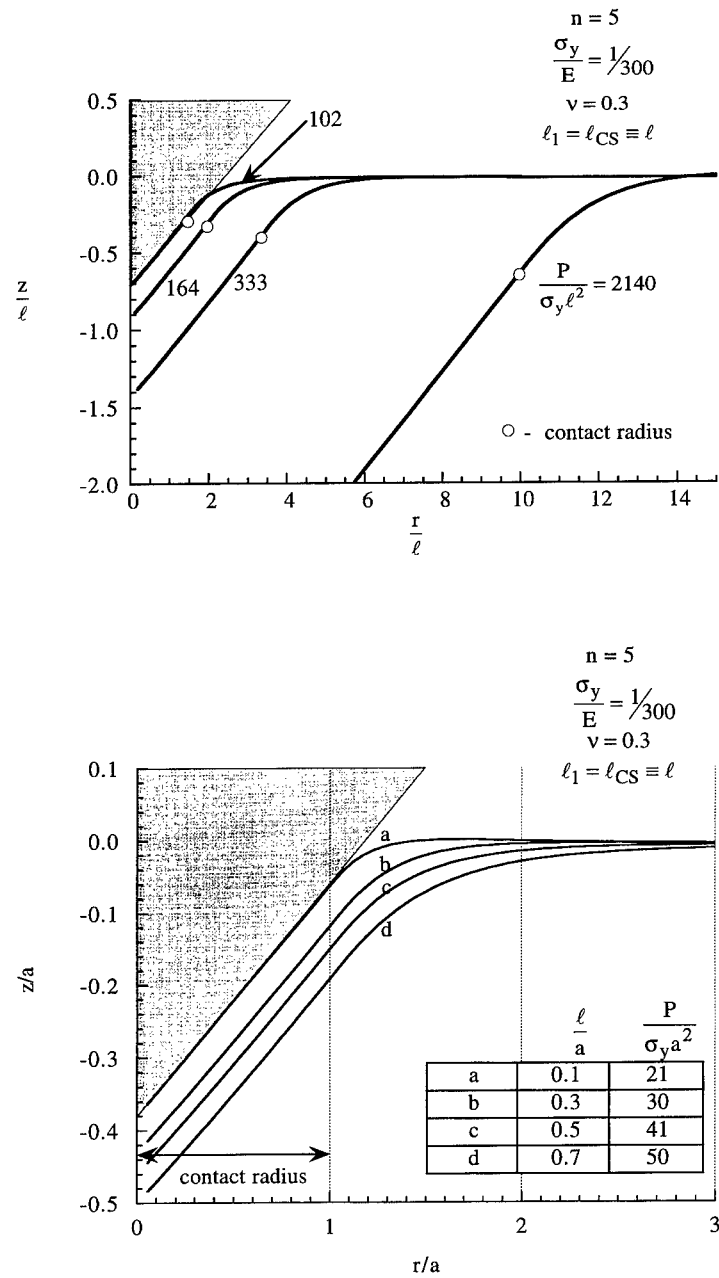


Fig. 3. (a) Deformed surface profiles for several indent sizes and constant material length scale. Given in the figure are normalized values of the indent load. (b) Deformed surface profiles for constant indent size and various length scales. Given in the figure are normalized values of material length scale and corresponding indent load.

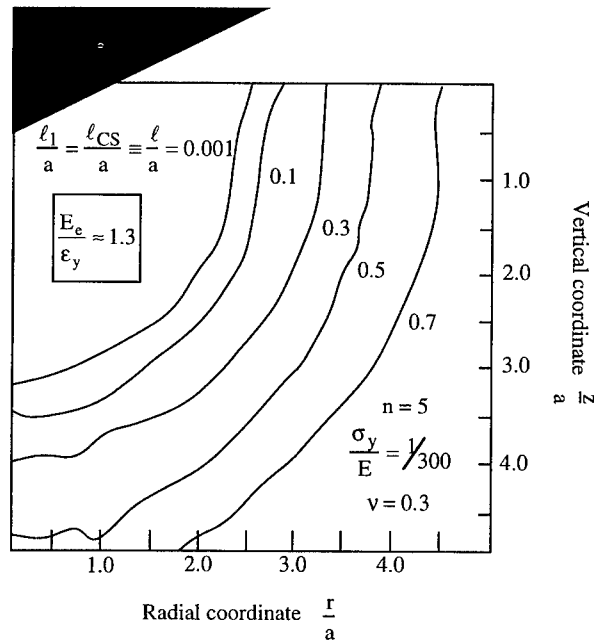


Fig. 4. Effective strain contours for various material length scales; each curve represents the estimated plastic zone size (i.e. $E_e \approx 1.3\epsilon_y$) for a given length scale to indent size ratio.

Figure 3(b) illustrates the effect of variations of material length parameter at constant indent size. These cases can be considered to be indents of the same size (defined as having the same contact radius) in materials with different length parameters l . The materials with the larger l are harder, and require greater loads to create the same contact radius. This is consistent with both the experimental behavior and anticipated behavior of the constitutive description, which dictates that the amount of hardening increases as l increases. The curves show that this increased hardening results in profiles that are increasingly similar to the elastic case where no pile-up occurs.

The effect of the material length parameter on the amount of plasticity underneath the indenter can be investigated by estimating the size of the plastic zone under the indenter. In Fig. 4, approximate boundaries to the plastic zone are shown for several length parameters l , all for the same contact radius a and the same strain hardening level, $n = 5$. The plastic zone is estimated as the region in which the effective stress measure is greater than σ_y , or, equivalently, $E_e > 1.3\epsilon_y$, as determined by the stress-strain relationship (8). The size of the plastic zone for the conventional plasticity limit, given approximately for the case $l/a = 0.001$ is consistent with previously published results (e.g. Bhattacharya and Nix, 1991; Giannakopoulos and Larsson, 1997; Shu and Fleck, 1997), regardless of whether flow or deformation plasticity theory was used. Figure 4 illustrates that increasing the material length parameter l , or, equivalently, decreasing the size of the indent a , increases the extent of the plasticity

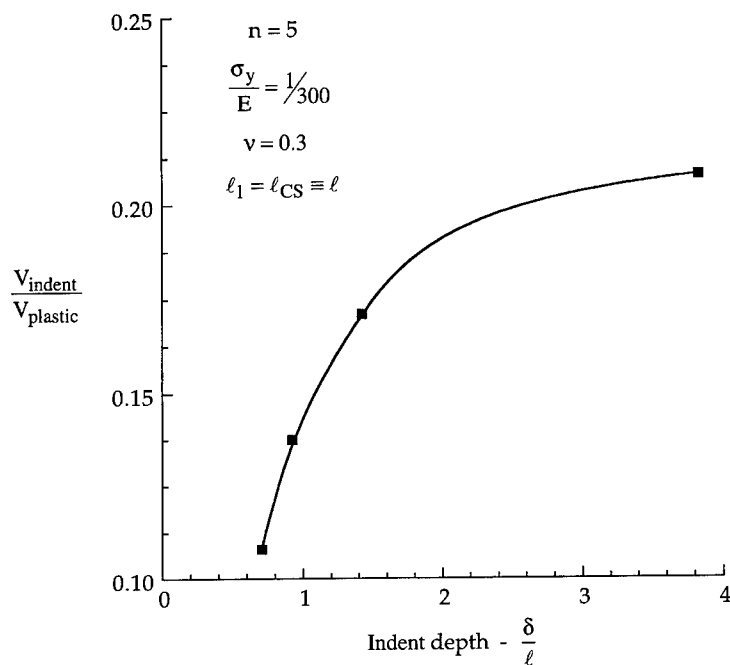


Fig. 5. Ratio of indentation volume over estimated plastic zone volume vs indentation depth. The volume of the plastic zone was estimated by fitting the curves in Fig. 4 with a half-ellipsoid of revolution.

zone relative to the indent size. When the indent radius is as small as $2l$, the extent of the plastic zone is nearly doubled. This is a large effect, but not surprising given the effect of l on the indentation load.

The effect is further illustrated in Fig. 5, which presents the ratio of the indentation volume over the volume of the plastic zone. The volume of the plastic zone was estimated by identifying the plastic zone as the region inside the appropriate contour in Fig. 4 and fitting the shape of the zone with a half-ellipsoid of revolution. Ma and Clarke (1995) have presented experimental results in a similar manner. They estimated the extent of plastic flow by measuring the size of the plastic zone at a given depth. Their results are presented in the same manner as in Fig. 5, with the ratio of indentation volume to plastic zone volume vs indentation depth. Their experiments confirm the trend displayed in Fig. 5: smaller indents have significantly larger relative plastic zone sizes.

4.3. Role of the individual length parameters, l_1 and l_{CS} .

The results presented above are for the SG solid for which the ratio of the amplitudes of the length parameters in (6) are fixed according to $l_1 = l_{CS} \equiv l$ (with $l_2 = \frac{1}{2}l_{CS}$ and

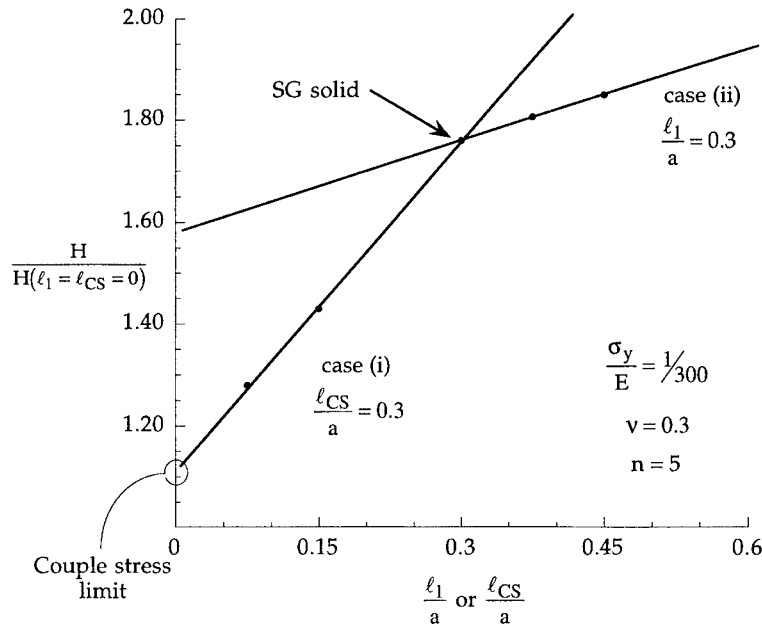


Fig. 6. Normalized hardness predictions as a function of individual length scale parameters; in case (i) l_{CS} is constant and l_1 varies, in case (ii) l_1 is constant and l_{CS} varies.

$l_3 = \sqrt{\frac{5}{24}} l_{CS}$). There is no physical basis for this particular choice of ratio, except that it ensures that both stretch and rotation gradients influence gradient hardening. This choice also ensures that E_c is positive definite because each of the three length parameters, l_i , in (2) are non-zero.

To gain some insight on the role of individual length parameters on hardness, calculations were carried out in which l_1 and l_{CS} were varied independently. Normalized hardness predictions are shown in Fig. 6 for a material with $\sigma_y/E = 1/300$, $n = 5$ and $\nu = 0.3$. Case (i) displays the dependence of the normalized hardness on l_1/a with l_{CS}/a fixed at 0.3, while case (ii) gives the dependence on l_{CS}/a with l_1/a fixed at 0.3. The point where the two curves cross at $l_1/a = l_{CS}/a = 0.3$ is the case of the SG solid. The relative slopes of the two cases illustrate that l_1 has much more effect on the hardness than l_{CS} . A decrease of l_1 by 50% [case (i)] drops the size-dependent hardness elevation by 60%. Conversely, the length parameter associated with the couple stress theory, l_{CS} , plays a relatively insignificant role. A 50% change in l_{CS} only results in approximately a 10% change hardness elevation. The results are consistent with the results of Shu and Fleck (1996), who found the couple stress theory did not predict significant hardness increases. Extrapolating the results for case (i) to $l_1/a = 0$ (see Fig. 6), one finds a size-dependent hardness elevation on the order of 10% for the couple stress solid with $l_{CS}/a = 0.3$. Shu and Fleck report a 5% elevation for this

case; the discrepancy can be explained by minor differences in the assumed tensile stress-strain law (8) and element performance.

An open question remains: What is the relative proportion of the material length parameters l_1 and l_{CS} ? Hopefully, insights will come from fundamental dislocation mechanics. It seems more likely, however, at least in the short term, that the answer will come from correlation with experiments which differentiate the two contributions, such as indentation and wire torsion. The parameter l_{CS} is clearly of secondary importance in indentation. By contrast, as noted earlier, l_1 has no influence on wire torsion. In the present study, a non-zero value of l_{CS} is required to ensure a positive definite formulation for the strain energy density. When the ratio l_{CS}/l_1 is taken to be too small, the finite element model becomes ill-conditioned. Thus, the SG solid with $l_1 = l_{CS} \equiv l$ provides a useful choice in the present study. Identification of l by fitting the solutions for the SG solid to experimental indentation data should be regarded as an approximate determination of l_1 with no implication for l_{CS} .

5. COMPARISON WITH EXPERIMENTS AND DISLOCATION MODELS: CHOICE OF THE MATERIAL LENGTH PARAMETER l

Indentation hardness data of Ma and Clark (1995) on silver single crystals with two orientations relative to the axis of the indenter are shown in Fig. 7(a), and another set of data on tungsten single crystals from Stelmashenko *et al.* (1993) at three orientations are shown in Fig. 7(b). In the first case, the hardness H is plotted against the indentation depth (h), while in the second it is plotted against the indent diagonal (D). Ma and Clarke used a Berkovich indenter (65.3° face angle) with the same area-depth ratio as the Vickers indenter (68° face angle) used by Stelmashenko *et al.* There is some dependence of the measured hardness on crystal orientation relative to the indentation direction in both sets of data, but size-dependence dominates. Superimposed on the data in Fig. 7 are the present theoretical predictions from Fig. 2 for $n = 3$, corresponding to a high strain hardening level characteristic of annealed metals.

The theoretical predictions were generated in the following manner. The results in Fig. 2 were fitted with second order polynomials to obtain H/H_0 as a function of l/a . The limiting macroscopic hardness ($H_0 \equiv H$ for $l/a = 0$) chosen for the fit is approximately the value of the hardness obtained in the experiments for the largest indent. These values are given in Table 1 and are indicated in each plot in Fig. 7. Indents of the same area are compared; the contact radius in the prediction was related to the experimental depth (or diagonal size) that would give the same projected area. Equating the areas for a 72° cone and a Berkovich indenter yields $a = 2.8h$, where h is the experimental depth. The relationship for a Vickers indenter is $a = 0.45D$, where D is the diagonal of the impression in the experiment.* These equations substituted into the polynomials yields an expression for the predicted hardness as a

* Since the cone used here has a slightly higher area/depth ratio than the Vickers and Berkovich indenters, the depth of the prediction is slightly smaller than the actual depth in the experiments. Using a cone angle of 70.3° gives the same area/depth relation and hence, compares indents of equal area and depth; the equations above would not change.

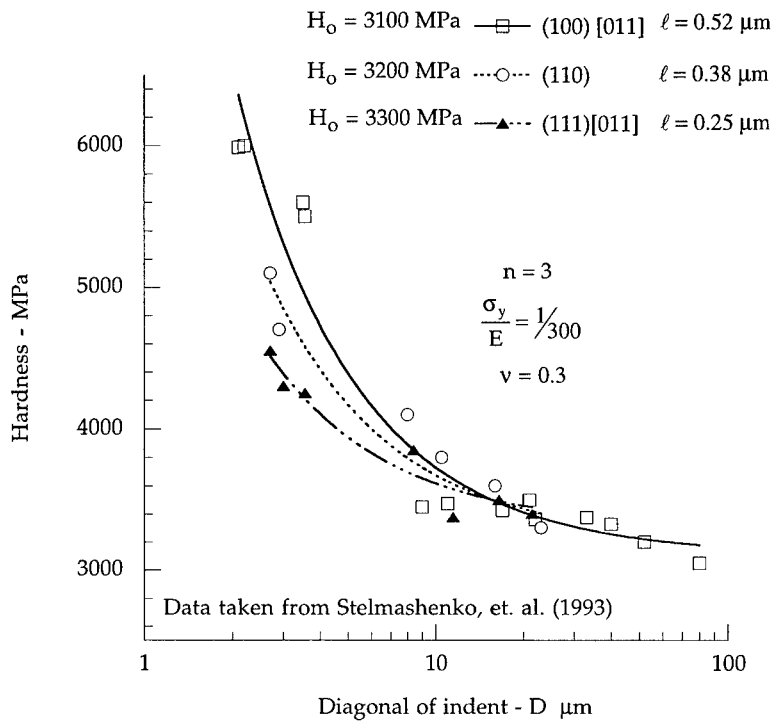
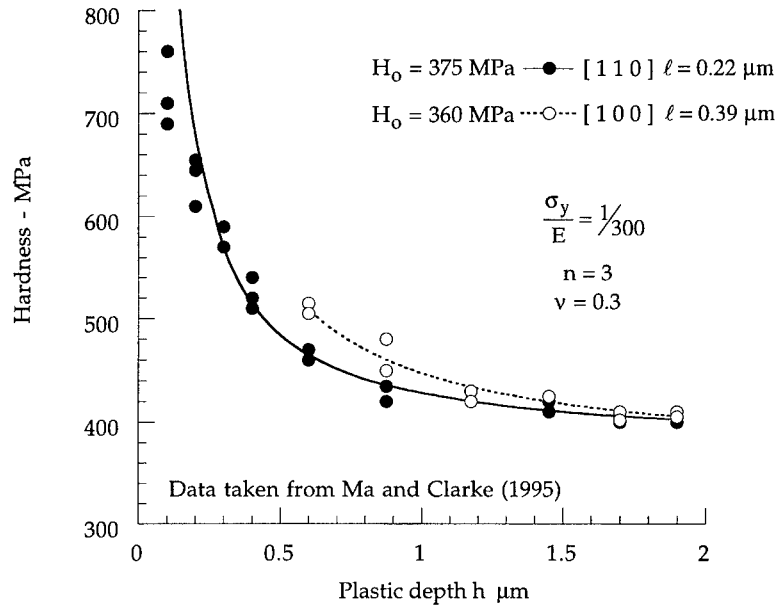


Fig. 7. (a) Comparison of the experimental results of Ma and Clarke (1995) and the theoretical predictions given in Fig. 2. The lines indicate the results of a least squares fit to determine the material length scale. The experiments were done using a Berkovich indenter with a 65.3° face angle. (b) Comparison of the experimental results of Stelmashenko *et al.* (1995) and the theoretical predictions given in Fig. 2. The lines indicate the results of a least squares fit to determine the material length scale. The experiments were done using a Vickers indenter with a 68° face angle.

function of experimental depth (or diagonal) and the material length scale l . The length scale was then determined by a least squares fit of the functions $H = f(h, l)$ to the experimental data. This was done for both $n = 3$ and $n = 5$, and the results are tabulated in Table 1. For all cases, values for l in the range 0.2–0.6 μm fit the data very well.

For hardnesses which do not exceed the macroscopic hardness, H_0 , by more than a factor of about 2, the numerical results of Fig. 2 can be well approximated by a linear dependence on the inverse indent radius according to

$$\frac{H}{H_0} = 1 + c(n, \sigma_y/E) \frac{l}{a}. \quad (17)$$

For $\sigma_y/E = 1/300$, the numerical results give $c \cong 1.85$ for $n = 3$ and $c \cong 2.43$ for $n = 5$.

A somewhat different dependence of H on the indent size has been suggested on the basis of dislocation arguments by De Guzman *et al.* (1993), Ma and Clarke (1995), Poole *et al.* (1997) and Nix (1997). Here, Nix's (1997) result will be quoted as it is the most detailed. The starting point of each of the above derivations is that the flow stress follows Taylor's relation $\tau = \alpha\mu b\rho^{1/2}$, where α is a constant depending on structure which is about 0.3 for FCC materials, μ is the shear modulus, b is the Burgers vector, and ρ is the total dislocation density. The total dislocation density is taken to be the sum of the statistically stored dislocations, ρ_s , and the geometrically stored dislocations, ρ_G , according to $\rho = \rho_s + \rho_G$. The statistically stored dislocations are related to the average plastic strain, while the geometrically necessary dislocations are tied to the incompatibility of the deformations induced by the indenter. Nix takes $\rho_G = 3(\cot\beta)^2/(16bh)$. His final result for the size-dependent hardness is

$$\left(\frac{H}{H_0}\right)^2 = 1 + \frac{h^*}{h} \quad (18)$$

where $H_0 = 3\sqrt{3}\alpha\mu b\sqrt{\rho_s}$ and $h^* = 3(\cot\beta)^2/(16b\rho_s)$. Note that h^*/h is equivalent to a^*/a , where $a^* = h^*/\cot\beta$. For small values of a^*/a , (18) also gives an inverse dependence on indent size as in (17). The two results are brought into coincidence if

$$c(n, \sigma_y/E)l = \frac{1}{2}a^*. \quad (19)$$

Differences between (17) and (18) become noticeable for values of a^*/a greater than about 1/2.

Nix (1997) plotted data for copper single crystals of McElhaney *et al.* (1997) as $(H/H_0)^2$ vs $1/h$, presented here in Fig. 8. This data is taken with a Berkovich diamond pyramidal indenter with a 65.3° face angle. The linear dependence of $(H/H_0)^2$ with $1/h$ displayed by the data over the range from $h = 1/5$ – $2 \mu\text{m}$ is striking. Nix extrapolated the unnormalized data to $1/h = 0$ to obtain $H_0 = 556 \text{ MPa}$. The value, $h^* = 1.68 \mu\text{m}$, in (18) gives the best fit to the data. Poole *et al.* (1996) also presented plots of H^2 vs $1/h$ for their micro-indentation data on two sets of copper polycrystals, one

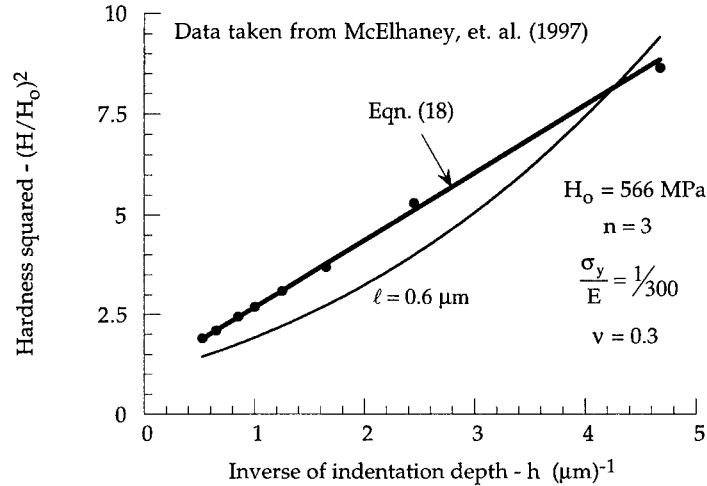


Fig. 8. (a) Comparison of the experimental results of McElhaney *et al.* (1997), the theoretical predictions of Nix [eqn (18)] and the theoretical predictions given in Fig. 2. The experiments were done using a Berkovich indenter with a 65.3° face angle.

annealed and one work hardened. Their data indicates a value of h^* for the work hardened copper, which is roughly one quarter that for the annealed copper. Their data, however, is less convincing as to the linear dependence of $(H/H_0)^2$ on $1/h$.

Superimposed onto Fig. 8 are the numerical results from the present analysis (from Fig. 2) for the case $n = 3$, using $H_0 = 556$ MPa and accounting for the difference between the pyramidal and conical indenters in the manner discussed earlier. The least squares fit outlined earlier results in the value $l = 0.6$ μm . (A summary of the fitting results is included in Table 1.) As mentioned above, the present results do not produce a linear dependence of $(H/H_0)^2$ on $1/h$ over the full range of $1/h$. The dependence of the present results seen in Fig. 8 is a consequence of the composition of the invariants employed in (6). In strain gradient plasticity, strain gradients are associated with geometric dislocations, while statistically stored dislocations are associated with the deviator strains (Fleck and Hutchinson, 1997). Thus, rather than a linear dependence of the form $\rho_s + \rho_G$, the effective strain E_c in (6) models a dependence composed according to the so-called harmonic mean as $\sqrt{\rho_s^2 + \rho_G^2}$. This choice has been made largely for mathematical convenience. Alternative compositions to (6) are discussed by Fleck and Hutchinson which are capable of modeling the linear dependence, $\rho_s + \rho_G$. Specifically, the choice

$$E_c = \left[\left(\frac{2}{3} \varepsilon'_{ij} \varepsilon'_{ij} \right)^{\lambda/2} + \left(l^2 \eta_{ijk}^{(1)} \eta_{ijk}^{(1)} + \frac{2}{3} l_{cs}^2 \chi_{ij} \chi_{ij} \right)^{\lambda/2} \right]^{1/\lambda} \quad (20)$$

models the linear dependence for $\lambda = 1$ and reduces to (6) for $\lambda = 2$. Until more data

becomes available, we leave for the future the investigation of whether an alternative composition such as (20) should be used in the strain gradient plasticity formulation.

Finally, the theoretical results in Fig. 2 have been fit to hardness data collected and analyzed by Atkinson (1995). Atkinson conducted indentation tests on a wide range of polycrystalline metals and extensively analyzed the data, with the goal of quantifying the size effect through relatively simple empirical formulae containing parameters to be determined by fitting the experimental hardness trends. One of the significant results of Atkinson's analysis is the finding that the variance of the fitting parameters is not greater for smaller indents than larger indents. This emphasizes that measurement error does not systematically increase with decreasing indent size. Atkinson's took data for relatively large indents, with the radius of the smallest indents no smaller than about $5\text{ }\mu\text{m}$. Consequently, his hardness measurements for the smallest indents were no more than 25–35% above the macroscopic hardness values. Atkinson found distinct differences among metals that divided along two lines: metals which were strain hardened by plastic working and those that were annealed. By choosing the material length parameter l for the present results in Fig. 2 to fit Atkinson's data for a given class of metals, we were able to accurately reproduce the variation of H/H_0 with indent size. Typically, the value of l for an annealed (soft) metal was found to be about $1.6\text{ }\mu\text{m}$. The corresponding value for a work hardened (hard) metal was between $1/2$ and $1\text{ }\mu\text{m}$. The values given in Table 1 are the results to fitting average results presented in Atkinson's paper.

In summary, indentation data appears to be an excellent means to infer the material length scale l in the strain gradient plasticity theory. As emphasized in Section 4, l should be identified with the length parameter l_1 associated with stretch gradients in (6), since l_{CS} has little influence on indentation. The values of l inferred from experimental data for a number of materials lies with the range for about $1/4$ – $1\text{ }\mu\text{m}$, with the hardest materials having the smallest values of l . This is consistent with the fact that the free slip distance of dislocations decreases with hardness, and that l is related to the free slip distance.

ACKNOWLEDGMENTS

This work was supported in part by the ONR through Grant N00014-96-10059, by the NSF through Grant NSF-CMS-96-34632, and by the Division of Engineering and Applied Sciences, Harvard University.

REFERENCES

- Acharya, A. and Bassani, J. L. (1996) On non-local flow theories that preserve the classical structure of incremental boundary value problems. In *IUTAM Symposium on Micromechanics of Plasticity and Damage*, ed. A. Pineau and A. Zaoui, pp. 3–10. Kluwer Academic Publishers.
- Acharya, A. and Bassani, J. L. (1997) Incompatibility and crystal plasticity. To be published.
- Atkinson, M. (1995) Further analysis of the size effective in indentation hardness tests of some metals. *J. Mater. Res.* **10**, 2908–2915.

- Atkins, A. G. and Tabor, D. (1965) Plastic indentation in metals with cones. *Journal of the Mechanics and Physics of Solids* **13**, 149–164.
- Bhattacharya, A. K. and Nix, W. D. (1991) Finite element analysis of cone indentation. *International Journal of Solids and Structures* **27**, 1047–1058.
- Brown, L. M. (1997) Transition from laminar to irrotational motion in plasticity. To be published.
- De Guzman, M. S., Neubauer, G., Flinn, P. and Nix, W. D. (1993) The role of indentation depth on the measured hardness of materials. *Mater. Res. Symp. Proc.* **308**, 613–618.
- Doerner, M. F. and Nix, W. D. (1986) A method for interpreting the data from depth sensing indentation measurements. *J. Mater. Res.* **1**, 601–609.
- Fleck, N. A. and Hutchinson, J. W. (1993) A phenomenological theory for strain gradient effects in plasticity. *Journal of the Mechanics and Physics of Solids* **41**, 1825–1857.
- Fleck, N. A. and Hutchinson, J. W. (1997) Strain gradient plasticity. In *Advances in Applied Mechanics*, ed. J. W. Hutchinson and T. Y. Wu, Vol. 33. Academic Press, New York.
- Fleck, N. A., Muller, G. M., Ashby, M. F. and Hutchinson, J. W. (1994) Strain gradient plasticity: theory and experiment. *Acta Metallurgica Materialia* **42**, 475–487.
- Gane, N. and Cox, J. M. (1970) The microhardness of metals at very low loads. *Philos. Mag.* **22**, 881–891.
- Giannakopoulos, A. E. and Larsson, P.-L. (1997) Analysis of pyramid indentation of pressure-sensitive hard metals and ceramics. *Mech. Matls* **25**, 1–35.
- Johnson, K. L. (1970) The correlation of indentation experiments. *Journal of the Mechanics and Physics of Solids* **18**, 115–126.
- Ma, Q. and Clarke, D. R. (1995) Size dependent hardness of silver single crystals. *J. Mater. Res.* **10**, 853–863.
- McElhaney, K. W., Vlassak, J. J. and Nix, W. D. (1997) *J. Mater. Res.*, to be published.
- Mindlin, R. D. (1965) Micro-structure in linear elasticity. *Arch. Ration. Mech. Anal.* **16**, 51–78.
- Nix, W. D. (1997) Elastic and plastic properties of thin films on substrates: nanoindentation techniques. *Mat. Sci. and Engr. A*, **234–236**, 37–44.
- Pethica, J. B., Hutchings, R. and Oliver, W. C. (1983) Hardness measurements at penetration depths as small as 20 nm. *Philos. Mag.* **A48**, 593–606.
- Poole, W. J., Ashby, M. F. and Fleck, N. A. (1996) Micro-hardness tests on annealed and work-hardened copper polycrystals. *Scripta Metall. Mater.* **34**, 559–564.
- Rubenstein, C. (1981) A critical appraisal of static hardness measurements. *Journal of Applied Mechanics* **48**, 796.
- Samuels, L. E. (1986) *Microindentation Techniques in Materials Science and Engineering*, ed. P. J. Blau and B. R. Law, pp. 5–24. ASTM STP 880, American Society for Testing and Materials, Philadelphia, PA.
- Shu, J. and Fleck, N. A. (1997) The prediction of a size effect in micro-indentation. *International Journal of Solids and Structures*, submitted.
- Shu, J. Y., King, W. E. and Fleck, N. A. (1997) Finite elements for materials with strain gradient effects. *International Journal of Numerical Methods in Engineering*, submitted.
- Smyshlaev, V. P. and Fleck, N. A. (1996) The role of strain gradients in the grain size effect for polycrystals. *Journal of the Mechanics and Physics of Solids* **44**, 465–496.
- Specht, B. (1988) Modified shape functions for the three node plate bending element passing the patch test. *International Journal of Numerical Methods in Engineering* **26**, 705–715.
- Stelmashenko, N. A., Walls, M. G., Brown, L. M. and Miman, Y. V. (1993) Microindentation on W and Mo oriented single crystals: An SEM study. *Acta Metallurgica Materialia* **41**, 2855–2865.
- Toupin, R. A. (1962) Elastic materials with couple stresses. *Arch. Ration. Mech. Anal.* **11**, 385–414.
- Xia, Z. C. and Hutchinson, J. W. (1996) Crack tip fields in strain gradient plasticity. *Journal of the Mechanics and Physics of Solids* **44**, 1621–1648.
- Zienkiewicz, O. C. and Taylor, R. L. (1989) *The Finite Element Method: Volumes I and II*, 4th edn. McGraw-Hill, London.

APPENDIX

Table A1. *Non-zero strain gradients for the general axisymmetric case*

Deviatoric strain gradients	Non-deviatoric components	Derivative components
η'_{rrr}	$\frac{1}{2}\eta_{rrr} - \frac{1}{2}(\eta_{r00} + \eta_{rzz})$	$\frac{1}{2}\frac{\partial^2 u_r}{\partial r^2} - \frac{1}{2}\left(\frac{1}{r}\frac{\partial u_r}{\partial r} - \frac{u_r}{r^2} + \frac{\partial^2 u_z}{\partial r \partial z}\right)$
η'_{rrz}	η_{rrz}	$\frac{\partial^2 u_z}{\partial r^2}$
$\eta'_{r00} = \eta'_{0r0}$	$\frac{3}{4}\eta_{r00} - \frac{1}{4}(\eta_{rrr} + \eta_{rzz})$	$\frac{3}{4}\left(\frac{1}{r}\frac{\partial u_r}{\partial r} - \frac{u_r}{r^2}\right) - \frac{1}{4}\left(\frac{\partial^2 u_r}{\partial r^2} + \frac{\partial^2 u_z}{\partial r \partial z}\right)$
$\eta'_{zr} = \eta'_{rrz}$	$\frac{3}{4}\eta_{zr} - \frac{1}{4}(\eta_{r00} + \eta_{rzz})$	$\frac{3}{4}\frac{\partial^2 u_r}{\partial r \partial z} - \frac{1}{4}\left(\frac{1}{r}\frac{\partial u_z}{\partial z} + \frac{\partial^2 u_z}{\partial z^2}\right)$
$\eta'_{zz} = \eta'_{zrz}$	$\frac{3}{4}\eta_{zz} - \frac{1}{4}(\eta_{rrr} + \eta_{r00})$	$\frac{3}{4}\frac{\partial^2 u_r}{\partial r \partial z} - \frac{1}{4}\left(\frac{\partial^2 u_r}{\partial r^2} + \frac{1}{r}\frac{\partial u_r}{\partial r} - \frac{u_r}{r^2}\right)$
η'_{00r}	η_{00r}	$\frac{1}{r}\frac{\partial u_r}{\partial r} - \frac{u_r}{r^2}$
η'_{00z}	η_{00z}	$\frac{1}{r}\frac{\partial u_z}{\partial r}$
$\eta'_{0z0} = \eta'_{z00}$	$\frac{3}{4}\eta_{0z0} - \frac{1}{4}(\eta_{zrr} + \eta_{zzz})$	$\frac{3}{4}\frac{1}{r}\frac{\partial u_r}{\partial z} - \frac{1}{4}\left(\frac{\partial^2 u_r}{\partial r \partial z} + \frac{\partial^2 u_z}{\partial z^2}\right)$
η'_{zzz}	$\frac{1}{2}\eta_{zzz} - \frac{1}{2}(\eta_{zrr} + \eta_{z00})$	$\frac{1}{2}\frac{\partial^2 u_z}{\partial z^2} - \frac{1}{2}\left(\frac{\partial^2 u_r}{\partial r \partial z} + \frac{1}{r}\frac{\partial u_z}{\partial r}\right)$
η'_{zrz}	η_{zrz}	$\frac{\partial^2 u_r}{\partial z^2}$

Table A2. *Hardness predicted for conventional plasticity*

	$(\sigma_y/E) = 1/300; \nu = 0.3; (l/a) = 0.001$ $(H/\sigma_y) = (P/\sigma_y \pi a^2)$	Approximate δ/a
$n = 3$	7.49	0.37
$n = 5$	5.57	0.35
$n = 10$	3.85	0.33



Pergamon

J. Mech. Phys. Solids, Vol. 46, No. 10, pp. 2069–2086, 1998

© 1998 Elsevier Science Ltd. All rights reserved

Printed in Great Britain

0022-5096/98 \$—see front matter

PII: S0022-5096(98)00023-4

DAMAGE IN GAMMA TITANIUM ALUMINIDES DUE TO SMALL PARTICLE IMPACTS

P. S. STEIF,^{†*} M. P. RUBAL,[†] G. T. GRAY III[‡] AND J. M. PEREIRA[§]

[†]Department of Mechanical Engineering, Carnegie Mellon University, Schenley Park, Pittsburgh,

PA 15213. [‡]Los Alamos National Laboratory, Group MST-5, Materials Research and

Processing Science, Mail Stop G755, Los Alamos, NM 87545. [§]NASA Lewis Research Center,

Mail Stop 333-1, 21000 Brookpark Road, Cleveland, OH 44135

(Received 20 December 1997; accepted 29 January 1998)

ABSTRACT

Initiation of cracking due to small particle impacts on low ductility intermetallics is investigated experimentally and theoretically. The gamma titanium aluminide alloys of interest which are being considered for elevated temperature structural applications in aircraft engines exhibit tensile ductilities on the order of 1–2%. Cracking due to any source, including small particle impacts, is of concern given the rapid growth of cracks in fatigue. This investigation focuses on a model geometry which reproduces the rear face cracking that is induced by a small particle impinging on an air foil leading edge. Small steel spheres are projected onto thin plates at velocities ranging from 76 to 305 m/s; cracking is thereby induced on the rear surface of the plates. Through finite element analyses of the dynamic impact event and some analytical estimates, we examine the hypothesis that crack initiation due to small particle impacts can be correlated with material ductility and with the severity and spatial extent of the straining during the impact event. In addition, with the use of static indentation tests in which similar strain distributions are present, some insight is gained into the difference in ductility between high and low strain rates. © 1998 Elsevier Science Ltd. All rights reserved.

Keywords: A. ductility, B. contact mechanics, C. finite elements, C. plate impact, intermetallics (not included in list).

1. INTRODUCTION

The intermetallic γ -TiAl offers attractive properties for aircraft engine applications, including low density, high modulus, and high burn resistance. These properties come at the expense of the low tensile ductility that is typical of intermetallics; the ductility of gamma ranges from below 1% up to approximately 3%. The relevance of low ductility, particularly in the case of engine component design, is not appreciated quantitatively; indeed, ductility is not traditionally accounted for in design. For materials used to date, there presumably has always been enough ductility. A critical question for engine manufacturers contemplating intermetallic components is whether tensile ductilities on the order of 1% are still sufficient.

Wright (1993) made an initial attempt to estimate the actual tensile ductility required in various circumstances. Very recently, Knaul *et al.* (1998) have shown that, indeed, elastic stress concentrations (up to 2.3) are effectively blunted even with tensile

* To whom correspondence should be addressed.

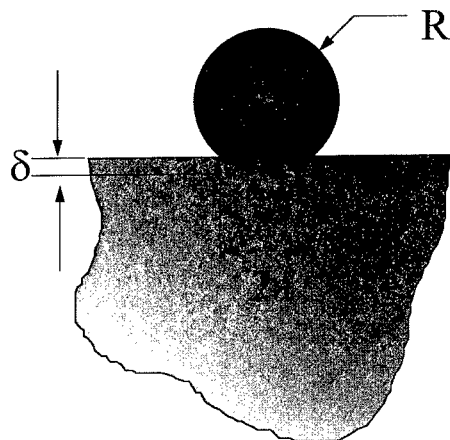


Fig. 1. Definition of geometric quantities for sphere impacting target.

ductilities as low as 1%. In contemplating the use of gamma in airfoils—turbine blades and certainly compressor blades—the threat of small particle impacts is also of considerable concern to designers. Significant amounts of foreign object damage have been documented for conventional titanium alloy compressor blades (Haake *et al.*, 1989), as well as on superalloy blades in other parts of aircraft engines. Given the low ductility in gamma, it is certainly possible that cracks may initiate from such impacts and thereby reduce the fatigue life.

This paper stems from an investigation (Steif *et al.*, 1997) which seeks to quantify the various factors controlling the fatigue strength or life reduction in gamma that may accompany small particle impacts. Relevant to this investigation is a parallel study carried out jointly by NASA Lewis Research Center and GE (Draper, Pereira and Nathal, 1997). They have cast to size “blade-simulative specimens” of gamma: fatigue specimens with the edge of the gage section shaped to simulate a blade leading edge. These specimens are to be subjected to conditions of load and temperature typical of those experienced by turbine blades, impacted with high speed particles, and tested in fatigue. Preliminary results of this investigation have been revealing as to the nature of damage to be expected. It has been found that small particle impacts perpendicular to the blade at the leading edge produce cracking on both the front (impacted) surface and on the rear surface. It is still unclear which of these forms of damage is more critical in determining the subsequent fatigue resistance, although the rear face damage tends to consist of cracks that are roughly perpendicular to the major loading direction in the blade.

For purposes of developing some quantitative understanding of the factors controlling damage in such impact situations, we have focused on one of these forms of damage: rear surface cracking. Further, we have devised a related, though more analyzable, configuration in which similar damage patterns are observed: a thin plate to be impacted at its centre perpendicular to the large free surface (Fig. 1). In this paper we compare observations of plasticity and cracking with finite element predictions of the rear face strain patterns. This comparison was also carried out for

static indentation tests which have been chosen so as to feature similar strain patterns on the rear face. In addition, simplified models and correlations are developed which may be useful in lieu of detailed numerical analyses.

The response of materials and structures to impacts has been the subject of investigation in many contexts. Most relevant to the present paper are studies of local damage induced by small impacts. This includes the effect of impacts on composites (which have been extensively studied; e.g., Choi and Chang (1992)) and on ceramics (Evans, 1973; Tsuruta *et al.*, 1990). Such impacts introduce damage which can grow subsequently in fatigue. The effect of small particle impacts on blades made of conventional titanium alloys has been investigated by Nicholas, Barber and Bertke (1980). They considered various impact conditions on a blade-like sample, and then assessed the resulting reduction in fatigue strength. They found that impacts which produce cracks had in fact a more severe effect on fatigue strength than higher energy impacts which cleanly cut out a portion of the blade leading edge. Very recently, Walston, Darolia and Demania (1997) have investigated the effect of small particle impacts on NiAl alloys.

2. MATERIALS, PREPARATION, AND EXPERIMENTAL PROCEDURE

2.1. *Materials*

The gamma TiAl alloy used principally in this investigation had a composition Ti-47.3Al-2.2Nb-0.5Mn-0.4W-0.4Mo-0.23Si (Bhowal, Merrick and Larsen, 1995). This alloy, designed as WMS alloy, was investment cast into plates measuring 3 mm \times 11 mm \times 75 mm. Following casting the material was subjected to a HIP treatment consisting of 1260°C and 172 MPa for 4 h, followed by a heat treatment of 1010°C for 50 h. The resulting microstructure was fully lamellar in character with significant amounts of the B_2 and α_2 phases, along with some degree of residual segregation. Rectangular flat plates of two thicknesses (1.75 mm and 2.25 mm) were electro-discharge machined from the cast plates. All samples were low stress ground, subjected to conventional mechanical polishing by hand with 600 grit paper and then electropolished in a solution containing 300 ml methanol, 175 ml *n*-butanol and 30 ml perchloric acid maintained at -50°C .

A second investment cast gamma alloy with a final composition of Ti-47.9Al-2.0Cr-1.9Nb (Huang, 1991) has also been the subject of study in concurrent investigations; this alloy will be referred to as 48-2-2 alloy. Plates measuring 12.6 mm \times 100 mm \times 140 mm were subjected to a pre-HIP treatment of 1093°C for 5 h, HIP'ed at 1205°C for 4 h at 172 MPa and given a subsequent heat treatment of 1205°C for 2 h, followed by rapid cooling. The resultant microstructure of 48-2-2 alloy was near-gamma in character, with an average grain size of about 70 μm and about 6 vol% of γ - α_2 lamellar colonies. The 48-2-2 alloy is relevant to the present investigation in that data at high strain-rates was obtained for this alloy, as described below.

2.2. *Material properties*

Room temperature tensile testing of the WMS alloy was carried out at strain rates of 0.3 s⁻¹ on cylindrical bars of gauge diameter 4.57 mm and length 23.4 mm. These

tests revealed a yield strength of 500 MPa, an ultimate strength of 540 MPa and a plastic strain to failure of 0.5%. The true-stress true-strain responses of the 48–2–2 alloy at large strains were measured in compression using solid-cylindrical samples 5.0 mm in dia. by 5.0 mm long, lubricated with molybdenum grease. Quasi-static compression tests were conducted on a screw-driven load frame at strain rates of 0.001 and 0.1 s⁻¹ at 77 and 298K. Dynamic tests, at strain rates of 1000–8000 s⁻¹, were conducted as a function of strain rate and temperature utilizing a Split-Hopkinson Pressure Bar (Follansbee, 1985). High temperature tests were performed in a vacuum furnace mounted on the Split-Hopkinson Pressure Bar (Frantz, Follansbee and Wright, 1984). The high temperature Hopkinson-Bar samples were lubricated with a boron nitride powder/alcohol slurry which was allowed to dry on the sample prior to testing. The samples were heated to temperature and allowed to stabilize prior to testing. The furnace used in the elevated temperature tests reached the equilibrium test temperature within an elapsed time of 7–10 minutes based upon thermocouple monitoring directly adjacent to the sample.

The results of these tests were then fit to a Zerilli-Armstrong model (Zerilli and Armstrong 1987), which features five fitting constants and involves a logarithmic dependence on strain rate and a power law dependence on strain. Computer programs were developed to optimize the fitting constants to the stress-strain data over a wide range of temperatures and strain rates. A range of corresponding constants are given to calculate the stress at a certain strain followed by comparing this value to the experimental values. This process is repeated for every curve of interest until the best agreement to the entire set of stress-strain data is achieved. A deviation parameter indicating the degree of fit is defined as:

$$\text{Deviation} = \frac{1}{n} \sum_{i=1}^n \frac{|\sigma_{\text{calculated}}(\epsilon_i) - \sigma_{\text{experimental}}(\epsilon_i)|}{\sigma_{\text{experimental}}(\epsilon_i)} \quad (1)$$

Two points representing the characteristic hardening behaviour on each stress-strain curve were taken to compare to the calculated stresses at the corresponding strain values. For the models presented, fits with deviation parameters of better than 4% were achieved. An in-depth description of the Zerilli-Armstrong model as well as other models was recently summarized in detail by Chen and Gray (1996). Additionally, a recent review of the high-strain rate mechanical response of aluminides by Gray (1996) details the numerous varied responses of Fe-, Ni-, and Ti-aluminides to high-strain rate deformation as a function of temperature.

From the fit so obtained, the flow stress as a function of the plastic strain (for the 48–2–2 alloy was expressed in the form

$$\sigma = 270 + 660 \exp[-0.00350T + 0.0001750T \ln(\dot{\epsilon})] + 3000\epsilon_p^{0.96} \quad (2)$$

where the stress σ is in MPa, $\dot{\epsilon}$ denotes the strain rate, ϵ_p is the plastic strain, and T is temperature. For the WMS alloy, the static yield stress is approximately 200 MPa higher than that of the 48–2–2 alloy to which the fit was made. The first term in the Zerilli-Armstrong fit represents essentially the static yield stress. Therefore, we raised that coefficient by 200 MPa (from 270 to 470) and assumed the same hardening behaviour and strain-rate sensitivity as was observed in the 48–2–2.

2.3. Impact Experiments

High speed impact damage was produced on the plates using a ballistic impact facility. Steel spherical projectiles were accelerated down a steel barrel by the release of compressed helium. The velocity of the projectile was measured at the end of the barrel by breaking two laser beams a known distance apart. The spheres were 1.587 mm in diameter and had velocities ranging from 76 m/s to 305 m/s. The particle impinged normal to the plate in the thickness direction and at its centre.

3. FINITE ELEMENT SIMULATION OF IMPACTS

Finite element simulations of the high speed, small particle impact experiments were based on the idealized problem of a circular, simply supported plate impacted perpendicularly (without friction) by a rigid sphere with mass density 7850 kg/m^3 . The impacted plate (representing the WMS alloy) was assumed to have a density of 3830 Kg/m^3 . The impacted plate was taken to occupy the region $0 < r < 19$ and $0 < z < t$, where $t = 1.75$ or 2.25 , depending on the plate thickness; the point of impact is at $r = 0, z = 0$. The calculations employed the commercial code ABAQUS EXPLICIT (Hibbit Karlsson and Sorenson, Inc.). The uniaxial behaviour described above was generalized to multiaxial states through the Mises stress invariant. The elastic modulus and Poisson ratio were taken to be 192 GPa and 0.3, respectively, and the transition in the stress-strain curve from the elastic regime to the fully plastic regime was assumed to have the same shape as for the 48-2-2 alloy. Meshes of various types have been used to assess convergence; the results to be presented below are based on a mesh of 2304 elements. The time integration steps are chosen automatically in ABAQUS EXPLICIT depending on the element size. The time steps were generally on the order of 2×10^{-9} s.

Typical results from the finite element simulations of high speed impacts (229 m/s on a 1.75 mm plate) are shown in Fig. 2. The peak force, the displacement at the impact point, as well as the rear surface deflection and the rear surface effective strain at $r = 0$, are plotted as functions of time. All have been normalized by their peak values (shown in Fig. 2); the peak values occur at different time instants. A second result of interest is the variation of the effective strain (the second invariant of the strain tensor) on the rear surface with r (distance from the central point beneath the point of impact). The results for three impacts (152, 229, 305 m/s on a 1.75 mm plate) are depicted as the solid curves in Fig. 3. These impacts produce successively higher peak effective strains; however, when the strains are normalized by their maximum values at $r = 0$, they can be seen to fall essentially along a single curve. For the lowest energy impact, at which no rear face damage was observed, the strain distribution is somewhat different.

The coincidence in the effective strain distributions for impacts of various energies has two useful implications. First, it indicates that strain at any point on the rear surface can be estimated if the maximum strain at $r = 0$ is known. Second, it provides the basis for constructing what we designate as "equivalent" static tests. Specifically, we entertain the possibility that static indentations of plates of the same dimensions

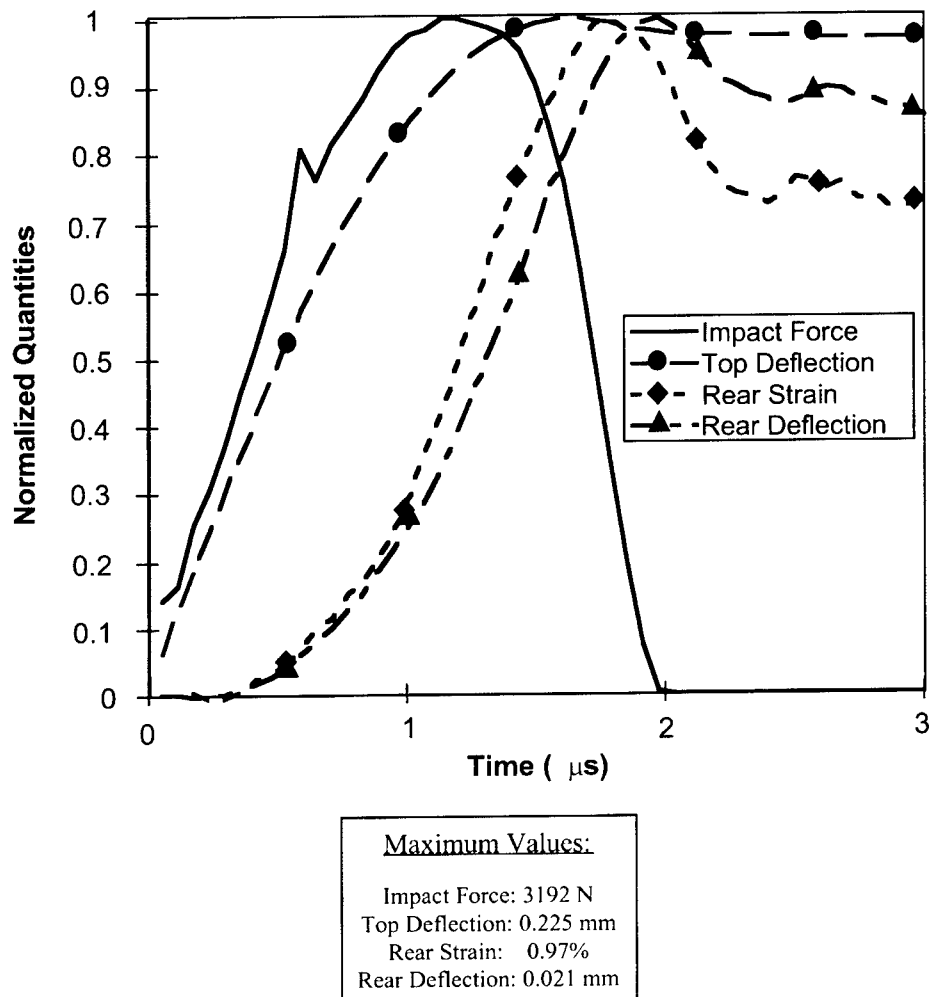


Fig. 2. Representative time traces from finite element analysis (229 m/s on 2.25 mm plate); quantities have been normalized by their maximum values.

could result in the same strain distribution if the plates were properly supported. Hence, we considered plates resting on a rigid support which contained a hole of diameter D concentric with the impact point. The strain distributions associated with such static indentations, again normalized with respect to their maximum values at $r = 0$, are also depicted (as the dashed curves) in Fig. 3 for several values of the hole diameter D . It can be seen that holes of diameter in the range shown lead to distributions that are rather close to the distributions from the dynamic case. Accordingly, static tests were carried out using a hole of diameter 6.35 mm, with indentation forces chosen to produce strains similar to those predicted by the simulation of high speed impacts.

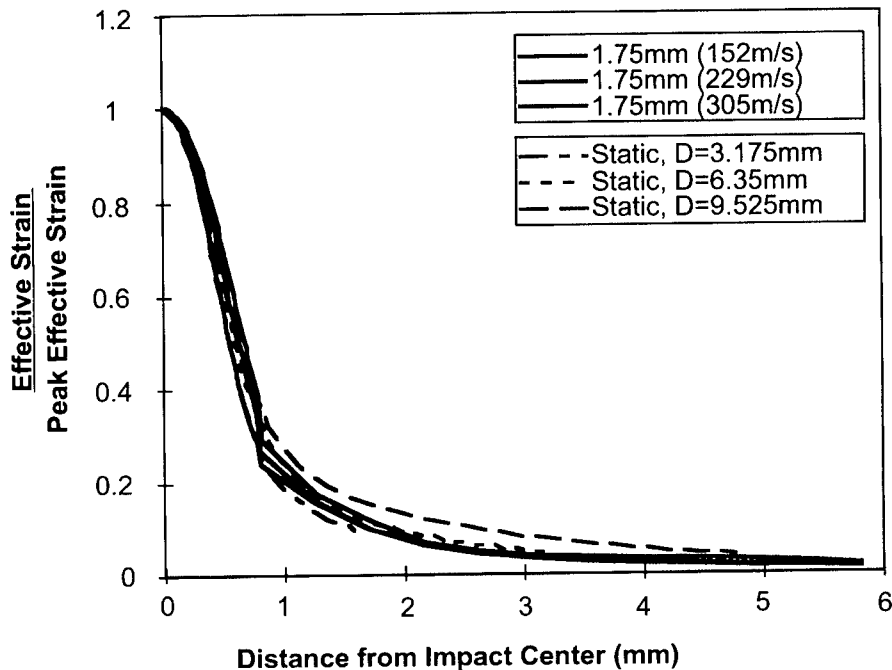


Fig. 3. Effective strains (normalized by their values at $r = 0$) as a function of radial distance from centre of impact. Note similarity of distribution for various high speed impacts, as well as effect of hole diameter D on distribution for static indentations.

4. RESULTS

4.1. Comparison of impact experiments with numerical predictions

We now present observations of plastic deformation and cracking produced by high speed impacts and static indentations and relate these observations to predictions of rear surface strains. First, we note that while there are substantial dents on the impacted face, there is little or no cracking. While gamma can withstand substantial strains when the stresses are compressive (as they predominantly are in the contact region), plastic straining and tensile stresses, such as takes place on the rear surface, do produce cracking. Selected optical images of the rear surfaces are shown in Fig. 4. From these images, a plastic zone was identified as that region in which plastic slip is observable at the surface. The size of this zone was defined as the diameter of the smallest circle which included all the observed surface slip. Selected secondary electron images of the rear surfaces are shown in Fig. 5. From these images, a cracking zone can be discerned; this zone includes larger cracks at the center and smaller cracks at the periphery. Selected optical images of the rear surfaces are shown in Fig. 4. The size of the cracking zone was defined as the diameter of the smallest circle which included all the observed cracking. The zones of plasticity and cracking are referred to collectively as the damage zones.

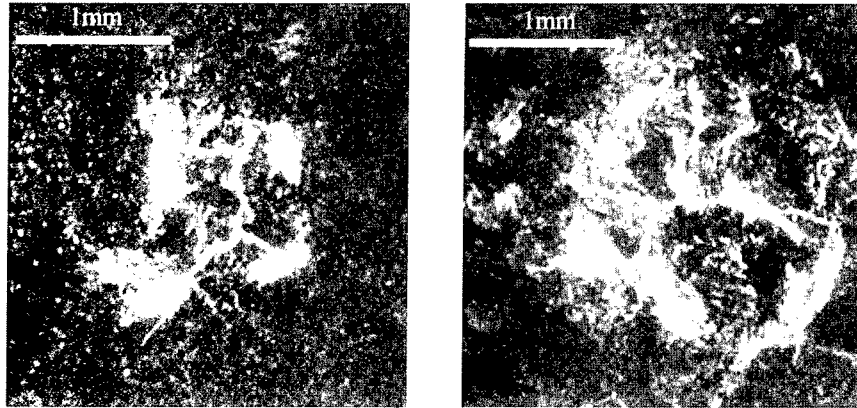


Fig. 4. Selected optical images of the rear face of plates impacted at high speed showing plastic zones.

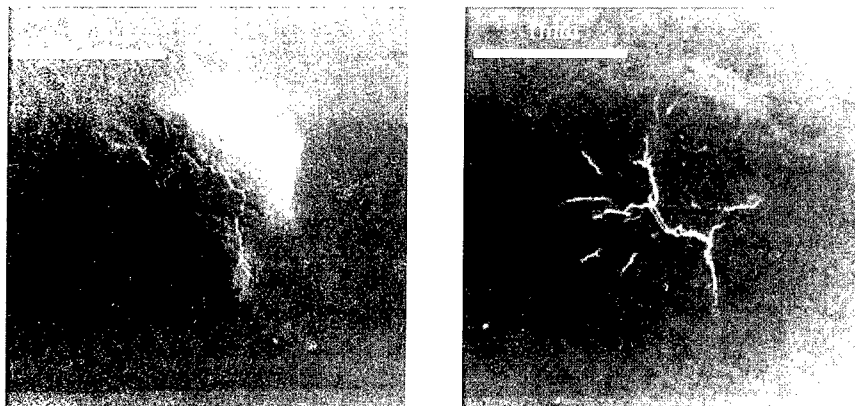


Fig. 5. Selected secondary electron images of the rear face of plates impacted at high speed showing cracking zones.

The sizes of the plastic zone and the cracking zone for high speed impacts on two plate thicknesses are plotted in Fig. 6 as a function of impact velocity; the expected increase of damage with velocity is observed. Additionally, the damage zones tend to be larger for thinner plates. Likewise, the damage zones associated with static indentation increase in size with static indentation force and tend to be larger for thinner plates (Fig. 7).

We consider now whether the strains computed from finite element analysis and continuum plasticity can be used to predict the extent of damage during impact. For each of the above high speed impacts and static indentations, the distribution of effective plastic strain on the rear surface was determined (from FEA) at the radial positions corresponding to the periphery of the plastic and cracking zones. Thus, this strain corresponds to the minimum straining necessary to initiate plastic slip or cracking. The inferred strains to initiate plasticity and cracking are plotting in Fig. 8

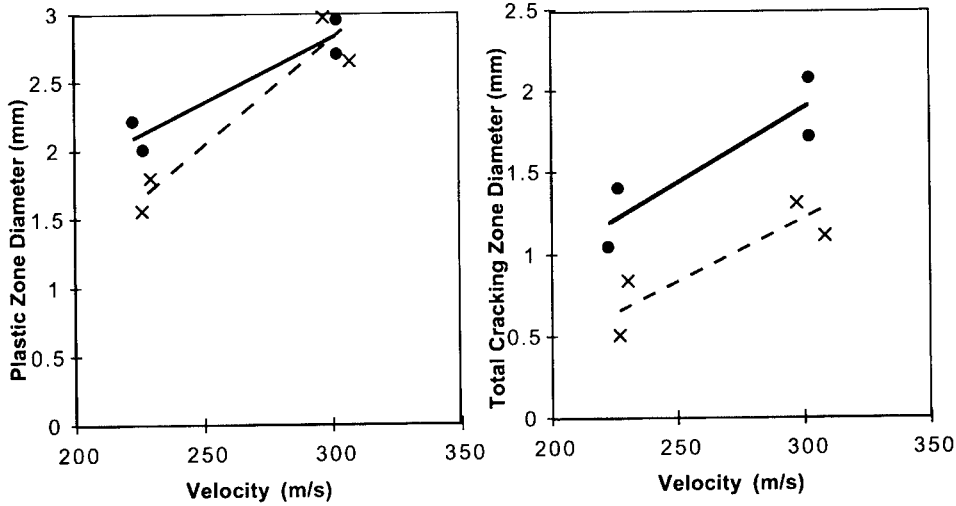


Fig. 6. Diameters of plastic zones and cracking zones for high speed impacts as a function of impact velocity (—●— 1.75 mm plate, -X- 2.25 mm plate).

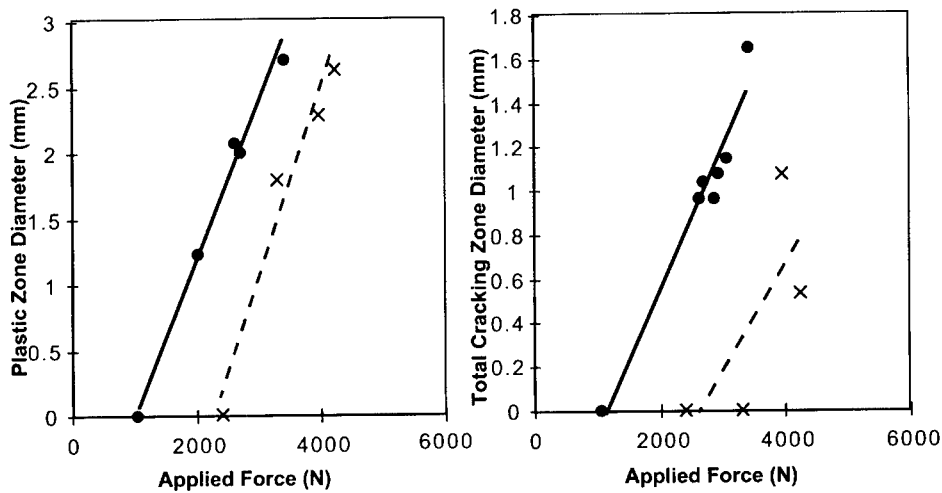


Fig. 7. Diameters of plastic zones and cracking zones for static indentations as a function of indentation force (—●— 1.75 mm plate, -X- 2.25 mm plate).

as functions of the damaged zone size. If plastic yielding were perfectly reproducible, then the inferred strains would be constant for all impacts sufficient to induce some plasticity; likewise, perfectly reproducible ductility would lead to constant strains for crack initiation. As can be seen, plasticity becomes visible when the strains reach values on the order of 0.2–1%. Interestingly, there is little discernable difference between the strains to produce visible plasticity with high speed impacts and with

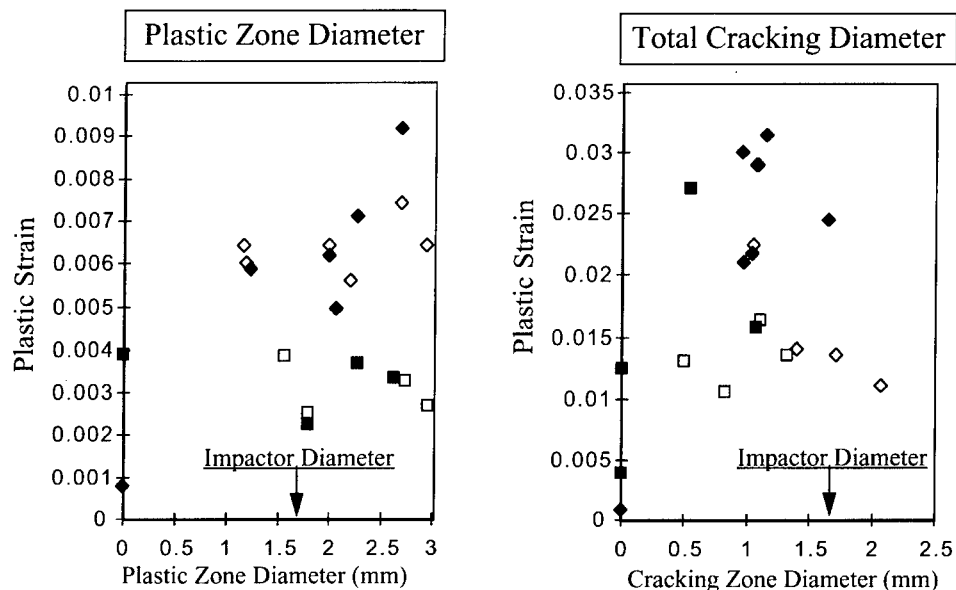


Fig. 8. Effective plastic strains at the peripheries of plastic and cracking zones for high speed impacts (\diamond 1.75 mm plate, \square 2.25 mm plate) and static indentations (\blacklozenge 1.75 mm plate, \blacksquare 2.25 mm plate).

static indentations. However, thinner plates tend to require somewhat higher strains to produce visible plasticity; this is not understood at present.

The effective plastic strain to initiate cracking spans the range from 1–3%. Note that these strains correspond to a range of cracking zone sizes. The strain level may be compared with the uniaxial tensile ductility of 0.5% measured for this material, although the strains in the configuration studied here are biaxial, and the strained volume is rather small. While there is a range of strains at which cracking initiates, these strains appear to be consistently lower for high speed impacts (from 1–2%) than for static indentations (from 2–3%). The data suggest that ductility decreases at higher strain rates, although this conclusion is somewhat premature given the known variability of γ and the small size of the data set examined here. However, there is other evidence (Y-W. Kim, private communication) that the uniaxial tensile ductility first increases with strain rate up to strain rates of the order 0.01 s^{-1} , and then decreases for higher strain rates. The strain rates associated with the impacts considered here can be much higher than 0.01 s^{-1} .

4.2. Approximate estimates of strains due to small particle impacts

It has been seen that strains on the rear face of the plate correlate reasonably well with damage zones. Therefore, it seemed potentially useful to devise simple approximate means of estimating the strain produced by any given impact. However, constructing a simple analysis of the impact event is very challenging: the event is dynamic, the material is strain-rate sensitive, and the strains in the rear portion of the

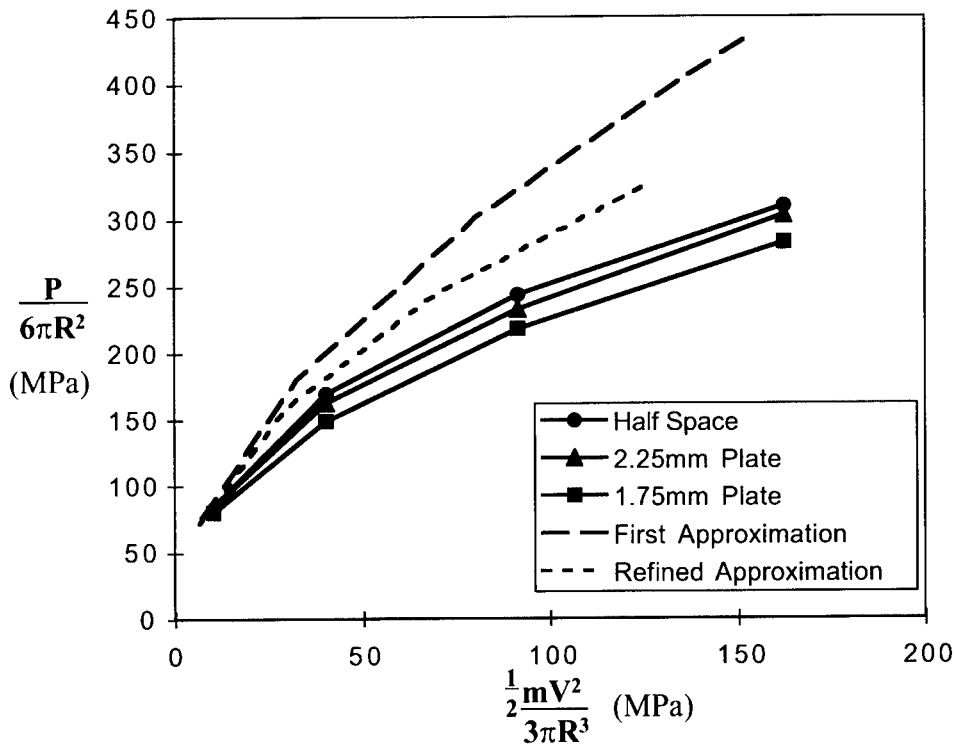


Fig. 9. Normalized peak impact force as a function of normalized impact energy.

impacted plate are barely into the elastic-plastic regime. Nevertheless, the beginnings of such a simplified analysis is put forth here. Our approach involves demonstrating how the peak contact force can be estimated, and then showing from numerical simulations that the rear surface peak strain can be correlated with the peak force suitably normalized.

Our first step in devising a method of estimating the peak force was to eliminate the strain-rate sensitivity and carry out strain-rate *insensitive* finite element computations for the set of high speed impacts described above on thin plates. This was done using the constitutive law (2), corresponding to the 48-2-2 alloy with the strain rate fixed at 0.001 s^{-1} . In addition, strain-rate *insensitive* finite element computations were carried out with the same constitutive law for the same set of impacts *on a half space*. The corresponding peak forces are plotted in Fig. 9 as the solid curves, with the forces and impact energies normalized by the sphere radius as shown. Note that all of these calculations included the effects of inertia.

To devise a simpler means of analyzing these impacts, we appeal to the classification of impacts given by Johnson (1985). One finds the impacts of interest here are quasistatic in that the impact velocity is much less than the elastic wave speed. In addition, ρV^2 tends to be the order of 0.1–1 times the yield stress; this corresponds to fully plastic contact, at the upper limit of shallow indentation theory but still short

of the hydrodynamic regime. One can, therefore, usefully employ Johnson's (1985) simplified formulation in which the "equation of motion of the particle" is combined with the "static force-indentation relation of the half-space". With reference to Fig. 1, the appropriate relations include the equation of motion of the particle

$$P = -m \frac{d^2 \delta}{dt^2} \quad (3)$$

where P is the contact force between the particle and the impacted body, m is the particle mass and δ is the indentation. This equation is subject to the initial conditions

$$\delta(0) = 0; \quad \frac{d\delta}{dt} = V \quad (4a, 4b)$$

where $t = 0$ coincides with the instant of first impact, and V is the velocity of the particle at impact.

The geometry of the rigid sphere implies a relation between contact radius and indentation of the form

$$a^2 = 2R\delta - \delta^2 \quad (5a)$$

where a is the contact radius and R is the particle radius. The relation (5a) can be approximated for shallow indentations ($\delta/R \ll 1$) as

$$a^2 = 2R\delta \quad (5b)$$

Finally, we use the approximate relation between contact force and contact radius (Johnson, 1995)

$$P = 3\pi a^2 \sigma_{rep} \quad (6)$$

where σ_{rep} is a representative flow stress. In taking the contact pressure to be 3 times the flow stress, fully plastic contact conditions have been assumed.

If the flow stress is approximated as constant during the impact $\sigma_{rep} = \sigma_0$, eqns (3), (4), (5b) and (6) can be integrated with the result

$$\frac{P}{6\pi R^2} = \sqrt{\frac{1}{2} m V^2} \sigma_0 \quad (7)$$

which suggests a feasible normalization scheme for other assumptions of flow stress. Note that the impact event is described completely by the impact energy of the particle in this approximate analysis; the inertia of half-space is neglected.

Alternatively, the representative flow stress in equation (6) may be taken to be dependent on the strain and on the strain-rate. This may be done by adopting the observation of Tabor (1951) that a representative strain beneath the contact depends on the contact radius according to

$$\epsilon_{rep} = 0.2a/R \quad (9)$$

and, therefore,

$$\sigma_{rep} = \sigma(0.2a/R)$$

where the function $\sigma(\epsilon)$ represents the uniaxial stress-strain curve. Although this has not been done, the strain-rate sensitivity can also be included using

$$\dot{\epsilon}_{rep} = 0.2\dot{a}/R \quad (10)$$

together with a relation between the indentation rate \dot{a} and the indentation rate.

Using a representative flow stress that depends on the contact area, the simplified analysis was also performed using the following linear hardening model

$$\sigma = \sigma_0 + k\epsilon \quad (11)$$

With $\sigma_0 = 434$ MPa and $k = 3682$ MPa, this linear approximation closely fits equations (2) for a temperature of $T = 298$ K and a strain rate of 0.001 s^{-1} .

For such a hardening model, the peak force and the energy are related parametrically to the peak indentation δ_{max} according to

$$\frac{P}{6\pi R^2} = \frac{\delta_{max}}{R} \left[\sigma_0 + 0.2k \sqrt{\frac{\delta_{max}}{R}} \right] \quad (12)$$

$$\frac{1}{2}mV^2 = \left[\frac{\delta_{max}}{R} \right]^2 \left[\sigma_0 + 0.2 \left(\frac{4}{5} \right) k \sqrt{\frac{\delta_{max}}{R}} \right] \quad (13)$$

The results of this first approximation simplified analysis are plotted as the dotted curve in Fig. 9 along with the finite element results.

It is interesting to note that while the peak forces associated with impacts on the thin plates are lower than those associated with impacts upon a half-space, they are only slightly lower. One expects inertia of the impacted body to play a more important role in impacts on thin plates. Studies of impact (Goldsmith, 1960) would suggest that the mass of the particle relative to that of the plate plays a role, in addition to the impact energy. For example, if the impact energy were to be held constant, but the impacting body had a much lower speed and a much higher mass, then the plate would flex statically during the impact. Much of the impact energy would go into gross deformation of the plate. Of course, the response to low speed impacts would depend on the diameter of the impacted plate, in contrast to the high speed impacts.

For the higher speeds considered here, however, the contact time is not long compared with the natural period of gross flexural vibrations. Thus, little gross deflection occurs and lower rear-face strains are realized. The impact energy instead goes into very local and more intense deformation in the contact region, leading to higher peak forces. Still, as for the impacts on the half space, the impact velocities are not high enough for there to be much inertial resistance to the local contact deformation. In this sense, within the range of impact conditions considered here, the precise combination of mass and velocity is less important than the energy: regarding the peak force, the plate reacts rather like a more massive body.

One can also see from Fig. 9 that the approximate analysis agrees fairly well with the half-space results, at least for lighter impacts; it overestimates the peak force for

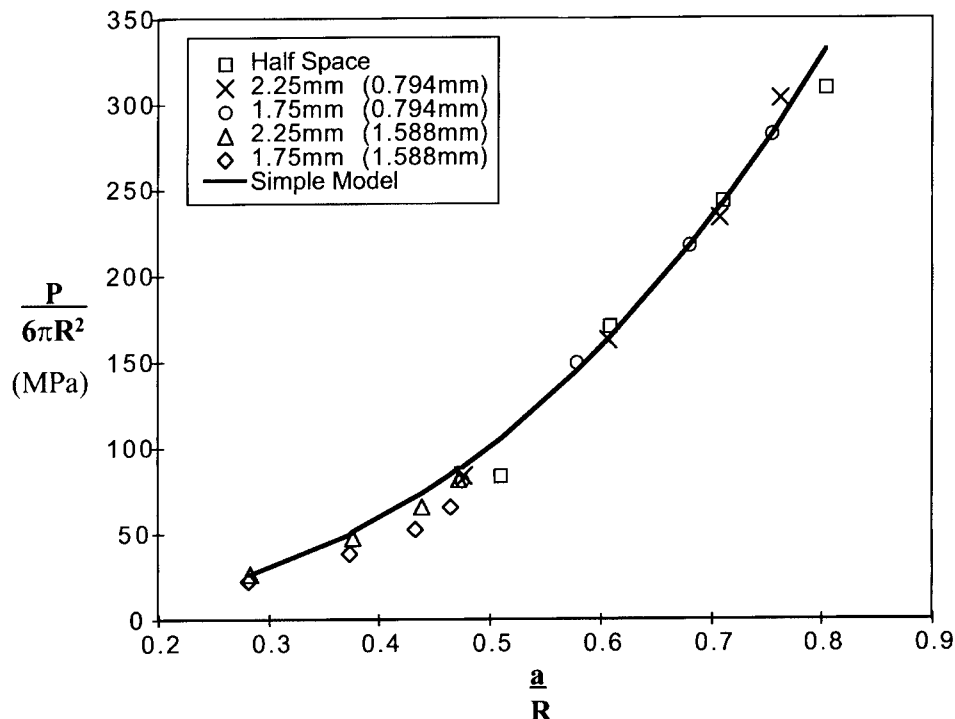


Fig. 10. Finite element predictions of contact force versus contact radius compared with fully plastic contact relation.

higher impacts. To gain some insight into the basis for the deviation between the finite element results and the approximate analysis, recall that the essential ingredients in the approximate analysis are the relations between force and contact radius and between contact radius and indentation depth. For this reason we have plotted these results from the finite element calculations for impacts on the half space in Figs 10 and 11, together with the predictions of the approximate analysis. Again, the half space has properties given by eq (2) with a strain-rate of 0.001 s^{-1} , and the approximate analysis uses the closely fitting linear hardening curve.

From Fig. 10, one can see that the relation between contact force and contact radius involving the representative flow stress fits the FE results remarkably well; this plot contains in addition numerical results for impacts of 3.175 mm spheres on the plates. However, from Fig. 11, one can see that the FE predictions of surface displacement versus contact radius, while reasonably captured by the simplified eq (5b) for small displacements, is poorly approximated by this shallow indentation formula for larger indentation (higher impact velocities). Even the more accurate approximation tends to overestimate the contact radius for a given indentation. Clearly, there is deflection of the surface outside of the contacting region. One expects these additional deflections to be more severe in the cases of impacted plates, where the contact area should be even more overpredicted as a function of the surface displacement.

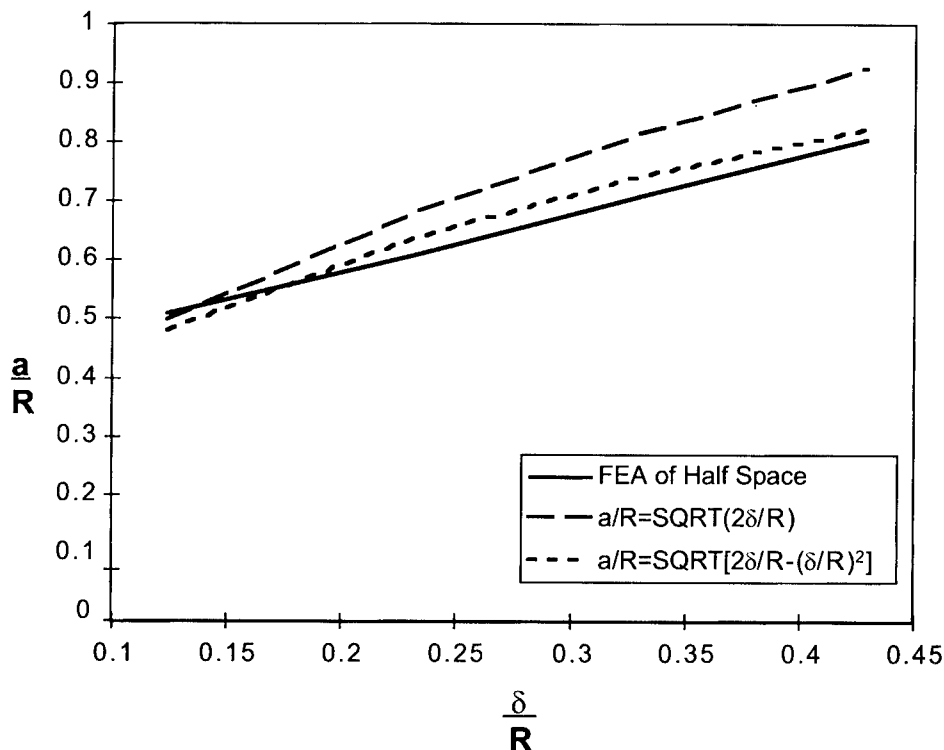


Fig. 11. Finite element predictions of contact radius versus surface displacement compared with simple geometric relations.

Accordingly, the approximate analysis was repeated, this time with the full expression (5a) for the contact radius in terms of the indentation (which requires numerical integration), rather than using eq (5b). The result of this analysis is plotted in Fig. 9, now as the dashed curve. While there is some improvement in the prediction (the peak force is lowered), it continues to overestimate the peak force somewhat for higher energy impacts.

While deformations near the contact surface are fully plastic, and hence amenable to the approximate analysis of the peak force given above, the deformations near the rear surface are within the elastic-plastic regime. This has made it difficult to devise an approximate analysis from which one can estimate in advance the rear surface strains. Of course, this difficulty is compounded by our use of realistic (experimentally determined) stress-strain curves, rather than, say, a perfectly plastic model. Nevertheless, we now show a correlation gleaned from the numerical results which might prove to be helpful in building such an approximate analysis. Figure 12 displays the peak force divided by the thickness squared (a stress-like quantity) plotted as a function of the peak strain on the rear surface. As indicated, Fig. 12 contains results for two materials: for the impacts on the WMS alloy (which includes strain-rate sensitivity), as well as for the impacts on the 48-2-2 alloy (for which the strain-rate has been fixed at 0.001 s^{-1}).

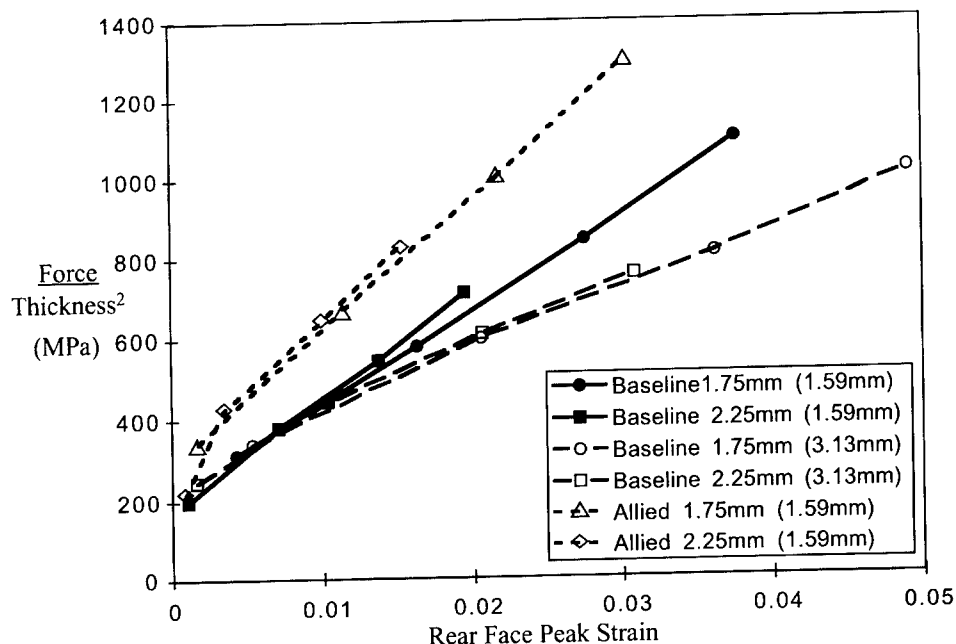


Fig. 12. Correlation between peak force normalized by thickness squared and peak rear surface strain as deduced from finite element results.

In each case, one discerns the data points to fall within a tolerable range of a single "stress-strain" curve. The dependence on the thickness of the plate is quite slight (after the normalization of the peak force); there is some dependence on the sphere radius, particularly as the peak strain extends beyond about 2%. Notice also that the curves for the WMS alloy (only simulations with 1.59 mm spheres were conducted with this alloy) tend to lie approximately 200 MPa above the curves for the 48-2-2 alloy. We suggest that it may be possible to combine this correlation with the approximate analysis of the peak force described above to estimate the likelihood of damage initiation given a contemplated impact. Certainly, to have a general tool for making quantitative predictions of damage, much additional study of the origin of the form of these curves and the dependence on the material stress-strain behaviour is required.

5. CONCLUSIONS

Our goal has been to gain insight into the factors which control the damage accompanying small particle impacts on air foils of low ductility intermetallics, such as gamma TiAl. To this end, experiments were conducted to study impacts of small particles on thin flat plates. Impacts over a range of energies have been produced which introduced differing degrees of damage on the plate rear faces. Damage was quantified in terms of two measurements: the size of the region in which plasticity

was visible and the size of the region in which cracking was visible. In addition, finite element analyses of the high speed impacts were performed, from which the plastic strain distributions were extracted. These finite element analyses also permitted us to devise static indentation tests which produce strain distributions on the rear face essentially matching the distributions from the high speed impacts.

For each impact and indentation, the strains necessary to initiate plastic deformation and to initiate cracking were taken to be the finite element predicted plastic strain at the periphery of the respective plastic or cracking zone. It was found that the strains to initiate plasticity ranged from 0.2–1.0%, independent of whether the damage was caused by a high speed impact or a static indentation. There was a higher strain to initiate plasticity in thinner (1.75 mm) plates than thicker (2.25 mm) plates. It was also found that strains ranging from 1–2% were necessary to initiate cracking in the high speed impacts, whereas higher levels of strain (from 2–3%) were required in the static indentations. These strain levels should be compared with strains to failure in uniaxial tension of 0.5% measured with standard cylindrical specimens. While the set of data reported here is still rather small, it does suggest that the strain to initiate cracking under high rate conditions is lower than that to initiate cracking under static conditions. Finally, it has been shown that reasonably accurate calculations of the peak force can be devised based on simple contact mechanics. In addition, there is a correlation between a suitably normalized peak force and the peak strain on the rear face. These provide a potential basis for simple means of estimating whether cracks will initiate under contemplated impact conditions.

ACKNOWLEDGEMENTS

The authors appreciate the assistance K. Muraleedharan with the microstructural observations. Useful discussions with C. M. Austin, J. L. Beuth, S. L. Draper, V. Z. Gandelman, T. Harding, J. W. Jones, J. Lasalle, M. V. Nathal, and T. M. Pollock are gratefully acknowledged. This research has been supported by AFOSR/PRET Program on Gamma Titanium Alloys under Grant F49620-95-0359.

REFERENCES

- Bhowal, P. R., Merrick, H. F. and Larsen, Jr., D. E. (1995) *Mater. Sci. Eng.* **A192/193**, 685–690.
- Chen, S. R. and Gray-III, G. T. (1996) *Metall. & Matls. Trans. A* **27A**, 2994–3006.
- Choi, H. Y. and Chang, F. K. (1992) A model for predicting damage in graphite/epoxy laminated composites resulting from low velocity point impact. *J. Comp. Mat.* **26**, (14), 2134–2169.
- Draper, S. L., Pereira, J. M. and Nathal, M. V. (1997) HITEMP Review 1997, NASA CP-10192, **II**, 25-1–25-13.
- Evans, A. G. (1973) Strength degradation by projectile impacts. *J. Am. Cer. Soc.* **56**, 405–409.
- Follansbee, P. S. (1985) *Metals Handbook-Mechanical Testing*. American Society of Metals, Metals Park, OH, **8**, 198–203.
- Frantz, C. E., Follansbee, P. S. and Wright, W. J. (1984) New experimental techniques with the Kolsky Bar. In *High Energy Rate Fabrication*, ed. I. Berman and J. W. Schroeder, pp. 229–236. Amer. Soc. Mech. Eng.

- Goldsmith, W. (1960) *Impact*. Edward Arnold Ltd., London.
- Gray-III, G. T. (1996) Influence of high-strain rate and temperature on the mechanical behaviour of Ni-, Fe, and Ti-Aluminides. In *Deformation and Fracture of Ordered Intermetallic Materials*, ed. W. O. Soboyejo, T. S. Srivatsan and H. L. Fraser, pp. 57–73, TMS, Warrendale, PA.
- Haake, F. K., Salivar, G. C., Hindle, E. H., Fischer, J. W. and Annis, Jr, C. G. (1989) Threshold fatigue crack growth behavior. U.S. Air Force Technical Report WRDC-TR-89-4085, Wright-Patterson Air Force Base, OH.
- Huang, S. C. (1991) U.S. Patent 5,076,858.
- Johnson, K. L. (1985) *Contact Mechanics*. Cambridge University Press, Cambridge.
- Knaul, D. A., Beuth, J. L. and Milke, J. G. (1998) Modeling and measurement of the notched strength of gamma titanium aluminides under monotonic loading. Unpublished manuscript.
- Nicholas, T., Barber, J. P. and Bertke, R. S. (1980) Impact damage on titanium leading edges from small hard objects. *Experimental Mechanics*, **20**, (10), 357–364.
- Steif, P. S., Jones, J. W., Harding, T., Rubal, M. P., Gandelsman, V. Z., Biery, N. and Pollock, T. M. (1997) Surface Damage Due to Impact and Fatigue Strength Reduction in Gamma Titanium Aluminides. In *Structural Intermetallics 1997*, ed. M. V. Nathal, R. Darolia, C. T. Lui, P. L. Martin, D. B. Miracle, R. Wagner and M. Yamaguchi, pp. 435–442. The Minerals, Metals and Materials Society.
- Tabor, D. (1951) *Harness of Metals*. Oxford University Press, U.K.
- Tsuruta, H., Masuda, M., Soma, T. and Matsui, M. (1990) Foreign object damage resistance of silicon nitride and silicon carbide. *J. Am. Cer. Soc.* **73**, 1714–1718.
- Walston, W. S., Darolia, R. and Demania, D. A. (1997) Impact resistance of NiAl alloys. Unpublished manuscript.
- Wright, P. K. (1993) On ductility and toughness requirements for intermetallics in aircraft engines. In *Structural Intermetallics*, ed. R. Darolia *et al.* The Minerals, Metals and Materials Society.
- Zerilli, F. J. and Armstrong, R. W. (1987) Dislocation-mechanics-based constitutive relations for material dynamics calculations. *J. Appl. Phys.* **61**, 1816–1825.



Pergamon

J. Mech. Phys. Solids, Vol. 46, No. 10, pp. 2087–2102, 1998

© 1998 Elsevier Science Ltd. All rights reserved

Printed in Great Britain

0022-5096/98 \$—see front matter

PII: S0022-5096(98)00058-1

STRAIN CHARACTERIZATION OF PROPAGATIVE DEFORMATION BANDS

WEI TONG

Department of Mechanical Engineering, Yale University, New Haven, CT 06520-8284 U.S.A.

(Received 20 December 1997; accepted 18 March 1998)

ABSTRACT

An experimental study on the formation and evolution of strain inhomogeneity in the form of deformation bands on the surface of polycrystalline sheet metals is presented. A whole field in-plane deformation measurement technique based on computer vision has been applied for *in situ* monitoring the development of plastic deformation patterns in annealed Al–5%Mg and recovered AA5182 aluminum sheet metals. The strain inhomogeneity over a rectangular area about 5 mm × 3 mm on the sheet metal surfaces is found to increase steadily with increasing elongation during a uniaxial tensile test. Propagative deformation bands have been detected in both aluminum alloys by incremental strain mapping although no band-like deformation patterns can be identified by direct visual observation of Al–5%Mg specimen surfaces. The effect of plastic deformation patterns on surface finish, tensile ductility, and formability of sheet metals are elucidated. The approach and results of this experimental investigation can be valuable to physically-based multiscale plasticity modeling of sheet metal forming. © 1998 Elsevier Science Ltd. All rights reserved.

Keywords: A. strain localization, B. polycrystalline materials, B. metallic materials, C. digital image correlation, C. mechanical testing.

1. INTRODUCTION

In the continuing efforts in reducing weights and increasing fuel efficiency of ground transportation vehicles, light-weight aluminum alloys are being developed and gradually used for automotive body sheet applications. Many important technical issues including surface finish and formability of newly developed aluminum sheet metals require in-depth investigation to ensure their defect-free production and smooth introduction. The surface finish is found to be particularly problematic for some aluminum alloy sheet metals. Beside the commonly known “orange peeling” due to surface grain roughening during forming, 5xxx aluminum alloys are susceptible to the growth of propagative Portevin-Le Chatelier (PLC) deformation bands (Chihab *et al.*, 1987). Formation of ridging or line surface defects during stamping has also been reported for 6xxx aluminum alloys that are being developed for automotive outer body panels (Roush, 1996). Existing aluminum alloy sheets also, in general,

show lower formability than that of low-carbon steel sheets currently used for auto body panels (Newby, 1982; Ghosh *et al.*, 1984). Three important parameters, (n , K and r) have been identified in forming of steel sheets over the years, where n and K are the material parameters in the Holloman constitutive equation $\sigma = K\epsilon^n$, r is the ratio of the true strain in the lateral direction to the true strain in the thickness direction of a sheet metal (Raghavan *et al.*, 1992; The Aluminum Assoc., 1996). The parameter n is known as the strain hardening exponent and a higher value of n implies a greater stretchability. However, the strain hardening exponent n alone may not be sufficient as a measure of stretchability across sheet metal material systems. For example, while an n value of 0.23 is obtained for both heat treated aluminum body sheet 6111-T4 and aluminum killed deep drawing quality steel based on stress-strain curves measured from uniaxial tensile testing, the actual stretchability of the aluminum sheet is much lower than that of the steel (The Aluminum Assoc., 1996).

The surface finish of sheet metal panels is closely related to the roughening of surface grains during stretch forming operations (Fukuda *et al.*, 1974). Free surface grain roughening are the manifestation of microscopic non-steady and non-uniform plastic deformation of individual grains or grain clusters even when a sheet metal undergoes a macroscopically uniform plastic deformation (Tong *et al.*, 1997; Weiland *et al.*, 1997). The existence of propagative PLC deformation bands and the appearance of accompanying surface markings in 5xxx and other aluminum alloy sheet metals have been attributed to the self-organization of microscopic plastic deformation processes correlated over a certain length scale and time scale (Kubin and Estrin, 1985; Estrin and Kubin, 1995). As the non-uniform deformation or strain inhomogeneity often also leads to tensile instability of sheet metals via the formation of macroscopic grooves and necking of the sheet metals (Marciniak and Kuczynski, 1967; Parmar *et al.*, 1977; McCarron *et al.*, 1988; Jain *et al.*, 1996), the spatial formation and temporal evolution of strain inhomogeneity in plastically deforming aluminum sheet metals may be one of the keys to achieve a better understanding of surface degradation and forming failure of the sheet metals.

An experimental study of characterizing whole-field strain inhomogeneity in two aluminum sheet metals subjected to a uniaxial tension is presented in this paper. A deformation measurement technique based on a computer vision approach was used to extract the whole field displacement data by comparing contrast features in a pair of digital images of a specimen surface before and after deformation. This technique, often called digital image correlation (DIC) in the literature, has been developed and improved over the years by Bruck *et al.* (1989), Sutton *et al.* (1991), Vendroux and Knauss (1994), and others. The sensitivity and accuracy of the DIC measured local strain variations of plastically deforming sheet metals have recently been evaluated by Tong (1997) and Smith *et al.* (1997) and are found to be sufficient for discerning the deformation patterns on both cumulative and incremental strain maps at a length scale of the order of 1 mm. The organization of the paper is as follows. Details of the experiment are described in Section 2. The results of macroscopically uniform uniaxial tension experiments on two aluminum sheet metals are presented in Section 3. Discussions on strain inhomogeneity, surface topography and finish, and tensile ductility of the aluminum sheet metals are given in Section 4. Finally, conclusions drawn from the present study are summarized in Section 5.

2. EXPERIMENTAL TECHNIQUE

2.1. Materials and specimen preparation

Two aluminum alloy sheet metals were investigated in this study, namely, Al-5%Mg (nominal thickness: 1.08 mm) and AA5182 (composition limits: 0.2 Si, 0.35 Fe, 0.15 Cu, 0.2–0.5 Mn, 4.0–5.0 Mg, 0.1 Cr, 0.25 Zn; nominal thickness: 0.203 mm). Dogbone-shaped flat tensile testing coupons were cut from rolled sheets so that the sheet rolling direction was aligned with the tensile loading direction. Al-5%Mg specimens had a nominal total length and width of 35 mm and 5 mm, respectively; their gauge section was nominally 15 mm long and 3 mm wide. The material Al-5%Mg was annealed to obtain a recrystallized grain structure consisting of equiaxed grains at an average size of about 70 μm . AA5182 specimens had a nominal total length and width of 50 mm and 6.8 mm, respectively and their gauge section was nominally 18 mm long and 4.6 mm wide. The material AA5182 was rolled and recovered and had an average grain size of about 12 μm . All specimen surfaces were mechanically lapped with #600 SiC paper to a smooth finish, free of any machining and processing marks. One flat surface of the tensile specimens was decorated with random white-and-black speckles by a fine mist of paint spray to facilitate the digital image processing for whole field deformation measurements.

2.2. Experimental set-up and procedure

In situ tensile tests of Al-5%Mg and AA5182 flat sheet specimens were carried out at the ambient temperature on a compact loading stage. The loading stage with a dimension of 100 mm \times 125 mm \times 50 mm was mounted to an x - y stage under a long-distance focus optical microscope with a CCD camera attached. The jaws of the tensile stage move in opposite directions to minimize the movement of the observation area which is kept close to the center of the tensile specimen. The maximum jaw travel is 50 mm and the maximum load capacity is 4.45 kN; these features enable the stage to stretch tensile specimens to large plastic deformation and fracture. The specimen fixture for testing Al-5%Mg was originally designed to hold a flat, dogbone-shaped tensile specimen close to the top surface of the tensile stage so that the specimen surface can also be directly measured *in situ* by atomic force microscopy (Tong *et al.*, 1997). Both displacement and load data were recorded via a computer-based data acquisition system. An eight-bit grayscale digital image (640 \times 480) of the flat surface of a specimen was captured after each prescribed displacement increment. Several dozens of images were acquired in a typical tensile test. Additional details of the experimental set-up, data acquisition procedures, and calibrations of load, displacement and digital images were given by Tong (1997) and Huang (1997).

2.3. Force-displacement data reduction

The displacement and load data collected during a tensile test were first corrected for the compliance of the loading stage and then used to compute the macroscopic true stress and true strain of the aluminum specimens by assuming that plastic deformation is volume preserving and the volume change due to elastic deformation

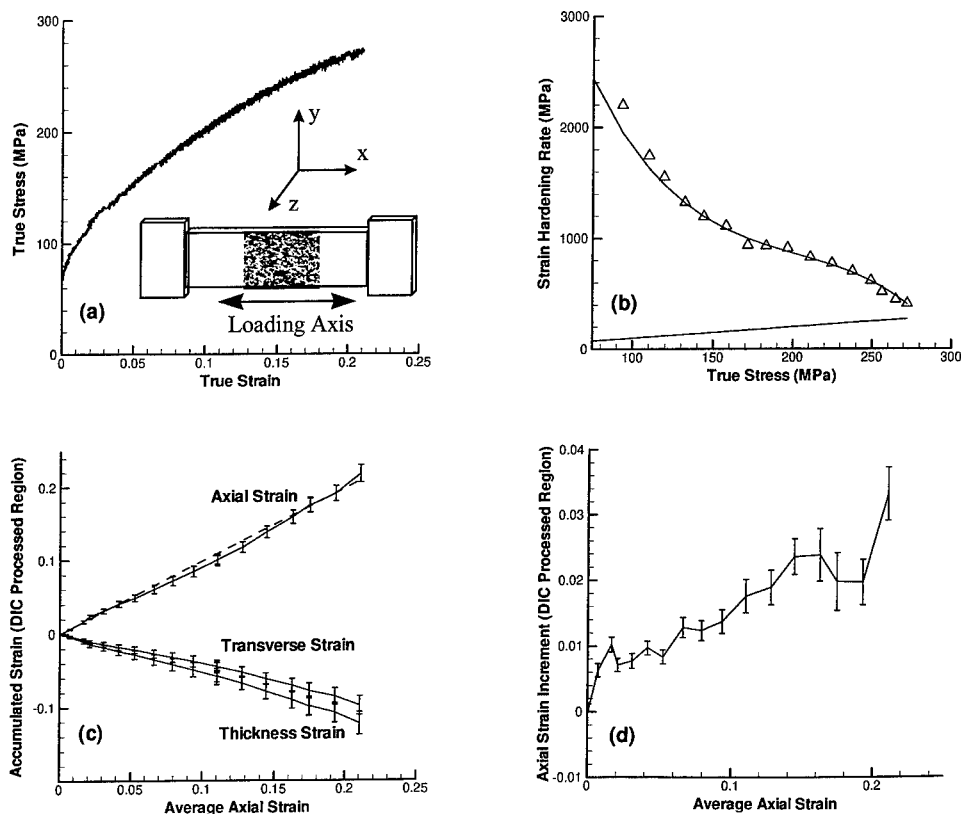


Fig. 1. Summary of a tensile test on an Al-5%Mg flat sheet specimen: (a) true stress-strain curve; (b) strain hardening rate vs true stress; (c) strain inhomogeneity of three accumulated strain components; and (d) strain inhomogeneity of axial strain increments. The insert in (a) shows the schematic of the specimen geometry, the region of the measurement, and the initial digital image of the specimen surface.

is negligible. The resulting stress-strain curve was approximated by a spline fit and the instantaneous strain hardening rate was calculated from the curve-fit. The calculated true strain was confirmed by comparing with the final dimension of the deformed specimens.

2.4. In-plane surface strain mapping

The following coordinate system is used throughout the paper (see the inserts in Fig. 1(a) and Fig. 2(a)): the x -, y - and z -axes are set to be the tensile loading direction, the transverse direction, and the normal or thickness direction of the sheet metals, respectively. The flat surface of a sheet metal tensile specimen forms the x - y plane. Two types of in-plane strain maps over the center region of a specimen gauge section, i.e. cumulative strain maps and incremental strain maps, were obtained by digital image correlation (DIC). A cumulative strain map was obtained by comparing each current deformed image with the initial, undeformed image of the specimen. An

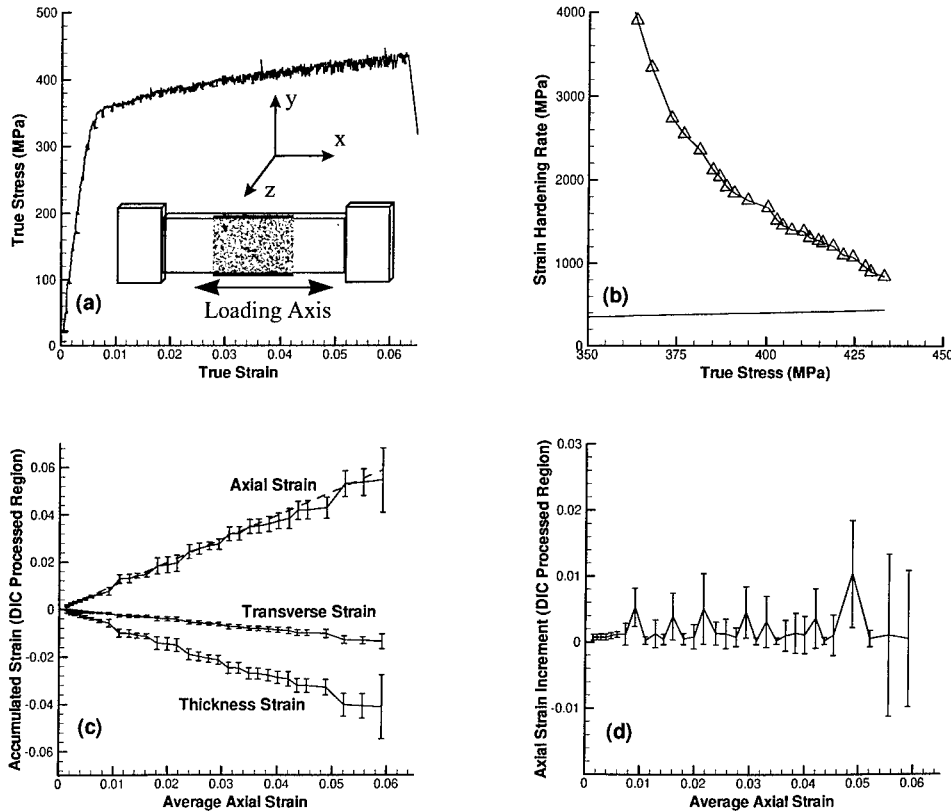


Fig. 2. Summary of a tensile test on an AA5182 flat sheet specimen: (a) true stress-strain curve; (b) strain hardening rate; (c) strain inhomogeneity of three accumulated strain components; and (d) strain inhomogeneity of axial strain increments. The insert in (a) shows the schematic of the specimen geometry, the region of the measurement, and the initial digital image of the specimen.

incremental strain map was computed by comparing the image at the current load step with the image recorded just before the current displacement increment. An image window size of 40×40 pixels was used as the subset in DIC calculations as well as the numerical gage in local strain calculations (Tong, 1997). The mean value and the standard deviation from the mean of each strain component were evaluated for each strain map consisting of $M \times N$ grid points. For the results reported here, the spacing between each grid point in either horizontal or vertical direction is 10 pixels and typically a total of more than 1600 ($= M \times N$) points were used for each strain map. An average strain ratio (ϵ_y/ϵ_z) was also computed for each map.

2.5. Surface topography and roughness

By assuming that plastic deformation is volume preserving and neglecting elastic strains, the cumulative normal strain of a sheet metal averaged through the sheet thickness, i.e. the thickness strain ϵ_z , was computed from the measured in-plane axial

(ε_x) and transverse (ε_y) strains via $\varepsilon_z = -\varepsilon_x - \varepsilon_y$. The non-uniform thinning of the sheet metal as the result of in-plane inhomogeneity of the normal strains was represented by the in-plane distribution of the current thickness of the deformed sheet metal via $h(x, y) = h_0 e^{-\varepsilon_z(x, y)}$, assuming the initial thickness h_0 of the sheet metal is uniform. The average surface topography or the surface height of the two flat surfaces of a sheet specimen was computed by $w(x, y) = [h(x, y) - h_{ave}]/2$, where h_{ave} is the average thickness of the deformed sheet metal. Three surface roughness parameters of sheet metals were then estimated, namely

$$\text{arithmetic mean value } R_a = \frac{1}{MN} \sum_{j=1}^N \sum_{i=1}^M |w(x_i, y_j)|, \quad (1)$$

$$\text{root-mean-square average } R_q = \sqrt{\frac{1}{MN} \sum_{j=1}^N \sum_{i=1}^M w(x_i, y_j)^2}, \quad (2)$$

$$\text{and maximum roughness height } R_{max} = \max[w(x, y)] - \min[w(x, y)]. \quad (3)$$

3. EXPERIMENTAL RESULTS

A uniaxial tensile test of a metal is typically divided into three regimes, namely, elastic deformation (up to plastic yielding), uniform plastic elongation and post-uniform elongation. Discussions of the tensile experimental results here are limited to the nominally uniform elongation regime. The limiting uniform strain ε_u is commonly assumed to be attained when the macroscopic strain hardening rate Θ becomes equal to the flow stress, that is

$$\Theta \equiv \frac{d\sigma_x}{d\varepsilon_x} = \sigma_x, \quad (4)$$

where σ_x and ε_x are the true axial stress and true axial strain.

Figure 1 summarizes the tensile testing of an Al-5%Mg specimen. In addition to the true stress-strain curve, Fig. 1(a) shows the schematic of the specimen geometry, the region of the measurement, and the initial digital image of the specimen. The specimen was not stretched to failure at the end of this test and the macroscopic strain hardening rate Θ was still larger than σ_x (the straight line in Fig. 1(b) corresponds to eqn (4)). Cumulative strains of the DIC processes region as a function of the overall axial strain averaged over the entire gauge section are shown in Fig. 1(c). The solid lines correspond to the mean values and the error bars indicate their standard deviations respectively; the dashed line represents the ideal case when the axial strain of the DIC processed local region is equal to the overall average axial strain. Results of the mean value and standard deviation of the increment in local axial strain after each increment of axial displacement are shown in Fig. 1(d). A similar summary is given in Fig. 2 for an AA5182 specimen; the specimen was broken in this test which was indicated by a large drop in stress at the end of the stress-strain curve in Fig. 2(a). Strain maps or spatial variations of both cumulative and incremental axial strain

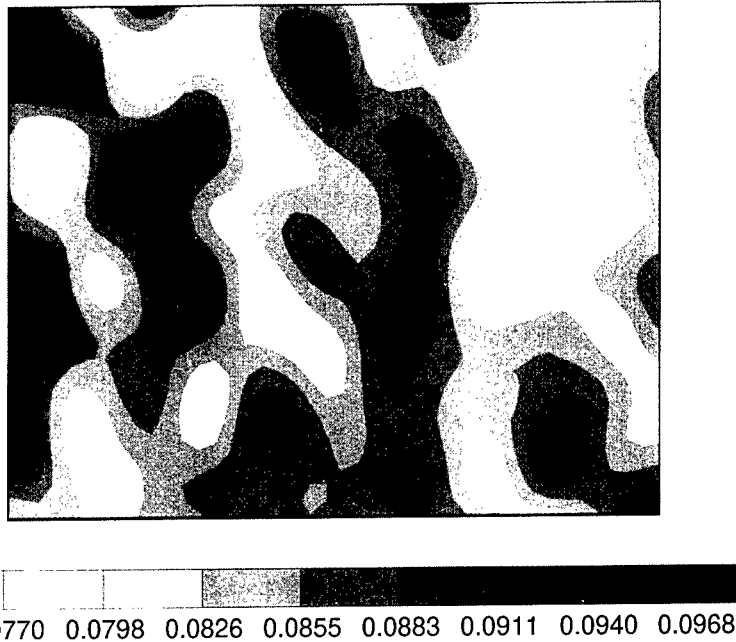


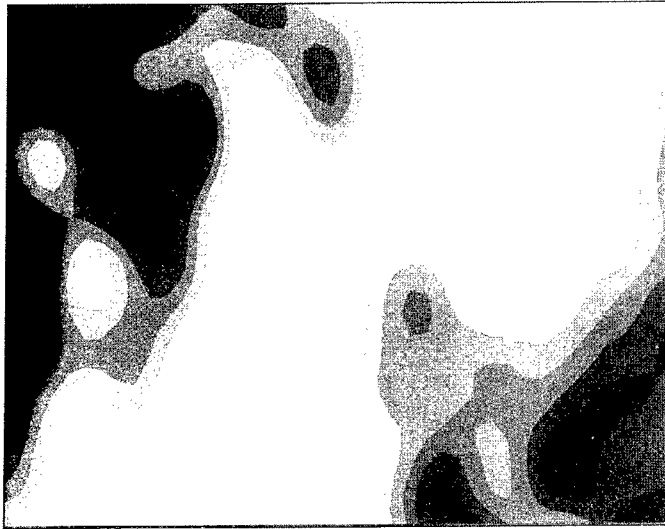
Fig. 3. Cumulative axial strain map of the deformed Al-5%Mg specimen surface with an average axial strain of 8.50%.

components are shown in Figs. 3 and 4 for the material Al-5%Mg and in Figs. 5 and 6 for the material AA5182, respectively. The strain maps in each figure correspond to a typical load step during each tensile test. All strain maps are plotted in the reference configuration (i.e. the initial undeformed region of each sheet metal).

Variations of the estimated surface roughness parameters with increasing axial strain are shown in Fig. 7(a) and (c) for aluminum sheet metals Al-5%Mg and AA5182 respectively. The change of the strain ratio with the axial strain of these two materials is shown in Fig. 7(b) and (d) respectively. The evolution of surface topography of the sheet metal Al-5%Mg due to plastic deformation is shown in Fig. 8, corresponding to the same step shown in Figs. 3 and 4. Unlike the strain maps, the surface topography is represented in the current configuration (i.e. the deformed surface of sheet metal specimens), which is consistent with the situation when the roughness of a deformed sheet metal specimen is measured by a surface profilometer. The predicted surface topography for the sheet metal AA5182 is given in Fig. 9. Finally, optical photographs of the two sheet metal surfaces after uniaxial plastic tensile deformation are shown in Fig. 10(a) and (b), respectively.

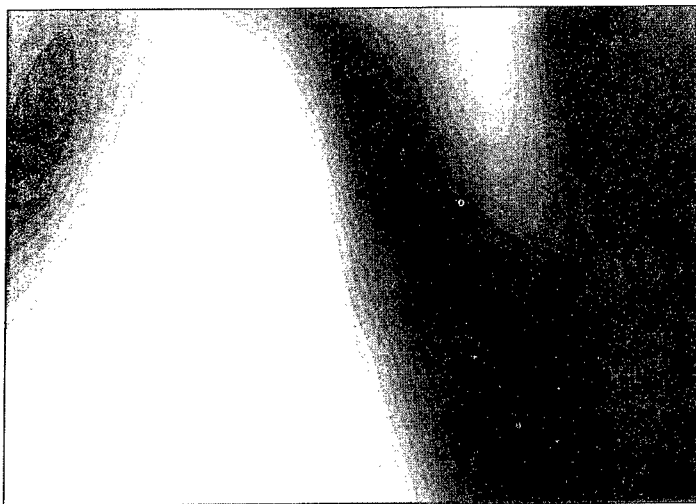
4. DISCUSSIONS

Plastic deformation of a single crystal due to dislocations is inherently heterogeneous at the microscopic level (Hähner and Zaiser, 1997). Each individual grain



0.0118 0.0123 0.0128 0.0133 0.0139 0.0144 0.0149 0.0154

Fig. 4. The incremental axial strain map of the deformed Al-5%Mg specimen surface at the load step shown in Fig. 3 (the average strain increment = 1.24%).



0.0199 0.0210 0.0222 0.0233 0.0245 0.0257 0.0268 0.0280

Fig. 5. Cumulative axial strain map of the deformed AA5182 specimen surface with an average axial strain of 2.41%.

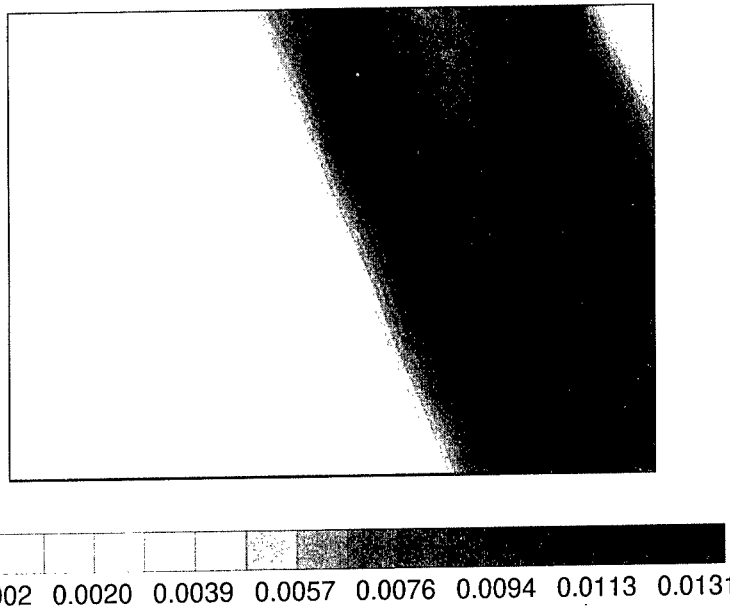


Fig. 6. The incremental axial strain map of the deformed AA5182 specimen surface at the load step shown in Fig. 5 (the average strain increment = 0.46%).

in a polycrystal aggregate deforms differently from an imposed macroscopically deformation field even when the field is nominally uniform (Weiland *et al.*, 1997). The experimental observation shows that a significant level of strain inhomogeneity exists over a field of view of several millimeters in two aluminum alloy sheet metals subjected to macroscopically uniform uniaxial tension. Such a field of view is larger than the thickness of the sheet metal and is much larger than the average size of individual grains in either sheet metal. The strain fluctuation measured in terms of the standard deviation from the mean value ranges from 10% to 30% of the average strain of the measured area, depending on the amount of cumulative deformation and materials. The origin of such a fluctuation can be attributed to non-homogeneous deformation of grains and grain clusters in Al-5%Mg (Figs. 3 and 4) and localized propagative deformation bands in AA5182 (Figs. 5 and 6).

Of two aluminum sheet metals tested, AA5182 shows a strong PLC effect (Fig. 6) and surface markings due to such deformation banding can be visually observed on the polished AA5182 specimen surface from a glancing angle (Fig. 10(b)). However, no band-like deformation patterns can be identified by direct visual observation of Al-5%Mg specimen surface (Fig. 10(a)). Nevertheless, the existence of propagative deformation bands has been unambiguously uncovered in Al-5%Mg, see Fig. 4. The major difference between these two aluminum sheet models is reflected in the level of strain inhomogeneity and the variation of the average strain in their incremental strain maps (see also Fig. 1(d) and Fig. 2(d)). The dynamic and heterogeneous nature of plastic deformation can thus be effectively described by spatial characterization of strain rates or strain increments (Tong, 1997). Experimentally, the incremental strain

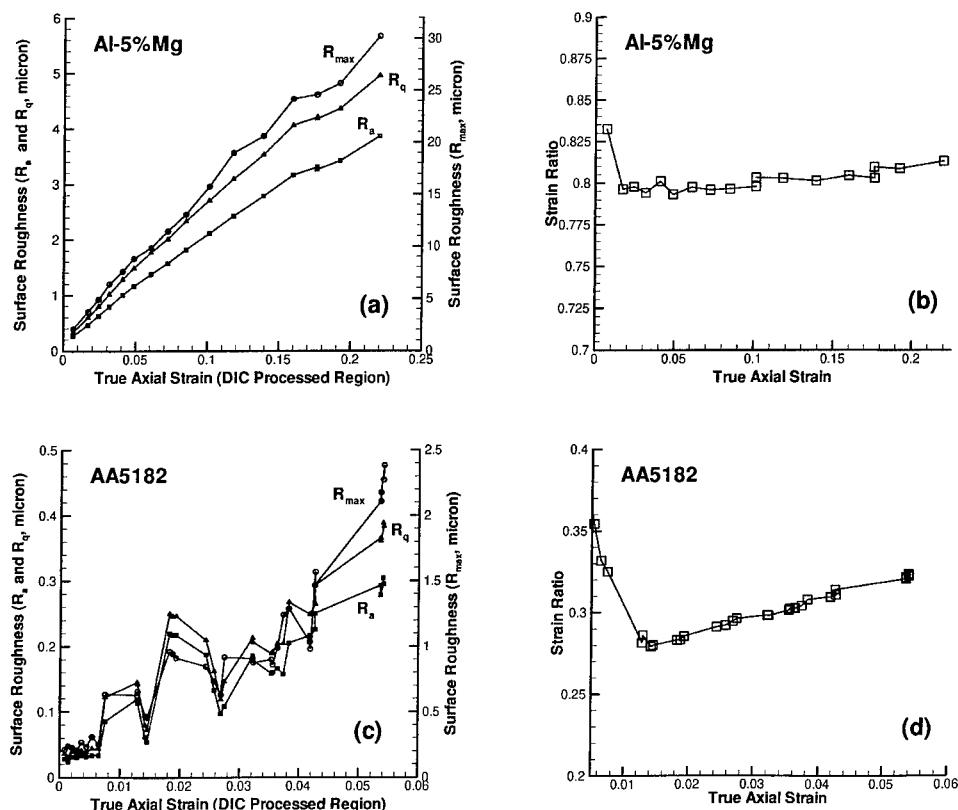


Fig. 7. Summary of the computed surface roughness parameters and strain ratio for Al-5%Mg (a) and (b) and AA5182 sheet metals (c) and (d), respectively.

mapping approach used in this study seems to be robust and sensitive in monitoring the deformation process in sheet metals and it can be applied to systematically study the spatial coupling effects of plastic deformation in metals and alloys.

Surface roughness in terms of the three parameters defined by eqns (1–3) increases monotonically with increasing deformation in Al-5%Mg (Fig. 7(a)). Up to 15% of axial strain, an approximately linear relation between the three roughness parameters and axial strain is observed. This linear dependence is consistent with observations by others (e.g. Fukuda *et al.*, 1974). An empirical relation was proposed by Fukuda *et al.* (1974) between the amplitude of surface roughening R and the average grain size d_0 and the effective strain ε , namely

$$R = R_0 + kd_0\varepsilon, \quad (5)$$

where R_0 and k are initial surface roughness and a material constant, respectively. Such a relation has been justified by assuming surface roughening is due primarily to surface grain rotation (Dai and Chiang, 1992). The surface roughness and topographical features estimated here for the two sheet metals are based on the in-plane

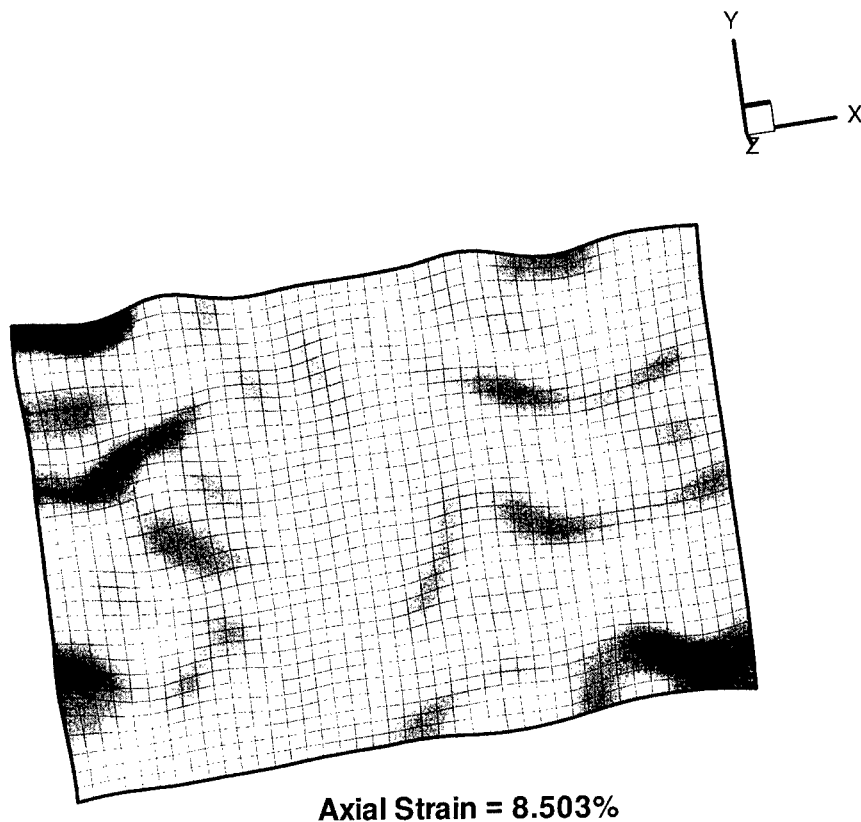


Fig. 8. Computed surface topography of the deformed Al-5%Mg specimen surface at the load step shown in Fig. 3. Each grid corresponds to a $67\ \mu\text{m} \times 67\ \mu\text{m}$ square on the undeformed surface.

strain inhomogeneity (see Section 2.5). The size of surface topographical features on the deformed Al-5%Mg surface is at least several times of that of grains (each grid in Fig. 8 corresponding approximately the average grain size of the sheet metal Al-5%Mg). Similarly, the periodicity of horizontal spacing of the peaks and valleys was found to be about an order of magnitude larger than the grain size in aluminum sheet metals by Jain *et al.* (1996). Surface roughening of Al-5%Mg at a field of view of several millimeters is thus dominated more likely by some collective deformation of a cluster of grains. Grains within certain small misorientation angles across grain boundaries can be the microstructural basis of such grain clusters (Adams, 1993; Randle, 1992). These results indicate that refining of grain size without controlling the microtexture of sheet metals may not result in any significant improvement in surface finish. Surface roughening of AA5182 is dominated by the strong PLC effects via propagative deformation bands: its surface roughness parameters change irregularly with increasing axial deformation within the field of view of the experimental measurements (Fig. 7(c)). Grooves aligned around 50° to the tensile loading direction are major surface topographical features of the deformed AA5182 surface, see Fig.

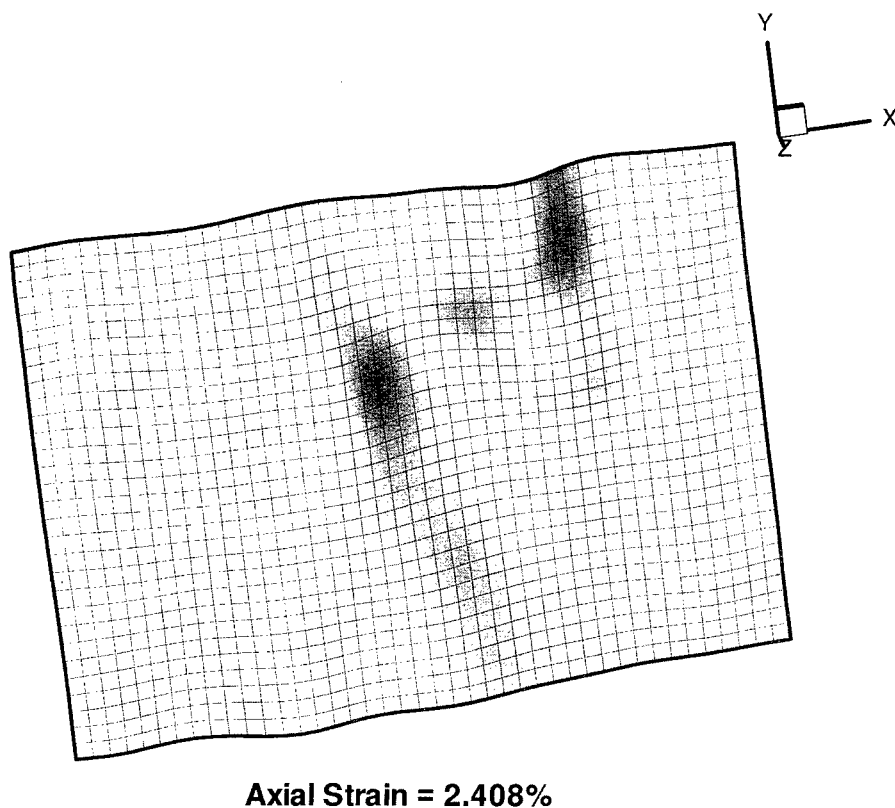


Fig. 9. Computed surface topography of the deformed AA5182 specimen surface at the load step shown in Fig. 5. Each grid corresponds to a $110\ \mu\text{m} \times 110\ \mu\text{m}$ square on the undeformed surface.

10(b). Surface roughness of both deformed Al-5%Mg and AA5182 specimens was measured over a sampling area of $1\ \text{mm} \times 1\ \text{mm}$ by an optical surface mapping microscope (Phase Shift Technology, Inc.). The measured surface roughness parameters R_a and R_q are consistent with the predicted values. The measured R_{max} is slightly smaller which may be due to the small sampling area. The size of major surface topographical features (“peaks”, “valleys”, and “grooves”) measured by the surface mapping microscope is also consistent with those in the predicted topography maps shown in Figs. 8 and 9.

Formability of metals has often been linked to the amount of uniform elongation in uniaxial tension. Consequently, macroscopic strain hardening behavior and its role in improving and predicting the formability of metals have been of considerable research (Kocks, 1976; Petch and Armstrong, 1990; Chu and Morris, 1996; Jain *et al.*, 1996). The success of such a macroscopic description of plastic deformation is largely limited to pure, well-annealed, poly-granular metals and it alone is not sufficient in characterizing resistance of engineering aluminum alloy sheet metals to tensile instability that leads to strain localization and thus forming failure. For

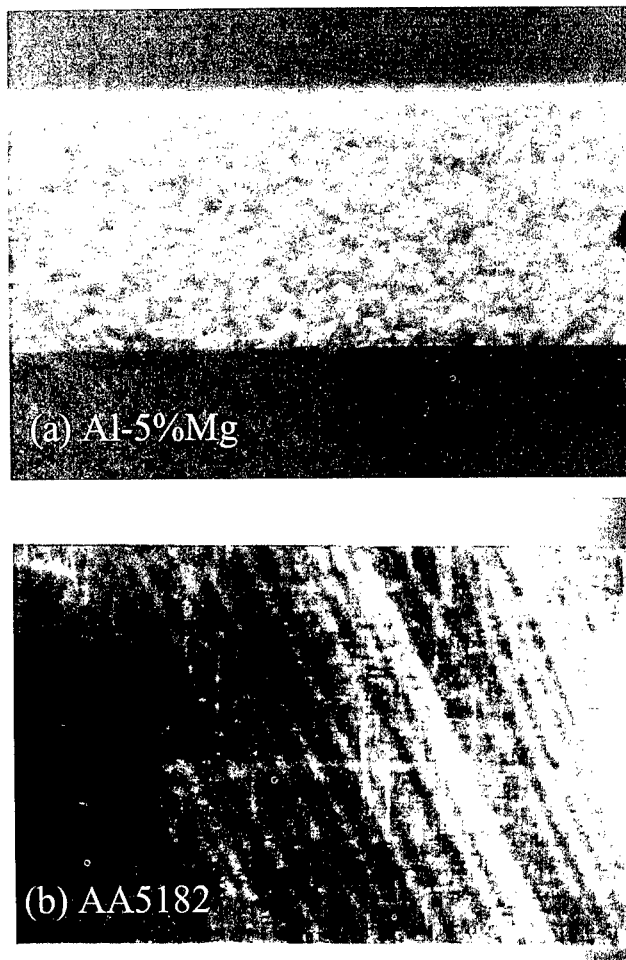


Fig. 10. Optical photographs of the deformed Al-5%Mg (a) and AA5182 (b) specimen surfaces.

example, the final failure of the AA5182 specimen was rather brittle-like as there was little necking process observed. In terms of the macroscopic stress-strain behavior of the material, its average strain hardening rate was well above the true stress level for initiating the macroscopic necking when the specimen broke (Fig. 2(b)) and hence was not the dominant factor determining its tensile ductility. The sudden loss of the potential ductility is attributed to the dynamic nature of a strong strain inhomogeneity within the sheet metal (Fig. 4).

It is well-established that ductile fracture of engineering materials involves void nucleation and growth from inclusions or second phase particles (Gurland and Plateau, 1963; McClintock, 1968). Failure of thin sheet metals has been observed however to occur primarily by the loss of tensile deformation stability and the growth of incipient grooves or necking. Marciniak and Kuczynski (1967) have subsequently

developed a theory of analyzing limit strains in the processes of stretch-forming sheet metals by assuming that necking develops from local regions of initial thickness inhomogeneity. Their approach has since been adopted widely to construct biaxial forming limit diagrams of sheet metals (for example, Parmar *et al.*, 1977; Jain *et al.*, 1996). While the Marciniak-Kuczynski type models provide a framework for rational discussion of limit strains in sheet metal forming, the resulting forming limit diagrams are found to be rather sensitive to the precise size and shape of the postulated groove (McCarron *et al.*, 1988). Efforts in removing the arbitrary assumption of the geometric defect include the introduction of a surface roughness parameter (Parmar *et al.*, 1997; Jain *et al.*, 1996). However, experimental observation of the incipient grooves or necks on deformed sheet metal surfaces has shown that the necks are very much longer and larger in magnitude than that of the surface roughness (Marciniak and Kuczynski, 1967; McCarron *et al.*, 1988). Based on the measured cumulative strain maps and predicted surface topography maps shown in Figs. 3–4 and Figs. 8–9, tensile instability and thus the initiation and growth of necks may be attributed to the interplay of strain hardening, material (and hence strain) inhomogeneity, and geometric imperfection (surface topography) over a length scale at least larger than the thickness of the sheet metals. Plasticity models incorporating the material inhomogeneity at proper length scales to capture the evolution of in-plane deformation patterning and surface topography may provide much more robust capabilities in analyzing sheet metal stretching processes.

5. CONCLUDING REMARKS

The lack of intrinsic length and time scales in conventional polycrystal plasticity theories make them inadequate in modeling some of technologically important metal plasticity problems. As an illustration as well as an application, the spatial characterization of strain inhomogeneity and its evolution in two aluminum alloy sheet metals have been successfully carried out using a digital image correlation technique. Under macroscopically uniform axial tension and over a physical field of view of several millimeters (which far exceeds the grain size of the materials), non-homogeneous plastic deformation with an inhomogeneity up to more than 30% of the average deformation has been observed via cumulative strain mapping. The dynamic nature of the plastic deformation process has been effectively monitored via incremental strain mapping as non-stationary deformation bands have been detected in both aluminum alloy sheets. The in-plane strain inhomogeneity of sheet metals has been identified as the leading factor that contributes to their local non-uniform thinning and consequently their surface roughening and formation of grooves at the same physical length scales. For the class of sheet materials similar to these two aluminum alloys, the conventional macroscopic plasticity models of strain hardening appear to be deficient for tensile ductility and formability analysis and completely inadequate for modeling the evolution of surface finish in sheet metal stretching operations.

There is an increasing recognition regarding the importance of the interactive hierarchy of length and time scales in modeling polycrystalline materials undergoing plastic deformation (Fleck and Hutchinson, 1997; Estrin and Kubin, 1995). Dynamic

in situ whole field strain mapping both cumulatively and incrementally over a range of corresponding scales, combining with effective characterization and representation of the evolution of spatial heterogeneity of material microstructure using the tools such as orientation imaging microscopy (Adams, 1993), should be valuable in studying the formation and evolution of plastic deformation patterns and their effect on surface finish, tensile ductility, and formability of newly developed sheet metal alloys.

ACKNOWLEDGEMENTS

The author would like to acknowledge Drs. L. G. Hector and H. Weiland of the Alcoa Technical Center (ATC) for providing the aluminum alloy sheets used in this investigation. The author is also indebted to Drs. O. Richmond, R. Becker, and M. Li at ATC for their valuable insights on the plastic deformation of sheet metals during the course of preparing this manuscript.

REFERENCES

- Adams, B. L. (1993) Orientation imaging microscopy: application to the measurement of grain boundary structure. *Mat. Sci. Eng.* **A166**, 59–66.
- Bruck, H. A., McNeill, S. R., Sutton, M. A. and Peters, W. H. (1989) Digital image correlation using Newton-Raphson method of partial differential correction. *Exp. Mech.* **29**, 261–267.
- Chihab, K., Estrin, Y., Kubin, L. P. and Vergnol, J. (1987) The kinetics of the Portevin-Le Chatelier bands in an Al–5at%Mg alloy. *Scripta Metall.* **21**, 203–208.
- Chu, D. and Morris, J. W., Jr. (1996) The influence of microstructure on work hardening in aluminum. *Acta Mater.* **44**(7), 2599–2610.
- Dai, Y. Z. and Chiang, F. P. (1992) On the mechanism of plastic deformation induced surface roughness. *J. Eng. Mater. Tech.* ASME **114**, 432–438.
- Estrin, Y. and Kubin, L. P. (1995) Spatial coupling and propagative plastic instabilities. In *Continuum Models for Materials with Micro-Structure*, ed. H. B. Muhlhaus, John Wiley & Sons.
- Fleck, N. A. and Hutchinson, J. W. (1997) Strain-gradient plasticity. *Adv. Appl. Mech.* **33**, 295–361.
- Fukuda, M., Yamaguchi, K., Takakura, N. and Sakano, Y. (1974) Roughening phenomenon on free surface of products in sheet metal forming. *J. Japan Soc. Tech. Plasticity* **15**(167), 994–1002.
- Ghosh, A. K., Hecker, S. S. and Keeler, S. P. (1984) Sheet metal forming and testing. In *Workability Testing Techniques*, ed. G. E. Dieter, pp. 135–195. American Society for Metals, Metals Park, OH.
- Gurland, J. and Plateau, J. (1963) The mechanism of ductile rupture of metals containing inclusions. *Trans. ASM* **56**, 442–456.
- Hähner, P. and Zaiser, M. (1997) From mesoscopic heterogeneity of slip to macroscopic fluctuations of stress and strain. *Acta Mater.* **45**(3), 1067–1075.
- Huang, S. (1997) Whole field in-plane surface deformation measurement by optical and scanning electron microscopy, MS Thesis, University of Nebraska.
- Jain, M., Lloyd, D. J. and Macewen, S. R. (1996) Hardening laws, surface roughness and biaxial tensile limit strains of sheet aluminum alloys. *Int. J. Mech. Sci.* **38**(2), 219–232.
- Kocks, U. F. (1976) Laws for work-hardening and low temperature creep. *J. Eng. Mater. Tech.* **98**, 76.
- Kubin, L. P. and Estrin, Y. (1985) The Portevin-Le Chatelier effect in deformation with constant stress rate. *Acta Metall.* **33**, 397–407.

- Marciniak, Z. and Kuczynski, K. (1967) Limit strains in the process of stretch-forming sheet metal. *Int. J. Mech. Sci.* **9**, 609–620.
- McCarron, T. J., Kain, K. E., Hahn, G. T. and Flanagan, W. F. (1988) Effect of geometrical defects in forming sheet steel by biaxial stretching. *Met. Trans.* **22A**(11), 2067–2074.
- McClintock, F. A. (1968) A criterion for ductile fracture by growth of holes. *J. Appl. Mech. ASME* **35**, 363–370.
- Newby, J. R. (1982) Formability tests contrasting ferrous materials and 2036-T4 aluminum. In *Formability of Metallic Materials—2000 A.D.*, ed. J. R. Newby and B. A. Niemeier, ASTM STP No. 753, pp. 60–83.
- Parmar, A., Mellor, P. B. and Chakrabarty, J. (1977) A new model for the prediction of instability and limit strains in thin sheet metal. *Int. J. Mech. Sci.* **19**, 389–398.
- Petch, N. J. and Armstrong, R. W. (1990) The tensile test. *Acta Metall. Mater.* **38**(12), 2695–2700.
- Raghavan, K. S., van Kuren, R. C. and Darlington, H. (1992) Recent progress in the development of forming limit curves for automotive sheet steels. SAE Technical Paper No. 920437, pp. 87–104.
- Randle, V. (1992) *Microtexture Determination and Its Applications*, The Institute of Materials, London.
- Roush, C. (1996) Aluminum sheet alloy stops formation of surface defects. *Adv. Mater. and Processes* **149**(5), p. 8.
- Smith, B. W., Li, X. and Tong, W. (1997) Error assessment for strain mapping by digital image correlation. *Exp. Tech.* (in press).
- Sutton, M. A., Turner, J. L., Bruck, H. A. and Chae, T. A. (1991) Full-field representation of discretely sampled surface deformation for displacement and strain analysis. *Exp. Mech.* **31**, 168–177.
- The Aluminum Association (1996) *Aluminum for Automotive Body Sheet Panels*, pp. 13–18. Publication AT3, Washington, D.C.
- Tong, W. (1997) Detection of plastic deformation patterns in a binary aluminum alloy. *Exp. Mech.* **37**(4), 452–459.
- Tong, W., Hector, L. G. Jr., Weiland, H. and Wieserman, L. F. (1997) *In situ* surface characterization of a binary aluminum alloy during tensile deformation. *Scripta Mater.* **36**(11), 1339–1344.
- Vendroux, G. and Knauss, W. G. (1994) Deformation measurements at the sub-micron size scale: II. Refinements in the algorithm for digital image correlation *SM Report 94-5* (Graduate Aeronautical Laboratories, California Institute of Technology).
- Weiland, H., Hector, L. G. Jr. and Tong, W. (1997) *In situ* observation of surface grain deformation on polycrystalline surfaces. In *Proc. 1997 Intl. Conf. On Plasticity and Its Applications*, Alaska.



Pergamon

J. Mech. Phys. Solids, Vol. 46, No. 10, pp. 2103–2138, 1998

© 1998 Elsevier Science Ltd. All rights reserved

Printed in Great Britain

0022-5096/98 \$—see front matter

PII: S0022-5096(98)00032-5

MODELLING OF ORTHOGONAL CUTTING WITH A TEMPERATURE DEPENDENT FRICTION LAW

A. MOUFKI, A. MOLINARI* AND D. DUDZINSKI

Laboratoire de Physique et Mécanique des Matériaux, UMR CNRS 7554, ISGMP,
Université de Metz, Ile du Sauley, 57045 Metz, France

(Received 20 December 1997; accepted 7 February 1998)

ABSTRACT

In this paper the process of orthogonal cutting is studied by analytical means. A thermomechanical model of the primary shear zone is combined with a modelling of the contact problem at the tool-chip interface. A friction law is introduced that accounts for temperature effects. The effects of cutting conditions and material behaviour on the temperature distribution along the contact zone, on the mean friction and on the global cutting forces are evaluated. The experimental trends are shown to be well described by the proposed model. © 1998 Elsevier Science Ltd. All rights reserved.

Keywords: A. cutting and forming, thermomechanical processes, B. viscoplastic material, friction.

1. INTRODUCTION

Machining of metals is a complex process. Two main mechanisms can be identified; firstly the chip is formed along the primary shear zone with a sudden change in the direction of velocities producing an intense shearing; secondly the chip sustains a sliding along the tool-chip interface accompanied by friction effects and the formation of a secondary shear zone. To fully describe the cutting process would involve accounting for the formation of a build-up edge (which might be important for low cutting velocities), and to model among other phenomena the wear of the tool, the chip segmentation, the chip curvature.

Before attaining these goals, our aim is to propose an analytical model of stationary orthogonal cutting based on a realistic description of the friction effects at the tool-chip interface.

A first modelling of orthogonal cutting was formulated by Merchant (1945). Cutting forces were predicted by considering a chip forming under shearing along a plane surface originated at the tool edge and inclined with an angle ϕ (the shear angle) with respect to the workpiece surface. The material was assumed to be perfectly rigid plastic. This model neglects thermomechanical effects. A Coulomb friction law at the tool-chip interface is assumed with a constant friction coefficient. The shear angle ϕ is determined by minimization of the work produced by the cutting forces.

* To whom correspondence should be addressed. Fax: 0033 0387315366.

A thermomechanical modelling was developed by Oxley (1989) which included temperature effects and material characteristics such as strain rate sensitivity and strain hardening. A semi-empirical thermal analysis was developed which provided satisfactory results at conventional cutting velocities. However the complexity of the model results from the existence of several parameters that have to be adjusted. This makes the interpretation of some trends of the model difficult.

A global analysis of the cutting process is made possible by use of finite element methods, (Strenkowski and Carroll, 1985; Strenkowski and Moon, 1990; Sekhon and Chenot, 1993; Marusich and Ortiz, 1995). The numerical solution depends on features such as the criterion of mesh opening and the mesh distortion in a Lagrangian formulation. Results obtained in this global analysis involve the whole cutting system; this makes the analysis of the influence of some parameters more difficult than in simple specific analytical models.

For industrial applications, a model should be able—from the cutting conditions, the thermomechanical properties of the workpiece and of the tool, and from the friction law—to predict the cutting forces, the stress, strain and temperature fields, the tool wear, the surface state, the instability conditions and chatter. There is no model at present that can efficiently account for all these effects together.

To model a cutting process, one has to characterize the thermomechanical behaviour of the workpiece at very large strain rates and a large range of temperatures. Indeed, strain rates larger than 10^5 s^{-1} can be attained in the primary shear zone even for conventional cutting velocities. In addition, high elevations of temperature are due to the important work of deformation associated to large shear strains in the primary shear zone (values of strains as high as 3 are usual), and to the friction effects along the tool interface. For steels, temperatures as high as $400\text{--}500^\circ\text{C}$ are typical of the primary shear zone, and temperatures higher than 1000°C are usual on the tool interface. Such an increase in temperature has a major effect on the material response by lowering the flow stress (thermal softening).

Contact conditions at the tool-chip interface are severe. The pressure is high and the sliding velocity may be large. This results in an important heating at the tool interface which affects the friction conditions. We shall propose a model of friction appropriate for the extreme conditions of pressure, velocities and temperature encountered during machining.

Data obtained from machining experiments indicate that the mean friction coefficient at the tool-chip interface depends upon the rake angle α —friction increases when α is getting larger; Bailey (1975)—upon the feeding t_1 —when the latter is increased, the friction coefficient decreases, Findley and Reed (1963)—upon the cutting speed, Schulz (1989) and the thermomechanical properties of the tool-workpiece pair. This list of parameters affecting friction, is not exhaustive. Empirical laws have been proposed where the mean friction coefficient increases exponentially with the rake angle, Usui *et al.* (1978), or decreases as a power law of the cutting speed, Schulz (1989). However it is difficult to generalize these laws so as to bring together all the effects of the cutting conditions (α , t_1 , V).

Experiments (using, for example, a high speed pin-on-disk test device) have shown that at large sliding velocities a reduction of the friction coefficient is obtained when the normal pressure or the sliding velocity are increased (Williams and Griffen, 1964;

Kadhim and Earles, 1967; Earles and Powell, 1967; Montgomery, 1976; Lim *et al.*, 1989). We postulate that for sliding velocities large enough (typically ≥ 1 m/s) these effects are related for a large part, to the change of the tool-chip interface temperature. This temperature is non uniform in general. However we simplify the situation by considering the mean temperature \bar{T}_{int} along the interface as the main parameter.

Our principal assumption consists of postulating a Coulomb friction law with a mean friction coefficient $\bar{\mu}$ depending on the mean temperature \bar{T}_{int}

$$\bar{\mu} = \bar{\mu}(\bar{T}_{\text{int}}) \quad (1)$$

We shall validate this assumption by comparison with experimental results under various cutting conditions. It may be noted that under our hypothesis the pressure and velocities effects have an action on the friction coefficient through the changes of the interface temperature which they produce. Although the real friction law might be a little more complicated, the main experimental trends are reproduced under the assumption, (1). Note that the present model is viewed as being specially suited for large sliding velocities (≥ 1 m/s). Note also that in our considerations, we shall be concerned with dry friction.

The model of orthogonal cutting presented here has two main aspects :

- (1) The primary shear zone is considered as a thin straight band. This idealization is specially appropriate for large cutting velocities. Within this band the thermomechanical problem and the material flow are modeled in a one dimensional approach (Molinari and Dudzinski, 1992; Dudzinski and Molinari, 1997).
- (2) Tool-chip contact is described by use of a mean friction coefficient depending upon the mean surface temperature \bar{T}_{int} (friction law (1)). The existence of a secondary shear zone where the material sustains shearing along the tool interface is not considered; this simplification is specially adequate for high cutting speeds. The thermomechanical problem to be solved has a two dimensional character. An analytical solution of the temperature distribution is obtained.

The characteristics of the friction law are deduced from the interpretation of data on machining of steels. Once this law is identified, various cutting conditions are considered so as to check the range of validity of the proposed model. Finally a large variety of results is provided by a parametric study.

2. MODELLING OF THE PRIMARY SHEAR ZONE

The following model of the primary shear zone has been proposed by Molinari and Dudzinski (1992). It is assumed that the chip is formed by shearing in a narrow straight band of thickness h , whose inclination with respect to the workpiece surface is defined by the shear angle ϕ , Fig. 1. It is supposed that the material is deformed by shearing in the shear band and that no deformation occurs before and after the band. The secondary shear zone that appears along the tool interface is not considered in the present modelling. The complex material flow near the tool is not accounted for either. We restrict our attention to the case of orthogonal cutting (cutting edge perpendicular to the cutting speed V).

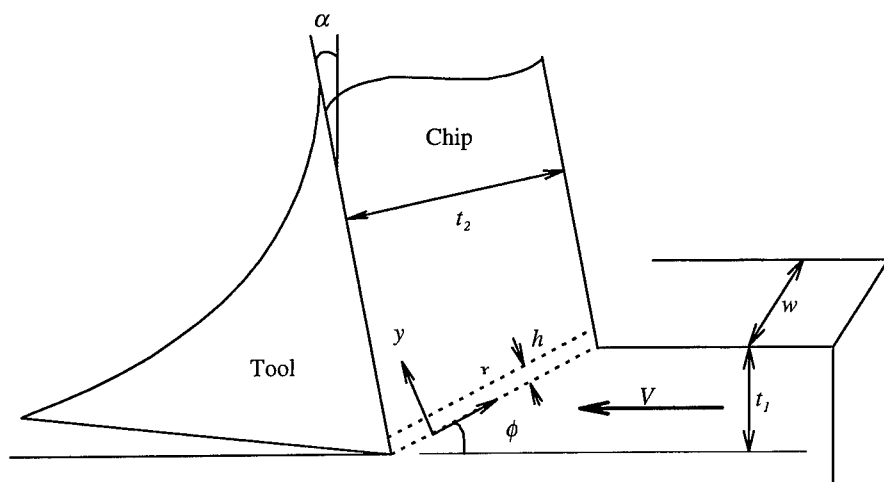


Fig. 1. The primary shear zone is modelled as a shear band of constant thickness h , inclined to the cutting direction at an angle ϕ .

The uncut chip thickness t_1 (or feeding) is presumed to be small with respect to the width of cut w . It is then justified to consider that the chip is formed under plane strain conditions. The cutting edge is taken as perfectly sharp and the tool is not deformable. The cutting conditions are given: it means that the feeding t_1 , the rake angle α and the cutting speed V , are known.

The workpiece material is postulated to be isotropic, rigid (elastic deformations neglected) and to have a thermomechanical response described under shear conditions by the following power law:

$$\tau = \mu_0 (\gamma + \gamma_p)^n \dot{\gamma}^m T^v \quad (2)$$

where γ , $\dot{\gamma}$ and T are the shear strain, the shear strain rate and the absolute temperature respectively. Characteristics of the material behaviour are defined as μ_p , the strain hardening exponent n ($n \geq 0$), the strain rate sensitivity exponent ($0 \leq m \leq 1$) and the thermal softening coefficient v ($v \leq 0$). At large strain rates an increase of the strain rate sensitivity is observed on metals (Campbell and Fergusson, 1970; Klepaczko, 1994). This can be included in the constitutive model, see Marusich and Ortiz (1995), and will be considered later in this paper, see section 5.4.

Velocity diagrams at the inflow and outflow of the primary shear zone are shown in Fig. 2. V_C is the chip velocity relative to the tool. V_{s0} and V_{s1} are the components of particle velocities tangential to the shear zone, respectively at the inflow and at the outflow; the normal velocity component V_N is constant through the thickness of the band, due to the incompressibility condition:

$$V_N = V \sin \phi \quad (4)$$

The analysis is limited to the case of stationary flow. The formulation is one dimensional, the variables depend solely on the coordinate y normal to the band and

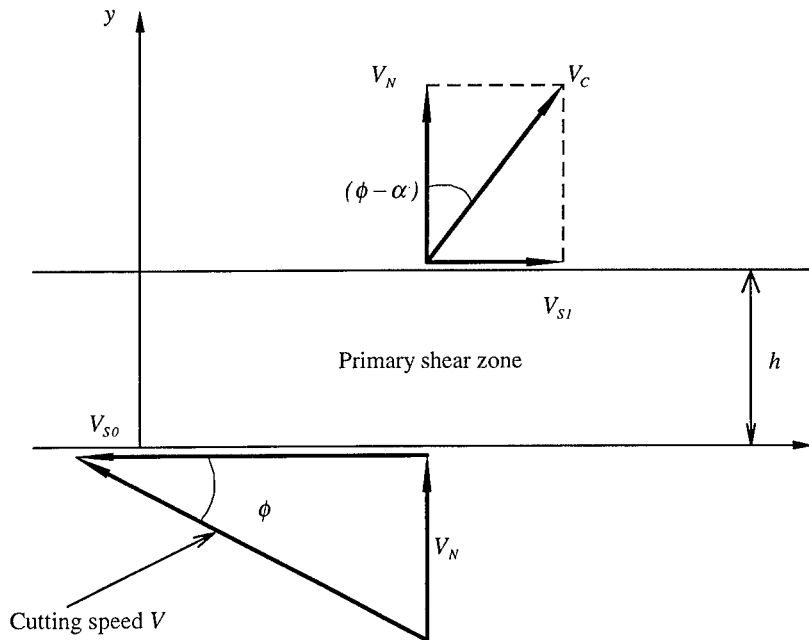


Fig. 2. Velocity diagrams at the boundaries of the shear zone.

do not depend on time. The equations of conservation of momentum, of conservation of energy, (assuming adiabatic conditions which are approached when high cutting speeds are considered), and the constitutive law (2) can be respectively written as (Dudzinski and Molinari, 1997) :

$$\begin{aligned}\tau &= \rho V_N^2 \gamma + \tau_0 \\ T &= T_w + \frac{\beta}{\rho c} \left(\rho V_N^2 \frac{\gamma^2}{2} + \tau_0 \gamma \right) \\ \dot{\gamma} &= \left(\frac{\tau}{\mu_0} \right)^{1/m} T^{-r/m} (\gamma + \gamma_p)^{-n/m}\end{aligned}\quad (5)$$

where ρ , c and β represent respectively the material density, the heat capacity and the fraction of the plastic work converted into heat (Taylor-Quinney coefficient). T_w is the absolute temperature of the workpiece. In addition, we have the compatibility condition :

$$\frac{d\gamma}{dy} = \frac{\dot{\gamma}}{V_N} = \frac{1}{V \sin \phi} \left(\frac{\tau(\gamma, \tau_0)}{\mu_0} \right)^{1/m} (T(\gamma, \tau_0))^{-r/m} (\gamma + \gamma_p)^{-n/m} \quad (6)$$

τ_0 is the stress at the entry of the band. The term ρV_N^2 represents the inertia effects.

Heat conduction effects could easily be added in this formulation, Dudzinski and Molinari (1997).

The boundary conditions are:

$$T = T_w \quad \text{at} \quad y = 0 \quad (7.1)$$

$$\gamma = 0 \quad \text{at} \quad y = 0 \quad (7.2)$$

$$\gamma = \gamma_1 = \tan(\phi - \alpha) + \frac{1}{\tan\phi} \quad \text{at} \quad y = h \quad (7.3)$$

Note that the temperature T given by (5.2) satisfies (7.1). When solving the differential equation (6) the value of τ_0 has to be determined iteratively so as to satisfy the boundary conditions (7.2) and (7.3).

To solve the foregoing equations, the value of the shear band thickness h (appearing as the length of the integration domain of the differential equation (6)) and the value of the shear angle ϕ are needed. The thickness h is assumed to be known (it can be measured). We shall determine ϕ by the following relationship due to Zvorykin (1893):

$$\phi = A + \frac{(\alpha - \lambda)}{2} \quad (8)$$

where α is the rake angle and λ the mean friction angle at the tool-chip interface:

$$\bar{\mu} = \tan\lambda \quad (9)$$

A is a constant that depends on the material considered. For $A = \pi/4$ the relationship (8) corresponds to the Merchant formula. There is no general proof of eqn (8) that should be considered rather a constitutive assumption validated experimentally for some materials. Experimental results shown later indicate for example, that a reasonable value of the angle A for steel would be:

$$A = 35^\circ \quad (10)$$

There are some materials for which ϕ would be of the form

$$\phi = A_1 + A_2(\alpha - \lambda) \quad (11)$$

3. MODELLING OF THE THERMAL EFFECTS AT THE TOOL-CHIP INTERFACE

The evaluation of the temperature at the tool-chip interface is an important step in the modelling of the cutting process. Friction effects are actually temperature dependent as proposed in our model (1). A realistic analysis of cutting can not be developed without accounting for the heat produced by friction. In addition one can note that the tool life depends strongly on the temperature level at the tool-chip interface, Taylor (1907). To increase the tool life, would involve a control of temperatures and

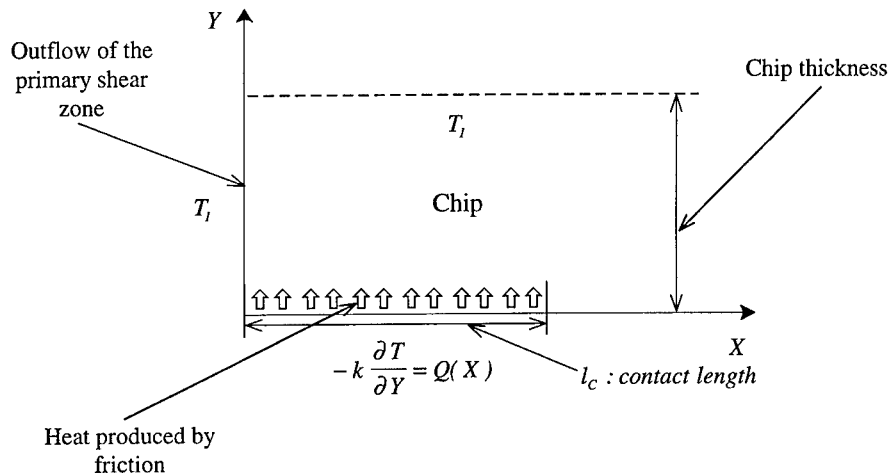


Fig. 3. Schematic view of the thermal boundary conditions used to solve the thermal problem in the vicinity of the tool-chip interface. T_l is the temperature at the outflow of the primary shear zone. $Q(X)$ is the surfacic heat source due to friction.

of pressures. To achieve this control by optimizing the cutting process would be a major goal.

Experimental data on the temperature distribution have been obtained by different means. Use of thermocouples and extrapolation of the results based on the solution of the heat equation in the tool provide an estimate of the temperature field and in particular of the mean contact temperature, Groover and Kane (1971). Other procedures are based on infrared technique measurements Boothroyd (1963), or on the analysis of the structural modifications in the tool material, Wright and Trent (1973). These measurements have indicated that temperatures at the tool-chip interface as high as 1200°C are not uncommon. The temperature distribution at the interface is shown to be non uniform and to have a maximum. Moreover, an important influence of cutting conditions such as the cutting speed and the depth of cut t_1 has been demonstrated, Trent (1977). The effect of the secondary shear zone was illustrated by Boothroyd (1963).

The modellings of the thermal problem on the rake face of the tool are based upon the following simplifying hypothesis:

- H1. The tool tip is perfectly sharp.
- H2. The heat produced by friction on the flank face is neglected.
- H3. The heat flow through the tool surface will be neglected. Actually, the part of the heat flowing into the tool was shown to be small by Boothroyd (1963). This was revealed by the analysis of isothermal contours in the chip.
- H4. The heat transfer in the flow direction due to conduction is neglected with respect to the heat convection due to the material flow.

Assuming that the heat sources are known, several solutions of the thermal problem at the interface have been proposed in the literature. The problem is considered as two-dimensional and time independent. The axes (X , Y) in Fig. 3 are taken along,

and perpendicular to the tool interface respectively. Rapier (1954) has solved the heat equation in the chip for a given heat source at the interface. The secondary shear zone which is disregarded in the Rapier calculations, is introduced in the work of Boothroyd (1963).

None of the former models consider the full coupling between the thermal problem and the friction effects. A full coupling is proposed in our approach based on the assumption of a temperature dependent friction coefficient, see eqn (1). With that assumption the friction characteristics will depend on the cutting conditions in a way that allows to reproduce the experimental trends. The totality of these trends could not be captured by other models.

The proposed model is the following: hypothesis H1 to H4 are adopted; the secondary shear zone is neglected—this is specially adequate at large cutting speeds; the heating of the chip is due to the viscoplastic deformation in the primary shear zone on the one hand, and to friction on the tool-chip interface on the other hand. The stationary temperature distribution in the chip beyond the primary shear zone is obtained by solving the following two dimensional thermal problem:

$$a \frac{\partial^2 T(X, Y)}{\partial Y^2} = V_c \frac{\partial T(X, Y)}{\partial X}, \quad (12)$$

where $a = k/\rho c$ is the thermal diffusivity of the workpiece material, and V_c is the chip velocity. The term in the right hand side is the material derivative of the temperature, providing that the partial time derivative vanishes in the stationary problem.

The outflow boundary of the primary shear zone is considered to be orthogonal to the tool interface (although it is not in general). This assumption, made for convenience, allows an analytical solution. Considering a different inclination of the primary shear band will not affect the solution at a distance X large enough with respect to the width of the layer thermally affected by friction, which is supposed to be small.

Boundary conditions associated to eqn (12) are:

$$T(0, Y) = T_1 \quad X = 0, Y \geq 0 \quad (\text{outflow of the primary shear zone}) \quad (13.1)$$

$$\lim_{Y \rightarrow \infty} T(X, Y) = T_1 \quad \text{for } X \geq 0 \quad (13.2)$$

$$-k \frac{\partial T(X, 0)}{\partial Y} = Q(X) \quad \text{for } X \geq 0 \quad (13.3)$$

T_1 is the temperature at the outflow of the primary shear band. It can be calculated using the thermomechanical model of Molinari and Dudzinski (1992). The condition (13.2) has the following meaning: the heat produced by friction affects a layer along the tool interface which gets smaller as the cutting speed is increased. Therefore, for a distance Y to the interface sufficiently large, the temperature of the chip is equal to T_1 . In eqn (13.3), k is the heat conductivity and $Q(X)$ is the surfacic heat source due to friction:

$$Q(X) = \bar{\mu} V_c P(X) \quad (14)$$

where $\bar{\mu}$ and V_c are the mean friction coefficient and the chip velocity respectively. $P(X)$ represents the pressure distribution.

Experimental data show that the pressure distribution is not uniform but is a decreasing function of X on the tool-chip interface (Usui and Takeyama, 1960; Zorev, 1963; Kato *et al.*, 1972; Buryta *et al.*, 1994). To account for this fact, we choose a distribution of pressure of the form:

$$P(X) = P_0 \left(1 - \frac{X}{l_c}\right)^\xi \quad (15)$$

where l_c is the chip-tool contact length and P_0 represents the pressure on the tool tip. The pressure profile is controlled by the parameter ξ (≥ 0). A parametric analysis of the influence of ξ will be provided. The contact length l_c and P_0 are calculated in Appendix A.

The chip velocity V_c is deduced from the incompressibility condition (4):

$$V_c = V \frac{\sin \phi}{\cos(\phi - \alpha)} \quad (16)$$

The foregoing problem (12)–(13) can be solved with the Laplace transform technique, using X as the transform variable, see Appendix B. The temperature distribution in the chip is shown to satisfy this relationship:

$$T(X, Y) = \frac{\bar{\mu} V_c P_0}{k} \sqrt{\frac{a}{\pi V_c}} \int_0^X \left(1 - \frac{X-u}{l_c}\right)^\xi \frac{1}{\sqrt{u}} \exp\left(\frac{-V_c Y^2}{4au}\right) du + T_1 \quad (17)$$

We now consider the case of ξ being an integer ($\xi = 0, 1, 2, \dots$). By developing the expression

$$\left(1 - \frac{X-u}{l_c}\right)^\xi$$

we obtain the mean interface temperature ($Y = 0$):

$$\bar{T}_{\text{int}} = \frac{\bar{\mu} P_0}{\sqrt{\pi k \rho c}} \sqrt{V_c l_c} \sum_{i=0}^{\xi} \frac{2}{2i+1} C_{\xi}^i \left(\sum_{j=0}^{\xi-i} (-1)^j C_{\xi-i}^j \frac{2}{2(i+j)+3} \right) + T_1 \quad (18)$$

with

$$C_{\xi}^i = \frac{\xi!}{(\xi-i)!i!}$$

Because of the dependence of $\bar{\mu}$ upon \bar{T}_{int} in our model, $\bar{\mu}$ is not known beforehand. The relationship (18) appears as an implicit equation in terms of \bar{T}_{int} . Once \bar{T}_{int} is calculated (iteratively), the friction coefficient $\bar{\mu}(\bar{T}_{\text{int}})$ is determined.

4. HOW THE MODEL WORKS

Let us consider that the friction law (1) has been identified (this will be discussed later in detail). In addition the values of ξ governing the variation of the pressure along the tool-chip interface are supposed to be given.

The following set of equations allows us to determine $\bar{\mu}$, ϕ , V_C , l_C , γ_1 , T_1 , τ_1 , P_0 , \bar{T}_{int} and τ_0 .

$$\bar{\mu} = \bar{\mu}(\bar{T}_{\text{int}}) = \tan(\lambda) \quad (19.1)$$

$$\phi = A + \frac{1}{2}(\alpha - \lambda) \quad (19.2)$$

$$V_C = V \frac{\sin \phi}{\cos(\phi - \alpha)} \quad (19.3)$$

$$l_C = t_1 \frac{\xi + 2 \sin(\phi + \lambda - \alpha)}{2 \sin \phi \cos \lambda} \quad (19.4)$$

$$\gamma_1 = \tan(\phi - \alpha) + \frac{1}{\tan \phi} \quad (19.5)$$

$$\tau_0 = \tau_0(\text{cutting conditions}, \phi, \text{material parameters}) \quad (19.6)$$

$$\tau_1 = \rho(V \sin \phi)^2 \gamma_1 + \tau_0 \quad (19.7)$$

$$T_1 = T_w + \frac{\beta}{\rho c} \left(\rho(V \sin \phi)^2 \frac{\gamma_1^2}{2} + \tau_0 \gamma_1 \right) \quad (19.8)$$

$$P_0 = 4 \frac{\xi + 1}{\xi + 2} \frac{\cos^2(\lambda)}{\sin(2(\phi + \lambda - \alpha))} \tau_1 \quad (19.9)$$

$$\bar{T}_{\text{int}} = \frac{\bar{\mu} P_0}{\sqrt{\pi k \rho c}} \sqrt{V_C l_C} \sum_{i=0}^{\xi} \frac{2}{2i+1} C_{\xi}^i \left(\sum_{j=0}^{\xi-i} (-1)^j C_{\xi-i}^j \frac{2}{2(i+j)+3} \right) + T_1 \quad (19.10)$$

Equations (19.1) to (19.5) come from (1), (8), (16), (A.12), (7.3); (the choice of the parameter A in (19.2) is made later). Equations (19.7) to (19.10) come from (5.1), (5.2), (A.9) and (18). The relationship (19.6) expresses the fact that τ_0 can be calculated in terms of the cutting conditions, the shear angle ϕ and the material parameters, using the model of the primary shear zone presented in section 2. In this model τ_0 is obtained iteratively by integration of the differential eqn (6).

The iterative scheme used to solve the preceding set of equations is as follows: let us consider that at the n th iteration $\bar{T}_{\text{int}}^{(n)}$ is known. $\bar{\mu}^{(n)}$, $\phi^{(n)}$ and $\gamma_1^{(n)}$ are given by (19.1), (19.2) and (19.5). $\tau_0^{(n)}$ follows from (19.6), $\tau_1^{(n)}$, $T_1^{(n)}$, $V_C^{(n)}$, $l_C^{(n)}$ and $P_0^{(n)}$ result from (19.7), (19.8), (19.3), (19.4) and (19.9). Finally a new estimate $\bar{T}_{\text{int}}^{(n+1)}$ of the tool-chip mean interface temperature is obtained from (19.10). The calculations stop when the accuracy on the estimate of \bar{T}_{int} is good enough.

5. RESULTS AND DISCUSSION

In this section the proposed model is applied to the analysis of orthogonal cutting of steels. We shall consider a CRS 1018 steel (U.S. norms) whose thermomechanical response has been characterized with high strain rate tests on Kolsky bars. The constitutive law (2) is used with the following values of material parameters, Clifton *et al.* (1984):

$$\begin{aligned}v &= -0.38 \quad n = 0.015 \quad m = 0.019 \\ \mu_0 &= 3579.10^6 \text{ SI} \quad c = 500 \text{ J/(kg}^\circ\text{K)} \quad \rho = 7800 \text{ kg/m}^3 \\ k &= 54 \text{ W/m}^\circ\text{K}\end{aligned}$$

Experimental results concerning the cutting of a 0.2% carbon steel, with characteristics close to the CRS 1018 steel, have been presented by Oxley (1989). The tool is made of tungsten carbide tips with a 6° clearance angle and negligible nose radius. These results are used to infer the friction law (1) and the relationship (8) providing the shear angle ϕ . A validation is later obtained by comparing the predictions of the model to experimental data under various cutting conditions.

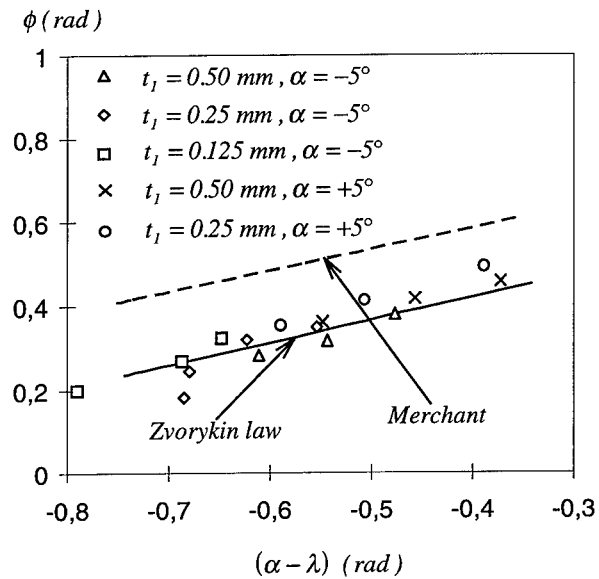
5.1. Experimental identification of the Zvorykin law and of the friction law

The identification of the laws (1) and (8) is made with experimental data of Oxley (1989). Values of the shear angle ϕ determined from measurements of the chip thickness, are reported in Fig. 4(a). They correspond to different cutting conditions ($\alpha = +5^\circ, -5^\circ, t_1 = 0.125, 0.25, 0.5 \text{ mm}, w = 4 \text{ mm}$) and various cutting velocities, Oxley (1989). It is seen that the Merchant formula overestimates the shear angle. The Zvorykin law (8) describes quite well the experimental trends for a value of the angle $A = 35^\circ$ (in place of $A = 45^\circ$ in the Merchant formula), see Fig. 4(a).

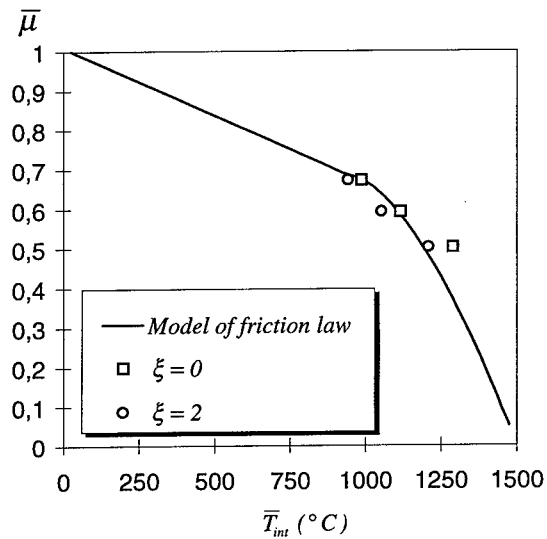
The mean friction coefficient $\bar{\mu}$ is deduced from the measurements of the components F_P and F_Q of the cutting forces, see (A. 13).

Since we do not have measurements of the interface temperature \bar{T}_{int} in the Oxley experiments, we propose to make an estimation using the following procedure. Two types of pressure distributions on the tool interface will be considered: a uniform and a parabolic profile ($\xi = 0$ and $\xi = 2$, resp.). The thickness h of the primary shear zone is taken as $h = 0.025 \text{ mm}$. This is a typical value found in the literature, Shaw (1984). Actually, under the adiabatic assumption made for the flow within the shear band, and for the constitutive law (2) (with m of low value) considered here, the precise value of h has no major influence on the results, Dudzinski and Molinari (1997). This point has to be reconsidered for material response with a larger strain rate sensitivity, see section 5.4.

From the value of F_P , we can deduce F_S and τ_1 with use of (A.4) and (A.2). Then τ_0 and T_1 are given by (19.6) and (19.8). P_0 and l_C are obtained with equations (19.9) and (19.4). The mean temperature \bar{T}_{int} at the tool interface is finally estimated by (19.10). For the following cutting conditions: $V = 100, 200, 400 \text{ m/mn}$, $\alpha = -5^\circ$, $t_1 = 0.25 \text{ mm}$, $w = 4 \text{ mm}$, $\bar{\mu}$ has been measured using Oxley data and \bar{T}_{int} has been estimated as shown before. The corresponding points calculated for $\xi = 0$ and $\xi = 2$



(a)



(b)

Fig. 4. (a) Experimental identification of the Zvorykin law (8) for the shear angle ϕ , (b) Experimental identification of the friction law (1). \bar{T}_{int} is the mean temperature at the tool-chip interface.

are reported on the $\bar{\mu}$ vs \bar{T}_{int} diagram of Fig. 4(b). It appears that the mean temperature \bar{T}_{int} is weakly affected by ξ , and consequently the identification of the friction law $\bar{\mu} = \bar{\mu}(\bar{T}_{\text{int}})$ seems not to be really dependent on the precise value of ξ .

More experimental measurements would be needed to have a complete identification of the friction law (1). However the temperature dependence of the friction coefficient can be extrapolated in the range of temperatures from 20–1500°C, with consideration of experimental results reported in the review by Lim *et al.* (1989). It appears that the dry friction coefficient decreases when the sliding velocity increases in the range $1 \text{ m/s} \leq V_c \leq 100 \text{ m/s}$. The maximum value of $\bar{\mu}$ for steel on steel friction, attained at velocities of the order of 1 m/s, is found to be close to unity. In addition, when the interface temperature is close to the melting temperature, a drop of the friction coefficient is assumed in our modelling. All these features are accounted for in the evolution of the friction law (1) reported in Fig. 4(b), and described by the following empirical equations:

$$\bar{\mu} = 1 - 3.44 \cdot 10^{-4} \bar{T}_{\text{int}} \quad \text{for } 25^\circ\text{C} \leq \bar{T}_{\text{int}} \leq 955^\circ\text{C}$$

$$\bar{\mu} = 0.68 \left(1 - \frac{\bar{T}_{\text{int}} - \bar{T}}{T_m - \bar{T}} \right)^q \quad \text{for } 955^\circ\text{C} \leq \bar{T}_{\text{int}} < 1500^\circ\text{C}$$

$$\text{with } q = 1.7, \bar{T} = 955^\circ\text{C}, T_m = 1500^\circ\text{C} \quad (\text{melting temperature})$$

In all the calculations presented in the following section ϕ and $\bar{\mu}$ are evaluated with reference to Zvorykin and the friction laws represented in Fig. 4(a) and 4(b).

5.2. Pressure and temperature distribution at the tool-chip interface

In this paragraph, the following cutting conditions are considered:

$$\alpha = -5^\circ, t_1 = 0.25 \text{ mm}, V = 250 \text{ m/mn}, w = 4 \text{ mm}$$

It should be remembered that in our calculations the heat flow toward the tool is neglected. The heat conductivity used for the chip is that of the CRS 1018 steel $k = 54 \text{ W/(m}^\circ\text{K)}$.

The temperature distributions along the interface presented in the Fig. 5 indicates the existence of a maximum located at a distance to the tool edge depending on the value of ξ . For $\xi = 2$, this distance is approximately equal to $l_c/3$, as observed in the experiments (this distance does not depend on the cutting conditions in the present model). Note that for $\xi = 0$ (uniform pressure distribution) the temperature maximum appears at the extremity $X = l_c$ of the contact zone. The prediction of the local temperature is important for the analysis of tool wear; then a realistic value of ξ must be considered. Note finally that, although the temperature distribution is ξ -dependent, the average temperature \bar{T}_{int} is just weakly dependent upon ξ . This fact is illustrated in Fig. 6 where a small increase of temperature (30°K) is obtained by replacing $\xi = 2$ with $\xi = 0$.

In Fig. 7, the pressure distribution at the tool-chip interface is represented with different values of ξ . The pressure P_0 at the tool tip is shown to attain high values when ξ is increased. A constant pressure profile ($\xi = 0$) is not observed in the experiments. It

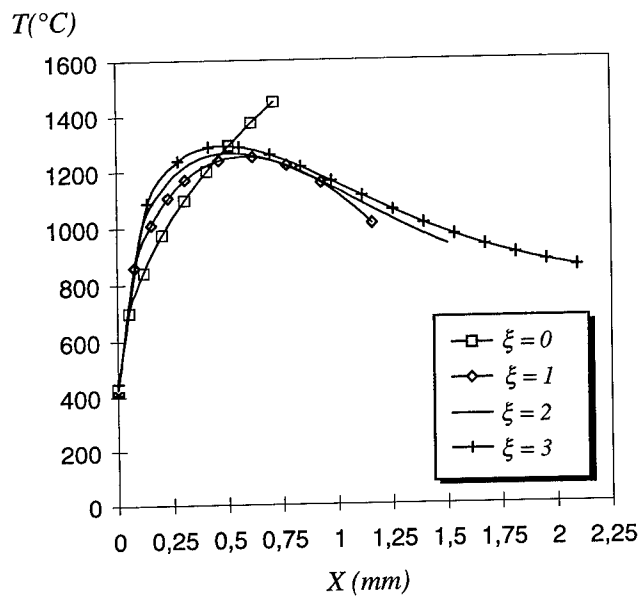


Fig. 5. Temperature distribution at the tool-chip interface, for different values of ξ .

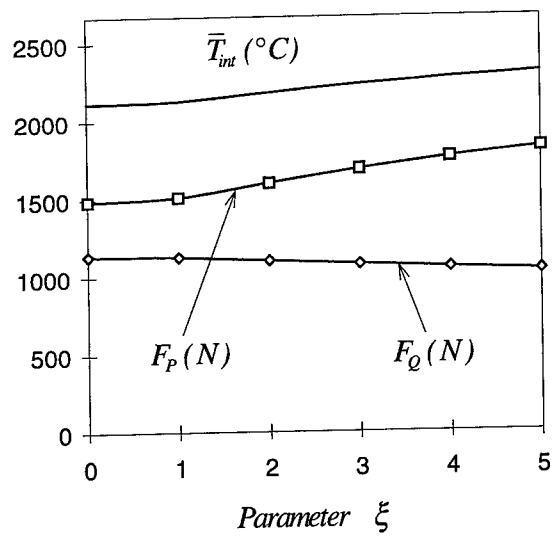


Fig. 6. Longitudinal, orthogonal cutting forces F_p , F_Q and mean temperature at the tool-chip interface \bar{T}_{int} as a function of the pressure parameter ξ .

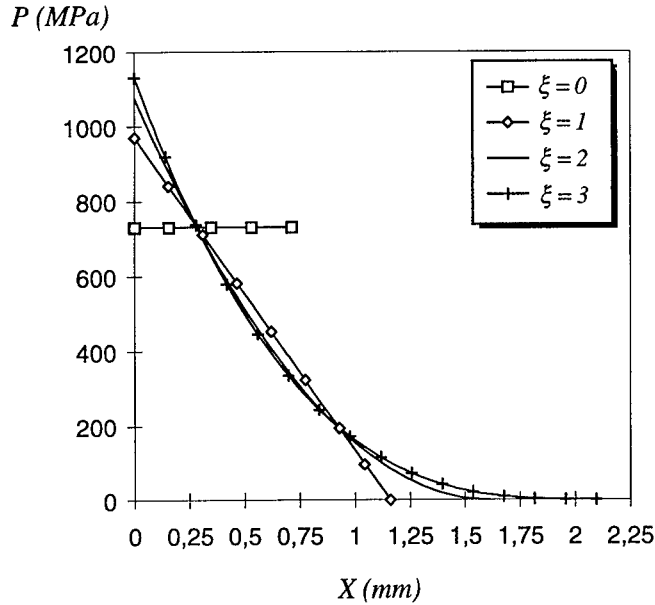


Fig. 7. Pressure distribution at the tool-chip interface, for different values of ξ .

appears that the global quantities F_p and F_Q are weakly dependent upon ξ , see Fig. 6.

Due to the foregoing discussion, the value of $\xi = 2$ will be chosen for the following calculations.

5.3. Validation of the model

We shall now validate the model by varying the cutting conditions. Two different depths of cut t_1 (feeding) are considered: $t_1 = 0.25$ mm (for which the corresponding experimental data were used to identify the friction law) and $t_1 = 0.5$ mm.

The evolution of the longitudinal and orthogonal components F_p and F_Q of the cutting force (see Fig. 19) are reported in terms of the cutting velocity V in Fig. 8, for $t_1 = 0.25$ mm and $t_1 = 0.5$ mm. The decay of the forces for an increasing velocity is due to the lowering of the friction coefficient, see Fig. 9, as a consequence of the growth of the interface temperature. The growth of \bar{T}_{int} with V for a fixed t_1 is due to the term $V_C^{1/2}$ in (19.10).

We can also note from the experiments that the forces F_p and F_Q are not proportional to the feeding t_1 . This fact is restituted by the model, and will be explained later.

The experimental trends discussed before concerning the dependence of the friction coefficient $\bar{\mu}$ on the cutting velocity and the feeding t_1 are reproduced by the model, Fig. 9.

The shear angle ϕ predicted by the model when the cutting speed is varied is compared with experimental measurements, in Fig. 10. The increase of ϕ with V

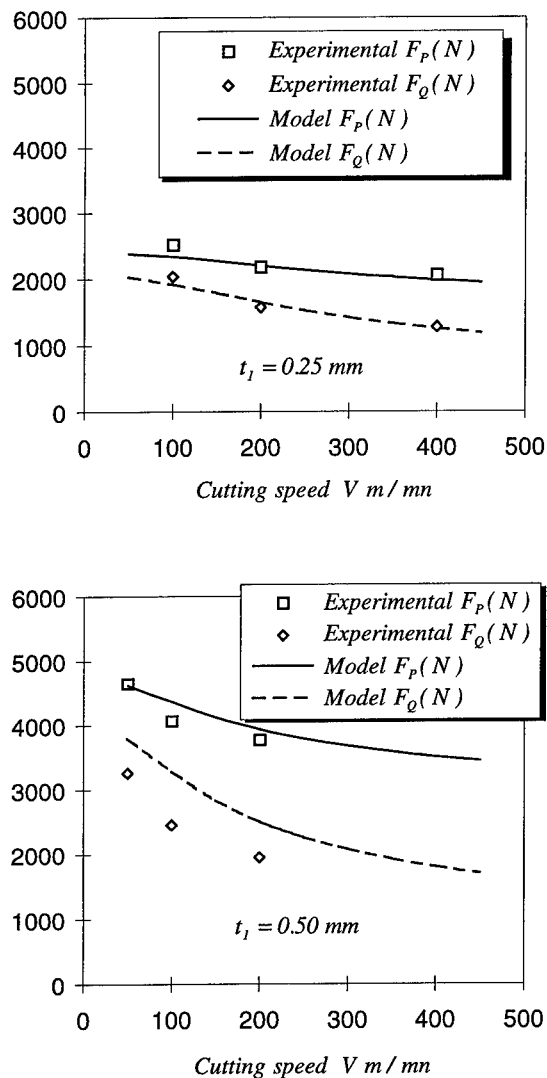


Fig. 8. Predicted cutting forces (for CRS 1018 steel) compared to the experimental values for a 0.20% carbon steel, (experimental data are from Oxley (1989)). The cutting conditions are: $\alpha = -5^\circ$, $w = 4$ mm, $t_1 = 0.25$ mm and $t_1 = 0.50$ mm.

results from the law (19.2) and the lowering of the friction angle λ . It is reminded that the rake angle and the width of cut have in these calculations the values $\alpha = -5^\circ$ and $w = 4$ mm.

5.4. Parametric analysis

A systematic analysis of the influence of cutting conditions is now presented. It will be shown how α , t_1 and V affect the cutting forces, the friction coefficient and the

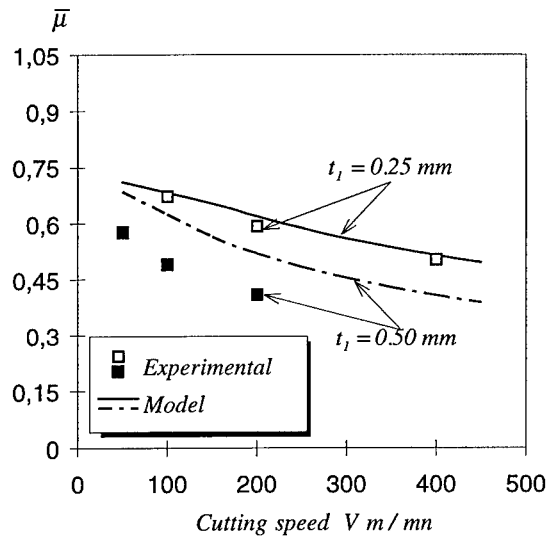


Fig. 9. Predicted and experimental values of the mean friction coefficient $\bar{\mu}$. The cutting conditions are: $\alpha = -5^\circ$, $w = 4$ mm, $t_1 = 0.25$ mm and $t_1 = 0.50$ mm.

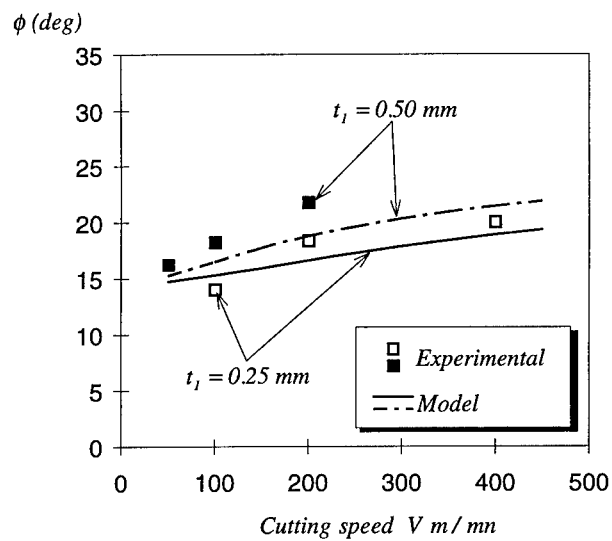


Fig. 10. Predicted and experimental values of the shear angle ϕ . The cutting conditions are: $\alpha = -5^\circ$, $w = 4$ mm, $t_1 = 0.25$ mm and $t_1 = 0.50$ mm.

temperature distribution at the outflow of the primary shear zone and at the tool-chip interface.

5.4.1. Influence of the cutting speed V . The rake angle and the cutting width have the values $\alpha = -5^\circ$ and $w = 4$ mm. The cutting velocity is varied from conventional to high speeds. The mean temperature \bar{T}_{int} at the tool interface is represented in Fig. 11(a) in terms of the cutting velocity V , for two different values of the feeding t_1 . A large increase of \bar{T}_{int} can be observed for velocities less than 1000 m/mn. This results in an important decay of the friction coefficient $\bar{\mu}$ and of the cutting forces F_p and F_Q , as shown in Fig. 11(b) and 11(c).

The variation of the temperature T_1 at the outflow of the primary shear band, versus the cutting velocity is reported in Fig. 11(d). The large decay of T_1 when V increases up to the value 1000 m/mn can be explained in the following way. Due to the decrease of the friction angle λ , the shear angle ϕ increases, see eqn (19.2) and Fig. 11(e). This results in a reduction of the shear strain γ_1 . Consequently the work of plastic deformations and the heat produced by dissipation are reduced, and so is T_1 .

The decay of $\bar{\mu}$ also implies an important reduction of the contact length l_c , as illustrated in Fig. 11(f), in agreement with the experimental observations of Gad *et al.* (1992).

Because of the term $V_C^{1/2}$ in expression (19.10) of the mean interface temperature, it is expected that for large cutting velocities, the dependence of \bar{T}_{int} upon the cutting speed is attenuated, while strongly marked for $V \leq 1000$ m/mn, see Fig. 11(a). This weakening of the velocity dependence for $V \geq 1000$ m/mn is clearly transmitted to the evolution of $\bar{\mu}$, F_p , F_Q , T_1 and l_c , see Fig. 11.

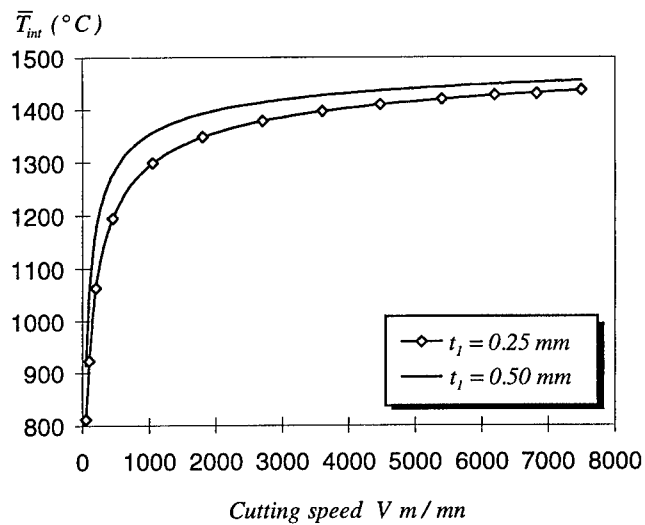
A slight increase of the force F_p and of T_1 can be observed for $V \geq 4000$ m/mn. This is due to inertia effects that become apparent at large cutting velocities. These effects are conducive to a rise of the flow stress τ_1 at the outflow of the primary shear zone (Dudzinski and Molinari, 1997; Recht, 1984) which explains the trends noticed on F_p and T_1 .

5.4.2. Influence of the rake angle α . For the present analysis, the feeding is fixed at the value $t_1 = 0.25$ mm and the width of cut is $w = 4$ mm. The influence of the rake angle α on the cutting process will be studied for three cutting velocities: 250 m/mn, 2500 m/mn and 6000 m/mn.

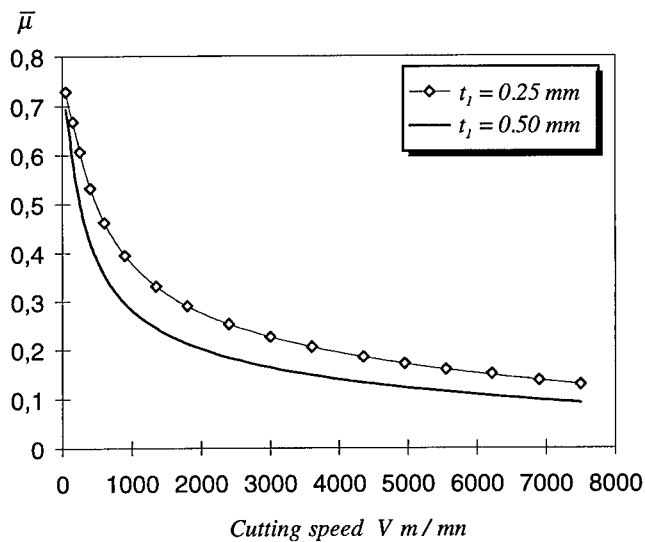
It is observed in Fig. 12(a) that the mean interface temperature \bar{T}_{int} is a decreasing function of α . The decrease in T_1 and l_c reported in Fig. 12(e) and Fig. 12(f) for an increasing α are responsible for the evolution of \bar{T}_{int} , see eqn (19.10).

As a result of the variation of \bar{T}_{int} presented in Fig. 12(a), the mean friction coefficient $\bar{\mu}$ varies in terms of α as shown in Fig. 12(b). These trends are in agreement with the experimental observations of Bailey (1975). We have evaluated the function $\bar{\mu}(\alpha)$ with the Oxley model (1989), using the constitutive law (2). These calculations have shown that $\bar{\mu}$ decreases with α , in contradiction with the experimental observations.

The shear angle ϕ undergoes two opposite effects. When α is made larger, it is seen in the law (19.2) that this geometric effect induces an augmentation of ϕ . However the increase of the friction angle λ in (19.2) has the reverse consequence. Eventually

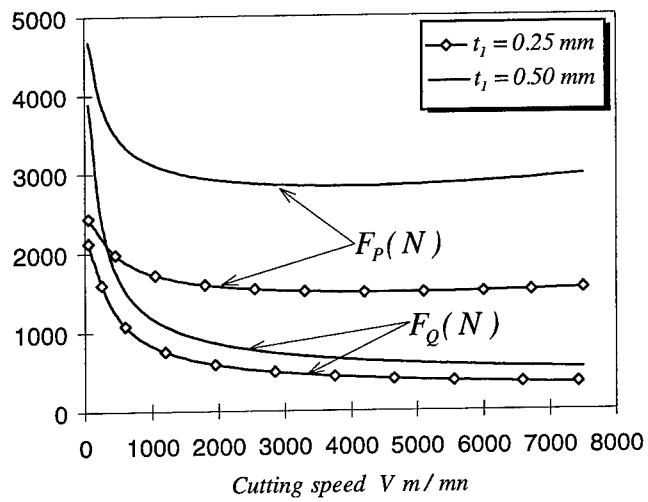


(a)

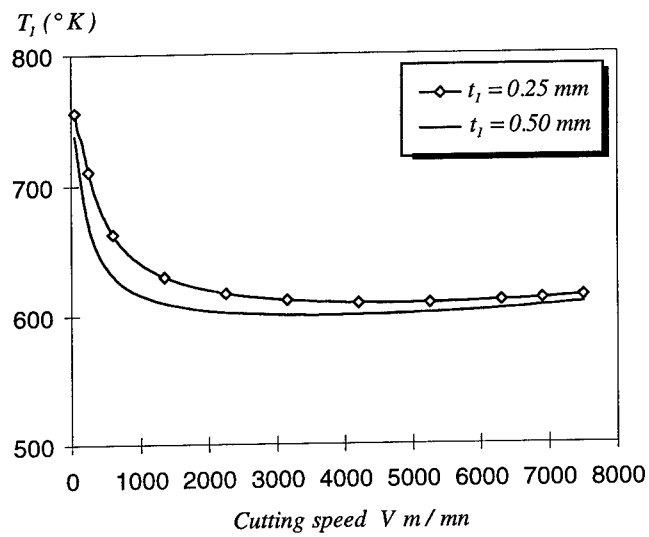


(b)

Fig. 11. Analysis of the effects of the cutting speed V on: (a) the interface temperature \bar{T}_{int} , (b) the mean friction coefficient $\bar{\mu}$, (c) the cutting forces F_P and F_Q , (d) the temperature at the outflow of the primary shear zone T_1 , (e) the shear angle ϕ , and (f) the contact length l_C . A CRS 1018 steel is considered. The cutting conditions are: $\alpha = -5^\circ$, $w = 4$ mm, $t_1 = 0.25$ mm and $t_1 = 0.50$ mm.

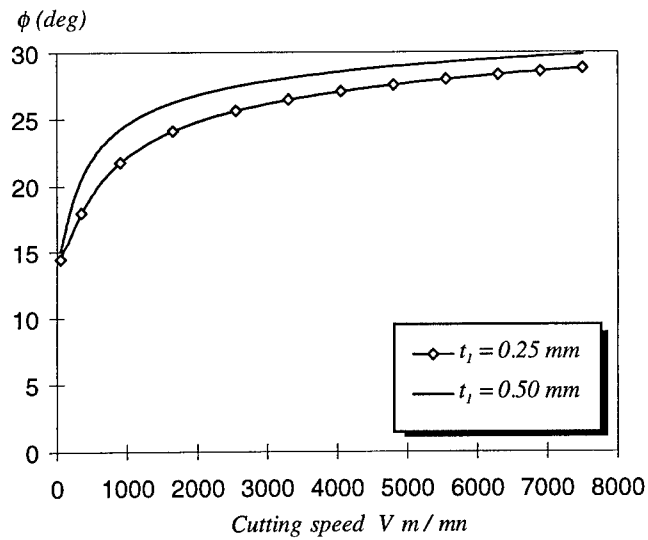


(c)

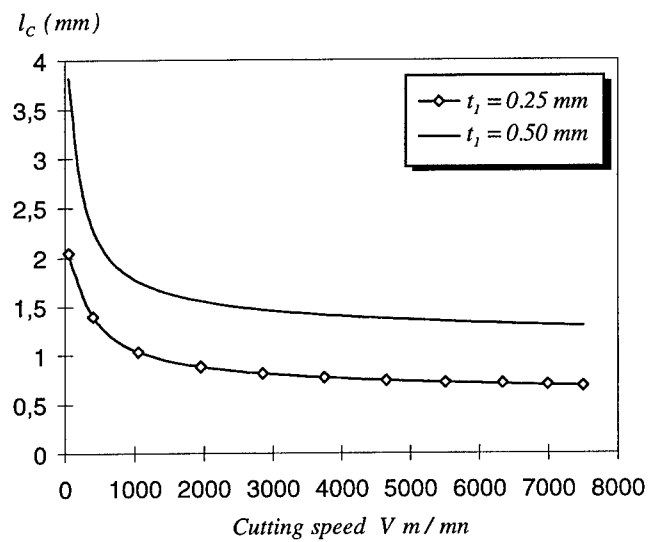


(d)

Fig. 11. (c) and (d).



(e)



(f)

Fig. 11. (e) and (f).

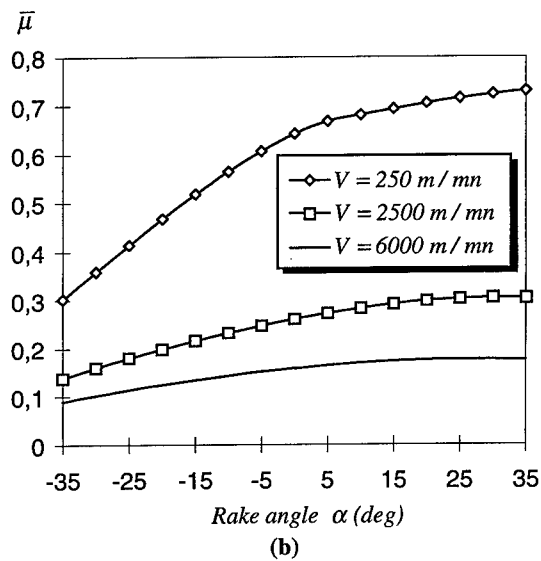
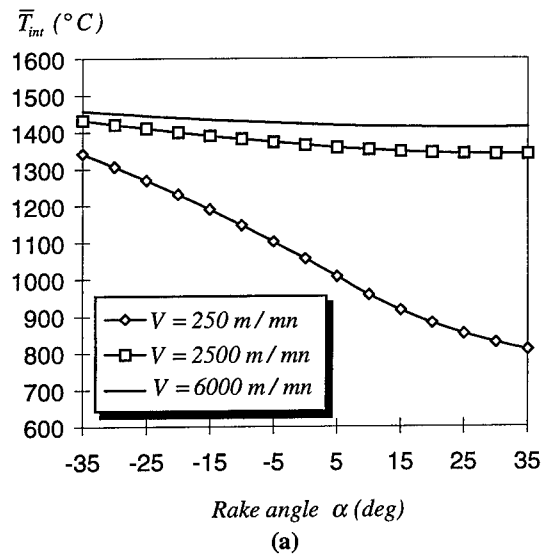


Fig. 12. Analysis of the effects of the rake angle α on: (a) the interface temperature \bar{T}_{int} , (b) the mean friction coefficient $\bar{\mu}$, (c) the longitudinal cutting force, F_p , (d) the shear angle ϕ , (e) the temperature at the outflow of the primary shear zone T_1 and (f) the contact length l_c . A CRS 1018 steel is considered. The cutting conditions are: $V = 250, 2500, 6000$ m/mn, $w = 4$ mm and $t_1 = 0.25$ mm.

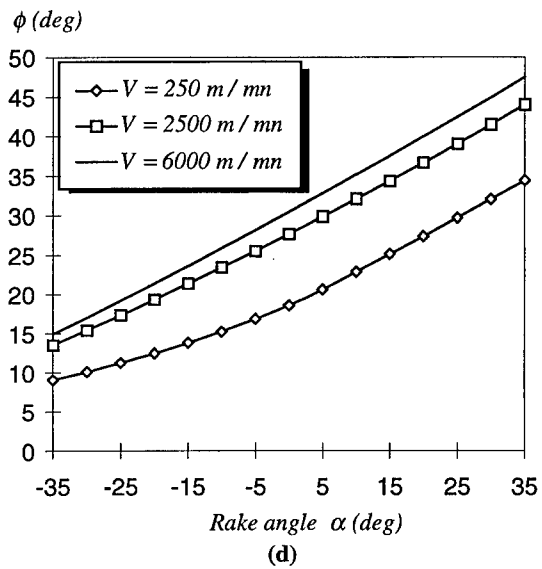
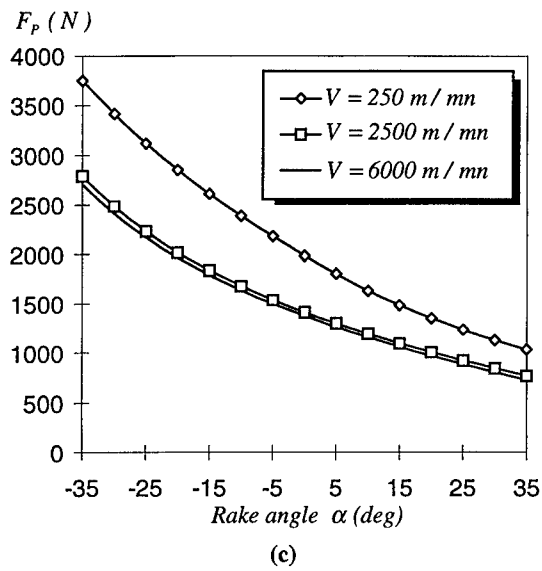


Fig. 12. (c) and (d).

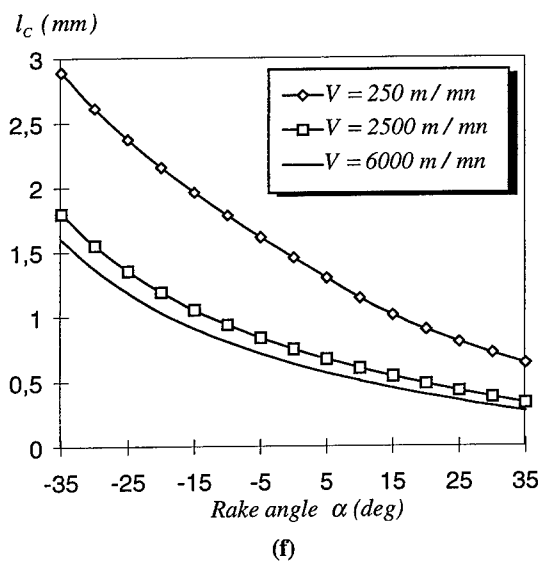
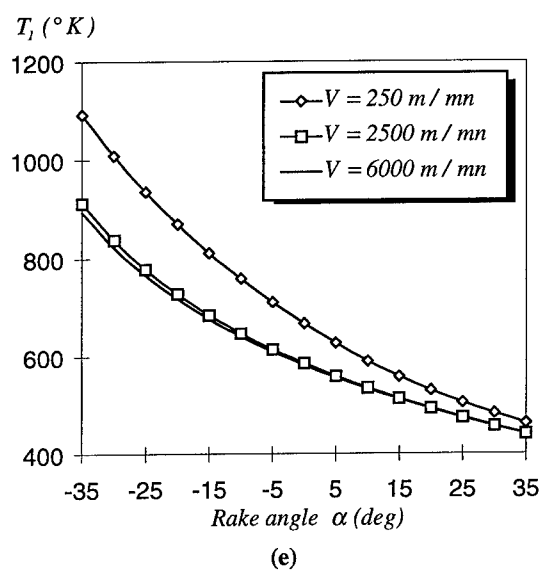


Fig. 12. (e) and (f).

the first effect outweighs the second and ϕ is shown in Fig. 12(d) to follow the variation of α .

The reduction of ϕ when α is decreased, leads to larger plastic deformations $\gamma_1 = tg(\phi - \alpha) + 1/tg\phi$, and thus to a larger plastic work and a larger increase of temperature T_1 at the outflow of the primary shear band, as reported in Fig. 12(e). Note that the large increase of T_1 for negative values of α , can be indicative of a situation favourable to thermomechanical instability and to chip segmentation.

The cutting force component F_p increases when α is reduced Fig. 12(c), in spite of the decay of friction. This is a consequence of the decay of ϕ .

In Fig. 12(f), it is shown that the contact length is increased when α is made smaller. Indeed a decrease of α produces a reduction of the friction angle λ and of the contact length, see (19.4). However the dependence of l_c upon α in the relationship (19.4) overcomes the effect of λ . This explains the trends shown in Fig. 12(f), which are in concordance with the experiments of Gad *et al.* (1992).

The effect of the cutting speed shown in the preceding figures conforms with the trends illustrated in the former paragraph.

5.4.3. Influence of the depth of cut t_1 . In the present paragraph, the rake angle and the width of cut have a fixed value $\alpha = -5^\circ$ and $w = 4$ mm. Experimental results have shown that the cutting forces are not proportional to the feeding t_1 . A proportional relationship would be incorrectly suggested by a first examination of eqns (A.4) and (A.5). However one cannot ignore in general the dependence of the friction angle upon t_1 which is the cause of the non proportional relationship between the cutting forces and the feeding. More precisely an increase in t_1 induces an augmentation of the interface temperature \bar{T}_{int} , Fig. 13(b), which in turn produces a reduction of friction, Fig. 13(c).

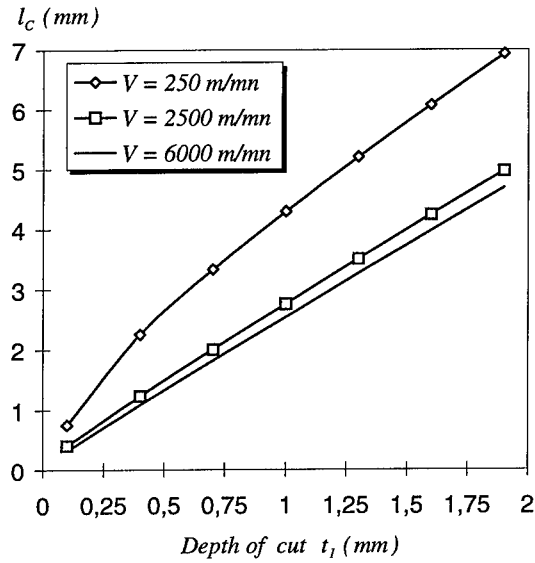
The variation of \bar{T}_{int} shown in Fig. 13(b) induces the decay of $\bar{\mu}$ in terms of t_1 shown in Fig. 13(c). This dependence of the mean friction coefficient with respect to the feeding agrees with the experimental data of Findley and Reed (1963).

The dependence of \bar{T}_{int} upon t_1 , cannot be explained in a simple way. On the one hand an increase of t_1 induces a growth of the contact length l_c , eqn (19.4) and Fig. 13(a), which leads to a rise of the interface temperature \bar{T}_{int} if T_1 were fixed, eqn (19.8). However, on the other hand T_1 is a decreasing function of t_1 , Fig. 13(e). This is a consequence of the decay of γ_1 resulting from the growth of the shear angle, Fig. 13(d), induced by the decay of the friction coefficient. Apparently the first effect overcomes the decay of T_1 and produces an increase of \bar{T}_{int} in terms of the feeding t_1 , Fig. 13(b). Note that the crossing of curves in Fig. 13(e) and 13(f) is a result of inertia forces.

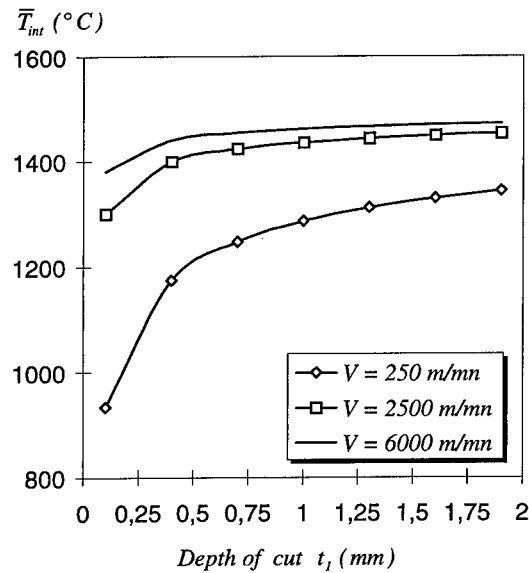
5.4.4. Influence of a change of mechanism in the constitutive law at large strain rates. In this paragraph, the following cutting conditions are considered :

$$\alpha = -5^\circ, t_1 = 0.25 \text{ mm}, w = 4 \text{ mm}$$

It is known that a significant increase of the strain rate sensitivity appears in metals subjected to strain rates higher than a critical value $\dot{\gamma}_l$ (Campbell and Fergusson, 1970; Follansbee and Kocks, 1988; Tong *et al.*, 1992; Klepaczko, 1994). The following



(a)



(b)

Fig. 13. Analysis of the effects of the depth of cut t_1 on: (a) the contact length l_c , (b) the interface temperature \bar{T}_{int} , (c) the mean friction coefficient $\bar{\mu}$, (d) the shear angle ϕ , (e) the temperature at the outflow of the primary shear zone T_1 , (f) the cutting force F_p . A CRS 1018 steel is considered. The cutting conditions are: $V = 250, 2500, 6000$ m/min, $w = 4$ mm and $\alpha = -5^\circ$.

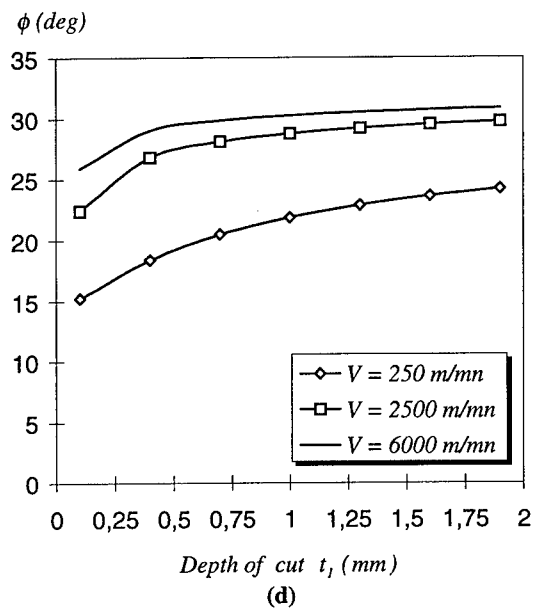
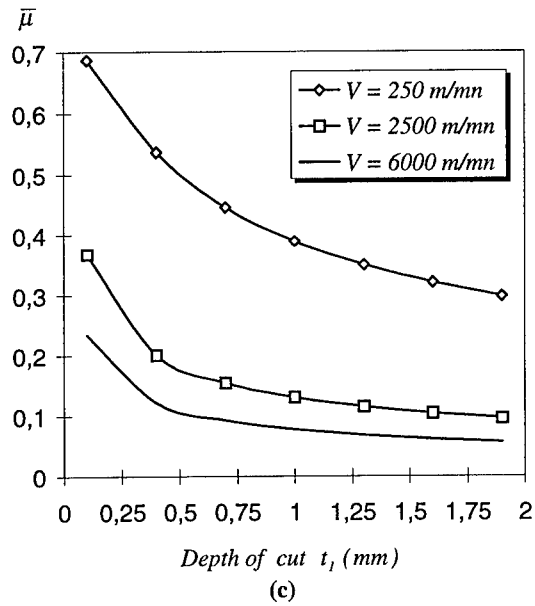


Fig. 13. (c) and (d).

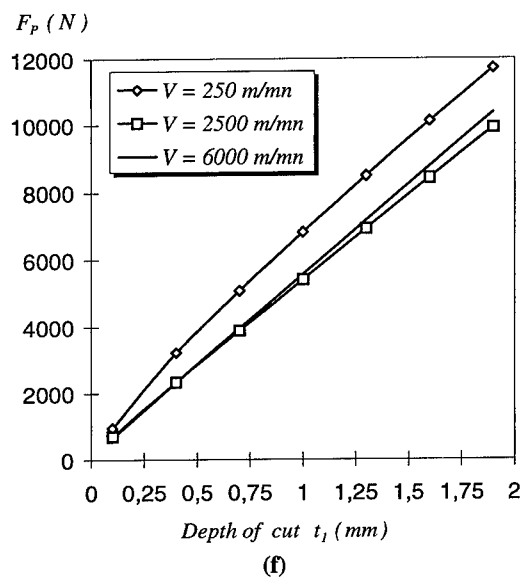
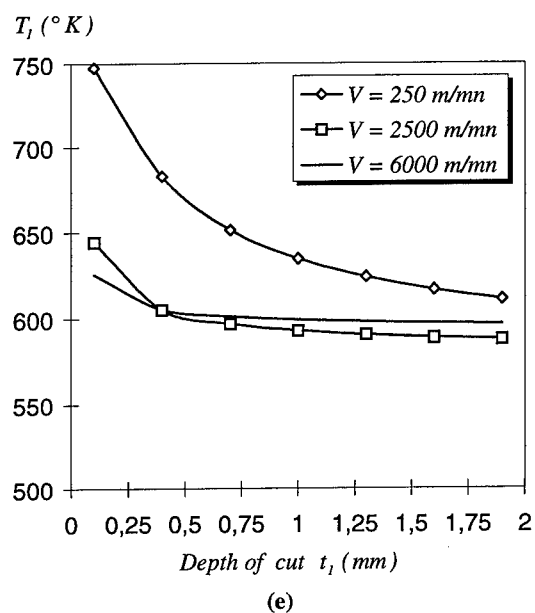


Fig. 13. (e) and (f).

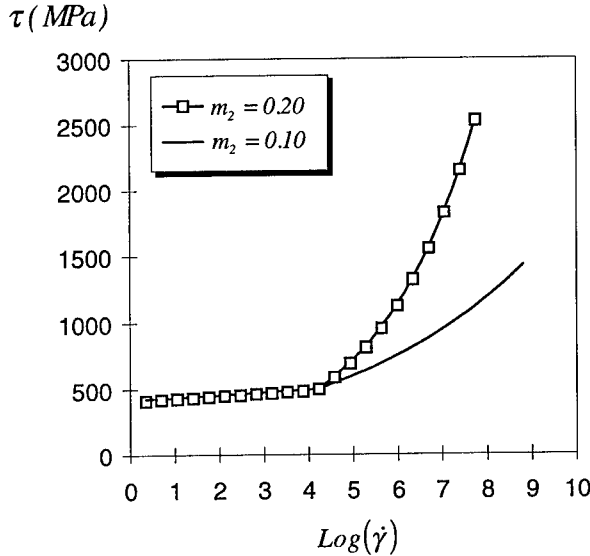


Fig. 14. Variation of the shear stress τ in terms of the shear strain rate $\dot{\gamma}$ (Logarithmic scale).

formulation of the constitutive law is a way to account for these experimental observations:

$$\begin{aligned} \tau &= \mu_0 (\gamma + \gamma_p)^n \dot{\gamma}^{m_1} T^r & \text{if } \dot{\gamma} \leq \dot{\gamma}_t \\ \tau &= \mu_0 (\gamma + \gamma_p)^n \dot{\gamma}_t^{(m_1 - m_2)} \dot{\gamma}^{m_2} T^r & \text{if } \dot{\gamma} \geq \dot{\gamma}_t \end{aligned} \quad (20)$$

with $\dot{\gamma}_t = 10^4 \text{ s}^{-1}$. The strain rate sensitivity $m_1 = 0.019$ has the same value as the one used in the preceding calculations. Two values of m_2 (0.1 and 0.2) are considered in our analysis to illustrate the effect on the cutting process of the change of mechanism at $\dot{\gamma}_t$. The strain rate dependence of the constitutive law (20) is illustrated in Fig. 14 for $m_2 = 0.1$ and $m_2 = 0.2$. The other values of parameters are those of the CRS 1018 steel, see section 5. Note the large increase of the stress for $\dot{\gamma} \geq \dot{\gamma}_t = 10^4 \text{ s}^{-1}$. The effect of the change of mechanism is important on the level of the cutting forces, Fig. 15. For $m_2 = 0.2$, the growth of the stress induced by the change of strain rate sensitivity overcomes the decrease of the cutting forces due to the friction effects. The influence of the cutting conditions (role of α , t_1 , V) is similar to the one illustrated by use of the constitutive law (2) (with no change of mechanism) as far as the following quantities are considered: \bar{T}_{int} , $\bar{\mu}$, ϕ , l_c , $T(X)$ (distribution of the interface temperature). As an example, the evolution of \bar{T}_{int} in terms of V is presented in Fig. 16 for the two constitutive laws (2) and (20). The temperature distribution at the tool-chip interface is presented in Fig. 17. The increase of strain rate sensitivity for $\dot{\gamma} \geq \dot{\gamma}_t$ seems to have little effect on this distribution.

The role of the thickness h of the primary shear zone is now important, because of the large strain rate sensitivity for $\dot{\gamma} \geq \dot{\gamma}_t$. We have kept in our calculations the value $h = 25 \text{ } \mu\text{m}$. An increase in h will produce a lowering of the strain rates within the

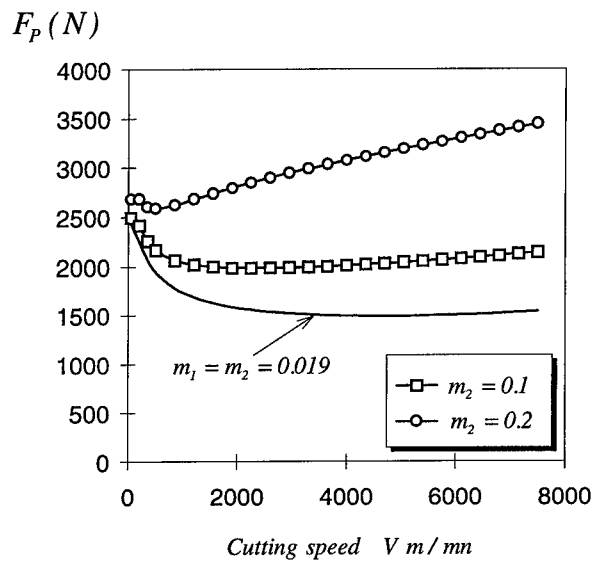


Fig. 15. Effect of the cutting speed V and of the change of mechanism in the constitutive law (20) on the longitudinal cutting force F_p . The cutting conditions are: $\alpha = -5^\circ$, $w = 4$ mm, $t_1 = 0.25$ mm.

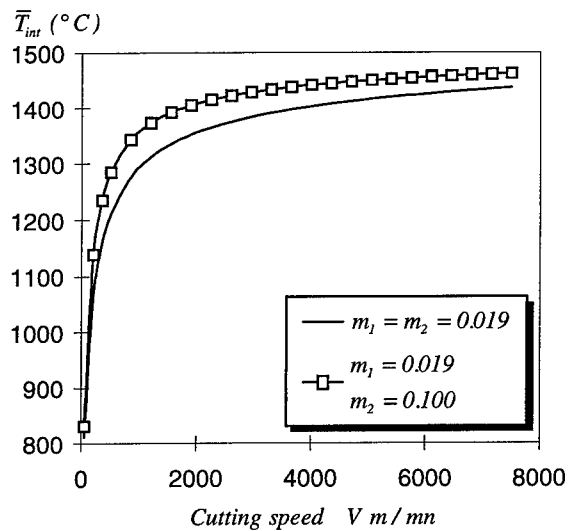


Fig. 16. Influence of the change of mechanism in the constitutive law (20) on the evolution of the mean interface temperature \bar{T}_{int} in terms of the cutting speed V . The cutting conditions are: $\alpha = -5^\circ$, $w = 4$ mm, $t_1 = 0.25$ mm.

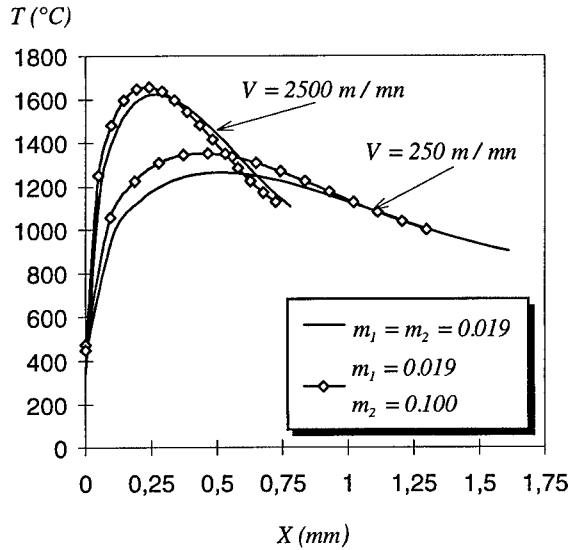


Fig. 17. Effect of the change of mechanism on the temperature distribution at the tool-chip interface. The cutting conditions are: $\alpha = -5^\circ$, $w = 4$ mm, $t_1 = 0.25$ mm.

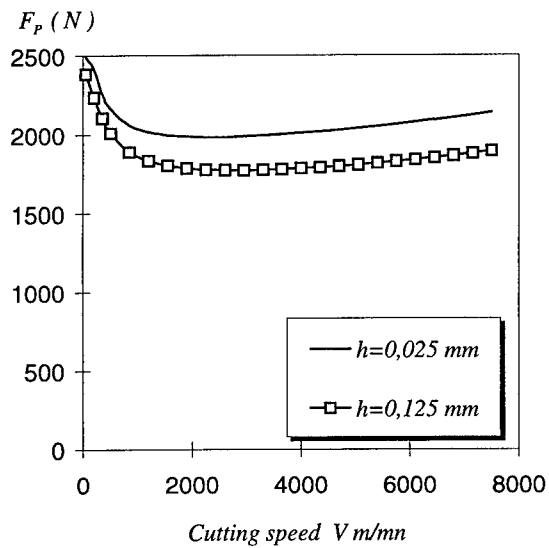


Fig. 18. Effect of the cutting speed V and of the thickness h of the primary shear zone on the longitudinal cutting force F_p , ($m_2 = 0.1$). The cutting conditions are: $\alpha = -5^\circ$, $w = 4$ mm, $t_1 = 0.25$ mm.

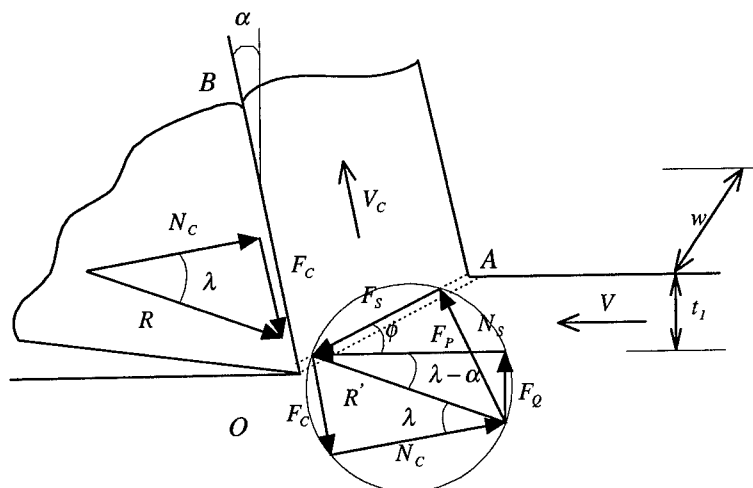


Fig. 19. Forces at the tool-chip interface and at the outflow of the shear zone.

primary shear zone, that could lead (if the strain rates are close to $\dot{\gamma}_i$) to a significant effect on the flow stress and on the cutting forces, see Fig. 18.

6. CONCLUSION

The model of orthogonal cutting presented in this paper combines a thermomechanical analysis of the material flow within the primary shear zone and a modelling of friction at the tool-chip interface. We have used a Coulomb law in which the friction coefficient is a decreasing function of the temperature. Other parameters could influence the friction characteristics. However due to the extreme temperature variations at the tool-chip interface observed in machining we consider that \bar{T}_{int} has a primary role.

Experimental trends such as the decay of the mean friction coefficient $\bar{\mu}$ in terms of the cutting velocity V , the feeding t_1 and the growth of $\bar{\mu}$ in terms of the rake angle α are reproduced by the present analysis. The last feature can not be captured by the Oxley model.

Some improvements could be made, for instance by including the effect of the secondary shear zone and the effect of the pressure distribution along the primary shear zone.

REFERENCES

- Abramowitz, M. and Stegun, I. A. (1964) *Handbook of Mathematical Functions*. National Bureau of Standards.
- Bailey, J. A. (1975) Friction in metal machining—Mechanical aspects. *Wear* **31**, 243–275.

- Boothroyd, G. (1963) Temperatures in orthogonal metal cutting. *Proc. Inst. Mech. Eng.* **177**, 789–802.
- Buryta, D., Sowerby, R. and Yellowley, I. (1994) Stress distributions on the rake face during orthogonal machining. *Int. J. Mach. Tools Manufact.* **34**, 721–739.
- Campbell, J. D. and Fergusson, W. G. (1970) The temperature and strain-rate dependence of the shear strength of mild steel. *Phil. Mag.* **21**, 63–81.
- Clifton, R. J., Duffy, J., Hartley, K. A. and Shawki, T. G. (1984) On critical conditions for shear band formation in high-strain rates. *Scripta Mater.* **18**, 443.
- Dudzinski, D. and Molinari, A. (1997) A modelling of cutting for viscoplastic materials. *Int. J. Mech. Sci.* **39**(4), 369–389.
- Earles, S. W. E. and Powell, D. G. (1966–1967) Variations in friction and wear between unlubricated steel surfaces. *Proc. IME* **181**, Part 30, 171–179.
- Findley, W. N. and Reed, R. M. (1963) The influence of extreme speeds and rake angles in metal cutting. *J. Eng. Ind.* **49**–67.
- Follansbee, P. S. and Kocks, U. F. (1988) A constitutive description of the deformation of copper based on the use of the mechanical threshold stress as an internal state variable. *Acta metall.* **36**(1), 81–93.
- Gad, G. S., Armarego, E. J. A. and Smith, A. J. R. (1992) Tool-chip contact length in orthogonal machining and its importance in tool temperature predictions. *Int. J. Prod. Res.* **30**(3), 485–501.
- Groover, M. P. and Kane, G. E. (1971) A continuing study in the determination of temperatures in metal cutting using remote thermocouples. *J. Eng. Ind.* 603–908.
- Kadhim, M. J. and Earles, S. W. E. (1966–1967) Unlubricated sliding at high speeds between copper and steel surfaces. *Proc. IME* **181**, Part 30, 157–162.
- Kato, S., Yamaguchi, K. and Yamada, M. (1972) Stress distribution at the interface between tool and chip in machining. *J. Eng. Ind.* **94**, 683–688.
- Klepaczko, J. R. (1994) An experimental technique for shear testing at high and very high strain rates. The case of a mild steel. *Int. J. Impact. Engng.* **15**(1), 25–39.
- Lim, S. C., Ashby, M. F. and Brunton, J. H. (1989) The effects of sliding conditions on the dry friction of metals. *Acta Metall.* **37**, 767–772.
- Marusich, T. and Ortiz, M. (1995) Modelling and simulation of high speed machining. *Int. J. Numer. Meth. Engng.* **38**, 3675–3694.
- Merchant, M. E. (1945) Mechanics of the metal cutting process, I. Orthogonal cutting. *J. Appl. Phys.* **16**, 267–275; II. Plasticity conditions in orthogonal cutting. *J. Appl. Phys.* **16**, 318–324.
- Molinari, A. and Dudzinski, D. (1992) Stationary shear band in high-speed machining. *C. R. Acad. Sci. Paris.* **315**(II), 399–405.
- Montgomery, R. S. (1976) Friction and wear at high sliding speeds. *Wear* **36**, 275–298.
- Oxley, P. L. B. (1989) *Mechanics of Machining*. Ellis Horwood, Chichester, U.K.
- Rapier, A. C. (1954) A theoretical investigation of the temperature distribution in the metal cutting process. *Brit. J. Appl. Phys.* **5**, 400–405.
- Recht, R. F. (1984) A dynamic analysis of high speed machining. In: *High Speed Machining*, ed. R. Komanduri *et al.* pp. 83–93. ASME, New York.
- Schulz, H. (1989) *Hoch-geschwindigkeits-fräsen, Metallischer und Nicht Metallischer Werkstoffe*. C. Hanser, 17–27.
- Sekhon, G. S. and Chenot, J. L. (1993) Numerical simulation of continuous chip formation during non steady-state orthogonal cutting. *Engng. Comput.* **10**, 31–48.
- Shaw, M. C. (1984) *Metal Cutting Principles*. Oxford Science Publications, Oxford.
- Strenkowski, J. S. and Carroll, J. T. (1985) A finite element method of orthogonal cutting. *J. Engng. Ind.* **107**, 349–354.
- Strenkowski, J. S. and Moon, K. J. (1990) Finite element prediction of chip geometry and workpiece temperature distributions in orthogonal metal cutting. *J. Engng. Ind.* **112**, 313–318.
- Taylor, F. W. (1907) On the art of cutting metals. *Trans. ASME* **28**, 31.
- Tong, W., Clifton, R. J. and Huang, S. (1992) Pressure-shear impact investigation of strain

- rate history effects in oxygen-free high-conductivity copper. *J. Mech. Phys. Solids* **40**, 1251–1294.
- Trent, E. M. (1977) *Metal cutting*. Butterworths, London.
- Usui, E., Hirota, A. and Masuko, M. (1978) Analytical prediction of three dimensional cutting process part I. Basic cutting model an energy approach. *J. Eng. Ind.* **100**, 222–228.
- Usui, E. and Takeyama, H. (1960) A photoelastic analysis of machining stresses. *J. Eng. Ind.* **82**, 303–308.
- Williams, K. and Griffen, E. (1964) Friction between unlubricated steel surfaces at sliding speeds up to 750 feet per second. *Proc. IME* **178**, Part 3N, 24–36.
- Wright, P. K., McCormick, S. P. and Miller, T. R. (1980) Effect of rake face design on cutting tool temperature distributions. *J. Eng. Ind.* **102**, 123–128.
- Wright, P. K. and Trent, E. M. (1973) Metallographic methods of determining temperature gradients in cutting tools. *J. Iron Steel Inst.* **211**, 364–368.
- Zorev, N. N. (1963) Interrelationship between shear processes occurring along tool face and on shear plane in metal cutting. *International Research in Production Engineering*. ASME, New York, 42–49.
- Zvorykin, K. A. (1893) Proceedings of the Kharko technological Institute, Ukraine.

APPENDIX A : FORCES AND CONTACT LENGTH CALCULATIONS

We consider the chip after the outflow of the primary shear band, see Fig. 1. The rate of change of the total momentum of the chip is equal to zero in a stationary process. Then, the equilibrium of the forces applied to the chip, reduces to :

$$R = R' \quad (\text{A.1})$$

where R is the force exerted by the tool on the chip and R' is the force exerted by the workpiece on the chip along the line OA (the outflow of the primary shear band), see Fig. 19.

The forces R and R' are conveniently resolved into three sets of components as indicated in Fig. 19 :

- (1) in the horizontal and vertical direction F_p and F_Q
- (2) along and perpendicular to the shear zone F_s and N_s
- (3) along the perpendicular to the tool face F_c and N_c .

The shear stress distribution on the shear plane OA is supposed uniform. Then the component F_s at the outflow of the layer is proportional to the shear stress τ_1 (τ_1 is given by the relation (19.7), t_1 is the depth of cut and w the width of cut) :

$$F_s = w OA \tau_1 = \frac{wt_1}{\sin\phi} \tau_1 \quad (\text{A.2})$$

The other forces are easily obtained from F_s , as it is evident in Fig. 19 :

$$N_s = F_s \tan(\phi + \lambda - \alpha) \quad (\text{A.3})$$

$$F_p = F_s \cos\phi + N_s \sin\phi = F_s \frac{\cos(\lambda - \alpha)}{\cos(\phi + \lambda - \alpha)} \quad (\text{A.4})$$

$$F_Q = -F_s \sin\phi + N_s \cos\phi = F_s \frac{\sin(\lambda - \alpha)}{\cos(\phi + \lambda - \alpha)} \quad (\text{A.5})$$

$$F_c = R' \sin\lambda = F_s \frac{\sin\lambda}{\cos(\phi + \lambda - \alpha)} \quad (\text{A.6})$$

$$N_C = R' \cos \lambda = F_s \frac{\cos \lambda}{\cos(\phi + \lambda - \alpha)} \quad (\text{A.7})$$

The force N_C can also be calculated as the following :

$$N_C = \int_0^{l_c} P_0 \left(1 - \frac{X}{l_c}\right)^\xi w dX = P_0 \frac{wl_c}{\xi + 1} \quad (\text{A.8})$$

P_0 is obtained with :

$$P_0 = F_s \frac{\cos \lambda}{\cos(\phi + \lambda - \alpha)} \frac{\xi + 1}{wl_c} \quad (\text{A.9})$$

To calculate the contact length l_c , an assumption has to be made on the distribution of normal stresses at the outflow of the primary shear band. This distribution is assumed to be uniform in the present analysis. Considering the momentum equilibrium of the chip at the tool-tip (point O in Fig. 19), we obtain $M_{OA} = M_{OB}$, with :

$$M_{OB} = \int_0^{l_c} X P_0 \left(1 - \frac{X}{l_c}\right)^\xi w dX = P_0 \frac{wl_c^2}{(\xi + 1)(\xi + 2)} = F_s \frac{\cos \lambda}{\cos(\phi + \lambda - \alpha)} \frac{l_c}{(\xi + 2)} \quad (\text{A.10})$$

$$M_{OA} = N_s \frac{OA}{2} = F_s \frac{t_1}{2 \sin \phi} \tan(\phi + \lambda - \alpha) \quad (\text{A.11})$$

The tool-chip length l_c is then determined :

$$l_c = t_1 \frac{\xi + 2}{2} \frac{\sin(\phi + \lambda - \alpha)}{\sin \phi \cos \lambda} \quad (\text{A.12})$$

The mean friction coefficient $\bar{\mu}$ and the associated friction angle λ at the tool-chip interface are defined by :

$$\bar{\mu} = \tan \lambda = \frac{F_c}{N_c} = \frac{F_p \tan \alpha + F_Q}{F_p - F_Q \tan \alpha} \quad (\text{A.13})$$

APPENDIX B: SOLUTION OF THE THERMAL PROBLEM AT THE TOOL-CHIP INTERFACE

The thermal problem at the tool chip interface is solved with use of the Laplace transform technique with lines similar to what was done by Wright *et al.* (1980), although the problem is set differently. We consider the Laplace transform $T^*(S, Y)$ of the temperature with respect to the variable X :

$$T^*(S, Y) = \int_0^\infty T(X, Y) \exp(-SX) dX$$

Expressions (12) and (13) are transformed into :

$$a \frac{d^2 T^*(S, Y)}{dY^2} = V_c (ST^*(S, Y) - T_1) \quad (\text{B.1})$$

$$T^*(S, \infty) = \frac{T_1}{S} \quad (\text{B.2})$$

$$-k \frac{dT^*(S, Y)}{dY} \Big|_{Y=0} = f(S) \quad (\text{B.3})$$

With :

$$f(S) = \int_0^{l_c} Q(X) \exp(-SX) dX$$

$$Q(X) = 0 \quad \text{for } X \geq l_c$$

where $f(S)$ is the Laplace transform of the surfacic heat source $Q(X)$ due to friction. The solution of (B.1) is :

$$T^*(S, Y) = C_1 \exp\left(Y \sqrt{\frac{SV_c}{a}}\right) + C_2 \exp\left(-Y \sqrt{\frac{SV_c}{a}}\right) + \frac{T_1}{S} \quad (\text{B.4})$$

with C_1 and C_2 determined by the boundary conditions (B.2) and (B.3) :

$$C_1 = 0$$

$$C_2 = \frac{f(S)}{k} \sqrt{\frac{a}{SV_c}} \quad (\text{B.5})$$

Finally (B.4) has the form :

$$T^*(S, Y) = \frac{f(S)}{k} \sqrt{\frac{a}{SV_c}} \exp\left(-Y \sqrt{\frac{SV_c}{a}}\right) + \frac{T_1}{S} \quad (\text{B.6})$$

The temperature distribution in the chip is calculated with use of the inverse Laplace transform, Abramowitz and Stegun (1964) :

$$T(X, Y) = \frac{\bar{\mu} V_c P_0}{k} \sqrt{\frac{a}{\pi V_c}} \int_0^X \left(1 - \frac{X-u}{l_c}\right)^\xi \frac{1}{\sqrt{u}} \exp\left(-\frac{V_c Y^2}{4au}\right) du + T_1 \quad (\text{B.7})$$

Considering that $a = k/\rho c$, by developing the expression

$$\left(1 - \frac{X-u}{l_c}\right)^\xi$$

we obtain the interface temperature $T(X, Y = 0)$:

$$T(X, Y = 0) = \frac{\bar{\mu} P_0 \sqrt{V_c}}{\sqrt{\pi k \rho c}} \left(\frac{1}{l_c^\xi} \sum_{i=0}^{\xi} \frac{2}{2i+1} C_\xi^i (l_c - X)^{\xi-i} X^{\frac{2i+1}{2}} \right) + T_1 \quad (\text{B.8})$$

with

$$C_\xi^i = \frac{\xi!}{(\xi-i)!i!}$$

The mean temperature is given by :

$$\bar{T}_{\text{int}} = \frac{1}{l_c} \int_0^{l_c} T(X, Y = 0) dX \quad (\text{B.9})$$

By developing the expression $(l_c - X)^{\xi-i}$ we obtain

$$\bar{T}_{\text{int}} = \frac{\bar{\mu} P_0}{\sqrt{\pi k \rho c}} \sqrt{V_c l_c} \sum_{i=0}^{\xi} \frac{2}{2i+1} C_\xi^i \left(\sum_{j=0}^{\xi-i} (-1)^j C_{\xi-i}^j \frac{2}{2(i+j)+3} \right) + T_1 \quad (\text{B.10})$$



Pergamon

J. Mech. Phys. Solids, Vol. 46, No. 10, pp. 2139–2153, 1998

© 1998 Elsevier Science Ltd. All rights reserved

Printed in Great Britain

0022-5096/98 \$—see front matter

PII: S0022-5096(98)00025-8

REMARKS ON IMPACT SHEARING

J. R. KLEPACZKO

Laboratory of Physics and Mechanics of Materials, ISGMP, Metz University, Ile du Saulcy, F-57045
Metz Cedex, France

(Received 20 December 1997; accepted 29 January 1998)

ABSTRACT

A review is presented on recent progress in shear testing of materials at high and very high strain rates. Some experimental techniques are discussed which allow for materials testing in shear up to 10^6 l/s. More detailed informations are provided on experimental techniques based on the Modified Double Shear specimen loaded by direct impact. This technique has been applied so far to test a variety of materials, including construction, armor and inoxidable steels, and also aluminum alloys. The double shear configuration has also been applied to test sheet metals, mostly used in the automotive industry, in a wide range of strain rates. Details of both techniques, including measuring systems and elastic wave propagation in tubes, are discussed. In addition, a new experimental configuration which can be applied for experimental studies of adiabatic shear propagation and high speed machining is discussed.

The role of adiabatic heating at different rates of shearing is also discussed, including transition from pure isothermal to pure adiabatic deformation. It appears that the initial impact velocity is an important parameter in development of plastic localization.

Finally, a new development is discussed in determination of the Critical Impact Velocity in shear. A comparison is shown between recent experimental findings and a simple analytic estimation. The CIV in shear is a certain mode of adiabatic failure which occurs at relatively high shear velocities of adjacent material layers. Numerical simulations support the existence of the CIV in shear which can be recognized to some extent as a material constant. © 1998 Elsevier Science Ltd. All rights reserved.

Keywords: A. dynamics, B. metallic materials, B. stress waves, B. viscoplastic material, C. impact testing.

1. INTRODUCTION. GENERAL REMARKS ON FAST SHEARING

Shear is the fundamental mode of plastic deformation in materials. Testing of materials in shear over a wide range of strain rate and temperature can provide a fundamental knowledge in the development and improvement of constitutive relations used nowadays in large numerical codes. Advances in experimental techniques made it possible to determine plastic properties of materials in a wide range of strain rates, from 10^{-4} l/s to 10^6 l/s, that is nine decimal orders. However, when the nominal strain rate, that is the mean strain rate over the gauge length, is high enough, or time of plastic deformation is relatively short (order of hundred of ms and less), adiabatic instability and strain localisation can occur and dominate the process of plastic deformation. At still higher strain rates in shear (impact velocities ~ 100 m/s and higher) plastic waves in a deforming material can completely change the mechanics of deformation. In addition, at strain rates typically higher than $\sim 10^3$ l/s and above the so called threshold stress, the rate sensitivity of metals substantially increases. This

phenomenon can be approximated by the pseudo-viscosity approach, for example Campbell and Fergusson (1970); Klepaczko (1988).

On the other hand, it is well known that experiments with strain rates higher than 10^3 l/s constitute a formidable task concerning technical difficulties, and only a limited number of reliable experimental techniques provide reliable results. Each setup configuration, that is specimen geometry and type of loading, offers some advantages and deficiencies in comparison to another one. Sometimes the roles may be completely inverted. It is then very important to test the same materials at high strain rates with different experimental techniques and compare the results.

Most studies of both constitutive modeling and adiabatic instabilities in shear, are based so far on results from the Split Hopkinson Torsion Bar technique (torsional Kolsky apparatus), (Duffy *et al.*, 1971, Lewis and Campbell, 1972). This experimental technique is quite reliable within a narrow range of strain rates, typically from 3×10^2 l/s to 2×10^3 l/s. A thin-walled tubular specimen of a short length, 2–5 mm, and wall thickness 0.5–1.0 mm, is loaded by the incident shear wave. The incident, reflected and transmitted torsional waves are analysed in a similar way as in the Split Hopkinson Pressure Bar (Kolsky, 1949, Lindholm, 1964, Klepaczko, 1971). The SHTB technique has been modified later to perform incremental/decremental strain rate tests (jump tests) (Frantz and Duffy, 1972). The thin-walled tubular specimens were used much earlier to test materials at different strain rates with specially designed torsion machines and also at impact shearing, typically up to 10^2 l/s, for example Klepaczko, 1965, 1967, 1969. The SHPB technique (original Kolsky apparatus) can also be used in shear by loading of specimens with special geometries. One such technique is the so called "hat" specimen, for example Hartman *et al.*, 1981, Beatty *et al.*, 1992. Because of a non-uniform deformation of the radial field within the shear zone in the "hat" specimen, determination of the shear stress vs shear strain is very difficult and needs an application of an FE technique. This technique is relatively well suited for a study of controlled initiation of Adiabatic Shear Bands (Beatty *et al.*, 1992).

A unique experimental technique is the pressure-shear plate configuration introduced by Clifton *et al.* for example Clifton and Klopp (1985). This technique represents an attractive configuration for studying dynamic plastic flow at shear strain rates from 10^5 l/s to 10^6 l/s. In this experiment, the strain rate of the order 10^5 l/s is achieved by sandwiching a very thin specimen between two hard elastic plates. The specimen is attached to the flyer and launched with the velocity of a few hundred m/s. The flyer impacts the stationary anvil in a vacuum at a small angle. Because of the inclined impact, the specimen is deformed in shear with a relatively high component of pressure. The elastic wave profiles, shear and normal components, which are transmitted by the specimen and the anvil plate, are recorded on the free external surface of the anvil. The wave analysis permits to find shear stress vs shear strain characteristics at strain rates in excess of 10^5 l/s. The characterisation of materials in shear at strain rates below 10^5 l/s must be complemented by a different experimental technique, for example SHTB. These two techniques are quite different, including the way of loading and specimen geometries.

Because of the effects of wave propagation in a specimen, every change of the specimen geometry and experimental technique introduces changes in the specimen response to fast or impact loading. The best solution is to use one specimen geometry

for the widest possible spectrum of strain rates, for example from 10^{-4} l/s– 10^5 l/s or even 10^6 l/s.

An effective specimen geometry which can be used in studies of dynamic plasticity at low, medium and high strain rates is the double-notch specimen. Such a specimen was first proposed by Fergusson *et al.* (1967), to study dynamic plasticity of single crystals. Later, the Double Shear specimen was applied, with the loading scheme consisting of the incident Hopkinson bar and transmitter Hopkinson tube by Campbell and Fergusson (1970), to study temperature and strain rate dependence of the yield stress of a mild steel. A very small gage length of 0.84 mm was used in the study mentioned above. Because of a small gage length of the original DS specimen, application of the conventional mass velocities occurring in the incident bar, from ~ 1.2 m/s to ~ 11 m/s in the work of Campbell and Fergusson, provided the nominal strain rates in shear up to $\sim 10^4$ l/s. Determination of higher shear strains from the DS specimen geometry, more than a few percent, by use of the method of the net displacement between the Hopkinson bar and Hopkinson tube (Campbell and Fergusson, 1970), leads to large errors due to a non-uniform shear and severe plastic deformation of the specimen supports. Some improvements, mainly to the DS specimen geometry, but with the gage length 0.8 mm, have been introduced later by Harding and Huddart (1979).

In order to study dynamic plasticity and adiabatic instabilities within a wide range of strain rates and at large strains, the concept of the double shear test has been completely modified to load specimens of the same geometry at very different velocities, from quasi-static to impact. This test technique is briefly discussed in the next part of this paper.

2. DIRECT-LOAD MODIFIED SHEAR TEST

This relatively new experimental technique was briefly described by Klepaczko (1991) and a more complete outline was given later (Klepaczko, 1994). It combines some advantages in comparison to the original DS technique developed by Fergusson *et al.* The fundamental change in comparison to the bar-tube configuration has been introduced by elimination of the incident bar and application of the direct impact by a projectile. Within the quasi-static region of strain rates, from 10^{-4} l/s up to ~ 500 l/s, a special rig was constructed to load specimens by a fast servo-hydraulic machine. On the other hand, the specimen geometry has been substantially modified, the shearing zones have been enlarged to 2.0 mm and the external parts enforced, to eliminate plastification of the support regions, the Modified Double Shear geometry is given elsewhere (Klepaczko, 1994). Because of the direct impact the risetime of the incident wave has been reduced to ~ 2 μ s in comparison to ~ 30 μ s in the bar-tube configuration. This experimental technique is shown schematically in Fig. 1. The flat-ended projectiles of different lengths made of maraging steel and of diameter $d_p = 10$ mm are launched from an air gun with desired velocity V_0 ; $1.0 < V_0 < 200$ m/s. Impact velocity is measured by three optic chains: source of light, photodiode and input/output optic fibers. Electric signals from the photodiodes are recorded by two time counters. The setup with three light axes makes it possible to determine

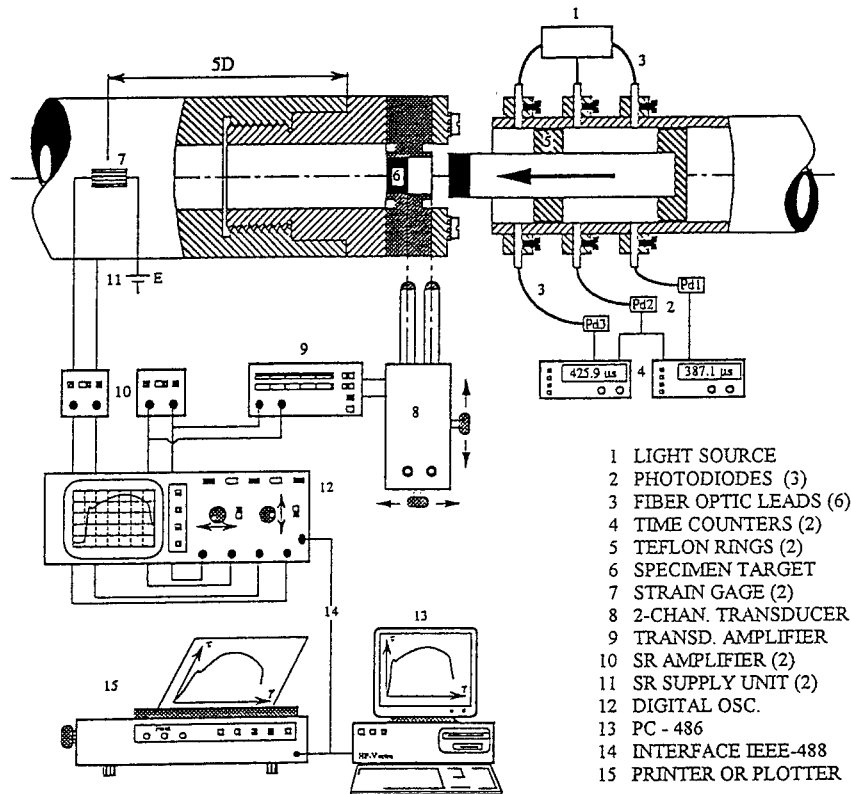


Fig. 1. Configuration of experimental setup for impact shearing of the MDS specimen (Klepaczko, 1991, 1994).

acceleration/deceleration of a projectile just before impact, so the exact value of V_0 at the impact face of the MDS specimen can be found. Axial displacement $\delta_A(t)$ of the central part of the specimen is measured as a function of time by an optical transducer, acting as a non-contact displacement gage. Since the double channel transducer is used, the second channel controls displacement $\delta_F(t)$ of the impact face of the MDS specimen. Measurements of V_0 and $\delta_F(t)$ make it possible to determine the coefficient of restitution for each test. A black and white target is cemented on the side of the MDS specimen (No. 6 in Fig. 1) and at the same time the impact end of the projectile is black; in this way the non-contact displacement transducer also reacts to the movement of the impact face. The axial force transmitted by the specimen symmetric supports into the Hopkinson tube can be determined as a function of time, $F(t)$, from the transmitted longitudinal elastic wave $\varepsilon_t(t)$. The transmitted wave $\varepsilon_t(t)$ is measured by strain gages 7, DC supply units 11 and amplifier 10. All electric signals, that is voltages of displacements $\delta_A(t)$ and $\delta_F(t)$ and transmitted wave $\varepsilon_t(t)$ are recorded by the digital oscilloscope 12 and stored later in the PC hard disk for further analyses. After an analysis of recorded signals and elimination of time, a force-net

displacement curve $F(\delta)$ can be constructed for each test and $\tau(\Gamma)$ and also $\dot{\Gamma}(\Gamma)$ characteristics determined, where τ is the shear stress, Γ strain, and $\dot{\Gamma} = d\Gamma/dt$ is the strain rate. The complete theory of the test is given elsewhere (Klepaczko 1994).

The experimental technique based on the direct impact on the MDS specimen has appeared to be quite effective and flexible in materials testing in shear at high strain rates, $10^3 \text{ l/s} < \dot{\Gamma} < 10^5 \text{ l/s}$. In addition, the special rig permits loading of the MDS specimen at low and medium strain rates, $10^{-4} \text{ l/s} < \dot{\Gamma} < 5 \times 10^2 \text{ l/s}$. A fast, closed-loop hydraulic testing machine is used together with this device (Klepaczko, 1991). Thus, the experimental technique based on the MDS specimen assures a wide spectrum of the nominal strain rates, typically from 10^{-4} l/s – 10^5 l/s .

Several alloys, mostly varieties of steel, were tested by this method; almost all of them show a very high rate sensitivity above 10^3 l/s . One typical example is given in Fig. 2 (Klepaczko and Rezaig, 1994), where the maximum shear stress (Fig. 2(a)) and shear deformation at the final adiabatic localisation (Fig. 2(b)) is shown as a function of the logarithm of the shear strain rate in $\log [\text{l/s}]$ for a hot-rolled low alloy steel, 0.41% C, 5% Cr, 1.4% Mo. Above strain rate 10^3 l/s , a substantial increase of the maximum shear stress is observed. On the contrary, the adiabatic localisation strain increases initially, again up to $\sim 10^3 \text{ l/s}$ and next, in excess of $\sim 2 \times 10^4 \text{ l/s}$, decreases rapidly. This is called the Critical Impact Velocity (CIV) in shear, which is discussed in the next part of this paper.

3. MACHINING BY DIRECT IMPACT

The idea of the direct impact on the MDS specimen has also been applied for high-speed machining. A new experimental setup has been put into operation in LPMM Metz which permits a ballistic high-speed machining up to $\sim 100 \text{ m/s}$ as well as for the testing of the dynamics of adiabatic shearing (Sutter *et al.*, 1997, Faure, 1996). The main modification lies in application of the projectile of a large diameter, $d = 50 \text{ mm}$, guided without rotation in the air gun tube. The specimen to be cut is attached to the projectile and a pair of knives is fixed to the Hopkinson tube. The schematic picture of this arrangement is shown in Fig. 3. The specimen in the form of the parallelepiped, can be cut before testing with high precision to assure an exact chip thickness predetermined by the distance of two knives attached with sufficient precision to the Hopkinson tube. The length of cutting is predetermined by the length of the specimen, dimension L in Fig. 3. During the cutting process the mean force is transmitted by two knives into the Hopkinson tube in the form of the transmitted longitudinal elastic wave which is recorded by strain gages, signal conditioners, amplifiers and a digital oscilloscope. The whole scheme of the setup is shown in Fig. 4. The projectile mass can be adjusted according to the energy needed for an almost constant cutting speed and for the impact velocity. The typical range of cutting speeds is within the limits of 10 m/s – 100 m/s . The impact velocity is determined in the same way as in the double shear technique: three sources of light S, fiber optics, three photodiodes PH and three time counters CT1 and CT2 (Klepaczko, 1994). The oscillograms obtained in the form of the transmitted wave as a function of time $\varepsilon_i(t)$ permit the force-projectile displacement characteristic to occur, with the assumption that the

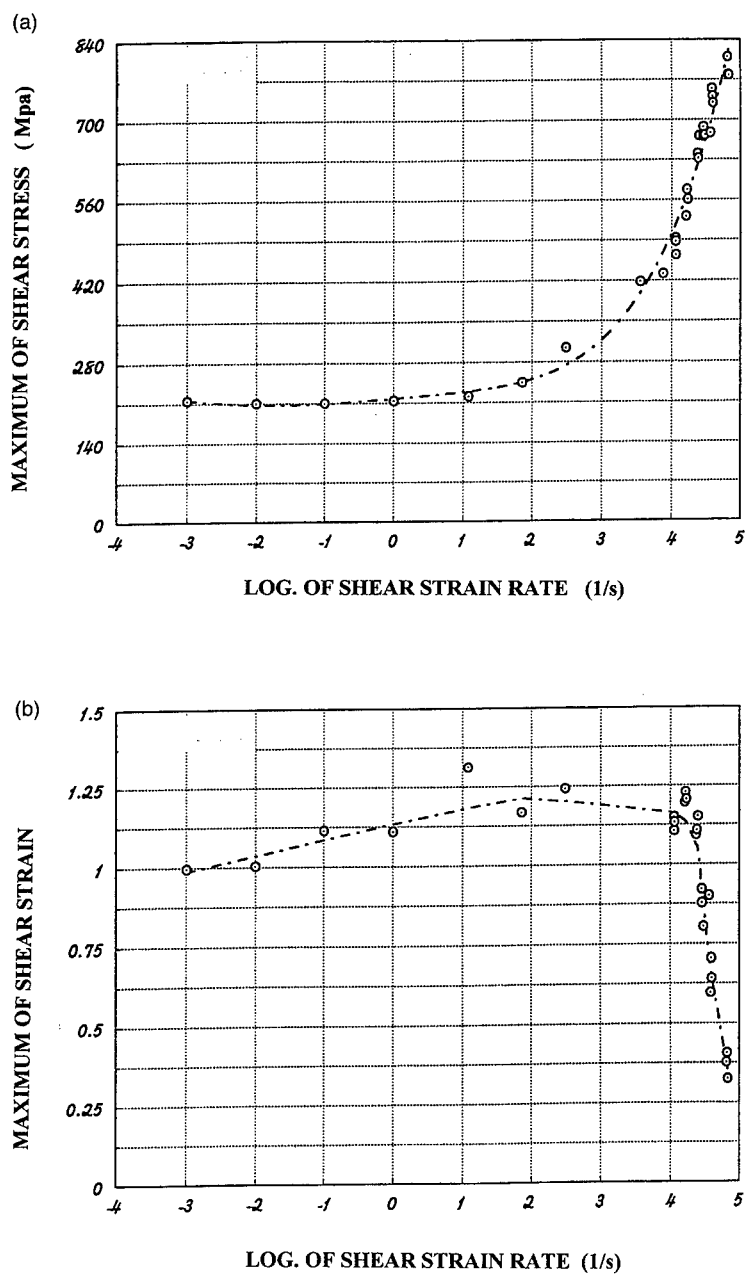


Fig. 2. Wide spectrum of shear strain rate for C-Cr-Mo hot-rolled steel; (a) Maximum shear stress vs log of shear strain rate (1/s); (b) Maximum shear strain of localisation vs log. of shear strain rate (1/s), (Klepaczko and Rezaig, 1995).

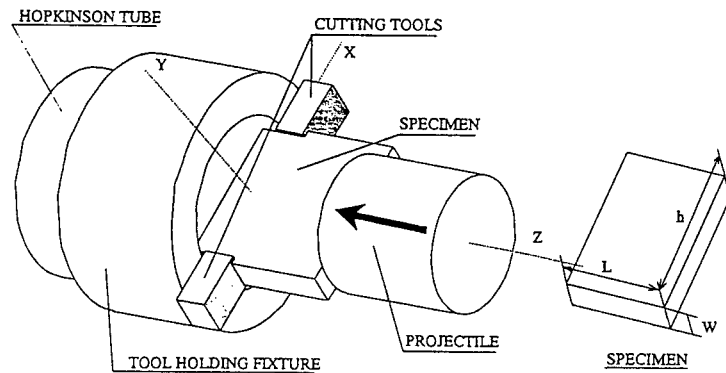


Fig. 3. Configuration of the specimen attachment to the projectile and tools fixed to the Hopkinson tube, projectile diameter 50 mm, (Sutter *et al.*, 1997).

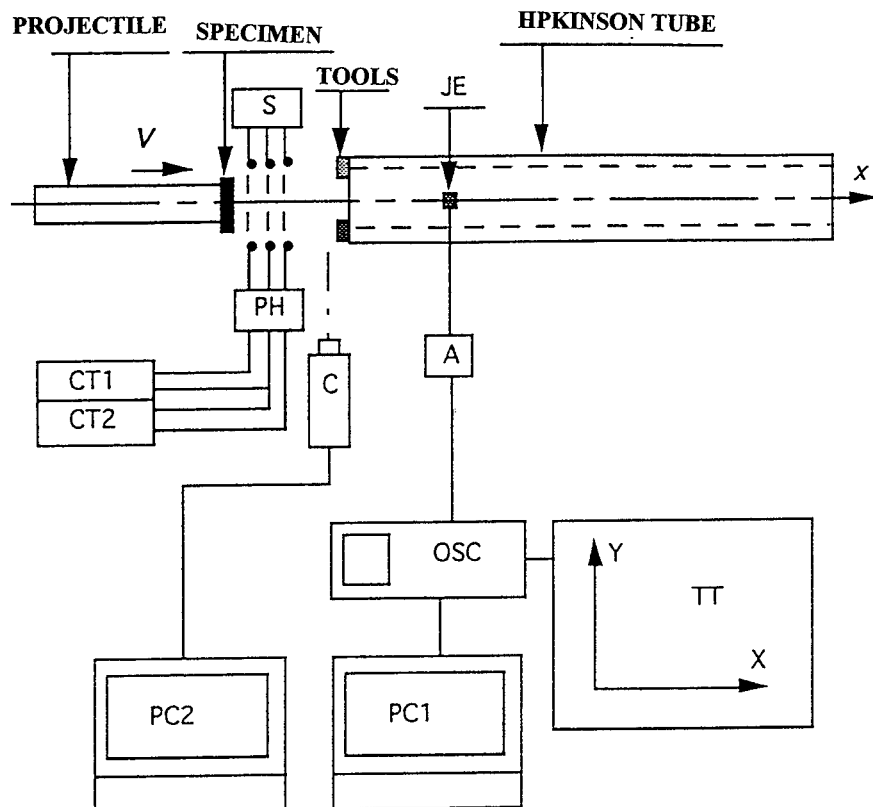
projectile deceleration is negligible. In general, the decrease of the velocity due to the cutting process was less than 4% (Sutter *et al.*, 1997). The theory of the test is practically the same as given by Klepaczko (1994).

Another recent application of the experimental setup shown in Fig. 4 was a study of the propagation of the adiabatic shear bands (Faure, 1996). The flat projectile made of a hard martensitic steel, and guided in the air gun tube, impacts a flat specimen attached to the Hopkinson tube. The scheme of loading is to some extent similar to that introduced by Kalthoff for Mode-II impact loading of cracks, for example Kalthoff (1990). The main difference is that in the LPMM setup, the force transmitted by the specimen supports can be determined from the transmitted elastic longitudinal wave measured in the Hopkinson tube. For instance, the mean crack velocity can be determined in this way. During crack propagation in Mode II, the force transmitted by the tube diminishes in proportion to the non-fracture ligaments in the specimens, and at the instant when the specimen breaks the force, it drops to zero. Because the initial length of the shear crack is known and the total time of the transmitted wave is measured, a mean crack speed can be determined, (Faure, 1996). It appears that in the case of a mild steel being tested, the mean crack speeds are not constant but increase with impact velocities.

In materials testing and machining at very different strain rates, additional effects like transition from isothermal to adiabatic deformation, adiabatic instability and localisation, and finally deformation wave trapping, complicate interpretation of the experimental results. Some of those features are addressed in the next part of this review.

4. ADIABATIC HEATING, INSTABILITY AND LOCALISATION

It is well known that during plastic deformation of materials, a large part of plastic work is converted into heat (Taylor and Quinney, 1934). When deformation is slow,



CT - TIME COUNTERS

PH - PHOTODIODES

S - LIGHT SOURCES

JE - STRAIN GAGES

A - AMPLIFIER

OSC - DIGITAL OSCILLOSCOPE

PC - COMPUTERS

TT - PLOTTER

C - SET OF 6 FAST CCD CAMERAS

Fig. 4. Configuration of experimental setup for impact machining, LPMM—Metz.

all heat generated is evacuated into surroundings by heat diffusion or by direct emission. However, when the process of deformation is short enough, there is no time for heat transfer and almost all plastic work is converted locally into volume heating. In a certain range of strain rates, the transition occurs between entirely isothermal and entirely adiabatic modes of plastic deformation. Some preliminary study on this subject was reported by Kaminski, 1976 and Litonski, 1985.

Because this transition depends, in the first place, on the geometry of the deformed body and also on the intensity of the heat extraction from the heated zones, a numerical analysis is very helpful in determining the region of strain rates and for

which specimen geometry the transition occurs. When the thickness of deformed layer is ~ 2.0 mm, like in the MDS specimen, the transition occurs at the following critical strain rates: copper ~ 85 l/s, aluminum ~ 68 l/s and a mild steel ~ 48 l/s (Oussouaddi and Klepaczko, 1991). The finite difference technique has been applied, and the calculations were carried out at $T_0 = 300$ K, the initial temperature. The results support quantitatively the physical intuition that the critical strain rate increases in proportion to the thermal conductivity, which is the lowest for steel and the highest for copper. Since those values are based on the maximum temperature gradients, a complete transition into the entirely adiabatic conditions occurs at strain rates at least 5 l/s higher than the mean value. Variations in the specimen geometry also change the transition region, (Oussouaddi and Klepaczko, 1991).

Thermal softening during adiabatic heating leads directly to instability and localization, for example early works (Litonski, 1977, Rogers, 1979, Zener and Hollomon, 1944). In the case of pure shear, the condition for stability is reduced to maximum shear stress $d\tau = 0$, where τ is the shear stress (Litonski, 1977, Rogers, 1979). This condition can be rewritten into the form of zero tangent modulus $d\tau/d\Gamma = 0$ and $\Gamma = \Gamma_c$, the instability strain. A schematic stress-strain curve showing different stages of deformation during fast (adiabatic) shearing is shown in Fig. 5.

All stages shown in Fig. 5 were identified by high-speed photography during deformation of a tubular specimen made of HY-100 steel loaded in SHTB (Marchand and Duffy, 1988). During the first stage of deformation, that is, in between the yield point (τ_y, Γ_y) and the instability point (τ_c, Γ_c) where $d\tau/d\Gamma = 0$, strain distribution over the gage length is homogeneous. During stage 2, shown in Fig. 5, the strain distribution becomes inhomogeneous, and localization begins. Finally, during stage 3, localization occurs by catastrophic shear, the flow stress drops rapidly and the Adiabatic Shear Band is well formed. However, during this stage the high-speed

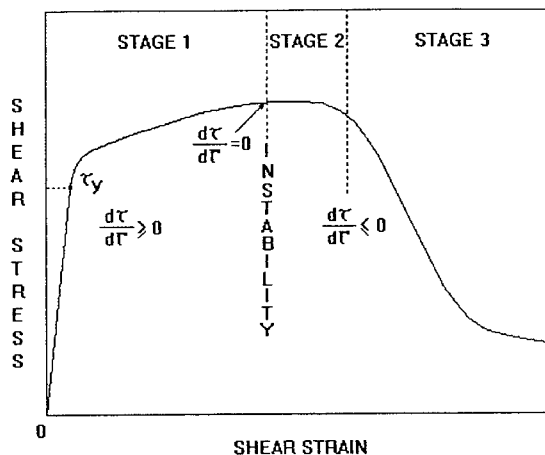


Fig. 5. Schematic stress-strain curve showing different stages of fast (adiabatic) shearing, τ_y is the yield stress and $d\tau/d\Gamma = 0$ is the instability point.

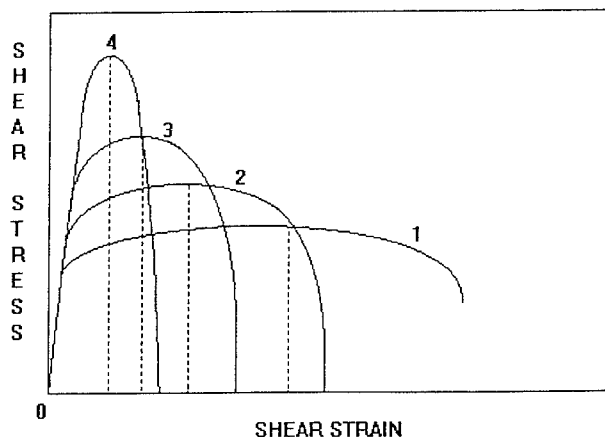


Fig. 6. Schematic evolution of stress-strain curves of industrial steels at strain rates higher than 5×10^2 l/s; (1) $\sim 5 \times 10^2$ l/s; (2) $\sim 5 \times 10^3$ l/s; (3) $\sim 1 \times 10^4$ l/s; (4) $\sim 5 \times 10^4$ l/s.

photography revealed some circumferential nonuniformities in formation of the ASB (Marchand and Duffy). The last part of stage 3 shows, which should be called stage 4, is typically observed for more ductile metals, a slowdown of the rate of the flow stress. Such behavior is caused by cooling of a very thin layer of material situated very close to the ASB (Litonski, 1985).

The instability point (τ_c , Γ_c) can be found for different constitutive relations, for example (Dormevail, 1987). A more general analysis of the condition $d\tau/d\Gamma = 0$ has been discussed by (Klepaczko, 1991, 1994b). Application of the condition for stability $d\tau/d\Gamma = 0$, and some form of equation for constitutive modeling, leads to the final result in the form $\Gamma_c(\dot{\Gamma}, T)$, when the adiabatic process of deformation is assumed together with a constant strain rate (Klepaczko, 1991). It has been found that an increase of flow stress when the strain rate is increased, has a negative effect on the onset of adiabatic instability, that is Γ_c is reduced when strain rate is increased (Klepaczko, 1994). The positive rate sensitivity increases production of plastic work converted into heat, this process accelerates formation of the instability, so the value of Γ_c is a diminishing function of the nominal strain rate. Several industrial steels tested so far in shear at strain rates from 10^{-3} – $\sim 10^5$ l/s with the MDS method (Klepaczko, 1991, 1994a), showed a substantial evolution of the stress-strain curve. Schematic changes of the $\tau(\Gamma)$ curves observed for many industrial steels at increasing rates are shown in Fig. 6.

In this schematic Figure, the mean proportions are conserved to show the effect of the very high rate sensitivity on the yield stress and instability stress above $\sim 10^3$ l/s. Contrary to the positive rate sensitivity of the critical stress τ_c , the critical strains of instability Γ_c always show a tendency to diminish when the strain rate is above $\sim 10^3$ l/s. The same happens with the fracture strains. At very high strain rates this feature is even more abrupt; this occurs because of a superposition of the ASB formation and plastic waves in shear.

5. CRITICAL IMPACT VELOCITY IN PLASTIC SHEARING

It has been shown recently (Klepaczko, 1994b, 1995), that during shear deformation imposed by a high-velocity, plastic waves excited in a deformed material can completely change the mechanics of plastic field. As a rule, an intense plastic deformation will appear near the impact end of a specimen. For the MDS specimen with the gage length 2.0 mm, the nominal strain rate when the plastic waves start to dominate is 5×10^4 1/s, that is, the velocity of shearing reaches value ~ 100 m/s.

Since formulation of the rate independent theory of elasto-plastic waves in solids by K arman, Taylor and Rakhmatulin, in the late forties and early fifties (for a review, see Cristescu, 1967), it is known that the longitudinal plastic deformation can be localised in thin bars by a high velocity impact (K arman and Duvez, 1950). This deformation trapping by longitudinal plastic waves is called the Critical Impact Velocity in tension (K arman and Duvez, 1950, Klepaczko, 1968). It has been shown recently that the Critical Impact Velocity in shear can be determined experimentally using the MDS specimen and the direct impact loading, (Klepaczko, 1994b, 1995). This is demonstrated in Fig. 2(b), where a systematic drop in the critical strain of shear localisation is observed for a low alloy steel around impact velocity 100 m/s. An existence of the CIV in shear was predicted by a numerical method by Wu and Freund (1984).

A more detailed analytic study was published elsewhere (Klepaczko, 1995); here, only a brief discussion is offered. It is clear that the CIV in shear is closely related with adiabatic heating and thermal softening. The CIV in shear is caused by an instantaneous instability and strain localisation superimposed on plastic wave propagation in shear. The rate-independent wave propagation theory has been applied to analyse CIV in shear and the final formula was derived by Klepaczko (1995).

Preliminary numerical estimation of the CIV values for 1018 steel (French Standard XC18) have confirmed the usefulness of the analytic procedure proposed by Klepaczko (1994b, 1995). The value of CIV obtained with a simplified constitutive relation was $V_{cr} = 98.0$ m/s and $\Gamma_C = 4.9 \times 10^4$ 1/s for 2.0 mm gage length, the value very close to the one determined by the MDS direct impact technique, $V_{cr} \cong 90$ m/s. The experimental technique based on the MDS specimen and direct impact has been applied so far for determination of the CIV for three steels. Besides XC18 mild steel, the CIV determined for VAR 4340 steel (52 HRC) was $\cong 130$ m/s and in the case of hot-rolled C-Cr-Mo steel $\cong 100$ m/s.

Of course, the process of adiabatic shearing and localisation superimposed on the propagation of plastic waves leads to shear fracture. It is interesting to note that the superposition of those two processes leads to a substantial decrease of the energy to fracture. Such behavior of the MDS specimen is demonstrated for C-Cr-Mo hot-rolled steel in Fig. 7. The total energy to fracture normalised by the specimen cross section is plotted vs logarithm of shear strain rate in 1/s. Up to values of the nominal strain rate $\sim 1.5 \times 10^4$ 1/s, the energy slightly increases up to 0.87 J/mm², but above this value a substantial drop is observed, up to 0.4 J/mm² at strain rate $\sim 7 \times 10^4$ 1/s ($V_{cr} = 134$ m/s).

The phenomenon of the CIV in shear has been studied by FE technique for VAR 4340 steel, ~ 50 HRC (Klosak and Klepaczko, 1997). An infinite layer with a small

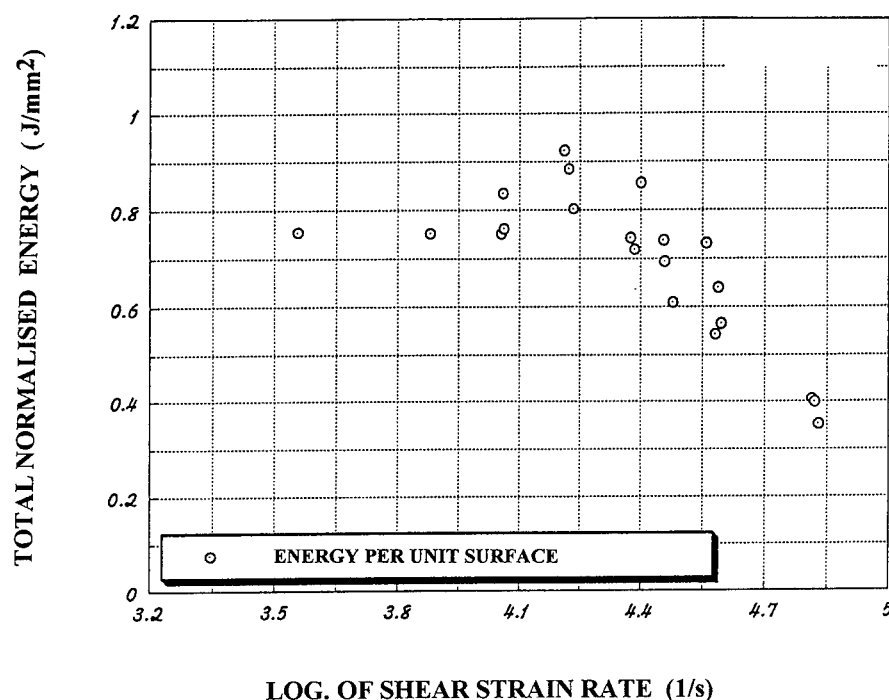


Fig. 7. Total fracture energy of the MDS specimen vs log of the nominal strain rate in shear (1/s); C-Cr-Mo hot-rolled steel (Klepaczko and Rezaig, 1995).

geometrical imperfection was analysed. Seventeen loading velocities of the MDS specimen were assumed, and for each velocity the instability shear strain ($d\tau = 0$) and the deep localisation strain have been found. The final results are shown in Fig. 8. Both characteristic strains are shown as a function of the different velocities, from quasi-static to impact, 160 m/s. Those detailed calculations entirely support experimental observations discussed in the preceding parts of this paper. In between impact velocities from 105 m/s to around 130 m/s, a CIV transition occurs. The analytic approximation of the CIV in shear for this steel yielded a value of 114 m/s. However, the numerical study clearly indicates that the CIV phenomenon is a process. The fracture energies for the VAR 4340 steel (the MDS geometry) have been estimated as a function of the impact velocity by integration of the force-displacement curves found by the FE technique. The final result is shown in Fig. 9. At lower impact velocities, the energy to the final localisation increases up to 681 MJ/m³; however, at impact velocities higher than 100 m/s, the energy drops considerably, to the value of ~ 8.0 MJ/m³. Thus, the energy drop is slightly less than a hundred times. The striking similarity can be instantly spotted between the experimental results of Fig. 7 and the numerical results shown in Fig. 9. It is clear that the CIV in shear can be understood as a new material constant. More precise experiments could be performed to determine this value for different materials.

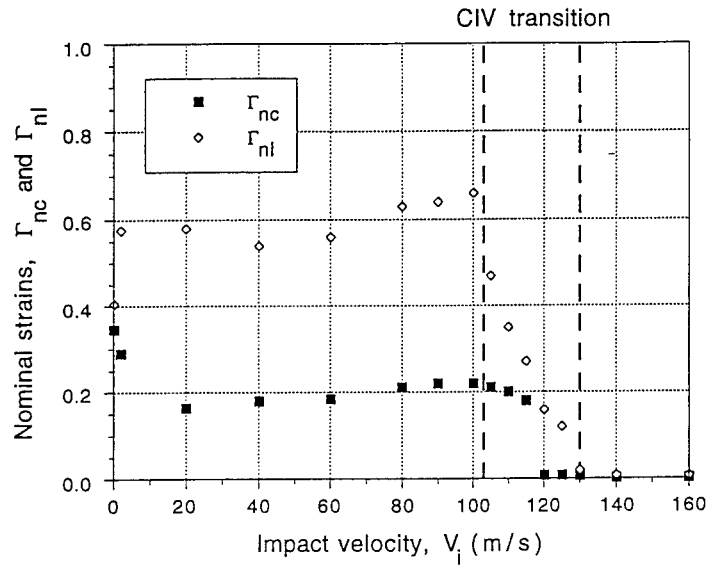


Fig. 8. Results of numerical calculations by FE method for VAR 4340 steel. Nominal shear strains of instability Γ_{nc} and localisation Γ_{nl} vs impact velocity; CIV indicates the Critical Impact Velocity transition, (Kłosak and Klepaczko, 1997).

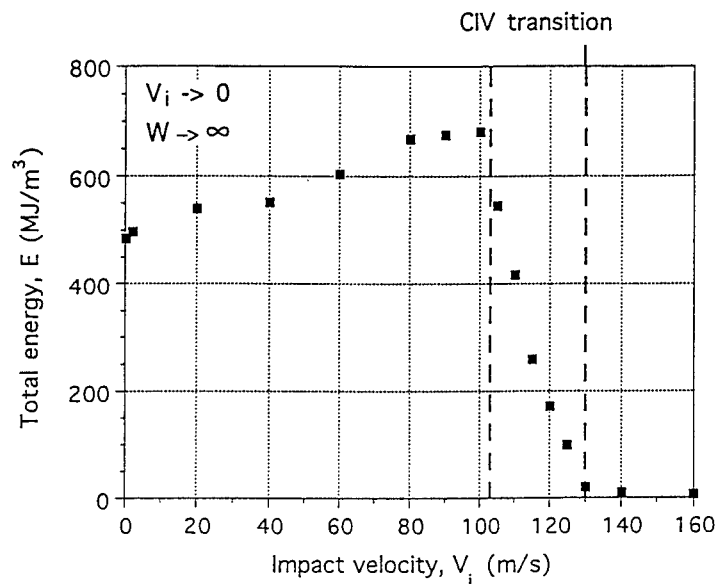


Fig. 9. Results of numerical calculations by FE method for VAR 4340 steel. Total energy to advanced localisation vs impact velocity; CIV indicates the Critical Impact Velocity transition (Klepaczko, 1996).

6. DISCUSSION AND CONCLUSIONS

It has been shown in this review that materials testing in shear within a wide range of strain rates, from quasi-static to impact and up to 10^5 1/s, is possible using the MDS specimen loaded at moderate rates or by a direct impact. Since the duration of experiments occurs at very different time spans, additional effects like transition from isothermal to adiabatic deformation, adiabatic instability and localisation, and finally CIV in shear, change the deformation process. In each range of strain rates, different processes may dominate. Indeed, the thermal coupling associated with heat production due to plastic deformation and heat conduction plays an important role in dynamic plasticity during shearing. Characteristic values of the CIV in shear can be proposed as a new material constant. The FE numerical technique has confirmed quantitatively and qualitatively existence of the CIV in shear. Analytic methods to estimate the value of the CIV in shear may be used as a first approximation. Of course, a value found will depend on the quality of the constitutive relations used.

ACKNOWLEDGEMENTS

This review was supported, and some results in the references cited here, in part by CNRS-DRET Program No. 972 "Impact on Materials", and also by the United States Army through its European Office, Contract DAJA M68171-95-C-9071.

REFERENCES

- Beatty, J. H., Meyer, L. W., Meyers, M. A. and Nemat-Nasser, S. (1992) Formation of controlled adiabatic shear bands in AISI 4340 high strength steel. *Shock Waves and High Strain Rate Phenomena in Metals*. Plenum Press, N. Y., U.S.A. p. 645.
- Campbell, J. D. and Fergusson, W. G. (1970) The temperature and strain-rate dependence of the shear strength of mild steel. *Phil. Mag.* **21**, 63.
- Clifton, R. J. and Klopp, R. W. (1985) Pressure-shear plate impact testing. *Metals Handbook* Vol. 8, AMS, Metals Park, p. 230.
- Cristescu, N. (1967) *Dynamic Plasticity*. North-Holland Publ. Co., Amsterdam.
- Dormeval, R. (1987) The adiabatic shear phenomenon. *Materials at High Strain Rates*, p. 47. Elsevier Appl. Sci., London.
- Duffy, J., Campbell, J. D. and Hawley, R. H. On the use of a torsional split Hopkinson bar to study rate effects in 1100-0 aluminum. *J. Appl. Mech.* **38**, 89.
- Faure, L. (1997) *Etude experimentale de la fissuration par impact et usinage rapide*, Ph. D. Thesis, ISGMP-LPMM, Metz University.
- Fergusson, W. G., Hauser, F. E. and Dorn, J. E. (1967) Dislocation damping in zinc single crystals. *Brit. J. Appl. Phys.* **18**, 114.
- Frantz, R. A. and Duffy, J. (1972) The dynamic stress-strain behavior in torsion of 1100-0 aluminum subjected to a sharp increase in strain rate. *J. Appl. Mech.* **39**, 939.
- Harding, J. and Huddart, J. (1979) The use of double-notch shear test in determining the mechanical properties of uranium at very high rates of strain. *Proc. Inst. Phys. Conf. Ser.* No. 47. p.49, The Institute of Physics.
- Hartman, K. H., Kuntze, H. D. and Meyer, L. W. (1991) High strain rate deformation of steel. *Shock Waves and High Strain Rate Phenomena in Metals*. p. 325. Plenum Press.

- Kalthoff, J. F. (1990) Experimental fracture mechanics. *Crack Dynamics in Metallic Materials*, p. 69, Springer Verlag, Wien—New York.
- Kaminski, M. (1976) Coupling of strain and temperature fields in the problem of torsion of a thin-walled tube. *Engng. Trans.* **24**, 185, (in Polish).
- Kármán, Th. and Duwez, P. (1950) The propagation of plastic deformation in solids. *J. of Appl. Phys.* **21**, 987.
- Klepaczko, J. R. (1965) Rate Sensitivity and Strain Rate history Effects in Technically Pure Aluminum, Ph. D. Thesis, Institute of Fund. Techn. Res., Polish Acad. Sci., Warsaw.
- Klepaczko, J. R. (1967) A new device for dynamic torsional tests. *Theoretical and Appl. Mech.* **5**, 198.
- Klepaczko, J. R. (1968) Generalized conditions for stability in tension tests. *Int. J. Mech. Sci.* **10**, 297.
- Klepaczko, J. R. (1969) The strain rate behavior of iron in pure shear. *Int. J. Solids and Struct.* **5**, 533.
- Klepaczko, J. R. (1991) Adiabatic shear bands, review of experimental techniques and results. *Anniversary Volume LMA, Mechanics, Numerical Modelling and Dynamics of Materials*, p. 335, CNRS Marseille.
- Klepaczko, J. R. (1994a) An experimental technique for shear testing at high and very high strain rates, the case of mild steel. *Int. J. Impact Engng.* **15**, 25.
- Klepaczko, J. R. (1994b) Plastic shearing at high and very high strain rates. *Proc. Conf. on Mech. and Phys. Behavior of Materials Under Dyn. Loadings*, p. C8-35. Les éditions de physique, Les Ulis.
- Klepaczko, J. R. (1995) On the critical impact velocity in plastic shearing. *EXPLOMET'95, Proc. Int. Conf. On Metallurgical and Materials Applications of Shock Waves and High Strain Rate Phenomena*, p. 413. Elsevier Science, Amsterdam.
- Klepaczko, J. R. and Rezaig, B. (1995) Shear testing of hot rolled C-Cr-Mo steel, LPMM, Metz University, (unpublished data).
- Klepaczko, J. R. (1996) *Stress Concentrators and Rate Effects in Formation of Adiabatic Shear Bands*. Final Technical Report, Contract No. N68171-95-9071, USA-ERO, LPMM, Metz University.
- Klosak, M. and Klepaczko, J. R. (1997) Numerical study of the inelastic wave propagation and plastic instabilities with thermal coupling. *Proc. XIII Polish Conf. on Computer Methods in Mechanics*, p. 615. Poznan Univ. of Technology, Poznan.
- Kolsky, H. (1949) An investigation of the mechanical properties of materials at very high rates of loading. *Proc. Phys. Soc., London* **62-B**, 676.
- Lewis, J. L. and Campbell, J. D. (1972) The development and use of a torsional Hopkinson bar apparatus. *Exp. Mech.* **12**, 520.
- Lindholm, (1964)
- Litonski, J. (1977) Plastic flow of a tube under adiabatic torsion. *Bull. de L'acad. Polonaise des Sciences, série des Sciences Techniques* **XXV**, 7.
- Litonski, J. (1985) Numerical Analysis of Plastic Torsion Process With Account of a Heat Generated During Deformation. IFTR Reports, No. 33, Warsaw, (in Polish).
- Marchand, A. and Duffy, J. (1988) An experimental study of the deformation process of adiabatic shear band formation in a structural steel. *J. Mech. Phys. Solids* **36**, 251.
- Oussouaddi, O. and Klepaczko, J. R. (1991) An analysis of transition between isothermal and adiabatic deformation for the case of torsion of a tube. *Proc. 3rd Int. Conf. on Mech. and Phys. Behaviour of Materials Under Dyn. Loading*, p. C3-237. Les éditions de physique, Les Ulis.
- Rogers, H. C. (1979) Adiabatic plastic deformation. *Ann. Rev. Mat. Sci.* **9**, 238.
- Sutter, G., Molinari, A., Faure, L. and Klepaczko, J. R. (1998) An experimental study of high-speed orthogonal cutting. *J. Engng. for Industry, Trans. ASME* **120**, 169.
- Taylor, G. I. and Quinney, H. (1934) The latent energy remaining in a metal after cold working. *Proc. Roy. Soc., London* **143A**, 307.
- Wu, F. H. and Freund, L. B. (1984) Deformation trapping due to thermoplastic instability in one dimensional wave propagation. *J. Mech. Phys. Solids* **32**, 119.
- Zener, C. and Hollomon, J. H. (1944) Effect of strain rate upon plastic flow of steel. *J. Appl. Phys.* **15**, 22.



Pergamon

J. Mech. Phys. Solids, Vol. 46, No. 10, pp. 2155–2170, 1998

© 1998 Elsevier Science Ltd. All rights reserved

Printed in Great Britain

0022-5096/98 \$—see front matter

PII: S0022-5096(98)00020-9

AN ANALYSIS OF THE DYNAMIC SHEAR FAILURE RESISTANCE OF STRUCTURAL METALS

K. MINNAAR AND M. ZHOU*

The George Woodruff School of Mechanical Engineering, Georgia Institute of Technology, Atlanta,
GA 30332-0405, U.S.A.

(Received 20 December 1997; accepted in revised form 23 January 1998)

ABSTRACT

The localization of shear deformation and the eventual rupture inside shear bands are analyzed experimentally. The shear failure resistance of several structural metals is compared. The materials studied are HY-80, HY-100, HSLA-80, 4340VAR, and Ti-6Al-4V. The evaluation of failure progression focuses on the evolution of both the stress-carrying capacities and material microstructures. Experiments show that despite its significantly stronger rate sensitivity, Ti-6Al-4V is more susceptible to shear localization and rupture compared with the steels, as demonstrated by its relatively early and precipitous loss of stress-carrying capacity. This observation is supported by measurements of the shear band and rupture lengths in specimens deformed to various stages of failure development. Among the steels, the martensitic microstructure of HY-100 seems to be responsible for its higher susceptibility to localization. While all the steels studied show very similar dynamic constitutive responses, their significantly different shear failure behaviors suggest that macroscopic thermal-mechanical descriptions alone are not sufficient to account for the shear failure in the form of combined localization of strain and the eventual rupture through the shear bands. Consequently, microstructural damage mechanisms should also be considered. © 1998 Elsevier Science Ltd. All rights reserved.

Keywords: A. strain localization, B. viscoplastic material, ductile failure, C. Kolsky bar.

1. INTRODUCTION

Shear band formation rather than crack initiation is the principal form of failure for many structural metals under certain dynamic loading conditions. In most applications, this form of failure should be avoided. It is necessary to evaluate the resistance of similar materials to dynamic shear failure in order to achieve maximum structural integrity through design, materials selection and development of more advanced materials. Identifying the factors that determine the susceptibility or resistance of materials to the initiation and propagation of localized shear deformation has clear practical significance. Just as *fracture toughness* is a measure of material resistance to cracking, there may also be a toughness measure for material resistance to dynamic shear banding. Although the influences of many individual material properties on shear banding, such as strain hardening and rate sensitivity, are understood, no well-developed criterion is available for the comparison of the relative susceptibilities to shear localization of different materials. The difficulty arises partly because different

* To whom correspondence should be addressed. Fax: 001 404-894 8336.

materials have different combinations of properties. The lack of a criterion for the comparison of the relative resistance to shear failure is an issue in the design of structures and the selection of materials.

The occurrence of shear bands at high strain rates is a thermomechanical process driven mainly by heat due to plastic dissipation. Analyses of this phenomenon have either followed mechanics approaches, which are based on descriptions of the thermomechanical response of materials, or materials approaches, which focus on the microscopic evolution associated with the shear band development. The mechanics analyses have yielded understandings on the conditions for the onset and development of shear bands. For example, Clifton (1980) analyzed the effects of heat conduction and strain rate on the growth of perturbations in deformation fields. Molinari and Clifton (1987) obtained the critical condition for shear localization in closed form for several idealized models of simple shearing deformation. A sample of related work includes Rogers (1979), Bai (1981, 1982), Rogers and Shastry (1981), Merzer (1982), Freund *et al.* (1985), Wright and Walter (1987), Grady and Kipp (1987), Needleman (1989), Shawki and Clifton (1989), Batra and Kim (1991, 1992), Grady (1992), Needleman and Tvergaard (1992), Nemat-Nasser (1992), Shawki (1992), Zhib and Aifantis (1992), Gioia and Ortiz (1996), Kalthoff (1987), Mason *et al.* (1994), and Zhou *et al.* (1994, 1996a,b, 1997). On the other hand, microscopic studies have revealed material deformation, damage and failure mechanisms associated with the localization process. For example, Cho *et al.* (1990, 1993) analyzed the local temperature profiles inside shear bands in several metals. They also found that rotation and alignment of martensitic laths accompany shear band development. The experiments of Andrade *et al.* (1994) suggested the occurrence of dynamic recrystallization in copper during shear localization. Other microscopic studies have been reported by e.g. Rogers and Shastry (1981), Giovanola (1988), Machand and Duffy (1988), Duffy *et al.* (1992), Bai *et al.* (1994), Ramesh (1994), Zurek (1994), Meyers *et al.* (1995), and Xu *et al.* (1996).

Grady (1994) derived a shear band toughness measure which is indicative of the amount of energy dissipated in propagating shear bands approximated by a one-dimensional model. This quantity is a function of parameters in a simplified material constitutive model and does not account for microscopic damage and ultimate rupture which leads to the eventual failure of materials inside shear bands. Experiments have indicated that the dynamic shear failure of metals is controlled by ductile damage mechanisms as well as their thermomechanical constitutive behavior. Beatty *et al.* (1991) showed that 4340 steels with the same hardness value but different carbon distributions absorb varying amounts of energy in a split Hopkinson bar experiment. They also identified the importance of grain size on the susceptibility of copper to shear banding, Andrade *et al.* (1994). Bai *et al.* (1994) pointed out that shear band formation in Ti-6Al-4V does not necessarily cause a loss of load-carrying capability. Instead, a loss is observed only after the occurrence of a sudden rupture due to the coalescence of microcracks. Clearly, in order to assess realistically this form of failure, experiments and models accounting for both macroscopic constitutive response and microscopic characterizations are needed.

The objective of this research is to identify, on macro- and microscopic scales, the factors that determine the resistance of materials to dynamic shear failure in the form of shear band formation and eventual rupture and provide an assessment of the

relative resistance to this form of failure. The focus is on both the evolution of the load-carrying capacity of these materials during shear band development and associated microscopic changes. The materials studied are structural metals HY-80, HY-100, HSLA-80, 4340VAR and Ti-6Al-4V. These are the materials for many structures and shear banding is the major mode of failure under certain dynamic loading conditions. For example, Hanchak *et al.* (1993) have demonstrated that shear band formation dominates the dynamic perforation of HY-100 steel. The experiments used in this analysis provide a range of loading rates and superimposed hydrostatic pressures. Deformations can be controlled to occur to various stages of shear localization and failure, allowing shear bands to be "frozen" at different levels of straining and analyzed using optical and electron microscopy. The experiments will also allow the evolution of the load-carrying capacity of the materials to be obtained and evaluated. Since a range of materials with different macroscopic properties and microstructures are analyzed under similar conditions, the results of this research can contribute to the quantification of the "shear band toughness" of materials.

2. MATERIALS

The four structural steels and one titanium alloy studied are listed in Table 1 along with their chemical compositions. HY-80 and HY-100 are carbon steels with different levels of yield strength resulting from their different carbon and magnesium contents. HSLA-80 is a low alloy substitute of HY-80 with a lower amount of carbon and an increased amount of magnesium. The 4340VAR steel is a low alloy steel. Ti-6Al-4V is a high temperature titanium alloy. The heat treatment conditions and the resulting static strength and hardness parameters are shown in Table 2.

The microstructures of the four steels are shown in Fig. 1(a)–(d). The microstructures of HY-80, HSLA-80 and 4340VAR steels consist of ferrite (light) and pearlite (dark). The size scales for the two constituents vary, with HSLA-80 having the finest phase morphology and 4340 having the coarsest phase morphology. HY-100 has a martensitic microstructure, in contrast to those of the other three steels. This microstructure gives HY-100 a higher static strength than the other steels. The Ti-6Al-4V alloy has a microstructure consisting of equiaxial α -phase (light) and β -phase (dark), as shown in Fig. 2. The α -phase has a volume fraction of approximately 80%. The static strength of the titanium alloy is the highest among the materials analyzed.

3. DYNAMIC SHEAR FAILURE EXPERIMENT

An experimental configuration involving a hat specimen geometry is used. The geometry of the specimen is illustrated in Fig. 3. The specimens are machined from one inch plates, with their axes parallel to the plate normal. This experiment is used to subject the materials to nominal shear deformations in the strain rate range of 10^2 – 10^4 s⁻¹. This configuration was first used by Beatty *et al.* (1991), Andrade *et al.* (1994), and Meyers *et al.* (1995) to analyze the shear deformation of a 4340 steel and copper.

Table 1. Chemical compositions of materials analyzed

	C	FE	H	MN	P	S	CU	SI	NI	CR	MO	V	TI	AI	CB	SB	AS	SN	O ₂
HY-80	0.12			0.23	0.014	0.012	0.14	0.21	2.34	1.53	0.25	0.01	0.003			0.005	0.009	0.01	
HY-100	0.16			0.29	0.006	0.002	0.16	0.27	2.38	1.36	0.25	0.006	0.002			0.005	0.006	0.01	
HSLA-80	0.05			0.54	0.004	0.005	1.19	0.25	0.85	0.75	0.22	0.006	0.003	0.018	0.036	0.003			
4340VAR	0.43			0.79	0.005	0.001	0.06	0.31	1.8	0.83	0.26								
Ti-6Al-4V	0.028	0.15	0.0061						0.01			3.985	BAL	6.12					0.17

Table 2. Heat treatment and quasistatic properties

	HY-80	HY-100	HSLA-80	4340 VAR	Ti-6Al-4V
Tensile strength	737 MPa	841 MPa	717 MPa	700 MPa	979 MPa
Yield strength	662 MPa	765 MPa	662 MPa	620 MPa	903 MPa
Hardness	RC 21	RC 28	RC 22	RC 19	RC 36
Heat treatment	1650 F for 70 min, WQ 1240 F for 46 min, WQ	1650 F for 31 min, WQ 1160 F for 98 min, WQ	1650 F for 18 min, WQ 1180 F for 42 min, A/C	1700 F for 60 min, A/C below 600 F 1250 F for 120 min, A/C	Anneal at 1450 F for 8 h

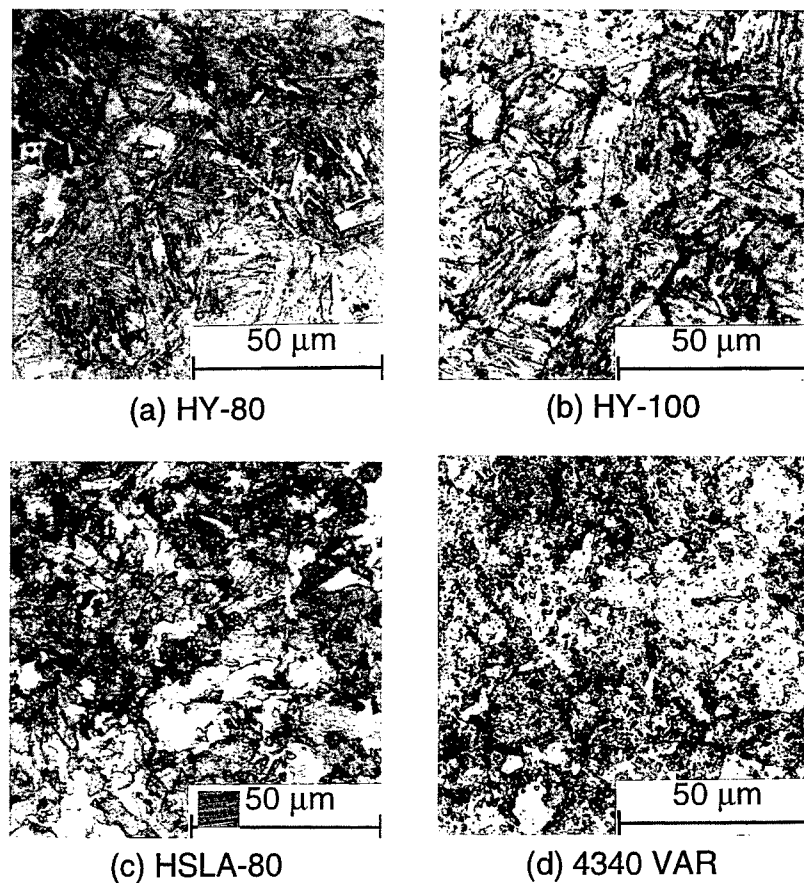
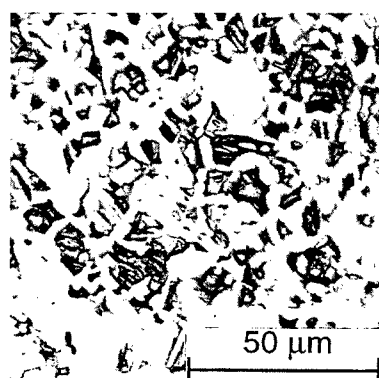
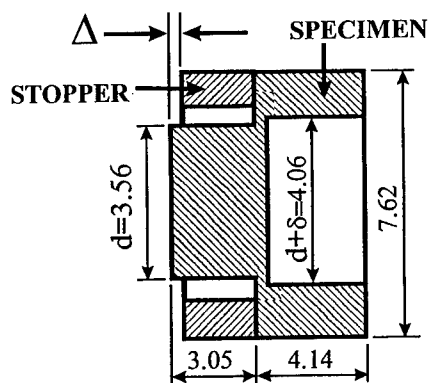


Fig. 1. Microstructures of the steels analyzed ; (a) HY-80, (b) HY-100, (c) HSLA-80, and (d) 4340VAR.



TI-6Al-4V

Fig. 2. Microstructure of Ti-6Al-4V alloy.



All Dimensions in mm

Fig. 3. A schematic illustration of specimen configuration.

This technique has also been used by Subhash and Ravichandran (1993) in a study of the deformation and failure of hafnium. A split Hopkinson compression bar as described by Follansbee (1985) is used to cause the compressive loading to the specimen along its axis. The specimen geometry is such that upon compressive loading at the two ends, intense shear deformation is obtained in the ligament between the smaller top section and the hollow cylinder section. A stopper ring is placed around the hat during the experiment to control the amount of shear deformation imparted to the ligament. The hat section protrudes above the ring surface and the amount of protrusion (Δ) determines the maximum amount of deformation allowed. Upon loading of the specimen, the hat section deforms until the incident bar touches the ring surface. The relatively small size of the ligament ensures that deformations in the hat and hollow cylinder sections are small and negligible compared to the deformation in the ligament. The maximum average shear strain in the ligament is $\gamma_{\max} = 2\Delta/\delta$. By varying the thickness of the stopper ring, a range of shear deformations can be obtained for each material. After the experiment, the specimens are sectioned in halves and polished. The steels are etched with a 3% nital solution and the titanium is etched with Kroll's solution. The length and width of the shear band are measured on a Reickerd optical microscope. The length of any visible rupture within the shear band is measured. Optical and scanning electron microscopy are used to examine the fracture surfaces for the specimens with completely ruptured ligaments.

4. RESULTS

4.1. Dynamic constitutive response

The dynamic constitutive behaviors of the materials are analyzed using the same split Hopkinson compression bar apparatus. The specimen is a cylinder 3 mm in diameter and 3 mm in length. The stress-strain curves for the five materials over the

strain rate range of 10^2 – 10^4 s $^{-1}$ are shown in Fig. 4(a)–(e). A comparison of the dynamic responses of the materials for similar strain rates between 2.1 – 2.4×10^4 s $^{-1}$ is given in Fig. 4(f). The curves show that like their similar quasistatic yield strengths and ultimate tensile strengths, the steels have similar dynamic constitutive behaviors in the strain rate range of 10^2 – 10^4 s $^{-1}$. The similar quasistatic and dynamic responses indicate that the steels have nearly the same rate-sensitivities in the strain rate range analyzed. It can be seen in Fig. 4(f) that the steels also have nearly the same rate of strain hardening.

Ti-6Al-4V has a much stronger rate-sensitivity than those of the steels. In addition, its rate of strain hardening is slightly higher. Despite these factors, this material is more susceptible to shear banding and ductile rupture than the steels, as suggested by the precipitous drops in stress at strains of approximately 0.2. Postmortem analysis revealed that the shear bands occurred along plane approximately 45° from the loading axis. This is inconsistent with the understanding that strong rate-sensitivity and higher strain hardening enhance resistance to shear localization, indicating factors other than rate-sensitivity play a more dominant role in determining shear failure under the conditions analyzed. Further discussions on this will follow in later sections. Shear bands are not observed for the steels in uniaxial compression experiments.

4.2. Evolution of stress-carrying capacity throughout deformation and failure

The nominal shear stress-strain curves obtained from shear failure experiments for all five materials are shown in Fig. 5(a)–(e). The stress and strain are average values in the specimen ligament. The shear stress is obtained by dividing the total load applied to the specimen by the cylindrical surface area in the ligament. The shear strain is obtained via

$$\gamma = \frac{2u(t)}{\delta},$$

where $u(t)$ is the decrease in the length of the hat specimen. This calculation assumes that all the deformation occurs in the ligament. For each material, results for several stopper thickness values are shown. The precipitous drops in shear stress signifies the loss of stress-carrying capacity associated with shear failure development. The increase in stress following the drop on each curve results from the contact of the incident bar and the stopper. It does not represent material behavior. Rather, it signifies the cessation of deformation in the specimen. To facilitate comparison, the curves for all five materials for the stopper thickness allowing complete failure are shown in Fig. 5(f). Clearly, all materials show a total loss of stress-carrying capacity indicated by the drop of stress to near zero levels. The shape of the curves indicate that the strains at which materials lose all of their stress-carrying capacities increase in the order Ti-6Al-4V → HY-80 → HY-100 → HSLA-80 → 4340VAR. The critical strain level for Ti-6Al-4V is approximately 1.6—significantly lower than those of the steels. Ti-6Al-4V does not display a period of gradual decrease of stress. Instead, a rapid loss of stress is observed immediately after the onset of localization. The steels, on the other hand, show gradual softening preceding the rapid losses of load-carrying capacity, indicating higher resistance to shear failure.

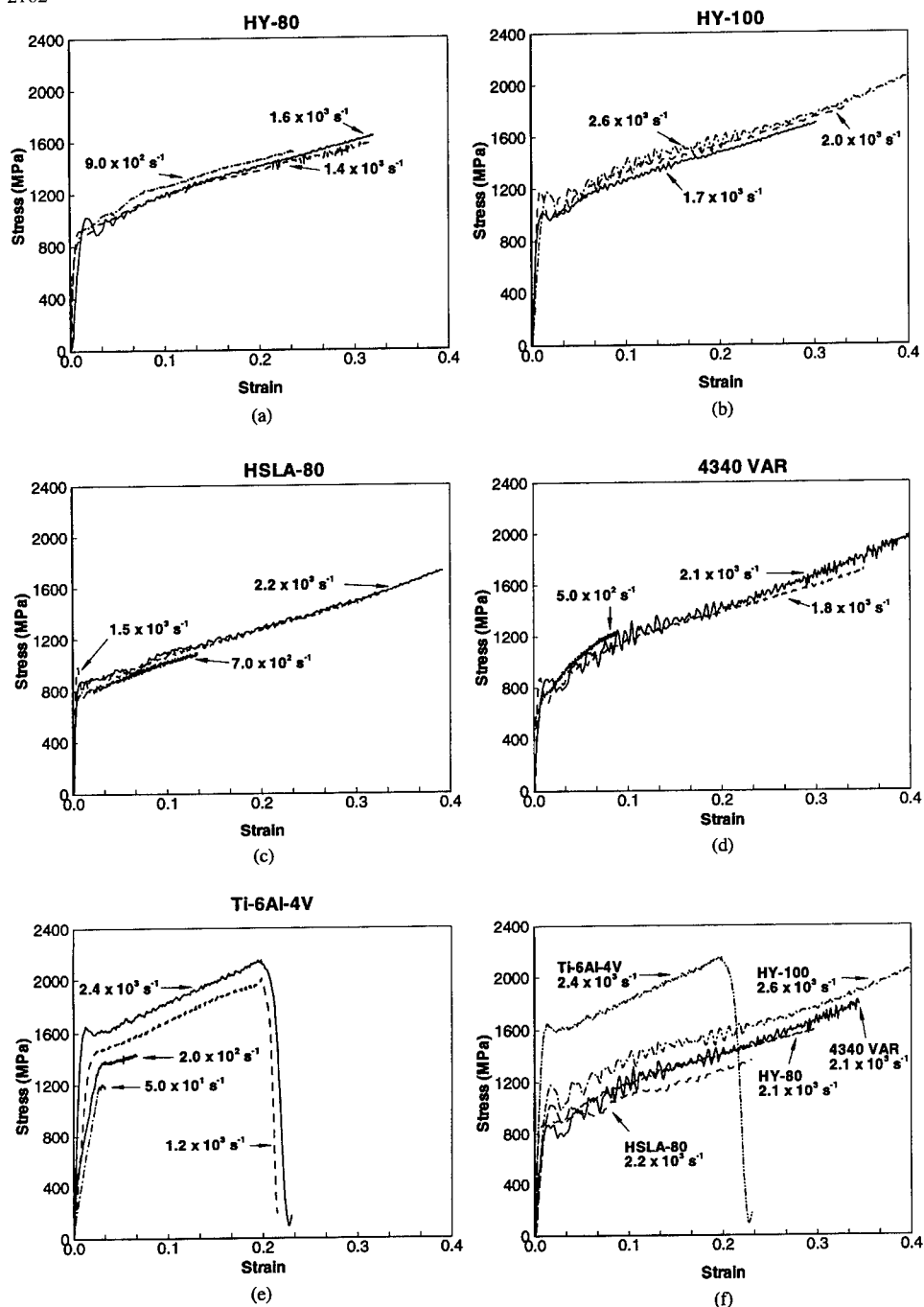


Fig. 4. Constitutive response over a range of strain rates for (a) HY-80, (b) HY-100, (c) HSLA-80, (d) 4340VAR, (e) Ti-6Al-4V alloy; (f) is a comparison of all materials at similar rates.

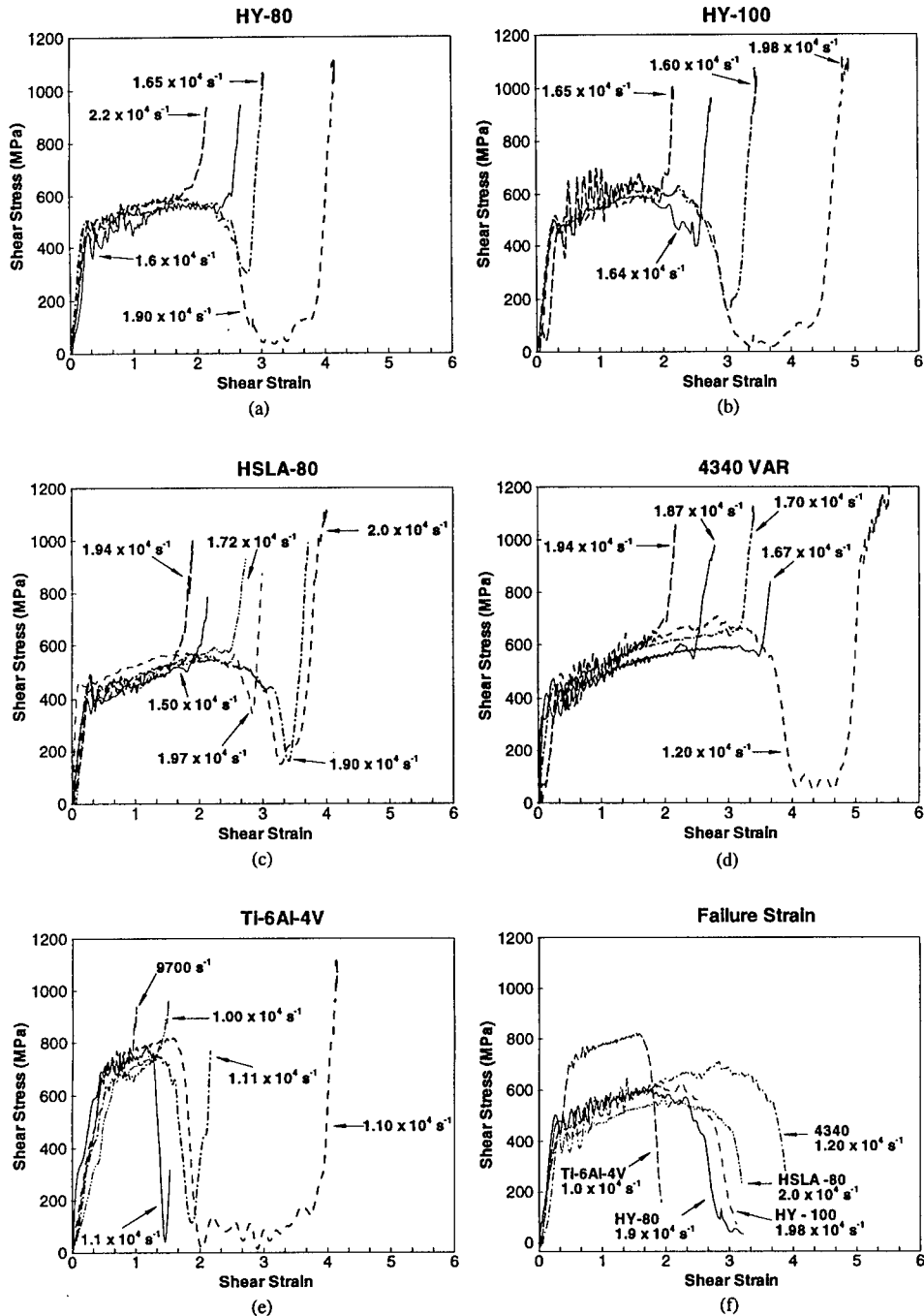


Fig. 5. Nominal stress-strain curves during shear deformation and failure for; (a) HY-80, (b) HY-100, (c) HSLA-80, (d) 4340VAR, (e) Ti-6Al-4V alloy, and (f) a comparison of all materials deformed until complete failure occurs.

4.3. Microscopic observations

To compare microstructural evolution during the shear failure process, the deformed microstructures of the steels at nominal shear strain levels of 2.0 and 2.5 are shown in Fig. 6. This series of pictures illustrates the progression of localization and rupture in each material. HY-100 shows distinct shear band formation across the whole ligament of the specimen at $\gamma = 2.0$. The band is narrow ($\sim 60\text{--}70\text{ }\mu\text{m}$ in width) compared with those in the other steels. At $\gamma = 2.5$, complete rupture has occurred along the shear band. This material shows the most extensive microscopic damage among the steels. For HY-80, a shear band is emerging from one side of the ligament at $\gamma = 2.0$. The band has propagated through the ligament at $\gamma = 2.5$ but no crack is seen. Note that the notch on the right hand corner is formed by the motion of the initial free surfaces and does not represent a crack. SEM photographs of the ruptured specimens indicate that the original radius of the specimen folds inward as the shear deformation increases. This folded surface is noticeable in all the specimens in which the shear band has not completely propagated across the ligament. A shear band is emerging from one side of the ligament at $\gamma = 2.0$. The localization of deformation in 4340VAR occurs later than in all other steels. In addition, the deformation is diffuse and the shear band has a width of approximately $260\text{ }\mu\text{m}$, 3–4 times those in HY-80, HY-100 and HSLA-80. The increasing order of shear failure resistance for the steels appears to be HY-100 \rightarrow HY-80 \rightarrow HSLA-80 \rightarrow 4340. This is different from the order of decreasing critical shear strain indicating the onset of loss of stress-carrying capacity seen in Fig. 5. It seems that the martensitic microstructure of HY-100 makes it more susceptible to the development of intensely localized shear bands. However, its earlier development of localization does not necessarily result in early loss of stress. Rather, significant loss of strength follows more closely the subsequent ductile rupture of materials. This observation is consistent with what was reported by Bai *et al.* (1994).

The deformed microstructures of Ti-6Al-4V at $\gamma = 1.3$ and 2.0 are shown in Fig. 7. Note that the strains here are from those in Fig. 6, indicating shear failure occurs significantly earlier in the titanium alloy than in the steels. The shear band in this material has a width of only $10\text{ }\mu\text{m}$ (Fig. 8), nearly an order of magnitude smaller than those in the steels. In addition to the extremely intense shear deformation, the shear band is closely followed by cracks formed through the microrupture of damaged materials inside the shear band, Fig. 8. Note that while no shear band is seen in Fig. 7(a) at $\gamma = 1.3$, nearly complete fracture has occurred in Fig. 7(b) at $\gamma = 2.0$, indicating the full development of localization and rupture in this material is within a nominal shear strain increment of 0.41. This rapid occurrence of failure has been observed in the stress-strain profiles for this material in Fig. 5(e).

To quantify the extent of shear localization and rupture, the lengths of shear bands and cracks following the shear bands are measured and plotted in Fig. 9. These two lengths increase with the nominal shear strain inside the ligament. For each of the steels, there is an appreciable difference in the shear band length and the crack length, suggesting development of rupture after localization of strain. For Ti-6Al-4V, the shear band length and the rupture length are very close to each other. This lack of difference for the titanium alloy indicates the near simultaneous occurrence of localization and rupture.

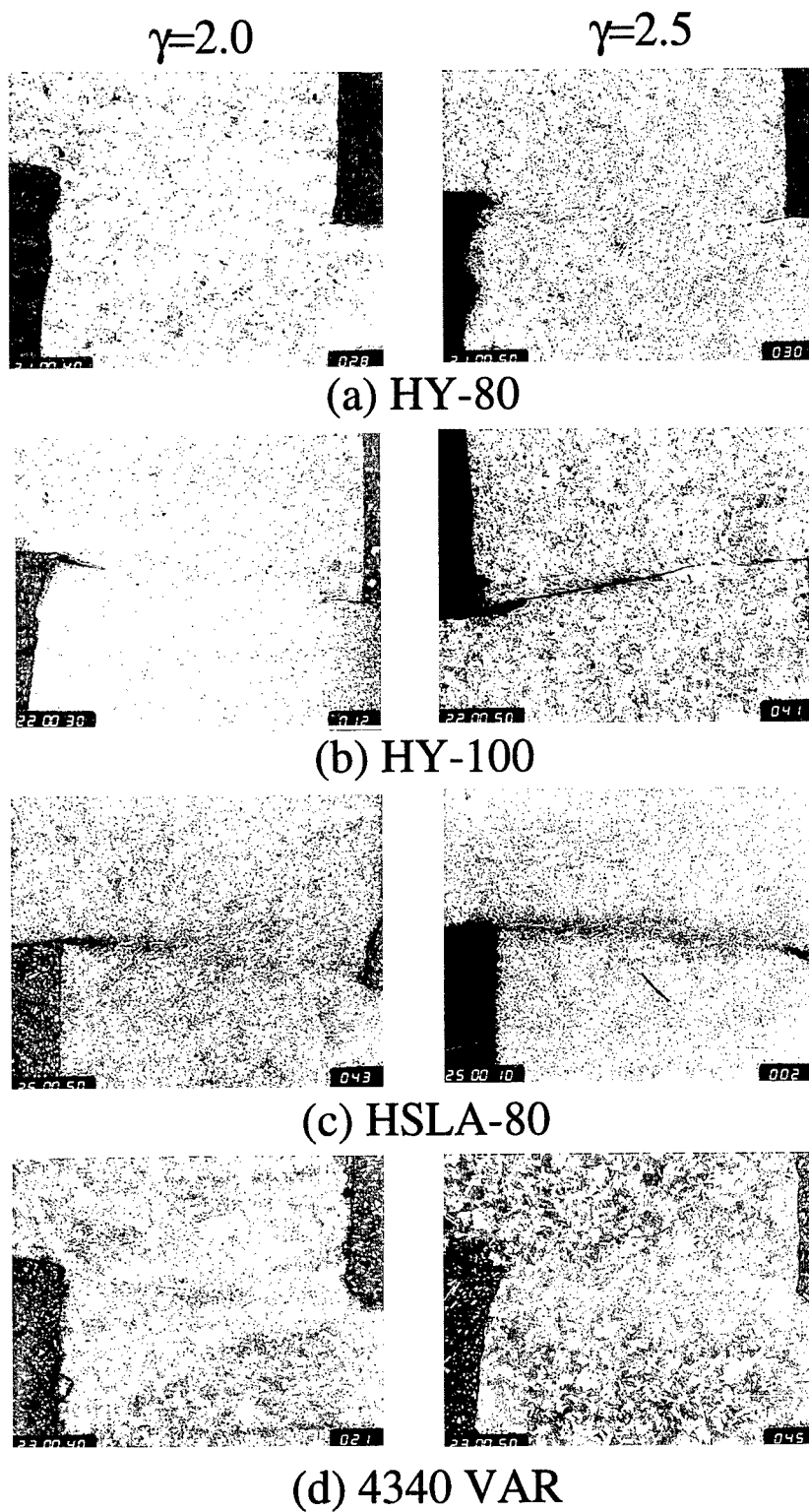


Fig. 6. Morphologies of shear bands and ductile rupture at $\gamma = 2.0$ and 2.5 for (a) HY-80, (b) HY-100, (c) HSLA-80, (d) 4340VAR.

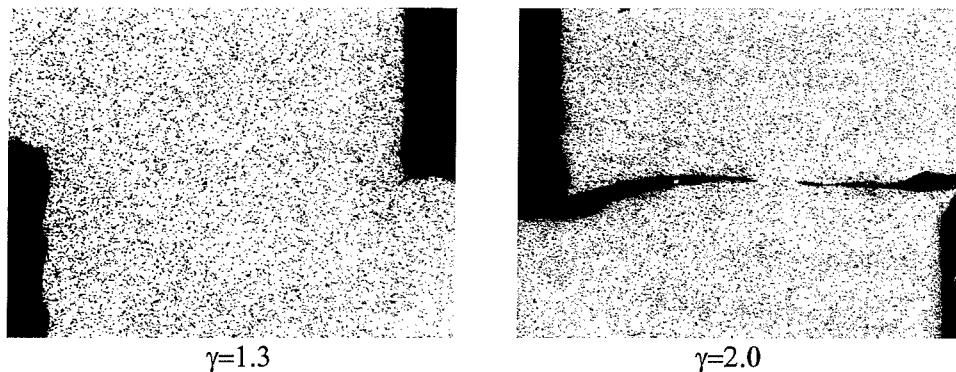


Fig. 7. Morphologies of shear bands and ductile rupture at $\gamma = 1.3$ and 2.0 for Ti-6Al-4V.

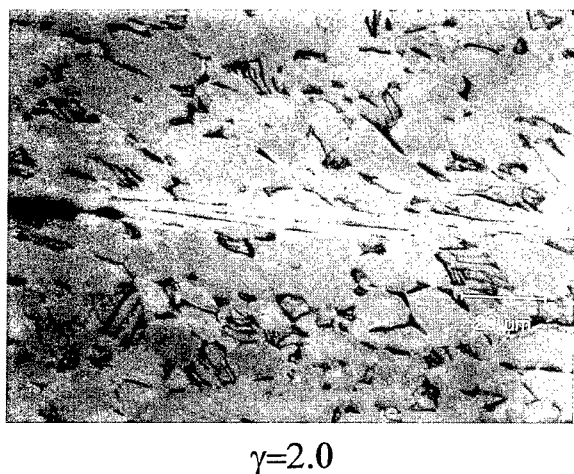


Fig. 8. A close up look of the shear band in Ti-6Al-4V at $\gamma = 2.0$.

Partly because of this rapid development of rupture, Ti-6Al-4V exhibits a much higher degree of susceptibility to the loss of stress-carrying capacity than those of the steels.

5. DISCUSSION AND SUMMARY

Although it is based on an approximate characterization of the thermomechanical response and a one-dimensional deformation model, the shear band dissipation energy derived by Grady (1994) allows the energy dissipated per unit area of shear band growth for different materials to be estimated and compared. This shear band dissipation energy is

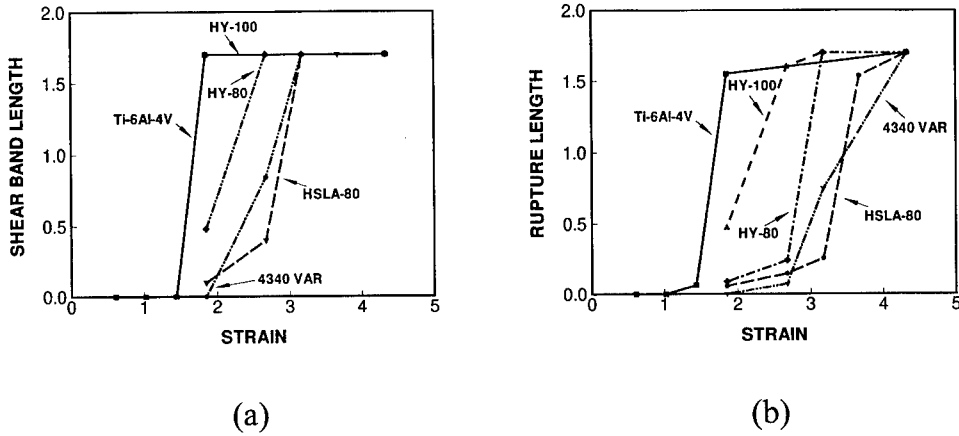


Fig. 9. Shear band and rupture lengths as a function of shear deformation; (a) shear band length, (b) rupture length.

Table 3. Dissipation energy and shear band toughness

Material	Flow stress (MPa)	Dissipation energy Γ_s (KJ/m ²)	Shear band toughness K_s (MPa \sqrt{m})
HY-80	1460	125.2	142.221
HY-100	1530	120.9	139.745
HSLA-80	1280	138.2	149.414
4340VAR	1450	125.9	142.588
Ti-6Al-4V	2000	3.935	18.861

$$\Gamma_s = \frac{\rho c}{\alpha} \left(\frac{9\rho^3 c^2 \chi^3}{\tau_y^3 \alpha^2 \dot{\gamma}} \right)^{1/4}$$

where ρ is density, χ is thermal diffusion coefficient, α is a thermal softening coefficient, c is specific heat, τ_y is the flow stress at strain rate $\dot{\gamma}$. This parameter is calculated for the materials analyzed in the experiments. For the steels, their densities, thermal diffusion coefficients, and thermal softening coefficients are similar (due to similar melting points) and are taken as $\rho = 7.85 \times 10^3 \text{ kg m}^{-3}$, $\alpha = 6.5 \times 10^{-4} \text{ m}^2 \text{ s}^{-1}$, and $c = 503 \text{ J} \cdot (\text{kg} \cdot \text{K})^{-1}$, respectively. For Ti-6Al-4V, these parameters are $\rho = 4.43 \times 10^3 \text{ kg m}^{-3}$, $\alpha = 5.6 \times 10^{-4} \text{ m}^2 \text{ s}^{-1}$, and $c = 526 \text{ J} \cdot (\text{kg} \cdot \text{K})^{-1}$. The flow stress τ_y for each material is taken from its stress strain curves in Fig. 4 at a strain rate of $\dot{\gamma} = 1.7 \times 10^4 \text{ s}^{-1}$. The values are listed in Table 3 along with the values of calculated Γ_s . A shear band toughness parameter is defined by Grady as $K_s = \sqrt{2G\Gamma_s}$, where G is the shear modulus. It can be seen that the dissipation energy and shear band toughness values for the steels are very close to each other due to their similar thermal and mechanical properties. This similarity is in contrast to the significantly different shear failure

behaviors observed in the experiments. In addition to the approximate nature of the model on which the calculation of Γ_s is based, the lack of agreement between the values of these quantities and the shear failure resistance of the materials observed has to do with the influence of microscopic damage not accounted for in the analysis.

The shear stress-shear strain curves obtained in the experiments described above and the microscopic observations assign mostly consistent shear failure toughness rankings for the materials analyzed. From the most susceptible to the least susceptible, the ranking is Ti-6Al-4V, HY-80, HY-100, HSLA-80, 4340VAR based on the stress-strain curves or Ti-6Al-4V, HY-100, HY-80, HSLA-80, 4340VAR based on the microscopic morphologies of shear bands and fracture behind the shear band tips. The stress-strain response and the microscopic analysis showed that Ti-6Al-4V is more susceptible to dynamic shear failure than the steels considered. This is in contrast to its much higher rate sensitivity than those of the steels. Similarly, among the steels, significant difference in the shear failure behavior is observed, despite their similar thermal and mechanical constitutive behavior over the strain rate range of 10^2 – 10^4 s⁻¹. The discrepancies can be partly attributed to the fact that the formation of a well-deformed shear band does not necessarily cause an instantaneous loss in load carrying capability. The subsequent coalescence of cracks or development of rupture also plays a significant role in determining the evolution of the load-carrying capacity of materials during shear deformation. Clearly, microscopic damage as well as the thermal-mechanical response of materials needs to be considered in evaluating the dynamic shear failure resistance of materials.

The calculated dissipation energy value for Ti-6Al-4V and the calculated shear band toughness value are only fractions of those for the steels. This partly explains its much higher susceptibility to shear failure compared with those of the steels and demonstrates that thermomechanical behavior plays a very important role in determining material shear failure resistance. However, the experiments showed that rupture closely follows the propagating shear bands in this material, further expediting the progression of failure through rapid release of stress. Like in the case of the steels, this effect should not be neglected. A comparison of the microscopic rupture mechanism in the form of void growth and coalescence in these materials is being carried out using scanning electron microscopy. The result and its implications for the shear failure resistance of these materials will be reported in a future publication.

ACKNOWLEDGEMENTS

Support from the Office of Naval Research through grant No. N00014-96-1-1195 to Georgia Institute of Technology is gratefully acknowledged.

REFERENCES

- Andrade, U., Meyers, M. A., Vecchio, K. S. and Chokshi, A. H. (1994) Dynamic recrystallization in high-strain, high-strain-rate plastic deformation of copper. *Acta Metall. Mater.* **42**, 3183–3195.
- Bai, Y. L. (1981) A criterion for thermo-plastic shear instability. Proceedings of the Inter-

- national Conference on Metallurgical Effects of High-Strain-Rates Deformation and Fabrication, Albuquerque, NM, Plenum, NY, 277–283.
- Bai, Y. L. (1982) Thermo-plastic instability in simple shear. *J. Mech. Phys. Solids* **30**, 195–207.
- Bai, Y., Xue, Q., Xu, Y. and Shen, L. (1994) Characteristics and microstructure in the evolution of shear localization in Ti-6Al-4V alloy. *Mech. Mater.* **17**, 155–164.
- Batra, R. C. and Kim, C. H. (1992) Analysis of shear banding in twelve materials. *Int. J. Plasticity* **8**, 425–452.
- Batra, R. C. and Kim, C. H. (1991) Effect of thermal conductivity on the initiation, growth and band width of adiabatic shear bands. *Int. J. Engng Sci.* **29**, 949–960.
- Beatty, J. H., Meyer, L. W., Meyers, M. A. and Nemat-Nasser, S. (1991) Formation of controlled adiabatic shear bands in AISI 4340 high strength steel. *12th Army Symposium on Solid Mechanics*, Plymouth, MA.
- Cho, K., Chi, Y. C. and Duffy, J. (1990) Microscopic observations of adiabatic shear bands in three different steels. *Metall. Trans. A* **21A**, 1161–1175.
- Cho, K., Lee, S., Nutt, S. R. and Duffy, J. (1993) Adiabatic shear band formation during dynamic torsional deformation of an HY-100 steel. *Acta Metall. Mater.* **41**, 923–932.
- Clifton, R. J. (1980) Adiabatic shear banding. *Material Response to Ultra-High Loading Rates*, NMAB-356, National Materials Advisory Board (NRC), Washington, D.C., Chap. 8.
- Duffy, J. and Chi, Y. C. (1992) On the measurement of local strain and temperature during the formation of adiabatic shear bands. *Mat. Sci. Engng A* **157**, 195–210.
- Follansbee, P. S. (1985) The hopkinson bar, *Metals Handbook*, **8**, American Society for Metals, Metals Park, Ohio, 198–217.
- Freund, L. B., Wu, F. H. and Toullos, M. (1985) *Proc. Considere Memorial Symposium*. Presse de l'Ecole Nationale des Pontes et Chaussées, Paris, France, p. 125.
- Gioia, G. and Ortiz, M. (1996) The two-dimensional structure of dynamic shear bands in thermoviscoplastic solids. *J. Mech. Phys. Solids* **44**, 251–292.
- Giovanola, J. H. (1988) Adiabatic shear banding under pure shear loading, Part I: Direct observation of strain localization and energy dissipation measurements; Part II: Fractographic and metallurgical observations. *Mech. Mater.* **7**, 59–87.
- Grady, D. E. (1992) Properties of an adiabatic shear-band process zone. *J. Mech. Phys. Solids* **40**, 1197–1215.
- Grady, D. E. (1994) Dissipation in adiabatic shear bands. *Mech. Mater.* **17**, 289–293.
- Grady, D. E. and Kipp, M. E. (1987) The growth of unstable thermoplastic shear with application to steady-wave shock compression in solids. *J. Mech. Phys. Solids* **35**, 95–118.
- Hanchak, S. J., Altman, B. S. and Forrestal, M. J. (1993) Perforation of HY-100 steel plates with long rod projectiles. *Proceedings of the 13th Army Symposium on Solid Mechanics*, Plymouth, MA, pp. 247–257.
- Kalthoff, J. F. (1987) Shadow optical analysis of dynamic shear fracture. *SPIE* **814**, Photo-mechanics and Speckle Metrology, 531–538.
- Marchand, A. and Duffy, J. (1988) An experimental study of the formation process of adiabatic shear bands in a structural steel. *J. Mech. Phys. Solids* **36**, 251–283.
- Mason, J. J., Rosakis, A. J. and Ravichandran, G. (1994) Full field measurements of the dynamic deformation field around a growing adiabatic shear band at the tip of a dynamically loaded crack or notch. *J. Mech. Phys. Solids* **42**, 1679–1697.
- Merzer, A. M. (1982) Modelling of adiabatic shear band development from small imperfections. *J. Mech. Phys. Solids* **30**, 323–338.
- Meyers, M. A., Andrade, U. R. and Chokshi, A. H. (1995) The effect of grain size on the high-strain, high-strain-rate behavior of copper. *Metall. & Mater. Trans. A* **26A**, 2881–2893.
- Molinari, A. and Clifton, R. J. (1987) Analytical characterization of shear localization in thermoviscoplastic materials, *Trans. of ASME. J. Appl. Mech.* **54**, 806–812.
- Needleman, A. (1989) Dynamic shear band development in plane strain. *J. Appl. Mech.* **56**, 1–9.
- Needleman, A. and Tvergaard, V. (1992) Analysis of plastic flow localization in metals. *Appl. Mech. Rev.* **45**(Suppl.), S3–S15.
- Nemat-Nasser, S. (1992) Phenomenological theories of elastoplasticity and strain localization at high strain rates. *Appl. Mech. Rev.* **45**(Suppl.), S19–S45.

- Ramesh, K. T. (1994) On the localization of shearing deformations in a tungsten heavy alloy. *Mech. Mater.* **17**, 165.
- Rogers, H. C. (1979) Adiabatic plastic deformation. *Ann. Rev. Mat. Sci.* **9**, 283–311.
- Rogers, H. C. and Shastry, C. V. (1981) Material factors in adiabatic shearing in steels. *Shock Waves and High Strain-rate Phenomena*, ed. M. A. Meyers and L. E. Murr, Chap. 18, pp. 285–298. Plenum Press.
- Shawki, T. G. (1992) The phenomenon of shear strain localization in dynamic viscoplasticity. *Appl. Mech. Rev.* **45**, S46–S60.
- Shawki, T. G. and Clifton, R. J. (1989) Shear band formation in thermal viscoplastic materials. *Mech. Mat.* **8**, 13–43.
- Subhash, G. and Ravichandran, G. (1993) High strain rate behavior and localization in hafnium. *Experimental Techniques in the Dynamics of Deformable Solids*, ed. K. T. Ramesh, AMD-Vol. 165, pp. 79–88. ASME.
- Wright, T. W. and Walter, J. W. (1987) On stress collapse in adiabatic shear bands. *J. Mech. Phys. Solids* **35**, 701–720.
- Xu, Y. B., Bai, Y. L., Xue, Q. and Shen, L. T. (1996) Formation, microstructure and development of the localized shear deformation in low-carbon steels. *Acta Mater.* **44**, 1917–1926.
- Zbib, H. M. and Aifantis, E. C. (1992) On the gradient-dependent theory of plasticity and shear banding. *Acta Mechanica* **92**, 209–255.
- Zhou, M., Needleman, A. and Clifton, R. J. (1994) Finite element simulations of dynamic shear localization in plate impact. *J. Mech. Phys. Solids* **42**, 423–458.
- Zhou, M., Rosakis, A. J. and Ravichandran, G. (1996(a)) Dynamically propagating shear bands in impact-loaded prenotched plates, I—Experimental investigations of temperature signatures and propagation speed. *J. Mech. Phys. Solids* **44**, 981–1006.
- Zhou, M., Ravichandran, G. and Rosakis, A. J. (1996(b)) Dynamically propagating shear bands in impact-loading prenotched plates, II—Numerical simulations. *J. Mech. Phys. Solids* **44**, 1007–1032.
- Zhou, M. and Clifton, R. J. (1997) Dynamic constitutive and failure behavior of a two-phase tungsten composite. *J. App. Mech.* **64**, 487–494.
- Zurek, A. K. (1994) The study of adiabatic shear band instability in a pearlitic 4340 steel using a dynamic punch test. *Metall. & Mater. Trans. A* **25A**, 2483–2489.



Pergamon

J. Mech. Phys. Solids, Vol. 46, No. 10, pp. 2171–2181, 1998

© 1998 Elsevier Science Ltd. All rights reserved

Printed in Great Britain

0022-5096/98 \$—see front matter

PII: S0022-5096(98)00026-X

ENERGY-BASED MODEL OF COMPRESSIVE SPLITTING IN HETEROGENEOUS BRITTLE SOLIDS

K. BHATTACHARYA, M. ORTIZ and G. RAVICHANDRAN*

Division of Engineering and Applied Science, California Institute of Technology, Pasadena CA 91125,
U.S.A.

(Received 20 December 1997; in revised form 29 January 1998)

ABSTRACT

Confined heterogeneous brittle solids loaded under far-field uniaxial compression are often observed to split along the loading axis. We develop a theory which accords this phenomenon an energetic interpretation: the solid splits because in so doing it reduces its total energy, defined as the sum of bulk strain energy and surface energy. The heterogeneous microstructure gives rise to a complex stress distribution in the intact solid. We show that the change in energy due to the release of the microstructural stresses may exceed the cost in fracture energy. Critical conditions for splitting are formulated for polycrystalline solids as a function of readily measurable material properties and applied stresses. The predictions of the theory are found to be in remarkably good agreement with experimental observations in ceramics and rocks. © 1998 Elsevier Science Ltd. All rights reserved.

Keywords: A. fracture, B. ceramic material, polycrystalline material, rock, C. energy methods.

1. INTRODUCTION

Confined heterogeneous brittle solids loaded in uniaxial compression are often observed to split along the loading axis (Wastiels, 1979; Cannon *et al.*, 1990; Smith and Schulson, 1994; Espinosa and Brar, 1995; Chen and Ravichandran, 1996). While brittle fracture in compression has been the subject of study since the pioneering work of Griffith (1920), an unambiguous understanding of this phenomenon is yet to emerge. Models based on the extension of inclined or tortuous cracks have been proposed by a number of authors (e.g. Brace and Bobolakis, 1963; McClintock and Walsh, 1963; Hoek and Bieniawski, 1965; Nemat-Nasser and Horii, 1982; Ortiz, 1985; Ashby and Hallam, 1986; Vekinis *et al.*, 1991; Ravichandran and Subbash, 1995; Espinosa and Brar, 1995; Wang and Shrive, 1995). Some of these models are based on the nucleation and growth of tension cracks, or “wing” cracks, from the tips of isolated inclined flaws. While wing cracks have been observed in some cases (Horii and Nemat-Nasser, 1986; Cannon *et al.*, 1990; Vekinis *et al.*, 1991), it has been shown by Lehner and Kachanov (1996) that the crack-tip driving force quickly approaches zero with crack extension, especially in the presence of frictional resistance, which calls the effectiveness of the mechanism into question.

* To whom correspondence should be addressed. E-mail: ravi@atlantis.caltech.edu

Most of the existing models of compressive fracture fail to account for heterogeneity on the microscale and envision the growth of flaws under the action of the nominal applied stresses. However, the heterogeneous microstructure of polycrystals and composites may lead to substantial local tensile stresses even under compressive applied loads. For instance, by treating concrete as a two-phase composite, Ortiz and Popov (1982) found that large tensile stresses may develop in the matrix under applied uniaxial compression. Furthermore, the tensile stresses are normal to the axis of loading, which promotes axial splitting. Indeed, compressive fracture is often observed in materials with heterogeneous microstructures such as rocks and concrete, which suggests a link between heterogeneity and compressive fracture.

Studying the energy release rate associated with a crack in the complicated stress field of a microstructurally heterogeneous solid appears to be a hopelessly complicated task. Therefore, we instead take a more macroscopic and energetic approach. We develop a theory which accords compressive fracture an energetic interpretation: splitting is driven by an attendant reduction of the total energy of solid, defined as the sum of bulk strain energy and surface energy. Similar energetic interpretations of fracture have been used successfully in studying cavitation in rubber-like solids (e.g., Ball, 1982; James and Spector, 1991; Hou and Abeyaratne, 1992). We combine this energetic approach with ideas of effective properties and the principle of minimum complementary energy. Hashin (1996) has used this principle to obtain a bound on the energy release rate for fracture in laminated composites. We will find that this macroscopic energetic approach allows us to easily account for the underlying heterogeneity.

For definiteness, we restrict our discussion to polycrystals, but other microstructures can likewise be treated within the theory. In a polycrystal, each grain is made up of the same material but at a different orientation. Therefore, the heterogeneity arises due to the anisotropy of the properties like elastic moduli of the single crystal. The microstructural heterogeneity gives rise to a complex stress distribution in the intact solid. We show that the change in the microstructural stresses induced by splitting results in a reduction of the elastic energy. By equating the energy released by splitting to the fracture energy required for the creation of new surface, critical conditions for splitting follow readily as a function of well-characterized material properties and applied stresses. The predictions of the theory are found to be in good agreement with experimental observations in ceramics and rocks.

2. A MODEL OF COMPRESSIVE SPLITTING

Consider the polycrystalline specimen of height h and thickness t shown schematically in Fig. 1(a). Suppose it is subjected to a macroscopic uniaxial compression σ . Suppose for the moment that the lateral confinement σ_c is zero. As σ increases, cracks appear as shown in Fig. 1(b) and the specimen splits into the columns as shown in Fig. 1(c) at a critical value of the applied stress σ^* . If the lateral confinement σ_c is nonzero but small, the behavior is still similar except the failure strength σ^* is known to increase with σ_c (e.g., Wastiels, 1979; Cannon *et al.*, 1990; Smith and Schulson, 1994; Espinosa and Brar, 1995; Chen and Ravichandran, 1996).

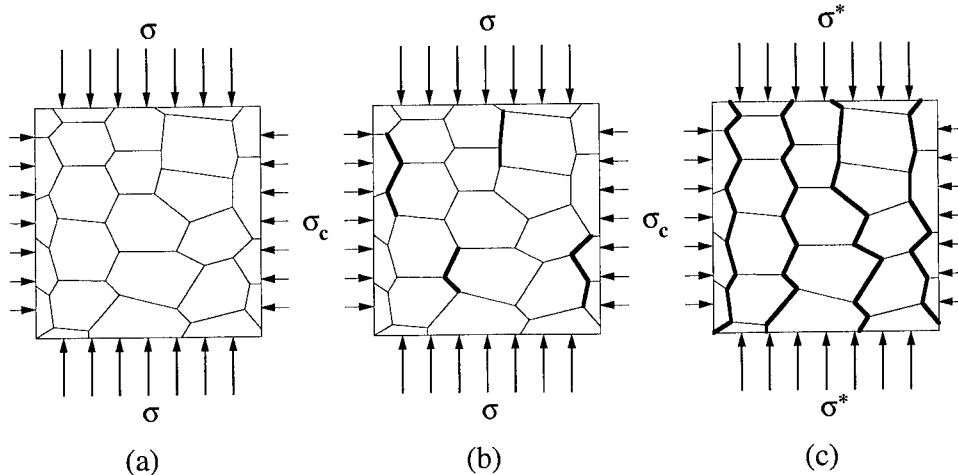


Fig. 1. Compressive splitting in ceramics.

In our model, we compare the energy of the unsplit specimen (Fig. 1(a)) with that of the split specimen (Fig. 1(c)). We estimate the elastic energy of both the split and the unsplit specimen using ideas of effective properties of polycrystals. The unsplit specimen has less total energy when the applied load σ is small while the split specimen has less total energy when σ is large. The failure strength or the critical compressive stress required for splitting σ^* is defined as the applied stress at which there is an exchange of stability from the unsplit to the split specimen. We obtain σ^* as a function of the confinement stress σ_c and easily measurable material properties: the elastic moduli of both the single crystal and the bulk polycrystal, the surface energy and the grain size.

2.1. Energy of the unsplit specimen

We assume that our specimen is subjected to dead loading corresponding an overall stress T . Therefore, the total energy of the unsplit specimen is equal to its elastic energy which is given by

$$\begin{aligned} \mathcal{E}_u &= \int_{\Omega} \left\{ \frac{1}{2} C(x) e(x) \cdot e(x) - T(x) \cdot e(x) \right\} dx = -\frac{1}{2} \int_{\Omega} \{ S(x) T(x) \cdot T(x) \} dx \\ &= -\frac{h t^2}{2} S_u^* T \cdot T. \end{aligned} \quad (1)$$

Above, $C(x)$ is the fourth-order elastic modulus tensor at point x , $S(x)$ is the fourth-order compliance tensor, S_u^* is the effective compliance tensor of the unsplit specimen, $e(x)$ is the strain field, $T(x)$ is the stress field and V is the volume of the specimen Ω .

We assume that the specimen is macroscopically isotropic so that S_u^* is described by the effective Young's modulus E_u and effective Poisson's ratio ν_u . The applied stress shown in Fig. 1 corresponds to

$$T = - \begin{pmatrix} \sigma & 0 & 0 \\ 0 & \sigma_c & 0 \\ 0 & 0 & \sigma_c \end{pmatrix} \quad (2)$$

in an orthonormal basis where the primary loading axis is chosen to be the 1-direction. Therefore,

$$S_u^* T = \frac{1+v_u}{E_u} T - \frac{v_u}{E_u} (\text{tr } T) I = \frac{1}{E_u} \begin{pmatrix} \sigma - 2v_u\sigma_c & 0 & 0 \\ 0 & \sigma_c - v_u(\sigma + \sigma_c) & 0 \\ 0 & 0 & \sigma_c - v_u(\sigma + \sigma_c) \end{pmatrix} \quad (3)$$

Finally, we assume that the specimen is a cuboidal with dimension $h \times t \times t$. Substituting all this into (1), we obtain the elastic energy of the unsplit specimen

$$\mathcal{E}_u = - \frac{ht^2}{2E_u} (\sigma^2 + 2\sigma_c^2(1-v_u) - 4v_u\sigma\sigma_c). \quad (4)$$

2.2. Energy of the split specimen

There are two components to the energy of the split specimen. First, is the elastic energy while the second is the surface energy. Calculating the exact value of either can be rather daunting; however, they may be estimated very simply with a few approximations.

We assume that the splitting produces columns of grains with a uniform stress field. Therefore, the elastic energy is given by

$$\mathcal{E}_s = - \frac{1}{2} \int_{\Omega} \{S(x) T \cdot T\} dx = - \frac{ht^2}{2} \langle S \rangle T \cdot T \quad (5)$$

where $\langle S \rangle$ is the average of the compliance tensor over the entire specimen. The discerning reader will recognize that $\langle S \rangle$ is the Reuss bound for the effective compliance of the polycrystal. Typically, the grains are much smaller than the specimen. Therefore, we may assume that the average is taken over all possible orientations; so $\langle S \rangle$ is isotropic with some Young's modulus E_s and Poisson's ratio v_s . Therefore,

$$\mathcal{E}_s = - \frac{ht^2}{2E_s} (\sigma^2 + 2\sigma_c^2(1-v_s) - 4v_s\sigma\sigma_c). \quad (6)$$

To calculate the surface energy, we assume that the splitting produces columns which are all one grain wide and that the surface energy density γ is constant independent of orientation. Therefore, the number of surfaces after splitting is $2t/d$ (where d is the typical grain size), each with area ht . Therefore, the total surface energy is

$$\mathcal{S} = 2\gamma \frac{ht^2}{d}. \quad (7)$$

2.3. Criterion for splitting

We recall that the constant stress Reuss bound always provides a lower bound for the energy: this is easily seen from the application of the principle of minimum complementary energy. Therefore, $\mathcal{E}_u - \mathcal{E}_s \geq 0$ and splitting reduces the elastic energy.

Our criterion for fracture is that the reduction in elastic energy must overcome the surface energy associated with the newly created surfaces. Therefore, at the critical state,

$$\mathcal{E}_u - \mathcal{E}_s = \mathcal{S}. \quad (8)$$

Substituting from (4), (6) and (7), we conclude that when the applied stress σ reaches the critical value σ^* ,

$$(\sigma^*)^2 \left(\frac{1}{E_u} - \frac{1}{E_s} \right) + 2\sigma_c^2 \left(\frac{1-\nu_u}{E_u} - \frac{1-\nu_s}{E_s} \right) - 4\sigma^* \sigma_c \left(\frac{\nu_u}{E_u} - \frac{\nu_s}{E_s} \right) = -4 \frac{\gamma}{d} \quad (9)$$

We solve this quadratic equation to obtain the failure strength,

$$\sigma^* = \frac{1}{\Delta_1} \left\{ 2\Delta_2 \sigma_c - \sqrt{2\sigma_c^2 (2\Delta_2 - \Delta_1)(\Delta_2 + \Delta_1) - 4\Delta_1 \frac{\gamma}{d}} \right\}$$

where

$$\Delta_1 = \left(\frac{1}{E_u} - \frac{1}{E_s} \right) \quad \text{and} \quad \Delta_2 = \left(\frac{\nu_u}{E_u} - \frac{\nu_s}{E_s} \right). \quad (10)$$

We will compare this result with experimental observations shortly. Before we do so, let us try to understand this result with some comments. First, the failure strength at zero confinement is given by

$$\sigma^*|_{\sigma_c=0} = \sqrt{\frac{4\gamma/d}{-\Delta_1}}. \quad (11)$$

Notice that it automatically contains the effect of the grain size d .

Second, to understand the effect of lateral confinement, we find from (10) that

$$\left. \frac{d\sigma^*}{d\sigma_c} \right|_{\sigma_c=0} = 2 \frac{\Delta_2}{\Delta_1}. \quad (12)$$

Let us now assume that the symmetry of the underlying material is cubic. Then, the bulk modulus is independent of texture and hence the bulk moduli of the split and the unsplit ceramic are equal. Using this fact, it is possible to show that for a cubic material,

$$\left. \frac{d\sigma^*}{d\sigma_c} \right|_{\sigma_c=0} = 1. \quad (13)$$

3. COMPARISON WITH EXPERIMENTS AND DISCUSSION

We now apply our model to various materials.

The measure elastic moduli of the unsplit specimen are readily available. Similarly,

the elastic moduli of the single crystals are also readily available; from this, we may easily calculate the Reuss bounds which are effective moduli for split specimen. However, it often turns out that the measured elastic moduli of the unsplit specimen violates the Reuss lower bound. This is believed to be a result of the porosity and texture in these materials. We could correct the Reuss bound for the porosity; unfortunately, the exact value of the porosity is difficult to measure and often unavailable. Under these circumstances we decided to estimate the elastic moduli of the unsplit specimen based on the single crystal elastic moduli.

We use the average of the Reuss lower and the Voigt upper bound as an estimate of the elastic moduli of the unsplit specimen. It is important to be careful here. The quantities that are really bounded are the bulk and the shear moduli. So, we average the bounds on the bulk and shear moduli and then obtain the Young's modulus and the Poisson's ratio from these. Clearly, we are not proposing this as a model of the effective elastic moduli for the polycrystal; instead we use this as the simplest possible estimate. The choice of other estimates would not change the qualitative features of the predictions. In particular, one can use various self-consistent estimates. However, one must choose amongst a variety of approximations. Further, these estimates are known to be suspect when the contrast or anisotropy is severe; and the anisotropy can be severe in some of these ceramics.

Finally, we need the surface energy density γ and the grain size d ; unfortunately, these are not always available. Therefore, we use (11) to fit γ/d to the experimental observations.

We list the single crystal elastic moduli for various materials in Table 1. We list the estimates of the elastic moduli for the split and the unsplit specimen in Table 2. Also listed in Table 2 is the fit value of the parameter γ/d . We can now calculate the failure strength as a function of the lateral confinement using (10). The results are shown in Figs 2 and 3 along with experimental observations. We find reasonable agreement.

Further, the fit values of the parameter γ/d are listed in Table 2. We notice that they are of the order of 10^{-5} GJ/m³. Since d is typically of the order of 10^{-6} m, we

Table 1. *Single crystal elastic moduli*

Material (symmetry)	Elastic moduli (GPa)
LiF (cubic)	$C_{11} = 119, C_{12} = 54, C_{13} = 53$ [1]
MgO (cubic)	$C_{11} = 286, C_{12} = 87, C_{13} = 148$ [1]
NaCl (cubic)	$C_{11} = 49, C_{12} = 12, C_{13} = 12$ [2]
AlN (hexagonal)	$C_{11} = 424, C_{12} = 103, C_{13} = 71, C_{33} = 455, C_{55} = 138$ [3]
BeO (hexagonal)	$C_{11} = 471, C_{12} = 168, C_{13} = 119, C_{33} = 494, C_{55} = 153$ [1]
TiB ₂ (hexagonal)	$C_{11} = 690, C_{12} = 410, C_{13} = 320, C_{33} = 440, C_{55} = 250$ [1]
Al ₂ O ₃ (trigonal-I)	$C_{11} = 466, C_{12} = 127, C_{13} = 117, C_{14} = 94, C_{33} = 506,$ $C_{44} = 235$ [1]
CaCO ₃ (trigonal-I)	$C_{11} = 137, C_{12} = 45, C_{13} = 45, C_{14} = -21, C_{33} = 79,$ $C_{44} = 34$ [1]

[1] Simmons and Wang (1971); [2] Bass (1995); [3] Azuhata, Soha and Suzuki (1996).

Table 2. Failure data for various materials

Material	Unsplit		Split		σ^* (GPa) at $\sigma_c = 0$	γ/d (GJ/m ³)
	E_u (GPa)	ν_u	E_s (GPa)	ν_s		
LiF	110	0.257	107	0.263	0.8	3.63×10^{-5}
MgO	297	0.177	292	0.182	1	1.27×10^{-5}
NaCl	36.9	0.253	36.5	0.256	0.045 [1, 2]	1.7×10^{-7}
AlN	372	0.188	370	0.191	4.6 [3, 4]	8.5×10^{-5}
BeO	394	0.237	393	0.238	0.4 [5]	1.18×10^{-6}
TiB ₂	456	0.322	419	0.325	40 [6, 7]	5.83×10^{-4}
Al ₂ O ₃	431	0.201	391	0.228	4.77 [5]	1.34×10^{-3}
CaCO ₃	84	0.29	72.7	0.312	0.35 [8, 2]	5.67×10^{-5}

[1] Handin (1953); [2] Ashby and Sammis (1990); [3] Rosenberg *et al.* (1991); [4] Chen and Ravichandran (1996); [5] Heard and Cline (1990); [6] Rosenberg *et al.* (1992); [7] Dandekar (1994); [8] Heard (1960).

obtain a value of γ to be of the order 10^{-2} J/m². It is low, though reasonable. We speculate that the low value is a consequence of the porosity.

Notice that in general, our theory slightly underestimates the failure strength with increasing lateral confinement. We speculate the following. As the lateral confinement increases, columns no longer achieve the Reuss lower bound and the failure mode changes from splitting to crushing. We can repeat the arguments above for crushing failure and we obtain results similar to (10): indeed, it is the same result except the term $4\gamma/d$ is changed to $6\gamma/d$. This increases the failure strength.

The theory failed to predict the observed behavior in TiB₂—see Fig. 4. The curve marked “Theory 1” is the one predicted using the procedure above. However, we noticed that for this material, the measured elastic moduli of the ceramic exceeds the Voigt upper bound! If we use the measured moduli rather than the average of Voigt and Reuss, we get the curve marked “Theory 2”. Based on this observation, we suspect that typical specimens of TiB₂ are textured. The wide spread of reported Poisson’s ratios—0.05–0.11—also points to possible texturing in this material.

4. CONCLUSION

In this paper, we have presented an energy-based model of the compressive failure of brittle heterogeneous solids. The basic idea is that the solid splits because in so doing it reduces its total energy, defined as the sum of bulk elastic energy and surface energy. The heterogeneous microstructure gives rise to a complex stress distribution in the intact solid. The material fractures to release the excess elastic energy associated with this complex stress field. We have applied this idea to macroscopically isotropic polycrystalline solids like ceramics and rocks. We have obtained a predictive model. Notice that we have explained a large amount of data based on simply the elastic

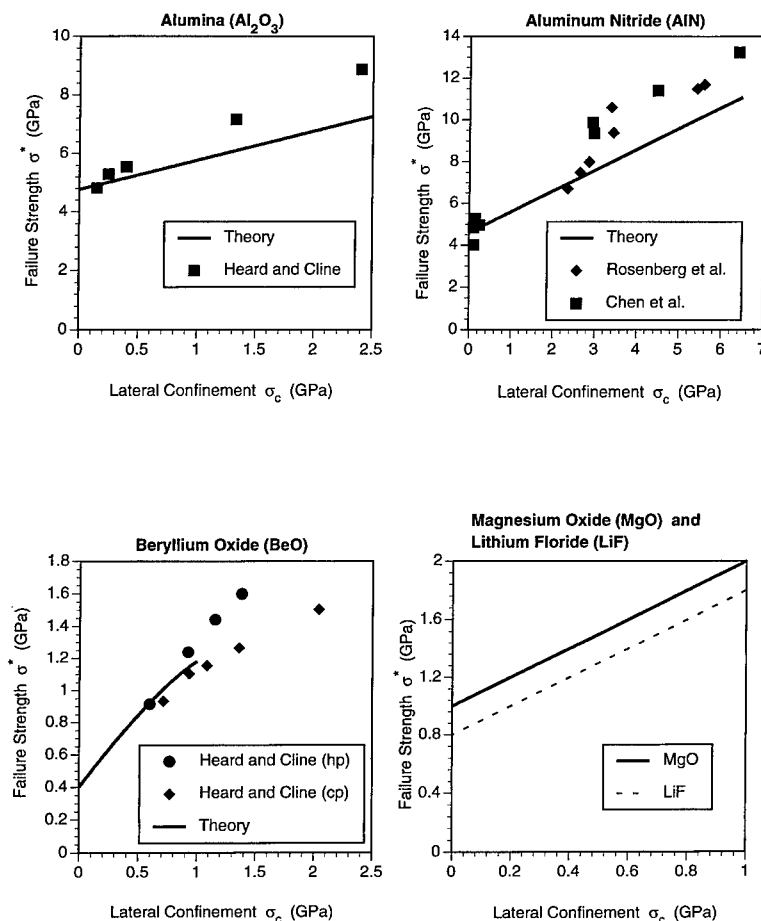


Fig. 2. The theoretical prediction eqn (9) of failure strength vs lateral confinement is compared with the experimental observations in various ceramics. The experimental data in Al_2O_3 is taken from Heard and Cline (1990), in AlN from Rosenberg *et al.* (1991) as well as Chen and Ravichandran (1996) and in hot-pressed (hp) and cold-pressed (cp) BeO from Heard and Cline (1990).

moduli and one fit parameter $-\gamma/d$. Thus, the model is able to capture in an essential manner the effect of the underlying heterogeneity on failure strength.

We close by noting that it is possible to apply this model to a variety of other situations including textured materials and composites. In particular, this energy-based model can provide a direct link between texture and failure strength in advanced structural ceramics.

ACKNOWLEDGEMENTS

We gratefully acknowledge the partial financial support of the following agencies. K.B.: AFOSR (F49620-95-1-0109) and NSF (CMS-9457573); M.O.: ARO (DAAH04-96-1-0056); G.R.: ARO (DAALO3-02-G-0192) and NSF (CMS-9157846).

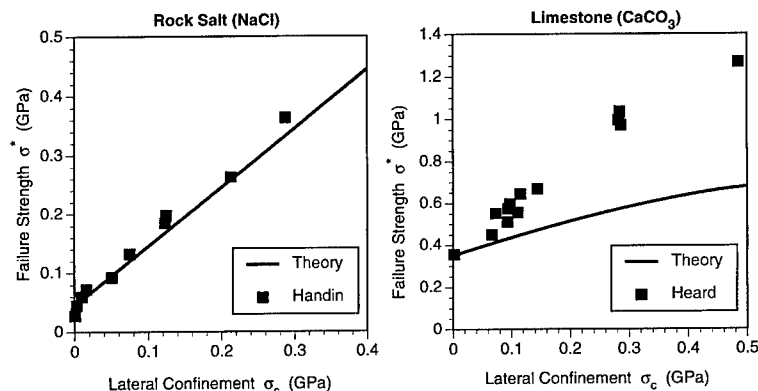


Fig. 3. The theoretical prediction eqn (9) of failure vs lateral confinement is compared with the experimental observations in rocks. The experimental data in rock salt is taken from Handin (1953) and in limestone from Heard (1960) as reported by Ashby and Sammis (1990).

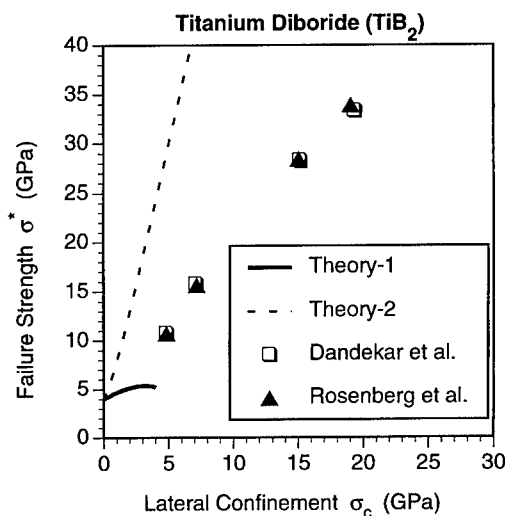


Fig. 4. The failure strength vs lateral confinement in TiB₂. The curve marked Theory 1 is based on eqn (9) using the estimated elastic moduli shown in Table 2 while the curve marked Theory 2 is based on eqn (9) using the measured elastic moduli: $E_u = 523$ GPa, $\nu_u = 0.05$ (Grady, 1995). The experimental data is taken from Rosenberg *et al.* (1992) and Dandekar (1994).

REFERENCES

- Ashby, M. F. and Hallam, S. D. (1986) The failure of brittle solids containing small cracks under compressive stress states. *Acta Metallurgica* **34**, 497–510.
- Ashby, M. F. and Sammis, C. G. (1990) The damage mechanics of brittle solids in compression. *J. Geoph.* **133**, 489–521.
- Azuhata, T., Soha, T. and Suzuki, K. (1996) Elastic constants of III–V compound semiconductors: modification of Keyes' relation. *J. Phys.: Condens. Matter* **8**, 3111–3119.

- Ball, J. M. (1982) Discontinuous equilibrium solutions and cavitation in non-linear elasticity. *Phil. Trans. Royal Soc. London A* **306**, 557–611.
- Bass, J. (1995) Elasticity of minerals, glasses and melts. In *Handbook of Physical Constants*, ed. T. J. Ahrens, **2**, 45–63.
- Brace, W. F. and Bombolakis, E. G. (1963) A note on brittle crack growth in compression. *J. Geophys. Res.* **68**, 3709–3713.
- Cannon, N. P., Schulson, E. M., Smith, T. R. and Frost, H. J. (1990) Wing cracks and brittle compressive fracture. *Acta Metallurgica Materiala* **38**, 1995–1962.
- Chen, W. and Ravichandran, G. (1966) Static and dynamic compressive behavior of aluminum nitride under moderate confinement. *Journal of the American Ceramic Society* **79**, 579–584.
- Dandekar, D. P. (1994) Shear strengths of aluminum nitride and titanium diboride under plane shock wave compression. *Journal de Physique III* **4**, 379–384.
- Espinosa, H. D. and Brar, N. S. (1995) Dynamic failure mechanism of ceramic bars—experiments and numerical simulations. *Journal of the Mechanics and Physics of Solids* **43**, 1615.
- Grady, D. E. (1995) Dynamic properties of ceramic materials. Sandia Report SAND94-3266, Sandia National Laboratories, Albuquerque, NM.
- Griffith, A. A. (1920) The phenomena of rupture and flow in solids. *Phil. Trans. Royal Soc. London A* **221**, 163–198.
- Handin, H. (1953) An application of high pressure in geophysics: experimental rock deformation. *Trans. Am. Soc. Mech. Engrs* **75**, 315–324.
- Hashin, Z. (1996) Finite thermoelastic fracture criterion with application to laminate cracking analysis. *Journal of the Mechanics and Physics of Solids* **44**, 1129–1145.
- Heard, H. C. (1960) Transition from brittle to ductile flow in Solenhofen limestone as a function of temperature, confining pressure and interstitial fluid pressure. *Geol. Soc. Am. Memoir*, ed. D. Grigg and J. Handin, **79**, 193–226.
- Heard, H. C. and Cline, C. F. (1990) Mechanical behavior of polycrystalline BeO, Al₂O₃ and AlN at high pressures. *J. Mat. Sci.* **15**, 1889–1897.
- Horii, H. and Nemat-Nasser, S. (1986) Brittle failure in compression: splitting, faulting and brittle-ductile transition. *Phil. Trans. Royal Soc. Lond. A* **319**, 337–374.
- Hoek, E. and Bieniawski, Z. T. (1965) Brittle fracture propagation in rock under compression. *International Journal of Fracture Mechanics* **1**, 137–155.
- Hou, H. S. and Abeyaratne, R. (1992) Cavitation in elastic and elastic-plastic solids. *Journal of the Mechanics and Physics of Solids* **40**, 571–592.
- James, R. D. and Spector, S. J. (1991) The formation of filamentary voids in solids. *Journal of the Mechanics and Physics of Solids* **39**, 783–813.
- Lehner, F. and Kachanov, M. (1996) On modelling of winged cracks forming under compression. *International Journal of Fracture* **7**, R69–R75.
- McClintock, F. A. and Walsh, J. B. (1963) Friction on Griffith cracks under pressure. *Proceedings of the U.S. National Congress on Applied Mechanics—1962*, **2**, 1015–1021. ASME Press, New York.
- Nemat-Nasser, S. and Horii, H. (1982) Compression induced non-planar crack extension with application to splitting, exfoliation and rockburst. *J. Geophys. Res.* **87**, 6805–6821.
- Ortiz, M. and Popov, E. P. (1982) Plain concrete as a composite material. *Mech. Mater.* **1**, 139.
- Ortiz, M. (1985) A constitutive theory for the inelastic behavior of concrete. *Mech. Mater.* **4**, 67–93.
- Ravichandran, G. and Subhash, G. (1995) A micromechanical model for high strain rate behavior of ceramics. *International Journal of Solids and Structures* **32**, 2627–2646.
- Rosenberg, Z., Brar, N. S. and Bless, S. J. (1991) Dynamic high-pressure properties of AlN ceramic as determined by flyer plate impact. *Journal of Applied Physics* **70**, 167–171.
- Rosenberg, Z., Brar, N. S. and Bless, S. J. (1992) Shear strength of titanium diboride under shock loading measured by transverse Manganin gauges. In *Shock Compression of Condensed Matter—1991*, ed. S. C. Schmidt, R. D. Dick, J. W. Forbes and D. G. Tasker, pp. 471–473. Elsevier, Amsterdam.

- Simmons, G. and Wang, H. (1971) *Single Crystal Elastic Constants and Calculated Aggregated Properties*. The MIT Press, Cambridge.
- Smith, T. R. and Schulson, E. M. (1994) Brittle compressive failure of salt-water columnar ice under biaxial loading. *Journal of Glaciology* **40**, 265–276.
- Vekinis, G., Ashby, M. F. and Beaumont, P. W. R. (1991) The compressive failure of alumina containing controlled distribution of flaws. *Acta Metallurgica Materiala* **39**, 2583–2588.
- Wang, E. Z. and Shrive, N. G. (1995) Brittle fracture in compression—mechanisms, models and criteria. *Engr. Fract. Mech.* **52**, 1107–1126.
- Wastiels, J. (1979) Behavior of concrete under multiaxial stresses—a review. *Cement and Concrete Research* **9**, 35.